Edited by
Vikas Mittal

**Characterization Techniques
for Polymer Nanocomposites**

Polymer Nano-, Micro- & Macrocomposite Series

Mittal, V. (ed.)

Surface Modification of Nanotube Fillers

Series: Polymer Nano-, Micro- and Macrocomposites (Volume 1)

2011
ISBN: 978-3-527-32878-9

Mittal, V. (ed.)

In-situ Synthesis of Polymer Nanocomposites

Series: Polymer Nano-, Micro- and Macrocomposites (Volume 2)

2012
ISBN: 978-3-527-32879-6

Mittal, V. (ed.)

Modeling and Prediction of Polymer Nanocomposite Properties

Series: Polymer Nano-, Micro- and Macrocomposites (Volume 4)

2013
ISBN: 978-3-527-33150-5

Related Titles

Mittal, V. (ed.)

Polymer Nanotube Nanocomposites

Synthesis, Properties, and Applications

2010
ISBN: 978-0-470-62592-7

Mittal, V. (ed.)

Miniemulsion Polymerization Technology

2010
ISBN: 978-0-470-62596-5

Mittal, Vikas (ed.)

Optimization of Polymer Nanocomposite Properties

2010
ISBN: 978-3-527-32521-4

Thomas, S., Joseph, K., Malhotra, S. K., Goda, K., Sreekala, M. S. (eds.)

Polymer Composites

Volume 1

2012
ISBN: 978-3-527-32624-2

Cosnier, S., Karyakin, A. (eds.)

Electropolymerization

Concepts, Materials and Applications

2010
ISBN: 978-3-527-32414-9

Leclerc, M., Morin, J.-F. (eds.)

Design and Synthesis of Conjugated Polymers

2010
ISBN: 978-3-527-32474-3

Edited by Vikas Mittal

Characterization Techniques for Polymer Nanocomposites

WILEY-VCH

WILEY-VCH Verlag GmbH & Co. KGaA

The Editor

Dr. Vikas Mittal
The Petroleum Institute
Chemical Engineering
Department
Room 2204, Bu Hasa Building
Abu Dhabi
UAE

Contents

Preface

Polymer layered silicate nanocomposites are relatively a new class of nanoscale materials, in which at least one dimension of the filler phase is smaller than 100 nm. They offer an opportunity to explore new behaviors and functionalities beyond that of conventional materials. A large number of advancements have been made in the techniques to modify the filler surface as well as to synthesize the polymer nanocomposites. Such advances need to be supplemented with robust characterization of the resulting composite morphology and properties to gain insights into the various factors affecting the nanocomposite microstructure and properties to be able to design them according to the need. The book summarizes a large number of characterization techniques that have been employed to analyze various aspects of polymer nanocomposites. The aim of the book is also to establish right practices for characterizing the nanocomposite materials with any specific technique.

Chapter 1 provides an overview of the most common characterization techniques for the polymer nanocomposites including thermogravimetric analysis, differential scanning calorimetry, X-ray diffraction, scanning electron microscopy, transmission electron microscopy, and permeation resistance. Chapter 2 details the thermal characterization of the modified fillers as well as nanocomposites. Correlations of the thermal information with other techniques like X-ray diffraction have also been presented. Chapter 3 focuses on the flame retardancy characterization of nanocomposites. Various flame retardants as well as flammability tests have been described in light of a large number of polymer clay nanocomposites. PVT characterization of the polymer nanocomposites is described in Chapter 4. The chapter deals with characterization of clays, *PVT* measurements, derivative properties, thermodynamic theories, interaction parameters, and theoretical predictions. Chapter 5 reports on the nanocomposites synthesis analysis by Raman spectroscopy, and X-ray photoelectron spectroscopy (XPS). Both POSS and nanotube-based polymer nanocomposites are reviewed. Tribological characterization of the nanocomposites is described in Chapter 6. First, the basics of tribology are discussed, followed by the description of possibilities in order to develop tribologically optimized nanocomposites. Afterward their characterization by special tribological methods is focused as well as selected results in respect of the tribological properties of nanocomposites. Chapter 7 reports on the use of dielectric

relaxation spectroscopy for polymer nanocomposites based on poly(vinylidene fluoride) (PVDF). A variety of nanofillers such as clay with platelet structure and functional nanoparticles like $BaTiO_3$ and Fe_3O_4 is explored. Chapter 8 is devoted to describing how atomic force microscope (AFM) is used to characterize polymer nanocomposites. In particular, a newly developed AFM-based technique is introduced to obtain Young's modulus map for various types of polymeric materials. Electron paramagnetic resonance and solid-state NMR studies of the surfactant interphase in polymer–clay nanocomposites are described in Chapter 9. The information from NMR and EPR on structure and dynamics of surfactant molecules in OMLS is used to provide a solid foundation for discussion of the more complex interphase behavior in the nanocomposites. Chapter 10 focuses on the rheological characterization of polymer nanocomposites. Basic rheological theories are introduced and a brief review of the current status of the understanding of rheological properties of polymer nanocomposites is provided. Chapter 11 reports on the segmental dynamics of polymers in polymer clay nanocomposites studied by spin-labeling electron spin resonance (ESR). This is a powerful technique for discerning properties of specific labeled regions or components in complex systems and can provide information on the dynamics on time scales in the range 10^{-11}–10^{-7} s.

Chapter 12 reports the characterization of the polymer inorganic hybrid colloidal particles by the use of analytical and preparative ultracentrifugation. Biodegradability characterization of nanocomposites is focused on in Chapter 13. The methodologies used to measure and understand biodegradation of nanocomposites are discussed. The standards associated with methods are also described followed by a discussion on the biodegradation of a number of nanocomposites types.

I am grateful to Wiley VCH for their kind acceptance to publish the book. I dedicate this book to my mother for being a constant source of inspiration. I express heartfelt thanks to my wife Preeti for her continuous help in co-editing the book as well as for her ideas to improve the manuscript.

Vikas Mittal

List of Contributors

Chetan Chanmal
National Chemical Laboratory
Polymer Science and Engineering
Division
Dr. Homi Bhabha Road
Pashan
Pune, Maharashtra 411008
India

Katherine M. Dean
CSIRO Materials Science and
Engineering
Gate 5 Normanby Rd
Clayton, Vic. 3168
Australia

Andrew R. Drews
Ford Motor Company
Ford Research and Advanced
Engineering
MD 3179
P.O. Box 2053
Dearborn, MI 48121
USA

Markus Englert
University of Kaiserslautern
Gottlieb Daimler Strasse
Gebäude 44
67663 Kaiserslautern
Germany

Sorina Alexandra Garea
University Politehnica of Bucharest
Advanced Polymer Materials Group
149 Calea Victoriei
010072 Bucharest
Romania

Horia Iovu
University Politehnica of Bucharest
Advanced Polymer Materials Group
149 Calea Victoriei
010072 Bucharest
Romania

Gunnar Jeschke
Lab. Phys. Chem.
ETH Zürich
Wolfgang-Pauli-Strasse 10
8093 Zürich
Switzerland

Jie Jin
Loughborough University
Department of Materials
Ashby Road
Loughborough LE11 3TU
UK

Jyoti Jog
National Chemical Laboratory
Polymer Science and Engineering
Division
Dr. Homi Bhabha Road
Pashan
Pune, Maharashtra 411008
India

Joseph H. Koo
The University of Texas at Austin
Department of Mechanical
Engineering
Texas Materials Institute
Center for Nano and Molecular
Science and Technology
1 University Station
C2200
Austin, TX 78712-0292
USA

Si Chon Lao
The University of Texas at Austin
Department of Mechanical
Engineering
Texas Materials Institute
Center for Nano and Molecular
Science and Technology
1 University Station
C2200
Austin, TX 78712-0292
USA

Jason C. Lee
Institute for Soldier Nanotechnologies
Department of Chemical Engineering
Massachusetts Institute of Technology
77 Massachusetts Ave.
Cambridge, MA 02139
USA

Vikas Mittal
The Petroleum Institute
Chemical Engineering Department
Room 2204, Bu Hasa Building
Abu Dhabi
United Arab Emirates

Yohei Miwa
University of Detroit Mercy
Department of Chemistry and
Biochemistry
4001 West McNichols Road
Detroit, MI 48221-3038
USA

Ken Nakajima
WPI-Advanced Institute for
Materials Research (WPI-AIMR)
Tohoku University
2-1-1 Katahira, Aoba-ku, Sendai
Miyagi 980-8577
Japan

Melissa A.L. Nikolic
CSIRO Materials Science and
Engineering
Gate 5 Normanby Rd
Clayton, Vic. 3168
Australia

Toshio Nishi
WPI-Advanced Institute for
Materials Research (WPI-AIMR)
Tohoku University
2-1-1 Katahira, Aoba-ku, Sendai
Miyagi 980-8577
Japan

Parveen Sangwan
CSIRO Materials Science and
Engineering
Gate 5 Normanby Rd
Clayton, Vic. 3168
Australia

Alois K. Schlarb
University of Kaiserslautern
Gottlieb Daimler Strasse
Gebäude 44
67663 Kaiserslautern
Germany

Shulamith Schlick
University of Detroit Mercy
Department of Chemistry and
Biochemistry
4001 West McNichols Road
Detroit, MI 48221-3038
USA

Mo Song
Loughborough University
Department of Materials
Ashby Road
Loughborough LE11 3TU
UK

Leszek A. Utracki
National Research Council Canada
Industrial Materials Institute
75 de Mortagne
Boucherville, QC
Canada J4B 6Y4

Dong Wang
WPI-Advanced Institute for
Materials Research (WPI-AIMR)
Tohoku University
2-1-1 Katahira, Aoba-ku, Sendai
Miyagi 980-8577
Japan

Cameron Way
CSIRO Materials Science and
Engineering
Gate 5 Normanby Rd
Clayton, Vic. 3168
Australia

1

Characterization of Nanocomposite Materials: An Overview

Vikas Mittal

1.1
Introduction

Polymer layered silicate nanocomposites are relatively new class of nanoscale materials, in which at least one dimension of the filler phase is smaller than 100 nm [1–9]. They offer an opportunity to explore new behaviors and functionalities beyond that of conventional materials. Owing to nanometer thick platelets in layered silicates, incorporation of such fillers strongly influences the properties of the composites at very low volume fractions because of much smaller interparticle distances and the conversion of a large fraction of the polymer matrix near their surfaces into an interphase of synergistically improved properties. As a result, the desired properties are usually reached at low filler volume fraction, which allows the nanocomposites to retain the macroscopic homogeneity and low density of the polymer.

Montmorillonite has been a layered silicate of choice for most of the studies on polymer nanocomposites. Montmorillonite is an expandable dioctahedral smectite belonging to the family of the 2:1 phyllosilicates [10, 11] with a general formula of $M_x(Al_{4-x}Mg_x)Si_8O_{20}(OH)_4$. The particles in montmorillonites consist of stacks of 1 nm thick aluminosilicate layers (or platelets) held electrostatically with each other with a regular gap in between (interlayer). Each layer consists of a central Al-octahedral sheet fused to two tetrahedral silicon sheets. Isomorphic substitutions of aluminum by magnesium in the octahedral sheet generate negative charges, which are compensated for by alkaline-earth or hydrated alkali-metal cations. Based on the extent of the substitutions in the silicate crystals, a term called layer charge density is defined. Montmorillonites have a mean layer charge density of 0.25–0.5 equiv. mol^{-1}. The layer charge is also not constant and can vary from layer to layer; therefore, it should be considered more of an average value. The electrostatic and van der Waals forces holding the layers together are relatively weak in smectites and the interlayer distance varies depending on the radius of the cation present and its degree of hydration. As a result, the stacks swell in water and the

1 nm thick layers can be easily exfoliated by shearing, giving platelets with high aspect ratio. This thus helps to easily exchange their inorganic cations with organic ions (e.g., alkylammonium) to give organically modified montmorillonite (OMMT) [12, 13]. An exchange of inorganic cations with organic cations renders the silicate organophilic and hydrophobic and lowers the surface energy of the platelets and increases the basal-plane or interlayer spacing (*d*-spacing) [12–16]. This improves the wetting, swelling, and exfoliation of the aluminosilicate in the polymer matrix. Alkyl ammonium ions like octadecyltrimethylammonium, dioctadecyldimethyl-ammonium, etc., have been conventionally used for the organic modification of silicates.

Nanocomposites with practically all the polymer matrices have been reported with varying degrees of property enhancements. Polar polymers have been generally reported to achieve better filler dispersion owing to better match of the surface polarities of filler and polymers. On the other hand, the dispersion of filler in the nonpolar polymers like polyethylene, polypropylene, etc., is challenging owing to the absence of any positive interactions between the organic and inorganic phases. To circumvent these difficulties, either low molecular weight compatibilizers are added to the system or the filler surface is specifically modified by additional chemical or physical processes. The synthesis of nanocomposites has also been reported by a number of different ways, for example, melt compounding, *in situ* synthesis, solution mixing, gas phase processing, living polymerization, etc. All the different techniques to modify the filler surface as well as to synthesize the polymer nanocomposites need to be supplemented with robust characterization of these processes as well as resulting composite properties to gain insights into the various factors affecting the nanocomposite microstructure and properties so as to be able to design them according to the need.

1.2
Characterization of Morphology and Properties

Characterization of the nanocomposite materials is necessary to understand/analyze various facets of polymer nanocomposites. A few of them are listed as follows:

a) quality of dispersion of filler in the polymer matrix along with its orientation or alignment related to the processing method used,
b) effect of filler surface modification on filler dispersion and composite properties,
c) interactions of the filler modification with the polymer chains including chemical reactions between the two,
d) changes in the process parameters on the resulting morphology and properties, and
e) apart from that, analysis of a wide spectrum of properties to ascertain the application potential of the nanocomposites.
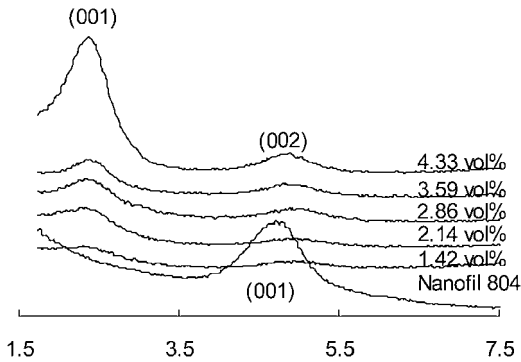
Figure 1.1 X-ray diffractograms of the Nanofil 804 filler as well as polyurethane nanocomposites with different filler volume fractions. Reproduced from reference [17] with permission from American Chemical Society.

It is also, in many instances, necessary to employ more than one characterization technique in order to accurately characterize the nanocomposite material. For example, over the years, it has become common to divide the nanocomposites into intercalated and exfoliated types based on the reflections observed in the detection range of wide-angle X-ray diffraction (WAXRD). However, this classification is arbitrary because the observation of a peak in the diffractogram depends not only on the periodicity but also on other factors, such as the concentration and orientation of the aluminosilicates, and does not exclude the presence of exfoliated part. Its absence also does not exclude the presence of small or randomly oriented intercalated particles and, therefore, does not indicate complete exfoliation as often postulated. Figure 1.1 shows an example of polyurethane nanocomposites generated with montmorillonite filler modified with different surface modifications [17]. The nanocomposites were synthesized by a solution casting method. The X-ray diffractograms of the filler Nanofil 804 (modified with bis(2-hydroxyethyl) hydrogenated tallow ammonium) as well as polyurethane nanocomposites with different filler volume fractions are shown. The diffraction signals of the filler in the composites were shifted to lower angles confirming the intercalation of the polymer in the interlayers; however, the presence of diffraction peaks also signified that the filler was not exfoliated. The extent of filler intercalation or exfoliation could not be quantified. When the same nanocomposites were characterized by transmission electron microscopy as shown in Figure 1.2, extensive filler exfoliation was noticed. The intercalated platelets also had varying thicknesses. Thus, to generate better insights into the nanocomposite microstructures, synergistic combinations of different characterization techniques are useful.

A number of different nanocomposite characterization methods are available which include thermogravimetric analysis, differential scanning calorimetry,
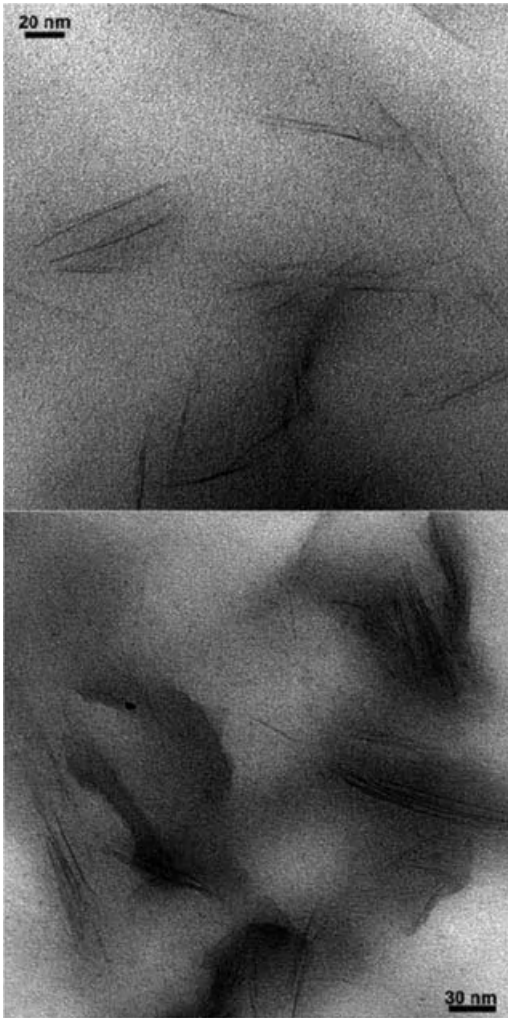
Figure 1.2 TEM micrographs of the 2.86 vol% Nanofil 804-PU composite. Reproduced from reference [17] with permission from American Chemical Society.

transmission electron microscopy, scanning electron microscopy, X-ray diffraction, nuclear magnetic resonance, IR spectroscopy, Raman spectroscopy, X-ray photoelectron spectroscopy, dielectric relaxation spectroscopy, atomic force microscopy, electron spin resonance, continuous-wave and pulsed ESR spectroscopy, etc. Apart from that, numerous characterization techniques to ascertain nanocomposite properties like mechanical performance, fire behavior, barrier performance, biodegradability, rheological properties, PVT characterization, tribo-

logical behavior, etc., are also used. The following section shows the overview examples of nanocomposite characterization performed with a few of these techniques; however, this section is not meant to be exhaustive.

1.3
Examples of Characterization Techniques

Figure 1.3 [18] shows an example of thermogravimetric analysis (TGA) of the modified fillers. The characterization was carried out to ascertain the filler surface cleanliness so as to use them in high-temperature compounding or in *in situ*
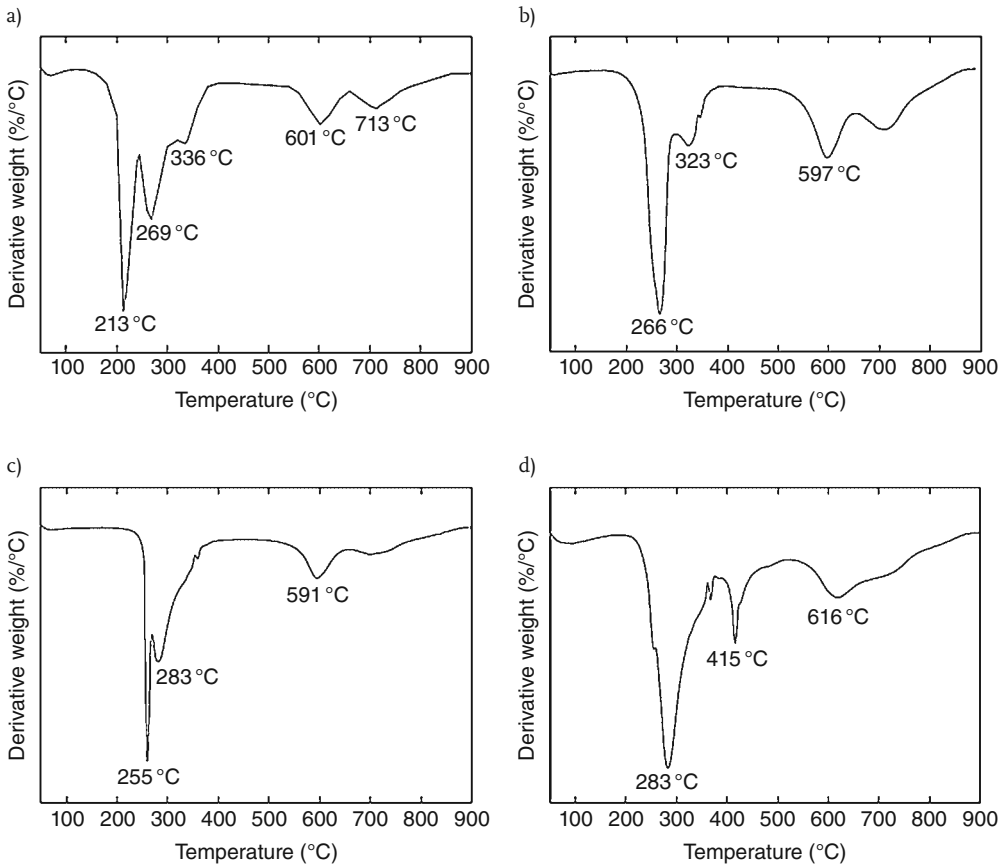
Figure 1.3 TGA thermograms of the (a) commercially modified BzC16; (b) self-treated BzC16; (c) commercially modified 2C18, and (d) self-treated 2C18. Reproduced from reference [18] with permission from Springer.
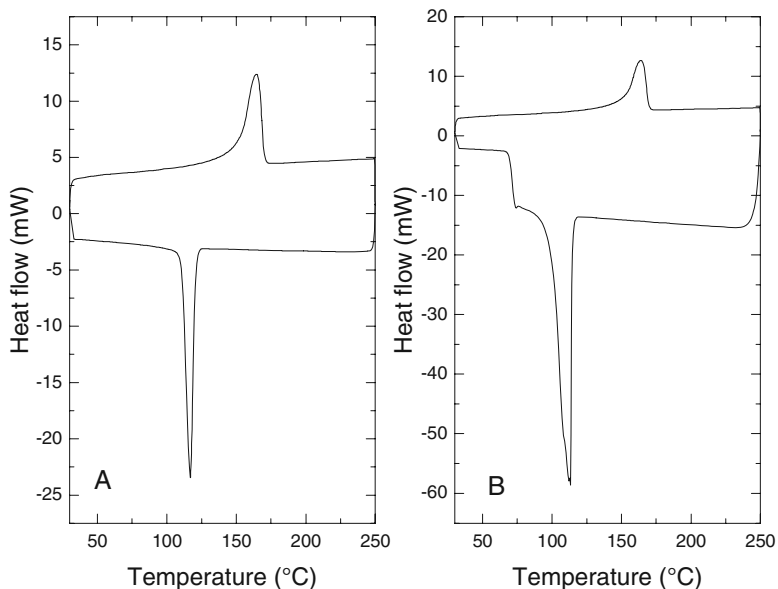
Figure 1.4 DSC thermograms of polypropylene using heating rate of 10°C min^{-1} and cooling rate of (A) 10°C min^{-1} and (B) 40°C min^{-1}.

polymerization processes. Fillers modified with sioctadecyldimethylammonium chloride (2C18) and benzylhexadecyldimethylammonium chloride (BzC16) were analyzed. As can be observed, the commercially treated fillers had an additional low-temperature degradation peak, which indicated the presence of excess surface modification molecules in the filler interlayers which were not ionically attached to the filler surface, but were physically trapped in the modification monolayers, thus forming pseudo bilayers. On the other hand, the self-treated fillers were free from any such excess molecules as no low-temperature degradation signal was observed in their thermograms.

Figure 1.4 shows an example of differential scanning calorimetry (DSC) characterization of pure polymer to generate information on the melting and crystallization transitions as well as to obtain information on the extent of crystallinity from the area under the melting transition (melt enthalpy). The nanocomposite materials can be similarly analyzed to know the effect of fillers on the crystallization behavior of the pure polymer. The organically modified fillers are also characterized by DSC in order to obtain information on the phase dynamics and transitions associated with the monolayers present on the filler surface.

Figure 1.5 [19] presents the WAXRD patterns of octadecytrimethylammonium (C18), dioctadecyldimethylammonium (2C18), and trioctadecylmethylammonium (3C18) modified fillers and their 3 vol% polypropylene nanocomposites. The analysis is used to ascertain the increase in interlayer spacing of the fillers after com-
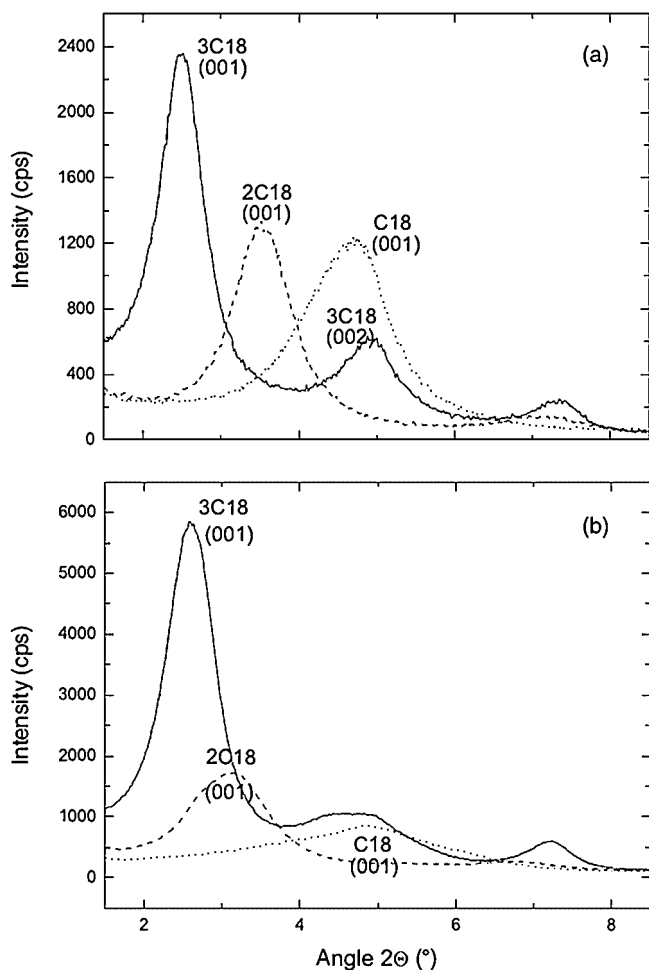
Figure 1.5 Wide angle X-ray diffractograms of (a) 1-3C18 ammonium modified fillers and (b) their PP nanocomposites. Reproduced from reference [19] with permission from Sage Publishers.

pounding with polymers, which is related to the shifting of the diffraction peaks to lower diffraction angles. However, as mentioned earlier, the method does not provide quantification of the extent of intercalation and exfoliation. The filler in the composites in Figure 1.5 was observed to have similar basal plane spacing (as minimal shift in the diffraction peak angle) as the filler powders indicating no intercalation, but the tactoid thickness was observed to be decreased in the microscopy analysis and a partial exfoliation of the filler was achieved. The peak intensity in the diffractograms is also not an accurate indication of the extent of intercalation
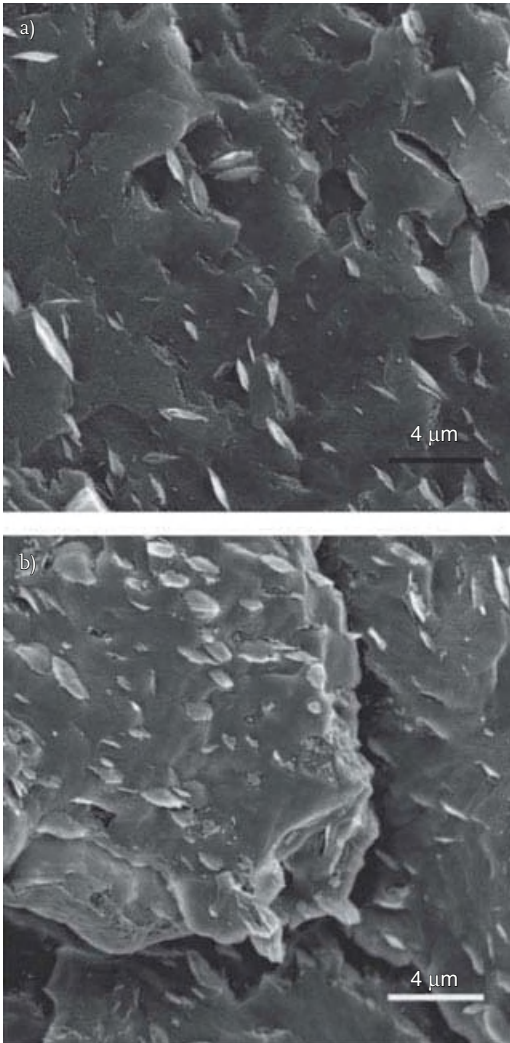
Figure 1.6 SEM micrographs of 3 vol% 2C18 modified filler-PP nanocomposites. The filler platelets are visible in different orientation states. Reproduced from reference [19] with permission from Sage Publishers.

as it depends on other factors like filler concentration, filler orientation, defects in the crystal, and sample preparation methods, etc. Small-angle X-ray analysis is also carried out to analyze the materials in a very low diffraction angle range, which is not possible in the wide-angle X-ray techniques.

Microscopy is commonly used to complement the findings from X-ray diffraction. Figures 1.6 and 1.7 show the scanning and transmission electron microscopy analysis of polymer nanocomposites [19, 20]. It should be noted that the filler
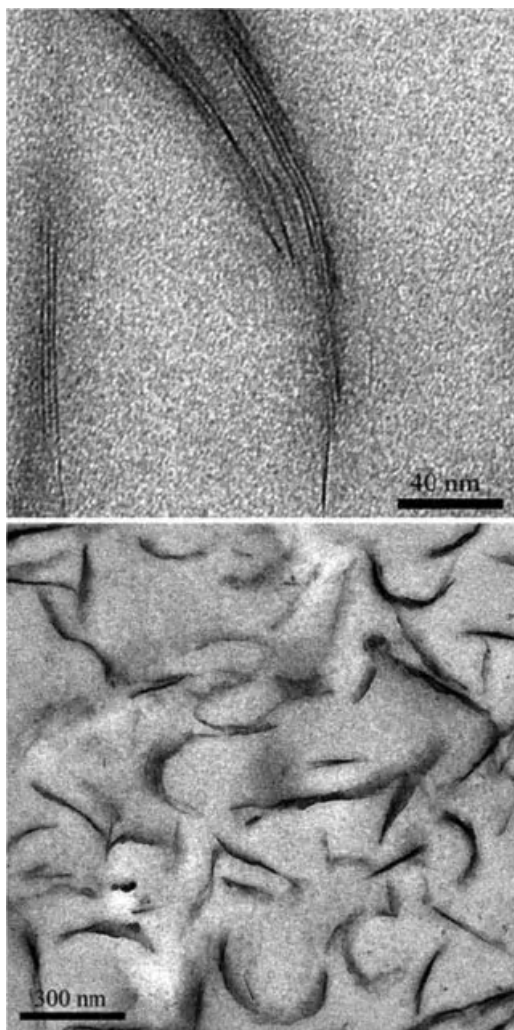
Figure 1.7 TEM micrographs of the 3.5 vol% BzC16 filler−epoxy nanocomposite. The dark lines are cross-sections of aluminosilicate layers. Reproduced from reference [20] with permission from American Chemical Society.

platelets are generally observed to be randomly aligned. Apart from misalignment, the platelets are also occasionally bent and folded. The particles of different thicknesses also indicate that varying degrees of polymer intercalation in the filler interlayers takes place.

Similarly, out of a number of techniques available for characterization of functional properties of nanocomposites, two examples of gas barrier property and mechanical property characterization are shown in Figures 1.8 and 1.9, respectively
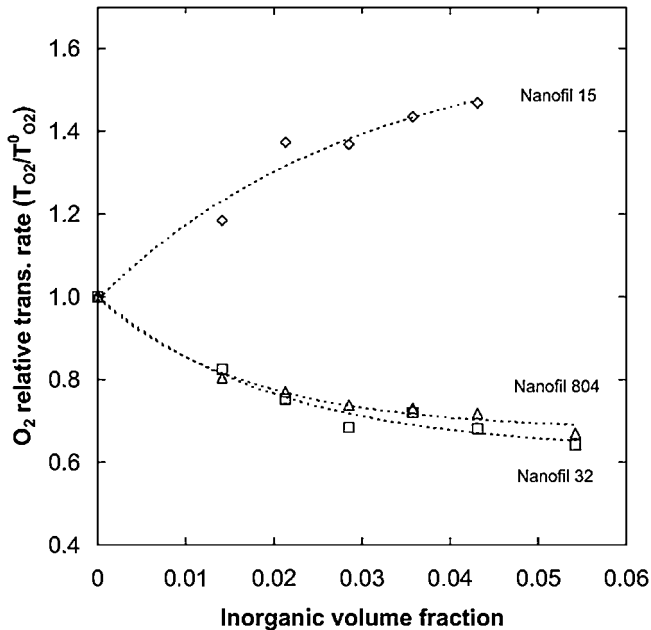
Figure 1.8 Dependence of the oxygen transmission rate through the PU-nanocomposites on the inorganic volume fraction. Reproduced from reference [17] with permission from American Chemical Society.

[17, 21]. The oxygen permeation of the polyurethane nanocomposites as shown in Figure 1.8 is an interesting example as out of the three different fillers, two caused a decrease in oxygen permeation through the polymer, whereas the third filler led to an increase in the oxygen permeation as a function of filler volume fraction. The filler that led to an increase in the permeation was observed to have a least increase in the basal lane spacing as compared to the other two fillers. Also, the microscopy analysis had revealed minimum filler exfoliation in this case. Thus, such microstructure characterizations of the system could also be related to the resulting properties of the nanocomposites. In the example of the mechanical property characterization shown in Figure 1.9 for polypropylene nanocomposites generated with imidazolium modified filler, tensile modulus was observed to increase as a function of filler content, whereas the yield stress was observed to decrease. It indicated that though the load transfer from the polymer chains to the filler particles could take place resulting in an increase in modulus, the filler was still partially exfoliated and the thicker filler tactoids led to reduction in yield stress, which also corresponded with the microscopic characterization of the morphology which was partially exfoliated.

a)

b)
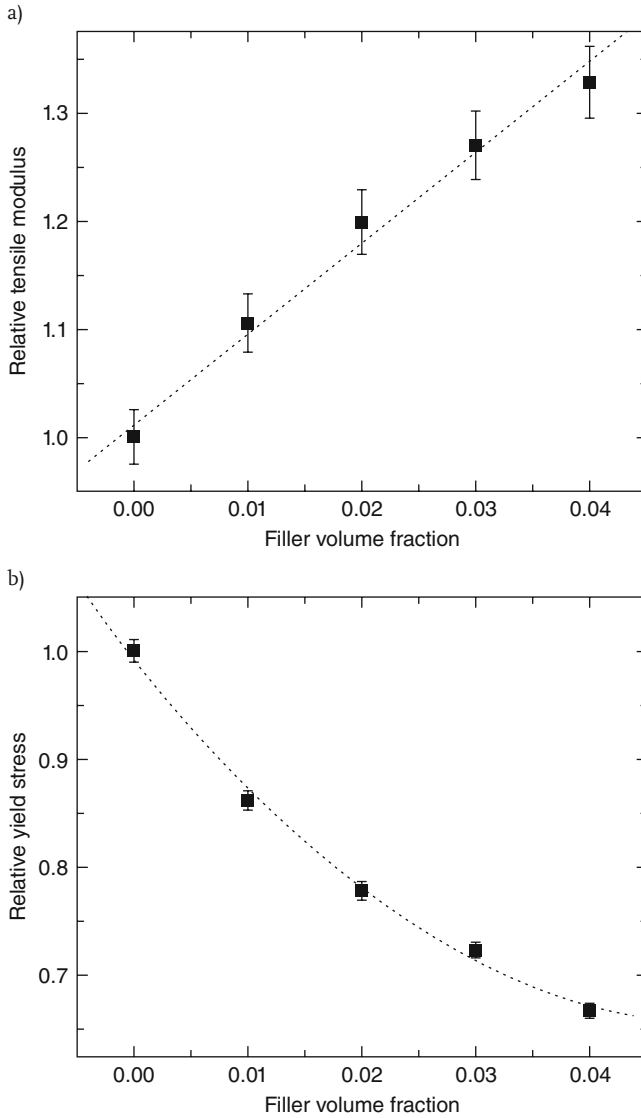
Figure 1.9 Relative (a) tensile modulus and (b) yield stress of polypropylene nanocomposites plotted as a function of the inorganic volume fraction of imidazolium modified filler. Dotted lines serve as a guide. Reproduced from reference [21] with permission from Elsevier.

References

1 Lan, T., Kaviratna, P.D., and Pinnavaia, T.J. (1994) *Chem. Mater.*, **6**, 573.

2 Chin, I.-J., Thurn-Albrecht, T., Kim, H.-C., Russell, T.P., and Wang, J. (2001) *Polymer*, **42**, 5947.

3 Lim, S.K., Kim, J.W., Chin, I.-J., Kwon, Y.K., and Choi, H.J. (2002) *Chem. Mater.*, **14**, 1989.

4 Wang, Z., and Pinnavaia, T.J. (1998) *Chem. Mater.*, **10**, 3769.

5 Messersmith, P.B., and Giannelis, E.P. (1995) *J. Polym. Sci. [A1]*, **33**, 1047.

6 Yano, K., Usuki, A., and Okada, A. (1997) *J. Polym. Sci. [A1]*, **35**, 2289.

7 Shi, H., Lan, T., and Pinnavaia, T.J. (1996) *Chem. Mater.*, **8**, 1584.

8 Giannelis, E.P. (1996) *Adv. Mater.*, **8**, 29.

9 LeBaron, P.C., Wang, Z., and Pinnavaia, T.J. (1999) *Appl. Clay Sci.*, **15**, 11.

10 Bailey, S.W. (1984) *Reviews in Mineralogy*, Virginia Polytechnic Institute and State University, Blacksburg.

11 Brindley, G.W., and Brown, G. (1980) *Crystal Structures of Clay Minerals and Their X-Ray Identification*, Mineralogical Society, London.

12 Theng, B.K.G. (1974) *The Chemistry of Clay-Organic Reactions*, John Wiley & Sons, Inc., New York.

13 Jasmund, K., and Lagaly, G. (1993) *Tonminerale und Tone Struktur*, Steinkopff, Darmstadt.

14 Osman, M.A., Ploetze, M., and Suter, U.W. (2003) *J. Mater. Chem.*, **13**, 2359.

15 Pinnavaia, T.J. (1983) *Science*, **220**, 365.

16 Krishnamoorti, R., and Giannelis, E.P. (1997) *Macromolecules*, **30**, 4097.

17 Osman, M.A., Mittal, V., Morbidelli, M., and Suter, U.W. (2003) *Macromolecules*, **36**, 9851.

18 Mittal, V. (2008) *J. Mater. Sci.*, **43**, 4972.

19 Mittal, V. (2007) *J. Thermoplastic Compos. Mater.*, **20**, 575.

20 Osman, M.A., Mittal, V., Morbidelli, M., and Suter, U.W. (2004) *Macromolecules*, **37**, 7250.

21 Mittal, V. (2007) *Eur. Polym. J.*, **43**, 3727.

2
Thermal Characterization of Fillers and Polymer Nanocomposites

Vikas Mittal

2.1
Introduction

The evaluation of the thermal performance of surface-modified fillers as well as polymer nanocomposite materials is required as it affects the properties of the materials significantly. The modified fillers or polymer nanocomposites with inferior thermal performance would not be suitable for high-temperature processing as well as applications. The thermoplastic polymers like polypropylene, polystyrene, etc., require very high compounding and processing temperatures; therefore, in order to ascertain the suitability of organically modified filler to be used for such operations, it is important to characterize its thermal performance. Similarly, the thermal performance of the final composite materials is necessary in order to analyze the effect of the organically modified filler on the microstructure of the polymer as well as to ascertain the suitability of the nanocomposite product for different applications which would require exposure to temperature during service life. Two most versatile techniques for the thermal characterization are thermogravimetric analysis (TGA) and differential scanning calorimetry (DSC). It is also important to note that high-resolution (Hi-Res) TGA, in which the heating rate is coupled to the mass loss, that is, the sample temperature is not raised until the mass loss at a particular temperature is completed, is more useful for accurate analysis of the thermal performance of materials. The following sections present examples of information achieved from these thermal characterization techniques.

2.2
TGA of Fillers

In the pristine inorganic form, the fillers are thermally very stable. However, to achieve their good dispersion with the polymers, their hydrophilic surfaces need

to be converted to organophilic [1, 2]. This is achieved by surface modification of the fillers by exchanging their surface cations with long alkyl chain ammonium ions, thus generating organically modified fillers. Owing to the organic coating around the inorganic filler particles, the thermal performance of the filler is affected, which thus is required to be quantified. Apart from that, the extent of surface modification of the filler is also required to be quantified to ensure its better dispersion when mixed with the polymer. It should however be noted that the environment of measurement of TGA (e.g., air or nitrogen) also affects the thermal performance of the materials.

2.2.1
Quantification of the Extent of Surface Modification

TGA is beneficial in quantifying the amount of the organic matter exchanged on the surface of the filler particles, thus generating an idea of the success or extent of ion exchange process. If the amount of organic matter does not correspond to the satisfactory extent of cation exchange, the ion exchange reaction has to be repeated. Thus, TGA provides an efficient tool to determine the organophilization of the filler surface. One has to be careful while treating the total weight loss achieved in a TGA analysis. Mass loss due to high-temperature dehydroxylation of the mineral has to be subtracted from the total mass loss to attain information on the mass loss corresponding to the organic layer. Apart from that, the weight loss between 50 and 150 °C corresponding to the evaporation of physisorbed water and solvent molecules should also be subtracted from the total weight loss. The total exchanged moles of the ammonium cation per gram of clay φ_{amm} is then calculated using the following expression:

$$\varphi_{amm} = W_{corr}/[(1 - W_{corr}) * M_{amm}]$$

where W_{corr} is the corrected mass loss corresponding to organic weight loss owing to only alkyl ammonium ions and M_{amm} is the molecular mass of the organic cation exchanged on the surface. This value can then be compared with the cation exchange capacity (number of exchangeable cations present on the filler surface) of the filler to quantify the extent of surface exchange.

2.2.2
Cleanliness of the Filler Surface

During the ion exchange process on the surface of the filler, an excess of surface modification molecules is used to ensure complete surface exchange. The removal of any excess unbound surface modification molecules after the exchange is also necessary as these excess molecules have lower thermal stability and thus degrade the thermal performance of the filler. The low-temperature degradation of the unbound surface modification molecules can also cause unwanted interactions with the polymer leading to the reduction in the molecular weight as well as dete-
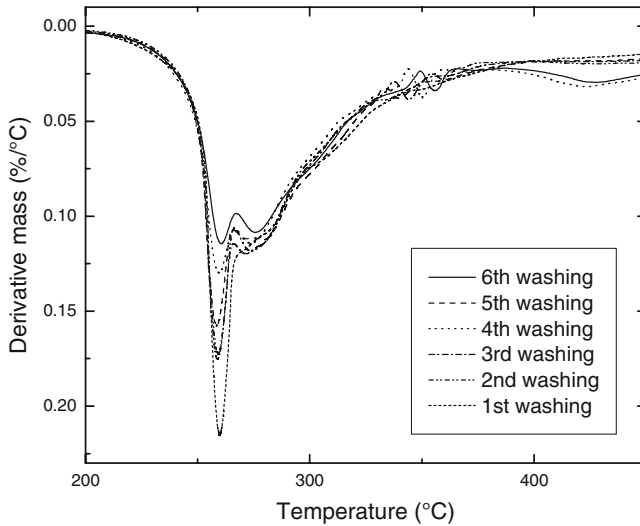
Figure 2.1 Effect of washing protocols on the thermal behavior of the surface-treated montmorillonite modified with octadecyltrimethylammonium.

rioration of the interface between the polymer and filler phases [3, 4]. These excess surface modification molecules are not ionically bound to the surface of platelets, but are entrapped as a pseudo bilayer in the filler interlayers. High-resolution thermogravimetric analysis is useful to ascertain the presence (or absence) of any excess surface modification which may be present in the interlayers. It is also worth noting that other characterization methods like X-ray diffraction do not detect such an excess and it is only the high-resolution thermogravimetric analysis which is able to provide information on such systems. Figure 2.1 shows the TGA thermograms of the surface-treated montmorillonite modified with octadecyltrimethylammonium [5] as a function of different washing cycles. It is obvious that at the initial washing stages, there was a presence of an excess surface modification which degraded at lower temperature represented by a sharp degradation peak. The montmorillonite after sixth washing was observed to be relatively free from this excess as the low-temperature degradation peak is almost eliminated.

2.2.3
Comparing the Stability of Different Fillers

TGA is also the most important tool to compare the thermal stability of the different organically modified fillers. Figure 2.2 [6] shows the differential and cumulative TGA thermograms of commercially treated Tixogel VP (with dehydrogenated tallow dimethyl ammonium) before and after washing the excess of the surface modification molecules. The filler after washing could be observed to have

a)

b)
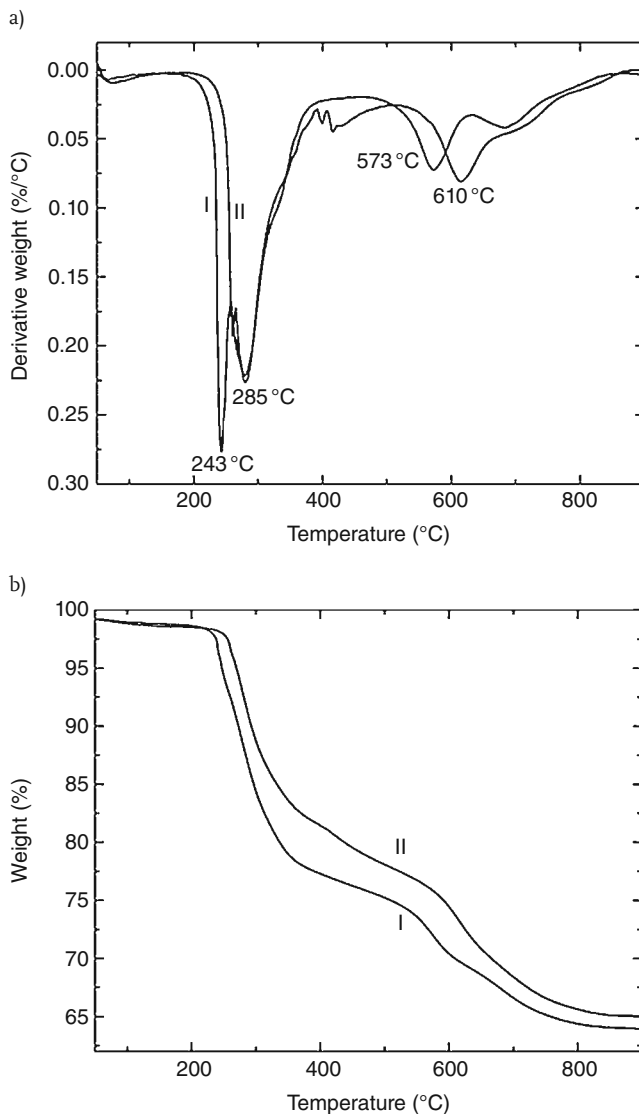
Figure 2.2 (a) Derivative weight and (b) weight loss thermograms of organically modified montmorillonite Tixogel VP before (I) and after (II) washing. Reproduced from reference [6] with permission from Elsevier.

higher thermal stability as the onset of thermal degradation occurred at higher temperature.

Apart from that, no sharp degradation peak at lower temperatures associated with the excess modification molecules was observed. Similarly, Figure 2.3a also shows the TGA thermograms of the imidazolium- and ammonium-modified

a)

b)
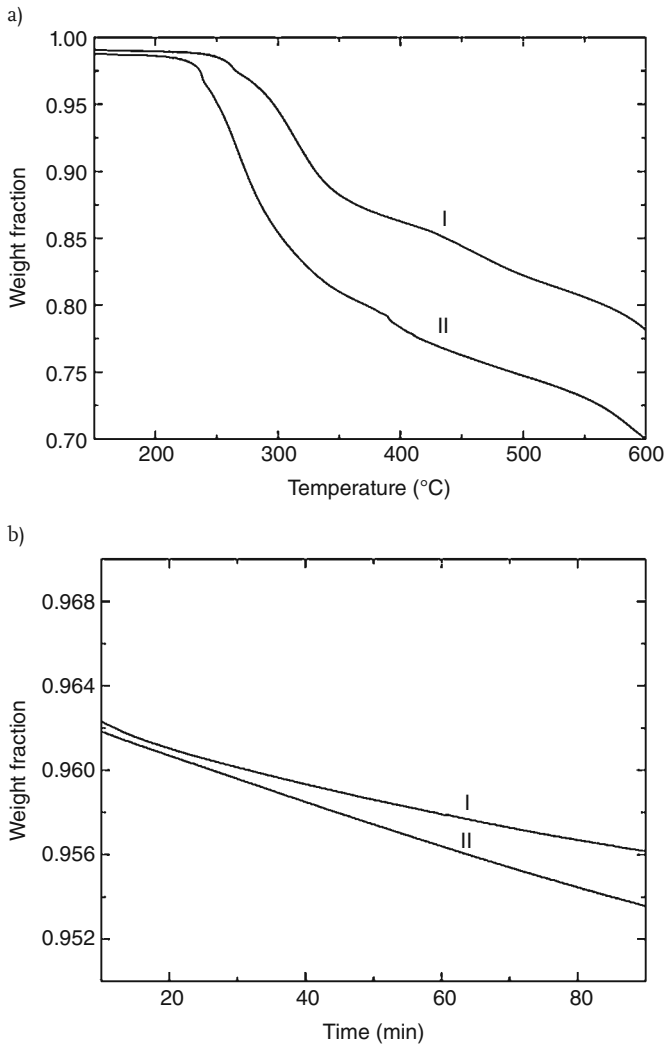
Figure 2.3 (a) TGA thermograms depicting the thermal degradation behavior and (b) dynamic thermogravimetric analysis; I: imidazolium-treated montmorillonite and II: ammonium-modified montmorillonite. Reproduced from reference [7] with permission from Elsevier.

montmorillonite fillers [7]. The two surface modifications had much different thermal performance owing to their different chemical architecture and subsequently different mechanisms of degradation. The imidazolium modification was observed to have significantly delayed onset as well as peak degradation temperature as compared to the ammonium modification. Such a better thermal stability

was observed to contribute more efficiently to the nanocomposite properties generated with imidazolium-modified filler.

2.2.4
Dynamic TGA Analysis of the Fillers

Figure 2.3b shows an example of the dynamic TGA testing to evaluate the thermal resistance of the filler as a function of time. The imidazolium as well as ammonium-modified montmorillonite fillers are compared. For this method, the fillers are equilibrated at a certain temperature and the weight loss is then measured over time. As can be observed in Figure 2.3b, the imidazolium-treated filler had lesser weight loss as compared to the ammonium-modified substrate, which had a steeper slope of the weight loss curve. Though the weight loss between the two fillers is not significantly different, however, it should be noted that the mechanism of degradation in ammonium modifications is the breaking of weaker C–N bonds which directly knocks the chains attached to the head group, thus completely changing the structure of the modification mole cues and its interaction with the polymer. Thus, breaking of even a small number of such bonds can significantly impact the performance. Another thing to note is that the modification molecules have different molecular weights; therefore, the different amounts of weight loss in the TGA thermogram can be caused by such differences in molecular weight rather than thermal stability. Therefore, it is also important to supplement the analysis with quantification of the time taken by the fillers to have a certain percent of weight loss. For example, the ammonium-treated filler took 23.5 min to lose 1% of the weight, whereas 33.5 min were taken by the imidazolium-modified filler to have the same weight loss when kept at 190 °C, thus, confirming its better thermal resistance during compounding with the polymer. Table 2.1 also shows further the comparison of the time taken by octadecyltrimethylammonium (C18) and dioctadecydimethylammonium (2C18)-modified volclay (montmorillonite) and mica fillers when kept isothermally at 200 °C [8]. The modified mica had much lower thermal stability as compared to the clay

Table 2.1 Thermal stability of the fillers.

Organo-mineral	Surface coverage (%)		
	70	100	150
C18-volclay	44.7	11.5	6.0
2C18-volclay	121.1	45.1	28.9
C18-mica	2.8	1.3	1.3
2C18-mica	13.5	10.2	7.2

Reproduced from reference [8] with permission from ACS.

filler owing to much longer thermal resistance of the C18- and 2C18-modified clay mineral.

2.2.5
Characterization of the Surface Reactions

Figures 2.4 [9] and 2.5 [6] underline the usefulness of TGA in analyzing the physical adsorption or chemical reactions taking place on the surface of organically modified fillers. Figure 2.4a shows the TGA thermograms of commercially treated clay carrying the modification bis(2-hydroxyethyl)methyl-hydrogenated tallow ammonium (C182OH) before and after its esterification with dotriacontanoic acid. Not much change in the weight loss was observed, which indicated that the esterification reaction did not take place possibly owing to the excess of the surface modification molecules present on the surface of the commercially treated filler. Figure 2.4b shows the differential and cumulative TGA thermograms of the esterification trials with same C182OH-modified clay, but after washing. Much higher weight loss was observed in the TGA thermogram of the esterified filler confirming that the surface reaction took place. The peak degradation temperature was also shifted to higher temperature as compared to the unreacted clay. Similarly, Figure 2.5 shows the differential and cumulative thermograms of organically modified montmorillonite (dehydrogenated tallow dimethylammonium) before adsorption (I), and after adsorption with 1.5 g (II) and 1 g (III) of initially added poly(vinylpyrrolidone) (PVP) (for 2 g of organically modified montmorillonite). Enhancement of the weight loss in the TGA thermogram confirmed that the physical adsorption took place and the amount was also dependent on the initial amount of PVP used in the process. Apart from that, the thermal stability of the filler also enhanced after physical adsorption of PVP chains on the surface of the filler. It should also be noted that fillers were extensively washed before the TGA analysis.

2.2.6
Different Measurement Environments

Another important factor affecting the thermal performance of materials is the environment in which the TGA analysis is carried out. Figure 2.6 shows the cumulative TGA plots of C18–4C18 ammonium-modified filler platelets when the fillers were analyzed both in air and nitrogen. Both the atmospheres led to different thermal response of the modified fillers. The thermal stability of the fillers was better in the case of nitrogen atmosphere as compared to air atmosphere. The onset of degradation as well as peak degradation temperatures of the surface modification in the filler was higher in the nitrogen atmosphere for all the four modified fillers. In the case of air atmosphere, the presence of oxygen in the air can lead to detrimental effects on the stability of surface modification as well as polymer chains whereas nitrogen being inert in nature does not interact negatively with the polymer or surface modification. Apart

a)

b)
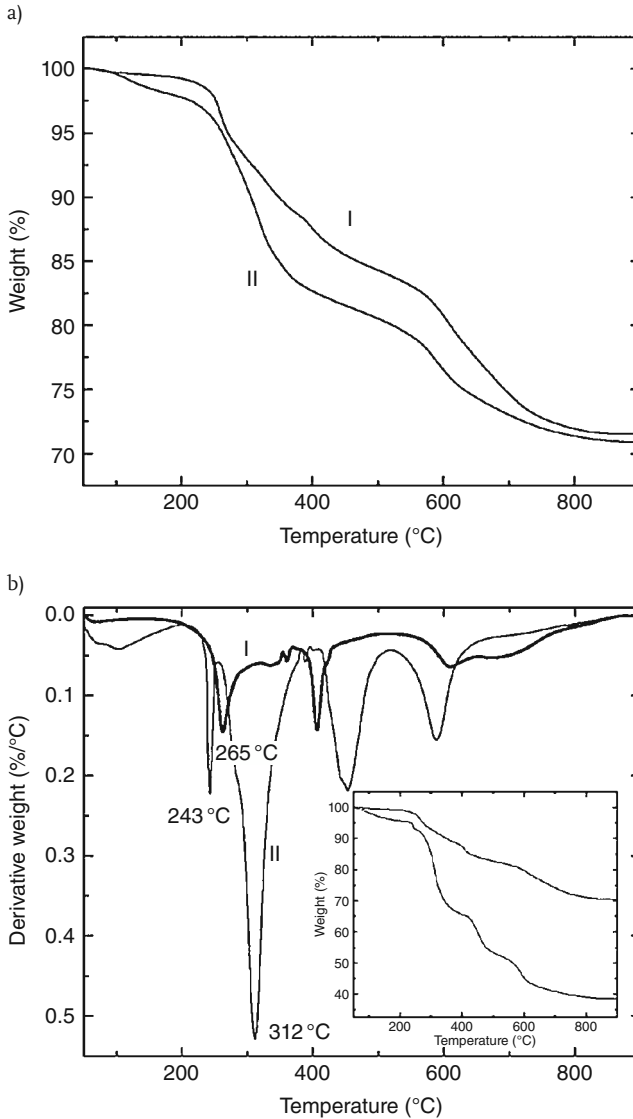
Figure 2.4 (a) TGA thermograms of (I) commercially treated clay (bis(2-hydroxyethyl) methyl-hydrogenated tallow ammonium (C18 2OH)) and (II) clay of I esterified with dotriacontanoic acid. (b) Differential and cumulative TGA thermograms of (I) washed filler and (II) clay of I esterified with dotriacontanoic acid. Reproduced from reference [9] with permission from Taylor and Francis.

a)

b)
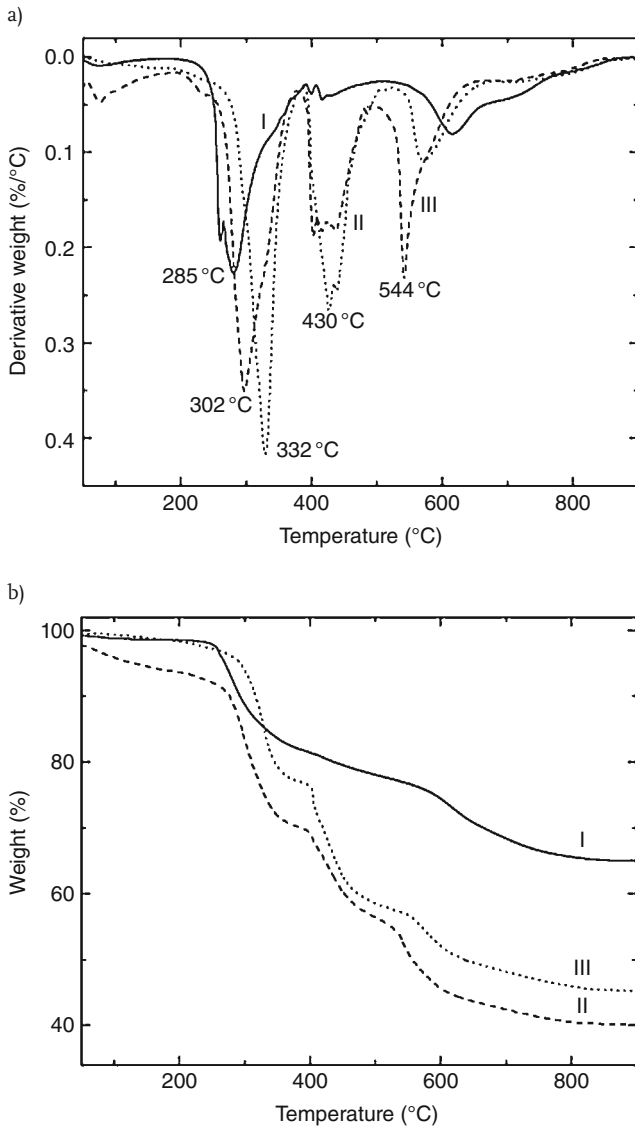
Figure 2.5 (a) Derivative weight and (b) weight loss thermograms of organically modified montmorillonite before adsorption (I), after adsorption with 1.5 g of initially added PVP (for 2 g of organically modified montmorillonite) (II), and after adsorption with 1 g of initially added PVP (for 2 g of organically modified montmorillonite) (III). Reproduced from reference [6] with permission from Elsevier.
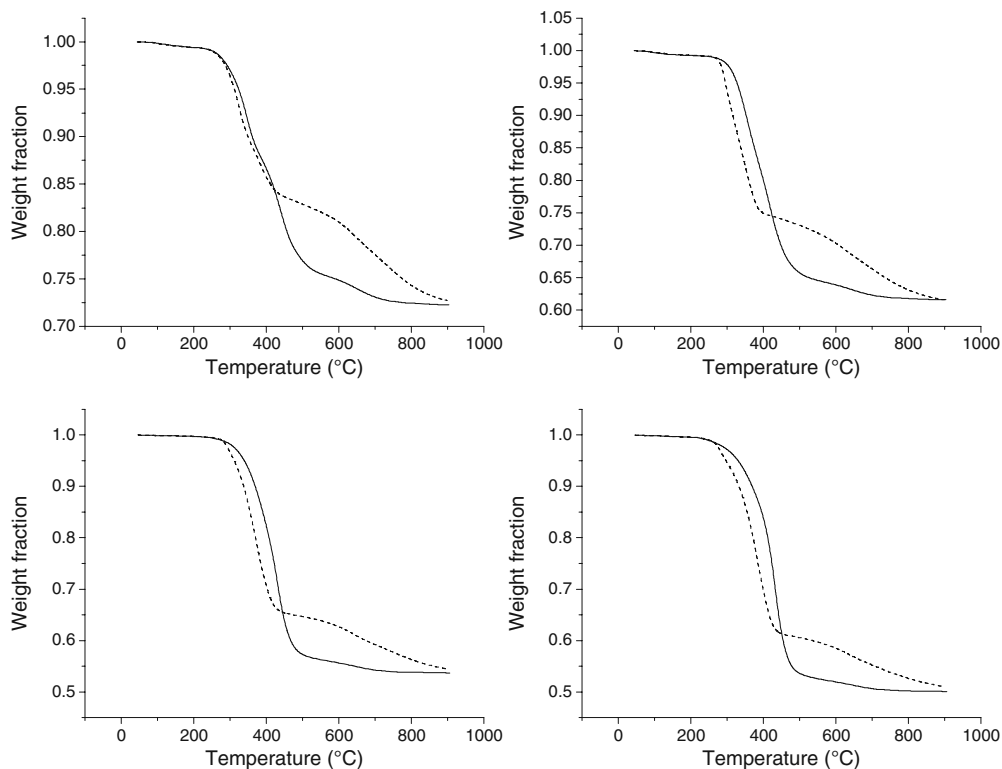
Figure 2.6 TGA thermograms of C18–4C18 ammonium modified clay platelets representing the effect of atmosphere in which the samples were tested. Solid lines represent nitrogen whereas dotted lines represent air atmosphere.

from the onset and peak degradation temperature, the use of different atmospheres also resulted in different degradation mechanisms as their TGA curves in nitrogen and air atmospheres were significantly different especially after 400–500 °C.

2.2.7
Correlation of Organic Matter with Basal Spacing

The findings of TGA on the amount of organic matter exchanged on the filler surface can also be correlated with the other techniques like X-ray diffraction as shown in Figure 2.7 [10]. The organic matter ionically attached to the clay surface calculated from TGA has been plotted with respect to the basal spacing of the fillers to obtain a correlation between the two quantities. Such a relation is beneficial in designing the surface modifications so as to achieve a certain basal spacing in the fillers, which in turn is dictated by the processing as well as filler polymer interactions.
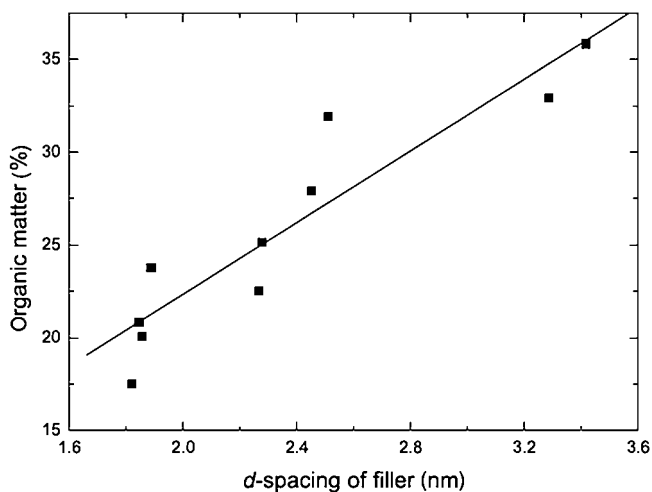
Figure 2.7 Organic matter ionically attached to the clay surface calculated from TGA with respect to the basal spacing of the fillers. The line shown acts as a guide. Reproduced from reference [10] with permission from Sage Publishers.

2.3
TGA of Polymer Nanocomposites

As mentioned above, the TGA characterization of nanocomposites is equally important to be performed in order to ascertain the effect of organically modified filler on the performance. Generally, it is observed that the thermal behavior of the nanocomposite is better than both the filler and pure polymer matrix indicating the synergistic improvement in the thermal behavior. However, low molecular weight additives like compatibilizers are generally added to the polymers to enhance compatibility with the organically modified fillers. Incorporation of even small amount of such additives can significantly affect the thermal performance.

2.3.1
Effect of Filler Concentration

Figure 2.8a shows the TGA thermograms of pure polypropylene (PP) and 2C18-modified filler and the corresponding 3 vol% composite [10]. The addition of filler significantly improved the thermal performance of the polymer as the onset of degradation temperature in the nanocomposite was roughly 50 °C higher as compared to the pure polymer. The nanocomposite had the maximum onset of degradation temperature, which also confirmed the synergistic improvement of the thermal performance in which the properties are better than any of the components. Figure 2.8b also shows the TGA thermograms of pure PP and 2C18

a)

b)
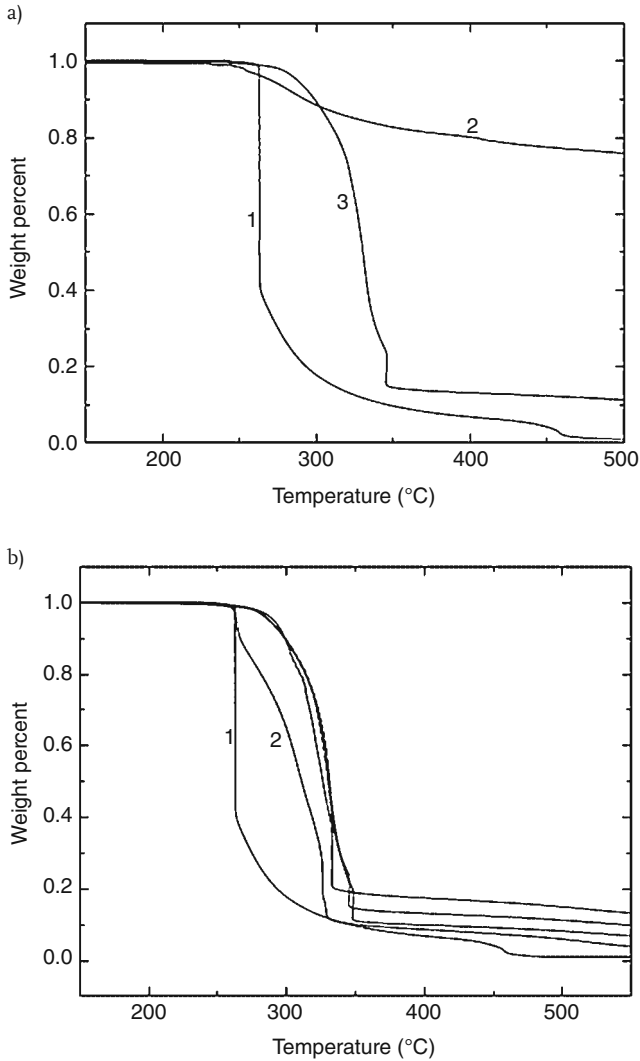
Figure 2.8 (a) TGA thermograms of pure PP (1), 2C18-modified filler (2) and the corresponding 3 vol% composite (3); (b) TGA thermograms of pure PP and 2C18 nanpcomposites containing different volume fractions. 1: pure PP, 2: 1 vol% nanocomposite. Curves of the nanocomposites containing higher volume fractions of fillers are indistinguishable. Reproduced from reference [10] with permission from Sage Publishers.

nanocomposites containing different volume fractions of filler. The addition of even 1 vol% of the filler was observed to cause significant improvement in the thermal performance. However, 2 vol% was needed to achieve maximum improvement, which remained unchanged even when the amount of filler was increased.
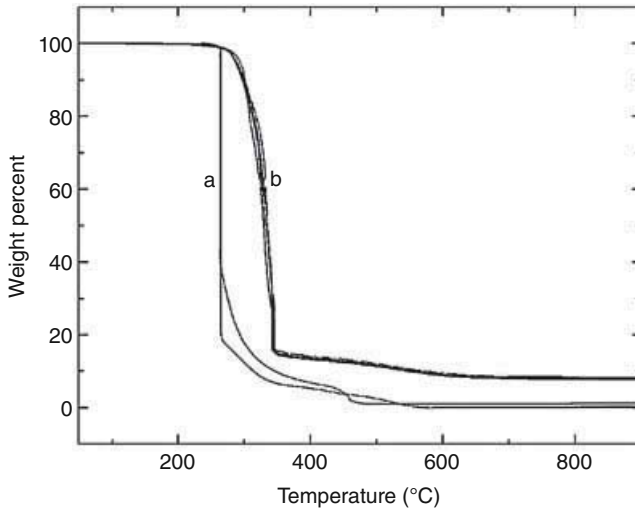
Figure 2.9 TGA thermograms of (a) pure PP; a blend of PP & PP-*g*-MA and (b) 3 vol% 2C18 nanocomposites with varying amounts of PP-*g*-MA compatibilizer. Reproduced from reference [11] with permission from Wiley.

2.3.2
Effect of Compatibilizer

Figure 2.9 demonstrates the TGA thermograms of pure PP, blend of PP with polypropylene-graft-maleic anhydride (PP-*g*-MA) compatibilizer, and 3 vol% 2C18 nanocomposites with varying amounts of PP-*g*-MA compatibilizer (0, 2, 4, 6, 8 wt%). The thermograms of polymer and polymer blend were observed to be similar. The thermograms of nanocomposites were also indistinguishable irrespective of the amount of compatibilizer indicating that the presence of compatibilizer in composites did not lead to any unwanted premature thermal degradation of composites irrespective of the low molecular weight of the compatibilizer.

2.4
DSC of Fillers

Vaia *et al.* [12] reported that the modification chains intercalated in the filler interlayers exist in states with varying degrees of order. In general, as the interlayer packing density or the chain length decreases (or the temperature increases), the intercalated chains adopt a more disordered, liquid-like structure resulting from an increase in the gauche/trans conformer ratio. In order to quantify such phase behavior transitions and chain dynamics for organic monolayers immobilized on the surface of montmorillonites, DSC analysis is performed.

2.4.1
Thermal Transitions in the Modified Fillers

Figure 2.10 shows an example of determination of thermal transitions in the C18–4C18-modified filler using DSC [13]. Two heating cycles and one cooling cycle were used. C18-modified filler did not show any transition indicating that the modifications chains did not pack in an ordered fashion possibly owing to incomplete coverage of the filler surface as well as more area available per cation on the filler surface as compared to the cross-sectional area of the C18 ammonium molecules. 2C18-, 3C18-, and 4C18-modified fillers exhibited phase transition temperatures of 57, 51, and 37 °C, respectively. The transitions signals also became sharper as the chain density in the ammonium modification molecules was enhanced.

2.5
DSC of Composites

DSC of nanocomposites is necessary to ascertain the presence (or absence) of transitions associated with filler modification monolayers. This helps to gain insights on the interphase mixing of polymer chains with the surface modification molecules. Similarly, transitions associated with the polymer and impact of filler or additives on such transitions can also be characterized with DSC. Apart from that, in the case of thermosetting polymers, the DSC analysis can also be used to optimize the curing conditions.

2.5.1
Transitions in Composites

Figure 2.11 shows an example of transitions associated with both filler and polymer in the composite [9]. In the DSC thermogram of 1-bromodocosane, a melting transition at 45 °C was observed. In the ammonium salt synthesized using 1-bromodocosane, a weak order–disorder transition and a strong melting transition were observed at 44 and 96 °C, respectively. The filler after modification with the ammonium salt also indicated similar transitions, but at higher temperature, it indicated the shielding effect of the inorganic substrate. The polypropylene nanocomposite generated by the surface-modified montmorillonite also showed the presence of similar peaks. The lower temperature transition was shifted by only 2 °C compared to the filler, but the higher temperature transition was shifted by 17 °C. The polypropylene bulk melting peak appeared at 165 °C. Similarly, Figure 2.12 also demonstrates an example of 3C18-modified filler and its 3 vol% polypropylene nanocomposites. The order–disorder transition of 3C18 monolayer in the modified filler was observed to take place at the same temperature in polypropylene composites indicating that the compound may not be thermodynamically stable owing to the absence of complete mixing between the modification
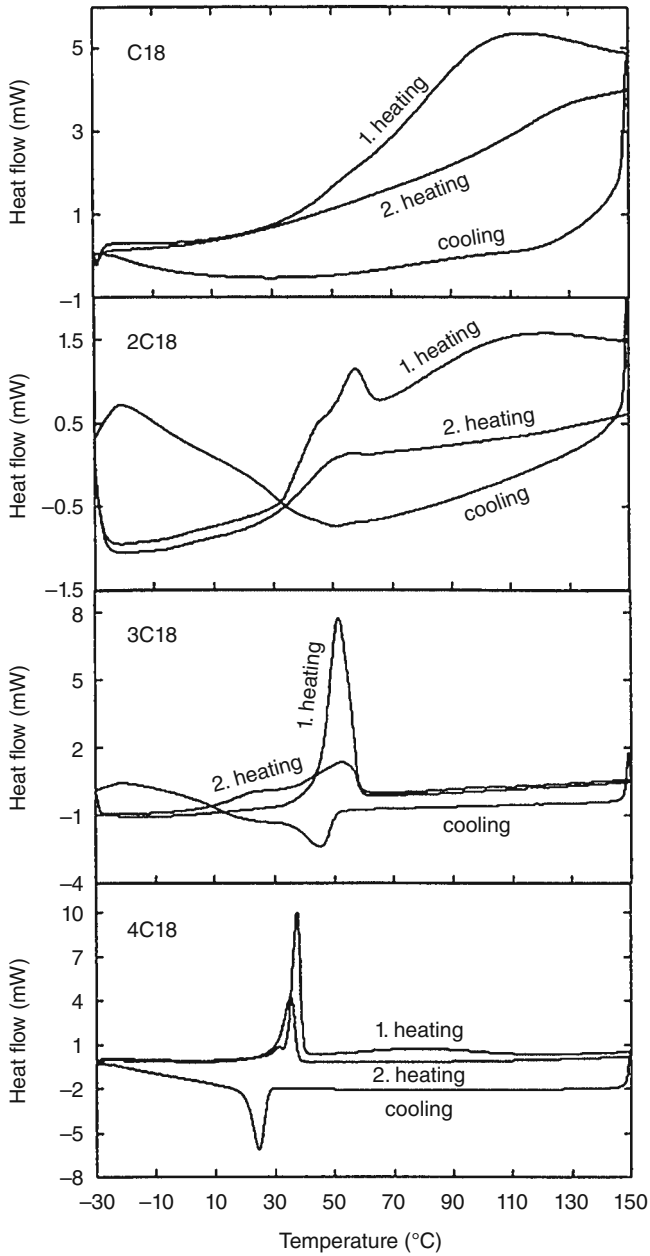
Figure 2.10 DSC thermograms of C18–4C18 modified clay mineral. Reproduced from reference [13] with permission from ACS.
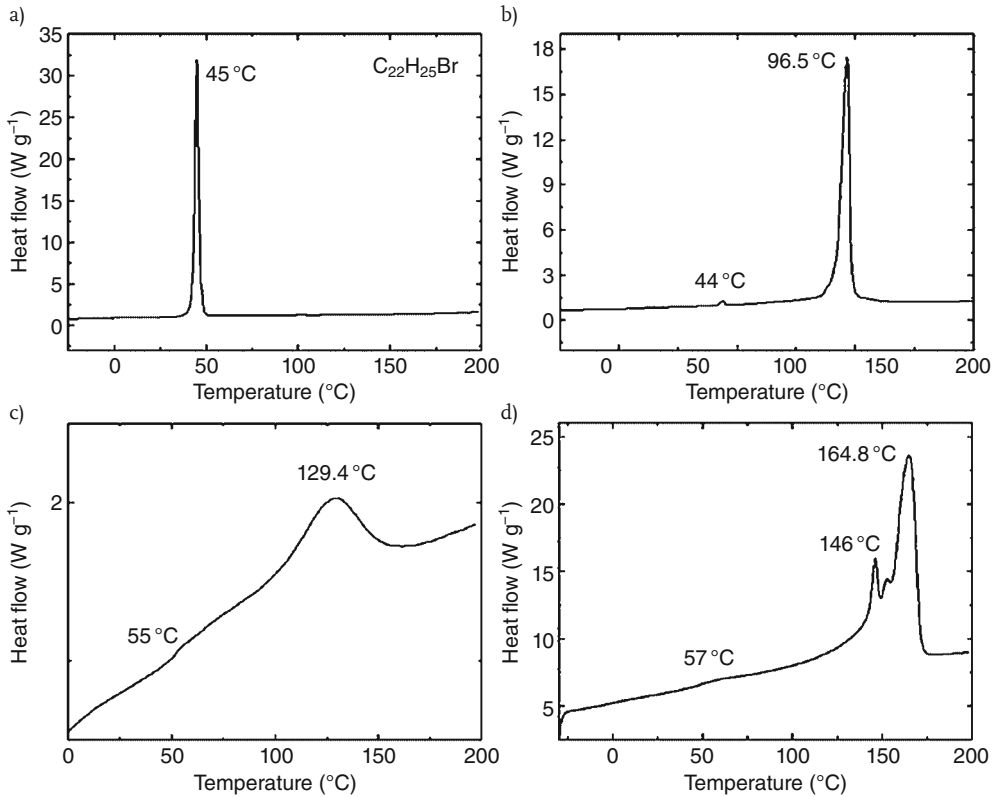
Figure 2.11 DSC thermograms of (a) 1-bromodocosane, (b) docosyltriethylammonium bromide, (c) clay exchanged with docosyltriethylammonium, and (d) polypropyl- ene nanocomposite incorporated with docosyltriethylammonium modified clay. Reproduced from reference [9] with permission from Taylor and Francis.

monolayers and polymer chains at the interface. Thus, complete mixing of the phases is not ensured even if the polymer and the surface modifications have similar chemical architecture. This is different from the earlier example mentioned in Figure 2.11, where the transition associated with the filler was observed at higher temperature when compounded with polymer. Such an effect can only take place if the polymer chains at the interface with the filler modifications mixed well thereby creating a high melting layer at the interface.

Figure 2.13 and Table 2.2 also show examples of the characterization of calorimetric behavior of the nanocomposites as compared to the pure polymer [5]. The effect of both increasing filler concentration as well as different surface-modified fillers on the crystallization and melting behavior of the polymer has been demonstrated. It is observed that under the processing conditions used to generate the
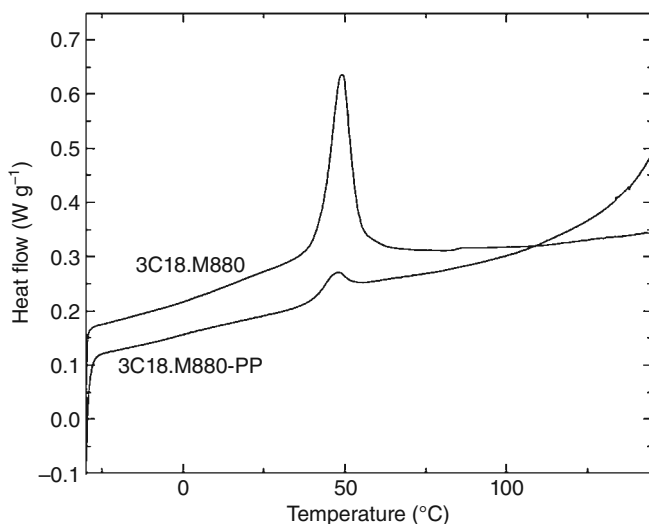
Figure 2.12 DSC thermograms of 3C18·M880 OM and its 3 vol% composite.

nanocomposites, no impact on the crystallization behavior of the polymer could be seen. Peak melting and crystallization temperatures of the polymer and polymer in composites were similar.

Degree of crystallinity ascertained by comparing the polymer enthalpy with that of enthalpy of purely crystalline polymer [14, 15] was also observed to be similar in all the cases. It should be noted that the composites depicted here were generated by fast cooling after compression molding. However, any change in the processing conditions can be expected to bring a change in the calorimetric behavior of the polymer.

2.5.2
Optimization of Curing Conditions

Optimization of the curing conditions in the case of thermosetting polymers, especially in the presence of filler, is of utmost importance as the rates of curing inside as well as outside the filler interlayers need to be controlled. The curing parameters such as time, temperature, and mole ratio of the curing agent to epoxy were required to be optimized in order to have the curing process which provides time for the intercalation of polymer or prepolymer and crosslinker in the clay interlayers, but is also quick enough to avoid excessive extragallery polymerization. Figure 2.14 shows the DSC plots of epoxy curing runs at different temperatures of 40, 55, 60, 70, and 100 °C, while keeping the amine to epoxy mole ratio constant at 1 : 1.

a)

b)
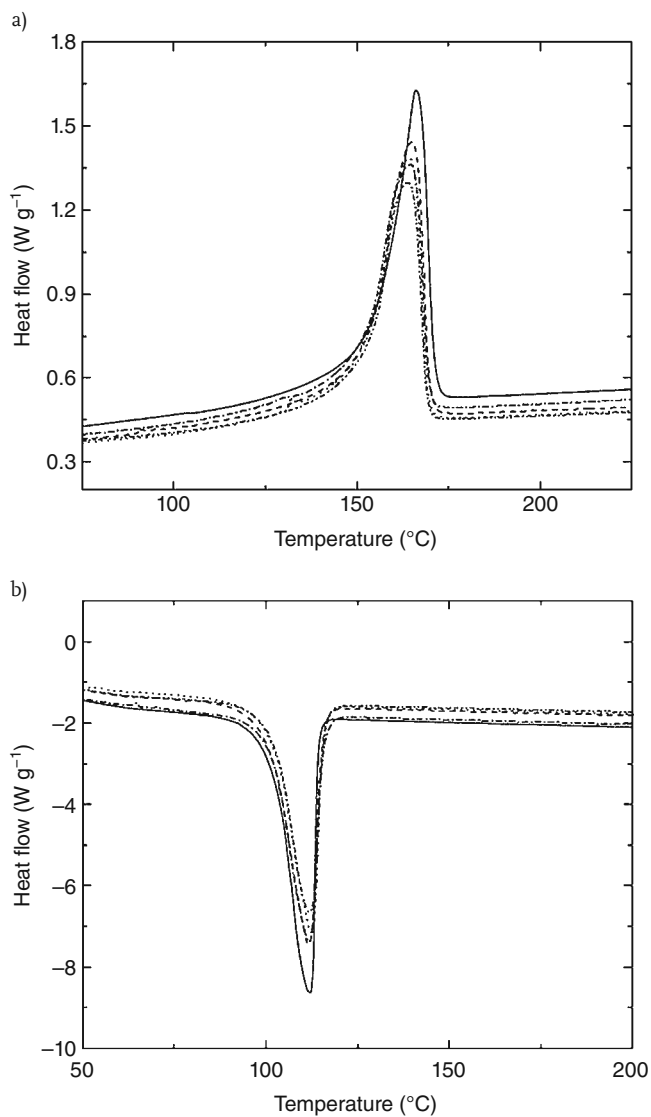
Figure 2.13 DSC melting and crystallization plots for polypropylene (solid line) and 2C18 polypropylene nanocomposites containing 1, 2, 3, and 4 vol% organically modified filler (dotted lines).

Table 2.2 Calorimetric behavior of PP and its 3 vol% nanocomposites (Cloisite).

Filler	$T_{m,onset}$[a]	T_m[b]	ΔH_m[c]	Crystallinity (X_c)[d]	$T_{c,onset}$[e]	T_c[f]
	(°C)	(°C)	(J g^{-1})		(°C)	(°C)
Neat PP	152	162	96	0.58	114	112
Na Cloisite	151	163	95	0.58	118	116
C18 · M880	153	163	94	0.57	118	115
2C18 · M880	152	163	94	0.57	115	112
3C18 · M880	152	162	96	0.58	116	112
BzC16 · M880	153	162	95	0.58	116	112

a) Melt onset temperature.
b) Melt peak temperature.
c) Polymer melt enthalpy.
d) Degree of crystallinity calculates using ΔH of 100% crystalline PP = 165 J g^{-1}[14, 15].
e) Crystallization onset temperature.
f) Crystallization peak temperature.
Reproduced from reference [5] with permission from Wiley.
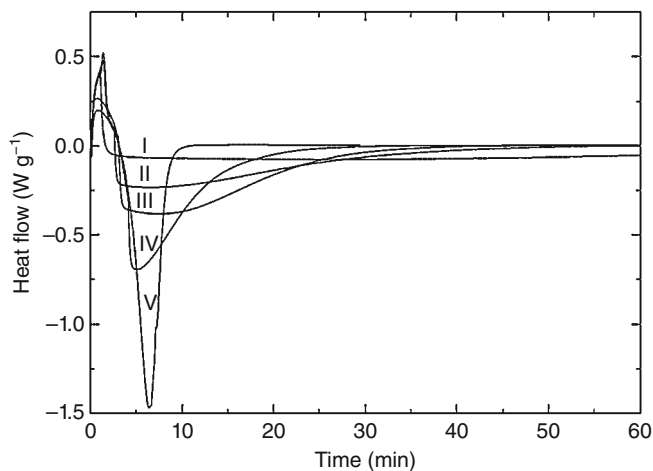
Figure 2.14 DSC thermograms showing the curing of epoxy at different temperatures at a fixed amine to epoxy mole ratio of 1:1; I: 40°C, II: 55°C, III: 60°C, IV: 70°C, and V: 100°C.

References

1 Usuki, A., Kojima, Y., Kawasumi, M., Okada, A., Fukushima, Y., Kurauchi, T., *et al.* (1993) *J. Mater. Res.*, **8**, 1179.

2 Gilman, J.W., Jackson, C.L., Morgan, A.B., Harris, R., Manias, E., Giannelis, E.P., *et al.* (2000) *Chem. Mater.*, **12**, 1866.

3 Mittal, V. (2009) *Optimization of Polymer Nanocomposite Properties* (ed. V. Mittal), Wiley-VCH Verlag GmbH, Weinheim.

4 Mittal, V. (2009) *Polymer Nanocomposites: Advances in Filler Surface Modifications* (ed. V. Mittal), Nova Science Publishers, New York.

5 Osman, M.A., Mittal, V., and Suter, U.W. (2007) *Macromol. Chem. Phys.*, **208**, 68.

6 Mittal, V., and Herle, V. (2008) *J. Colloid Interface Sci.*, **327**, 295.

7 Mittal, V. (2007) *Eur. Polym. J.*, **43**, 3727.

8 Osman, M.A., Ploetze, M., and Suter, U.W. (2003) *J. Mater. Chem.*, **13**, 2359.

9 Mittal, V. (2010) *Phil. Mag.*, **90**, 2489.

10 Mittal, V. (2007) *J. Thermoplastic Compos. Mater.*, **20**, 575.

11 Mittal, V. (2008) *J. Appl. Polym. Sci.*, **107**, 1350.

12 Vaia, R.A., Teukolsky, R.K., and Giannelis, E.P. (1994) *Chem. Mater.*, **6**, 1017.

13 Osman, M.A., Ploetze, M., and Skrabal, P. (2004) *J. Phys. Chem. B*, **108**, 2580.

14 Fatou, J.G. (1971) *Eur. Polym. J.*, **7**, 1057.

15 Wunderlich, B. (1980) *Macromolecular Physics*, Academic Press, New York.

3
Flame-Retardancy Characterization of Polymer Nanocomposites

Joseph H. Koo, Si Chon Lao, and Jason C. Lee

3.1
Introduction

This chapter provides an overview on the fundamentals, properties, and applications of flammability of polymer nanocomposites (PNCs). The structures, properties, and surface treatment of the different types of commonly used flame-retardant (FR) nanoadditives will be introduced. These FR nanomaterials are subdivided based on their nanoscale dimensions: one-dimensional nanoscale, such as nanoclay and nanographene platelets; two-dimensional nanoscale, such as carbon nanofibers (CNFs), carbon nanotubes (CNTs), and Halloysite nanotubes (HNTs®); and three-dimensional nanoscale, such as nanosilica, nanoalumina, nanomagnesium hydroxide, and polyhedral oligomeric silsequioxanes (POSS®). The test methods that are commonly used to evaluate thermal and flammability of polymer nanocomposites are briefly reviewed. The effects of one-dimensional, two-dimensional, three-dimensional, combined nanoadditives, as well as combined nanoadditives with conventional FR additives on thermal and flammability properties of the polymer nanocomposites are discussed. The mechanisms of the effect of nanoadditives on flammability of the PNCs are proposed. The section on concluding remarks and trends for the study of polymer nanocomposites completes this chapter. The readers who need to have more detailed description of the nanomaterials and their detailed influence on a specific matrix polymer may peruse some reviews, books, and papers in this emerging research area, which is listed in the reference section of this chapter.

3.2
Types of Flame-Retardant Nanoadditives

There are many different types of flame-retardant nanoadditives that can be incorporated into polymer systems to enhance their thermal and/or flammability available in the market. Some are inorganic while some are organic. If they are

classified by the length in different dimensions, they fall into one of the three categories: one-dimensional, two-dimensional, and three-dimensional nanomaterials. There has not been a fine definition for the size of nanoparticles. However, it is generally accepted that a single nanoparticle should have at least one dimension of 100 nm or less [1].

3.2.1
One-Dimensional Nanomaterials

One-dimensional nanoparticles have one dimension of 100 nm or less. Examples are montmorillonite (MMT) clays and nanographene platelets (NGPs). They are platelets in shape and their thickness is in the nanoscopic scale while length and width are in the microscopic scale.

3.2.1.1 Montmorillonite Clay

Montmorillonite clay is a sheet silicate material which consists mainly of Si and O, and various metals such as Al, Mg, Ca, etc. [2]. A single clay platelet has thickness of about 1 nm. However, clay platelets tend to stack together into larger micron-sized aggregates. They need to be opened up, or exfoliated, in order to take advantage of the high surface to volume ratio of a single platelet, which yields the enhancement of different properties on polymer resins (Figure 3.1). High shear processing is always required to achieve the exfoliation of clay platelets.

Functionalizations and surface treatments of nanoclays can also help exfoliating the platelets when they are mixed with polymer resins. Ammonium salt is a common chemical used in the surface treatment of nanoclay. However, different functional groups should be used to surface treat the nanoclay when it is used with various polymer resins for the best compatibility. Nanoclay can enhance char formation on some polymer resins [3], which in turns improves the thermal stability and flammability properties of the resins. Figure 3.2 shows an example of exfoliated nanoclay in polyamide 11 (PA11) resin.

8μm Particle   >1 Million Platelets
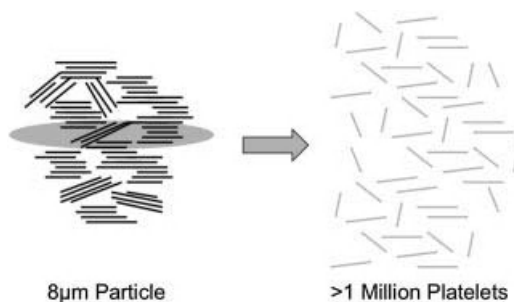
Figure 3.1 Aggregated nanoclay platelets need to be exfoliated to single platelets (courtesy of Southern Clay Products).
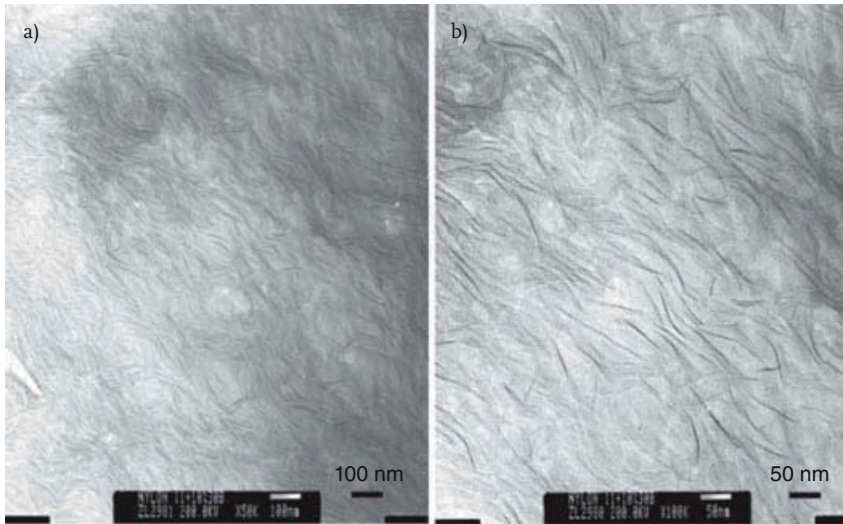
Figure 3.2 TEM micrographs of PA11/10%Cloisite® 30B nanoclay. (a) 50 kX, (b) 100 kX.
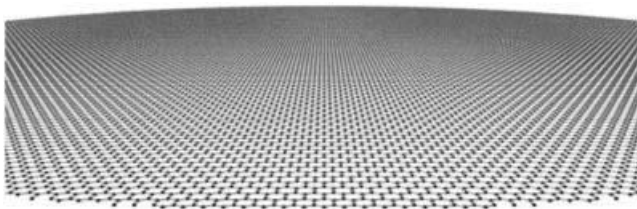
Figure 3.3 Perspective view of the flat graphene crystal in real space [6].

3.2.1.2 Nanographene Platelets

Graphene sheet is an atomic scale honeycomb structure (hexagonal lattice) of sp^2-bonded carbon atoms. It is essentially a single planar sheet of graphite [4]. The thickness of a single graphene platelet is <1 nm [5]. Commercially available graphene flakes consist of stacks of graphene platelet so shear force is also required to open up these platelets when being dispersed into polymer resins. Figure 3.3 shows a perspective view of flat graphene crystal [5], and Figure 3.4 shows the plate-like, flake-like morphology of the as-received nanographene particles. These flake-like nanographene networks may work as heat shield and reduce the dripping of polymer resin when the polymer nanocomposite is burned.

Mag = 10.17 KX   2 μm   EHT = 10.00 KV   Signal A = Inlens   Date :31 Oct 2008
                          WD = 13 mm   Photo No. = 5035   Time :19:54
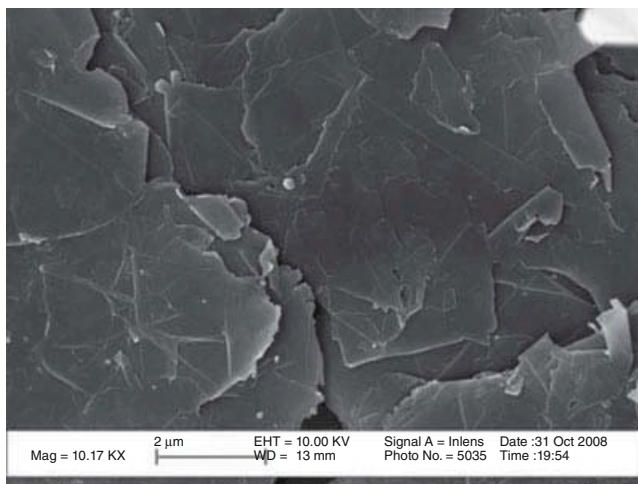
Figure 3.4   SEM image of nanographene obtained from XG Sciences.

3.2.2
Two-Dimensional Nanomaterials

Two-dimensional nanoparticles have two dimensions of lengths less than 100 nm. This type of nanoparticles is mostly tube, fiber, or filament shaped. Examples are carbon nanofibers, carbon nanotubes, and clay nanotubes.

3.2.2.1 Carbon Nanofibers

CNFs are discontinuous graphitic filament produced by catalytic chemical vapor deposition (CCVD) [2]. They have stacked-cup structures with hollow core (Figures 3.5 and 3.6), and their diameters are 100–150 nm in average [2, 7]. CNFs have good mechanical properties, electrical conductivity, and thermal conductivity, so CNF nanocomposites can offer multifunctional performance, such as EMI shielding, thermal conductivity of spacecraft, etc. CNF is also a good char promoter, which makes it a good additive for fire retardancy. Commercially available CNFs aggregate/entangle to micron-sized particles (Figure 3.7). Processing techniques such as extrusion, roll milling, ball milling, ultrasonication, etc. are able to debundle and/or disperse CNFs into polymer matrix. Therefore, processing parameters need to be fine tuned for different polymer resins and CNFs to reduce the breakage or shortening of nanofibers.

3.2.2.2 Carbon Nanotubes

Depending on the number of layers, carbon nanotubes can be single-wall carbon nanotubes (SWNTs), double-wall carbon nanotubes (DWNTs), and multiwall carbon nanotubes (MWNTs). A SWNT can be thought as a seamless roll-up of a
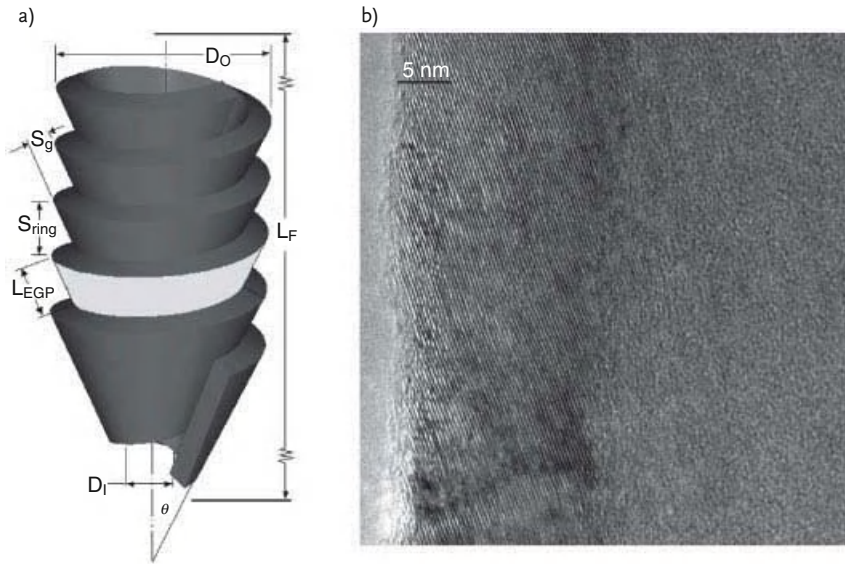
Figure 3.5 Stacked-cup structure of carbon nanofiber shown by schematic diagram (a) and shown by TEM micrograph (b) (courtesy of Pyrograf Products, Inc.).
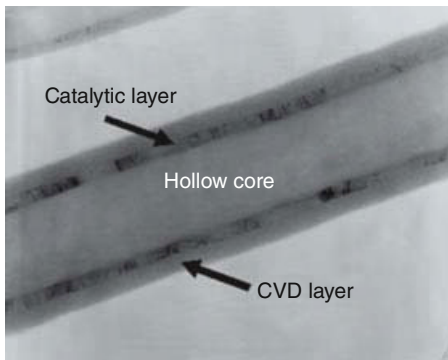
Figure 3.6 TEM micrograph of a single CNF showing the hollow core structure (courtesy of Pyrograf Products, Inc.).

monolayer graphene sheet into a cylinder (diameter: 1–2 nm) [4], while DWNT and MWNT are concentric tubes of two or more layers (inner and outer tube diameters are 2–4 nm and 10–70 nm, respectively). Figure 3.8 shows a schematic structure of a CNT while Figure 3.9 shows a TEM image of a MWNT. CNTs can be synthesized by arc discharge, pyrolysis, laser ablation, chemical vapor deposition, etc. [2]. As-received CNTs from manufacturers also entangled to micron-sized particles so they also require debundling (Figure 3.10). CNTs have excellent mechanical properties, electrical conductivity, and thermal conductivity.
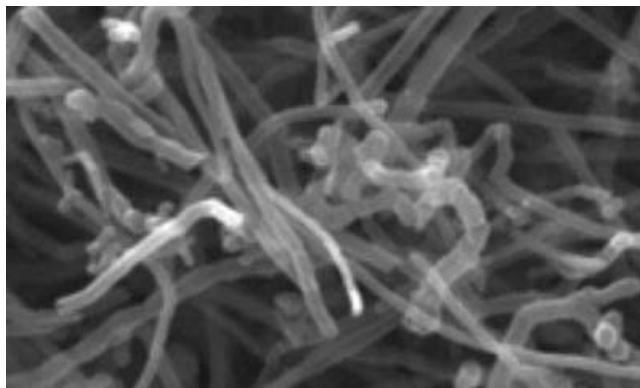
Figure 3.7 TEM micrograph of commercially available CNFs (courtesy of Carbon NT&F 21).
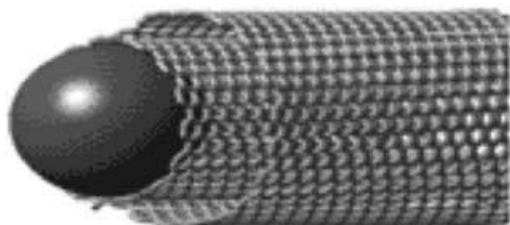
Figure 3.8 Carbon nanotube showing the concentric tube structure (courtesy of Pyrograf Products, Inc.).

5 nm
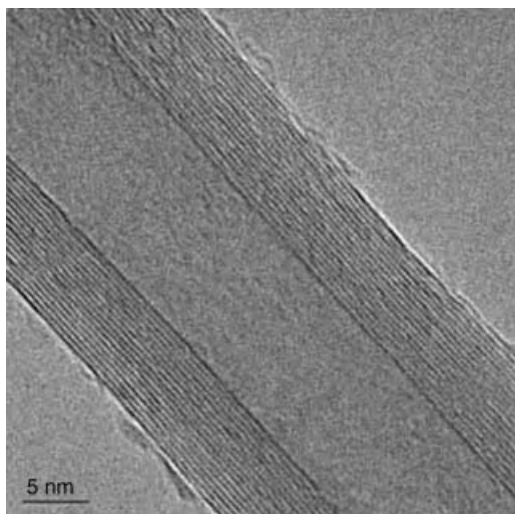
Figure 3.9 TEM image of an individual MWNTs (copyright of Nanotech Innovations).
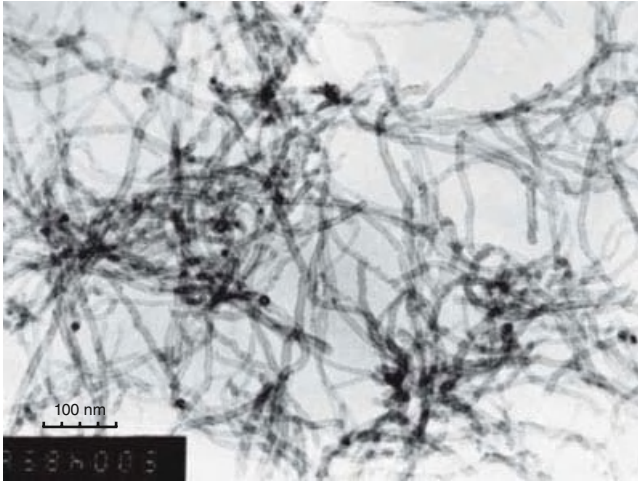
Figure 3.10 TEM image showing entanglement of the as-received multiwalled carbon nanotube (courtesy of Cheaptubes, Inc.).
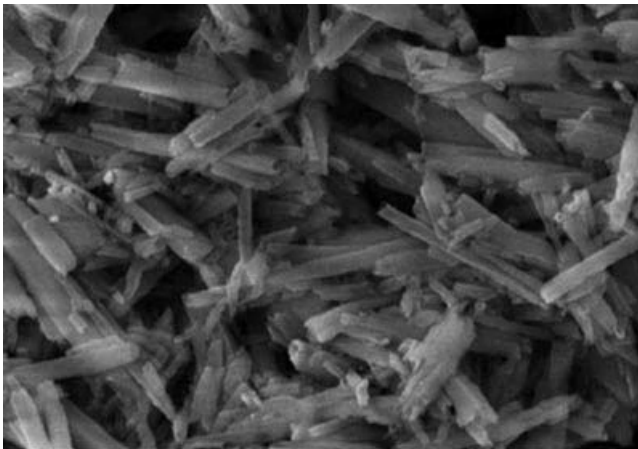
Figure 3.11 Halloysite nanotubes imaged at Cornell University (copyright NaturalNano, Inc.).

3.2.2.3 Halloysite Nanotubes

Halloysite is a type of kaolinite aluminosilicate clay naturally formed in the Earth. HNTs are hollow multilayered tubes with diameter 50–100 nm [8]. Unlike MMT clay, layers of HNTs cannot be exfoliated because the clay layers keep intact, but similar to CNFs and CNTs, HNTs aggregate/entangle to each other as-received from the manufacturer so they also require debundling (Figure 3.11). HNTs have
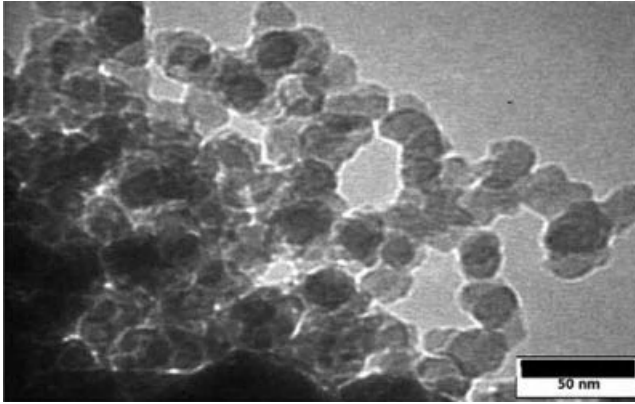
Figure 3.12 TEM micrographs of nanosilica particles [11].

been incorporated into polymer for improved mechanical strength, higher degradation temperature, and improved flame retardancy in the industry [8–10].

3.2.3
Three-Dimensional Nanomaterials

All three dimensions of this type of nanoparticles are in nanoscopic scale. Examples are nanosilica, nanoalumina, POSS, and nanomagnesium hydroxide.

3.2.3.1 Nanosilica
Dispersed nanosilica ranges from 5 to 70 nm in size [2] and can be spherical or irregular in shape (Figure 3.12). It can be produced by high temperature hydrolysis or sol–gel method [11]. Nanosilica has been used as adsorbent, thermal insulation, concrete fabrication, etc.

3.2.3.2 Nanoalumina
The particle size of nanoalumina (*n*-alumina) ranges from 20 to 800 nm [12]. It can be synthesized by the sol–gel technique [13], hydrothermal synthesis, precipitation, and combustion method [14]. Nanoalumina may improve hardness, thermal conductivity and stability, wear resistance, strength, and stiffness. Like other nanoparticles, nanoalumina aggregates to micron-sized particles and can be broken down by mechanical and chemical methods (Figure 3.13). Figure 3.14 shows the SEM micrograph of an as-received nanoalumina.

3.2.3.3 Nanomagnesium Hydroxide
Since magnesium hydroxide undergoes endothermic dehydration in fire conditions, it has been used as fire retardant additive in composite materials [15]. Figure 3.15 shows TEM and SEM images of MgOH nanoparticles [16]. Nanomagnesium hydroxide has platelet structure and it requires exfoliation; otherwise
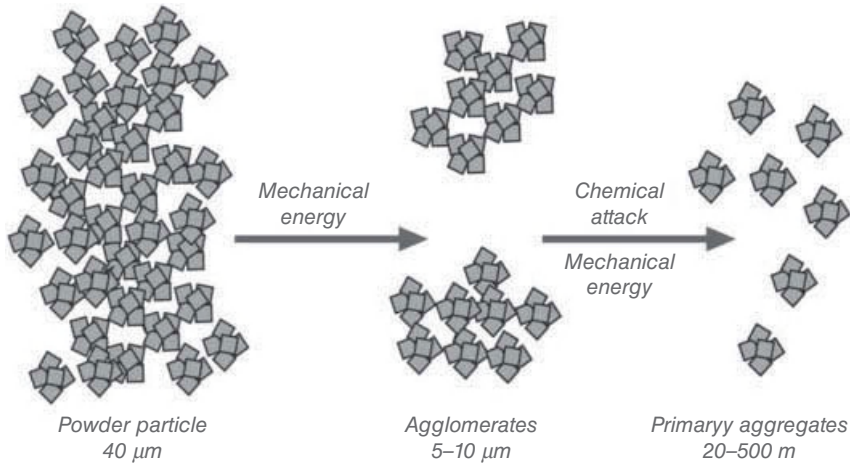
Figure 3.13 Dispersion of nanoalumina (courtesy of Sasol).
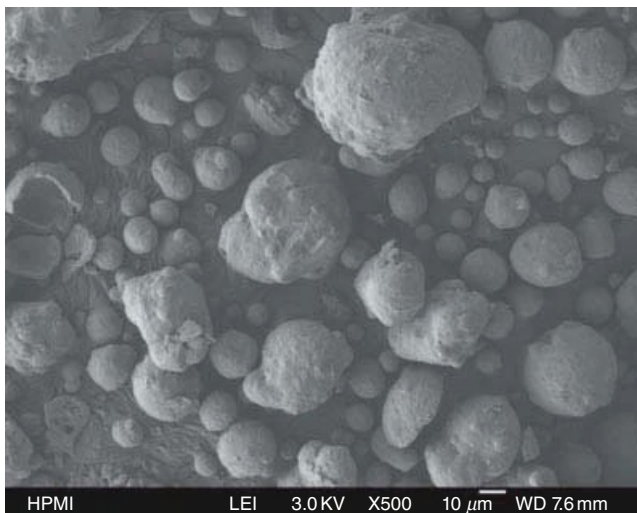
Figure 3.14 SEM image of as-received *n*-alumina.

the mechanical properties of the resulting polymer nanocomposites would reduce [17].

3.2.3.4 Polyhedral Oligomeric Silsequioxanes

A POSS molecule is the nanoscopic silicon–oxygen cage with size ranging from 1 to 3 nm (Figure 3.16) [2]. POSS is versatile because the each silicon in the cage could be functionalized with different functional groups to enhance the interfacial
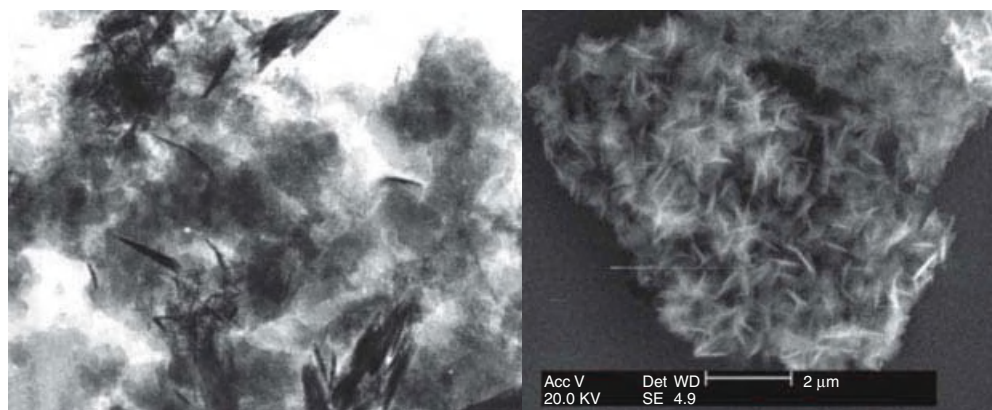
Figure 3.15 TEM (a) and SEM (b) images of neat MgOH nanoparticles [16].
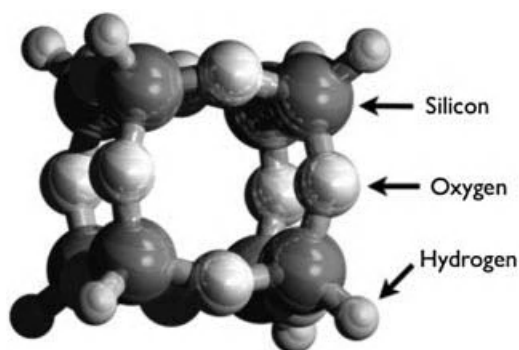
Figure 3.16 Cage structure of POSS (courtesy of NSDL).

adhesion to polymer resin. This nanoparticle possesses better thermal properties and chemical resistivity than silica. It has been shown that POSS nanocomposites have excellent fire resistance performance [18].

3.3
Thermal, Flammability, and Smoke Characterization Techniques

3.3.1
Introduction to Test Methods

There are numerous techniques to evaluate the thermal, flammability, and smoke of the polymer nanocomposites, depending on the type of information desired. A

brief discussion of the techniques is not intended to be exhaustive or authoritative, but only as an aide to the reader in identifying the test methods used worldwide; the reader should refer to the original ASTM, UL, and other organizations for more detailed information. The reader is referred to Troitzsch [19] and Hirschler [20] for an overview of all test methods.

3.3.2
Thermogravimetric Analysis (TGA)

Thermogravimetric analysis (TGA) is a technique in which the mass of a substance is monitored as a function of temperature or time as the sample specimen is subjected to a controlled temperature program in a controlled atmosphere. TGA is a technique in which, upon heating a material, its weight increases or decreases. TGA consists of a sample pan that is supported by a precision balance. The pan resides in a furnace and is heated or cooled during the experiment. The mass of the sample is monitored during the experiment. A sample purge gas controls the sample environment. This gas may be inert or a reactive gas that flows over the sample and exits through an exhaust. TGA can determine the thermal stability of the polymer nanocomposites compared to the base polymer.

3.3.3
The UL 94 Vertical Flame Test

Underwriters Laboratories UL 94 Test [21] (also known as ASTM D 3801 and ISO 1210) is designed for assessing "flammability of plastic materials for parts in devices and appliances." It is run on a sample of plastic itself, at specific dimensions. This test measures how long a bar of polymer burns after exposure to a small gas burner flame, and it is a reasonable measure of material's response to a small ignition source, such as a candle or a match. It is accepted for standardization internationally. Five different classifications from the vertical burn configuration are included, but only V-0, V-1, and V-2 classification are introduced, because it is most often cited in the literature.

  To assign this set of classifications, a plastic bar of 125 mm length × 13 mm width, with smooth edges, is positioned vertically and held from the top. Depending on the application of the plastic, bars may have a thickness of 3.2, 1.6, or 0.8 mm. Thinner specimens are usually more flammable. A wad of surgical cotton is placed 300 mm below the specimen to detect flaming drips which will ignite the cotton. The Bunsen burner flame (ca. 19 mm high, fed with methane) is applied twice to the test bar (10 s each). After each application the burning time is recorded. The second application of the flame should follow immediately after the bar ceases to burn from the first application. A V-0 classification is given when the five test bars extinguish in less than 10 s after any flame application. The average burning time for five bars tested (10 flame applications) should not be greater than 5 s and there should be no burning drips that ignite the cotton. The individual specimen after flame plus afterglow must not exceed 30 s. A V-1 classification is given to

samples with maximum total combustion time <50 s and average burning time for five specimens <25 s. The individual specimen after flame plus afterglow must not exceed 60 s. There should be no flaming drips. The sample is classified as V-2 if it meets the flaming time criteria of V-1 or V-0 but has flaming drips that ignite the cotton.

3.3.4
Oxygen Index (Limiting Oxygen Index) (ASTM D2863-97)

Limiting Oxygen Index (LOI) is another test commonly used in the R&D laboratory; it is also known as the Oxygen Index (OI). It is included in some national or international standards, such as ASTM D2863-97 [22] or BS ISO 4589-2. The specimen size and shape are not as strictly specified as the UL 94 test, but usually bars of about 100 mm × 65 mm × 3 mm are used in testing of rigid plastics. The specimen is positioned in a candle-like position vertically at the exit of a glass chimney and clamped at the bottom. The chimney is continuously fed with a controlled mixture of nitrogen and oxygen. The flame of a small igniting burner is applied to the top of the specimen until the entire top surface is ignited. If the specimen does not ignite or extinguishes in less than 30 s, the concentration of oxygen is then increased, in steps with repeated trial ignitions, until the specimen shows stable candle-like combustion for more than 3 min after removal of the ignition source or if more than 5 cm length of the sample is consumed, a new specimen should be put in place and tested at a slightly lower oxygen concentration. By iteration of these steps, finally the LOI value is determined; this is the highest concentration of oxygen at which the tested sample self-extinguised is less than 3 min and less than 5 cm of the material is consumed. The LOI test does not represent any real fire scenario, but it is quite reproducible, and fairly insensitive to the sample thickness. It is often used as a screening, research statistical design tool, because it gives a numerical value typically to two significant figures, instead of a mere classification as given by the UL 94. It can even be run on films and textiles with suitable clamping.

Materials which melt and flow readily will give high LOI values, and in the case of such as nylon, it is even possible to arrive two different LOI values depending on whether they are reached from the oxygen side or the high oxygen side.

3.3.5
Cone Calorimeter (ASTM E 1354)

The cone calorimeter test is a bench scale test which was originally developed at NIST and quickly gained popularity in the academic community and was transformed into ASTM E 1354 [23] or ISO 5660-1 standard tests. It is also used as a tool for fire protection engineering, because it allows prediction of some large-scale

test results, in particular flash-over time which is important for time to escape. In the cone calorimeter, heat and smoke release rate is measured together with mass loss and ignitability, under a wide range of radiant heat exposure conditions. At the start of a test, a square specimen of 100 mm × 100 mm is placed on a load cell and exposed to a preset incident heat flux from a truncated cone radiant heater, which can be set to fluxes representing small fires to fully developed fires. An electric spark ignition source is used for piloted ignition. The combustion products and entrained air are collected by a hood and extracted through a duct by a blower. The heat release rate is calculated from oxygen concentration measurement based on the oxygen consumption principle. Apart from the heat release rate, the cone calorimeter can also monitor time to ignition, weight loss of the sample during combustion, effective heat of combustion (heat generated per unit mass loss), rate of smoke generation, carbon monoxide, carbon dioxide, and optionally some corrosive gases like HCl or HBr.

3.3.6
Microscale Combustion Calorimeter (ASTM D 7309)

The microscale combustion calorimeter was developed by Federal Administration (FAA) to offer industry a research tool to assist FAA in its mandate to dramatically improve the fire safety of aircraft materials. It is a standardized ASTM D 7309 test method [24]. The tester is becoming a useful research tool due to its ability to obtain meaningful test data with a sample size in the range of 0.5–50 mg. Its potential measurements are heat of combustion, ignition temperature, heat release, heat release capacity, and flame resistance.

3.3.7
Steiner Tunnel Test (ASTM E 84) [25]

This test is mainly used for building materials in the United States and is written in various building codes. The test apparatus is a tunnel measuring 8.7 m × 0.45 m × 0.31 m (25 ft × 1.5 ft × 1 ft) with viewing windows along its length. The sample to be tested is 7.6 m (24 ft) long and 0.51 m (1.67 ft) wide, mounted on the ceiling position. It is exposed for 10 min at one end of the tunnel to an 88 kW (5000 Btu/min) gas burner, with a forced draft through the tunnel, from the burner end, at an average initial air velocity of 1.2 m/s (240 ft/min). The flame spread index (FSI) is calculated on the basis of the area under the curve of the flame tip location as a function of time, compared to assigned values of 0 for an inert board and 100 for a standard red oak flooring. The smoke developed index (SDI) is calculated from the area under the curve of the light obscuration versus time as measured at the tunnel outlet, and is compared to the reference values of 0 for inert board and 100 for the red oak. Some codes require that the test be run on the minimum and maximum thickness and with construction similar to the manner in which the laminate will be used.

3.4
Thermal and Flame Retardancy of Polymer Nanocomposites

Although polymer nanocomposites show improved thermal and flame retardancy, it has been shown that different nanoadditives have different effects on improvement in flame retardancy. The thermal and flammability properties of polymer nanocomposites depend on the types of nanofillers, types of polymers, and the nanostructures obtained. In this section, the thermal and flammability properties of these polymer nanocomposites will be subdivided into (i) one-dimensional nanomaterial polymer nanocomposites which include clay-based and graphene-based nanocomposites; (ii) two-dimensional nanomaterial polymer nanocomposites which include carbon nanofiber-based, carbon nanotube-based, and halloysite nanotube-based polymer nanocomposites; and (iii) three-dimensional nanomaterial polymer nanocomposites which include nanosilica-based, nanoalumina-based, nanomagnesium hydroxide-based, and POSS-based polymer nanocomposites. Different types of polymers, such as thermosets, thermoplastics, and elastomers, will be included.

3.4.1
One-Dimensional Nanomaterial-Based Nanocomposites

3.4.1.1 Polymer–Clay Nanocomposites
Clay-based nanomaterial is the most commonly used for nanocomposites because it has been around the longest and can be obtained in high purity at low cost. In the following discussions, the clay used to create the polymer nanocomposites is MMT unless otherwise identifying differently. More information can be found in several recent books on polymer–clay nanocomposites [26–28].

The polyamide 6 (PA6)–clay nanocomposite was the first discovered polymer nanocomposites. FR of polymer–clay nanocomposites has received much attention because FR was one of the first desirable properties noted by researchers. Initially all the polymers exhibit improved FR, as evaluated by the cone calorimeter, upon the incorporation of clay. The following summarizes the research progress on clay nanocomposites using different polymers.

Flammability of Polyamide–Clay Nanocomposites The PA6–clay nanocomposite was the first discovered polymer nanocomposite and studied by Gilman *et al.* [29] at NIST, USA. The cone calorimeter was used as the characterization tool to evaluate the PA6–clay nanocomposites. The peak heat release rate (PHRR) is reduced by 32% and 63% in a PA6–clay nanocomposite containing 2% and 5% of the clay. The PA6–clay nanocomposite not only showed improved FR, but the mechanical properties also improved compared to neat PA6. Foster Corp., USA (www.fostercomp.com), demonstrated that high levels (13.9%) of clay can be added to PA12 elastomers to achieve UL 94 V-0 ratings at a 3.175 mm thickness. The clay can be used as a char former allows the typical 50% loading of the halogen/antimony oxide flame-retardant system to be cut into half that reduces
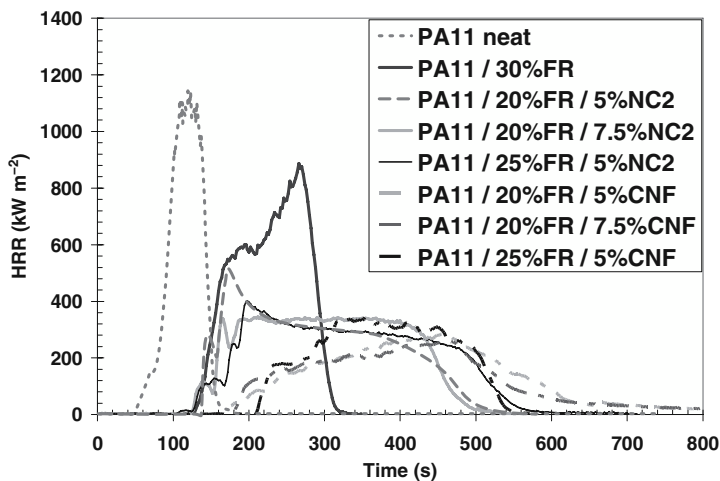
Figure 3.17 Heat release rate of neat and nanoparticle-filled PA11 with and without FR additive as a function of time (cone calorimeter, $35\,kW\,m^{-2}$). FR is flame-retardant additives, NC2 is nanoclay, and CNF is carbon nanofiber.

the detrimental effects on physical properties of the polymer. Foster Corp. introduced PA12–clay nanocomposites for tubing and film in 2001.

Lao and Koo have recently carried out extensive research on flame-retardant PA11–clay and PA12-clay composites for selective laser sintering application [30–32]. Their research group demonstrated with PA11 at 7.5% and 10% of nanoclay (NC); the PHRR was reduced by 68% and 73%, respectively [30]. Figure 3.17 shows the PHRR of the neat PA11 and several PA11 polymer blends at a radiant heat flux of $35\,kW\,m^{-2}$. When 20% of conventional intumescent FR additives and 7.5% NC were added to PA11, PHRR was reduced to 70% and achieving a UL 94 V-0 rating [30]. The heat deflection temperatures (HDT) of neat PA11 and PA11/20% FR/7.5% NC were 48 and 97 °C, respectively. A synergistic effect exists between conventional FR intumescent additives with nanoclay allowing the author to lower the FR intumescent additive from 30% to 20% by incorporating 5–7.5% NC in PA11.

Flammability of Epoxy–Clay Nanocomposites Epoxy resins are used in a variety of applications, such as coatings, adhesives, and electronics or in composites in the aerospace and transportation industries. Although the polyfunctional reactivity of most epoxy systems leads to a high crosslink density, brittleness of epoxy systems is always a concern. In most applications, the polymer matrix is combined with one or more phases, such as short or long fibers or a rubbery phase for toughening to form epoxy fiber-reinforced composites. Epoxy nanocomposites have attracted a lot of attention within nanocomposites research to enhanced modulus, strength, fracture toughness, impact resistance, gas and liquid barrier, and improve flame
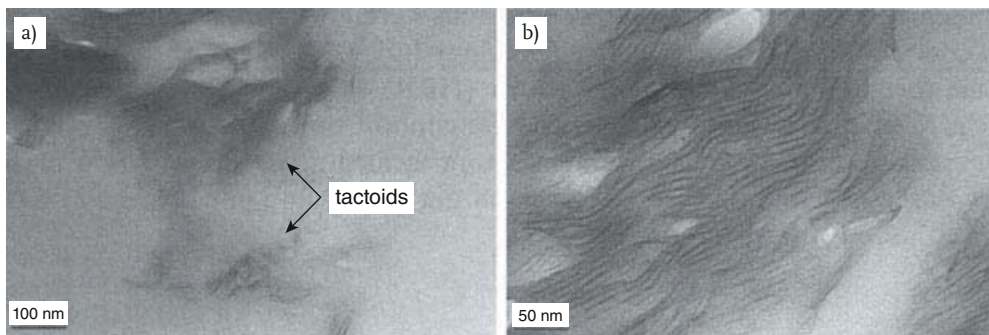
Figure 3.18 TEM images at low magnification (a) and high magnification (b) of an epoxy nanocomposite.

retardancy. However, like all organic materials, epoxy is flammable, and its use for replacing traditional nonflammable materials has increased the fire hazard in the past years. Evolved smoke and toxic gases from these fires create hazards for both people and the environment. At present, nanoclays are by far the most investigated nanofillers in flame retardancy. In this section, we focus on epoxy nanocomposites based on nanoclays.

The additive effect of resorcinol bis(diphenyl phosphate) (RDP) and nanoclay on epoxy was studied by Katsoulis *et al.* [33]. The epoxy resin, tetraglycidy1-4,4′-diaminodiphenylmethane (TGDDM), the curing agent, 4,4′-diaminodipheny sulfone (DDS), RDP flame retardant, and nanoclay of different loadings were synthesized. Figure 3.18 shows TEM images of epoxy-RDP-I.30E (80/15/5) at low magnification showing intercalated nanoclay with gallery spacing at 5–10 nm. Formulations with RDP alone at 5% and 10% gave the best flame resistance in LOI and UL 94 experiments, while going beyond 10% RDP had an adverse effect. In the cone calorimeter, the addition of RDP at 10% results in remarkable reductions in PHRR and enhanced char formation. The addition of nanoclay alone did not improve the thermal stability of the epoxy resin, nor did it improve its flame resistance using the cone calorimeter. The addition of clay with RDP did not show an advantage. It also did not produce any significant improvement in the fire properties as measured by the cone calorimeter and LOI. This may be attributed to possible antagonistic interactions between the constituent components. The addition of a known flame retardant, RDP, and nanoclay yielded mixed results with respect to thermal stability and improved fire performance.

In nitrogen, residue yields from epoxy–clay nanocomposite reveal little improvement in the carbonaceous char yield once the presence of silicate in the residue is accounted for [33–36]. In air, the char yield increase is more relevant [37]. Hussain *et al.* [38] studied the effect of clay and an organophosphorus epoxy modifier, DOPO on DGEBA and TGDDM epoxies cured with amine curing agent. They prepared 3% P-containing epoxies by reacting DGEBA or TGDDM with DOPO.
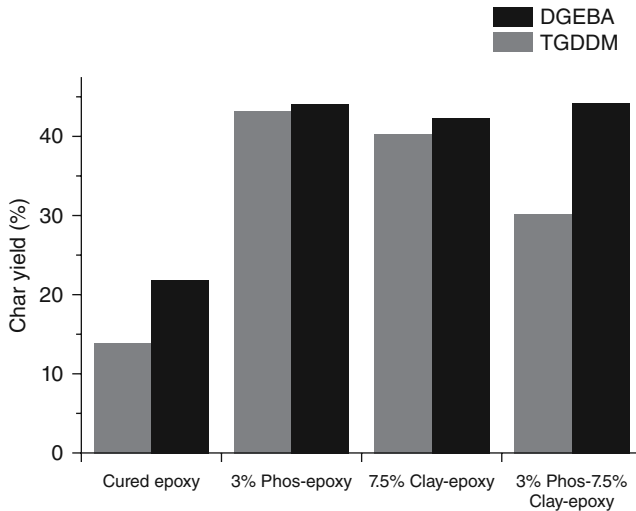
Figure 3.19 Char yields at 600 °C for DGEBA and TGDDM control samples, 3% P-epoxies, and 7.5% clay nanocomposites.

Standard and modified epoxies were used to prepare clay nanocomposites which show a mixed intercalated–exfoliated structure. The clay enhanced char formation significantly. The results are shown in Figure 3.19. The char yield at 600 °C increases from 14% in the near DGEBA to 38% and 42% for 5% clay-DGEBA nanocomposite and 3% P-modified epoxy, respectively. Similar results were observed for TGDDM-based formulations.

Polymer nanocomposites showed that clays can reduce the amount of tradition flame retardants required to comply with the standards; the approach to nanocomposites itself alone is not sufficient to facilitate passing commercial tests. In terms of LOI, the improvement achieved by using clays is generally not relevant. A typical increase between 1% and 2% in LOI values is seen with 5% nanoclay [39]. Hussain *et al.* [38] reported an increase in LOI values from 25% for neat DGEBA to 32.7% and 34.5% for 5.0% and 7.5% nanocomposites, respectively. For a tetrafunctional TGDDM epoxy, the LOI values increase from 26.3% in neat polymer to 35.1% and 36.7% in nanocomposites containing 5% and 7.5% clay, respectively.

Cone calorimeter results of nanoclay in DGEBA cured with either methylenedianiline (MDA) or benzyldimenthylamine (BDMA) [40] were impressive. The PHRR and the average heat release rate (HRR) are significantly improved with 6% nanoclay. The HRR plots for DGEBA–MDA and the DGEBA–MDA clay nanocomposites are compared in Figure 3.20. The PHRR, HRR, and average mass loss rate (MLR) decrease by about 40%. The heat of combustion, smoke obscuration, and carbon monoxide yields are unchanged. The results suggest that the clay nanocomposite is operating primarily in the condensed phase. A shorter ignition time
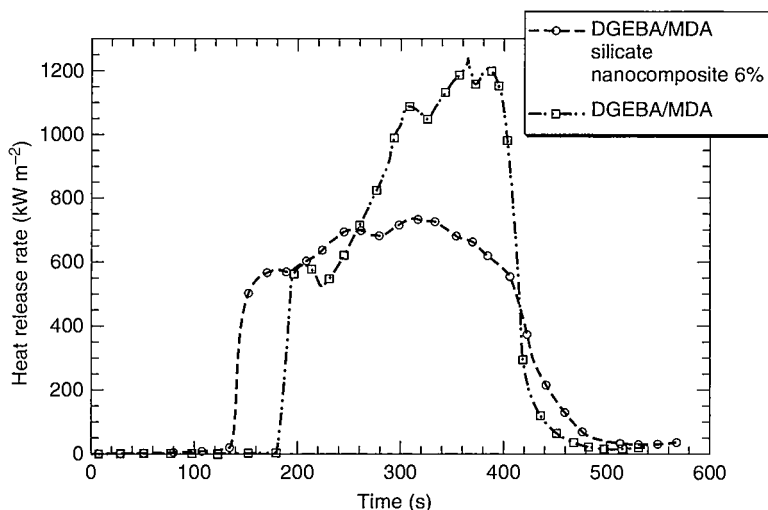
Figure 3.20 HRR plots for DGEBA/MDA and DGEBA/MDA silicate nanocomposites.

is observed in the nanocomposite, may be due to the low stability of the organic modifier.

Flammability of Elastomer–Clay Nanocomposites   The combustion behavior of thermoplastic elastomer has been studied by Koo *et al.* [41, 42]. Two types of commercially available thermoplastic polyurethane elastomer (TPU) (Pellethane® and Desmopan®) were melt blended with various loadings (2.5–10%) of MMT nanoclay (Cloisite® 30B) using twin screw extrusion. The morphological, physical, thermal, flammability, thermophysical properties, and kinetic parameters of these two families of polymer–clay nanocomposites were characterized. The *processing–structure–property* relationships of this class of novel thermoplastic polyurethane elastomer–clay nanocomposites (TPUNs) were established. The WAXD plots of the four different nanoclay loadings of Desmopan TPUNs are shown in Figure 3.21. No peaks were observed in WAXD, which indicated that all loadings of nanoclays were exfoliated in the TPU polymer. No stacks are observed in any of the three 40 kX TEM images in Figure 3.22; the scale bar is 100 nm. The lack of platelet stacks indicates that the nanoclay is exfoliated and well dispersed in the Desmopan TPU material.

Cone calorimeter experiments at 50 kW m^{-2} are tested on the neat Desmopan TPU, neat Pellethane TPU, Desmopan-5% Cloisite 30B TPUN, and Pellethane-5% Cloisite 30B TPUN. Two or three experiments are performed to test for repeatability. The neat material experiments are the least repeatable due to the fact that the material melted and dripped off the test fixture; for this reason the test with the higher PHRR is used in the comparisons. The HRR graph of the materials is
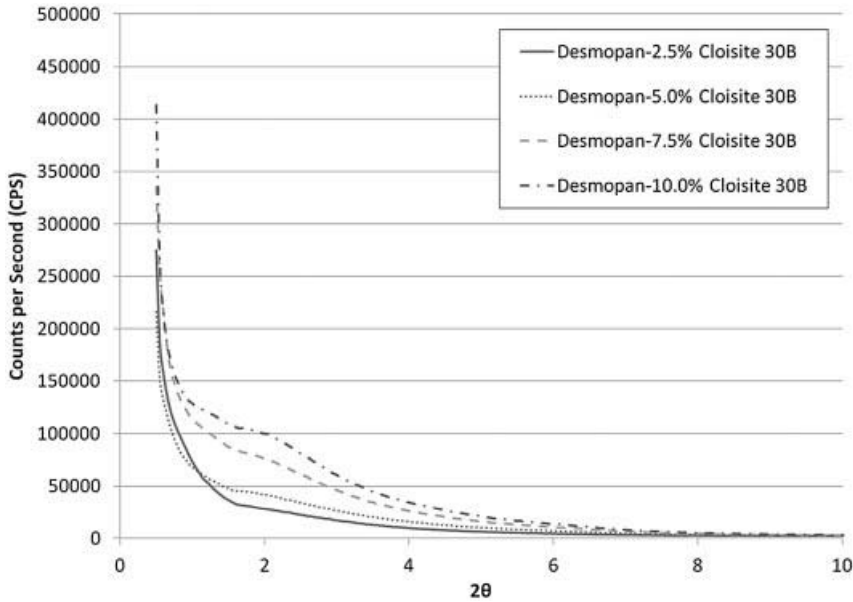
Figure 3.21 Wide-angle X-ray diffraction of Desmopan–clay TPUNs.
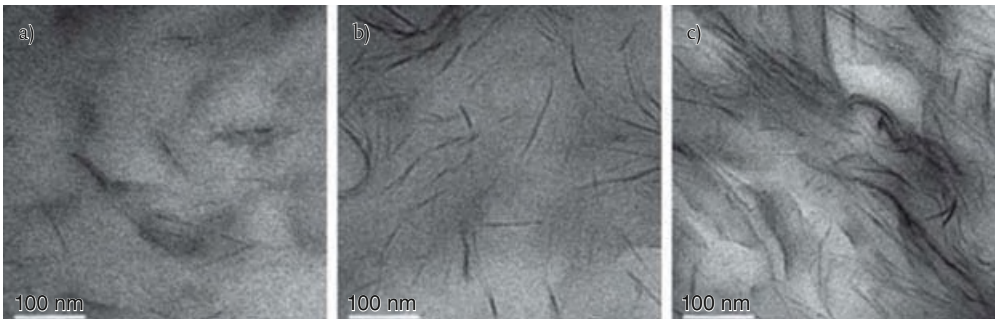
Figure 3.22 TEM micrographs at 40 kX of Desmopan with (a) 2.5%, (b) 5%, and (c) 10% Cloisite 30B nanoclay TPUNs with a unit bar of 100 nm.

shown in Figure 3.23. The flammability properties are shown in Table 3.1. The material's time to sustained ignition is not changed drastically with the addition of Cloisite 30B, +2 s for Pellethane TPUN and −1 s for the Desmopan TPUN. However, a dramatic decrease in peak heat release rates (PHRR) is observed. Pellethane TPU PHRR decreases by 73% and Desmopan TPU PHRR decreases by 50% with the addition of 5 wt% Cloisite 30B. In the first 60 s, the HRR is higher in the TPUN. This is due to a higher rate of decomposition at this stage observed in the mass loss graph.
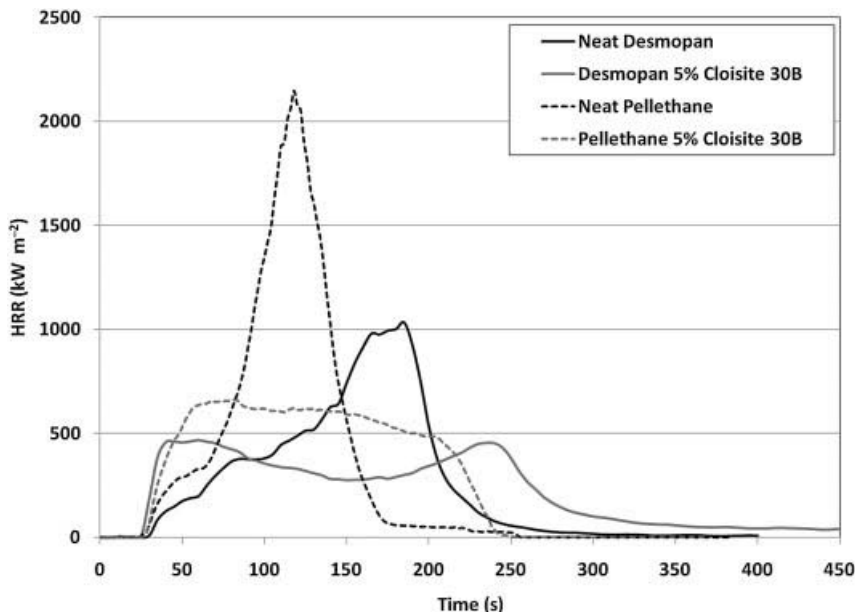
Figure 3.23 Heat release rate of Desmopan and Pellethane TPU and Cloisite 30B TPUNs.

Table 3.1 Summary of cone calorimetry data at an irradiance heat flux of $50\,kW\,m^{-2}$.

Material	t_{ig} (s)	PHRR (kW m⁻²)	Avg. HRR, 60 s (kW m⁻²)	Avg. HRR, 180 s (kW m⁻²)	Avg. Eff. H_c (MJ/kg)	Avg. SEA (m² kg⁻¹)
Neat Pellethane	32	2290	406	653	30	237
Pellethane-5% Cloisite 30B	34	664 (71% reduction)	560	562	25	303
Neat Desmopan	28	1031	228	515	27	311
Desmopan-5% Cloisite 30B	27	518 (50% reduction)	442	376	28	256

t_{ig} = iime to sustained ignition; PHHR = peak heat release rate; Avg. HRR = average heat release rate after ignition; Avg. Eff, H_c = effective heat of combustion; Avg. SEA = average specific extinction area.

3.4.1.2 Polymer–Graphene Nanocomposites

Researchers started using nanographene (NG) and graphene oxide (GO) in the polymer in recent years aiming to enhance the electrical and thermal conductivities of polymer resins. Both NG and GO also have the potential to work as heat barrier and char promoter when the polymer nanocomposites are subjected to fire

burning thus improving the flammability properties. However, this research area is not yet well developed. Major work of NG and GO used as flame retardant was on the epoxy resin.

Flammability of Epoxy–Graphene Nanocomposites   Avila [43] incorporated 3 wt% of NG into the epoxy resin and showed that fire resistance of the resin was enhanced. Specimens were burned under a large heat flux using an oxyacetylene torch for 2 min. The unburned thicknesses of the neat resin and nanocomposites at 60 s were ~1 and ~3.2 mm, while at 120 s were 0.16 and 2.74 mm, respectively. Also, the peak mass losses in TGA of the neat resin and the NG nanocomposite were 1.04 and 0.63 mg/min, respectively. These results indicated that the nanoparticle could act effectively as thermal barrier which protected the resin underneath the char layer. Koo [44] tested Avila's epoxy–graphene materials and showed similar results using the cone calorimeter. Guo [45] also found that by incorporating 0.3–5 wt% of NG, GO, and FGO (functionalized graphene oxide) into the epoxy resin increased the char yield under TGA of 14–16%. The PHRR and total heat release (THR) under a micro-combustion calorimeter (MCC) reduced up to 45% and 24%, respectively. Although all three nanoparticles could reduce the heat release, NG provided the greatest reduction. Guo concluded that there was a good flame-retardant effect of graphite sample in epoxy composites and the nanoparticles were good char promoters. Wang [46] showed that an epoxy nanocomposite with 1 wt% NGO showed 28.5% and 11% reduction in THR and PHRR under a heat flux of 50 kW m^{-2} in the calorimeter.

Flammability of HIPS–Graphene Oxide Nanocomposites   Higginbotham [47] incorporated 1, 5, and 10 wt% of GO in high impact polystyrene (HIPS). As the weight loading of GO increased in the HIPS resin (0–10 wt%), the THR reduced from 37.5 to 34 kJ/g (10% reduction), PHRR reduced from 840 to 610 W/g (28% reduction), and the char yield increased from 1 to 6 wt% (500% improvement) as observed from the MCC results. However, since HIPS is a very flammable material, dripping was observed when the HIPS–GO nanocomposites were burned in a vertical flame test and fire did not self-extinguish. Therefore, no correlation between flame retardancy and flammability was observed in this nanocomposite system.

Flammability of ABS–Graphene Oxide Nanocomposites   Higginbotham [47] incorporated 1, 5, and 10 wt% of the same GO as in the HIPS nanocomposites into the acrylonitrile butadiene styrene (ABS) resin. The GO had similar effects on the THR, PHRR, and char yield on the ABS polymer. As the weight loading of GO increased, the THR decreased (up to 11%), PHRR decreased (up to 17%), and the char yield decreased (up to 600 wt%). ABS–GO nanocomposites also exhibit dripping under the vertical flame test. Although self-extinguishment of fire was also observed, there was still no correlation of thermal retardancy and flammability in this system.

Flammability of PC–Graphene Oxide Nanocomposites   Higginbotham [47] also incorporated the same GO into polycarbonate (PC) with the same weight loadings.

A general trend of decreases in THR (up to 13%) and PHRR (up to 13%) with increasing GO weight loading was observed, with a couple of exceptions which were probably some random errors. The char yield increased 21 wt% when 10 wt% of GO was added. Since the PC itself was not very flammable (fire self-extinguished in 14 s in a vertical flame test), the addition of 1 wt% GO decreased the time to self-extinguish to 4 s, and thus no dripping was observed. The incorporation of 5 and 10 wt% of GO even made the PS nonflammable.

3.4.2
Two-Dimensional Nanomaterial-Based Nanocomposites

3.4.2.1 Polymer Carbon Nanofiber Nanocomposites
Flammability of Thermoplastic-CNF Nanocomposites   PA11 were melt-blended by dispersing low concentrations of CNFs by Lao and Koo [32] via twin-screw extrusion. To enhance their thermal and FR properties, an intumescent FR additive was added to the mechanically superior PA11 CNF formulations. Good dispersion of the CNFs and FR additives in the PA11 polymer was achieved. For neat and CNF-reinforced PA11 as well as for PA11 reinforced by both intumescent FR and select CNF, decomposition temperatures by TGA, flammability properties by UL 94, and cone calorimeter values were measured. All PA11 polymer systems infused with CNFs and FR additive had higher decomposition temperatures than those infused with solely FR additive. For the PA11/FR/CNF formulations, all Exolit® OP 1311 (FR1), OP 1312 (FR2), and OP 1230 (FR3) FR additives passed the UL 94 V-0 requirement with 20%.

Based on the decomposition temperatures at 50% mass loss, thermal stability of the PA11 was enhanced by CNF significantly. All FR/CNF-reinforced PA11 blends had higher decomposition temperatures than those reinforced with CNF only. The FR3 intumescent additive provided the best synergistic effect to CNF since PA11/20%FR3/7.5%CNF sample had a significant increase of $T_{50\%}$ ($\Delta \cong 66\,°C$).

It was shown that 30% FR3 was needed for PA11 to achieve a UL 94 V-0 rating. It was also observed that a minimum of 20% of either FR1, FR2, or FR3 is needed with either 5 or 7.5 wt% of CNF to achieve the V-0 rating. All three FR additives worked well with CNF. Since 15 wt% of FR intumescent additive will only achieve a V-1 rating. The optimal percentage of intumescent FR additive that is needed with CNF lies between 15% and 20% to achieve a V-0 rating. The CNF blend had no combustion at the first flame application and a lower total combustion time than the NC blend. Therefore, the FR/CNF blend outperformed its NC counterpart. Cone calorimeter peak heat release rates of FR/CNF blends are lowered than that of the FR/NC blends. This may suggest that CNF has a good synergistic effect with the FR2 additive.

3.4.2.2 Polymer Carbon Nanotube Nanocomposites
Carbon nanotubes (single-walled and multi-walled)-based polymer nanocomposites have been studied intensively by Kashiwagi and others. Heat release rates of
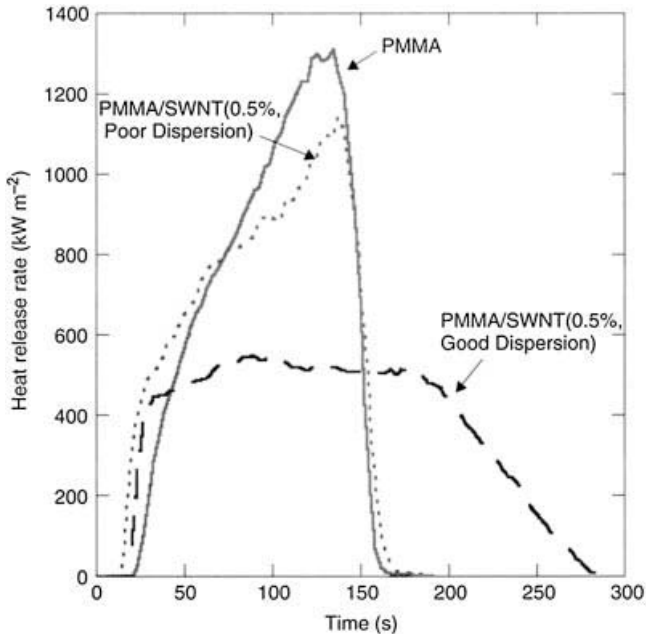
Figure 3.24 Effect of SWNT dispersion on the heat release rate of PMMA–SWNT (0.5%) nanocomposites at an external radiant flux of 30 kW m^{-2}.

three different samples – poly(methyl methacrylate) (PMMA), PMMA-SWNT (0.5%, good dispersion), and PMMA-SWNT (0.5%, poor dispersion) – were measured in a cone calorimeter at an external radiant flux of 50 kW m^{-2} as shown in Figure 3.24 [48, 49]. The 0.5% SWNT (good dispersion) showed more than 50% reduction in the PHRR compared with neat PMMA. It was proposed that the SWNTs formed a continuous network that acts as a heat shield to slow the thermal degradation of PMMA. The effects of SWNT concentration on flammability properties of PMMA—SWNT nanocomposites by a cone calorimeter that have good dispersion of SWNT at levels from 0.1% to 1% prepared by the coagulation method are shown in Figure 3.25 [48, 49]. The addition of a 0.1% of SWNT did not significantly reduce the heat release rate of PMMA. The most reduction in the heat release rate was achieved by 0.5% SWNT. A 60% PHHR reduction was achieved by 0.5% SWNT.

3.4.2.3 Polymer Halloysite Nanotube Nanocomposites
Bulter *et al.* [50] developed an enhanced PA11 composite with improved mechanical, thermal, and flammability properties through the addition of HNTs and a conventional intumescent FR additive. Polyamide 11 (nylon 11) is of particular interest, as it is the one of the major polymers used in the selective laser sintering (SLS) process. Unfortunately, PA11 has poor flammability properties that impose
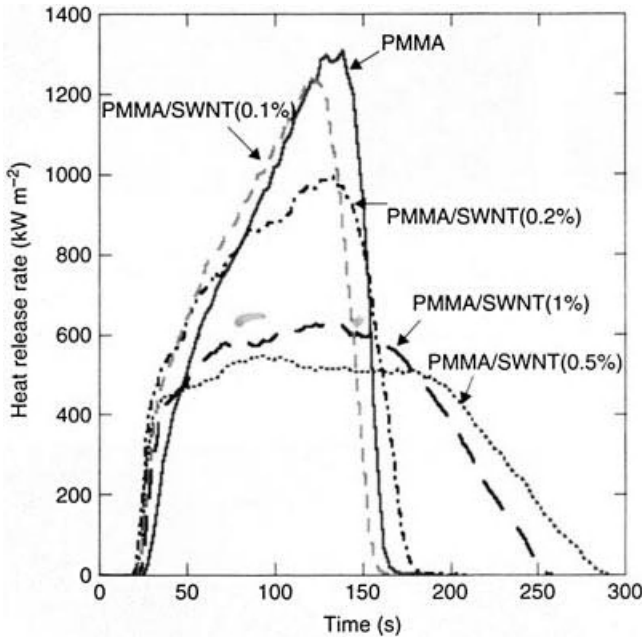
Figure 3.25 Effect of SWNT concentration on the heat release rate of PMMA–SWNT at 50 kW m^{-2}.

limitations upon the applications for this particular material via the additive manufacturing process. HNTs are an attractive additive as they occur naturally, are relatively easy to process, and are less detrimental to the elongation and toughness properties of the polymeric material compared to other additives. HNTs and FR additives were melt-compounded via twin-screw extrusion processing in PA11. Test specimens in this study were injected molded. The principal objective of this work is to study the combined effects of the addition of HNTs and a conventional intumescent FR additive to PA11. A matrix of nine formulations of PA11–HNT–FR was studied; properties are characterized using tensile and Izod impact testing, UL 94 flammability testing, TGA, and scanning electron microscopy (SEM).

None of the PA11–HNT nanocomposites (2.5, 5, 7.5, and 10 wt%) were able to achieve a UL 94 V-0 rating. When a Clariant FR intumescent component (Exolit® OP 1312) was added to the PA11–FR–HNT nanocomposites, they appear to be valuable high-performance materials for the SLS process. With only 2.5 wt% HNT in PA11, the tensile modulus is increased from 424 to 1867 MPa, and an elongation to break of 40% is obtained. In traditional composites, a substantial increase in the modulus almost always results in a brittle material. A 40% elongation at break may be considerably lower than the neat PA11 which had an elongation at break of 227%; however, 40% elongation at break is still a considerable

toughness for a material and is much higher than many other polymer nanocomposites which incorporate nanoparticles, such as MMT nanoclays [30, 31], carbon nanofibers [30, 31], and carbon nanotubes [51]. Traditional polymer nanocomposites often see elongations at break around 20% and lower for a similar increase in the modulus. The combination of stiffness and toughness in the PA11 nanocomposites is therefore very intriguing. In the PA11 nanocomposite formulation comprising 20 wt% FR and 5 wt% HNT, a nondripping formulation that achieved the UL 94 V-0 rating, 940 MPa tensile modulus, and 19% elongation at break was achieved. This balance of flame retardancy, stiffness, and toughness is also very promising. A design of experiment approach was adapted in this study to identify additional PA11–FR–HNT formulations. Future work will involve the development of surface treatments for HNT to improve the interfacial adhesion and thus the tensile strength and elongation at break of FR–HNT nanocomposites.

3.4.3
Three-Dimensional Nanomaterial-Based Nanocomposites

3.4.3.1   Polymer Nanosilica Nanocomposites

Nanosilica can have a huge interfacial area as long as the diameter of the particles is in the range of nanometers. Although they do not have the narrow gallery structure of the layered nanoclay, improvement in physical properties [52–55] and thermal stability [56, 57] by the addition of nanosilica to a polymer was reported. It was also reported that the addition of mesoscale silica to different polymers significantly reduced the HRR of polymers [58, 59]. Flammability properties of PMMA–nanosilica [60–62] and polyimide–nanosilica nanocomposites [62] have been reported. Dispersion of the particles in a polymer is critical for obtaining better flame retardant performance. Roughly 50% reduction in PHRR was reported with the addition of 13 wt% of silica particles [61] as shown in Figure 10.2 Little to no improvement was reported in LOI measurement with up to 10 wt% of nanosilica of diameter 7 nm. Although the LOI values increased from 36 to 44, the addition of 20 wt% of silica particles (diameter 50–300 nm) was required. The addition of nanosilica hardly reduced the HRR at the early stage of burning, and it was demonstrated that the addition of nanosilica did not significant modify the UL 94 rating [62]. The overall FR effectiveness of nanosilica appears to be less than that of the nanoclays as described in an earlier section in this chapter.

3.4.3.2   Polymer Nanoalumina Nanocomposites

Three types of nanoalumina (X-0 needle, X-25SR, and X-0SR) with different organic treatments manufactured by SASAL NA were incorporated into PA11 via twin-screw extrusion by Lao *et al.* [63]. A total of 10 formulations of PA11/ *n*-alumina nanocomposites, including the neat PA11, were melt-compounded and injection molded to test specimens. TEM demonstrated that *n*-alumina surface-treated particles are well dispersed in the PA11 matrix. TGA showed that

n-alumina improved the thermal stability of the nylon 11 substantially. The UL 94 test showed that all formulations did not pass the ideal V-0 rating. All of them exhibited flammable dripping that ignited the cotton under the specimens during the test. The X-0 needle formulations performed the best, followed by X-25 SR, and the X-0 SR performed the worst in performance. The addition of selective flame-retardant additives or antidripping agents should be incorporated into the system together with the *n*-alumina for enhanced flammability properties in the future.

Rallini *et al.* reported using nanoalumina (average diameter of 13 nm) to improve the flame resistance of a carbon fiber-reinforced composites [64]. Nanoalumina was dispersed in an epoxy resin as a matrix for carbon fiber reinforced by simple mechanical stirring. The 5 wt% nanoalumina allowed the authors to obtain a fiber-reinforced composite with improved fire resistance. After exposure to high temperature, the nanoalumina acts as a high temperature adhesive coating and has sintered onto the carbon fibers. This coating binds together the carbon fibers promoting residual structural integrity of the burnt composite. TGA data also demonstrated that the sintered alumina coating of the fibers acts as a barrier for the oxidation of carbon fibers. The morphological investigation of the samples burnt in a muffle has shown further evidence on the role of alumina particles. The 1 wt% content is insufficient to improve the residue strength of the burnt sample, whereas the 5 wt% content is sufficient to produce a ceramic skeleton on the entire volume of the composite.

3.4.3.3 Polymer Nanomagnesium Hydroxide Nanocomposites

Magnesium hydroxide [Mg(OH)$_2$/MH] has been used in a polymer as a flame-retardant additive. However, it commonly requires 60–70 wt% of the micron-sized (2–5 μm) MH to be added into polymer to make it truly fire retardant [65]. Since flame-retardant efficiency of MH is related to the interparticle distance which decreases with decreasing particle size at a given volume fraction of the filler [66, 67], it is believed that by using MH of smaller particle size, that is, nano-MH, effective flame retardancy can be achieved at a lower loading of the filler.

Flammability of EVA-Mg(OH)$_2$ Nanocomposites   Kalfus [65] incorporated 26 wt% of nano-MH (compared to conventional loading of 60–70 wt% of micro-MH) into ethylene vinyl acetate (EVA) resin, and found that the rate of weight loss was about the same as the micro-MH of the same weight loading. However, the thermal stability of the EVA–MH nanocomposite was slightly better. Qiao [68] added 33 wt% nano-MH into EVA and observed 43% reduction in PHRR, 43% reduction in mean HRR, and 182% increase in residue. Ly [69] also compared the effect of particle sizes on the flammability of EVA. Nano-MH and micro-MH of 80, 100, 120, and 150 phr (parts per hundred polymer) were incorporated into EVA, respectively. It was found that the LOI of the composite was increased from 18% to 39% by micro-MHs and to 46% by nano-MHs, respectively. However, all of the EVA nanocomposite, besides the 150 phr, failed the UL-94 burning test (while EVA-

150 phr nano-MH achieved V-2 rating). The addition of 100 phr nano-MH increased the time to ignition (TTI) from 87 to 148 s (70%), decomposition temperature from 438 to 470 °C (7%), and char yield from 0 to 6 wt%; and reduced the PHRR from 1655 to 423 kW m^{-2} (74%) and average HRR from 439 to 251 kW m^{-2} (43%). Ly then incorporated one more component (microcapsulated red phosphorus; MRP) into the nanocomposites and found a synergistic effect. While EVA with 100 phr nano-MH failed the UL-94 test, EVA with 100 phr of nano-MH and MRP (e.g., 95 phr nano-MH and 5 phr MRP) achieved a V-0 rating. The synergism also increased the LOI to 60%, TTI to 176 s (102% increase compared to neat EVA), decomposition temperature to 490 °C (12%), and char yield to 16 wt%; and reduced the PHRR to 148 kW m^{-2} (91%) and HRR to 72 kW m^{-2} (83.5%).

Flammability of PP-Mg(OH)$_2$ Nanocomposites   Mishra [70] incorporated 2, 4, 8, and 12 wt% of nano-MH into polypropylene (PP). It was found that the rate of burning per second was reduced with the increasing nanofiller composition. The reduction in the flammable property was as high as 35% compared to the neat PP. Mishra claimed that the reduction in flammability was due to the endothermic nature of the evenly dispersed nano-MH in the PP matrix.

Flammability of EPDM-Mg(OH)$_2$ Nanocomposites   Zhang [71] mixed 20–100 phr MH into ethylene-propylene-diene monomer rubber (EPDM) with particle sizes of 800 mesh, 1250 mesh, 2500 mesh, and nano. A decrease in PHRR with decreasing particle sizes was observed. Tang [72] incorporated 100MP (mass portion) of nano-MH into the EPDM (100MP)/Paraffin (100MP) system and found an increase of LOI from 17% to 28%. Tang claimed that a greater LOI value was obtained with higher content of nano-MH added and it was obvious that the addition of the nano-MH promote flame resistance.

Flammability of ABS-Mg(OH)$_2$ Nanocomposites   Cao [73] investigated the acrylonitrile–butadiene–styrene (ABS) system with nano-MH. The ABS/1 wt% nano-MH nanocomposite had similar flammability properties as the neat ABS polymer. However, when incorporating 5 wt% of the nano-MH, the PHRR reduced from 663 to 430 kW m^{-2} (35%), and THR from 107 to 96.8 MJ m^{-2} (9.5%); TTI increased from 30 to 67 s (123%), and time to reach PHRR from 169 to 245 s (45%). However, the combustion time was extended from 400 to 580 s (45%).

Flammability of SBR-Mg(OH)$_2$/PBR-Mg(OH)$_2$ Nanocomposites   Patil [74] incorporated 2–10 wt% of both conventional MH and nano-MH into styrene-butadiene rubber (SBR) and polybutadiene rubber (PBR), respectively. It was observed that the flame retardancy (improvement) in a burning test increased with increasing MH from 1.5 to 2.1 mm/s while conventional MH was used and from 1.6 to 2.3 mm/s when nano-MH was used. A similar trend was observed in the PBR/MH systems. The flame retardancy increased from 1.38 to 1.54 mm/s and 1.41 to 1.58 mm/s when conventional MH and nano-MH were used in the PBR

resin, respectively. According to the data, flame retardancy was noticeably enhanced by the MHs; however, the difference between the conventional MH and the nano-MH in both polymer systems was insignificant, although Patil claimed that the nano-MH provided a significant increase in flame retardancy in the SBR resin compared to the conventional filler.

Flammability of Epoxy-Mg(OH)$_2$ Nanocomposites Suihkonen [75] compared the flammability of epoxy resins filled with micro-MH and nano-MH. Weight loadings of 1%, 5%, and 10% of both fillers were incorporated into the epoxy, respectively. TTI of all samples were about the same. However, PHRR was reduced significantly from 933 kW m^{-2} (neat) to 572 kW m^{-2} (10% micro-MH) and 539 kW m^{-2} (10% nano-MH). THR and TSP (total smoke produce) were also decreased but the effects of micro-MH and nano-MH were about the same. THR was reduced from 124 to 114 MJ m^{-2} while TSP from 40 to 35–36 m^2. There was a significant decrease (71%) in the burning rate of the sample in the UL94HB burning test when 10 wt% of nano-MH was added, compared to the neat epoxy. Suihkonen also commented that the poor dispersion of the micro particles did not obstruct the functionality of the flame-retardant filler since the efficiency of MH in flammability was not significantly affected by the particle size of the filler or the surface treatment in this study.

3.4.3.4 Polymer POSS Nanocomposites

POSS-based nanocomposites have received increasing attention because of the unique three-dimensional structure of the POSS macromonomer [76] as shown in Figure 3.16. Early examples were presented with siloxane [77, 78] followed by numerous applications showing enhancement of thermal stability and improving the flammability properties of polymers. The thermal analysis study demonstrated the enhancement of thermal stability of polymer–POSS nanocomposites and suggested that there is a potential to improve the flammability properties of matrix polymers. Studies clearly demonstrating such improvement by means of the use of POSS-based nanocomposites are limited. Kashiwagi *et al.* [79] studied polytetramethylene ether-glyco-*b*-polyamide-12, 1% polyimide-12 (PTME-PA), polystyrene-polybutadine-polystrene (SBS), and polypropylene (PP) with POSS ranging from 10% to 20% via solution blending in tetrahydrofuran (THF). For comparison purposes, composites based on other silicone compounds, such as polycarbosilane (PCS) and polysilastyrene (PSS), were also prepared by solution blending. The flammability properties of these polymer blends were characterized using a cone calorimeter. The results shown in Figure 3.26 and Table 3.2 reveal that both PCS and POSS are reasonably effective for reducing the heat release rate measured at 35 kW m^{-2}. However, the total heat release of the nanocomposites was not significantly reduced from that of the polymer matrix. Furthermore, the residue yields are about the same as the theoretical yields as shown in Table 3.2. This means that the addition of POSS to the nanocomposites does not significantly increase the yield of carbonaceous char. The residue is mainly the inorganic component of the POSS.
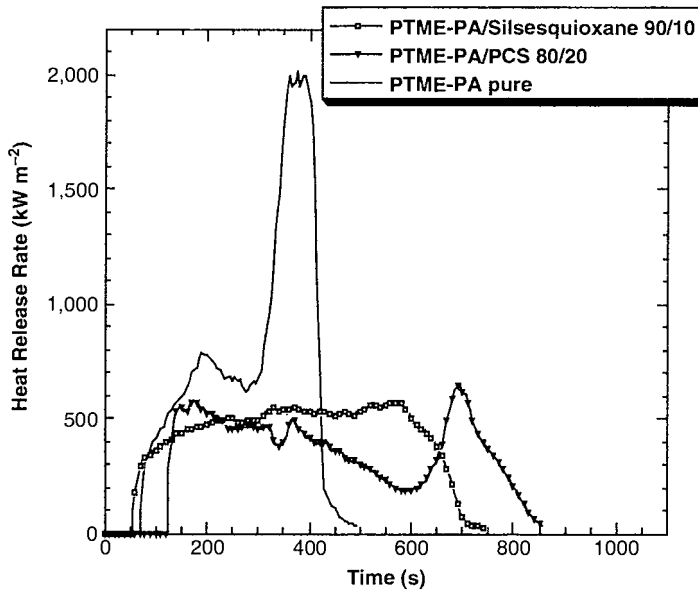
Figure 3.26 Heat release rates of PTME-PA with siloxane and the POSS at 35 kW m^{-2}.

Table 3.2 Summary of the cone calorimeter data of PP, PTME-PA, and SBS with siloxanes and POSS at 35 kW m^{-2}.

Sample	Residue yield[a] (%)	Mean mass loss rate (g m^{-2} s)	Peak HRR (kW m^{-2} (Δ%))	Mean HRR (kW m^{-2} (Δ%))	H_c (MJ kg^{-1})	SEA (m^2 kg^{-1})	Mean CO yield (kg kg^{-1})
PP	0	25.4	1466	741	34.7	650	0.03
PP/POSS 80/20	17 (16)	19.1	892 (40%)	432 (42%)	29.8	820	0.03
PTME-PA	0	34.2	2020	780	29.0	190	0.02
PTME-PA/PCS 80/10	15 (15)	14.8	699 (65%)	419 (46%)	28.5	260	0.02
PTME-PA/POSS 90/10	6 (8)	19.8	578 (72%)	437 (44%)	25.5	370	0.02
SBS	1	36.2	1405	976	29.3	1750	0.08
SBS/PCS 80/20	20 (15)	18.5	825 (42%)	362 (63%)	26.4	1550	0.07
SBS/POSS 90/10	6 (8)	31.2	1027 (27%)	755 (23%)	26.9	1490	0.07

H_c = mean heat of combustion; SEA = specific extinction area (smoke measurement). Uncertainties: ±5% of reported value of residue yields for heat release rate (HRR) and H_c data; ±10% for carbon monoxide and SEA data.
a) Theoretical residue yields in parentheses.

3.4.4
Multicomponent FR Systems: Polymer Nanocomposites Combined with Additional Materials

3.4.4.1   Polymer–Clay with Conventional FR Additive Nanocomposites

A combination of 65 wt% alumina trihydrate (ATH) and 35 wt% of a high level accepting polymer matrix, such as poly(ethylene-co-vinyl acetate) must often be used for cable outer sheaths [80]. The performances of two polymer blends were compared by Beyer [81, 82]. One blend was made from 65 wt% ATH and 35 wt% EVA (28 wt% vinyl acetate content), and a second blend was made from 60 wt% ATH, 5 wt% organoclay, and 35 wt% EVA. Both blends were investigated with TGA in air and by a cone calorimeter at $50 \, kW \, m^{-2}$. TGA in air clearly showed a delay in degradation by a small amount of organoclay [81, 82]. The char of the EVA–ATH–organoclay compound generated by the cone calorimeter was very rigid and showed only few small cracks. On the other hand, the EVA–ATH compound was much less rigid and with many big cracks. This could be the reason that the PHRR of nanocomposite was reduced to $100 \, kW \, m^{-2}$ compared to $200 \, kW \, m^{-2}$ for the EVA–ATH compound. To obtain the same decrease for PHRR by using just ATH in EVA, the content of ATH has to be increased to 78 wt% within the EVA–ATH system. To maintain $200 \, kW \, m^{-2}$ as a sufficient peak heat release rate level, ATH could be decreased from 65 to 45 wt% by the presence of 5 wt% organoclay within the EVA–ATH–clay system. The reduction of ATH resulted in improved mechanical and rheological properties of the EVA-based nanocomposite.

This research resulted in the commercial product FRNH cables passing UL-1666 as shown in Figure 3.27 [82]. The outer sheath was based on a nanocomposite with an industrial EVA–ATH–organoclay composition. The analogous coaxial cable was tested with an outer sheath based on EVA–ATH. Table 3.3 shows the results of the fire performance of these two coaxial cables [82]. The insulating and no burning char reduced the emission of volatile produce from polymer degradation into the flame area, and thus minimized the maximal temperature and height of the flames.
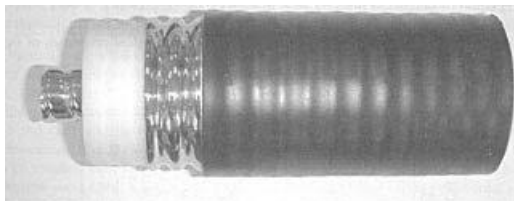
Figure 3.27   FRNH coaxial cable (1.27 cm diameter) with a nanocomposite-based outer sheath passing the UL-1666 cable fire test.

Table 3.3 Fire performance of FRNH coaxial cables with EVA–ATH and EVA–ATH–organoclay outer sheaths.

UL-1666 requirement	EVA–ATH compound	EVA–ATH–organoclay compound
Maximal temperature at 12 ft: <850 °F	1930 °F	620 °F
Maximal flame height <12 ft	>12 ft	6 ft

Table 3.4 Peak of heat release rates at 35 kW m^{-2} for various compounds with organoclays and multiwalled carbon nanotubes.

Sample	EVA[a] (parts resin)	MWCNT/ Purified (phr)	MWNCT/ Crude (phr)	Organoclay[b] (phr)	PHRR (kW m^{-2})
EVA[a]	100.0	–	–	–	580
1[c]	100.0	2.5	–	–	520
2	100.0	5.0	–	–	405
3	100.0	–	–	2.5	530
4	100.0	–	–	5.0	470
5[c,d]	100.0	2.5	–	2.5	370
6a[c]	100.0	–	5.0	–	403
6b[e]	100.0	–	5.0	–	405

a) Eaxorene UL-00328 with 28 wt% vinyl acetate content.
b) Nanofil 15.
c) The screw velocity was 45 rpm and the mass temperature was 136 °C.
d) The nanotubes and the organoclay were premixed before addition.
e) The screw velocity was 120 rpm and the mass temperature was 142 °C.

3.4.4.2 Polymer–Carbon Nanotubes with Conventional FR Additive Nanocomposites

EVA with purified MWNT, crude MWNT, and organoclay were investigated by Beyer [82–86] by a cone calorimeter at 35 kW m^{-2}. All compounds were melt-blended in a Brabender mixing chamber. It is evident from the results in Table 3.4 that all the filled polymers had improved flammability properties. The EVA and EVA-based nanocomposites containing 2.5 phr of the filler, the PHRR decreased as follows: EVA > organoclays ~ purified MWCNTs. For EVA and EVA-based composites containing 5.0 phr of the filler, the PHRR decreased as follows: EVA > organoclays > purified MWCNTs = crude MWNCTs. Crude MWCNTs were as effective as purified MWCNTs in the reduction of PHRR as purified MWCNTs. Increasing the filler content from 2.5 to 5.0 phr caused an additional flame-retardant effect that was most significant when purified or crude MWCNTs were used.
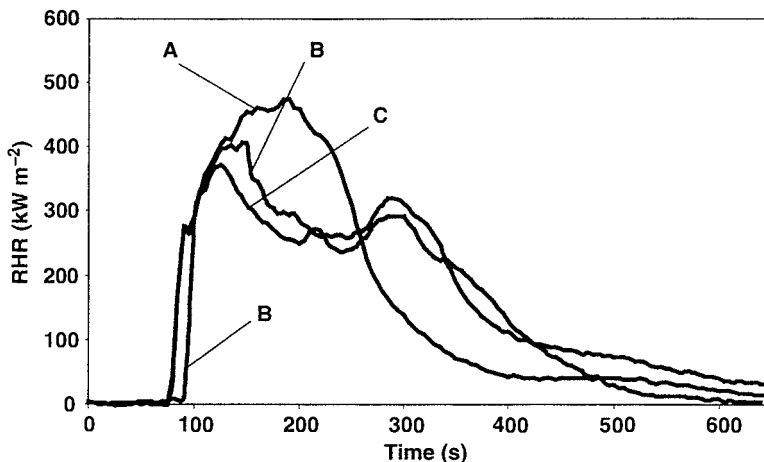
Figure 3.28 Heat release rates at 35 kW m^{-2} for various EVA-based materials: A is EVA + 5.0 phr organoclay; B is EVA + 5.0 phr pure MWCNT; C is EVA + 2.5 phr organo- clay + 2.5 phr pure MWCNT. EVA is Escorene UL-00328 with 28 wt% vinyl acetate content; organoclay is Nanofil 15 [59].

A synergistic effect for flame retardancy between MWNCTs and organoclays was observed for a nanocomposite containing 2.5 phr of purified MWCNTs and 2.5 phr of organoclays (Figure 3.28). The latter sample was found to be the best flame-retardant compound. The variation of screw velocity from 45 rpm (sample A) to 120 rpm (sample B) did not change the flame-retardant properties for composites containing 5.0 phr of crude MWCNTs. There was also no reduction in time to ignition for the EVA MWCNT-based composite, in contrast to the EVA organoclay-based composite.

3.4.4.3 **Polymer–Clay and –Carbon Nanotubes with Conventional FR Additive Nanocomposites**

Johnson *et al.* [87] studied the combined effects of MMT clay, CNF, FR additives on the mechanical and flammability properties of these PA11 nanocomposites for application in SLS. Test specimens of PA11 containing various percentages of intumescent FR additive, MMT clay, and CNF were prepared via the twin screw extrusion technique. Izod impact testing, tensile testing, and SEM analysis are used to characterize mechanical properties. UL-94 and SEM analysis of char surfaces are used to characterize the flammability properties of these materials. Results are analyzed to determine any synergistic effects among the additives to the material properties of PA11.

The results for the UL-94 vertical burn test of their materials are shown in Table 3.5. The baseline PA11 material received a V-2 rating because it produce burning drips, but was still self-extinguishing in less than 30 s. The two formulations with

Table 3.5 UL-94 vertical burn ratings for PA11 composites [87].

Formulation	MMT (%)	CNF (%)	FR (%)	UL-94 rating
Neat PA11	0	0	0	V-2
#1	2.5	2.5	0	Fail
#3	2.5	2.5	15	V-0
#4	2.5	2.5	20	V-0
#2	3.5	3.5	0	Fail
#5	3.5	3.5	15	V-0
#6	3.5	3.5	20	V-0
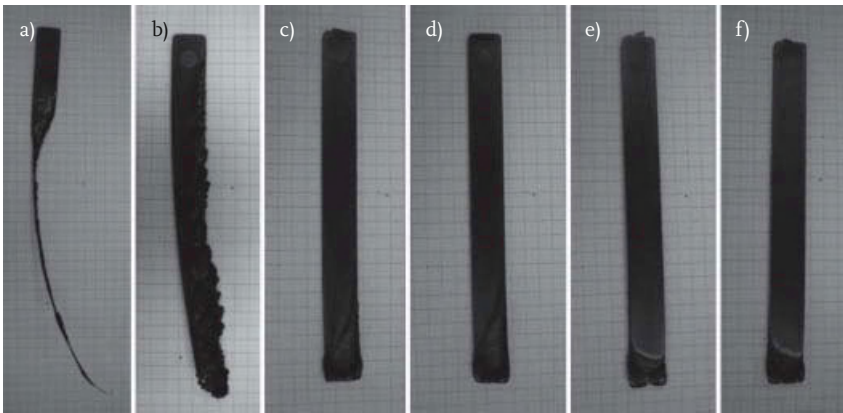
Figure 3.29 Posttest photos of UL-94 test specimens. Formulations 1 and 2 (a and b) can be seen to have burned significantly while formulations 3–6 (c–e) show no significant burn damage [87].

MMT clay and CNF, but no FR additive failed the test. In the PA11/2.5% MMT/2.5% CNF formulation, the material burned quickly once ignited and produced numerous viscous drips. The PA11/3.5% MMT/3.5% CNF also burned readily once it was ignited, but it only produced drips on 6 out of 10 tests and the drips were very viscous. All of the formulations with FR additive passed the test with V-0 ratings. They all immediately self-extinguished and produced no drips during testing. Photos of the posttest specimens are shown in Figure 3.29.

The results for the formulations without FR additive are as expected. It is not unusual for nanomaterial additives alone to fail to improve a material's flammability rating and there are typically most beneficial when used to improve the effectiveness of conventional FR additives [32]. The results for the remaining formulations are quite promising. In previous tests, where MMT clay and CNF

were combined with intumescent FR additives separately, such significant improvements in flammability properties were not observed with such low percentages of FR. In those experiments there were no formulations that were able to reach V-0 rating with only 15% FR, and there were several formulations that failed to reach it even at 20% FR [30, 32]. These results suggest that there is a synergistic effect between MMT clay and CNF in improving the flammability of PA11 composites when combined with conventional FR additives.

3.5
Flame Retardant Mechanisms of Polymer Nanocomposites

The mechanism of nanomaterials on the thermal and flammability properties of polymer nanocomposites has been widely investigated and different mechanisms have been proposed [88], but a comprehensive understanding of this phenomenon is not yet available. The enhancement of the thermal and flammability properties for the PNCs is very dependent on the matrix polymer as well as how the different types of nanomaterials are used to fabricate the PNCs. For polymer–clay nanocomposites, it is hypothesized that migration of the nanoclays to the surface of the matrix polymer occurs during combustion [88, 89]. One mechanism is due to the force of the volatile products produced in the bulk of the polymeric material. The numerous rising bubbles during combustion push the nanoclays upward from the burning area. Another mechanism is due to the recession of polymer from the surface during pyrolysis, leaving the dewetted nanoclay platelets behind. The decomposition of the organic modified in the clay will lead to aggregation of the clay. The migration of clay onto the surface was also confirmed by XRD and attenuated total reflectance Fourier transform infrared (ATR-FTIR) measurements on the isothermally heated samples [90]. It is observed, a minimum amount of clay platelets are needed to be present in order to have an effective char formation on the surface of the polymer nanocomposite.

It is proposed that the accumulation of clay at the surface of the degraded polymer acts as a barrier (ceramic shield) to both mass transport of degradation productions and thermal transfer of energy from the heat source to the polymer underneath the clay platelets. Figure 3.30 shows a schematic of the mechanism on how the clay barrier forms. This clay platelet barrier slows the rate of mass loss and will in term lower the HRR in a cone calorimeter experiment. The barrier function of the clay platelets can provide thermal insulation for the condensed phase and thus increased the thermal stability of the matrix polymer. No char formation were observed by burning the polyamide 6, but a significant amount of char was formed for polyamide 6 with 2 and 5 wt% clay. If the char is continuous, it will be more effective in enhancing flame retardancy [48].

The protective mechanisms for carbon nanofibers and carbon nanotubes are similar since they are both nanoscale diameter carbon fibers, but they are different from MMT nanoclay platelets. The carbonaceous residues from CNFs and CNTs form a continuous carbon network; as a result the CNFs and CNTs need to be
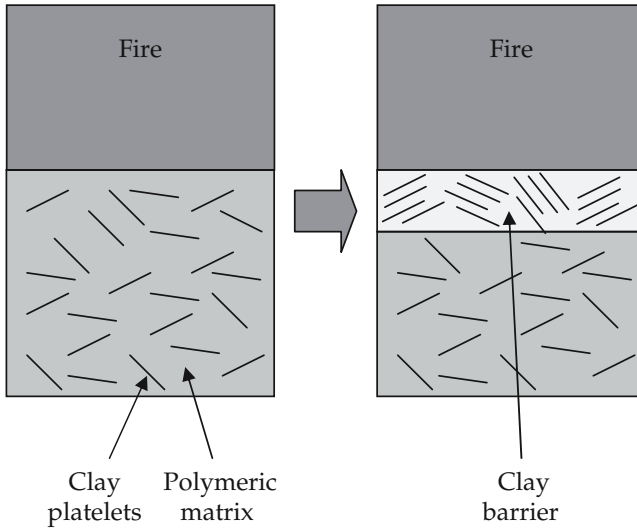
Figure 3.30 Schematic showing the mechanism of how the clay barrier forms.
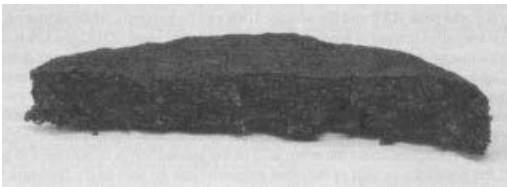
Figure 3.31 Cross section of the carbonaceous char residue of PP/1% MWNT [48].

uniformly distributed in the polymer nanocomposite. As the polymer degrades, a carbon network is formed. It is observed that a minimum amount of carbon network needs to be present in order to have an effective char formation on the surface of the polymer nanocomposite. Formation of a tougher char layer during the combustion process can also be observed in Figure 3.31 [48] for PP/MWNT on the surface of the matrix polymer is the primary pathway by which the nano-materials enhance the thermal and flammability properties of the matrix polymer. Crack-free and carbonaceous network barriers can significantly shield the heat and oxygen from the matrix polymer and reduce the heat release rate by slowing down the combustion process (Figure 3.32).
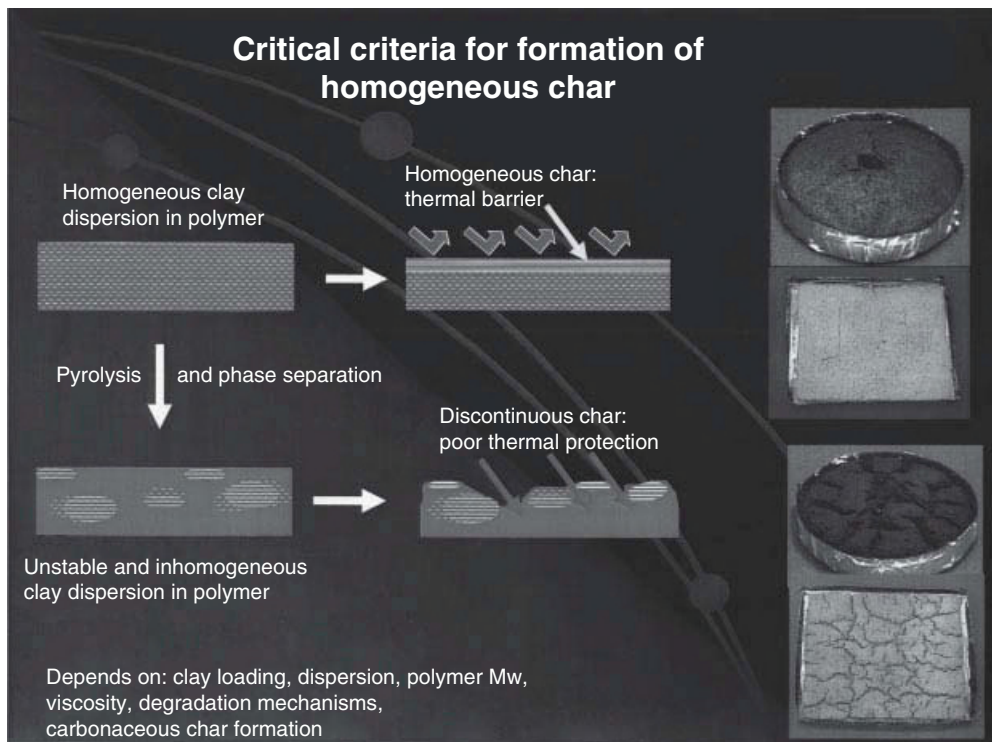
Figure 3.32 Mechanism of how crack-free and carbonaceous char network affects the thermal stability of the polymer matrix (courtesy of J. Gilman).

3.6
Concluding Remarks and Trends of Polymer Nanocomposites

Nanotechnology has a very bright future to improve the flame retardancy of polymeric materials. Although the nanomaterial by itself cannot achieve the fire properties required in industrial applications, the presence of the nanomaterial will enhance other desirable properties, such as mechanical, barrier, or electrical properties, and in combination with other conventional flame retardants, can provide better flame-retardant solutions. Finding new ways of applying nanomaterials cost effectively in polymers with desired properties, such as thermal and flammability, has been of increasing interest and is very challenging. Adaption of nanomaterials in polymers to promote the thermal and flame retardancy as well as other desired properties are warranted [91].

To promote the thermal and flame retardancy, and multifunctional properties of the polymer, one trend is to combine two or more nanomaterials into the polymer matrix to achieve a PNC which will consist of multicomponents. If synergism exists between these nanomaterials, the resulting PNC will exhibit better performance. Currently, MMT clay is considered as one component of the combined nanomaterials due to its low cost, availability, and its comprehensive per-

formance. Of increasing interest is the use of halloysite nanotubes and synthetic clays, such as fluorinated synthetic mica, magadiite, and layered double hydroxides (LDHs) to fabricate PNCs. However, the high cost and limited sources of the synthetic clays has been an obstacle for the wide usage of these nanomaterials.

Another trend is the use of other conventional FR additives, which are micron sized, to enhance the flame retardancy of the polymer matrix, such as using an additive that can form a glassy barrier to seal the crack in the char, resulting in self-extinguishing PNCs. One common and practical way is to use nanomaterials in the presence of conventional flame retardants, such as halogen-, or phosphorus-based, or as a nanosized component in a conventional FR system to achieve a flame-retardant polymeric composite. This includes nanoparticles, such as nano-$Mg(OH)_2$ and nano-$Al(OH)_3$, obtained from conventional inorganic FR additives that have original particle size in microns. Again, clay will be of great interest because of its excellent performance, such as the antidripping and charring properties, and/or the synergism with many conventional FR additives.

Other nanomaterials, such as CNFs, CNTs, POSS, NGPs, although expensive when comparing with MMT clay when used alone in the polymer matrix, can also be combined with the conventional FR system, to reduce the raw material cost and to improve the flame retardancy of the resulting PNCs.

Due to the thermal instability of the organic modifier of the nanoclays, it is most likely that advances in the future will occur with advanced polymers that can be processed below about 200 °C. As new surfactants are developed and commercialized, flame-retardant polymer nanocomposites that can be used for polymers that must be processed at higher temperatures may be developed. As the price of CNFs, CNTs, and POSS are coming down, they may be used as the next generation of flame-retardant nanomaterials. PNCs do offer many advantages – enhanced barrier, flame, mechanical, and electrical properties – so they will be used in multifunctional materials and the enhanced flame retardancy will be an added "bonus."

Acknowledgments

References

1 Lott, N. (2011) Introduction to nanoparticle, in *Nanoparticles in Nanotechnology* (ed. V.M. Rotello), The English Press, Delhi, India, p. 1.

2 Koo, J.H. (2006) An overview of nanoparticles, in *Polymer Nanocomposites*, McGraw-Hill, New York, pp. 12–30.

3 Bras, M.L., and Wilkie, C.A. (2005) Effect of clays on thermal degradation of flame retarded resin, in *Fire Retardancy of Polymers: New Applications of Mineral Fillers* (ed. M.L.E. Bras, C.A. Wilkie, S. Bourbigot, S. Duquesne, and C. Iama), Royal Society of Chemistry (Great Britain), Cambridge, UK, p. 158.

4 Saito, R., Jorio, A., Jiang, J., Sasaki, K., Dresselhaus, G., and Dresselhaus, M.S. (2010) Optical properties of carbon nanotubes and nano-graphene, in *Oxford Handbook of Nanoscience and Technology*, vol. 2 (ed. A.V. Narlikar and Y.Y. Fu), Oxford University Press, Oxford, UK, p. 1.

5 Huang, Y., Wu, J., and Hwang, K.C. (2006) Thickness of graphene and single-wall carbon nanotubes. *Phys. Rev. B*, **74** (24), 245413/1–9.

6 Meyer, J.C., Geim, A.K., Katsnelson, M.I., Novoselov, K.S., Booth, T.J., and Roth, S. (2007) The structure of suspended graphene sheets. *Nature*, **446** (1), 60.

7 Technical Bulletin Pyrograf®, Pyrograf Products, Inc., Cedarville, OH.

8 Shamsi, M.H., Luqman, M., Basarir, F., Kim, J.-S., Yoon, T.-H., and Geckeler, K.E. (2010) Plasma-modified halloysite nanocomposites: effect of plasma modification on the structure and dynamic mechanical properties of halloysite–polystyrene nanocomposites. *Polym. Int.*, **59** (11), 1492–1498.

9 Geckeler, K.E., and Rosenberg, E. (2006) *Functional Nanomaterials*, American Scientific Publishers, Valencia, CA.

10 Geckeler, K.E., and Nishide, H. (2009) *Advanced Nanomaterials*, Wiley-VCH Verlag GmbH, Weinheim.

11 Adam, F., Chew, T.-S., and Andas, J. (2011) A simple template-free sol–gel synthesis of spherical nanosilica from agricultural biomass. *J. Sol–Gel Sci. Tech.*, **59** (3), 580.

12 Technical Bulletin NanoArc® Aluminum Oxide, Nanophase Technology Corporation, 2011, Romeoville, IL.

13 Baskaran, R., Sarojadevi, M., and Vijayakumar, C.T. (2011) Unsaturated polyester nanocomposites filled with nano alumina. *J. Mater. Sci.*, **46**, 4864–4871.

14 Norouzbeigi, R., and Edrissi, M. (2011) Preparation of nano alumina powder via combustion synthesis: porous structure optimization via Taguchi L$_{16}$ design. *J. Am. Ceram. Soc.*, **94** (11), 4052–4058.

15 Yu, J.C., Xu, A., Zhang, L., Song, R., and Wu, L. (2004) Synthesis and characterization of porous magnesium hydroxide and oxide nanoplates. *J. Phys. Chem. B*, **108** (1), 64–70.

16 Xu, B.-Q., Deng, H., Dai, Y.-N., and Yang, B. (2007) Preparation of nanoparticles of magnesium hydroxide from bittern. *Trans. Nonferrous Met. Soc. China*, **17**, s671–s674.

17 Zheng, X.-T., Wu, D.-M., Meng, Q.-Y., Wang, K.-J., Liu, Y., Wan, L., and Ren, D.-Y. (2008) Mechanical properties of low-density polyethylene/nano-magnesium hydroxide composites prepared by an in-situ bubble stretching method. *J. Polym. Res.*, **15** (1), 59–65.

18 Sorathia, U., and Perez, I. (2004) Improving fire performance characteristics of composite materials for naval applications. *Polym. Mater. Sci. Eng.*, **91**, 292–296.

19 Troitzsch, J. (ed.) (2004) *Plastics Flammability Handbook*, 3rd edn, Hanser, Cincinnati, OH.

20 Hirschler, M.M. (2008), Chapter 3, in *NFPA Fire Protection Handbook*, 20th edn, NFFA, Quincy, MA.

21 UL (2006) 94. *Standard for Safety of Flammability of Plastic Materials for Parts in Devices and Appliances Testing*, Underwriters Laboratory, Northbrook, IL.

22 ASTM (1997) D 2863-97. *Standard Test Method for Measuring the Minimum Oxygen Concentration to Support Candle-Like Combustion Plastics (Oxygen Index)*, ASTM International, West Conshohocken, PA.

23 ASTM (2011) E 1354-11a. *Standard Test Method for Heat and Visible Smoke Release Rates for Materials and Products Using an Oxygen Consumption Calorimeter*, ASTM International, West Conshohocken, PA.

24 ASTM (2007) D 7309-07a. *Standard Test Method for Determining Flammability Characteristics of Plastics and Other Solid Materials Using Mircoscale Combustion Calorimetry*, ASTM International, West Conshohocken, PA.

25 ASTM (2011) E 84-11a. *Standard Test Method for Surface Burning Characteristics*

of Building Materials, ASTM International, West Conshohocken, PA.

26 Pinnavaia, T.J., and Beall, G.W. (eds) (2000) *Polymer–Clay Nanocomposites*, John Wiley & Sons, Ltd, West Sussex, England.

27 Utracki, L.A. (2004) *Clay-Containing Polymeric Nanocomposites*, Rapra Technology Limited, Shropshire, England.

28 Bhattacharya, S.N., Gupta, R.K., and Kamal, M.R. (2008) *Polymeric Nanocomposites—Theory and Practice*, Hanser, Cincinnati, OH.

29 Gilman, J.W., Kashiwagi, T., and Lichtenhan, J.D. (1997) Nanocomposites: a revolutionary new flame retardant approach. *SAMPE J.*, **33**, 40.

30 Lao, S.C., Wu, C., Moon, T.J., Koo, J.H., Morgan, A., Pilato, L.A., and Wissler, G. (2009) *J. Compos. Mater.*, **43** (17), 1803–1818.

31 Lao, S.C., Yong, W., Nguyen, K., Moon, T.J., Koo, J.H., Pilato, L.A., and Wissler, G. (2010) *J. Compos. Mater.*, **44** (25), 2933–2951.

32 Lao, S.C., Koo, J.H., *et al.* (2011) Flame-retardant polyamide 11 nanocomposites: further thermal and flammability studies. *J. Fire Sci.* **29**, 479–498.

33 Katsoulis, C.K., Kandare, E., and Kandola, B.K. (2009) Thermal and fire performance of flame-retarded epoxy resin: investigating interaction between resorcinol bis(diphenyl phosphate) and epoxy nanocomposites, in *Fire Retardancy of Polymers – New Strategies and Mechanisms* (ed. T. Richard Hull and B.K. Kandola), the Royal Society of Chemistry, Cambridge, England, pp. 184–205.

34 Zammarano, M. (2007) Thermoset fire retardant nanocomposites, in *Flame Retardant Polymer Nanocomposites* (eds A.B. Morgan and C.A. Wilkie), John Wiley & Sons, Inc., Hoboken, NJ, pp. 235–285.

35 Wang, Z., and Pinnavaia, T.J. (1998) Hybrid organic–inorganic nanocomposites: exfoliation of magadiite nanoclays in an elastomeric epoxy. *Polymer*, **10**, 1820–1826.

36 Triantafillidis, C.S., LeBaron, P.C., and Pinnavaia, T.J. (2002) Thermoset epoxy–clay nanocomposites: the dual role

of alpha, omega-diamines as clay surface modifiers and polymer curing agents. *J. Solid State Chem.*, **167**, 354–362.

37 Camino, G., Tartaglion, G., Frache, A., Manferti, C., and Costa, G. (2005) Thermal and combustion behavior of layered silicate–epoxy nanocomposites. *Polym. Degrad. Stab.*, **90**, 354–362.

38 Hussain, M., Varley, R.J., Mathys, Z., Cheng, Y.B., and Simon, G.P. (2004) Effect of organophosphorus and nano-clay materials on the thermal and fire performance of epoxy resins. *J. Appl. Polym. Sci.*, **91**, 1233–1253.

39 Hartwig, A., Purtz, D., Schartel, B., Bartholmai, M., and Wenschuh-Josties, M. (2003) Combustion behavior of epoxide based nanocomposites with ammonium and phosphonium bentonites. *Macromol. Chem. Phys.*, **204**, 2247–2257.

40 Gilman, J.W., Kashiwagi, T., Nyden, M., Brown, J.E.T., Jackson, C.L., Lomakin, S., Giannelis, E.P., and Manias, E. (1990) Flammability studies of polymer-layered silicate nanocomposites: polyolefin, epoxy, and vinyl ester resins, in *Chemistry and Technology of Polymer Additives* (eds S. Ak-Malaika, A. Colovoy, and C.A. Wilkie), Blackwell Science, Malden, MA, pp. 249–265.

41 Koo, J.H., Nguyen, K., Lee, J.C., Ho, W.K., Bruns, M.C., and Ezekoye, O.A. (2010) Flammability studies of a novel class of thermoplastic elastomer nanocomposites. *J. Fire Sci.*, **28** (1), 49–85.

42 Koo, J.H., Ezekoye, O.A., Lee, J.C., Ho, W.K., and Bruns, M.C. (2011) Rubber–clay nanocomposites based on thermoplastic elastomers, in *Rubber Clay Nanocomposites* (ed. M. Galimberti), John Wiley & Sons, Inc., New York, NY, pp. 489–521.

43 Avila, A.F., Dias, E.C., Lopes da Cruz, D.T., Yoshida, M.I., Bracarense, A.Q., Carvalho, M.G.R., and Avila, J., Jr. (2010) An investigation on graphene and nanoclay effects on hybrid nanocomposites post fire dynamic behavior. *Mater. Res.*, **13**, 143–150.

44 Koo, J.H., Leo, H., Clay, W., and Conaway, J. (2011) Methodology to evaluate epoxy nanocomposites for fire

protection application, in *AIAA Paper No. 2011-1799*, AIAA, Reston, VA.

45 Guo, Y., Bao, C., Song, L., Yuan, B., and Hu, Y. (2011) In situ polymerization of graphene, graphite oxide, and functionalized graphite oxide into epoxy resin and comparison study of on-the-flame behavior. *Ind. Eng. Chem. Res.*, **50**, 7772–7783.

46 Wang, Z., Tang, X.Z., Yu, Z.-Z., Guo, P., Song, H.-H., and Du, X.-S. (2011) Dispersion of graphene oxide and its flame retardancy effect on epoxy nanocomposites. *Chin. J. Polym. Sci.*, **3**, 368–376.

47 Higginbotham, A.L., Lomdea, J.R., Morgan, A.B., and Tour, J.M. (2009) Graphite oxide flame-retardant polymer nanocomposites. *Appl. Mater. Interfaces*, **1**, 2256–2261.

48 Kashiwagi, T., Du, F., Winey, K.I., Groth, K.M., Shield, J.R., Bellayer, S.P., Kim, H., and Douglas, J.F. (2005) Flammability properties of polymer nanocomposites with single-walled carbon nanotubes: effects of nanotube dispersion and concentration. *Polymer*, **46**, 471–481.

49 Kashiwagi, T. (2007) Progress in flammability studies of nanocomposites with new types of nanoparticles, in *Flame Retardant Polymer Nanocomposites* (eds A.B. Morgan and C.A. Wilkie), John Wiley & Sons, Inc., Hoboken, NJ, pp. 285–324.

50 Bulter, S., Kim, G., Koo, J.H., *et al.* (2011) Polyamide 11–halloysite nanotube nanocomposites: mechanical, thermal, and flammability characterization. Proceedings of 2011 SAMPE ISTC, SAMPE, Covina, CA.

51 Lao, S.C., Kan, M.F., Lam, C.K., Koo, J.H., Moon, T., Londa, M., Takatsuka, T., Kuramoto, E., Wissler, G., Pilato, L., and Luo, Z.P. (2010) Polyamide 11–carbon nanotubes nanocomposites: processing, morphological, and property characterization. Proceedings of 2010 Solid Freeform Fabrication Symposium, The University of Texas at Austin, Austin, TX.

52 Landry, C.J.T., Coltrain, B.K., Landry, M.R., Fitzgerald, J.J., and Long, V.K. (1993) Poly(vinyl acetate) silica filled materials: material properties of in-situ vs. fumed silica particles. *Macromolecules*, **26**, 3702–3712.

53 Hajji, P., David, L., Gerard, J.F., Pascault, J.P., and Vigier, G. (1999) Synthesis, structure, and morphology of polymer–silica hybrid nanocomposites based on hydroxyethyl methacrylate. *J. Polym. Sci. B*, **37**, 3172–3187.

54 Ou, Y., Yang, F., and Yu, Z.-Z. (1998) New conception on the toughness of nylon 6/silica nanocomposite prepared via in situ polymerization. *J. Polym Sci. B*, **36**, 789–795.

55 Reynaud, E., Jouen, T., Gauthier, C., Vigier, G., and Varlet, J. (2001) "Nanofiller in polymeric matrix" a study on silica reinforced PA6. *Polymer*, **42**, 8759–8768.

56 Hsiue, G.-H., Kuo, W.-J., Huang, Y.-P., and Jeng, R.-J. (2000) Microstructural and morphological characteristics of PS–SiO$_2$ nanocomposites. *Polymer*, **41**, 2813–2825.

57 Liu, Y.L., Hsu, C.Y., Wei, W.L., and Jeng, R.J. (2003) Preparation and thermal properties of epoxy–silica nanocomposites from nanoscale colloidal silica. *Polymer*, **44**, 5159–5167.

58 Kashiwagi, T., Gilman, J.W., Butler, K.M., Harris, R.H., and Shields, J.R. (2000) Flame retardant mechanism of silica gel/silica. *Fire Mater.*, **24**, 277–289.

59 Kashiwagi, T., Shields, J.R., Harris, R.H., and Davis, R.D. (2003) Flame-retardant mechanism of silica: effect of resin molecular weight. *J. Appl. Polym. Sci.*, **87**, 1541–1553.

60 Yang, F., and Nelson, G.L. (2004) PMMA/silica nanocomposite studies: synthesis and properties. *J. Appl. Polym. Sci.*, **91**, 3844–3850.

61 Kashwagi, T., Morgan, A.B., Antonucci, J.M., VanLandingham, M.R., Harris, R.H., Awad, W.H., and Shields, J.R. (2003) Thermal and flammability properties of a silica–poly(methylmethacrylate) nanocomposite. *J. Appl. Polym. Sci.*, **89**, 2072–2078.

62 Yang, F., Yngard, R., and Nelson, G.L. (2005) Flammability of polymer–clay and polymer–silica nanocomposites. *J. Fire Sci.*, **23**, 209–226.

63 Lao, S.C., Koo, J.H., Moon, T.J., Hadisujoto, B., Yong, W., Pilato, L., and Wissler, G. (2009) Flammability and

thermal properties of polyamide 11–alumia nanocomposites. Proceedings of 2009 Solid Freeform Fabrication Symposium, University of Texas at Austin, Austin, TX.

64 Rallini, M., Monti, M., Natali, M., Kenny, J.M., and Torre, L. (2011) Alumina nanoparticles as a filler of carbon fibre/epoxy composites for improved fire resistance. Proceedings of 2011 SAMPE ISTC, SAMPE. Covina, CA.

65 Kalfus, J., and Jancar, J. (2010) Effect of particle size on the thermal stability and flammability of $Mg(OH)_2$/EVA nanocomposites. *Comp. Interfaces*, **17**, 689–703.

66 Vesely, K., Rychly, J., Kummer, M., and Jancar, J. (1990) Flammability of highly filled polyolefins. *Polym. Degrad. Stab.*, **30**, 101–105.

67 Rychly, J., Vesely, K., Gal, E., Kummer, M., Jancar, J., and Rychla, L. (1990) Use of thermal methods in the characterization of the high-temperature decomposition and ignition of polyolefins and EVA copolymers filled with $Mg(OH)_2$, $Al(OH)_3$, and $CaCo_3$. *Polym. Degrad. Stab.*, **30**, 57–62.

68 Gui, H., Zhang, X.-H., Gao, J.-M., Dong, W.-F., Song, Z.-H., Lai, J.-M., and Qiao, J.-L. (2007) An EVA/unmodified nano-magnesium hydroxide/silicone rubber nanocomposite with synergistic flame retardancy. *Chin. J. Polym. Sci.*, **25**, 437–440.

69 Lv, J.-P., and Liu, W.-H. (2007) Flame retardancy and mechanical properties of EVA nanocomposites based on magnesium hydroxide nanoparticles/microcapsulated red phosphorus. *J. Appl. Polym. Sci.*, **105**, 333–340.

70 Mishra, S., Sonawane, S.H., Singh, R.P., Bendale, A., and Patil, K. (2004) Effect of nano-$Mg(OH)_2$ on the mechanical and flame-retarding properties of polypropylene composites. *J. Appl. Polym. Sci.*, **94**, 116–122.

71 Zhang, Q., Tian, M., Wu, Y., Lin, G., and Zhang, L. (2004) Effect of particle size on the properties of $Mg(OH)_2$-filled rubber composites. *J. Appl. Polym. Sci.*, **94**, 2341–2346.

72 Song, G., Ma, S., Tang, G., Yin, Z., and Wang, X. (2010) Preparation and characterization of flame retardant form-stable phase change materials composed by EPDM, paraffin and nano magnesium hydroxide. *Energy*, **35**, 2179–2183.

73 Cao, H., Zheng, H., Yin, J., Lu, Y., Wu, S., Wu, X., and Li, B. (2010) $Mg(OH)_2$ complex nanostructures with superhydrophobicity and flame retardant effects. *J. Phys. Chem. C*, **114**, 17362–17368.

74 Patil, C.B., Kapadi, U.R., Hundiwale, D.G., and Mahulikar, P.P. (2008) Effect of nano-magnesium hydroxide on mechanical and flame-retarding properties of SBR and PBR: a comparative study. *Polym.-Plast. Tech. Eng.*, **47**, 1174–1178.

75 Suihkonen, R., Nevalainen, K., Orell, O., Honkanen, M., Tang, L., Zhang, H., Zhang, Z., and Vuorinen, J. (2011) Performance of epoxy filled with nano- and micro-sized magnesium hydroxide. *J. Mater. Sci.* doi: 10.1007/s10853-011-5933-6

76 Hybrid Plastics, MS (2011) www.hybridplastics.com (accessed 15 October 2011).

77 Mantz, R.A., Jones, P.F., Chaffee, K.P., Lichtenham, J.D., Gilman, J.W., Ismail, I.M.K., and Burneister, M.J. (1996) Thermolysis of polyhedral oligomeric silsequioxane (POSS) macromers and POSS–siloxane copolymers. *Chem. Mater.*, **8**, 1250–1259.

78 Schwab, J.J., and Lichtenham, J.D. (1998) Polyhedral oligomeric silsesquioxane (POSS)-based polymers. *Appl. Orgamet. Chem.*, **12**, 707–713.

79 Kashiwagi, T., and Gilman, J.W. (2000) Silicon-based flame retardants, in *Fire Retardancy of Polymeric Materials* (eds A.F. Grand and C.A. Wilkie), Marcel Dekker, New York, pp. 353–389.

80 Herbert, M.J., and Brown, S.C. (1992) New developments in ATH technology and applications. Proceedings of the Flame Retardants '92 Conference, London, CT, January 12–13, 1992, pp. 100–119.

81 Beyer, G. (2007) Flame retardant properties of organoclays and carbon nanotubes and their combinations with alumina tri hydrate, in *Flame*

Retardant Polymer Nanocomposites (eds A.B. Morgan and C.A. Wilkie), John Wiley & Sons, Inc., Hoboken, NJ, pp. 163–190.

82 Beyer, G. (2005) Flame retardancy of nanocomposites: from research to technical products. *J. Fire Sci.*, **23**, 75–87.

83 Beyer, G. (2002) Carbon nanotubes as flame retardants for polymers. *Fire Mater.*, **26**, 291–293.

84 Beyer, G. (2002) Improvements of the fire performance of nanocomposites. Proceedings of the 13th Annual BCC Conference on Flame Retardancy for Polymers, Stamford, CT, June 3–6, 2002.

85 Beyer, G. (2005) Filler blend of carbon nanotubes and organoclays with improved char as a few flame retardant system for polymers and cable application. *Fire Mater.*, **29**, 61–69.

86 Beyer, G., Gao, F., and Yuan, Q. (2005) A mechanistic study of fire retardancy of carbon nanotube/ethylene vinyl acetate copolymers and their clay composites. *Polym. Degrad. Stab.*, **89**, 559–564.

87 Johnson, B., Allcorn, E., Baek, M.G., and Koo, J.H. (2011) Combined effects of montmorillonite clay, carbon nanofiber, and fire retardant on mechanical and flammability properties of polyamide 11 nanocomposites. Proceedings of 2011 SAMPE ISTC, SAMPE, Covina, CA.

88 Gilman, J.W. (2007) Flame retardant mechanism of polymer–clay nanocomposites, in *Flame Retardant Polymer Nanocomposites* (eds A.B. Morgan and C.A. Wilkie), John Wiley & Sons, Inc., Hoboken, NJ, pp. 67–87.

89 Kashiwagi, T., Harris, R.H., Zhang, X., Briber, R.M., Cipriano, B.H., Raghavan, S.R., Awad, W.H., and Shields, J.R. (2004) Flame retardant mechanism of polyamide 6–clay nanocomposites. *Polymer*, **45**, 881–891.

90 Lewin, M., *et al.* (2005) Nanocomposites at elevated temperatures: migration and structural changes. *Polym. Adv. Technol.*, **4**, 928.

91 Morgan, A.B., and Wilkie, C.A. (2007) Practical issues and future trends in polymer nanocomposite flammability research, in *Flame Retardant Polymer Nanocomposites* (eds A.B. Morgan and C.A. Wilkie), John Wiley & Sons, Inc., Hoboken, NJ, pp. 355–399.

4
PVT Characterization of Polymeric Nanocomposites

Leszek A. Utracki

4.1
Introduction

Two principal components of polymeric nanocomposites (PNCs) are polymeric matrix and nanoparticles dispersed in it, for example, natural or synthetic clays. In the IUPAC nomenclature, the nanoparticles must have at least one dimension in the nanometer range, ≤ 2 nm. The particles may be platy (only thickness being nanosized), two dimensional (i.e., fibers, nanotubes, or whiskers), or three dimensional (e.g., spherical metal or metal oxide atom clusters).

Depending on the volume and applications, PNCs are classified as structural (large volume) or functional (small volume for specialty applications). For the industrial production of structural PNC only layered nanoparticles are of interest. They are mainly crystalline natural clays with platelets ca. 0.7 to 1.7 nm thick, and the cation exchange capacity CEC = 0.8–1.2 meq g^{-1} [1].

Natural clays originate from the hydrothermal alteration of alkaline, 85–125 million years old volcanic ashes, deposited by winds in seas and lakes [2, 3]. As a consequence, chemical composition of even the same type of clay (e.g., montmorillonite, MMT) changes with geographical location and open mine strata. These clays contain impurities: (i) adsorbed organic compounds (e.g., humic substances, HS), (ii) nonexpandable clays (e.g., amorphous clays, vermiculite, kaolin), and (iii) diverse particulate minerals (e.g., quartz, sand, silt, feldspar, gypsum, orthoclase, apatite, halite, calcite, dolomite, quartz, biotite, muscovite, chlorite, opal, volcanic dust, fossil fragments, heavy minerals, sulfates, sulfides, carbonates, zeolites, hematite, etc.) [1, 4].

Originally, the resin manufacturers reactively produced PNCs, that is, polymerizing monomer(s) in the presence of preintercalated clay [5]. However, development of the melt compounding technology for PNC is more economic and it shifts their production to compounders and fabricators, adding flexibility and accelerating market penetration by PNC. In 2010 the PNC market reached 500 kton with the cost differential between the neat polymer and its PNC of about 10% [6]. Due to superior thermal and electrical conductivity as well as other properties, the

demand for PNCs is escalating for packaging, automotive, electrical, and coating applications.

4.2
Components of Polymeric Nanocomposites

In structural PNC ca. 2–5 wt% clay is dispersed in the polymer matrix: thermoplastic, thermoset, or elastomeric. However, since most clay/polymer systems are antagonistically immiscible, in analogy to immiscible polymer blends, compatibilization is required. The process comprises two steps: (1) conversion of clay into organoclay by intercalation with low molecular weight onium salts and (2) addition of functional compatibilizer(s). The amount of intercalant in organoclays is about 30–50 wt%, that is, 50–70 vol%. The amount of compatibilizer ranges from about 5 to 100 wt% of the polymeric phase.

Three types of clays are being used in industrial PNC: the natural, semisynthetic, and synthetic. Their characteristic feature is the ability to peel off individual layers, that is, to exfoliate. This ability is related to the imbalance of electronic charges in crystalline cells that must be compensated by hydrated ions in the interlayer galleries. Of prime interest are smectite clays with the general formula (Ca, Na, H) (Al, Mg, Fe, Zn)$_2$(Si, Al)$_4$O$_{10}$(OH)$_2$(xH$_2$O). The most important members of this group are MMT, hectorite (HT), saponite (ST), nontronite (NT), and beidellite (BT). These clays have three-layer structure of octahedral (Oc) sandwiched between two tetrahedral layers (Tc), namely MMT: [Al$_{1.67}$Mg$_{0.33}$(Na$_{0.33}$)]Si$_4$O$_{10}$(OH)$_2$, or HT: [Mg$_{2.67}$Li$_{0.33}$(Na$_{0.33}$)]Si$_4$O$_{10}$(OH/F)$_2$. Owing to substitution in Oc of Al^{+3} atoms by Mg^{+2} the MMT platelet has 0.25–1.2 negative charges per unit cell, that is, CEC $\approx$ 0.5–2 meq g^{-1}. In HT the charge imbalance is caused by replacing Mg^{+2} atoms in Oc by Li$^+$, while in ST replacement in Tc layers of Si^{+4} by Al^{+3} atoms, engender the CEC $\approx$ 1.3 meq g^{-1} [7].

The clays may be natural, semisynthetic, or synthetic. Thus, natural MMT from Wyoming has the aspect ratio $p = d/t \approx 280$, where d is the diameter and t is the clay platelet thickness. Its nominal orthogonal dimensions are: thickness $t \approx 1$ nm, width $W \approx 200$ nm, length $L \approx 300$ nm, with the ratio being nearly universal: $L/W \approx 1.5 \pm 0.1$. These dimensions follow the Gaussian distribution with the mean value $L_{av} \approx 280$ nm. The synthetic or semisynthetic clays have been produced with $p = 30$–6000; the ones with large platelets do not follow the Gaussian curve [1].

1) **Semisynthetic clays** are prepared by modification of natural minerals, for example, talc or obsidian. Thus, a powdery mixture of 10–35 wt% of a sodium hexafluorosilicate (Na$_2$SiF$_6$) and natural talc is heated for about 1 h at $T \approx 900\,°C$ producing fluoro hectorite (FH) or fluoro mica (FM). During this time, Na$^+$ or Li$^+$ partially replace Mg^{+2} in the talc Oc layer and fluorine partially replaces the –OH groups on the clay surface [8, 9].

2) **Fully synthetic clays** are formed starting with metal salts or oxides in appropriate proportions. Several subcategories are distinguished:

   a) Low-temperature, high-pressure hydrothermal synthesis that starts with aqueous solutions of appropriate salts, coprecipitated into crystallizing slurry [10, 11].

   b) The high-temperature melt process that starts with a mixture of, for example, Li_2O, MgO, SiO_2, and MgF_2; or SiO_2, MgO, and Na_2SiF_6, mixed in proper proportion, heated at 1300–1500 °C for 3h and then allowed to cool for 10h, yielding HT or FH [12].

   c) Synthesis of the layered double hydroxides (LDH) by coprecipitation of divalent and trivalent metal ions in an alkaline, aqueous medium [13, 14].

3) **Templated synthetic,** based on organic templates, which after synthesis may be pyrolyzed, or left in as intercalants (noncommercial) [15].

Recently three clays were tested [4]: (i) the natural MMT from Southern Clay Products Cloisite®-Na$^+$ (C-Na$^+$), (ii) the semisynthetic fluoro-mica or fluoro-hectorite, Somasif ME-100 from CBC Co., Japan (ME-100), and (iii) the fully synthetic fluoro-tetrasilicic mica from Topy Industries, Japan (Topy-Na$^+$). Their properties are listed in Table 4.1.

Three sets of information characterize the clays:

1) Size, size distribution, and shape of the clay platelets
2) Chemical composition
3) Impurities: type and quantity.

4.2.1
Size, Size Distribution, and Shape of the Clay Platelets

Clay sodium salt was exfoliated in demineralized water and a droplet of suspension deposited on a membrane filter with pore size = 220nm. Three orthogonal measures of platelets, L, W, and t, as well as their distribution, were determined in a

Table 4.1 Properties of the clays [4].

Property	C-Na$^+$	ME-100	Topy-Na$^+$
Specific/bulk density (g ml^{-1})	2.86/0.34	2.6/–	2.6/–
Particle diameter, d (µm)	2–13	5 to 7	4–10
Interlayer spacing, d_{001} (nm)	1.17	0.95	1.23
Platelets thickness, t (nm)	0.96	0.91	
Cation exchange capacity, CEC (meq g^{-1})	0.92	1.2	0.80
Nominal aspect ratio, p (–)	280	≤6000	≤5000
Clay reference	[16]	[9]	[17]
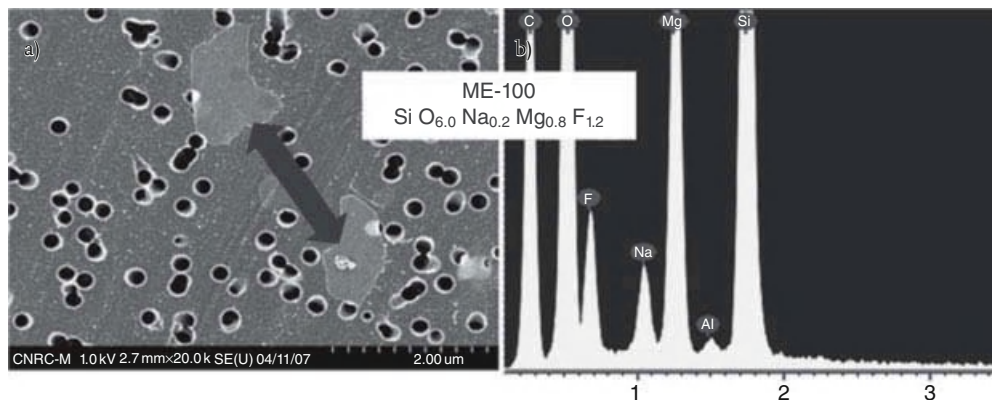
Figure 4.1 (a) SEM image of ME-100 clay platelets (the diameters of circular holes in the PC membrane are $d = 220\,nm$). (b) SEM/EDX spectrum of ME-100 [18].

Table 4.2 Statistical analysis of three clays [4].

Clay	Length L (nm)		Width, W (nm)		Ratios	
	L_n	L_w	W_n	W_w	$(L/W)_n$	$(L/W)_w$
Natural, C-Na$^+$	290	350	183	219	1.58	1.60
Semi-synthetic, ME-100	872	1097	572	743	1.52	1.48
Synthetic, Topy-Na$^+$	1204	1704	761	1186	1.58	1.44
Error					±0.2	±0.2

Note: Subscripts n and w indicate the number and weight averages, respectively.

scanning (SEM), transmission (TEM) or atomic force (AFM) microscope. Figure 4.1 displays an example and Table 4.2 the statistics.

4.2.2
Chemical Composition of Clays

Scanning electron microscopy and energy-dispersive X-ray analysis (SEM/EDX method) probes ca. $1\,\mu m^3$ of material at a time [19]; see the SEM/EDX spectrum in Figure 4.1. The SEM/EDS method analyzes the chemical composition and its crystalline cell size. A characteristic X-ray is produced when outer shell electrons replace the inner shell ones. Since clay may have locally diverse composition, it is important that several particles are sampled from at least five locations, each. An example of results is presented in Table 4.3.

The composition of minerals of micron-sized particles depends on their size (a core-shell compositional structure). Since there is a particle size distribution in

Table 4.3 Elemental composition of C-Na$^+$ and ME-100 clays [4].

Source	C-Na$^+$	ME-100
Nominal	$[Al_{3.34}Mg_{0.66}Na_{0.66}](Si_8O_{20})(OH)_4$	$(NaF)_{2.2}(MgF_2)_{0.1}(MgO)_{5.4}(SiO_2)_8$
Found	$[Al_{2.9}Fe_{0.6}Mg_{0.35}Na_{0.72}](Si_8O_{20})(OH)_4$	$(NaF)_{0.94}(MgF_2)_{2.3}(MgO)_{2.7}(SiO_2)_8$

commercial clay powders a large scatter of values (error $= \pm 5 - 15\%$) has been reported [20].

4.2.3
Impurities

Purification of natural clays into a polymer-grade material is a laborious, time-consuming process of about 300 steps. The patented method leads to clay sodium salt, which contains ≤ 5 wt% ("preferably less than about 2% by weight") of impurities, such as amorphous silicates, stacks of welded (by a crystallographic defect) platelets, and the residual 0.3–2 wt% quartz particles with size exceeding 300 nm [21]. Furthermore, the commercial clay contains about 2 wt% of moisture and 7 wt% of "loss on ignition," LOI (comprising organics, hygroscopic and bound H_2O, carbonic acid, etc.).

Table 4.4 lists impurities identified in natural (C-Na$^+$) and semisynthetic (ME-100) clays. For the analysis of contaminants clay was dispersed in water and centrifuged. The sediment was analyzed by the X-ray diffraction method.

Table 4.4 Impurities in C-Na$^+$ and ME-100 from XRD [22].

C-Na$^+$	ME-100
Vermiculite, quartz, cristobalite, rutile, albite, microcline, aragonite, vaterite, dolomite, gypsum, anhydrite, alunite, sylvite	Vermiculite, gypsum

4.3
Pressure–Volume–Temperature (*PVT*) Measurements

4.3.1
Transitions

Within the full temperature range from 0 K to the thermal decomposition temperature, $T_{dec} = 380–1170$ K [23] polymers undergo several transitions. Of these the best known are the melting temperature of crystalline polymers, T_m, and the glass

transition temperature of amorphous, T_g – the former is the first-order thermodynamic transition whereas the latter is a kinetic one. In addition to these major transitions there are others smaller ones detectable on the derivative properties, for example, the compressibility and the thermal expansion coefficients (κ and α, respectively):

$$\kappa \equiv (\partial \ln V / \partial P)_{T,P^o,q}; \quad \alpha \equiv (\partial \ln V / \partial T)_{T^o,P,q} \tag{4.1}$$

where P^o and T^o are solidification pressure and temperature, respectively, and q is the rate of heating or compressing.

The first transition at $T \leq 80\,K$ was theoretically predicted by Simha *et al.* [24] who assumed that at these low temperatures the intersegmental interactions follow Einstein's equation for harmonic oscillators with the universal Einstein reduced quantum temperature. Good agreement between the theory and experiments was demonstrated at ambient P for several chemically different polymers. At higher temperatures (but below T_g) there are other glass–glass transitions, identified by letters of the Greek alphabet [25]. Of these $T_\beta \approx 0.8T_g$ is the most important as it limits the region of physical aging of vitreous materials [26].

Also at $T > T_g$ there are transitions such as the cross-over one, $T_c/T_g \approx 1.15–1.35$. The magnitude of this ratio was found dependent on the fragility index [27, 28]:

$$m = \left(\frac{1}{T_g}\right)\left(\frac{d\log\eta}{d(1/T)}\right)_{T=T_g} \tag{4.2}$$

The transition at T_c is readily observed by neutron scattering and other vibrational spectra, in dielectric or rheological measurements, but not readily in *PVT*. The mode-coupling theory (MCT) considers liquid as an assembly of particles enclosed in cages formed by their neighbors with α-relaxation controlling the behavior. Only at $T > T_c$ the molecular vibrations dominate. Götze and Sjogren wrote: "T_c seems to be an equilibrium parameter of the system, which separates the supercooled liquid state in two regions" [29]. Semicrystalline polymers have a dual nature, in part being amorphous, in part crystalline. In most such polymers $T_m \approx 1.5T_g$ [30].

4.3.2
Determination of PVT

The *PVT* data are often represented as a surface in $V = V(T, P)$ coordinates. The measurements are carried out in two steps: (1) determination of the specific volume under well-defined ambient conditions, V_o, and (2) measurements of changes, ΔV, caused by programmed variation of T and P; thus,

$$V(T,P) = V_o(T_o,P_o) + \Delta V(T,P) \tag{4.3}$$

ΔV measurements are carried out in a pressure dilatometer. Several of these have been described in the literature, home-made or commercial, but most of the results originate from the Gnomix dilatometer (from Gnomix Inc., Boulder, CO)

[31, 32]. This fully automated instrument is based on the principle of confining the tested specimen in Hg. The pressure ranges from ambient to 200 MPa, and the temperature from ambient to 400 °C. Variations of ΔV may be determined with accuracy of 0.0002 ml g^{-1} at the heating or cooling rate ≤ 5 °C min^{-1}.

Before the *PVT* test, polymer samples need to be dried, and then V_o is determined. Dry samples are loaded to the dilatometer, premolded at $T \geq 130$ °C, and then cooled to room temperature (RT) at a rate of ca. 1 °C min^{-1}. The premolded specimens are tested following the selected procedure within the range of temperatures, $T = 300$–590 K, and pressures, $P = 0.1$–190 MPa. For example, following the "standard" procedure at each *T*-level P is increased from ca. 10 to 190 MPa in steps of 20 or 30 MPa. The T is increased from RT in steps of about 10 °C. Depending on the selected rate of heating or cooling, the measurement of 350–750 data points takes 16–36 h. The four procedures used for *PVT* tests are listed in Table 4.5.

Distinctly different PVT plots obtained from three procedures are seen in Figure 4.2. The "standard" test in Figure 4.2a and the isobaric cooling one (at a high cooling rate of 10 °C min^{-1}) in Figure 4.2c show large transitory regions below T_g. Only the isobaric heating in Figure 4.2b resulted in a regular behavior with nearly constant slopes (a measure of the thermal expansion coefficient, α) in the vitreous and molten phase. Evidently, different procedures are used for different purpose. For example, the standard procedure guarantees that specimens see the highest temperature only at the end of the test; thus the measurements are less affected by thermal degradation. The isobaric cooling from $T \approx T_g + 30$ °C has been used for studying the thermodynamics of glass transition [33, 34].

Table 4.5 Procedures of *PVT* measurements.

Procedures	Constant variable	Adjusted variable
Isothermal heating ("standard")	T is kept constant until *P*-sweep is completed, then T is increased to another level between the ambient and the maximum level, T_{max}	P increases from 10 to 200 MPa
Isothermal cooling	Initially $T \approx T_g + 30$ °C is constant until *P*-sweep is completed, then T is decreased to another level toward the ambient T	P increases from 10 to 200 MPa
Isobaric heating	P is kept constant until *T*-sweep is completed, then P is increased to another level between 10 and 200 MPa	T increases from ambient to T_{max}
Isobaric cooling	P is kept constant until *T*-sweep is completed, then P is increased to another level between 10 and 200 MPa	T decreases from $T \approx T_g + 30$ °C to ambient

Note: As P increases the resulting adiabatic heating increases the set T by up to 5 °C. In principle, the experiments may also be conducted reducing P.
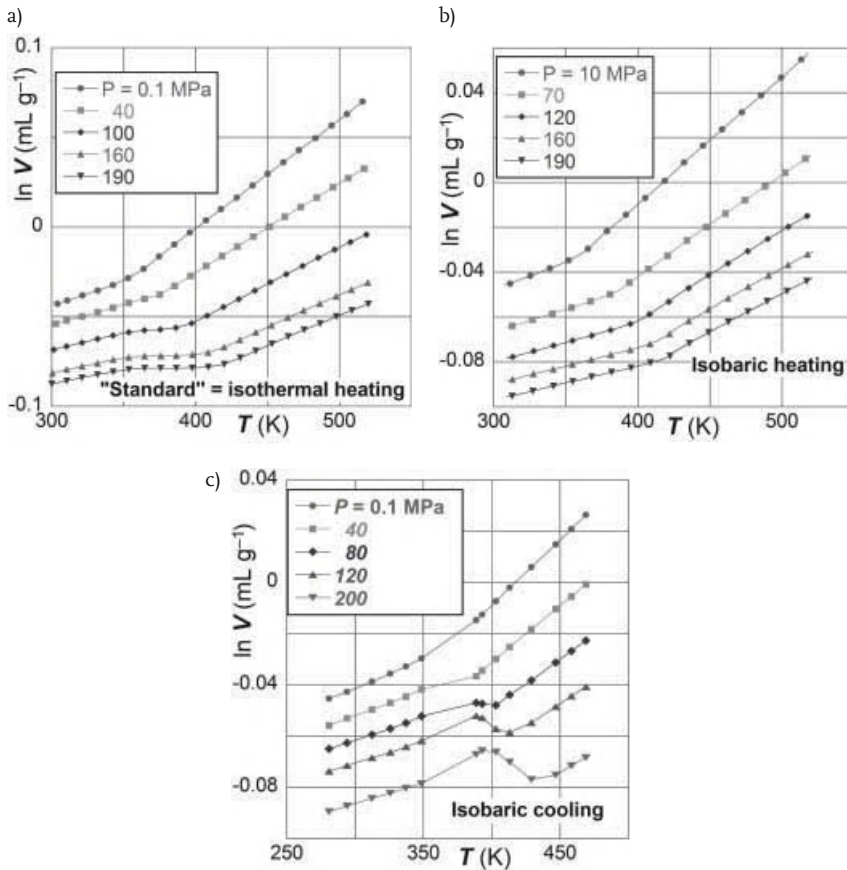
Figure 4.2 PVT dependences of polystyrene (PS). The measurements followed the procedures: (a) isothermal heating, (b) isobaric heating, and (c) isobaric cooling. For clarity only five constant *P* curves are displayed with 20% of the experimental points shown.

4.3.3
Effects of Clay, Intercalant, and Compatibilizer

The discussion in the preceding parts focused on neat polymers. In the case of PNC the procedure needs to be slightly modified. The expandable clay contains ca. 7 wt% of moisture that may falsify the high-*T* response. Furthermore, PNC shows barrier properties for vapors and gases dependent on the clay aspect ratio, its degree of dispersion, concentration, and orientation. Consequently, the drying time of PNC samples may be significantly longer than that of the neat resin. For example, to reach constant weight during vacuum drying at 80 °C PA-6 required 48 h but its PNC with 2 wt% organoclay 161 h [35, 36].

Commercial organoclay may contain 25–40 wt% excess of the intercalating onium salt. This low molecular weight compound brings into PNC a large quantity of free volume that may significantly affect the *PVT* behavior. Highly polar PA-6 strongly interacts with crystalline clays having high surface energy [37]. The interactions are so strong that PA-6 expels intercalant from the clay surface and forms a 4–6 nm thick solid layer of polymer, followed by an about 100 nm thick layer of organic molecules with increasing mobility as the distance from the clay surface increases [35, 38]. In these PNCs adsorption and solidification reduce the free volume by ca. 15%.

As in polymer alloys and blends (PAB), also in PNC the two principal components, polymer and organoclay, are thermodynamically immiscible and compatibilization is desirable. The thermodynamic theories of PNC treat nanosized clay platelets and polymeric macromolecules as statistical elements of the network; thus if exfoliation is required, system miscibility must be assured. Since macromolecular diffusion into the clay gallery decreases the entropy, $\Delta S < 0$, the miscibility might be expected only if enthalpy is negative, $\Delta H < 0$, that is, if the specific interactions are strong [39]. However as in PAB, compatibilizers may also be used for modifying the PNC performance, for example, by toughening the matrix, changing permeability, etc. Thus their overall effect on the *PVT* behavior is not necessarily predictable.

4.4
Derivatives, Compressibility, and Thermal Expansion Coefficient

4.4.1
Interpolating the Data

The raw data that come from automatic dilatometers usually have well-defined constant *P*-values, but because of the adiabatic effect *T* is different at each *P* level. Thus, if the derivatives α and κ are required, one needs to have evenly spaced data points at constant *T* and *P*. Three methods have been applied to accomplish this.

I)   Fitting the data to an equation and then computing the function value at desired intervals of *T* and *P*; for that an empirical Tait equation has been used [40, 41].

II) As an alternative to the first method, one may fit the data to a polynomial, which subsequently is differentiated according to definitions in Eq. (4.1).

III) The third approach is a simple interpolation to the same *T*-value at *P* = *constant*, thus correcting for the adiabatic heating. The interpolation may be linear or polynomial.

All three methods may find their usefulness, but if derivatives are to be used for detecting small transitions, only the last interpolative method III is acceptable.

4.4.2
Computation of the Thermal Expansion and Compressibility Coefficients, α and κ

According to definition in Eq. (4.1), α and κ are slopes of $\ln V$ as a function of T or P, respectively, while keeping the second independent variable constant. The experience shows that the most objective method for extracting these derivatives from *PVT* data is direct numerical differentiation of data at a constant value of the second variable, P or T. There are numerous computer programs that perform differentiation by the "moving arch" method, but the one that is most convenient permits selection of the number of data points used in each differentiation step. For fitting a curve, the minimum number of data points is 3 and usually the maximum number is 9 – the smaller the number the larger the scatter and high sensitivity to small functional variation, while the larger the number of data points the smoother the differential and with risk of erasing important local information [42, 43]. The most popular is the "5 point formula," equivalent to locally fitting a fourth-degree polynomial. The error of the derivation depends on the symmetry of the computation, the number of data points in formula, and the distance between the abscissa-independent variable, Δx. Thus, for symmetric computation with five points the derivative is

$$y'_o = [y_{-2} - 8y_{-1} + 8y_1 - y_2]/12\Delta x \tag{4.4}$$

The error depends on the size of the step Δx and the form of the $y = y(x)$ dependence.

4.4.3
Polymer α and κ from PVT

Numerical differentiation of dependences displayed in Figure 4.2 leads to the temperature-dependent thermal expansion and compressibility coefficients presented in Figures 4.3 and 4.4, respectively.

It is noteworthy that at $T > T_g$ the numerical values of α are similar for neat PS-686 and PS-667 with lubricant. The different *PVT* test procedure is reflected in the lower-T data. The sequence of data collection during "standard" isothermal heating starts with data point at lowest T and P, and then zigzagging down and up for each isothermal step ends in the uppermost point at the highest T. For $P > 40\,MPa$ the procedure results in densification of the vitreous phase and reduction of α to zero. For PS-686 the *beta*-temperature increases with pressure as $T_\beta = 265 + 0.59\ P$ (MPa) with $r = 0.991$, that is, for the range P it varies between 265 and 378 K [34]. When $T_\beta \leq T \leq T_g$ the compressed glass may relax. The simplest α-dependences were obtained by isobaric heating (Figure 4.3b) where the overcompression evident in Figure 4.3a is absent. In these two test procedures the data were collected at a rate of $\leq 25\,min/data$ point, that is, ca. 2 °C h^{-1}. The rate used during the isobaric cooling (Figure 4.3c) was higher, ca. 10 °C h^{-1}. Upon cooling at $P > 40\,MPa$ below T_g the coefficient α decreases down to negative values (volume expansion) and then increases to the value typical for the vitreous phase.

a)

b)

c)
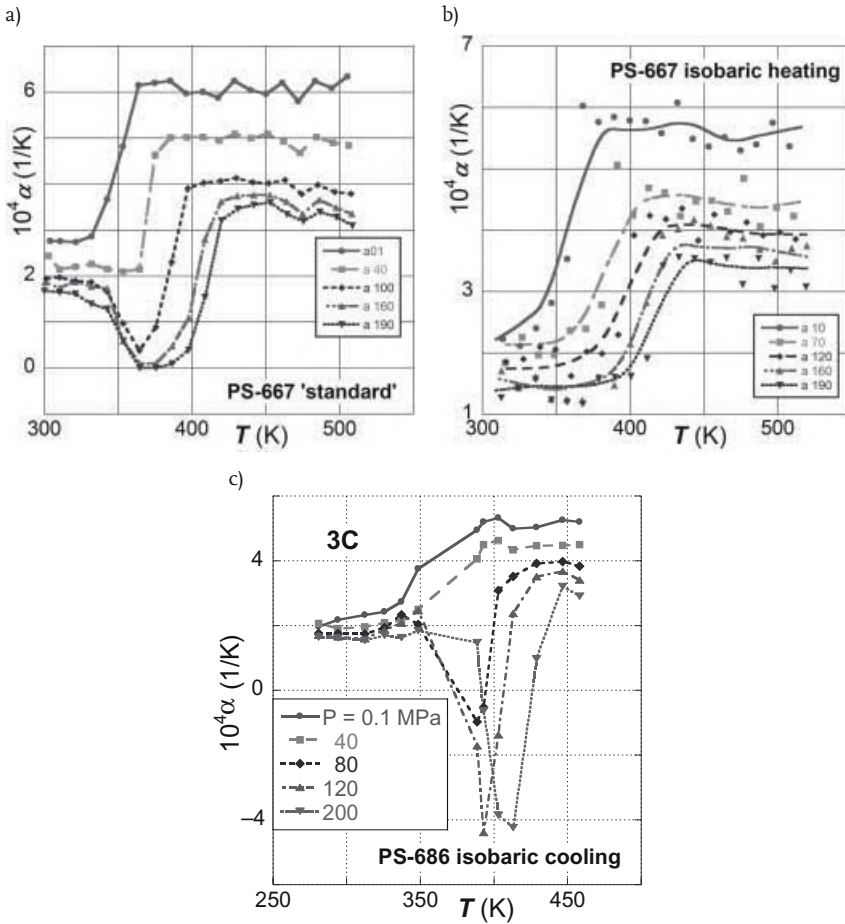
Figure 4.3 Volumetric thermal expansion coefficients versus T, computed from data in Figure 4.2. For clarity only five constant P curves and every fourth point are shown.

This kinetic effect is related to the presence of the nonequilibrium fractal structure of PS melt in the vicinity of T_g [44, 45].

Figures 4.3 and 4.4 show that while the thermal expansion coefficient, $\alpha = \alpha(T)$, within the vitreous and molten phase varies little with T, the compressibility coefficient, $\kappa = \kappa(T)$, increases in both phases. A transitory behavior of these two coefficients at $T \leq T_g$ is evident for isothermal heating and isobaric cooling PVT procedures at $P > 40$ MPa. It is worth noting that all three procedures lead to acceptable agreement of $\kappa = \kappa(T)$ functions at $T > T_g$, especially at lower P. Characteristically, in Figures 4.2–4.4 there is weak evidence for the presence of other transitions than T_g, for example T_c at 475 ± 5 K. On the other hand, $T_\beta \approx 0.8T_g = 290$ K is near the lowest temperature of the PVT scans and thus impossible to observe.
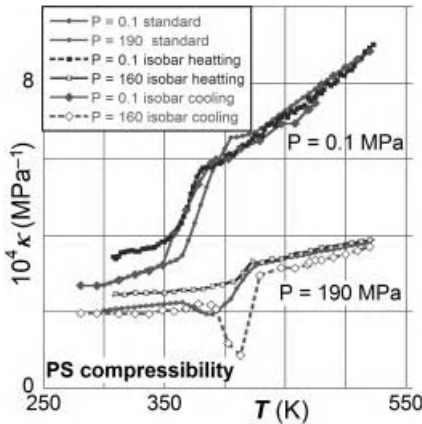
Figure 4.4 Volumetric compressibility coefficients versus *T*, computed from data in Figure 4.2. For clarity only curves for *P* = 0.1 and 190 MPa (with every fourth point) are shown.

4.4.4
Effect of Clay on α and κ in PS-Based PNC

In the following parts the data obtained from the "standard" *PVT* isothermal heating procedure will be discussed.

The PS-based CPNCs were prepared by melt compounding commercial, slightly lubricated PS-1301 (M_w = 270 kD) with 0–17.1 wt% of Cloisite® 10A organoclay (C10A = MMT + 39 wt% of di-methyl-benzyl hydrogenated tallow ammonium chloride, 2MBHTA) in a twin screw extruder (TSE). The details have been published by Tanoue *et al.* [46–48]. As it will be repetitively shown in this chapter, in PNCs there are two critical concentrations: w_1 limits the possibility of free rotation of exfoliated clay platelets and w_2, at which all matrix molecules are adsorbed by dispersed clay stacks. For the PS/C10A system, w = 1.1 and 3.6 wt% clay.

Figures 4.5–4.7 display computed values of α as a function of *P*, *T*, and *w*. In the glassy (subscript g) state α_g shows two types of behavior. For clay loadings $w \leq 2\%$ it has a low value decreasing with *P* to about zero, whereas for $w > 3.6\%$ its values are negative, that is, heated specimen shrinks with *T* instead of expanding. The magnitude of α_g at $T < T_g$ strongly depends on the cooling process from the melt. In the molten state (subscript m) the isobaric values of α_m are nearly constant, independent of *T*. As shown in Figure 4.6, the addition of clay reduces α_g in the full range of the investigated *P*. However, the decrease is nonuniform – in the vicinity of w_2 = 3.6 wt% the function takes a dip. A similar but stronger local decrease is observed in the melt; Figure 4.7 displays $\alpha_m = \alpha_m(w)$ at ambient pressure and its pressure gradient.

Figures 4.8 and 4.9 show the compressibility coefficients, κ, computed from *PVT*, as functions of *P*, *T*, and *w*. By contrast with α, compressibility tends to increase with *T*. However, the temperature dependence of κ decreases with *P* virtually to zero at the highest *P* and *w*. This observation is confirmed by the $\kappa = \kappa(w)$ dependences shown in Figure 4.9 – excepting a local dip of the func-
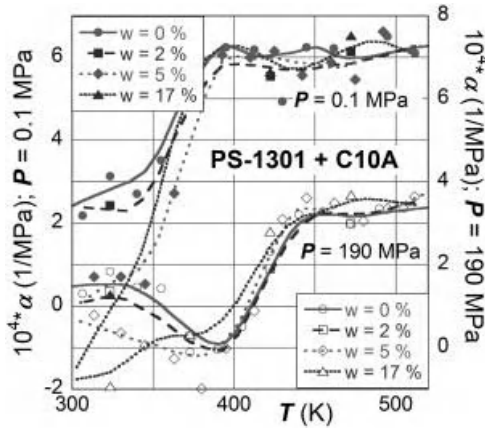
Figure 4.5 Temperature dependence of the volumetric thermal expansion coefficient at two pressures and four concentrations.
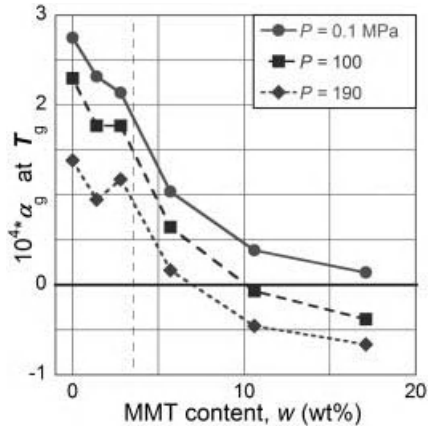
Figure 4.6 The thermal expansion coefficient at $T < T_g$ and $P = 0.1$, 100, and 190 MPa versus clay content.

tion near $w_2 = 3.6$ wt% at constant T and P the function is nearly constant. Thus, the dip observed in the vitreous and molten state in $\alpha = \alpha(w)$ is also evident in $\kappa = \kappa(w)$.

4.4.5
Effect of Clay on α and κ in PA-6 Based PNC

There are two transitions of interest in dry PA-6: the glass transition temperature T_g(PA-6) ≈ 323 K and the melting point at T_m(PA-6) ≈ 500 K, both dependent on P as well as on the method of material preparation. The *PVT* measurements of PA-6 ($M_w \approx 22$ kD), its PNC-2 and PNC-5 containing 2.29 ± 0.13 and 4.91 ± 0.24 wt% of clay (inorganic content), respectively, were carried out at $T = 300$–580 K and
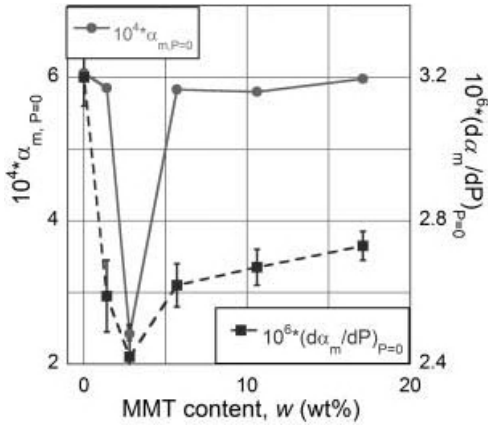
Figure 4.7 The thermal expansion coefficient at $T > T_g$ and its pressure gradient as a function of the clay concentration, w.
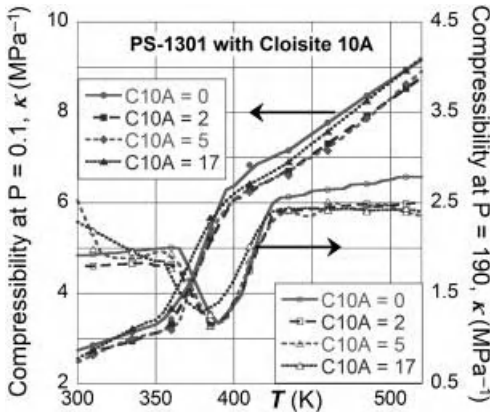
Figure 4.8 The compressibility coefficient versus T at $P = 0.1$ and 190 MPa for PNC containing: $w = 0$, 2, 5, and 17 wt%.

$P = 0.1–190$ MPa [49]. The PNCs were prepared reacting ε-caprolactam in the presence of MMT preintercalated with ω-amino-dodecyl-acid (ADA), thus forming a bonded structure: MMT↔ADA↔PA-6.

The derivatives α and κ were computed by numerical differentiation of the *PVT* isobaric or isothermal dependences, following Eq. (4.1). Because of the closeness of T_g to the starting temperature, this transition was ignored – the attention was focused on T_m and its variation with independent variables, *P*, *T*, and *w*.

The thermal expansion coefficient for PA-6 and its PNCs is shown in Figure 4.10. For ease of comparison the three graphs are on the same scale – the crystalline phase is separated from the melt by a "chimney-like" melting zone. It
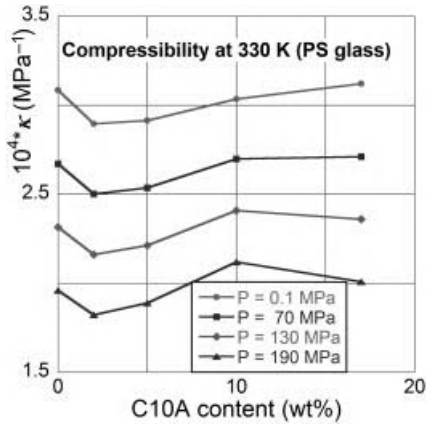
Figure 4.9 The compressibility coefficient at $T < T_g$ as a function of the clay concentration, w.

is evident that addition of clay affects both phases – it reduces α of the solid phase and significantly modifies the melt behavior. Comparing PNC-2 with PA-6 at $T > T_m$ one notes that while the shape of the dependences is similar, the low-P expansion is larger. By contrast, PNC-5 behavior at $T < T_m$ is similar to that of PA-6, but above T_m the function $\alpha = \alpha(T)$ decreases instead of increasing. This behavior might be related to the presence of high crystallinity regions in the vicinity of the MMT high-energy surface.

The compressibility coefficient versus T for PA-6 and its two PNCs is displayed in Figure 4.11. The data points were computed from PVT, whereas the lines represent polynomial fitted to all data except those in the melting zone at 470–500 K. Two aspects are noteworthy: (i) the dependence $\kappa = \kappa(T)$ follows the same dependence on both sides of T_m, and (ii) at low P compressibility slightly increases with clay content (at high P the behavior of all three materials is the same). As it will be shown in Section 4.7, the first aspect is fully predicted by the theoretical analysis of α and κ as functions of P and T [50, 51]. The enhanced compressibility at low P might be related to the presence of the low molecular weight ADA intercalant with its large free volume cushioning the MMT platelets in the PA-6 matrix.

4.5
Thermodynamic Theories

Up to this point all discussion was based on experimental data: measuring the PVT surface and then differentiating it for extracting the α and κ derivatives as functions of P, T, and w. However, with adequate theory one may determine other thermodynamic quantities such as binary interaction parameters, cohesive energy density, solubility parameters, internal pressure, and others. Furthermore, since the theory relates the material behavior to the presence of free volume, it offers

a)

b)

c)
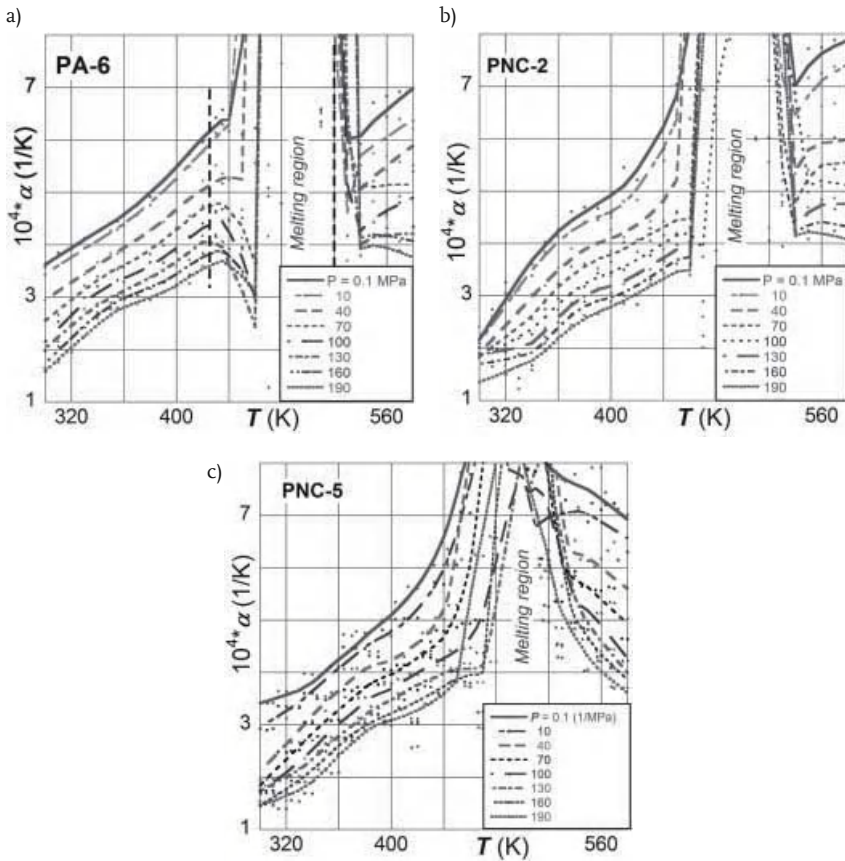
Figure 4.10 The thermal expansion coefficient versus T at $P = 0.1–190$ MPa for PA-6 and two its nanocomposites with 2 and 5 wt% of clay.

valuable insight into the thermodynamic equilibrium and nonequilibrium behavior such as diffusivity, rheology, positron annihilation lifetime spectroscopy (PALS), etc. [52].

4.5.1
Simha–Somcynsky Cell-Hole Theory

Any functional relation between volume, V, pressure, P, and temperature, T, belongs to the family of equations of state, eos [53]. While the early relations were empirical, applied to condensed gases, later on Lennard–Jones and Devonshire generalized the concept of intermolecular interactions in gases and liquids. The Prigogine *et al.* cell model for *s*-mer linear molecules was a big step toward development of eos suitable for polymeric systems [54]. The cell model offered good description for condensed fluids, where the intermolecular distance is comparable

a)

b)

c)
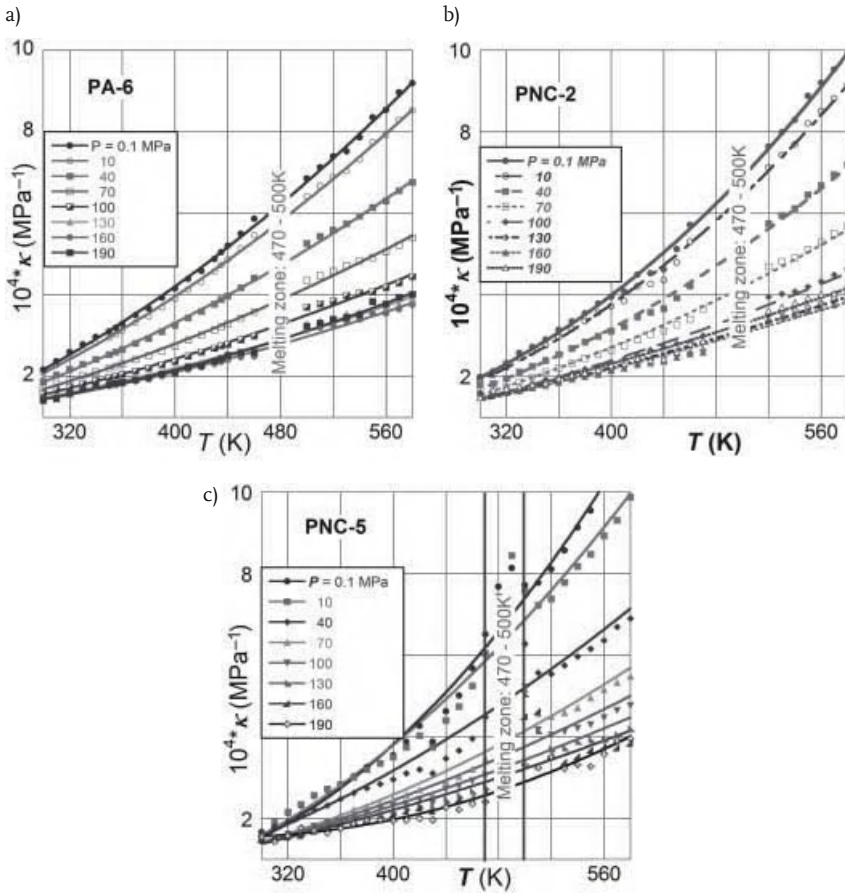
Figure 4.11 The compressibility coefficient versus T at $P = 0.1–190\,$MPa for PA-6 and two its nanocomposites PNC-2 and PNC-5.

to the lattice size, but progressively deviated with increased T. This problem was successfully treated in 1969 by Simha and Somcynsky by introduction of non-occupied cells in the lattice model [55, 56].

The Simha and Somcynsky (S–S) cell-hole theory is based on the lattice-hole model. The molecular segments of s-mer occupy y-fraction of the lattice sites, while the remaining randomly distributed sites, $h = 1 − y$, are left empty accounting for free volume. The theory was derived assuming thermodynamic equilibrium; thus, its direct applicability is to liquids: nonpolar or polar solvents, solutions, melts, and diversity of mixtures (alloys, blends, composites, foams, nanocomposites). Furthermore, assuming that at $T < T_g$ part of the free volume is frozen, the theory was extended to the vitreous and semicrystalline nonequilibrium states [34, 57].

The derivation starts with configurational partition function in the form

$$Z = g(N, \gamma)[v_f(V, \gamma)]^{cN} \exp\{-E_o(V, \gamma)/k_B T\}$$

$$g(N, \gamma) \propto \gamma^{-N}(1-\gamma)^{-Ns(1-\gamma)/\gamma} \tag{4.5}$$

$$E_o(V, \gamma) = (\gamma Nqz\varepsilon^*/2)\left[A(v^*/\omega)^4 - 2B(v^*/\omega)^2\right]; \quad \omega \equiv \gamma V/(Ns)$$

where g is the combinatorial factor. L–J "6-12 potential" cast in volume terms is incorporated as the potential energy of the system, E_o, with two interaction parameters: the maximum attractive energy, ε^*, and the segmental repulsion volume, v^*. Next, assuming the corresponding states principle (CSP), the variables are divided by the characteristic reducing parameters:

$$\left.\begin{aligned}\tilde{V} &\equiv V/V^* \\ \tilde{T} &\equiv T/T^* \\ \tilde{P} &\equiv P/P^*\end{aligned}\right\} \Rightarrow M_s \frac{P^*V^*}{RT^*} = \frac{c}{s} \Leftarrow \begin{cases}P^* = zq\varepsilon^*/(sv^*) \\ T^* = zq\varepsilon^*/(Rc) \\ V^* = v^*/M_s\end{cases} \tag{4.6}$$

where $zq = s(z-2) + 2$ is the number of interchain contacts between s segments (each of molecular weight: $M_s = M_n/s$) in a lattice of the coordination number z, and $3c$ is the number of the external degrees of freedom. The reduced free-volume function v_f in Eq. (4.5) is taken as a volume average of the solid-like and gas-like contributions:

$$\tilde{v}_f = \left[\gamma(\tilde{\omega}^{1/3} - 2^{-1/6}) + (1-\gamma)\tilde{\omega}^{1/3}\right]^3 \tag{4.7}$$

The configurational Helmholtz free energy is obtained as

$$\tilde{F} = \tilde{F}\left[\tilde{V}, \tilde{T}, h(\tilde{V}, \tilde{T})\right] = -RT \ln Z$$

$$\tilde{F}/k_B T = N \ln \gamma + sN[(1-\gamma)/\gamma]\ln(1-\gamma) - 3cN\left\{\ln\left[(\gamma\tilde{v})^{1/3} - 2^{-1/6}\gamma\right] + \right. \tag{4.8}$$

$$\left. Nqz(\varepsilon^*/2kT)\left[A(\gamma\tilde{v})^{-4} - 2B(\gamma\tilde{v})^{-2}\right]\right\}$$

In Eq. (4.8) the numerical values of the coefficients $A = 1.011$ and $B = 1.2045$ are for the assumed face-centered cubic lattice with the coordination number $z = 12$. It is noteworthy that in addition to the usual volume and temperature dependence, $\tilde{F}$ contains the hole fraction $h = h(\tilde{V}, \tilde{T})$.

The S–S eos is obtained by differentiation of the Helmholtz free energy:

$$(\partial \tilde{F}/\partial h)_{\tilde{T}, \tilde{V}} = 0 \quad \text{and} \quad \tilde{P} = -(\partial \tilde{F}/\partial \tilde{V})_{\tilde{T}} \tag{4.9}$$

The first partial derivative in Eq. (4.9) assumes the presence of the thermodynamic equilibrium at which the free-volume content is at optimum, while the second is a standard definition of pressure. Thus, the differentiation leads to eos in the form of coupled equations:

$$\tilde{P}\tilde{V}/\tilde{T} = (1-\eta)^{-1} + 2\gamma(AQ^4 - BQ^2)/\tilde{T}$$

$$3c\left[(\eta - 1/3)/(1-\eta) - \gamma(3AQ^4 - 2BQ^2)/6\tilde{T}\right] + \tag{4.10}$$

$$(1-s) - (s/\gamma)\ln(1-\gamma) = 0$$

$$Q \equiv 1/(\gamma\tilde{V}); \quad \eta \equiv 2^{-1/6}\gamma Q^{1/3}$$

The Helmholtz free energy also leads to the cohesive energy density, $\widetilde{CED}$, solubility parameter, $\delta = \delta(T, P)$, and the internal pressure, $\tilde{p}_i$ [58, 59]:

$$\widetilde{CED} \equiv \tilde{U}/\tilde{V} = (\gamma/2\tilde{V})\left[AQ^4 - 2BQ^2\right]; \quad \delta = \sqrt{CED} = \sqrt{\widetilde{CED} \times P^*}$$

$$\tilde{p}_i \equiv \left(\partial\tilde{U}/\partial\tilde{V}\right)_{\tilde{T}} = -\frac{1}{2}\left[3AQ^4 - 2BQ^2\right]\left(\partial\gamma/\partial\tilde{V}\right) + \left(2\gamma/\tilde{T}\right)\left[AQ^4 - BQ^2\right]$$

$$(4.11)$$

where $U = F + TS$ is the internal energy of the system.

The S–S theory [in the form of Eqs. (4.5)–(4.11)] is valid for a single component liquid at equilibrium. Its advantage over others eos is the explicit incorporation of the hole fraction, $h = 1 - y$, a measure of the free-volume fraction, $f(P, T) \equiv 1 - V_o/V(P, T)$ [60]. Equation (4.10) stipulates that all liquids cast in reduced variables obey the CSP. Once the characteristic parameters (P^*, V^*, T^*, and $3c/s = 1 + 3/s$) are known, the V, h, L–J interaction parameters and derivative properties may be computed in the full range of P and T. For linear polymers, where $s >> 3$, the external degree of freedom $3c/s \cong 1$, and only knowledge of P^*, V^*, and T^* is required [61].

4.5.2
Simha–Somcynsky eos for Multicomponent Systems

In the early 1980s Jain and Simha published an important extension of the S–S theory to homogeneous binary mixtures [62, 63]. Assuming that in multicomponent fluids there is only one type of vacancies and one cell size for all components the authors showed that Eq. (4.10) is applicable to multicomponent systems provided that the reducing and interaction parameters are expressed as composition-dependent averages indicated by the angular brackets $\langle\ \rangle$:

$$\langle P^* \rangle = qz\langle\varepsilon^*\rangle/(\langle s\rangle\langle v^*\rangle); \quad \langle T^* \rangle = qz\langle\varepsilon^*\rangle/R\langle c\rangle; \quad \langle V^* \rangle = \langle v^*\rangle/\langle M_o\rangle$$

$$\langle P^* \rangle\langle V^* \rangle/R\langle T^* \rangle = (\langle c\rangle/\langle s\rangle)(1/\langle M_o\rangle)$$

$$\langle c\rangle = \sum_i c_i x_i; \quad \langle s\rangle = \sum_i s_i x_i; \quad \langle M_o\rangle = \sum_i M_{si}s_i x_i \Big/ \sum_i s_i x_i$$

$$X_i = zq_i x_i \Big/ \sum zq_i x_i; \quad zq_i = s_i(z-2)+2; \quad z = 12$$

$$(4.12)$$

where the interacting site fractions, X_i, depend on the lattice interchain contact, zq_i, and the mole fraction x_i. The average interaction parameters $\langle\varepsilon^*\rangle$ and $\langle v^*\rangle$ are related to binary ones via

$$\langle\varepsilon^*\rangle\langle v^*\rangle^m = \sum_{i,k} X_i X_k \varepsilon_{i,k}^* \left(v_{i,k}^*\right)^m; \quad m \in (2,4)$$

$$(4.13)$$

where the two values of m reflect the assumed Lennard–Jones 6-12 potential. The S–S theory for multicomponent systems well describes the phase equilibria, CED, solubility as well as PVT behavior of polymer mixtures with gases (PS foam with physical foaming agents [60]), liquids (PS blends with poly(2,6-dimethyl phenyl ether), PPE [64]), or solids (composites [65–67] and nanocomposites [1, 52]).
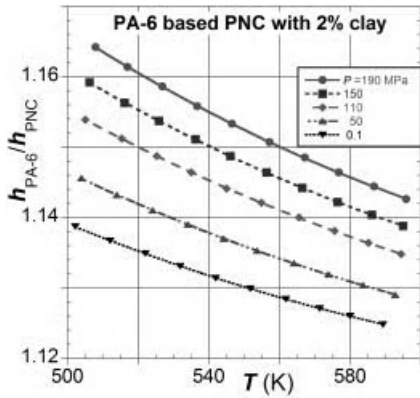
Figure 4.12 Relative free volume versus T and P for PNC with 2 wt% clay [35].
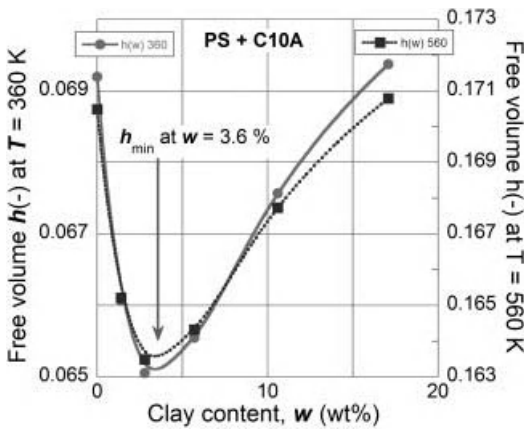
Figure 4.13 Loss of free volume versus clay content in PS-based PNC at $P = 0.1$ MPa and $T = 360$ and 560 K.

Equation (4.13) has six parameters, out of which up to four are accessible from the *PVT* measurements of neat components (e.g., polymer-1 and polymer-2), while the two cross-interaction parameters, ε_{12}^* and v_{12}^*, may be computed from the two relations in Eq. (4.13). The PNC behavior was analyzed for systems with PA-6 [35, 36], PS [68], or polypropylene, PP [69], as the matrix. Details of the calculations are provided in the cited articles.

Figures 4.12 and 4.13 illustrate the effect of clay on the free-volume parameter h in molten PNC with the PA-6 and PS matrix, respectively. At constant clay loading of 2% reduction of the free-volume parameter is related to the interlayer spacing, d_{001} [46]:

$$\Delta h = 2.51 + 0.833 d_{001}; \quad r = 1.000 \tag{4.14}$$
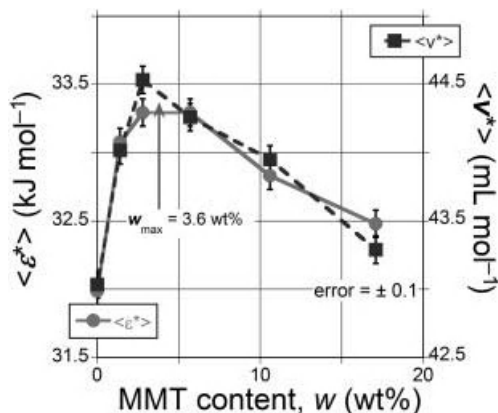
Figure 4.14 Concentration dependence of the volume-average L–J interaction parameters for PS and its PNC.

Since the reactively prepared PA-6-based PNCs are the closest to full exfoliation, here the addition of 2 wt% clay has the largest effect – it reduces h by about 15%. In Figure 4.13 for PS-based PNCs the h versus w dependence goes through a local minimum of about 6% at $w_2 = 3.6$ wt% clay – further addition of organoclay reduces the interlayer spacing and dilutes the intercalated stacks. It is noteworthy that the shape of dependences presented in Figure 4.13 resembles the effects of clay on the derivative properties in Figures 4.7 and 4.10, indicating that α and κ dependences are indeed related to the hole fraction in the S–S lattice-hole theory. However, fundamentally h is a result of interactions; thus it is interesting to see how the L–J interaction parameters vary with w.

The results of computations, using Eqs. (4.10), (4.12), and (4.13), presented in Figure 4.14 again show the expected similarity of behavior with the maxima for $\langle \varepsilon^* \rangle$ and $\langle v^* \rangle$ at $w_2 \approx 3.6$ wt%. Table 4.6 lists the reducing and L–J interaction parameters for a series of PNC with PA-6, PP, and PS matrix. It is noteworthy that the effect of clay addition depends on its intercalant and the method of PNC manufacture.

Before leaving discussion on the *PVT* behavior in molten phase it is worth mentioning that contrary to the earlier concept that equilibrium liquid exists at $T > T_g$, there is experimental evidence from several test methods that indicate the presence of dynamic solid-like aggregates near but above T_g – only above the crossover temperature, T_c, the true liquid-like behavior was found. For example, Wool and his colleagues used AFM in the tapping mode for detecting the percolating twinkling fractal solid aggregates in PS below and above T_g [71, 72]. Given that the tapping mode detects variation of substrate modulus, the results evidence the presence of the twinkling solid clusters in the liquid matrix.

Table 4.6 The characteristic reducing parameters for PNC with PA-6, PP, and PS matrix [70].

Polymer	Clay (wt%)	$\langle P^* \rangle$ (MPa)	$\langle T^* \rangle$ (K)	$10^4 \times \langle V^* \rangle$ (ml g^{-1})	M_s (g mol^{-1})	$\langle \varepsilon^* \rangle$	$\langle \nu^* \rangle$	R^2
1	2	3	4	5	6	7	8	10
PA-6	0	1257.4 ± 8.2	11134 ± 32	8919.3 ± 9.6	27.51	31.23	24.54	0.999999
PA-6	0.8	1185.7 ± 11.1	11364 ± 49	8943.1 ± 14.3	29.70	31.49	26.56	0.999998
PA-6	1.6	1163.9 ± 12.6	11307 ± 54	8888.6 ± 16.2	30.29	31.71	26.92	0.999998
PA-6	0	1232.8 ± 6.0	11157 ± 22	8935.5 ± 6.9	28.07	30.92	25.08	0.999998
PA-6	1.6	1310.4 ± 6.9	10962 ± 22	8779.3 ± 7.4	26.41	30.98	23.18	0.999998
PA-6	4.0	1312.0 ± 8.6	10956 ± 28	8685.2 ± 9.2	26.64	30.36	23.14	0.999997
PA-6	0	1064.1 ± 10.8	12287 ± 61	9199 ± 15	34.78	34.05	32.00	0.999999
PA-6	2.29	1180.8 ± 12.2	11338 ± 52	8895 ± 15	29.82	31.42	26.52	0.999998
PA-6	4.91	1217.3 ± 14.3	11204 ± 57	8795 ± 17	29.00	31.05	25.51	0.999998
PP	0	572.7 ± 6.8	10449 ± 57	11728 ± 22	43.1	28.95	50.56	0.999998
PP	1.14	516.9 ± 10.3	10712 ± 98	11874 ± 37	48.4	29.68	57.43	0.999998
PP	1.59	545.7 ± 5.5	10775 ± 49	11712 ± 18	46.7	29.86	54.70	0.999998
PP	2.42	502.8 ± 9.3	10917 ± 92	11857 ± 34	50.7	30.25	60.17	0.999997
PS	0	743.5 ± 2.6	11723 ± 22	9525.9 ± 4.7	45.87	31.98	43.03	0.999999
PS	1.4	749.2 ± 5.2	11938 ± 46	9583.7 ± 9.6	46.08	33.07	44.02	0.999998
PS	2.8	747.5 ± 3.2	12010 ± 29	9567.8 ± 5.9	46.54	33.29	44.53	0.999999
PS	5.7	755.6 ± 5.6	11975 ± 48	9458.8 ± 9.8	46.43	33.29	44.26	0.999998
PS	10.6	747.1 ± 8.4	11834 ± 74	9259.6 ± 15.1	47.41	32.83	43.95	0.999994
PS	17.1	751.0 ± 8.9	11711 ± 73	9011.2 ± 14.6	47.77	32.48	43.29	0.999992

Analysis of the *PVT* surface by means of the S–S eos leads to the hole content, h, which should correlate with liquid viscosity following the dependence [73–76]

$$\ln \eta_{\sigma_{ij}=\text{const}} = a_0 + a_1 Y_s; \quad Y_s \equiv 1/(h + a_2) \tag{4.15}$$

The relation predicts that $\eta_{\sigma_{ij}=\text{const}}$, that is, the zero-shear or constant stress quantity is a function of T and P only through $h = h(T, P)$. This indeed was observe for low molecular weight *n*-paraffins or silicon oils; good superposition was found at $T = 20$–$204\,°C$ and $P = 0.1$–$500\,\text{MPa}$, with constants: $a_1 = 0.79 \pm 0.01$ and $a_2 = 0.07$. The method was applied to eight molten polymers, whose *PVT* and $\eta = \eta(P, T)$ were measured [77]. By contrast with the previously found superposition for solvents and silicone oils, the polymer data plotted as $\log\eta$ versus $1/h$ did not superpose on a "master curve." The discrepancy could be eliminated by introducing an empirical characteristic reducing pressure, $P_R^* = \zeta P^*$, with ζ ranging from 1 to 2.1. The origin of the behavior difference between solvents and molten polymers is the presence of structures in the latter at $T_g \leq T \leq T_c$. The TFT model supports this explanation as the liquid entrapped within the aggregate does not contribute to flow. The presence of structure at $T_g \leq T \leq T_{LL}$ has been postulated by Boyer and his colleagues; only above T_{LL} the melt behaved as regular liquid [30, 78–80].

PALS has also been used for determining the free-volume holes. The method is based on the rate of annihilations of *ortho*-positronium (*o*-PS) by external electrons of a free-volume cavity. The method has been applied to the polymer and is well reviewed in part III of [52]. In particular, Dlubek has discussed correlation between the hole volume obtained from PALS and the hole volume fraction obtained from *PVT* [81]. The chapter reviews a decade of intensive research in the field, to a large extent focused on the determination of hole density through the use of S–S eos. The specific volume obtained from the high-pressure dilatometry is divided into the specific occupied volume, $V_{occ} = \gamma V$, and the specific hole free volume, $V_f = hV$. Differentiation leads to α and κ coefficients for the occupied and free-volume parts, consistent with: $\alpha_{occ} = 0$ and $\kappa_{occ} = \text{constant}$. The interrelation between the *PVT* volume, V, and the PALS average hole volume, $\langle v_h \rangle$, is set up by calculating the effective number of holes from $N_h = V_f/\langle v_h \rangle = (V - V_{occ})/\langle v_h \rangle$. Thus, correlation of information from these two methods and their analysis using S–S eos leads to the consistent description of material behavior. Furthermore, a connection between the hole-size distribution and relaxation phenomena was noted [82].

4.5.3
The Vitreous Region

The properties of the vitreous phase vary with the way they were produced by cooling or compressing the molten phase [83]. The analysis follows the procedure developed by Simha and his colleagues [34, 68, 84–86]. Accordingly, from *PVT* data the hole fraction was calculated for the molten and vitreous phase (omitting the transitory region). For the glasses, $h_{glass} = h(T', P')$ was computed substituting
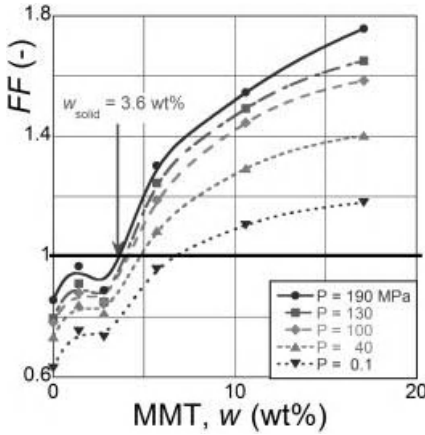
Figure 4.15 Free-volume-frozen fraction, $FF = FF(w)$, for PS-1301 with 0–17 wt% of C10A at the selected (for clarity) five pressures, $P = 0.1$–190 MPa. See the text.

$V = V(T', P')$ into Eq. (4.10) with the known $\langle P* \rangle$, $\langle T* \rangle$ and $\langle V* \rangle$ parameters from the $T > T_g$ data (*nota bene*, the variables with prime refer to the vitreous region). The hole fraction that the melt would have at the vitreous state at T' and P', $h_{extrapol} = h(T', P')$, was computed the S–S eos. Next, the frozen fraction of free volume, FF, was calculated from the relation

$$FF = 1 - (\partial h / \partial T')_{P,glass} / (\partial h / \partial T')_{P,extrapol} \tag{4.16}$$

Evidently, since FF is a fraction its value should be FF < 1. Figure 4.15 displays the $FF = FF(w)$ dependence at several pressures calculated for PS + C10A.

Only in PNCs with low clay content, $w < w_2 = 3.6$ wt%, FF < 1 is found; at higher clay concentration FF > 1. This behavior stems from rapid adsorption and solidification during cooling from the melt, which takes place at $T \leq T_g + 50\,°C$ for samples with higher w. In other words, once the free PS melt is exhausted additional incorporation of organoclay brings along a large quantity of free volume associated with the 2MBHTA intercalant. Additionally, while in the neat polymer h always increases with increasing T, in the highly loaded PNC-17 glass it decreases at $T/T_g \approx 0.86 \pm 0.02$, thus above but near T_β.

4.5.4
Equation of State for Semicrystalline PNC

Thermodynamic theory for semicrystalline polymeric systems originates from several sources: theory of polymeric glasses at $T \leq 80\,K$ by Simha *et al.* [24], Prigogine *et al.* cell model for condensed systems [87], cell model for crystals Midha and Nanda [88], and Simha and Jain refinements [89, 90]. Thus, the MNSJ theory

has five parameters: P^*, T^*, V^*, c/s, and the characteristic frequency at $T = 0\,K$, v_0. The cell lattice does not have holes; thus, the reducing parameters (P^*, T^*, V^*) are different than those computed using S–S eos cell-hole theory for equilibrium liquids. The theory for crystalline solids in reduced variables is

$$\tilde{P}\tilde{V} = \left(2/\tilde{V}^2\right)\left[\left(A/\tilde{V}^2\right) - B\right] + 3\gamma_G F_1\left(\tilde{\theta},\tilde{T}\right) - \left(9s/4c\right)ab\tilde{V}^2\tilde{\theta}'^2\left[\frac{1}{2} + \frac{2X}{(X-1)^2}\right] +$$
$$\left(9s/8c\right)\gamma_G b\tilde{V}^2\tilde{\theta}'^2\left[\frac{1}{2} + \frac{3X+1}{(X-1)^2} - \left(\tilde{\theta}/\tilde{T}\right)\frac{X(3+X)}{(X-1)^3}\right] \tag{4.17}$$

With the secondary functions given by

$$\gamma_{G,0} = -\left(\partial\ln v_0/\partial\ln V\right)_T = 4/3 + A_1/\left(A_1 - 2B_1V^2\right)$$
$$\gamma_G = \gamma_{G,0}\left\{1 - (s/2c)b\tilde{V}^2\left[F_1\left(\tilde{\theta}_0,\tilde{T}\right) - \left(\tilde{\theta}_0^2/\tilde{T}\right)\frac{X_0}{(X_0-1)^2}\right]\right\} -$$
$$\quad (s/c)ab\tilde{V}^2F_1\left(\tilde{\theta}_0,\tilde{T}\right)$$
$$\tilde{\theta}_0\left(v_0\right) \equiv hv_0/kT^* = 4.794 \times 10^{-11}v_0/T^*$$
$$\quad = 13.189(c/s)V_0^{-4/3}\frac{\left(A_1/2V_0^2 - B_1\right)^{1/2}}{M_0^{5/6}\sqrt{T^*}\sqrt[3]{V^*}}$$
$$X\left(\tilde{\theta},\tilde{T}\right) = \exp\left\{\tilde{\theta}/\tilde{T}\right\}; \quad F_1\left(\tilde{\theta},\tilde{T}\right) = \tilde{\theta}\left[\frac{1}{2} + \frac{1}{X-1}\right];$$
$$Y = (3s/8c)\left(\tilde{\theta}_0/\tilde{\theta}'\right)^2\left(\tilde{\theta}_0\tilde{V}\right)^2b/\tilde{T}$$
$$\tilde{\theta} = \tilde{\theta}'\left[1 + (3s/8c)b\tilde{V}^2\tilde{\theta}'\right]; \quad \tilde{\theta}' = \tilde{\theta}_0\left[1 + \left(4\tilde{T}/3\tilde{\theta}_0^2\right)F_1\left(\tilde{\theta}_0,\tilde{T}\right)Y\right] + 0(Y)$$
$$a = 1 - \frac{A_2}{\left[A_2 - 2B_2\tilde{V}^2\right]} + \frac{2A_1}{\left[A_1 - 2B_1\tilde{V}^2\right]};$$
$$b = \left[\left(A_2/\tilde{V}^2\right) - 2B_2\right]/\left[\left(A_1/\tilde{V}^2\right) - 2B_1\right]^2 \tag{4.18}$$

In the above relations $A_1 = 22.1060$, $B_1 = 5.2797$, $A_2 = 200.653$, and $B_2 = 14.334$ are lattice constants.

Equations (4.17) and (4.18) have been derived for the crystalline phase at $T_g \leq T \leq T_m$. Their applicability for describing the PVT dependences has been examined for PE [89, 90] and more recently for PA-6 [49–51]. In the latter publications the additivity of the crystalline and noncrystalline domains was assumed. For rigorous calculations the crystalline content should be determined as $X = X(T, P, w)$. However, owing to the nonavailability of high-pressure calorimeter, only the ambient P tests could be conducted. These data were supplemented by the pressure effect on crystallinity, deduced from the difference, $\Delta V_{m,c}$, in specific volume, V, between the experimental PVT data and computed from the assumption of additivity of crystalline and molten phases. The results are displayed in Figure 4.16 with lines given by second-order polynomials. The sequence of the computation steps and the assumed models are detailed in the original publication [49]. An example of the final fit is presented in Figure 4.17.
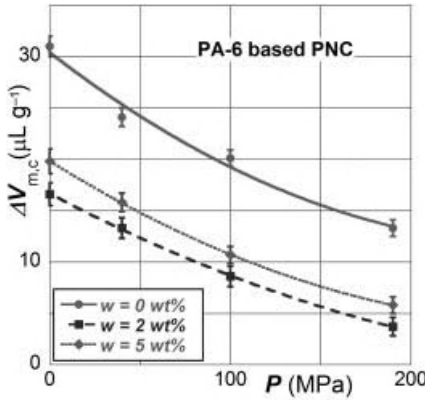
Figure 4.16 Incremental volume of PA-6 with $w = 0$–5 wt% clay at $P = 0.1$–190 MPa. Error bars of the computer fit are marked.
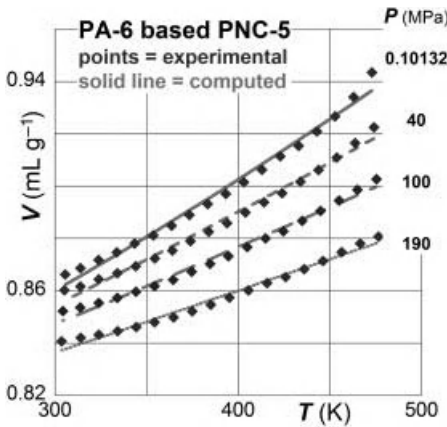
Figure 4.17 Experimental (points) and computed (lines) specific volume of PA-6 with 5 wt% clay at $P = 0.1$–190 MPa.

4.6
Thermodynamic Interaction Coefficients

All theories discussed in this chapter employ the L–J potential, initially written in the general form $E_o = (\lambda/r^n) - (\mu/r^m)$ with the adjustable exponents: $m = 10$–13, $n = 6$–7 [91–93]

$$E_o(r) = 4\varepsilon_{ij}\left[A\left(\frac{\sigma_{ij}}{r}\right)^m - B\left(\frac{\sigma_{ij}}{r}\right)^n\right]; \quad m = 12; \quad n = 6$$

or   (4.19)

$$E_o(V,\gamma) = \left(\frac{\gamma Nqz\varepsilon^*}{2}\right)\left[A\left(\frac{\omega}{v^*}\right)^4 - 2B\left(\frac{\omega}{v^*}\right)^2\right]; \quad \omega \equiv \gamma V/(Ns)$$

where ω is cell volume. The present form of the "6-12 potential" originates from the quantum mechanics derivation of attractive forces between H–H atoms that lead to $n = 6$, while the exponent for the short-range repulsive interactions was taken as $m = 2n$ [93]. The 6–12 potential was incorporated into the S–S cell-hole theory in the form given by the second relation in Eq. (4.19).

In the text above, the intersegmental L–J interaction parameters ε^* and v^* are for single component systems, and averaged, $\langle\varepsilon^*\rangle$ and $\langle v^*\rangle$, for multicomponent ones [see Eq. (4.12)]. For extracting the individual binary interactions from the averages one needs a model. Note that the Simha–Jain assumption was for random-mixed two systems, $i = 1$ customarily assigned for the major phase and $i = 2$ for the dispersed one.

The situation is relatively simple for the single-phase polymeric systems such as solutions [58, 59], mixtures of the molten polymer with a foaming agent [60], or miscible polymer blends [64]. In the case of immiscible binary polymer blends, where *PVT* of each component can be measured directly, only the heterogeneous ones, ε_{ij}^* and v_{ij}^*, must be determined from the blend behavior. It is noteworthy that such a treatment ignores the presence of the interphase whose importance increases with the enhanced dispersion and is inacceptable for the finer than micron-sized dispersions [94].

PNCs are complex systems comprising matrix, nanosized particles, intercalant, compatibilizer(s), and various industrial additives. Furthermore, the clay usually exists in a wide spectrum of dispersion ranging from fully exfoliated to micron-size aggregates. Clay also adsorbs the organic phase creating a gradient of molecular mobility stretching up to 120 nm from the clay surface [1]. During the last 20 years PNCs with immiscible polymer blends have become interesting [95]. Thus, it is a challenge to convert these systems into a model mixture of the matrix and dispersed in it solid particles that will realistically simulate the physical behavior.

The organic-phase adsorption on the high-energy solid surface has been observed using the surface force analyzer (SFA) and the neutron scattering method [96–99]. Similarly, molecular dynamics (MD) and Monte Carlo (MC) computations predicted formation of the solidified layer [100–102]. Thus, in the z-direction (perpendicular to the clay surface) there are two layers with reduced molecular dynamics: a $z_1 < 2$–9 nm thick solid layer of organic molecules followed by a $z_2 - z_1 = 100$–120 nm thick layer where molecular mobility progressively increases from z_1 to z_2. Luengo *et al.* determined that on a freshly cleaved mica flake polybutadiene (PBD) forms a 5–6 nm solid layer, followed by an about 100 nm thick layer of increasing with distance z mobility. Thus, the bulk melt behavior of PBD (e.g., steady-state or dynamic viscosity) was observed only at $z_2 \geq 110$ nm from the mica surface [38].

Accordingly, the basic model of PNC should specify the composition of the matrix and dispersed solid phase. Experimentally, the solid particles are made of clay platelets or their stacks covered with a $z_1 \approx 4$–6 nm thick solidified organic layer (intercalant, compatibilizer and/or polymer). Their L–J interaction parameters are ε_{22}^* and v_{22}^*. Consequently, the remaining materials must be treated as a matrix, that is, the organic layer at $z > z_1$ having variable molecular mobility, with the L–J parameters ε_{11}^* and v_{11}^*. In consequence, the model implicitly assumes that

the L–J parameters depend on the clay content. Obviously, the variability may be observed only at low clay content, below its second critical value ($w_2 = 3.6$ wt% in the PS matrix; see Section 4.4) at which the molten polymer with the bulk properties disappears. The expression used for describing variation of L–J parameters with distance from the clay surface, $\varepsilon_{ij}^*(z)$ or $v_{ij}^*(z)$, is [69]

$$\gamma(z) = \frac{\gamma_1\gamma_2}{\gamma_1 - (\gamma_1 - \gamma_2)\exp\{n[(z-z_1)/(z-z_2)]\}}; z_1 \leq z \leq z_2; \gamma \in [\varepsilon^*, v^*] \qquad (4.20)$$

In this expression the steepness index $n \approx 2$ is adjustable, and γ represents the L–J parameters at $z_1 \leq z \leq z_2$. At the low limit, $\gamma(z) = \gamma_1 \in [\varepsilon_{22}^*, v_{22}^*]$ and at high limit, $\gamma(z) = \gamma_2 \in [\varepsilon_{11}^*, v_{11}^*]$.

Because of differences in clay–polymer interactions, one should not assume that a single model will be applicable to all PNCs. For example, owing to polarity of PA-6 and strong interaction with negatively charged clay platelets, the PA-based PNC are relatively easily prepared with high degree of exfoliation following the synthetic or compounding method. However, since the intercalant location and molecular structure are different, the model for extracting the L–J parameter should account for the difference [103]. Flow analysis of these PNCs led to the "hairy clay particle" (HCP) model [104]. By contrast with these PNCs, the ones with polyolefin (PO) or the PS matrix, which does not bond to the clay surface, are immiscible with most intercalants; thus they need a compatibilizer.

In conclusion, before devising a realistic model for tested PNC, information about composition, thermodynamic interactions, and resulting degree of dispersion is needed [70]. Considering the adopted definition of the solid and liquid phase the molar and site fractions [x_i and X_i in Eq. (4.12), respectively] must be recalculated, for example,

$$x_1 = \frac{(m_1/M_{s1}) - (m_{1,\text{solid}}/M_{s1})}{(m_1/M_{s1}) + (m_2/M_{s2})}; \quad x_2 = \frac{(m_2/M_{s2}) + (m_{1,\text{solid}}/M_{s1})}{(m_1/M_{s1}) + (m_2/M_{s2})} \qquad (4.21)$$

where m_1 is the weight fraction of the polymer, $m_{1,\text{solid}}$ is the weight fraction of the solidified matrix, m_2 is the weight fraction of clay, and $M_{si} = M_i/s_i$ is the molecular weight of a statistical segment of component "i."

The interrelation between the L–J parameters and site fractions X_i is given by Eq. (4.13), which for ease of computation was transformed into:

$$\langle v^* \rangle^2 = v_{11}^{*2}\Xi_4/\Xi_2; \quad \text{and} \quad \langle \varepsilon^* \rangle^2 = \varepsilon_{11}^*\Xi_2^2/\Xi_4$$

$$\Xi_2 \equiv X_1^2 + 2X_1X_2e_{12}v_{12}^2 + X_2^2e_{22}v_{22}^2 = (\langle v^* \rangle/v_{11}^*)^2 \cdot (\langle \varepsilon^* \rangle/\varepsilon_{11}^*)$$

$$\Xi_4 \equiv X_1^2 + 2X_1X_2e_{12}v_{12}^4 + X_2^2e_{22}v_{22}^4 = (\langle v^* \rangle/v_{11}^*)^4 \cdot (\langle \varepsilon^* \rangle/\varepsilon_{11}^*) \qquad (4.22)$$

$$e_{12} \equiv \varepsilon_{12}^*/\varepsilon_{11}^*; \quad e_{22} \equiv \varepsilon_{22}^*/\varepsilon_{11}^*; \quad v_{12} \equiv v_{12}^*/v_{11}^*; \quad v_{22} \equiv v_{22}^*/v_{11}^*$$

For PNCs, of the six parameters only two (ε_{11}^* and v_{11}^*) can be measured directly. The two cross-interaction parameters, ε_{12}^* and v_{12}^*, follow Berthelot's rule and the algebraic average, respectively [1]:

$$\varepsilon_{12}^* = \sqrt{\varepsilon_{11}^*\varepsilon_{22}^*}; \quad v_{12}^* = [v_{11}^{*1/3} + v_{22}^{*1/3}]^3/8 \qquad (4.23)$$
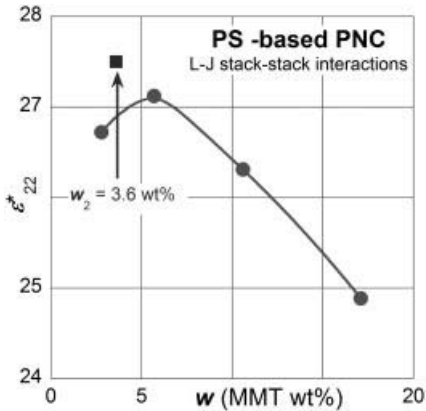
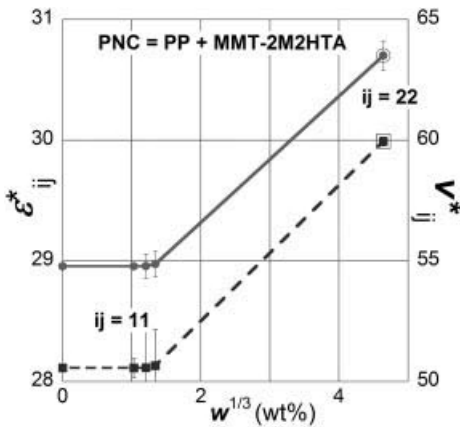**Figure 4.18** Computed stack–stack interaction in intercalated PS-based PNCs.

Figure 4.19 L–J interaction parameters in PP-based PNCs.

The remaining two parameters, ε_{22}^* and v_{22}^*, are then calculable from the two relations in Eq. (4.13) or (4.22). The concentration dependence of ε_{22}^* for PS-based PNC is displayed in Figure 4.18. The solid line is a smooth curve fitting dependence with the critical concentration, $w_2 = 3.6$ wt% [68]. Figure 4.19 displays the concentration dependence of the computed binary interaction parameters in the full range of clay content, $w = 0$–100 wt% for PP-based PNC with MMT preintercalated with *di*methyl *di*hydrogenated tallow ammonium chloride (2M2HTA). The computations lead to ε_{11}^* and v_{11}^* for all points, excepting the two last ones at $w = 100$ wt% clay corresponding to ε_{22}^* and v_{22}^* interactions. From these two sets of numbers the cross-interactions, ε_{12}^* and v_{12}^*, can be calculated according to Eq. (4.23).
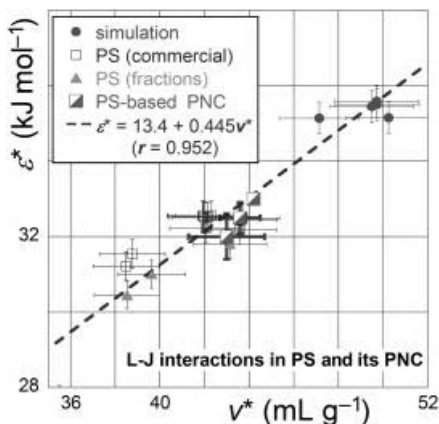
Figure 4.20 L–J interaction parameters for PS and PS-based PNCs.

Equation (4.6) suggests that the L–J parameters may not be independent, namely

$$v* P* = \varepsilon*(zq/s), \quad \text{where} \quad zq/s = z - 2 + 2/s \to 10 \tag{4.24}$$

Since for a given polymer $P*$ varies by about $\pm 5\%$ one may expect that parameters are interrelated: $\varepsilon* \propto v*P*$ [61]. Indeed, Figure 4.20 shows $\varepsilon*$ versus $v*$ for PS and its PNCs. The data seem to follow a linear dependence, but as for each set the range of values is limited the observation may not be always valid, although similar linear dependences have been obtained for other polymers, blends, and composites.

The binary interaction parameters for the matrix (ε_{11}^*, v_{11}^*) and for the solid phase (ε_{22}^*, v_{22}^*) are listed in Table 4.7. The cross-interaction parameters, ε_{12}^* and v_{12}^*, can be calculated using Eq. (4.23). On a first sight it may seem odd that the difference between the interaction parameters of the matrix and solid part is small. However, for solids there is no clay–clay interaction, but rather between the polymeric solid layers that enrobe the high-energy solid platelets.

Table 4.7 The binary interaction parameters for PNC with PA-6, PP, and PS matrix.

Polymer	Matrix		Solid		References
	ε_{11}^*	v_{11}^*	ε_{22}^*	v_{22}^*	
PA-6	34.1 ± 0.3	32.0 ± 0.1	31.2 ± 0.3	25.9 ± 0.3	[36, 49]
PP	28.9 ± 0.1	50.6 ± 0.4	30.7 ± 0.4	59.9 ± 0.3	[69]
PS	32.0 ± 0.6	43.0 ± 1.7	33.0 ± 0.1	44.2 ± 0.1	[68]

4.7
Theoretical Predictions

Theories are constructed following assumptions that on the one hand should represent the phenomenon and on the other still permit derivation of analytical expressions and their use for comparison with experiment. The notorious assumptions for theories of polymer systems are omission of polydispersity, the presence of "customary" industrial additives, and the nonrandom distribution of properties, for example, introduced by mixing or temperature gradients. Furthermore, the thermodynamics theories assume thermodynamic equilibrium within a phase located between two transitions while in practice the transitions are complex, introducing serious physical changes even to such first-order transition as T_m.

It is interesting to check how well the accepted theories represent the *PVT* data, in particular their derivatives, α and κ. Dependencies in Figure 4.21 show their variability within a wide range of independent variables, T/T^*; P/P^*. The variables are expressed in reduced form – one needs to multiply these by the reducing parameters (e.g., see Table 4.6) to convert these to SI variables such as °C, MPa, 1/K, and 1/MPa. Thus, the variables for PS range are as follows: $T = 20–313\,°C$, $P = 11–189\,MPa$, $10^4\alpha = 3.52–8.44\,K^{-1}$, and $\kappa = 0.07–0.60\,(kPa)^{-1}$. Similarly, for PA-6 these ranges are $T = 5–284\,°C$, $P = 25–314\,MPa$, $10^4\alpha = 3.35–8.02\,K^{-1}$, and $\kappa = 0.13–1.01\,(kPa)^{-1}$. In short, they do represent the customary ranges of variables.

Comparing the theory with experiment one may look for similarities in pairs of figures:

- (1) The pair 21A & 3A (PS) shows similar effects of P on both sides of T_g, but while the experimental data are nearly constant on both sides of the transition, the theory predicts a slight increase seen in Figure 4.5 for another PS.

- (2) The pair 21B & 11 (PA-6) shows that on both sides of T_m α increases with T, but while theory increases across the transition, the experimental data are horizontally displaced.

- (3) For neat PS the pair 21C and 8 show a similar behavior – better agreement for κ than for α.

- (4) An excellent agreement between theory and experiment is observed comparing 21D & 12 (PA-6) – κ versus T follow the same dependence across the first-order melting point transition.

The comparison of the four theoretical plots of α and κ for PS and PA-6 with the dependences extracted from the *PVT* data is acceptable (Figure 4.21). For the amorphous polymer (PS) the experimental plots well compare with predictions of the S–S eos. Considering the difficulties with numerical differentiation of the *PVT* data the agreement is considered good. The theoretical dependences for PA-6 were computed assuming the presence of PA-6 crystals dispersed in the molten polymer, thus using MNSJ and S–S theories, respectively. The agreement with experiments is excellent.
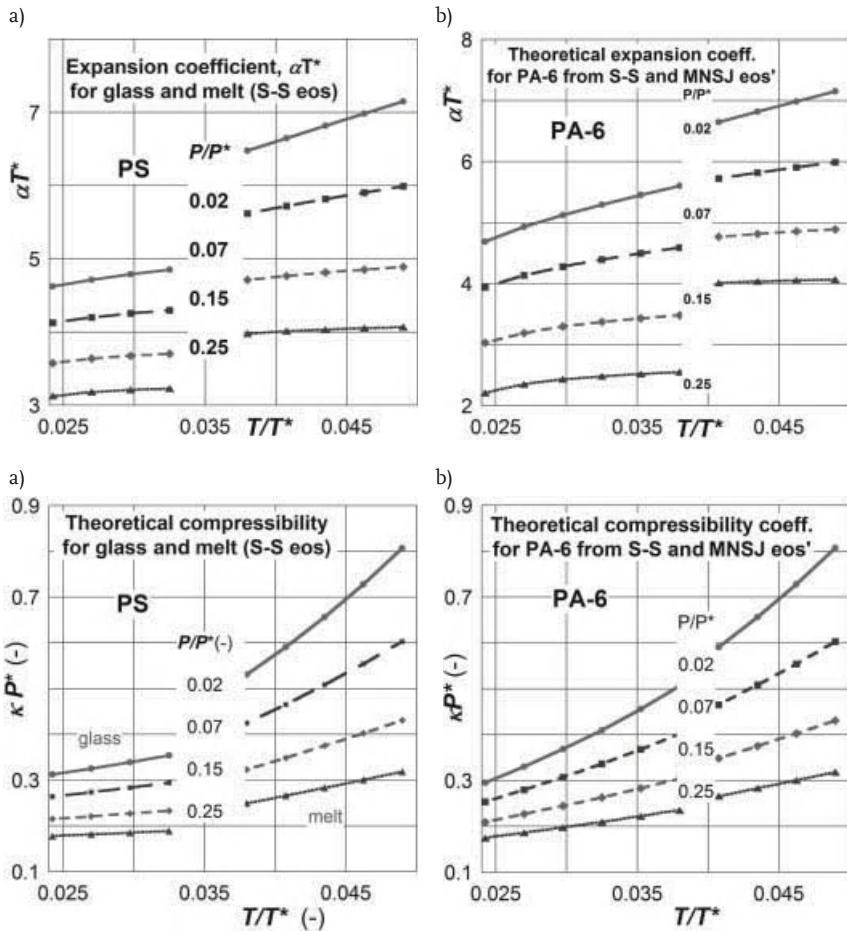
a)

b)

a)

b)

Figure 4.21 Theoretical predictions of the thermal expansion and compressibility coefficients in reduced variables for amorphous glass/melt (left column) and semicrystalline/molten polymeric systems computed from S–S eos and from combination of S–S and MNSJ eos [50, 51].

4.8
Summary and Conclusions

This chapter discusses the use of high-pressure dilatometry for characterization of the clay-containing polymer nanocomposites. The central six parts of the chapter deal with the following:

1) Characterization of clays
2) *PVT* measurements

3) Derivative properties
4) Thermodynamic theories
5) Interaction parameters
6) Theoretical predictions.

Over the last 80 years or so there has been an evolution in the approach to experimental polymer physics, reflected in the ossified statement "used without further purification." Indeed, the early research on polymers inherited from physics and physical chemistry the need to work with well-characterized substances, fractionated polymers, rectified or recrystallized additives, well-characterized ingredients, etc. At the same time, the industrial materials are getting progressively complex, loaded with diverse additives designed to stabilize the polymer during forming, facilitate production by incorporation of internal lubricants, extend the lifetime of the finished part or modified the performance by blending in small (≤ 5 wt%) of another polymer. As a result, results of measurements of supposedly the same polymer originating from different manufacture may show significant differences. PNC characterization is even more complex, especially of these containing natural minerals.

4.8.1
Characterization of Clays

Natural clays significantly differ (depending on the geographical location and local strata) in platelet shape, size and size distribution, chemical composition, and impurities. For example:

1) The average clay platelet dimensions in three orthogonal directions are thickness $t \approx 1\,nm$, width $W \approx 20$–$4000\,nm$, length $L \approx 30$–$6000\,nm$, with nearly universal ratio $L/W \approx 1.5 \pm 0.1$. The distribution of clay platelet size is approximately Gaussian.

2) The chemical composition of clay varies greatly due to (i) nonuniform atomic substitution in the crystalline cells, (ii) tendency of natural clays to vary composition with particle size, (iii) presence of mineral impurities. The chemical heterogeneity may cause batch-to-batch variability of the mechano-chemical sensitivity during compounding, degradability, weatherability, sensitivity or lack of it toward antioxidants and stabilizers, etc.

3) The natural clays contain 2–5 wt% of impurities, such as $< 300\,\mu m$ diameter quartz, cristobalite, rutile, and other particles, which may seriously affect the reproducibility of PNC performance. Since they do not bond to the matrix, they may initiate premature specimen fracture, reduction of the barrier property of PNC films, etc.

In short, characterization of PNC should start with examination of the three discussed aspects of the reinforcing clay.

4.8.2
PVT Measurements

Four test procedures may be used for the determination of the *PVT* surface: iso-thermal or isobaric increasing or decreasing the second independent variable. Under thermodynamic equilibrium conditions, all four procedures should and mostly do lead to the same results. However, the test results show a significant influence of the test procedure in the vitreous phase, as well as near the transition temperature, T_g or T_m. The most regular $V = V(P, T)$ behavior is obtained in the isobaric heating, but for thermally sensitive material the "standard" isothermal heating procedure is recommended. Evidently, the test strategy should depend on the reason for testing, dictated by a part application. It is recommended that the transient behavior of the matrix polymer at and below the transition temperatures will be disregarded.

Since PNCs are multicomponent systems, their behavior depends on the con-centration and the nature of the additives, for example, clay, intercalant, compati-bilizer. In particular, since the intercalant has low molecular weight and large free volume its effect on *PVT* and its derivatives may be disproportionately large.

4.8.3
Derivative Properties

The thermal expansion and compressibility coefficients, α and κ, are important derivatives of the function $\ln V = \ln V(P, T)$. They are of interest for the processing and application of PNCs as well as for detecting finer variations of the material structure reflected in specific volume. The numerical differentiation of raw data is recommended, preceded by an interpolation step assuring constant values of V for the selected level of P and T. Care must be taken that the fine structure of experimental data is not affected.

There is a significant difference in α and κ behavior for the amorphous and semicrystalline polymers. The former ones show a large transient effect for both coefficients below T_g, which depend on the test procedure. For the latter systems there is also a transient effect in α, originating in variability of the crystalline content and structure near T_m. However, the temperature variation of κ is smooth right across T_m.

4.8.4
Thermodynamic Theories

Simha–Somcynsky (S–S) cell-hole theory was developed for equilibrium single-component liquids, and then extended to multicomponent systems (alloys, blends, foams, micro, and nanocomposites) in the molten and vitreous state. Since the theory explicitly includes free-volume parameter, its application was extended to rheology, PALS, physical aging, diffusion, surface/interface tension, and other phenomena.

Midha and Nanda cell theory (no free volume!) was developed for crystalline polymers and subsequently modified by Simha and Jain by incorporating elements of the earlier theory for polymers at $T < 80\,\mathrm{K}$, in which the intersegmental interactions followed Einstein's equation for harmonic oscillators. The modified theory was used to describe the *PVT* behavior of the crystalline part of PNC based on semicrystalline PA-6. However, since crystallinity amounts to ca. 40%, the molten fraction was described by the S–S theory. The combined theories well followed the observed *PVT* behavior.

4.8.5
Interaction Parameters

For a single or bicomponent system the interaction parameters can be directly calculated from the derived equations. However, for PNCs one must define which part of composition belongs to the solid phase and which one to the matrix. Furthermore, owing to adsorption of the organic phase on the high-energy clay surface the progressive variability of molecular mobility with distance from the surface must be taken into account.

Depending on the system, that is, polymeric matrix and dispersed solids, the interaction parameters and their relative magnitude change. Thus for example, exfoliated clay in the polar polymer (PA-6) matrix shows a significant difference between matrix and solid parameters. By contrast, the interactions between clay stacks in the PS matrix for these two components are similar. In PP systems the energetic interaction are small, but the volumetric expulsion contribution is large, as it could be expected from the low polymer density.

4.8.6
Theoretical Predictions

The last part compares the measured and theoretically predicted α and κ coefficients for the amorphous polymer and its PNC and for the semicrystalline system. Good agreement between these two sets of data was found.

References

1 Utracki, L.A. (2004) *Clay-Containing Polymeric Nanocomposites, 2 Volumes Monograph*, RAPRA, Shawbury, Shrewsbury, UK.

2 Theng, B.K.G. (1974) *The Chemistry of Clay–Organic Reactions*, John Wiley & Sons, Inc., New York.

3 Lagaly, G., and Zismer, S. (2003) Colloid chemistry of clay minerals: the coagulation of montmorillonite dispersions. *Adv. Colloid Interface Sci.*, **100–102**, 105–128.

4 Utracki, L.A., Broughton, W., Gonzalez Rojano, N., Hecker de Carvalho, L., and Achete, C. (2011) Clays for polymeric nanocomposites. *Polym. Eng. Sci.*, **51** (3), 559–572.

5 Okada, A., and Usuki, A. (2006) Twenty years of polymer–clay nanocomposites. *Macromol. Mater. Eng.*, **291**, 1449–1476.

6 Brauer, S. (2004) Polymer nanocomposites: nanoparticles, Nanoclays and Nanotubes. *Business Communications Company report P-234R*; Ruban, L., Lomakin S., Zaikov G.E. (2000) Polymer nanocomposites based on layer aluminum-silicates, *Intern. J. Polym. Mater.*, **47**, 117–137; Global nanocomposites market (2008) http://www.strategyr.com/Nanocomposites_Market_Report.asp

7 Carretero, M.I., Pozo, M., Sánchez, C., García, F.J., Medina, J.A., and Bernabé, J.M. (2007) Comparison of saponite and montmorillonite behaviour during static and stirring maturation with seawater for pelotherapy. *Appl. Clay Sci.*, **36** (1–3), 161–173.

8 Orlemann, J.K. (1972) Process for producing synthetic hectorite-type clays, US Patent 3,666,407.

9 Tateyama, H., Tsunematsu, K., Kimura, K., Hirosue, H., Jinnai, K., and Furusawa, T. (1993) Method for producing fluorine mica, US Patent 5,204,078.

10 Neumann, B.S. (1971) Synthetic hectorite-type clay minerals, US Patent 3,586,478; 1972, US Patent 3,671,190.

11 Jaffe, J. (1974) Hydrothermal method for manufacturing a novel catalytic material, catalysis containing said material, and process using said material, US Patent, 3,803,026.

12 Daimon, N., and Izawa, T. (1976) Sol of ultra-fine particles of synthetic hectorite, US Patent 3,936,383.

13 Zhao, Y., Li, F., Zhang, R., Evans, D.G., and Duan, X. (2002) Preparation of layered double-hydroxide nanomaterials with a uniform crystallite size using a new method involving separate nucleation and aging steps. *Chem. Mater.*, **14**, 4286–4291.

14 Stamires, D., O'Connor, P., Jones, W., and Brady, M. (2004) Process for producing anionic clay using boehmite which has been peptized with an acid. US Patent 6,800,578.

15 Carrado, K.A. (2000) Synthetic organo- and polymer-clays: preparation, characterization and materials applications. *Appl. Clay Sci.*, **17**, 1–23.

16 Typical Physical Properties Bulletin, Southern Clay Products, a subsidiary of Rockwood Specialties, Inc., Cloisite® Na⁺; http://www.scprod.com/product_bulletins/PB%20Cloisite%20NA%2B.pdf (accessed February 2012).

17 Synthetic Mica, TOPY Industries Ltd. (Information from Dr. Shun-ichi OHTA, received 9 February 2005) Mica Division, 1, Akemi-cho, Toyohashi-city, Aichi, JAPAN; http://www.topy.co.jp/ (accessed February 2005).

18 Perrin-Sarazin, F., and Sepehr, M. (2007) Determination of shape size and size distribution of nano-filler particles, Test procedure for VAMAS TWA-33, Project #1, Montreal.

19 Laskin, A., and Cowin, J.P. (2001) Automated single-particle SEM/EDX analysis of submicrometer particles down to 0.1 μm. *Anal. Chem.*, **73** (5), 1023–1029.

20 Olubambi, P.A., Ndlovu, S., Potgieter, J.H., and Borode, J.O. (2008) Mineralogical characterization of Ishiagu (Nigeria) complex sulphide ore. *Int. J. Miner. Process.*, **87**, 83–89.

21 Clarey, M., Edwards, J., Tsipursky, S.J., Beall, G.W., and Eisenhour, D.D. (2000) Method of manufacturing polymer-grade clay for use in nanocomposites, US Patent 6,050,509.

22 Cabrera-Torres, J.L., Rosas-Gutierrez, F., Ramirez-Maldonado, E., Juarez-Garcia, J.M., and Gonzalez-Rojano, N. (2009) Report on the determination of shape size and size distribution of nano-filler particles, Centro Nacional de Metrologia, Mexico.

23 Beyler, C.L., and Hirschler, M.M. (2008) Thermal decomposition of polymers, in *SFPE Handbook of Fire Protection Engineering*, 4th edn (eds D. Drysdale and J. Hall), Natl. Fire Protection Assn., Bethesda, MD, http://kutenk2000.blogspot.com/2008/10/fire-protection-engineering-books.htmlpp

24 Simha, R., Roe, J.M., and Nanda, V.S. (1972) Low-temperature equation of state for amorphous polymer glasses. *J. Appl. Phys.*, **43**, 4312–4317.

25 Boyer, R.F. (1980) Dynamics and thermodynamics of the liquid state $T > T_g$ of amorphous polymers.

J. Macromol. Sci. Phys., **B183**, 461–553; Boyer R.F. (1987) in *Order in the Amorphous State* (eds R.L. Miller and J.K. Rieke), Plenum, New York.

26 Struik, L.C.E. (1978) *Physical Aging in Amorphous Polymers and Other Materials*, Elsevier, Amsterdam.

27 Kisliuk, A., Mathers, R.T., and Sokolov, A.P. (2000) Crossover in dynamics of polymer liquids. *J. Polym. Sci. B Polym. Phys.*, **38**, 2785–2790.

28 Surovtsev, N.V. (2007) Interrelation between fast relaxation and mode-coupling theory temperature in glass formers. *J. Phys. Condens. Mater.*, **19**, 196101 (8 pp).

29 Götze, W., and Sjogren, L. (1992) Relaxation processes in supercooled liquids. *Rep. Prog. Phys.*, **55**, 241–370.

30 Boyer, R.F. (1985) T_{LL} and related liquid state transitions–relaxations: a review, in *Polymer Yearbook 2* (ed. R.A. Pethrick), Harwood Academic Publishers, Chur–London–Paris–New York, pp. 233–343.

31 Zoller, P. (1986) Dilatometry, in *Encyclopedia of Polymer Science and Engineering*, vol. 5, 2nd edn (eds H. Mark, N. Bikales, C. Overberger, and G. Menges), John Wiley & Sons, Inc., New York, pp. 69–78.

32 Zoller, P., and Walsh, D. (1995) *Standard Pressure–Volume–Temperature Data for Polymers*, Technomic Pub. Co., Lancaster-Basel.

33 Breuer, H., and Rehage, G. (1967) Zur Thermodynamilr der glasigen Erstarrung. *Klloid-Z. Z. Polymere*, **216–217**, 159–179.

34 Quach, A., and Simha, R. (1971) Pressure–volume–temperature properties and transitions of amorphous polymers; polystyrene and poly(o-methyl-styrene). *J. Appl. Phys.*, **42**, 4592–4606; Quach, A., and Simha, R., (1972) Statistical thermodynamics of the glass transition and the glassy state of polymers, *J. Phys. Chem.*, **76**, 416–421.

35 Simha, R., Utracki, L.A., and Garcia-Rejon, A. (2001) Pressure–volume–temperature relations of a poly-ε-caprolactam and its

nanocomposite. *Compos. Interfaces*, **8**, 345–353.

36 Utracki, L.A., Simha, R., and Garcia-Rejon, A. (2003) Pressure–volume–temperature relations in nanocomposite. *Macromolecules*, **36**, 2114–2121.

37 Tanaka, G., and Goettler, L.A. (2002) Predicting the binding energy for nylon 6,6/clay nanocomposites by molecular modeling. *Polymer*, **43**, 541–553.

38 Luengo, G., Schmitt, F.-J., Hill, R., and Israelachvili, J.N. (1997) Thin film rheology and tribology of confined polymer melts: contrasts with bulk properties. *Macromolecules*, **30**, 2482–2494.

39 Kim, K., Utracki, L.A., and Kamal, M.R. (2004) Numerical simulation of polymer nanocomposites using a self-consistent mean-field model. *J. Chem. Phys.*, **121**, 10766–10777.

40 Tait, P.G. (1889) On some of the physical properties of fresh water and of sea-water, in *Report on the Scientific Results of the Voyage of H.M.S. Challenger* (issued in fifty volumes between 1850 and 1895), Ed. Thomson C. W., *Phys. Chem.*, **2** (IV), 1.

41 Nanda, V.S., and Simha, R. (1964) Theoretical interpretation of Tait equation parameters. *J. Chem. Phys.*, **41**, 1884–1885.

42 List of numerical analysis software, http://en.wikipedia.org/wiki/List_of_numerical_analysis_software; http://en.wikipedia.org/wiki/Numerical_differentiation (accessed February 2012).

43 Collins, G.W., II (2003) *Fundamental Numerical Methods and Data Analysis*, Case Western Reserve University, Cleveland, OH.

44 Wool, R.P. (2008) Twinkling fractal theory of the glass transition. *J. Polym. Sci. B Polym. Phys.*, **46**, 2765–2778.

45 Utracki, L.A., and Sammut, P. (2011) Polystyrene structures above the glass transition, $T > T_g$. *J. Polym. Sci. Part B: Polym. Phys.*, **49** (19), 1369–1380.

46 Tanoue, S., Utracki, L.A., Garcia-Rejon, A., Tatibouët, J., Cole, K.C., and Kamal, M.R. (2004) Melt compounding of different grades of polystyrene with organoclay: part 1. Compounding and

characterization. *Polym. Eng. Sci.*, **44**, 1046–1060.

47 Tanoue, S., Utracki, L.A., Garcia-Rejon, A., Sammut, P., Ton-That, M.-T., Pesneau, I., Kamal, M.R., and Lyngaae-Jørgensen, J. (2004) Melt compounding of different grades polystyrene with organoclay: part 2. Rheological properties. *Polym. Eng. Sci.*, **44**, 1061–1076.

48 Tanoue, S., Utracki, L.A., Garcia–Rejon, A., Tatibouët, J., and Kamal, M.R. (2005) Melt compounding of different grades of polystyrene with organoclay: part 3. Mechanical properties. *Polym. Eng. Sci.*, **45**, 827–837.

49 Utracki, L.A. (2009) Equation of state of polyamide-6 and its nanocomposites: 1. Fundamentals and the matrix. *J. Polym. Sci. B Polym. Phys.*, **47** (3), 299–313; (2009) Equation of state of polyamide-6 and its nanocomposites: 2. Effects of clay. *J. Polym. Sci. B Polym. Phys.*, **47** (10), 966–980.

50 Utracki, L.A. (2009) Compressibility and thermal expansion coefficients of nanocomposites with amorphous and crystalline polymer matrix. *Eur. Polym. J.*, **45** (7), 1891–1903.

51 Utracki, L.A. (2010) PVT of amorphous and crystalline polymers and their nanocomposites. *Polym. Degrad. Stab.*, **95** (3), 411–421.

52 Utracki, L.A., and Jamieson, A.M. (eds) (2010) *Polymer Physics: From Suspensions to Nanocomposites to Beyond, Book*, John Wiley & Sons, Inc., New York.

53 Moulinié, P., and Utracki, L.A. (2010) Equations of state and free volume content, in *Polymer Physics: From Suspensions to Nanocomposites to Beyond* (eds L.A. Utracki and A.M. Jamieson), John Wiley & Sons, Inc., New York, Chapter 6, pp. 227–281.

54 Prigogine, I., Bellemans, A., and Mathot, V. (1957) *The Molecular Theory of Solutions*, North-Holland, Amsterdam.

55 Simha, R., and Somcynsky, T. (1969) On the statistical thermodynamics of spherical and chain molecule fluids. *Macromolecules*, **2**, 342–350.

56 Somcynsky, T., and Simha, R. (1971) Hole theory of liquids and glass

transition. *J. Appl. Phys.*, **42**, 4545–4548.

57 Jain, R.K., and Simha, R. (1979) High-pressure isotherms of polyethylene crystals. *J. Polym. Sci. Polym. Lett. Ed.*, **17**, 33–37.

58 Utracki, L.A. (2004) Statistical thermodynamics evaluation of solubility parameters and polymer miscibility. *J. Polym. Sci. B Polym. Phys.*, **42**, 2909–2915.

59 Utracki, L.A., and Simha, R. (2004) Statistical thermodynamics predictions of the solubility parameter. *Polym. Int.*, **53**, 279–286.

60 Utracki, L.A., and Simha, R. (2001) Free volume and viscosity of polymer-compressed gas mixtures during extrusion foaming. *J. Polym. Sci. B Polym. Phys.*, **39**, 342–362.

61 Utracki, L.A. (2005) Pressure–volume–temperature dependencies of polystyrenes. *Polymer*, **46**, 11548–11556.

62 Jain, R.K., and Simha, R. (1980) On the statistical thermodynamics of multicomponent fluids: equation of state. *Macromolecules*, **13**, 1501–1508.

63 Jain, R.K., and Simha, R. (1984) Statistical thermodynamics of multicomponent fluids. *Macromolecules*, **17**, 2663–2668.

64 Utracki, L.A., and Simha, R. (2001) Analytical representation of solutions to lattice-hole theory. *Macromol. Theory Simul.*, **10**, 17–24.

65 Simha, R., Jain, R.K., and Jain, S.C. (1984) Bulk modulus and thermal expansivity of melt polymer composites: statistical versus macro-mechanics. *Polym. Compos.*, **5**, 3–10.

66 Papazoglou, E., Simha, R., and Maurer, F.H.J. (1989) Thermal expansivity of particulate composites: interlayer versus molecular model. *Rheol. Acta*, **28**, 302–308.

67 Simha, R., Papazoglou, E., and Maurer, F.H.J. (1989) Thermal expansivity and bulk modulus of polymer composites: experiment versus theory. *Polym. Compos.*, **10**, 409–413.

68 Utracki, L.A. (2008) Free volume of molten and glassy polystyrene and its nanocomposites. *J. Polym. Sci. B Polym. Phys.*, **46**, 2504–2518.

69 Utracki, L.A., and Simha, R. (2004) Pressure–volume–temperature dependence of polypropylene/organoclay nanocomposites. *Macromolecules*, **37**, 10123–10133.

70 Utracki, L.A. (2010) Free volume of molten and glassy polystyrene and its nanocomposites, in *Polymer Physics: From Suspensions to Nanocomposites to Beyond* (eds L.A. Utracki and A.M. Jamieson), John Wiley & Sons, Inc., New York, Chapter 14, pp. 553–604.

71 Wool, R.P., and Campanella, A. (2009) Twinkling fractal theory of the glass transition: rate dependence and time–temperature superposition, in polymers. *J. Polym. Sci. B Polym. Phys.*, **47**, 2578–2590.

72 Stanzione, J.F., III, Strawhecker, K.E., and Wool, R.P. (2011) Observing the twinkling fractal nature of the glass transition. *J. Non-Crystalline Solids*, **357** (2), 311–319.

73 Utracki, L.A. (1983) Pressure dependence of Newtonian viscosity. *Polym. Eng. Sci.*, **23**, 446–452.

74 Utracki, L.A. (1983) Temperature and pressure dependence of liquid viscosity. *Can. J. Chem. Eng.*, **61**, 753–758.

75 Utracki, L.A. (1986) Correlation between PVT behavior and the zero–shear viscosity of liquid mixtures, in *Thermodynamics and Rheology* (ed. B. Hartmann), Special issue of *J. Rheol.* **30**, 829–841.

76 Utracki, L.A. (1985) A method of computation of the pressure effects on melt viscosity. *Polym. Eng. Sci.*, **25**, 655–668.

77 Utracki, L.A., and Sedlacek, T. (2007) Free volume dependence of polymer viscosity. *Rheol. Acta*, **46** (4), 479–494

78 Hyun, K.S., and Boyer, R.F. (1970) Melt rheology in Encyclopedia of polymer science and technology, in *Encyclopedia of Polymer Science and Technology: Plastics, Resins, Rubbers*, vol. 13 (ed H.F. Mark), Wiley-Interscience New York, pp. 349–375.

79 Stadnicki, S.J., Gillham, J.K., and Boyer, R.F. (1976) The T_{ll} (>T_g) transition of atactic polystyrene. *J. Appl. Polym. Sci.*, **20**, 1245–1275.

80 Keinath, S.E., and Boyer, R.F. (1981) Thermomechanical analysis of T_g and $T > T_g$ transitions in polystyrene. *J. Appl. Polym. Sci.*, **26**, 2077–2085.

81 Dlubek, G. (2010) Local free-volume distribution from pals and dynamics of polymers, in *Polymer Physics: From Suspensions to Nanocomposites to Beyond* (eds L.A. Utracki and A.M. Jamieson), John Wiley & Sons, Inc., New York, Chapter 11, pp. 421–472.

82 Dlubek, G., Pionteck, J., Shaikh, M.Q., Hassan, E.M., and Krause-Rehberg, R. (2007) Free volume of an oligomeric epoxy resin and its relation to structural relaxation: evidence from positron lifetime and pressure–volume– temperature experiments. *Phys. Rev. E*, **75**, 021802.

83 Schmidt, M. (2000) Macroscopic volume and free volume of polymer blends and pressure-densified polymers. Ph.D. Thesis, Chalmers University, Göteborg.

84 McKinney, J.E., and Simha, R. (1974) Configurational thermodynamic properties of polymer liquids and glasses. Poly(vinyl acetate). *Macromolecules*, **7**, 894–901; *ibid.* (1976) **9**, 430–441; (1977) *J. Res. NBS Phys. Chem.*, **81A**, 283–297.

85 Curro, J.G., Lagasse, R.R., and Simha, R. (1981) Use of a theoretical equation of state to interpret time-dependent free volume in polymer glass. *J. Appl. Phys.*, **52**, 5892–5897.

86 Utracki, L.A. (2007) Pressure–volume– temperature of molten and glassy polymers. *J. Polym. Sci. B Polym. Phys.*, **45**, 270–285.

87 Prigogine, I., and Mathot, V. (1952) Application of cell method to the statistical thermodynamics of solutions. *J. Chem. Phys.*, **20**, 49–57; Prigogine I., Trappeniers N., and Mathot V. (1953) Application of the cell method to r-mer liquids, *J. Chem. Phys.*, **21**, 559–560; Prigogine I., Trappeniers N., and Mathot V. (1953) Statistical thermodynamics of r-mers and r-mer solutions, *Discuss. Faraday Soc.*, **15**, 93–107.

88 Midha, Y.R., and Nanda, V.S. (1977) Equation of state for a polymer crystal. *Macromolecules*, **10**, 1031–1035.

89 Simha, R., and Jain, R.K. (1978) Statistical thermodynamics of polymer crystal and melt. *J. Polym. Sci. B Polym. Phys. Ed.*, **16**, 1471–1489.

90 Jain, R.K., and Simha, R. (1979) Equation of state of semicrystalline and crystalline polymers. *J. Polym. Sci. Polym. Phys. Ed.*, **17**, 1929–1946.

91 Lennard-Jones, J.E. (1929) The theory of properties of matter in equilibrium, in *Statistical Mechanics* (ed. R.H. Fowler), Cambridge Univ. Press, Cambridge, pp. 292–337.

92 Lennard-Jones, J.E. (1931) Cohesion. *Proc. Phys. Soc.*, **43**, 461–482.

93 Lennard-Jones, J.E., and Devonshire, A.F. (1937) Critical phenomena in gases I. *Proc. R. Soc.*, **163**, 53–70.

94 Utracki, L.A. (1989) *Polymer Alloys and Blends*, Hanser, Munich; Utracki L.A. (ed.) (2002) *Polymer Blends Handbook*, Kluwer Academic Publishers, Dordrecht.

95 Utracki, L.A. (2011) Rheology of polymer blends, in *Encyclopedia of Polymer Blends* (ed. A. Isayev), Wiley-VCH Verlag GmbH, Weinheim, Germany, Chapter 2 in Volume 2, pp. 27–107.

96 Israelachvili, J.N., Tirrell, M., Klein, J., and Almog, Y. (1984) Forces between two layers of adsorbed polystyrene immersed in cyclohexane below and above the Θ-temperature. *Macromolecules*, **17**, 204–209.

97 Horn, R.G., and Israelachvili, J.N. (1988) Molecular organization and viscosity of a thin film of molten polymer between two surfaces as probed by force measurements. *Macromolecules*, **21**, 2836–2841.

98 Cosgrove, T., Heath, T.G., Ryan, K., and Crowley, T.L. (1987) Neutron scattering from adsorbed polymer layers. *Macromolecules*, **20**, 2879–2882.

99 Cosgrove, T., Heath, T.G., Phipps, J.S., and Richardson, R.M. (1991) Neutron reflectivity studies of polymer adsorbed on mica from solution. *Macromolecules*, **24**, 94–98.

100 Fleer, G., Cohen-Stuart, M.A., Scheutjens, J.M.H.M., Cosgrove, T., and Vincent, B. (1993) *Polymers at Interfaces*, Chapman and Hall, London.

101 Hentschke, R. (1997) Molecular modeling of adsorption and ordering at solid interfaces. *Macromol. Theory Simul.*, **6**, 287–316.

102 Termonia, Y. (2009) Monte Carlo modeling of dense polymer melts near nanoparticles. *Polymer*, **50**, 1062–1066.

103 Tokihisa, M., Yakemoto, K., Sakai, T., Utracki, L.A., Sepehr, M., Li, J., and Simard, Y. (2006) Extensional flow mixer for polymer nanocomposites. Proceedings of the NRCC-IMI Polymeric Nanocomposites onference, Boucherville, QC, Canada, 2005.09.28–30. *Polym. Eng. Sci.*, **46** (8), 1040–1050.

104 Utracki, L.A., and Lyngaae-Jørgensen, J. (2002) Dynamic melt flow of nanocomposites based on poly-ε-caprolactam. *Rheol. Acta*, **41**, 394–407.

5
Following the Nanocomposites Synthesis by Raman Spectroscopy and X-Ray Photoelectron Spectroscopy (XPS)

Sorina Alexandra Garea and Horia Iovu

5.1
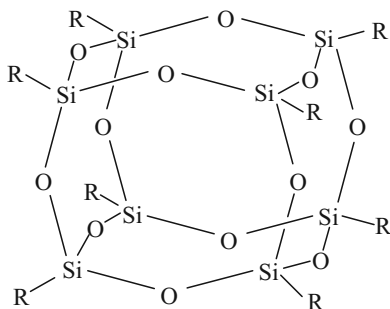## Nanocomposites Based on POSS and Polymer Matrix

5.1.1
Introduction

Polyhedral oligomeric silsesquioxanes (POSS) are considered intermediate compounds between the silica (SiO_2) and silicone compounds (R_2SiO) with the general formula ($RSiO_{1.5})_n$, where R is an organic substituent attached to the inorganic cage formed by silicon and oxygen atoms (Figure 5.1) [1–3].

POSS in comparison with other nanostructured agents like silica, layered silicates, and carbon nanotubes includes both organic and inorganic parts in the structure, each of them with a well-defined role. Thus, the inorganic structure $(SiO_{1.5})_8$ of POSS acts as a reinforcing agent while the organic substituent provides a good compatibility with polymer matrices or their monomers and even covalent bonds between the POSS structure and the polymer matrix if it contains various groups like vinylic, methacrylic, etc. [2].

The organic substituents may include polymerizable functional groups like vinyl, acrylic, and epoxy. By choosing a certain organic substituent several properties such as crosslinking density and dispersion, the degree of polyhedral structures can be strictly controlled. The POSS molecules were introduced into various polymer matrix types (vinyl ester resins, polyimides, epoxy resins, polybenzoxazines, polymethylmethacrylates, polyethylene oxide, and polyurethanes) in order to increase some properties like thermal stability and mechanical properties [4–12].

R = alkyl or aryl substituent

Figure 5.1 The general structure of POSS.

5.1.2
Raman Spectroscopy Applied for Following the Synthesis of Nanocomposites Based on Polymer Matrix and POSS

Spectroscopic methods like Raman and FTIR spectroscopy are often used to monitorize the evolution of complex reactions like copolymerization and crosslinking reactions of various thermoset matrices [13–16].

The Raman spectroscopy is a suitable method used for monitoring the conversion of C=C bonds from vinylic, methacrylic, and unsaturated polyesters because these bonds exhibit intense Raman signals in comparison with other spectroscopic methods (especially, e.g., FTIR spectroscopy).

Figure 5.2 shows a comparison between the Raman and FTIR spectra of two acrylic resins (bisphenol A glycerolate dimethacrylate [BisGMA] and triethylene glycol dimethacrylate [TEGDMA]).

As the C=C bond from the methacrylic group is nonpolar, the assigned band (1638 cm^{-1}) exhibits a higher intensity in the Raman spectrum than in the FTIR spectrum and because of this feature Raman spectroscopy can be successfully used to follow the crosslinking reaction of methacrylic and acrylic resins. Figure 5.3 shows an example of monitoring crosslinking reaction of an acrylic resin (bisphenol A ethoxylate dimethacrylate-BisEMA) with benzoyl peroxide at 80°C using Raman spectroscopy.

During the polymerization reaction of BisEMA the peak at 1638 cm^{-1} significantly decreases due to the consumption of methacrylic groups. In the aromatic methacrylic resins the peak assigned to the aromatic ring was used as reference in order to establish the conversion. After 90 min of reaction the conversion of the double bond tends to be constant. The restricted mobility of radical chain ends is responsible for this limited conversion of the methacrylic bond which was founded in many methacrylic systems.

Moreover, Raman spectroscopy is also useful in the synthesis of nanocomposites based on POSS and polymer matrix. The special structure of POSS enables

a)

b)
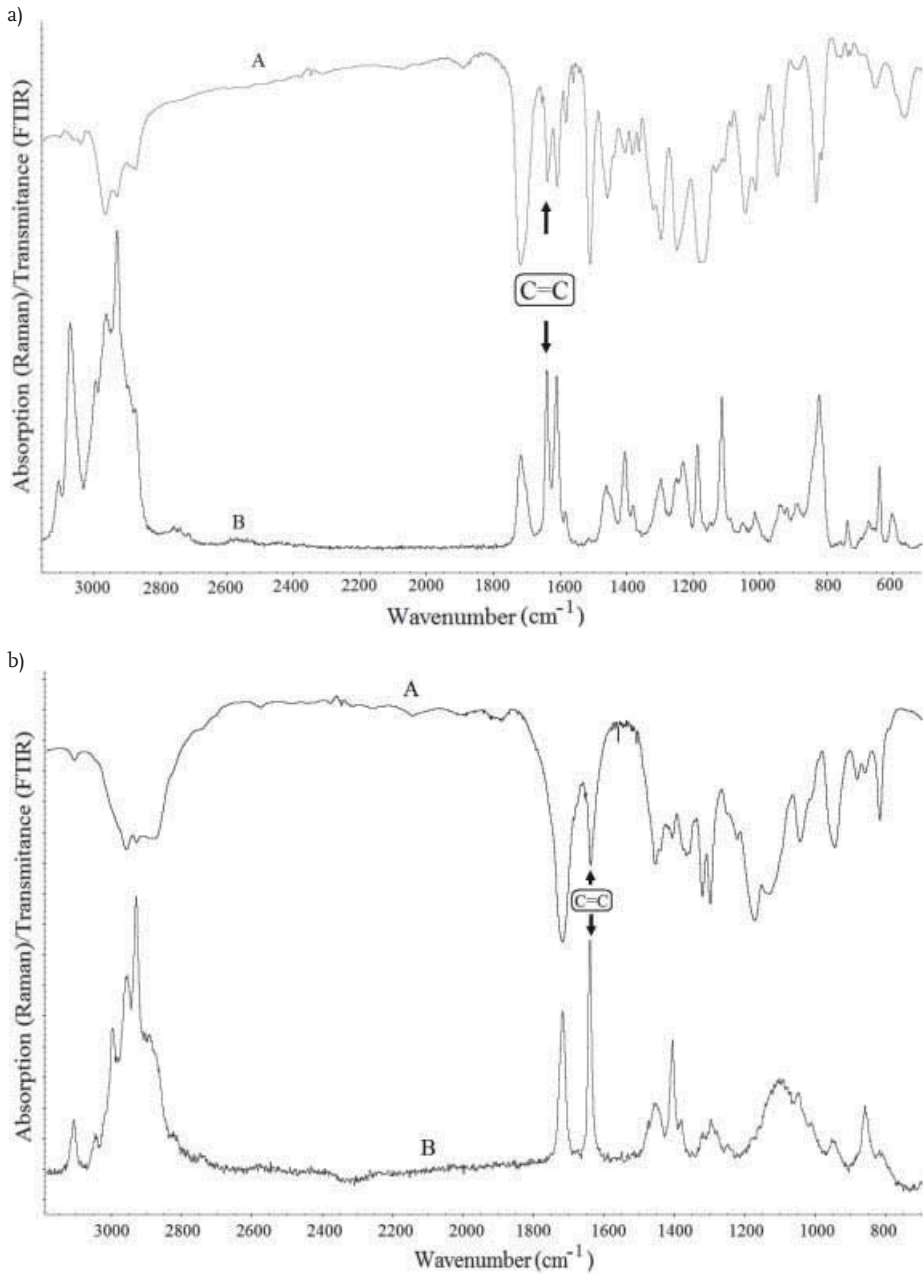
Figure 5.2 FTIR and Raman spectra for (a) BisGMA and (b) TEGDMA methacrylic resins.
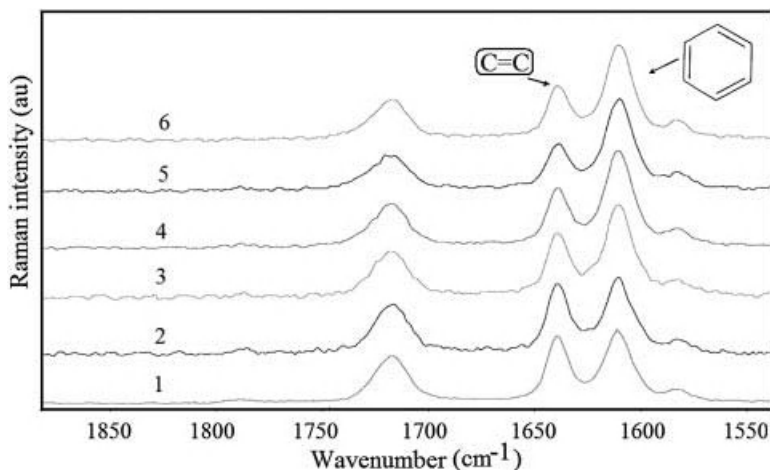
Figure 5.3 Raman spectra recorded during the polymerization reaction of BisEMA with benzoyl peroxide (1 wt%) at different reaction times: (1) 0 min, (2) 30 min, (3) 60 min, (4) 90 min, (5) 120 min, (6) 150 min.

us to develop a variety of hybrid materials (nanocomposites) which exhibit specific properties. POSS with various organic substituents can be considered multifunctional nanomaterials that may be used as additives if they are dispersed in the matrix polymer or macromers when they are copolymerized with other monomers. The nanocomposites based on a polymer matrix and POSS could be synthesized through various methods like physical mixing of POSS with polymer matrix, *in situ* polymerization, copolymerization or grafting of POSS with widely monomers, and sol–gel methods [17–19]. The proper method is chosen depending on the type and structure of the polymer matrix and POSS.

The physical mixing method was used mainly to introduce different POSS types with no reactive groups in thermoplastic polymer matrices such as polypropylene oxide (PPO), polypropylene (PP), high-density polyethylene (HDPE), polymethylmethacrylate (PMMA), polyvinyl chloride (PVC) polyethylene terephtalate (PET), polystyrene (PS), and poly(bisphenol A carbonate) (PBAC) [20–23]. A common problem of this method is how to obtain a stable dispersion of POSS at molecular level within the polymer matrix [21].

The *in situ* polymerization method involves several types of synthesis according to the raw materials, namely, polymerization of functional groups already existed in the structure of POSS substituents by different polymerization mechanisms [22–24], polymerization of monomers in which the POSS has been dispersed, and copolymerization of monomers with functional groups from the POSS organic substituents [24–26].

There are several factors that must be taken into account for the synthesis of nanocomposites based on polymer matrices and POSS. Thus, the reactivity of
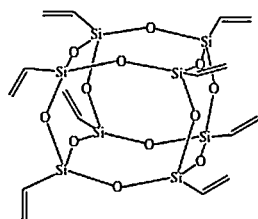
Octa-vinyl POSS
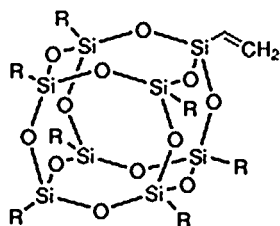
Mono-vinyl POSS
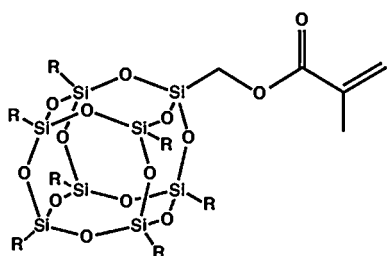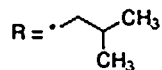
R = /-butyl

Monofunctional-methacrylic POSS
(HISO-POSS)
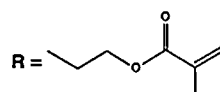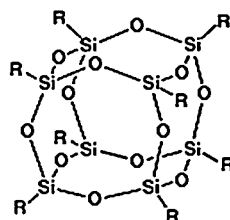
Multifunctional methacrylic POSS
(MA-POSS)

Figure 5.4 The chemical structures of various POSS with polymerizable functional groups.

functional groups from POSS organic substituents and the copolymerization reaction rate of POSS with other monomers are two examples of factors which may influence the final properties of obtained hybrid materials [27].

Raman spectroscopy may be successfully used in the synthesis of nanocomposites based on POSS which include vinylic or methacrylic functional groups into the organic substituents on the inorganic cage (Figure 5.4) in order to follow the evolution of the functional groups *homopolymerization* or *copolymerization reaction* with other acrylic/methacrylic groups from the matrix structure.

The FTIR and Raman spectra of POSS molecules bring important information about the chemical structures of these compounds. Thus, the FTIR spectra exhibit a strong absorption band at $1105\,cm^{-1}$ assigned to the asymmetric stretching vibrations of Si–O–Si linkage from the inorganic cage. This band shows a low intensity in the Raman spectrum.

The main feature of the Raman spectra of vinylic POSS (octavinyl-POSS and monovinyl-POSS) is that these hybrid molecules exhibit higher intensity of the C=C bond from vinylic groups ($1605\,cm^{-1}$) in the Raman spectra in comparison with the FTIR spectra, especially for monovinyl-POSS (Figure 5.5).

a)

b)
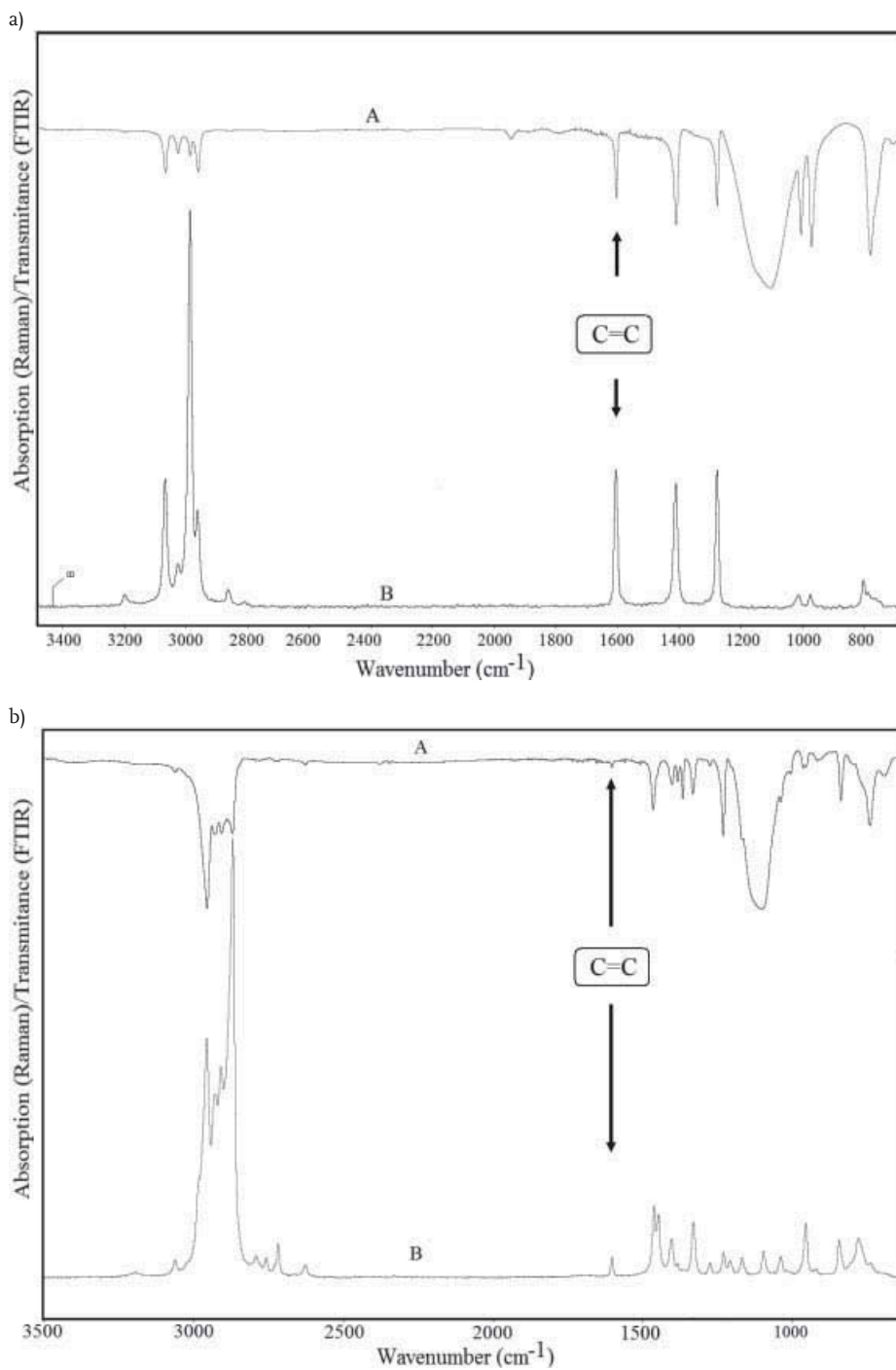
Figure 5.5 FTIR and Raman spectra for (a) octavinyl-POSS and (b) mono-vinyl-POSS.

Also the POSS molecules substituted with methacrylic groups exhibit a higher intensity of the C=C bond in the Raman spectra [28].

The difference in intensity of the band corresponding to the C=C bond between Raman and FTIR is more significant for POSS compounds compared with acrylic resin.

Figure 5.6 shows an example of monitoring by Raman spectroscopy the copolymerization reactions between BisGMA and two types of methacrylic POSS, one with only one reactive group (HISO-POSS) and the other with eight methacrylic groups (MA-POSS).

The homopolymerization reaction of BisGMA initiated by benzoyl peroxide involves a radicalic process consisting of initiation, propagation, and termination. A similar reaction mechanism is also assigned for the reactions of BisGMA with POSS macromers (HISO-POSS/MA-POSS) but these hybrids may be considered complex systems for which different reactions like homopolymerization of BisGMA, homopolymerization of HISO-POSS and BisGMA followed by POSS grafting may occur (Figure 5.7).

Considering the case of monofunctional POSS one should also take into account its ability to homopolymerize. Thus mono-methacrylate-functionalized POSS reagents are capable of being polymerized into novel linear silsesquioxane-based materials [23–24].

If the POSS compound includes more than one functional group (e.g., MA-POSS), the crosslinking reactions between POSS molecules may occur despite the sterical hindrance exhibited by POSS cages (Figures 5.8 and 5.9).

As can be seen in Figure 5.9 the peak at $1638\,cm^{-1}$ attributed to C=C bonds from methacrylic groups substantially decreases especially if compared with a reference peak ($1713\,cm^{-1}$ assigned to C=O groups which do not suffer any chemical reactions).

The Raman data are useful to establish the conversion of methacrylic groups for the studied hybrid systems (Figure 5.10). Thus, the conversion of methacrylic bonds can be calculated considering two bands: one at $1638\,cm^{-1}$ assigned to the C=C bond from the methacrylic group and the other at $1609\,cm^{-1}$ assigned to the benzene ring from the BisGMA structure used as reference. The degree of methacrylate conversion was established using the following equation:

$$\eta = \left[\frac{\left(\dfrac{A_{1638}}{A_{1609}} \right)_t}{\left(\dfrac{A_{1638}}{A_{1609}} \right)_0} \right] \times 100$$

where

η = conversion (%);

$\left(\dfrac{A_{1638}}{A_{1609}} \right)_t$ = the ratio between the area of 1638 and $1609\,cm^{-1}$ at time t;

$\left(\dfrac{A_{1638}}{A_{1609}} \right)_0$ = the ratio between the area of 1638 and $1609\,cm^{-1}$ at time 0.
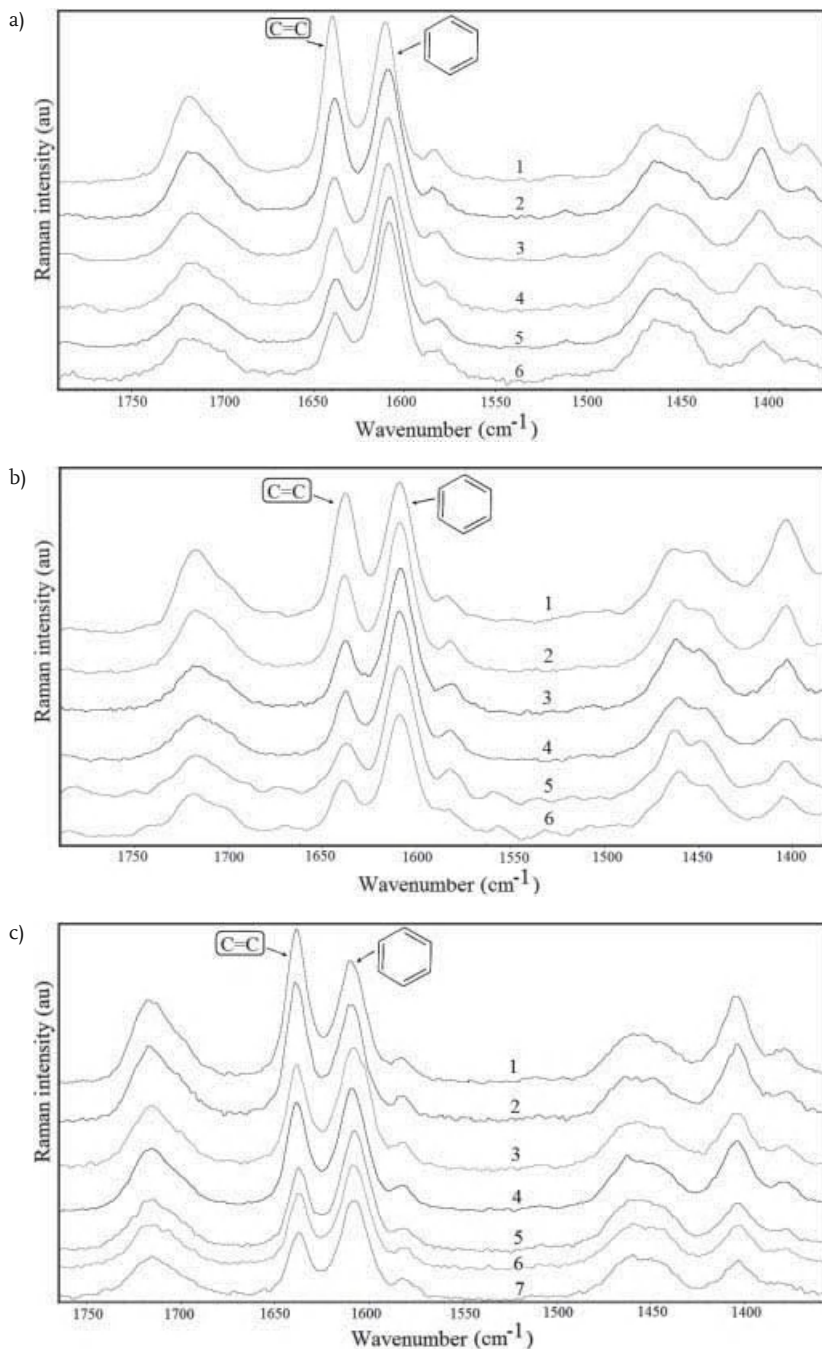
Figure 5.6 The Raman spectra recorded during the reaction of (a) BisGMA homopolymerization, (b) BisGMA with HISO-POSS, and (c) BisGMA with MA-POSS at various reaction times: (1) 0 min, (2) 20 min, (3) 30 min, (4) 60 min, (5) 95 min, (6) 135 min, (7) 160 min. Initiator = benzoyl peroxide (1%); BisGMA/POSS = 85:15.
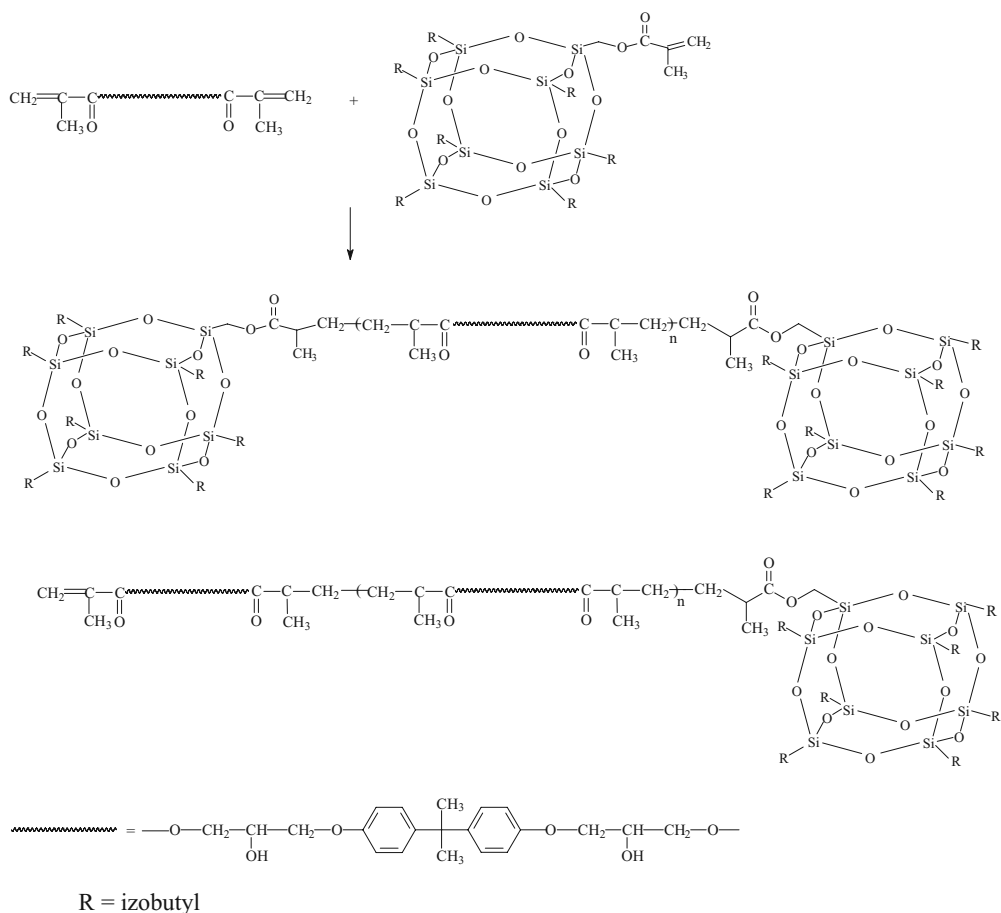
Figure 5.7 The copolymerization reaction of BisGMA with HISO-POSS.

As one may notice the POSS type exhibits a strong influence on the final conversion of methacrylic groups. Thus the conversion of methacrylic bonds decreases for the hybrid systems which contain POSS in comparison with the reference (BisGMA). The hybrid system based on BisGMA and MA-POSS exhibits the lowest conversion of methacrylic groups because of the fact that the eight methacrylic groups from each POSS cage are trapped within the POSS agglomerates, thus being more difficult to reach by the MA groups from the BisGMA monomer. This behavior was also encountered for multifunctional epoxy–POSS systems [29] and methacrylated POSS in the polyimide matrix[30].

As it was previously reported the reactivity of the pendant POSS methacrylic groups depends on the inert POSS substituents, that is, on their sterical demand [28, 31].
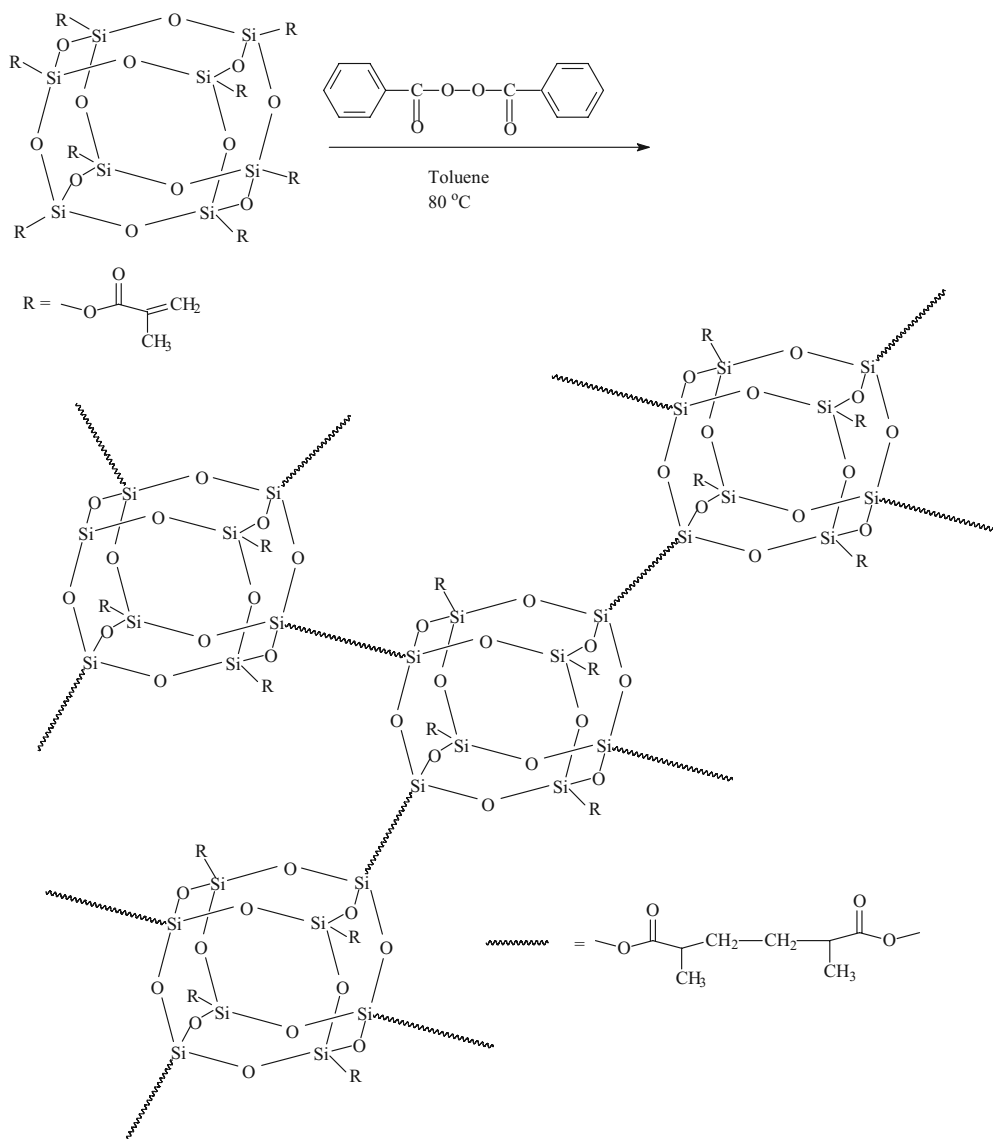
Figure 5.8 The reaction of MA-POSS using BP as an initiator.

The aspects regarding the reactivity of functional groups from the hybrid exhibit a strong influence on the properties of the final nanomaterials. Thus the lower POSS reactivity leads to a low incorporation rate of POSS into the networks which mainly occurs in the late (post-gel) stages of the reaction and therefore the formation of POSS-rich domains due to the tendency of POSS to phase separation is enhanced.
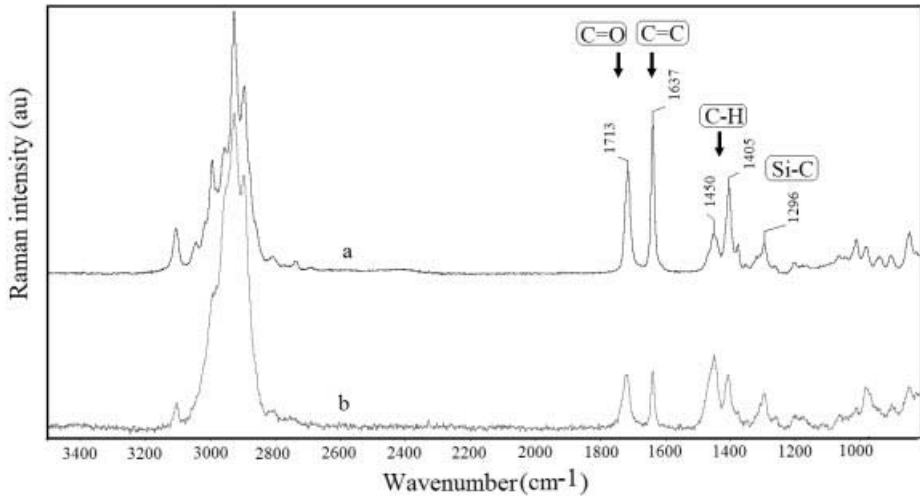
Figure 5.9 Raman spectra of (a) MA-POSS and (b) product obtained by MA-POSS polymerization with BP (1 wt%) at 75 °C for 24 h.
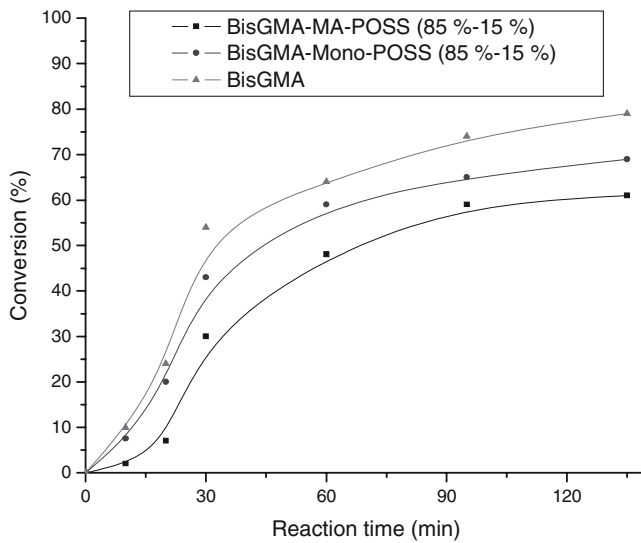
Figure 5.10 The dependence of methacrylic group conversion on reaction time for BisGMA and BisGMA-POSS nanocomposites with different POSS calculated from Raman data.

5.1.3
XPS Applied for Characterization of Polymer-POSS Nanocomposites

5.1.3.1 Analysis of Functionalized POSS Molecules

Unlike the other nanostructured agents (carbon nanotubes, nanosilica, montmorillonite), POSS compounds may be synthesized in a large variety of structures with certain functional groups in organic substituents that influence a range of properties like solubility, reactivity, and compatibility with various polymer matrices used in the synthesis of polymer nanocomposites [32].

The presence of these functional groups from organic substituents can be proved using X-ray photoelectron spectroscopy (XPS).

Figure 5.11 shows the XPS survey and C 1s and Si 2p high-resolution spectra of POSS-amino. As one may observe the XPS survey spectrum shows distinct peaks assigned to carbon, silicone, and oxygen. The C 1s peak was deconvoluted into two peaks assigned as follows: the lower energy peak corresponds to the C–Si bond while the second peak at 285.11 eV was attributed to the C–C bonds. The
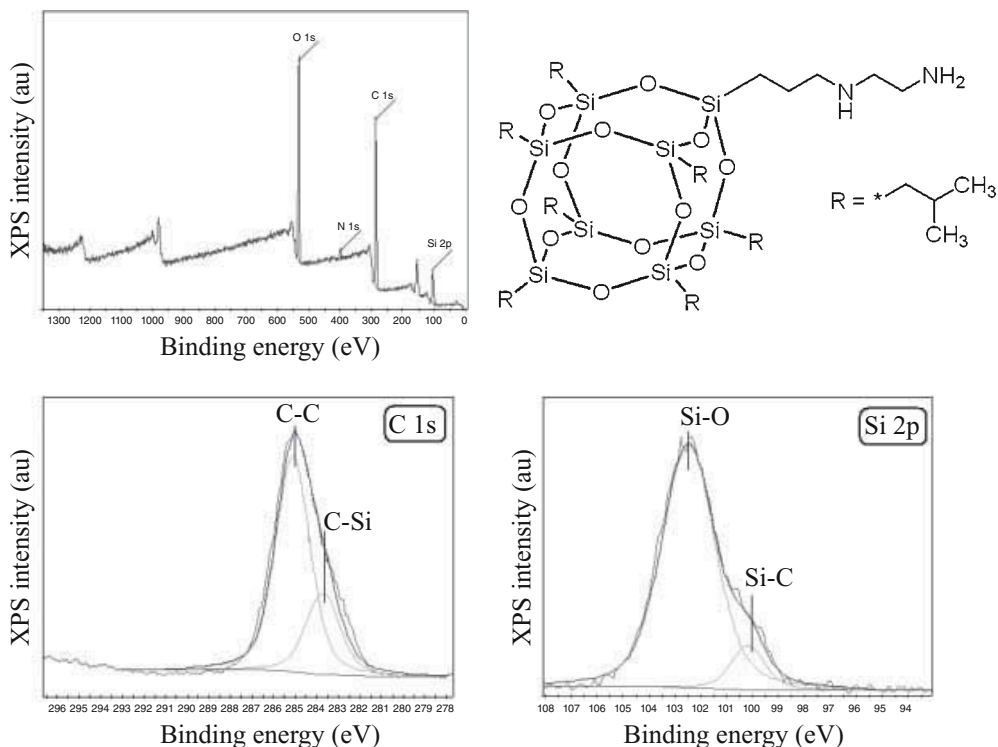
Figure 5.11 XPS survey and C 1s and Si 2p high-resolution spectra of POSS-amino.
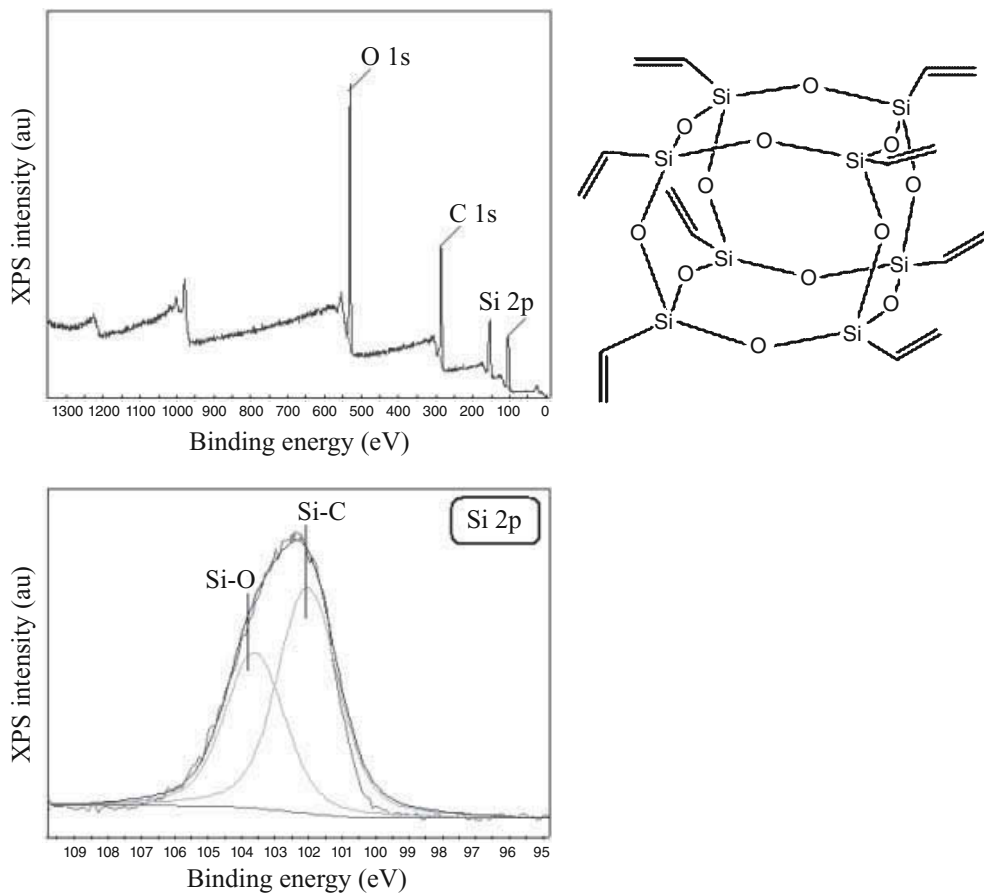
Figure 5.12   XPS survey, C 1s and Si 2p high-resolution spectra of octa-vinyl-POSS.

C–N bond was not identified probably due to its low concentration compared to the other bonds (C–C and C–Si).

For the Si 2p deconvoluted spectrum two different types of Si 2p peaks centered at 102.4 and 100.2 eV are identified. The first peak is assigned to the Si–O bonds from the inorganic core of the POSS and the second one to the Si–C bonds making the link with the organic substituents.

Figure 5.12 shows another example of the XPS survey and Si 2p deconvoluted spectra of POSS substituted with eight vinyl groups (octa-vinyl POSS).

As was expected the XPS survey spectrum shows peaks assigned to carbon, silicone, and oxygen. In the case of this POSS structure the C 1s deconvoluted spectrum shows only one peak assigned to both C–Si and C=C bonds, the individual peaks for these groups being overlapped.
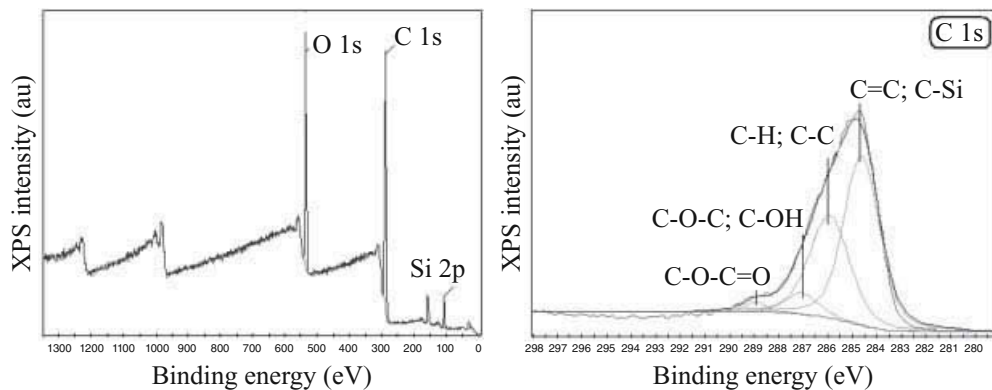
Figure 5.13 XPS survey and C 1s deconvoluted spectra of nanocomposite based on BisGMA and mono-POSS (85–15%).

The Si 2p peak was deconvoluted into two peaks corresponding to the Si–O bond from the inorganic cage (103.6 eV) and the Si–C bond formed between inorganic POSS structure and organic substituents (102 eV). It may be observed that these peaks are shifted to higher values of binding energies than for POSS-amino due to the higher polar environmental exhibited by the eight methacrylic groups surrounding the POSS cages.

5.1.3.2 Characterization of Nanocomposite Materials

Another application of the XPS method consists in the characterization of polymer nanocomposites [33–36].

Figure 5.13 shows an example of XPS survey and C 1s deconvoluted spectra for a nanocomposite based on acrylic resin (BisGMA) and mono-metacrylic-POSS.

It can be seen that the C 1s is deconvoluted into four main peaks according to different carbon atoms from the nanocomposite final structure. Thus, the peak around 284.6 eV is assigned to unreacted C=C bonds and to C–Si bonds. The peak at 285.9 eV is characteristic for C–H and C–C bonds from aliphatic and aromatic species. The peak at 287 eV is characteristic to C–O–C and C–OH bonds from the BisGMA structure and the last peak at 288.9 eV is attributed to C=O bonds from C–O–C=O groups.

5.1.4
Conclusions

For synthesis of polymer-polyhedral oligomeric silsesquioxanes (POSS) nanocomposites Raman spectroscopy is a useful method to study the influence of POSS organic substituents on the conversion degree. Thus the methacrylic group consumption is strictly evaluated by Raman considering all the polymerization proc-

esses involved, monomer and POSS homopolymerization, and copolymerization between the monomer and POSS compound. The final degree of methacrylic group conversion is important since the main thermal and mechanical properties of the synthesized nanocomposite depend on its value. The significant target is to increase the final conversion which is however limited by the sterical hindrances occurred at POSS level and furthermore due to the POSS agglomeration within the polymer matrix.

The XPS is a valuable technique for identifying the main structure of the polymer–POSS nanocomposite considering the main signals given by the bonds present within the hybrid structure. However the application of this method to POSS-based nanocomposites is limited to the material surface and also its reliability is influenced by the low dispersability of the POSS compound within the polymer matrix even if some bonds are formed by copolymerization between the methacrylic bonds from monomer and POSS.

5.2
Raman and XPS Applied in Synthesis of Nanocomposites Based on Carbon Nanotubes and Polymers

5.2.1
Introduction

Carbon nanotubes (CNTs) discovered in 1991 by Iijima defined as unique tubular nanostructures characterized by a very high length/diameter ratio can be considered another allotropic form of carbon atoms [37]. These nanostructured materials exhibit a chemical composition similar to graphite but they are rather considered as isotropic materials which make the difference between CNT and other carbon structures and give unique properties.

The chemical reactivity of CNT is generally similar to that of carbon and in particular with graphite reactivity but the unique structure gives the specific properties. CNT could suffer some changes in the molecular orbitals of carbon atoms and shifting the electronic density to the external surface of nanotubes due to the walls bending. The ends of CNT are considered to be their most reactive parts because in this area the highest strain is achieved and therefore the carbon atoms are rather sp^3 than sp^2 species [38].

CNTs are classified as single-walled carbon nanotubes (SWCNTs) or multi-walled carbon nanotubes (MWCNTs) depending on the number of graphene layers from which a single nanotube is composed [39].

Both SWCNT and MWCNT are recommended in many fields like electronics, biomedical, and polymer-based nanocomposites due to their remarkable properties (mechanical, thermal, electric) [40].

The compatibilization of a nanostructured agent with a polymer matrix is the most important step in the synthesis of polymer-based nanocomposites. Depending on the type of nanostructured agent several methods for increasing the

compatibility with the polymer matrix have been developed. For instance in the case of montmorillonite nanostructured clay that exhibits a high cationic exchange capacity the compatibilization process consists in a cationic exchange process between the raw clay and different organic cations like protonated amines, for example, polyetheramines [41–42], protonated adducts synthesized from the reaction of epoxy resin and amines [43–46],, and polyhedral oligomeric silsesquioxane [47]. Another case is of the halloysite nanostructured agent for which the functionalization surface consists in the reaction of coupling agents with the hydroxyl groups from the clay surface [48].

Like other nanostructured reinforcing agents, carbon nanotubes are difficult to be uniformly dispersed into the polymer matrix due to the strong surface interactions between the tubes [49]. Therefore the CNT surface modification is considered the most important step in the synthesis of polymer-based nanocomposites. The surface functionalization presents a dual role, namely to ensure a uniform dispersion of CNT into the polymer matrix as well as to stabilize dispersion. It is achieved by modifying the CNT surface with different agents depending on the polymer matrix type used and the desired application of CNT. Surface functionalization of carbon nanotubes is also very important because their use and processing are limited due to the insolubility in most organic solvents.

The most used CNT surface modifier agents include amines (octadecylamine, nonylphenoxy polypropylene oxyamine, diamine like 4,4′-(4,4′-isopropylidenedip henyl-1,1′ diyldioxy)dianiline-IDDA, ethylenediamine) [50–54], glucozamine [55], polystyrene [56], polyethyleneimine [57], hydrophilic dendrons [58], silanization agents [59–61], magnetic silica [62], and polyhedral oligomeric silsesquioxane (aminopropylisooctil-POSS) [63].

CNT surface modification can be achieved using different methods like defects functionalization, noncovalent functionalization, covalent functionalization, electrochemical methods, and click chemistry. These methods were classified as physical, chemical, or electrochemical methods [64].

Functionalization of carbon nanotubes is difficult to prove by conventional methods and in addition the CNTs include a significant amount of impurities (amorphous carbon, graphite particles) which apparently show the same nature as that of carbon nanotubes.

Raman spectroscopy, X-ray photoelectron spectroscopy (XPS), transmission electron microscopy (TEM), and scanning electron microscopy (SEM) are the main techniques used for characterization of CNT and nanocomposites based on polymers and CNT respectively [65–66].

5.2.2
X-Ray Photoelectron Spectroscopy (XPS) Used to Monitorize the Synthesis of Polymer-CNT-Based Nanocomposites

Nowadays XPS is considered a modern tool for carbonaceous materials characterization used to determine the chemical composition, impurity presence, and nature of chemical bonds [67].

The most important application of XPS in nanocomposites based on polymer-CNT is to identify the chemical composition of the modified carbon nanotubes surface in order to confirm if the surface modification has occurred or not.

The XPS analysis performed on the CNT surface was focused on measuring the binding energy of photoelectrons ejected when CNTs are irradiated with X-rays [68].

In the following section some examples of CNT surface modification with different agents pointed out by XPS analysis are detailed.

5.2.2.1 CNT Functionalization with Carboxylic Groups

The modification of the CNT surface with carboxylic groups is the most used method to increase the solubility, reactivity, and functionalization capacity of CNT. These functional groups may be introduced using different methods like oxidation with strong acids (e.g., HNO_3) and mixture of acids (H_2SO_4/HNO_3) [69]. The CNT modified with carboxylic groups may react with other compounds like amines and thus new multifunctional nanostructured materials can be obtained [70].

The CNT surface functionalization involves several steps that depend on the modifier agent used. For example, if the CNT is functionalized with amine, in the first step the CNT surface undergoes an oxidative process to obtain carboxylic groups onto the surface and in the second step the modified CNT react directly with the amine in the presence of activation agents (*N*(3-dimethylaminopropyl)-*N'*-ethyl carbodiimide hydrochloride (EDC) and *N*-hydroxysuccinimide (NHS) [51]. An example of CNT modification with octadecylamine is shown in Figure 5.14.

The XPS survey spectrum of SWCNT-COOH (Figure 5.15a) was recorded in order to identify the chemical composition of the CNT surface. As one may observe the XPS spectrum exhibits two peaks assigned to C 1s and O 1s. In order to obtain more information about the SWCNT-COOH structure the C 1s high-resolution spectrum was recorded (Figure 5.15b). Generally the CNTs exhibit three characteristic peaks in XPS analysis that can be identified as follows: a dominant peak at 284.9 eV attributed to the C–C sp^2 carbon atoms of the graphene sheets, a peak at 285.5 eV assigned to the defects on the nanotubes structure, and a peak at 291.5 eV assigned to the π–π* transitions [71–72].

For SWCNT-COOH two new peaks at 286.9 and 289.4 eV appear in the XPS spectrum which were assigned to the C–OH bond and the O–C=O group, respectively.

5.2.2.2 CNT Functionalization with Amines

If the goal is to synthesize a modified CNT with amine, an additional step is required. Thus the CNT oxidation step is followed by amidation reaction between carboxylic groups which exist on the CNT surface and amine. Figure 5.16 shows an example of XPS survey and C 1s high-resolution spectra of modified SWCNT with octadecylamine (ODA).

The XPS survey spectrum of SWCNT-ODA shows three distinct peaks assigned to C 1s (91.38%), O 1s (5.55%), and N 1s (3.07%). The presence of N 1s peaks confirms that the CNT functionalization with ODA has occurred. In the C 1s
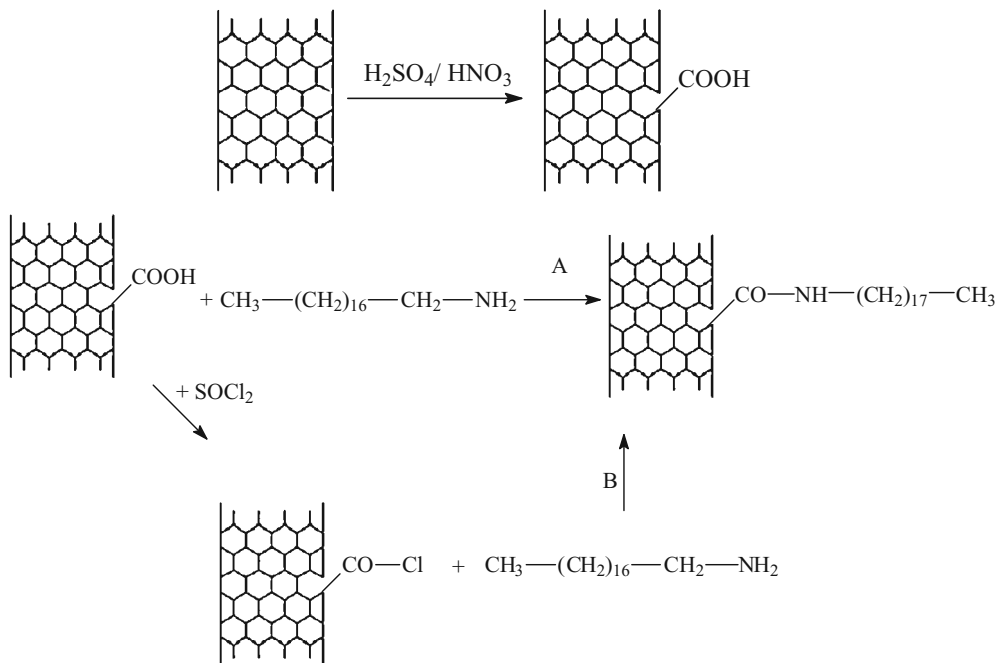
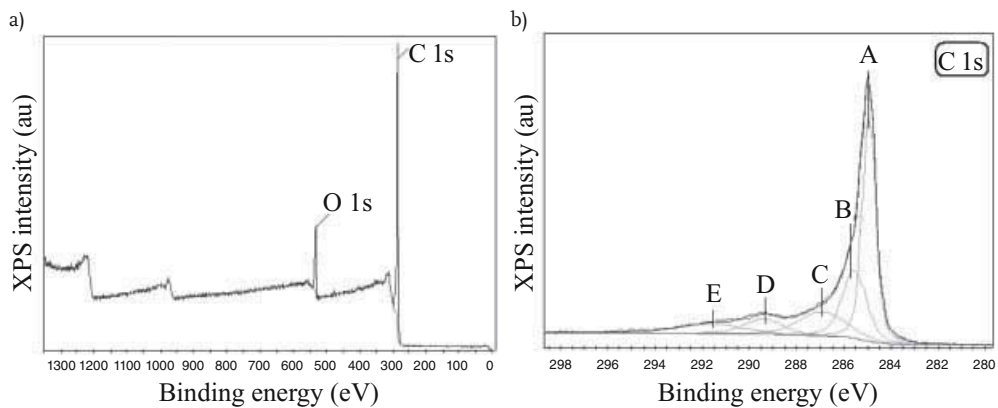**Figure 5.14** The steps followed for CNT modification with octadecylamine.

Figure 5.15 The XPS survey (a) and C 1s high-resolution (b) spectra of SWCNT-COOH.
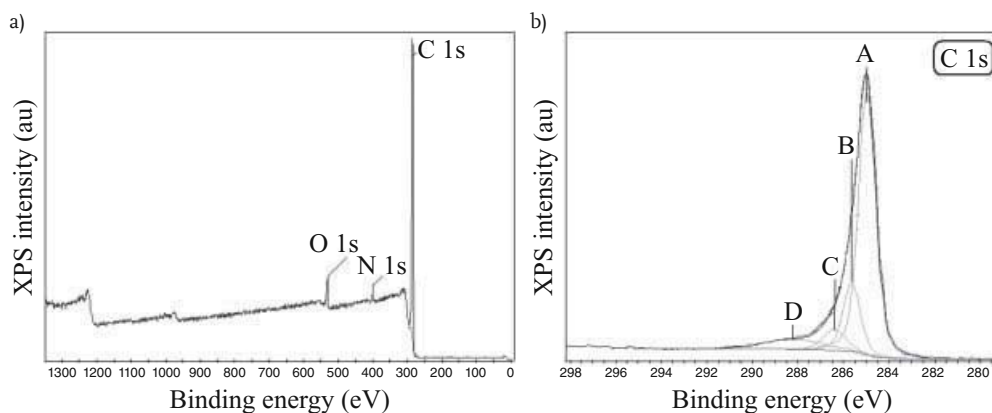
a)

b)

Figure 5.16 The XPS survey (a) and high-resolution C 1s (b) spectra of SWCNT-ODA.

deconvoluted spectrum of SWCNT-ODA four peaks are found. The characteristic peaks corresponding to the C–C sp^2 and C–C sp^3 from defects of CNT appear at the same energy like in SWCNT-COOH. In addition, for SWCNT-ODA, the $\pi–\pi^*$ transition peak disappears because of the ODA long chains which cover the nanotubes walls. A similar situation was encountered for the MWCNT surface functionalization with a nonylphenoxy polypropylene oxyamine (B 100) [51]. The formation of the amidic bond was further proved by the presence of new peak at 288.2 eV [73].

5.2.2.3 CNT Functionalization with Bioconjugated Systems Based on Dendritic Polymers and Antitumoral Drug

In the recent years CNTs were thoroughly studied to extend their applications in biomedical field due to unique physical properties, size, shape, and structure [74].

The CNTs used in biomedical applications as controlled drug delivery systems have been proposed in numerous studies due to the existence of spaces capable of drug encapsulation [66, 75]. For this special application it is necessary to modify the CNT surface in order to increase the biocompatibility and water solubility dispersion, and meanwhile, to maintain a low toxicity level. For instance several antitumoral drugs like doxorubicine, cisplatin, and paclitaxel were covalently conjugated onto the CNT surface [76].

Our group synthesized a bioconjugated system based on a high-generation polyamidoamine with hydroxyl terminated groups and paclitaxel as a drug which was further attached onto the SWCNT surface in order to obtain a drug delivery system. The SWCNT functionalization was pointed out by XPS analysis. The synthesis of the drug delivery system consists of two steps (Figure 5.17).

The XPS survey and C 1s high-resolution spectra for SWCNT modified with bioconjugated system are shown in Figure 5.18 and the XPS assignments are summarized in Table 5.1.

Step 1
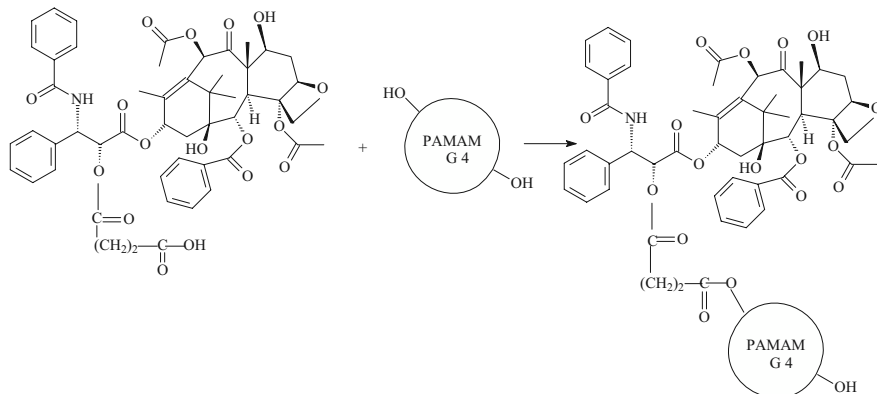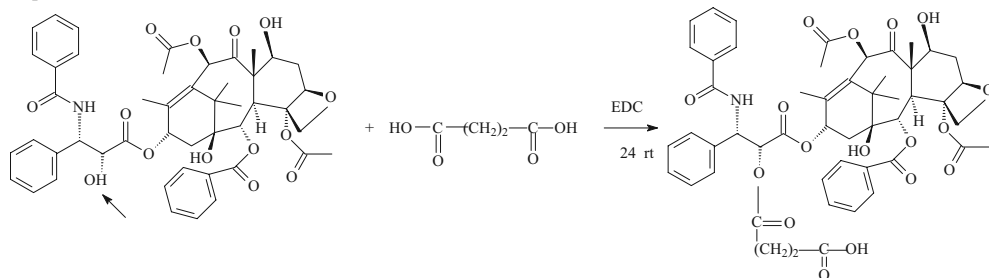
Step 2
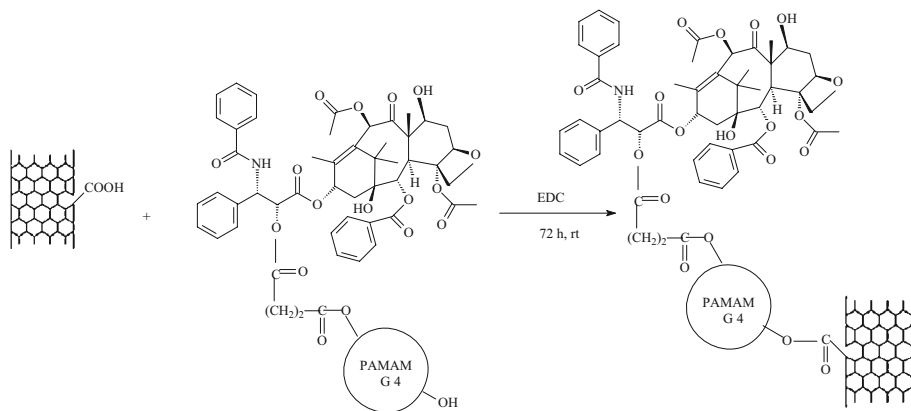
Figure 5.17 The steps for synthesis of the drug delivery system based on the modified SWCNT and PAMAM-G4-paclitaxel bioconjugated system. Step 1: the synthesis of bioconjugated systems based on fourth-generation polyamidoamine dendrimer with ethylenediamine core (PAMAM-G4-OH) and paclitaxel [77]. Step 2: the functionalization of the SWCNT surface with the bioconjugated system.
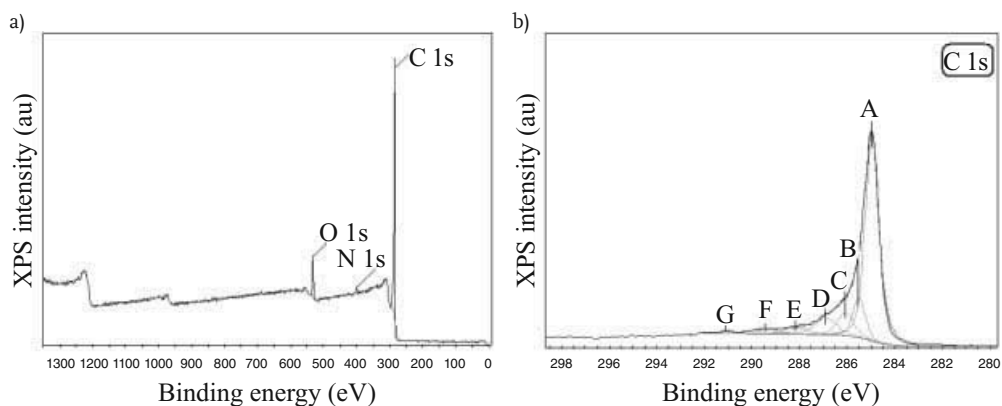
a)

b)

Figure 5.18 The XPS survey (a) and high-resolution C 1s (b) spectra of SWCNT modified with PAMAM-G4-paclitaxel bioconjugated system.

Table 5.1 The XPS assignments for the SWCNT modified with bioconjugated systems.

Code	Binding energy (eV)	Assignments
A	284.9	C–C from SWCNT
B	285.4	Defects from SWCNT
C	286.1	C–N from bioconjugate PAMAM-G4-OH-paclitaxel
D	286.8	C–O
E	288.1	N–C=O
F	289.4	O–C=O
G	291.1	π–π^* transitions

5.2.3
Polymer-CNT-Based Nanocomposites Synthesis Followed by Raman Spectroscopy

In Raman spectroscopy vibrational modes are identified by measuring the energy of scattered photons generated from a sample exposed to intense laser light [67]. Raman spectroscopy is a method that offers important information about electronic and vibrating properties of the CNT [57].

In order to identify the characteristic peaks of CNT an example of the Raman spectrum of commercially modified SWCNT with polyethyleneglycol (PEG) is shown in Figure 5.19.

The Raman spectrum of CNT typically consists of three specific zones (area):

1. *Radial breathing mode (RBM)* is situated between 75 and 300 cm^{-1} and is visible for carbon nanotubes which are characterized by a diameter of less than 3 nm, like SWCNT. In the case of nanotubes with diameters larger than 3 nm this
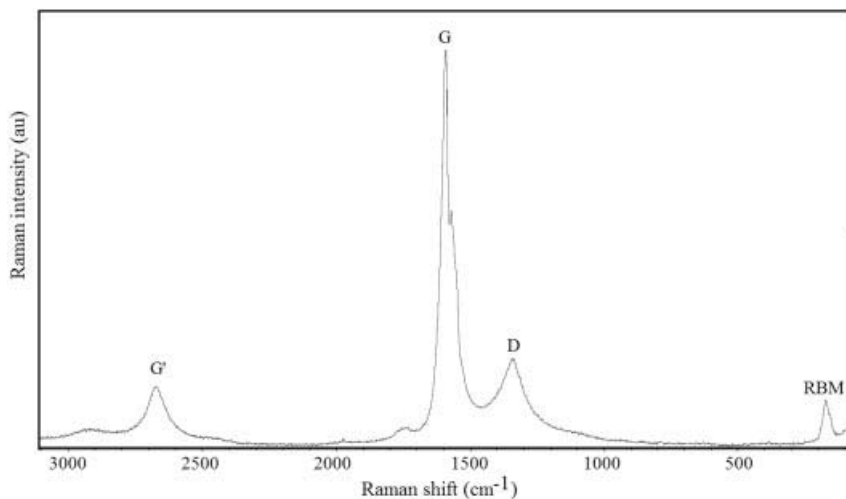
Figure 5.19 Raman spectrum of SWCNT modified with polyethyleneglycol (SWCNT-PEG). Excitation laser wavelength = 532 nm.

band may be absent. This band is associated with symmetrical movements of carbon atoms in the radial direction [78].

Some experimental data reported in the literature showed that the RBM can be useful for studying the diameter size of carbon nanotubes. In the case of aggregated carbon nanotubes the RBM band appears to be shifted with $6–20\,\text{cm}^{-1}$ at higher frequencies due to space restrictions imposed by neighboring tubes [78].

2. *In the frequency range between 1200 and $1600\,\text{cm}^{-1}$* the atoms tangential vibration movement generates two bands that provide supplementary characteristic information of CNT.

These bands called G band (graphitic band: $1500–1600\,\text{cm}^{-1}$) and D band (disorder band: $1300–1400\,\text{cm}^{-1}$) can give some information about the chemical changes and structural damage. The ratio between the intensity of the D band and the intensity of the G band, denoted as I_D/I_G, can be considered an indicator of the degree of disorder (defect density) in the CNT sidewall. An increase in this ratio corresponds to a high proportion of sp^3 carbon, which is generally attributed to the presence of structural defects in a higher percentage.

3. At higher frequencies ($2500–2900\,\text{cm}^{-1}$) the G′ band assigned to second-order processes is of less importance.

Figure 5.20 shows the Raman spectra of modified SWCNT with various agents and previously characterized by XPS analysis.

As one may observe all the analyzed samples exhibit the characteristic peaks of CNT (D band, G band, and RBM) which appear in the Raman spectrum.
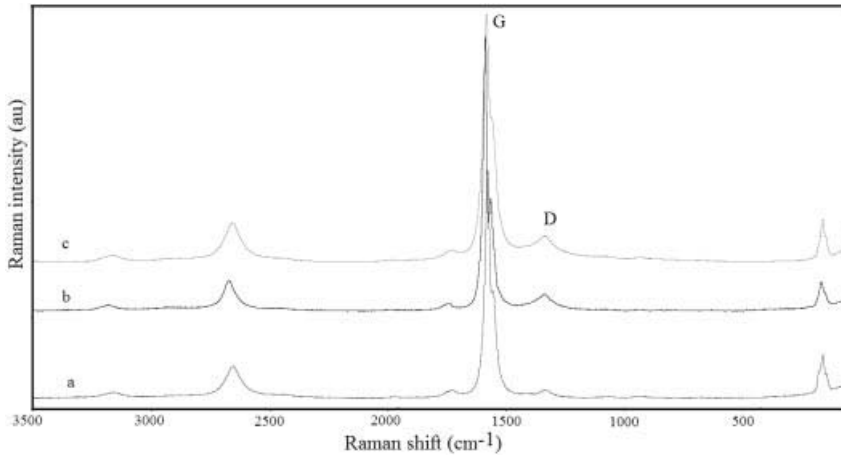
Figure 5.20 Raman spectra of SWCNT modified with different agents: (a) carboxylic groups (SWCNT-COOH), (b) octadecylamine (SWCNT-ODA), (c) bioconjugated system based on dendritic polymer PAMAM-G4-OH-paclitaxel (SWCNT-PAMAM-G4-OH-PACLIT-AXEL). Excitation laser wavelength = 532 nm.

Table 5.2 The ratio between the intensities of the D and G bands for carboxylated and modified SWCNT from Raman spectra.

SWCNT type	I_D/I_G	D peak (cm^{-1})	G peak (cm^{-1})
SWCNT-COOH	0.024	1335	1579
SWCNT-ODA	0.041	1341	1588
SWCNT-PAMAM-G4-PACLITAXEL	0.073	1339	1582

The results of Raman analysis summarized in Table 5.2 show an increase in the I_D/I_G ratio for the modified CNT which is a proof for the modification process. Also for MWCNT modified with various amines like B 100, benzylamine, the functionalization reaction was proved by the increase of the I_D/I_G ratio from Raman spectra [51].

5.2.4
Conclusions

Carbon nanotubes are good reinforcing nanoagents for polymer-based nanocomposites, but despite their unique properties their high dispersability in a polymer matrix is a demanded task due to the inert character and low reactivity of the nanotubes. Therefore the only way to form a proper nanocomposite material is

first to modify adequately the CNT surface in order to introduce functional groups and then to add and polymerize the organic monomer. Thus an enhanced compatibility between the CNT and polymer matrix will be achieved. All these steps of polymer–CNT nanocomposites synthesis may be accurate followed by Raman spectroscopy proving the nature of functional groups obtained on the CNT surface. This method is limited by the low absorption intensity of certain functional groups in Raman and/or by overlapping of some bands with those given by the polymer matrix as the final nanocomposite is synthesized. However, for all modified CNT the I_D/I_G ratio shown in Raman spectra is a good indicator of the degree of functionalization. As this ratio increases more desired groups are bonded onto the CNT surface.

The XPS spectra give the nature of atoms from the modified CNT surface and may even result in a quantitative analysis of atoms shown in the survey spectra. The deconvoluted spectra strictly show the types of certain atoms concerning their neighbors within the modified CNT structure. However, the conclusions from XPS are related only to the CNT surface and further advanced analysis like TEM is required to deeply analyze the morphology of nanomaterial.

Acknowledgments

References

1 Li, G., Wang, L., Ni, H., and Pittman, C.U. (2001) Polyhedral oligomeric silsesquioxane (POSS) polymers and copolymers: a review. *J. Inorg. Organomet. Polym.*, **11**, 123–154.

2 Douvas, A.M., Van Roey, F., Goethals, M., Papadokostaki, K.G., Yannakopoulou, K., Niakoula, D., Gogolides, E., and Argitis, P. (2006) Partially fluorinated, polyhedral oligomeric silsesquioxane-functionalized (meth)acrylate resists for 193 nm bilayer lithography. *Chem. Mater.*, **18**, 4040–4048.

3 Schwab, J.J., and Lichtenhan, J.D. (1998) Polyhedral oligomeric silsesquioxane (POSS)-based polymers. *Appl. Organomet. Chem.*, **12**, 707–713.

4 Laine, R.M., Zhang, C., Sellinger, A., and Viculis, L. (1998) Polyfunctional cubic silsesquioxanes as building blocks for organic/inorganic hybrids. *Appl. Organomet. Chem.*, **12**, 715–723.

5 Li, G., Wang, L., Toghiani, H., Daulton, T.L., and Pittman, C.U., Jr. (2002) Viscoelastic and mechanical properties of vinyl ester (VE)/multifunctional polyhedral oligomeric silsesquioxane (POSS) nanocomposites and multifunctional POSS–styrene copolymers. *Polymer*, **43**, 4167–4176.

6 Lee, Y.J., Huang, J.M., Kuo, S.W., Lu, J.S., and Chang, F.C. (2005) Polyimide and polyhedral oligomeric silsesquioxane

nanocomposites for low-dielectric applications. *Polymer*, **46**, 173–181.

7 Ni, Y., Zheng, S., and Nie, K. (2004) Morphology and thermal properties of inorganic–organic hybrids involving epoxy resin and polyhedral oligomeric silsesquioxane. *Polymer*, **45**, 5557–5568.

8 Wu, K., Song, L., Hu, Y., Lu, H., Kandola, B.K., and Kandare, E. (2009) Synthesis and characterization of a functional polyhedral oligomeric silsesquioxane and its flame retardancy in epoxy resin. *Prog. Org. Coating.*, **65**, 490–497.

9 Lee, Y.J., Kuo, S.W., Huang, C.F., and Chang, F.C. (2006) Synthesis and characterization of polybenzoxazine networks nanocomposites containing multifunctional polyhedral oligomeric silsesquioxane (POSS). *Polymer*, **47**, 4378–4386.

10 Yen, Y.C., Ye, Y.S., Cheng, C.C., Chen, H.M., Sheu, H.S., and Chang, F.C. (2008) Effect of LiClO$_4$ on the thermal and morphological properties of organic/inorganic polymer hybrids. *Polymer*, **49**, 3625–3628.

11 Huang, K.W., Tsai, L.W., and Kuo, S.W. (2009) Influence of octakis-functionalized polyhedral oligomeric silsesquioxanes on the physical properties of their polymer nanocomposites. *Polymer*, **50**, 4876–4887.

12 Wang, W., Guo, Y., and Otaigbe, J.U. (2009) The synthesis, characterization and biocompatibility of poly(ester urethane)/polyhedral oligomeric silsesquioxane nanocomposites. *Polymer*, **50**, 5749–5757.

13 Skrifvars, M., Niemela, P., Koskinen, R., and Hormi, O. (2004) Process cure monitoring of unsaturated polyester resins, vinyl ester resins, and gel coats by Raman spectroscopy. *J. Appl. Polym. Sci.*, **93**, 1285–1292.

14 Kim, Y.B., Kim, H.K., Choi, H.C., and Hong, J.W. (2005) Photocuring of a thiol-ene system based on an unsaturated polyester. *J. Appl. Polym. Sci.*, **95**, 342–350.

15 Nelson, E.W., and Scrantont, A.B. (1996) In situ Raman spectroscopy for cure monitoring of cationic photopolymerizations of divinyl ethers. *J. Raman Spectrosc.*, **27**, 137–144.

16 Edwards, H.G.M., and Day, J.S. (2004) Fourier transform Raman spectroscopic studies of the curing of cyanoacrylate glue. *J. Raman Spectrosc.*, **35**, 555–560.

17 Ni, Y., Zheng, S., and Novel, A. (2004) Photocrosslinkable polyhedral oligomeric silsesquioxane and its nanocomposites with poly(vinyl cinnamate). *Chem. Mater.*, **16**, 5141–5148.

18 Cho, H.S., Liang, K., Chatterjee, S., and Pittman, C.U., Jr. (2005) Synthesis, morphology, and viscoelastic properties of polyhedral oligomeric silsesquioxane nanocomposites with epoxy and cyanate ester matrices. *J. Inorg. Organomet. Polym. Mater.*, **15**, 541–554.

19 Mark, J.E. (2006) Some novel polymeric nanocomposites. *Acc. Chem. Res.*, **39**, 881–888.

20 Yoon, K.H., Polk, M.B., Park, J.H., Min, B.G., and Schiraldi, D.A. (2005) Properties of poly(ethylene terephthalate) containing epoxy-functionalized polyhedral oligomeric silsesquioxane. *Polym. Int.*, **5**, 47–53.

21 Hao, N., Bhning, M., and Schnhals, A. (2007) Dielectric properties of nanocomposites based on polystyrene and polyhedral oligomeric phenethyl-silsesquioxanes. *Macromolecules*, **40**, 9672–9679.

22 Bian, Y., Pejanovi, S., Kenny, J., and Mijovi, J. (2007) Dynamics of multifunctional polyhedral oligomeric silsesquioxane/poly(propylene oxide) nanocomposites as studied by dielectric relaxation spectroscopy and dynamic mechanical spectroscopy. *Macromolecules*, **40**, 6239–6248.

23 Lichtenhan, J.D., Otonari, Y.A., and Cam, M.J. (1995) Linear hybrid polymer building blocks: methacrylate-functionalized polyhedral oligomeric silsesquioxane monomers and polymers. *Macromolecules*, **28**, 8435–8437.

24 Haddad, T.S., and Lichtenhan, J.D. (1996) Hybrid organic–inorganic thermoplastics: styryl-based polyhedral oligomeric silsesquioxane polymers. *Macromolecules*, **29**, 7302–7304.

25 Zhang, H.X., Lee, H.Y., Shin, Y.J., Yoon, K.B., Noh, S.K., and Lee, D.H. (2008)

Preparation and characterization of styrene/styryl–polyhedral oligomeric silsesquioxane hybrid copolymers. *Polym. Int.*, **57**, 1351–1356.

26 Liu, Y., Zeng, K., and Zheng, S. (2007) Organic–inorganic hybrid nanocomposites involving novolac resin and polyhedral oligomeric silsesquioxane. *React. Funct. Polym.*, **67**, 627–635.

27 Perrin, F.X., Chaoui, N., and Margaillan, A. (2009) Effects of octa(3-chloroammoniumpropyl) octasilsesquioxane on the epoxy self-polymerisation and epoxy–amine curing. *Thermochim. Acta*, **491**, 97–102.

28 Sulca, N.M., Lungu, A., Gârea, S.A., and Iovu, H. (2009) Monitoring the synthesis of new polymer nanocomposites based on different polyhedral oligomeric silsesquioxane using Raman spectroscopy. *J. Raman Spectrosc.*, **40**, 1634–1640.

29 Constantin, F., Gârea, S.A., Sandu, T., and Iovu, H. (2010) Characterization of novel epoxy composites based on hybrid inorganic/organic polyhedral oligomeric silsesquioxane. *Int. J. Polym. Anal. Character.*, **15**, 119–128.

30 Chen, W.Y., Ho, K.S., Hsieh, T.H., Chang, F.C., and Wang, Y.Z. (2006) Simultaneous preparation of PI/POSS semi-IPN nanocomposites. *Macromol. Rapid Commun.*, **27**, 452–457.

31 Yuancheng, Q., Yutie, B., Hongbo, R., Fanghua, Z., Meiming, L., and Lin, Z. (2010) Poly(methyl methacrylate)/methacryl–POSS nanocomposites with excellent thermal properties. *Chin. J. Chem.*, **28**, 2527–2532.

32 Kuoa, S.W., and Chang, F.C. (2011) POSS related polymer nanocomposites. *Prog. Polym. Sci.*, **36**, 1649–1696.

33 Wang, X., Hu, Y., Song, L., Xing, W., Lu, H., Lv, P., and Jie, G. (2011) UV-curable waterborne polyurethane acrylate modified with octavinyl POSS for weatherable coating applications. *J. Polym. Res.*, **18**, 721–729.

34 Liu, Y.R., Huang, Y.D., and Liu, L. (2007) Influences of monosilanolisobutyl-POSS on thermal stability of polymethylsilxoane. *J. Mater. Sci.*, **42**, 5544–5550.

35 Monticelli, O., Waghmare, P., and Chincarini, A. (2009) On the preparation and application of novel PVDF–POSS systems. *J. Mater. Sci.*, **44**, 1764–1771.

36 Liu, L., and Wang, W. (2009) Synthesis and characterization of poly(methyl methacrylate) using monofunctional polyhedral oligomeric silsesquioxane as an initiator. *Polym. Bull.*, **62**, 315–325.

37 Iijima, S. (1991) Helical microtubules of graphitic carbon. *Nature*, **354**, 56–58.

38 Meyyappan, M. (2005) Carbon nanotubes. *Science and Applications*, CRC Press, Boca Raton, FL, London, New York, Washington, D.C.

39 Liu, Z., Tabakman, S., Welsher, K., and Dai, H. (2009) Carbon nanotubes in biology and medicine: *in vitro* and *in vivo* detection, imaging and drug delivery. *Nano Res.*, **2**, 85–120.

40 Dresselhaus, M.S., Dresselhaus, G., and Avouris, P. (eds) (2001) *Carbon Nanotubes, Synthesis, Structure, Properties and Applications*, Springer-Verlag, Berlin, Heidelberg.

41 Garea, S.A., and Iovu, H. (2006) New epoxy coating systems which contain multipurpose additives based on organophilic montmorillonite. *Prog. Org. Coating.*, **56**, 319–326.

42 Garea, S.A., Iovu, H., Nicolescu, A., and Deleanu, C. (2009) A new strategy for polybenzoxazine–montmorillonite nanocomposites synthesis. *Polym. Test.*, **28**, 338–347.

43 Garea, S.A., Nicolescu, A., Deleanu, C., and Iovu, H. (2010) New nanocomposites based on epoxy resins reinforced with modified montmorillonite. *Int. J. Polym. Anal. Charact.*, **15**, 1–12.

44 Gârea, S.A., Iovu, H., and Voicu, G. (2010) The influence of some new montmorillonite modifier agents on the epoxy–montmorillonite nanocomposites structure. *Appl. Clay Sci.*, **50**, 469–475.

45 Garea, S.A., Iovu, H., and Bulearca, A. (2008) New organophilic agents of montmorillonite used as reinforcing agent in epoxy nanocomposites. *Polym. Test.*, **27**, 100–113.

46 Gârea, S.A., Iovu, H., Stoleriu, S., and Voicu, G. (2007) Synthesis and characterization of new nanocomposites

based on epoxy resins and organophilic clays. *Polym. Int.*, **56**, 1106–1114.

47 Constantin, F., Gârea, S.A., Voicu, G., and Iovu, H. (2010) The influence of organic substituents from de polyhedral oligomeric silsesquioxane (POSS) cage on the epoxy–POSS hybrid materials properties. *High Perform. Polym.*, **22**, 905–915.

48 Gârea, S.A., Ghebaur, A., Constantin, F., and Iovu, H. (2011) New hybrid materials based on modified halloysite and unsaturated polyester resin. *Polym.-Plast. Technol. Eng.*, **50**, 1096–1102.

49 Liu, P. (2005) Modifications of carbon nanotubes with polymers. *Eur. Polym. J.*, **41**, 2693–2703.

50 Petrea, C.M., Andronescu, C., Pandele, A.M., Gârea, S.A., and Iovu, H. (2010) Epoxy-based nanocomposites with amine modified singlewalled carbon nanotubes. *e-Polymers*, **20**, 1–9.

51 Damian, C.M., Pandele, A.M., Andronescu, C., Ghebaur, A., Garea, S.A., and Iovu, H. (2011) Epoxy-based nanocomposites reinforced with new amino functionalized multi-walled carbon nanotubes. *Fuller. Nanotub. Car. N.*, **19**, 3, 197–209.

52 Chen, J., Hamon, M.A., Hu, H., Chen, Y., Rao, A.M., Eklund, P.C., and Haddon, R.C. (1998) Solution properties of single-walled carbon nanotubes. *Science*, **282**, 95–98.

53 Chen, J., Rao, A.M., Lyuksyutov, S., Itkis, M.E., Hamon, M.A., Hu, H., Cohn, R.W., Eklund, P.C., Colbert, D.T., Smalley, R.E., and Haddon, R.C. (2001) Dissolution of full-length single-walled carbon nanotubes. *J. Phys. Chem. B*, **105**, 2525–2528.

54 Chiu, P.W., Duesberg, G.S., Dettla.-Weglikowska, U., and Roth, S. (2002) Interconnection of carbon nanotubes by chemical functionalization. *Appl. Phys. Lett.*, **80**, 3811–3813.

55 Pompeo, F., and Resasco, D.E. (2002) Water solubilization of single-walled carbon nanotubes by functionalization with glucosamine. *Nano Lett.*, **2**, 369–373.

56 Jung, C.-H., Kim, D.-K., and Choi, J.-H. (2009) Surface modification of multi-walled carbon nanotubes by radiation-induced graft polymerization. *Curr. Appl. Phys.*, **9**, S85–S87.

57 Hu, H., Ni, Y., Mandal, S.K., Montana, V., Zhao, B., Haddon, R.C., and Parpura, V. (2005) Polyethyleneimine functionalized single-walled carbon nanotubes as a substrate for neuronal growth. *J. Phys. Chem. B*, **109**, 4285–4289.

58 Sun, Y.P., Huang, W., Lin, Y., Fu, K., Kitaygorodskiy, A., Riddle, L.A., Yu, Y.J., and Carroll, D.L. (2001) Soluble dendron-functionalized carbon nanotubes: preparation, characterization, and properties. *Chem. Mater.*, **13**, 2864–2869.

59 Velasco-Santos, C., Martinez-Hernandez, A.L., Lozada-Cassou, M., Alvarez-Castillo, A., and Castano, V.M. (2002) Chemical functionalization of carbon nanotubes through an organosilane. *Nanotechnology*, **13**, 495.

60 Ma, P.C., Kim, J.K., and Tang, B.Z. (2006) Functionalization of carbon nanotubes using a silane coupling agent. *Carbon*, **44**, 3232–3238.

61 Zhou, Z., Wang, S., Lu, L., Zhang, Y., and Zhang, Y. (2008) Functionalization of multi-wall carbon nanotubes with silane and its reinforcement on polypropylene composites. *Comp. Sci. Technol.*, **68**, 1727–1733.

62 Deng, Y., Deng, C., Yang, D., Wang, C., Fu, S., and Zhang, X. (2005) Preparation, characterization and application of magnetic silica nanoparticle functionalized multi-walled carbon nanotubes. *Chem. Commun.*, **44**, 5548–5550.

63 Chen, G.-X., and Shimizu, H. (2008) Multiwalled carbon nanotubes grafted with polyhedral oligomeric ilsesquioxane and its dispersion in poly(ʟ-lactide) matrix. *Polymer*, **49**, 943–951.

64 Sahoo, N.G., Rana, S., Cho, J.W., and Li, L. (2010) Polymer nanocomposites based on functionalized carbon nanotubes. *Prog. Polym. Sci.*, **35**, 837–867.

65 Vigoloa, B., Mamane, V., Valsaque, F., Ha Le, T.N., Thabit, J., Ghanbaja, J., Aranda, L., Fort, Y., and McRae, E. (2009) Evidence of sidewall covalent

functionalization of single-walled carbon nanotubes and its advantages for composite processing. *Carbon*, **47**, 411–419.

66 Tripisciano, C., Costa, S., Klaenczuk, R.J., and Borowiak-Palen, E. (2010) Cisplatin filled multiwalled carbon nanotubes – a novel molecular hybrid of anticancer drug container. *Eur. Phys. J. B*, **75**, 141–146.

67 Estrade-Szwarckopf, H. (2004) XPS photoemission in carbonaceous materials: a "defect" peak beside the graphitic asymmetric peak. *Carbon*, **42**, 1713–1721.

68 Wepasnick, K.A., Smith, B.A., Bitter, J.L., and Fairbrother, D.H. (2010) Chemical and structural characterization of carbon nanotube surfaces. *Anal. Bioanal. Chem.*, **396**, 1003–1014.

69 Curulli, A., Nunziante Cesaro, S., Coppe, A., Silvestri, C., and Palleschi, G. (2006) Functionalization and dissolution of single-walled carbon nanotubes by chemical–physical and electrochemical treatments. *Microchimica Acta*, **152**, 225–232.

70 Wang, Y., Iqbal, Z., and Malhotra, S.V. (2005) Functionalization of carbon nanotubes with amines and enzymes. *Chem. Phys. Lett.*, **402**, 96–101.

71 Zhang, G., Sun, S., Yang, D., Dodelet, J.-P., and Sacher, E. (2008) The surface analytical characterization of carbon fibers functionalized by H_2SO_4/HNO_3 treatment. *Carbon*, **46**, 196–205.

72 Papagelis, K., Kalyva, M., Tasis, D., Parthenios, J., Siokou, A., and Galiotis, C. (2007) Covalently functionalized carbon nanotubes as macroinitiators for radical polymerization. *Phys. Stat. Sol.*, **244**, 4046–4050.

73 Hadjiev, V.G., Lagoudas, D.C., Oh, E.-S., Thakre, P., Davis, D., Files, B.S., Yowell, L., Arepalli, S., Bahr, J.L., and Tour, J.M. (2006) Buckling instabilities of octadecylamine functionalized carbon nanotubes embedded in epoxy. *Comp. Sci. Technol.*, **66**, 128–136.

74 Yang, W., Thordarson, P., Gooding, J.J., Ringer, S.P., and Braet, F. (2007) Carbon nanotubes for biological and biomedical applications. *Nanotechnology*, **18**, 1–12.

75 Tripisciano, C., Kraemer, K., Taylor, A., and Borowiak-Palen, E. (2009) Single-wall carbon nanotubes based anticancer drug delivery system. *Chem. Phys. Lett.*, **478**, 200–205.

76 Liu, Z., Fan, A.C., Rakhra, K., Sherlock, S., Goodwin, A., Chen, X., Yang, Q., Felsher, D.W., and Dai, H. (2009) Supramolecular stacking of doxorubicin on carbon nanotubes for *in vivo* cancer therapy. *Angew. Chem. Int. Ed.*, **48**, 7668–7672.

77 Khandare, J.J., Jayant, S., Singh, A., Chandna, P., Wang, Y., Vorsa, N., and Minko, T. (2006) Dendrimer versus linear conjugate: influence of polymeric architecture on the delivery and anticancer effect of paclitaxel. *Bioconjug. Chem.*, **17**, 1464–1472.

78 Zhao, Q., and Daniel Wagner, H. (2004) Raman spectroscopy of carbon-nanotube-based composites. *Philos. Trans. R. Soc. Lond. A*, **362**, 2407–2424.

79 Lu, T., Liang, G., Peng, Y., and Chen, T. (2007) Blended hybrids based on silsesquioxane–OH and epoxy resins. *J. Appl. Polym. Sci.*, **106**, 4117–4123.

6
Tribological Characterization of Polymer Nanocomposites

Markus Englert and Alois K. Schlarb

6.1
Introduction

The development of materials with improved tribological properties has in regard to technical as well as economic aspects a huge importance. On the one hand the functionality and safety of technical systems by use of components with the highest possible service life are desired, and on the other hand, maintenance or downtime costs should be minimized. In addition to commercial and technical aspects, especially environmental objectives, such as sustainable business as global means for maintaining the environment, play an important role. In this context there is the possibility by minimizing friction with help of low-wear materials to directly save energy. Furthermore, by their higher lifetime material use is reduced which has the consequence of indirect energy savings. Caused by friction and wear the respective economics of the industrial nations record annual losses of about 5% concerning the national product. This means for Germany approximately €35 billion per year. By converting the existing tribological knowledge €5 billion could be saved per year. Through further tribological research, these potential savings can be increased [1].

Energy-efficient construction methods, therefore, require the reduction of friction losses and the use of optimized tribological systems. Here, polymer materials in recent decades have opened up a wide range of applications. Where high surface pressures must be possible, the reinforcement of polymer matrices with different additives is required. The beneficial combination of a polymer matrix and reinforcing materials which are well dispersed and distributed is the key to the development of high-performance tribomaterials.

Previous studies [2–4] have already shown how the tribological performance of polymer composite materials, such as specific wear rate and friction coefficient, can be positively influenced by nanoscale fillers, in particular by taking advantage of synergistic effects that are caused by a combination with micro-fillers. In addition to improved tribological properties the use of nanoparticles also leads to increases in mechanical properties [5–7], particularly the simultaneous increase in the strength and toughness what could not be realized with particles in the

macroscale in this range. To improve the characteristic material properties of nanocomposites, it is necessary to break up nanoparticle agglomerates, caused by van der Waals force, and distribute them homogeneously in the matrix.

The application of mechanical and tribological optimized materials is possible in a wide field of industries, ranging from the automotive and engine industry, manufacturing technology and aerospace to medical technology. For example calender rolls in the paper industry, tribologically optimized pistons by nanocoatings as light weight constructions, and bearings in pumps that transport aggressive and abrasive fluids can be mentioned in this context.

This section gives an overview concerning polymer nanocomposites in the field of tribology. Therefore in the first step the basics of tribology are discussed, followed by the description of possibilities in order to develop tribologically optimized nanocomposites. Afterward their characterization by special tribological methods is focused as well as selected results in respect of the tribological properties of nanocomposites.

6.2
Tribological Fundamentals

Tribology, derived from the Greek word tribein for friction, is considered as science and technology of surfaces acting on each other in relative motion [8]. It includes the entire area of friction and wear, including lubrication and concludes the interfacial interactions between solids as well as liquids or gases. Because of its interdisciplinary character, different fields have to work together to solve wear and friction problems. For engineering functions and structures of tribological systems in the micro- to nanometer range are of interest, while material sciences, physics, and chemistry are more dealing with micro- and nanoscale tribological processes [9] (Figure 6.1).
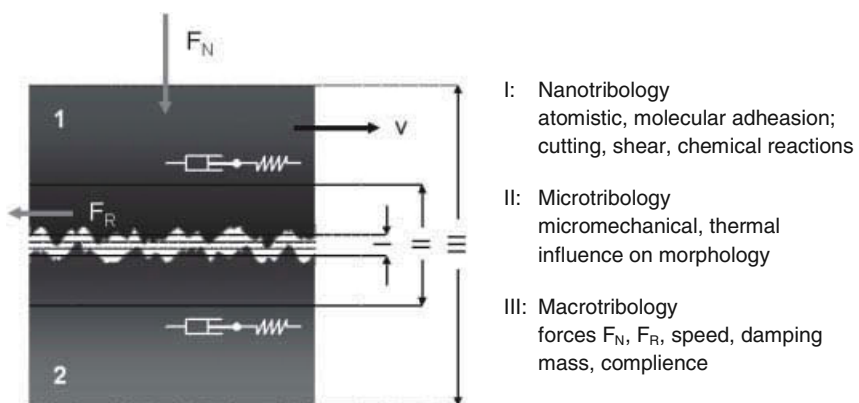
Figure 6.1 Schematic illustration of the dimensional range of tribological processes, according to [9].

Friction and wear in tribological systems result from tribological processes in the active surfaces of contacted triboelements. They range from dissipative nano-micro-effects in submicroscopic locations to the macro area of triboelements with measurable forces, velocities, and damping-mass-spring characteristics of the triboelements. Nanoscale friction and wear processes are investigated today with molecular modeling and electron and atomic force microscopy.

6.2.1
Tribological System

A tribological system consists of four elements (components or materials). This is the solid base body, the counterbody (solid, liquid, or gaseous), the interfacial medium (lubricants, dust, and other contaminants), and the surrounding medium (air, gases, other liquids or vacuum) (Figure 6.2) [10, 11]. These elements characterize the structure of the tribological system. Significant are, for example, dimensions, chemical composition, density, expansion coefficient, thermal conductivity, strength, hardness, and surface roughness.

The loading spectrum of a tribological system is time dependent. It is formed by the motion form, the direction of movement, the passing of relative motion, and by physical–technical stress parameters [10]. The relative motion is opposed by the friction whereby kinetic energy is irreversibly transformed into heat. Simultaneously, the interactions between the elements can lead to undesired wear (material loss by replacing of particles) and thus to material changes and/or
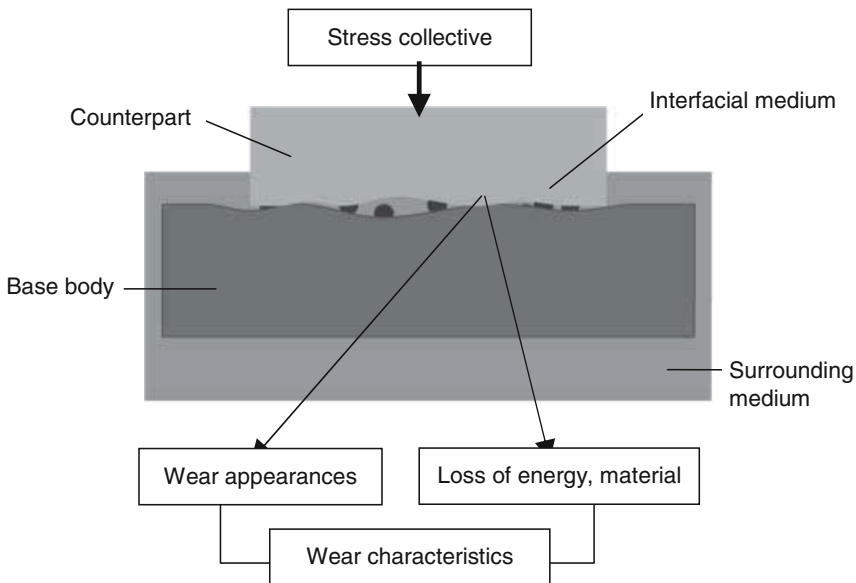
Figure 6.2 Tribological system; according to [11].

changes concerning the material surfaces. Friction leads to energy loss and wear causes material loss. Friction characteristics and wear characteristics are characteristics in contrast to the strength properties dependent of the respective system. They are dependent on the interaction of the elements of each tribological system under the individual stress collective. Mechanical stresses on a material, however, result in material parameters [10].

Friction is one of the longest-known phenomena, whose scientific exploration took place in the 15th century by Leonardo da Vinci and was extended by Guillaume Amatons, Leonard Euler, Charles Augustin Coulomb, and Jules Arthur-Morin [12]. Their investigations led phenomenologically to the equation formulated by Coulomb of sliding friction for sliding movements:

$$F_R = \mu \cdot F_N \tag{6.1}$$

where μ (also f) is the friction coefficient, F_N is the normal force, and F_R is the friction force.

According to current knowledge, however, these correlations are only approximately valid and in certain limits. In fact, friction force and friction coefficient are dependent on the stress parameters as well as the tribological structure of the involved materials [12]. The appearing friction forces in the case of dynamic friction between relatively moving bodies counteract the direction of movement and try to inhibit the movement. The dynamic friction is split according to kinematic considerations into sliding friction, drilling friction, rolling friction, and revolving friction.

In all types of friction the largest part of mechanical energy is changed into heat, while only a small quantity is transformed into sound emission. Another part of friction energy is changed into wear. The wear forms of sliding, rolling, and oscillating loads mostly occur in closed systems (elements of machines), whereby abrasive, abrasive sliding, three-body abrasive wear, and erosion are present in open systems.

6.2.2
Wear Mechanisms

Wear mechanisms are understood as physical and chemical interactions in the contact area of a tribological system [9]. These trigger elementary processes and lead to substance and shape changes of the contact partners. Their contribution to wear depends on structure and stress collective of the tribological system. For the formation of wear the basic mechanisms of adhesions, abrasion, surface distress, tribo-chemical reaction, and ablation are essentially responsible (Figure 6.3). These mechanisms occur only in a few cases individually [12]. Usually they are overlaid and their part of the wear process changes during the stress [9, 12]. Therefore, the wear behavior in practical operation cannot be estimated theoretically but determined experimentally by appropriate wear experiments.

In the following the principles of the different wear mechanisms as they can be observed by the tribological stress of polymer materials are explained [9, 13, 14].
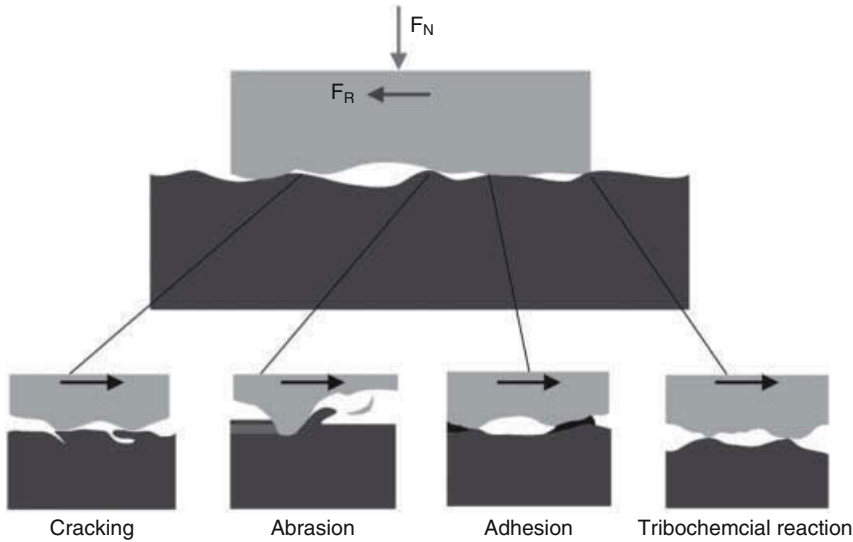
Figure 6.3 Schematic illustration of fundamental wear mechanisms; according to [9].

Adhesion: under the action of a normal force, at the contact surfaces considerable mechanical stresses are caused in the contact area. By tangential relative movements of the wear bodies, these stresses are increased. The stresses can become so large that the asperities are deformed elastically or elastic–plastic. If the existing adsorption and reaction layers at the surface are locally destroyed, an atomic contact between surfaces is caused so that atomic bonds are formed. Because of relative movements between the basebody and the counterbody during the wear process, these bondings are released again.

Surface fatigue: cyclic loads lead to changing mechanical stresses in the surface area of the basebody and the counterbody. Caused by locally repeated elastic and plastic deformation crack formation and gradual extension occur until small wear particles are separated from the surface. Cracks, pits, or holes are formed.

Abrasion: abrasion occurs in tribological contacts when the counterbody is considerably harder and rougher than the tribologically stressed basebody or when hard particles are pressed into a tribologically stressed material. Due to the usually small size of the contact points between the abrasive and the surface of the basebody locally very high surface pressures occur, so that the penetration is possible, and during the relative movement, the typical wear forms for this the mechanism of wear such as scratches, grooves, vats, and waves are formed.

Tribochemical reactions: by tribochemical reactions, reaction products are formed under tribological stress if basebody, counterbody, and adjacent medium enter into chemical reactions with each other. Tribochemical reactions lead to a change of the structure and properties of the outer boundary layer of the surface. The

educated layer, depending on their thickness and hardness, can increase the amount of wear or reduce. Forms of wear occur in the case of tribochemical reactions layers and particles.

6.2.3
Transfer Film Formation

A large number of interactions between a polymer and a metal surface (polymer-on-metal system) in sliding contact result in the formation of a transfer film [2, 15]. According to Lancaster [15] a transfer film can, in dependence of the polymer, either increase or decrease the wear rate. Under its considerations, polymers with high elongations, for example, PTFE, polyamides, and polyolefins are beneficial candidates in order to reduce the wear rate, whereby less ductile polymers, for example, epoxies, polyester, polystyrene, and PMMA increase wear [15]. During the sliding process soft polymer is removed by harder metal asperities so that a transfer film is caused. This polymer adheres to the metal surface of the counterbody and is able to protect the polymer from the counter-face asperities. The transfer film is influenced by sliding parameters, polymer composition, and counterface characteristics. These factors are discussed in detail in [2].

Based on studies using micro- and nanoparticles it can be summarized that it is necessary for wear reduction to realize a thin and uniform transfer film which is well bonded on the counterface. A uniform coverage of the counterface avoids the abrasion of the softer polymer surface by hard metal asperities. The advantage of a thin transfer film in comparison to a thicker one lies in a stronger bonding to the counterface. The use of nanofillers can affect the tribological performance of polymers by mechanical and chemical action during the sliding process. Their task is to enhance the uniformity of the transfer film and its adhesion to the counterface.

6.2.4
Temperature Increase

Due to friction kinetic energy is dissipated into heat during a tribological process. This results in a temperature decrease ΔT of the friction partners which is dependent on friction coefficient μ, normal force F_N, relative velocity v between the friction partners, and a thermal resistance parameter R. The temperature increase is calculable according to the following equation [14]:

$$\Delta T = \mu \cdot F_N \cdot v \cdot R \tag{6.2}$$

The thermal resistance parameter is dependent on the cross-sectional surface A of the heat paths n, their lengths l, and their thermal conductivity λ:

$$R = (1/A) \cdot \left(\sum_{i=1-n} \frac{\lambda_i}{l_i} \right)^{-1} \tag{6.3}$$

Physical properties of polymers are temperature dependent [16]. With increasing temperature the hardness decreases under tribological loading with the result of softening, creeping or even surface melting [14]. On the other hand the temperature increase in surface areas depends on the hardness [14]. As a consequence the temperature increase can lead to changes of the morphology and/or structure of the polymer.

6.3
Wear Experiments

Field tests in real tribological systems are complex and cost intensive in comparison to trials with the individual components [17]. Model tests with specimens of the interested material are repeatable and variable regarding the influencing factors. Considering that the tribological values friction and wear are no properties of the material but represent characteristics of a complex tribological system, wear tests need to be classified in terms of their practical similarity [18]. In DIN 50320 [19] an evaluation is proposed which is scaled in six categories. It starts from a practical operation test, whereby the tribological system is gradually reduced. In Table 6.1 these six categories are presented, where with increasing category number an increasing distance from the real operating state is related. But it also decreases the safety of the portability, while conversely, the possibilities of a clear assignment due to tribological mechanisms and the quantitative and reproducible determination of wear data increases [18].

Table 6.1 Reduction of a tribo-system according to categories of tribological tests [18].

Category	Kind of test		System structure	
	Stress collective			
I	Operational or operation-like trials	Operational test (field experiment)	Original components	Complete machine, system
II		Test stand with complete machine or plant		Complete machine, system
III		Test stand with aggregate or subassembly		Complete unit, assembly
IV	Tests with model systems	Experiment with unchanged or reduced component	Model samples	Extracted components, scaled aggregate
V		Stress a similar experiment with specimens		Components with similar stress
VI		Model experiment with simple test specimens		Simple specimens

Wear tests are technically the most important and comprehensive tribological tests [20]. The main aims are defined in DIN 50322 [14, 21]:

- Optimization of components or tribo-technical systems in order to achieve a specified wear determined lifetime.

- Determination of wear-determined influences on the general function of machines or optimization of components and tribo-technical systems to realize a predefined function.

- Monitoring of wear-determined functionality of machines.

- Preselection of materials and lubricants for practical application cases.

- Quality control of material and lubricants.

- Wear research- and mechanism-oriented wear testing.

- Diagnostics of operating conditions.

- Creation of data for instant maintenance.

6.3.1
Selected Wear Models

The wear behavior of polymers cannot be understood by the determination of characteristics of individual materials. Actually, for each material combination, the behavior of both components and their interaction has to be examined [22].

For the tribological characterization of polymer (nano)composites different test methods are established which can be classified by the tribological loads. Sliding wear is realized by a specimen (block or plate) which is pressed with a defined force against a rotating counterbody (ring or disk) (Figure 6.4a–c). By the use of a ball-shaped counterbody the specimen can be tested by a rolling motion (Figure 6.4d and f). In a vibration wear test experiment the counterbody makes a leaded oscillating movement against the specimen.

It is obvious that the tribological loads in the individual systems are different with respect to contact geometry (point, line, area), kinematics, and friction-induced thermal processes are to analyze and to observe concerning their influence [9]. Regarding the measuring technology of the laboratory tribological test it is important monitoring stress variables, for example, normal force, sliding velocity, and temperature and to record the main tribological variables. Disturbances, such as vibration or thermal expansion, must be registered and their influence on the measured results has also to be taken into account [9].

6.3.2
Characteristic Values of Tribological Systems

Tribological characteristics are in contrast to substance-related variables system-related parameters, that is, these variables can only be assigned to a material with
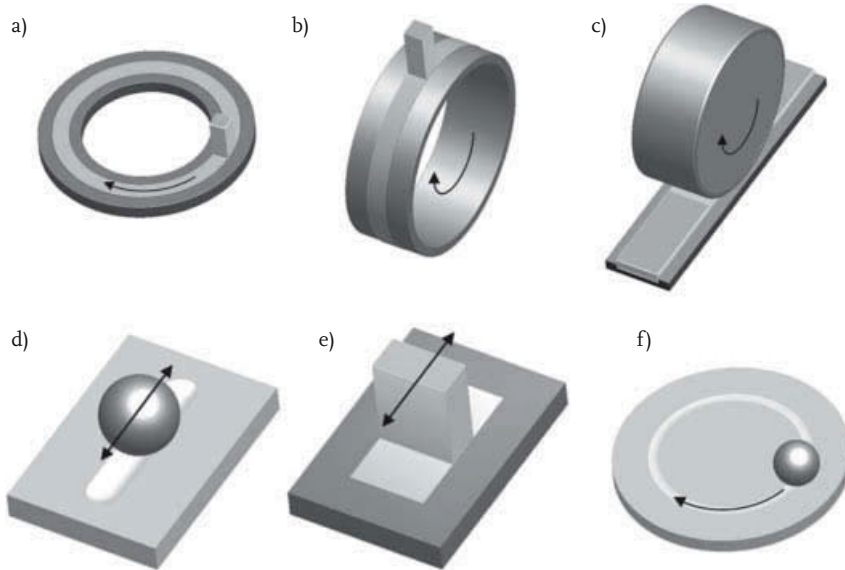
Figure 6.4 Tribological test principles: (a) pin on disk, (b) block on ring, (c) roller on plate, (d) and (e) oscillating wear, (f) roll wear.

knowledge of the tribological system. In tribological tests, depending on the task and test category, the following principal parameters are determined [20]:

- *Friction parameters:* friction force and friction torque, friction coefficient, friction work, and friction performance.

- *Wear parameters:* wear amount (length, area, volume, or mass change of the test specimen), wear resistance, (reciprocal of the wear amount), wear rate, wear-way relationship, wear-determined use life.

- *Wear appearance:* light and scanning electron micrographs analysis of wear surfaces, surface roughness measurement, surface analysis, and investigation of near-surface structure.

- *Acoustic parameters:* friction-induced air or acoustic emission measurement.

- *Thermal parameters:* friction-induced temperature increase of specimens or components.

- *Electrical parameters:* electrical contact resistance as indicative of the presence of a lubricating oil film or a foreign film formation on the contact partners.

In modern tribology research also new high-resolution techniques such as scanning tunneling microscopy and atomic force microscope are used. The function-related parameters of the system structure and the collective stress form the basis for a systematic handling of wear problems [20].
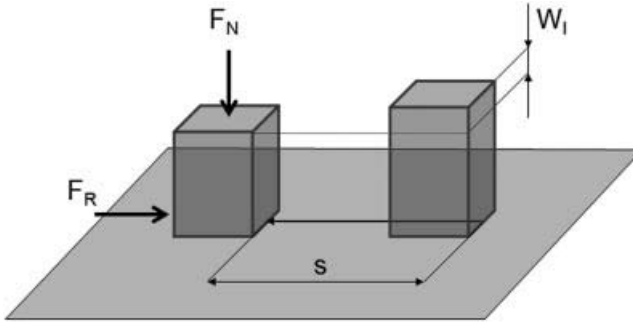
Figure 6.5 Illustration of the determination of the linear wear rate.

6.3.2.1 Wear Rate

For the specification of wear in tribological systems linear wear is based on the sliding distance s, or the stress time t [23, 24]. These results in the linear distance-related wear rate $W_{l/s}$ and the linear time-related wear rate $W_{l/t}$ according to the equations (Figure 6.5):

$$W_{l/s} = W_l / s \tag{6.4}$$

$$W_{l/t} = W_l / t \tag{6.5}$$

The specific wear rate w_s relate the volumetric wear W_V on the sliding distance s and the normal force F_N [25].

$$w_s = \frac{W_V}{F_N \cdot s} \tag{6.6}$$

6.4
Selection Criteria

As essential tribological characteristics and selection criteria, sliding speed, mechanical, and thermal stresses are considered [26]. The product of pressure p and sliding velocity v is a measure of thermal stress and the operating load (wear) of elements of a tribological system [24]. The friction-induced increase of the bear temperature and the linear wear are proportional to the pv value. This value is system related and can only be used for a specified tribological system. In a p–v-diagram the pv value is split into a pv factor and pv limit value (Figure 6.6).

The pv factor indicates the limit to which a constant time-related linear wear rate sets whereby the specific wear rate k is constant [24]. The wear increases progressively with increasing the pv value. For the maximum permissible limit of pv value concerning stress different definitions are existing. The criteria are that the surface of the material is just not melted or a maximal accepted wear rate [24].
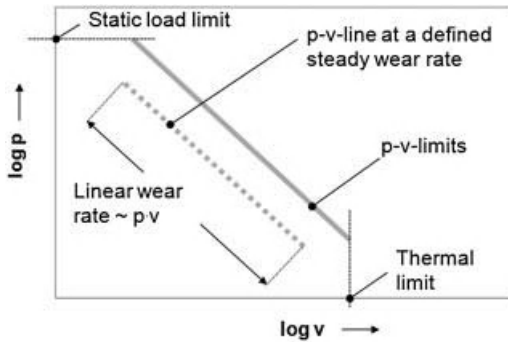
Figure 6.6 *p–v* diagram for dry-running slide bearings; according to [14].

6.5
Design of Polymer Nanocomposites and Multiscale Composites

Wear and friction properties of polymers can be improved by reduced adhesion, increased stiffness, and strength of the material [27]. A successful method for achieving these properties is the modification of polymeric materials with reinforcements. In order to reduce the adhesion normally internal solid lubricants such as PTFE and graphite (Figure 6.7b) are used. The increase of stiffness and strength is realized by short armid, carbon (Figure 6.7a) or glass fibers. Additionally, the combination of microparticles (Figure 6.7d) and ceramic particles in the nanoscale (Figure 6.7c) causes synergetic effects which in comparison with the implication of the individual components lead to a significant improvement of the tribological behavior of the material. The efficient wear properties, which can be caused by the nanoparticles, are thus further improved.

The reinforcing effects of nanoparticles are caused by their large total surface. If the nanoparticles are well dispersed in the polymer a very large interface between the particles and the matrix is created which enhance the interaction. Therefore, the fragmentation of nanoparticle agglomerates in primary particles and their homogeneous distribution in the matrix is a necessary precondition for the realization of nanocomposites with enhanced properties.

6.6
Selected Experimental Results

6.6.1
Particulate Fillers

The modification of polymeric matrices by using spherical ceramic particles has a high potential to optimize tribological performance of the material [28, 29].
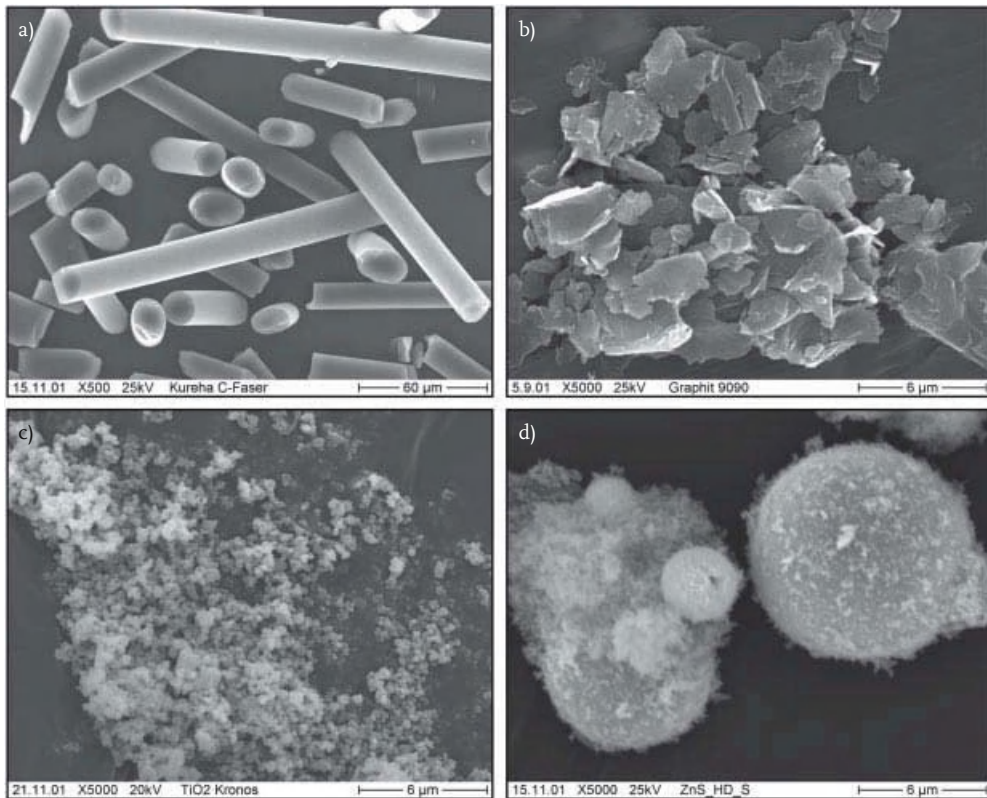
Figure 6.7 SEM pictures of (a) carbon fibers, (b) graphite, (c) titanium dioxide, and (d) zinc sulfide.

Numerous studies can demonstrate the beneficial influence of particulate fillers on the specific wear rate of thermoplastic as well as thermosetting nanocomposites (Figure 6.8) [30].

Wetzel *et al.* incorporate titanium dioxide particles with a diameter of 300 nm into epoxy resin and could decrease the specific wear rate until an optimum value of 4 vol%. A higher filler content, however, deteriorated the wear resistance. Badur *et al.* filled PPS by the use of TiO_2 and CuO nanoparticles in the range from 30 to 50 nm and observed a decrease of the specific wear rate at 2 vol% for both nanoparticle systems. A further increase of the filler content of 3 vol% and higher results in comparison with the neat PPS matrix to a reduced wear resistance. Zhang *et al.* incorporate SiO_2 nanoparticles in epoxy resin and applied the grafting polymerization technique with polyacrylamide (PAAM) in combination with SiO_2 nanoparticles (9 mm) for the modification of epoxy. Because of the chemical bonding it was possible to enhance the interfacial adhesion between the nanopar-
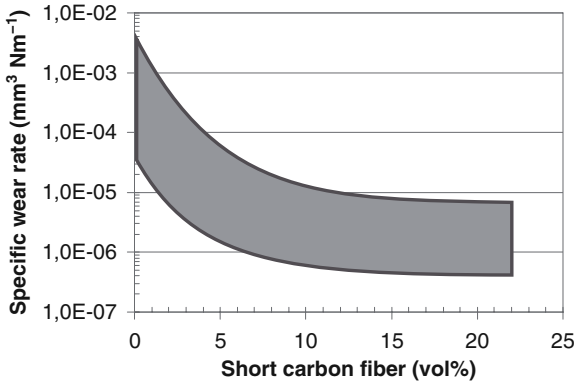
Figure 6.8 Specific wear rate for selected polymer nanocomposites as a function of nanoparticle volume fraction; data range from [30].

ticles and the epoxy matrix. Filler contents in the range from 2 to 6 vol% increased the wear resistance of the epoxy by a factor of 20. Studies with PEEK and different inorganic particles consisting of Si_3N_4, SiO_2, SiC, and ZrO_2 were performed by Wang *et al.* A change in wear mechanisms from adhesive wear for the neat PEEK to slight fatigue and transfer wear for the reinforced PEEK could be observed. A filler content of more than 4 vol% causes abrasive wear and deteriorates the cohesion of the nanocomposite.

6.6.2
Short Fibers

Another possibility to enhance the properties of polymers is the addition of short fibers (aramid, carbon, glass) [30]. The typical benefits in this case are improved mechanical properties (i.e., compressive strength, creep resistance, and impact strength), thermal conductivity, and wear properties. For triboloigical enhancement carbon fibers are considered as fundamental fillers. They provide excellent mechanical properties and have in comparison to glass fibers a less abrasive nature. Further, carbon fibers form a smooth carbon film on the counterbody during the process, increase the thermal conductivity, and the resistance to heat distortion of the polymer matrix. Therefore, different authors investigated the role of fiber volume content on the wear perfomance of polymer composites. Selected results are summarized in Figure 6.9.

Chang *et al.* incorporate short carbon fibers in epoxy and received the lowest specific wear rate at a filler content of 15 vol%. Xian *et al.* reinforced polyetherimide (PEI) by the addition of short carbon fibers and observed a tribological improvement of the polymer, especially in the high temperature and *pv*-range (80 times lower specific wear rate at 150 °C). The specific wear rate of the PEI composite is
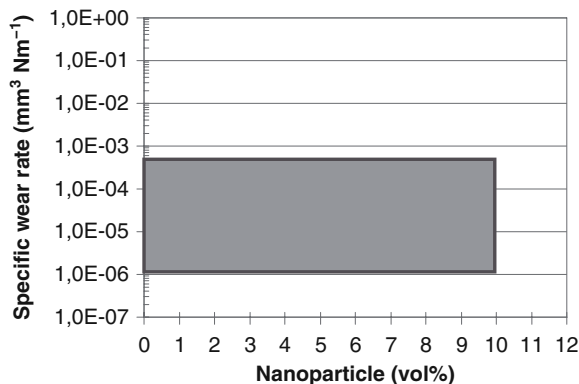
Figure 6.9 Influence of short fiber loading fraction on the specific wear rate of various polymer matrices; data range from [30].

for a carbon fiber volume fraction in the range of 5–20 vol% approximately constant.

Based on different studies it can be concluded that a beneficial friction and wear behavior can be obtained with a carbon fiber loading in the range of 10–20 vol%. If higher volume contents, especially at a higher *pv*-range are applied, stick-slip occurrence can be the consequence.

6.6.3
Combination of Fillers

6.6.3.1 Internal Lubricants and Short Carbon Fibers
Table 6.2 displays the formulations of different thermoplastic composites including their specific wear rates. The materials were tested by means of a block-on-ring test configuration against steel counterparts. The aim of these formulations is to realize materials with low friction, high wear resistance, and capable thermal conductivity under sliding wear conditions against steel counterparts. According to Table 6.2 the lowest specific wear rate can be achieved with a polytetrafluorethylene (PTFE) matrix together with 10 vol% carbon fibers and 10 vol% bronze. Because of the remarkable thermal conductivity of bronze it is possible to improve significantly the tribological properties of this composite.

In Figure 6.10 the microstructure of a PTFE-based composite modified by various fillers is displayed. The function of the different fillers is explained in [31].

PTFE, polyphenylene-sulfide (PPS), and graphite flakes serve as internal lubricants in order to reduce the adhesion. One important mechanism regarding the decrease in the coefficient of friction is the development of a PTFE-transfer film on the counterbody's surface. Short carbon fibers enhance the creep resistance and the compressive strength of the polymer matrix.

Table 6.2 Various polymer nanocomposites with excellent wear properties for different loading conditions (block-on-ring tests)[a].

Material compositions (vol%)							Specific wear rate (10^{-6} mm^3 N^{-1} m^{-1})
PTFE	PPS	PEEK	Graphite	CF	Bronze	Al$_2$O$_3$	
51.6	31.8	–	4.8	11.8	–	–	1.53
51	31.6	–	3.9	13.5	–	–	1.40
51.9	32.4	–	2.6	13.1	–	–	1.20
12.4	–	61.8	11.7	14.1	–	–	4.31
9.7	–	49.7	12.5	28.1	–	–	6.33
76.8	–	–	19.8	–	–	3.4	22.40
84.1	–	–	–	12.6	–	3.3	1.25
52.5	28	–	–	19.5	–	–	1.69
78.6	–	–	–	21.4	–	–	1.75
80	–	–	–	10	10	–	0.565

a) Test conditions: $p = 2$ MPa; $v = 1$ m s^{-1}; $T =$ RT; $t = 8$ h; counterpart: steel). Reproduced from reference [31] with permission.
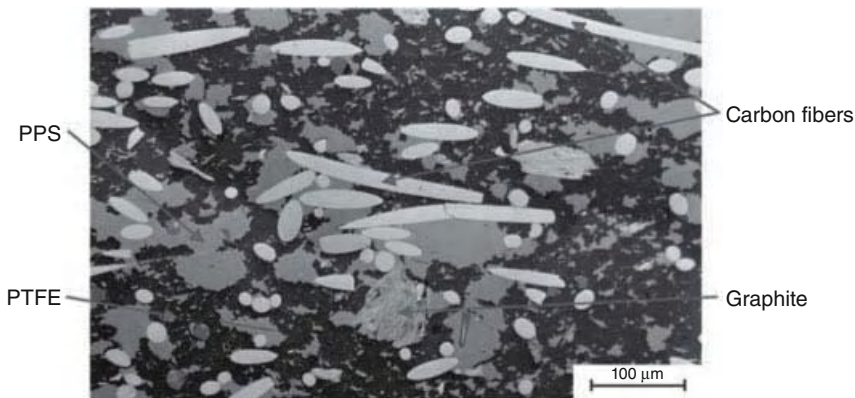
Figure 6.10 Reflected light micrograph of a PTFE composite containing a second-polymer phase of 31.6 vol% polyphenylene sulfide (PPS), short carbon fibers (13.5 vol%), and graphite flakes (3.9 vol%). Reproduced from reference [31] with permission.

6.6.3.2 Short Carbon Fibers and Nanoparticles

Investigations were also carried out for composites consisting of short carbon fibers and graphite additionally filled with submicron particles regarding the investigation of beneficial effects. Figure 6.11a displays the specific wear rate of neat epoxy and epoxy composites with different formulations. The investigations were
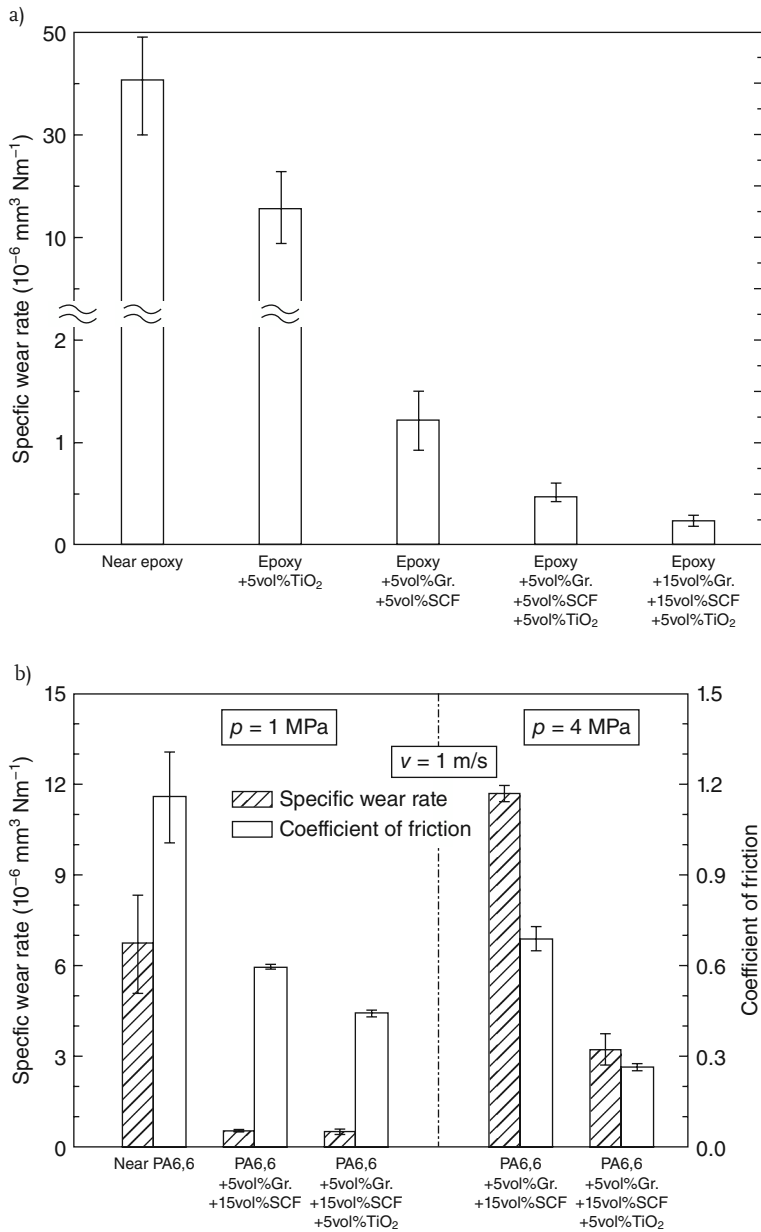
Figure 6.11 (a) Specific wear rate of neat epoxy and epoxy-based composites with and without TiO$_2$ particles (300 nm) determined by means of a block on ring configuration. Reproduced from reference [31] with permission; (b) specific wear rate and coefficient of friction of neat PA66 and PA66-based composites with and without TiO$_2$ particles (300 nm) at different contact pressures measured with a pin on disk device.

carried out by means of a block on ring apparatus equipped with ball bearing steel rings (100Cr6).

By the addition of 5 vol% TiO_2 nanoparticles (300 nm) the specific wear rate could be enhanced by nearly a factor of 3 in comparison with the unfilled epoxy. The use of traditional fillers such as short carbon fibers (M-2007S, Kureha Chemicals, Japan) and graphite flakes (Superior 9039), however, leads to a wear improvement which is more effective than just the nanoparticles alone. But the combination of these traditional fillers and nanoparticles cause synergistic effects whereby both advantageous mechanisms superimposed each other.

In regard to thermoplastic polymers similar correlations which have been found for epoxy resin concerning the cooperative effects of nano- and microparticles are valid. Figure 6.11b shows the specific wear rate and the friction coefficient of neat polyamide 66 (PA66) in comparison to polyamide composites filled with and without TiO_2 particles. It is demonstrated that traditional fillers enhance the friction and the wear properties significantly, as also seen in the case of epoxy (Figure 6.11a). But by the addition of TiO_2 particles further improvements, especially at the higher contact pressure of 4 Pa, are realizable. The decrease of the coefficient of friction is associated with a reduction of temperature in the contact area from 95 to 45 °C under the test conditions: $p = 4\,MPa$ and $v = 1\,m\,s^{-1}$.

In addition to the specific wear rate it is also useful to observe the depth wear rate in dependence on the pv factor concerning epoxy composites filled with and without TiO_2 nanoparticles (Figure 6.12). As can be clearly seen in Figure 6.12,
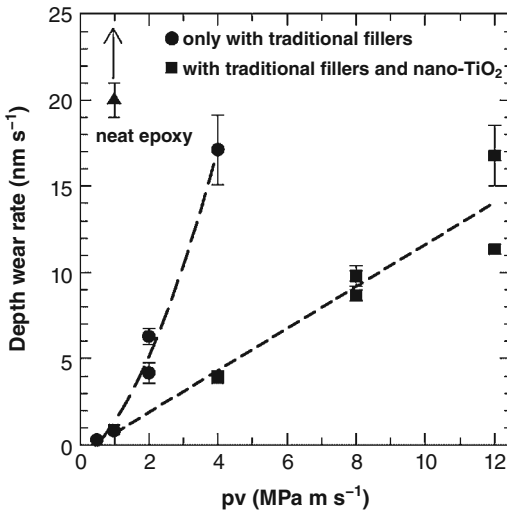
Figure 6.12 Depth wear rate of neat epoxy, epoxy filled without (5 vol% graphite, 5 vol% PTFE, and 15 vol% SCF) and with TiO_2 nanoparticles (5 vol% graphite, 5 vol% PTFE, 15 vol% SCF, and 5 vol% TiO_2 nanoparticles) in dependence on the pv factor. Wear conditions: pin on disk device, counterbody: steel (100Cr6). Reproduced from reference [31] with permission.
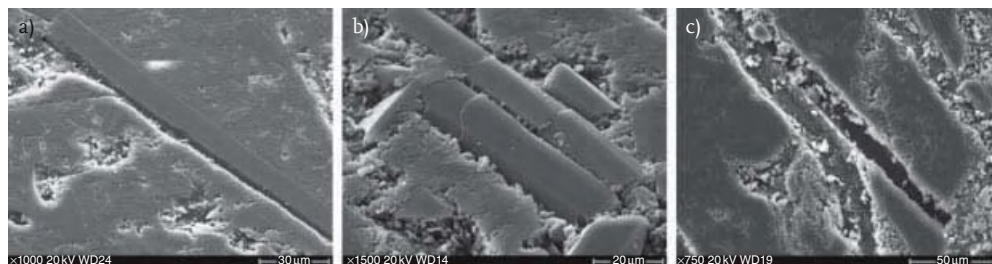
Figure 6.13 SEM micrographs of worn epoxy composite surfaces reinforced with 5 vol% graphite, 5 vol% PTFE, and 15 vol% SCF; (a) fiber thinning, (b) fiber breakage, and (c) fiber pulverization and interfacial removal. Wear conditions: normal pressure = 1 MPa, sliding velocity = 1 m s^{-1}, duration = 20 h; pin on disk device. Reproduced from reference [31] with permission.

the neat epoxy resin has a very high depth wear rate of about 20 nm s^{-1} at a *pv* value of 1 MPa m s^{-1}. Therefore this material is not operable. As already observed in regard to the specific wear rate, the incorporation of traditional fillers, that is, 15 vol% SCF, 5 vol% graphite, and 5 vol% PTFE, also allows a significant reduction of the depth wear rate. But with rising *pv* values the depth wear rate of the traditional filled composites increases strongly. By the addition of TiO$_2$ nanoparticles, however, the depth wear rate is much lower under this condition and shows a low-rising function in dependence on increasing low *pv* values (e.g., 12 MPa and 1 m s^{-1} or 4 MPa and 3 m s^{-1}).

Investigations of worn surfaces using scanning electron microscopy (SEM) and atomic force microscopy (AFM) offer information about the wear mechanisms. Figure 6.13 demonstrates the wear process of epoxy composites filled with 5 vol% graphite, 5 vol% PTFE, and 15 vol% SCF. The major wear mechanisms in this case are fiber thinning, fiber breakage, fiber pulverization, and interfacial removal.

The incorporation of TiO$_2$ nanoparticles leads in comparison to the composite without nanoparticles to a much smoother wear surface (Figure 6.14) at a load of 1 and 12 MPa, respectively.

Investigations by means of AFM show a smooth fiber surface for the composites without nanoparticle (Figure 6.15) which lies tilted in the cross-section of the wear surface (Figure 6.15b). In the case of the nanoreinforced composite, the fiber was finely scratched by the very small nanoparticles (Figure 6.15c and d). The scratches occur parallel to the sliding direction. The interface between the fibers and the matrix is retained under a capable condition. Based on this observation a positive rolling effect of the nanoparticles is supposed which reduces the frictional coefficient during the sliding process. In addition, the shear stress and the contact temperature are decreased. Therefore, the short carbon fibers were protected of more severe wear mechanisms, especially at high sliding pressures and velocities. This nanorolling effect was also found in the case of thermoplastic composites based on, for example, PA66 [32], PEEK, and PEI.
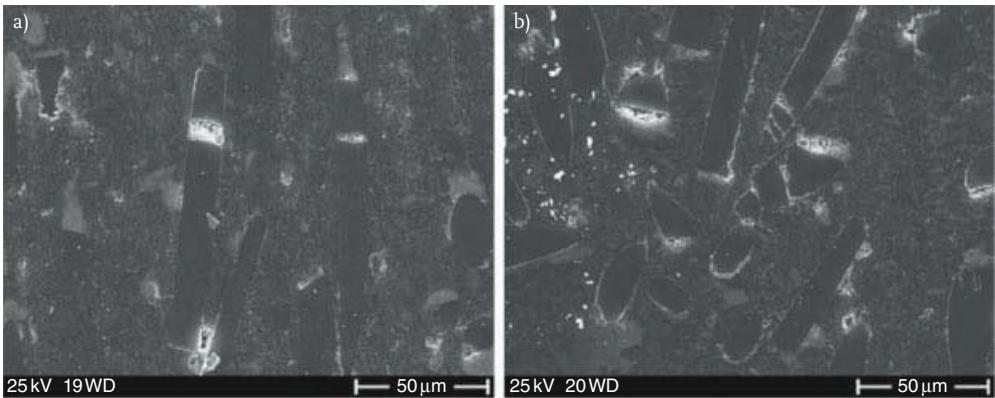
Figure 6.14 SEM micrographs of worn epoxy composite surfaces reinforced with 5 vol% graphite, 5 vol% TiO$_2$ nanoparticles, and 15 vol% SCF. Reproduced from reference [31] with permission; wear conditions: sliding velocity = 1 m s^{-1}, duration = 20 h, pin on disk device; (a) 1 MPa, (b) 12 MPa.

Figure 6.16 represents the frictional coefficient and the contact temperature in dependence on the sliding time of PA66 composites with and without TiO$_2$ nanoparticles. The experiments were carried out with the help of a pin on disk device. At the beginning of the running-in stage, the sliding behavior is similar for both composites. But after approximately 1 h the frictional coefficient and the contact temperature of the nanoreinforced composite is significantly reduced.

6.6.4
Wear Mechanisms

6.6.4.1 Ball Bearing ("Rolling") Effect on a Submicro Scale

The so-called ball bearing effect is a construction in order to get a better understanding of the wear scenario for sliding wear of multiphase polymer composites against steel 100 CR6 [33, 34]. A schematic illustration of this effect is shown in Figure 6.17. During the wear process the soft polymer matrix is removed and fillers which are near to the surface are exposed. Thereby, submicron particles from the polymer matrix attain the contact surface. These submicron particles enter the roughness valley of the counterpart and fill it up under the assumption that they are free to roll and/or slide under the resulting shear forces. During their movement these particles form agglomerates and are mixed with soft matrix material and iron (FE) from the counterpart. By means of the accumulated debris which is acting as spacers the contact between the soft polymer and the hard steel asperities is prevented. In this way solid friction is transferred to a kind of mild three-body abrasion.

In the further consideration a polymer matrix filled with short carbon fibers (SCFs) and titanium dioxide (TiO$_2$) particles which have almost the same hardness
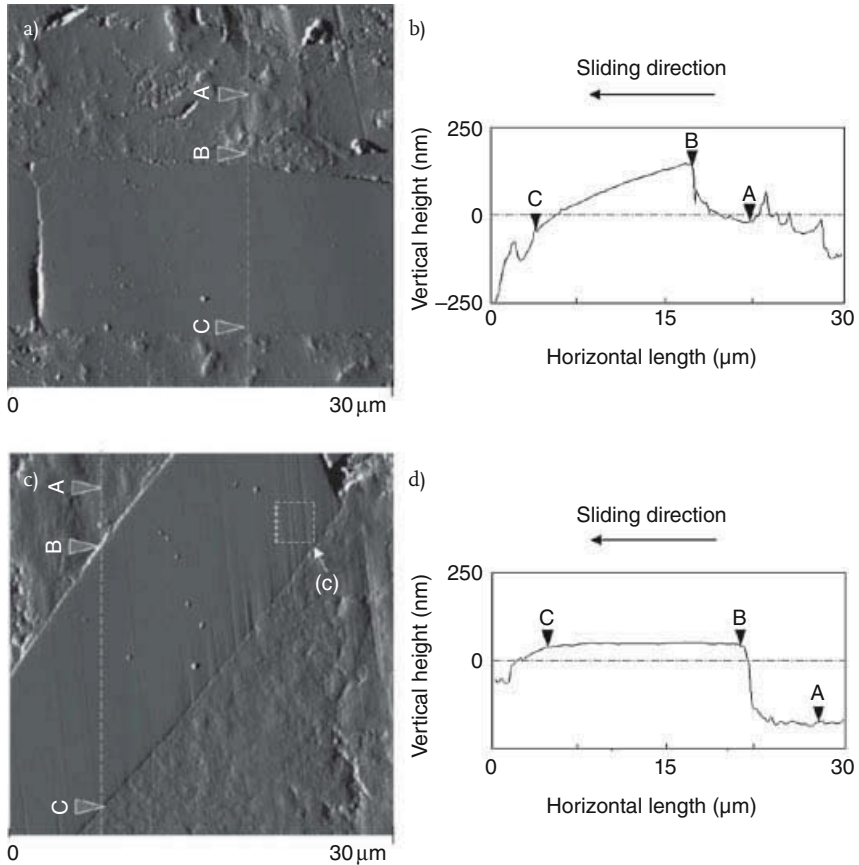
Figure 6.15 AFM micrographs of worn composite surfaces. Reproduced from reference [31] with permission: (a) and (b) 15 vol% graphite, 5 vol% PTFE, and 15 vol% SCF; (c) and (d) 15 vol% graphite, 5 vol% TiO$_2$ nanoparticles, and 15 vol% SCF. Wear conditions: normal pressure = 1 MPa, sliding velocity = 1 m s^{-1}, duration = 20 h, pin on disk device.

as the fibers is focused. The exposed fiber hinders the rolling debris which is partially resting at the front edge. In the following this quasispherical debris rolls over the fiber surface and prevents fiber damage caused by much harder steel asperities. By reaching the trailing edge of the fiber the quasispherical debris is transferred on the polymer matrix and is partially embedded there. The remains move and expand again. Thus, the transfer particles act as very small ball bearings in the sliding contact zone which protect the fibers from damage and consequently reduce friction and prevent wear.
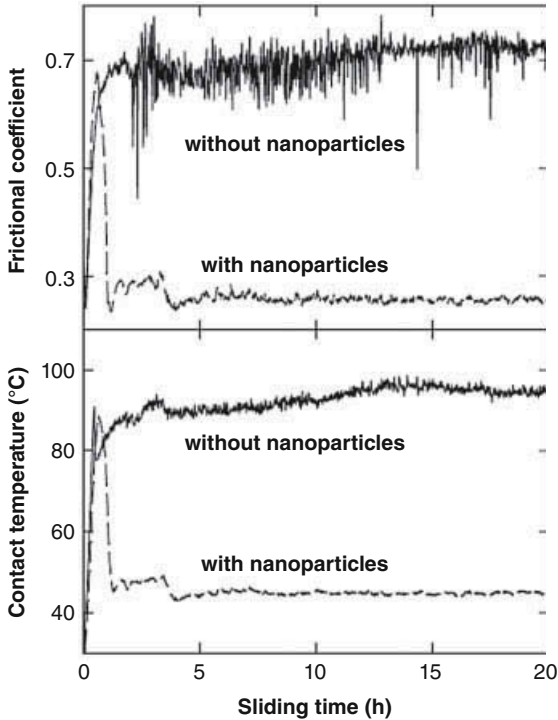
Figure 6.16 Sliding process (frictional coefficient and contact temperature) of PA66 composites without (5 vol% graphite and 15 vol% SCF) and with nanoparticles (5 vol% TiO₂ nanoparticles, 5 vol% graphite + 15 vol% SCF). Reproduced from reference [31] with permission. Wear conditions: normal pressure = 4 MPa, sliding velocity = 1 m s⁻¹, duration = 20 h, pin on disk device.

6.6.5
Summary

In contrast to material properties, friction and wear characteristics are dependent on the respective system. Such a tribological system consists of the test material, the counterpart, the interfacial medium, the surrounding medium, and the loading collective. The achievement of useable results requires the transaction of tribological experiments which are based on a well-chosen wear model and the adaption to the real wear conditions.

During the last few years the importance of nanomodified polymeric composites has grown up more and more. Especially, there exists the possibility of tailoring a material in dependence on the individual application by a purposive variation and combination of individual fillers, such as nano-, microparticles, fibers, and internal lubricants.
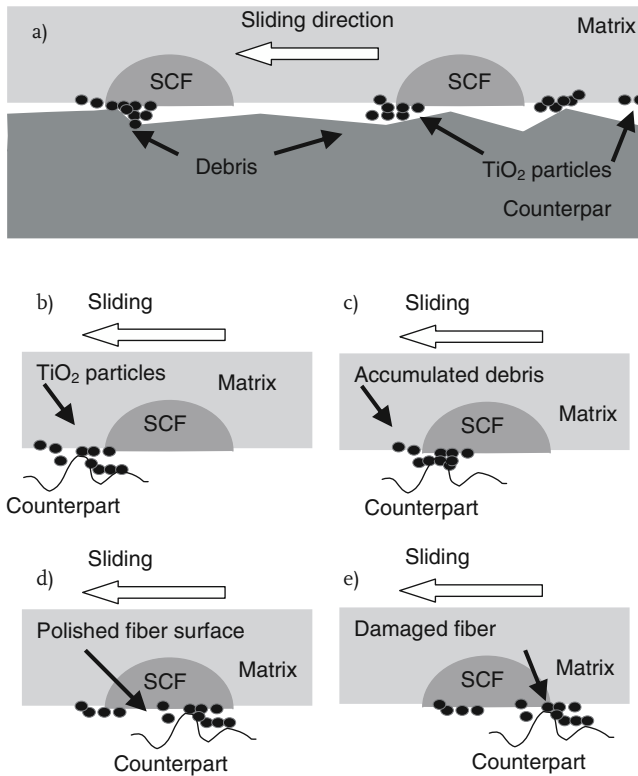
Figure 6.17 Schematic illustration of the ball bearing effect on a submicro scale according to [33, 34]. (a) Overview, (b) matrix-wrapped particles roll on the matrix, and reduce the abrasion of matrix, (c) particles prevent the counterpart tip from directly scraping the fiber, (d) particles act as an abrasive component to polish the fiber surface, (e) the counterpart tip moves through the fiber surface, sometimes result in the damage of the fiber edge. The small black arrows at the leading edge of the counterpart tip indicate the rolling direction of the transfer particles.

By the incorporation of inorganic nanoparticles into thermosetting as well as thermoplastic polymer matrices an improvement of the wear resistance at low filler content can be achieved. The combination of nanoparticles and fillers in the microscale leads to synergistic effects which allow a significant enhancement of the tribological performance. In addition to a decreased specific wear rate, friction coefficient and contact temperature are reduced. Therefore, it is possible to apply these composites under higher normal pressures and sliding velocities.

The beneficial wear mechanisms are supposed in an interaction of nanoparticles and the carbon fibers whereby nanoparticles perform a rolling movement which protects the carbon fibers from pulling out from the matrix and the counterpart asperities. Another reason is that the development of a smooth transfer film during the wear process reduces the severity of wear.

Finally, further investigations are necessary to develop a fundamental understanding of the existing wear mechanisms in polymer-based nanocomposites and those interaction and function.

References

1 http://www.gft-ev.de (accessed 2 May 2011).

2 Friedrich, K., and Schlarb, A.K. (2008) *Tribology of Polymeric Nanocomposites*, Elsevier Verlag, Amsterdam.

3 Friedrich, K., Fakirov, S., and Zhang, Z. (2005) *Polymer Composites – From Nano- to Macro-Scale*, Springer-Verlag, Berlin.

4 Oster, F. (2005) Hochtemperaturbeständige Polymer-Beschichtungen für tribologische An-wendungen. Dissertation. Technische Universität Kaiserslautern.

5 Zhang, M., and Singh, P. (2004) Mechanical reinforcement of unsaturated polyester by Al_2O_3 nanoparticles. *Mater. Lett.*, **58**, 408–412.

6 Singh, R.P., Zhang, M., and Chan, D. (2002) Toughening of a brittle thermosetting polymer: effects of reinforcement particle size and volume fraction. *J. Mater. Sci.*, **37**, 781–788.

7 Wetzel, B. (2006) Mechanische Eigenschaften von Nanoverbundwerkstoffen aus Epoxidharz und keramischen Nanopartikeln. Dissertation. Technische Universität Kaiserslautern.

8 Bushan, B. (2008) *Nanotribology and Nanomechanics*, Springer-Verlag, Berlin.

9 Czichos, H., and Habig, K.-H. (2010) *Tribologie-Handbuch*, Vieweg und Teubner Verlag, 3. Auflage Wiesbaden.

10 Jünemann, H. (1997) *Tribometrie*, Expert-Verlag, Renningen-Malmsheim.

11 GfT (2002) Arbeitsblatt 7, Tribologie.

12 Sommer, K., Heinz, R., and Schöfer, J. (2010) *Verschleiß metallischer Werkstoffe*, Vieweg und Teubner Verlag, Wiesbaden.

13 Riehle, M., and Simmchen, E. (2000) *Grundlagen der Werkstofftechnik*, Deutscher Verlag für Grundstoffindustrie, Stuttgart.

14 Grellmann, W., and Seidler, S. (2007) *Polymer Testing: Friction and Wear*, Carl Hanser Verlag, München.

15 Swallowe, G.M. (1999) *Mechanical Properties and Testing of Polymers*, Kluwer Academic Publishers, Dordrecht, the Netherlands.

16 Eyerer, P., Hirth, T., and Elsner, P. (2008) *Polymer Engineering*, Springer-Verlag, Heidelberg.

17 Weißbach, W. (2010) *Werkstoffkunde*, Vieweg und Teubner Verlag, Wiesbaden.

18 Menning, G., and Lake, M. (2008) *Verschleißminimierung in der Kunststoffverarbeitung*, Carl Hanser Verlag, München.

19 DIN (1979) 50320. *Verschleiß: Begriffe, Systemanalyse von Verschleißvorgängen, Gliederung des Verschleißgebietes*, Beuth-Verlag, Berlin.

20 Czichos, H., and Hennecke, M. (2008) *Hütte, das Ingenieurwissen*, Springer Verlag, Berlin.

21 DIN (1986) 50322. *Verschleiß: Kategorien der Verschleißprüfung*, Beuth-Verlag, Berlin.

22 Hellerich, W., Harsch, G., and Haenle, S. (2004) *Werkstoff-Führer Kunststoffe*, Carl Hanser Verlag, München.

23 DIN (Dezember 1979) 50321. *Verschleiß-Meßgrößen*, Beuth Verlag, Berlin.

24 Mäurer, M. (2002) Tribologische Untersuchungen an Radialgleitlagern aus Kunststoffen. Dissertation. TU Chemnitz.

25 DIN (Mai 1985) 31680. *Gleitlager; Prüfung des tribologischen Verhaltens von Kunststoffen*, Beuth Verlag, Berlin.

26 Bartz, W.J. (1993) *Selbstschmierende und wartungsfreie Gleitlager*, Expert Verlag, Ehningen.

27 Grellmann, W., and Seidler, S. (1998) *Deformation und Bruchverhalten von Kunststoffen*, Springer Verlag, Berlin.

28 Zhang, G., Schlarb, A.K., Tria, S., and Elkedim, O. (2008) Tensile and tribological behaviors of PEEK/nano-SiO$_2$ composites compounded using a ball milling technique. *Compos. Sci. Technol.*, **68**, 3073–3080.

29 Zhang, G., Chang, L., and Schlarb, A.K. (2009) The roles of nano-SiO$_2$ particles on the tribological behavior of short carbon fiber reinforced PEEK. *Compos. Sci. Technol.*, **69**, 1029–1035.

30 Gyrova, L., and Schlarb, A.K. (2008) On the action of various reinforcing fillers and additives for improving the sliding friction and wear performance of polymer composites: Part 1. Short fibers, internal lubricants, particulate fillers. *J. Plast. Technol.*, **4**, 6.

31 Friedrich, K., Zhang, Z., and Schlarb, A.K. (2005) Effects of various fillers on the sliding wear of polymer composites. *Compos. Sci. Technol.*, **65**, 2329–2343.

32 Chang, L., Zhang, Z., Zhang, H., and Schlarb, A.K. (2006) On the sliding wear of nanoparticle filled polyamide 66 composites. *Compos. Sci. Technol.*, **66**, 3188–3198.

33 Gyrova, L. (2010) Sliding friction and wear of polyphenylene sulfide matrix composites: experimental and artificial neural network approach. Dissertation. Technische Uni-versität Kaiserslautern.

34 Jiang, Z., Gyurova, L., Schlarb, A.K., Friedrich, K., and Zhang, Z. (2008) Study on friction and wear behavior of polyphenylene sulfide composites reinforced by short carbon fibers and sub-micro TiO$_2$-particles. *Compos. Sci. Technol.*, **68**, 734–742.

7
Dielectric Relaxation Spectroscopy for Polymer Nanocomposites

Chetan Chanmal and Jyoti Jog

7.1
Introduction

Over the past decade polymer nanocomposites have been the subject of significant interest. This is because of the enhancement in the bulk properties that can be achieved at very low filler content (up to 5 wt% filler loading). The enhancement in the bulk properties of polymer nanocomposites is attributed to the colossal increase in the particle polymer interfacial area which in turn affects the polymer mobility in the interfacial area [1–3]. As a result changes in the glass transition temperature as well as subglass transition relaxations are often noticed. A large number of scientific methods such as dielectric relaxation spectroscopy (DRS), nuclear magnetic resonance (NMR), dynamic mechanical analysis (DMA), and quasi-elastic light scattering, neutron scattering are used to probe the structural and molecular interaction between the polymer matrix and nanofiller inclusion [4–6]. Among these techniques, the broadband DRS has emerged as a powerful technique in probing the relaxation dynamics of the polymer matrix at molecular level [7–10]. The major advantage of using dielectric spectroscopy compared to other techniques is the broad frequency range covered in this technique. The broad frequency range allows investigating different characteristic relaxation processes having a wide range of time and length scales. In dielectric spectroscopy, by observing the dipolar relaxation as a function of temperature and frequency, effects due to intermolecular cooperative segmental motion and hindered dipole orientation can be elucidated. In recent years, the dielectric relaxation spectroscopic study of polymer nanocomposites based on various polymers such as polystyrene (PS), poly-1-butene (PB), polyethylene terephthalate (PETG), and poly(3-hydroxy butyrate) (PHB) has been reported [11–16].

In this chapter, we present the results of the dielectric spectroscopic study of poly(vinylidene fluoride) (PVDF)-based nanocomposites. A variety of nanofillers such as clay with platelet structure and functional nanoparticles such as $BaTiO_3$

and Fe_3O_4 are explored. The effect of these nanofillers on the relaxation dynamics of PVDF is investigated.

7.2
Theory of Dielectric Relaxation Spectroscopy

In dielectric spectroscopy, a small electric perturbation in the form of sinusoidal voltage is applied to samples. The electric field produces polarization, causing oscillation of the same frequency as that of the applied field but with a phase shift (θ). The phase angle shift is measured by comparing the applied voltage to the measured current. The measured response is represented into a complex form (ε*) that can be separated into capacitive and conductive components giving the real part of permittivity (ε′) and loss factor (ε″) [17, 18].

The complex permittivity is defined as

$$\varepsilon^*(f) = \varepsilon'(f) - i\varepsilon''(f) \tag{7.1}$$

where ε' is the real part of permittivity and ε'' is the imaginary part of permittivity. The ratio of the imaginary to the real part ($\varepsilon''/\varepsilon'$) is termed as "dissipation factor," which is represented by tan δ, where δ is the angle between the voltage and the charging current.

In a typical dielectric experiment, samples are initially coated with a thin layer of conducting silver paste to ensure good electrical contacts. Then the sample is sandwiched between gold-coated metal electrodes and a sinusoidal alternating voltage with low amplitude is applied to the sample inducing an alternating current of same frequency. The real part of dielectric permittivity (ε′) and imaginary part of permittivity (ε″) are recorded as a function of frequency or temperature.

7.2.1
Dielectric Relaxations in Polymer Nanocomposites

The various relaxation processes with different time scales and length scales can be studied using dielectric spectroscopy. The following are the characteristic relaxation processes seen in polymer nanocomposites as a function of frequency and temperature:

- Cooperative relaxation (α_a) – Cooperative segmental relaxation in the amorphous phase of polymer associated with the onset of glass transition temperature (T_g).

- Crystalline relaxation (α_c) – Relaxation in local crystalline chains of polymer.

- Maxwell–Wagner–Sillars (MWS) polarization – MWS polarization is associated with the charge trapping at the interface of composites having materials with large difference in the permittivity.

7.2.2
Fitting to Experimental Data

Frequency-dependent dielectric permittivity can be studied using several models. Debye was the first to predict the frequency dependence of dielectric relaxations in polymers [19].

The Debye equation for fitting the dielectric spectra is given by

$$\varepsilon(\omega) = \varepsilon_\infty + \frac{\Delta\varepsilon}{1 + i\omega\tau} \tag{7.2}$$

where $\Delta\varepsilon = \varepsilon_s - \varepsilon_\infty$ is relaxation strength (ε_s is low-frequency permittivity and ε_∞ is high-frequency permittivity), τ is the relaxation time, and $\omega = 2\pi f$.

Generally the relaxation time distribution in polymers is much broader and asymmetric than a single Debye process. A phenomenological model that accounts for the broader and asymmetric nature of the relaxation was developed by Havriliak–Negami (H–N) based on empirical modification to the Debye equation [20, 21]. The H–N equation also takes into consideration the dc conductivity contribution and is given by following equation:

$$\varepsilon(\omega) = \varepsilon' - \varepsilon'' = -i\left(\frac{\sigma_{dc}}{\varepsilon_0\omega}\right)^N + \left(\frac{\Delta\varepsilon}{(1 + (i\omega_{\tau_{HN}})^\alpha)^\beta}\right) \tag{7.3}$$

where σ_{dc} is the dc conductivity, α and β are the shape parameters describing the symmetric and asymmetric broadening parameters, respectively, τ_{HN} is the relaxation time, $\Delta\varepsilon = \varepsilon_s - \varepsilon_\infty$ is the relaxation strength, and $\omega = 2\pi f$.

The H–N equation is the generalized equation for fitting the dielectric relaxation of polymer as it also includes the Cole–Cole equation ($\beta = 1$), Cole–Davidson equation ($\alpha = 1$), and Debye equation ($\alpha = \beta = 1$) as a special case. H–N analysis provides better understanding of the relaxation time scale (τ), the magnitude (relaxation strength), and the shape (α, β) of each relaxation process, particularly, time scale of relaxation processes that can be extracted from the H–N equation fitting. This relaxation time can be further analyzed in terms of the Arrhenius equation for determining the activation energy of the relaxation process.

7.2.3
Activation Energy of the Relaxation Process

The temperature dependence of a relaxation process can be analyzed by plotting the frequency maximum, obtained at each temperature from H–N fitting, against the reciprocal temperature. The maximum frequency (or temperature) of the peak in the loss spectrum is related to the mean relaxation time of the process and characterizes the molecular mobility.

The crystalline relaxation and MWS relaxation were known to follow the Arrhenius-type equation given by the following equation [22]:

$$f_{\max} = f_0 \exp\left(\frac{-E_a}{KT}\right) \tag{7.4}$$

where $f_{\max}$ is the frequency maximum in permittivity loss spectra, E_a is the activation energy, and K is Boltzmann's constant.

Unlike the crystalline and MWS relaxation, the time–temperature relationship of the segmental relaxation corresponding to glass transition temperature normally follows a nonlinear behavior and can be described by the Vogel–Fulcher–Tammann (VFT) equation given by

$$\tau = \tau_0 \exp\left(\frac{BT_0}{T - T_0}\right) \tag{7.5}$$

where τ is the segmental relaxation time and τ_0 is the prefactor correlated with the time scale at which the molecules are attempting to overcome some energy barrier. B is a parameter related to the strength for glass forming. T_0 is a temperature below T_g and at which the segments would be frozen if they were at equilibrium. The width and the asymmetry associated with the distribution of the relaxation times result from a local structural heterogeneity.

7.2.4
Modulus Formalism

The electric modulus formalism was introduced by McCrum *et al.* [23] and it is used to study electrical relaxation phenomena in many polymers [24, 25]. According to its definition, variations in the large values of permittivity and conductivity at low frequencies are minimized and hence common difficulties like electrode nature and contact, space charge injection phenomena, and absorbed impurity conduction effects can be resolved. Electric modulus is an electrical analog to the mechanical shear modulus.

Electric modulus is defined as a quantity inversely proportional to permittivity and is given by the following equation:

$$M^* = \frac{1}{\varepsilon^*} = \frac{1}{\varepsilon' - j\varepsilon''} = \frac{\varepsilon'}{\varepsilon'^2 + \varepsilon''^2} + j\frac{\varepsilon''}{\varepsilon'^2 + \varepsilon''^2} = M' + jM'' \tag{7.6}$$

where M' and M'' are the real and the imaginary part of electric modulus, and ε' and ε'' are the real and the imaginary part of dielectric permittivity, respectively. The electric modulus formalism has unique advantages in the interpretation of slow relaxation phenomena processes like MWS relaxation.

To elucidate the importance of electric modulus, we present the dielectric relaxation spectra of PVDF in permittivity and electric modulus formalism shown in Figure 7.1. The dielectric permittivity (ε'') curve for PVDF shows single relaxations at around 10^{+04} Hz and is attributed to crystalline chain relaxation in PVDF. However when the same data are presented in modulus presentation, two relaxations are clearly discernible. An additional peak (around 10^{+00} Hz) in the low-
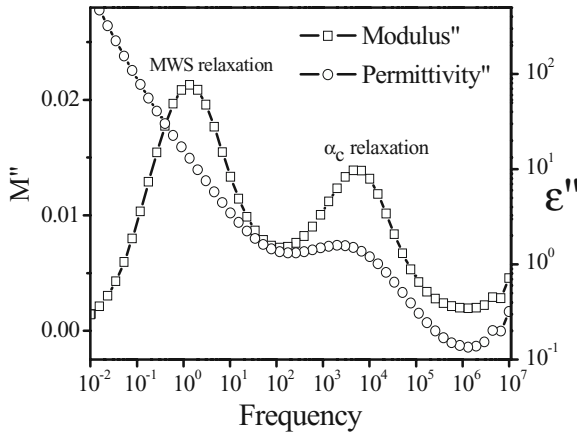
Figure 7.1 Dielectric relaxation spectra of PVDF in permittivity and modulus formalism.

frequency region appears in modulus presentation, which was completely masked in permittivity spectra in the low-frequency region. This low-frequency relaxation is identified as MWS relaxation and is observed in many crystalline polymers. This MWS relaxation is attributed to the trapping of ionic charges at the interface between the amorphous and the crystalline regions of the polymer [4, 26].

7.3
PVDF/Clay Nanocomposites

Polymer clay nanocomposites represent a new class of materials based on reinforcement of polymer chain by dispersion of nanoscale clay particles. From the fundamental point of view, polymer/clay nanocomposites serve as model systems to study the confinement effect on various properties of polymers. Dielectric spectroscopy is indeed found to be an excellent tool to understand the confinement effects in these systems. Depending on the type of clay and polymer matrix, due to the confinement effect, the glass transition temperature will increase, decrease, or sometimes may not change. The studies of the effect of intercalation on microstructure and the dynamics of relaxation in polymer clay nanocomposites have been reported [27–29].

7.3.1
Frequency Dependence of Dielectric Permittivity

PVDF/clay nanocomposites have been studied by a number of researchers as the incorporation of clay in the PVDF matrix results in facilitating formation of polar crystal form of PVDF, namely the β phase [30]. The dielectric properties of the
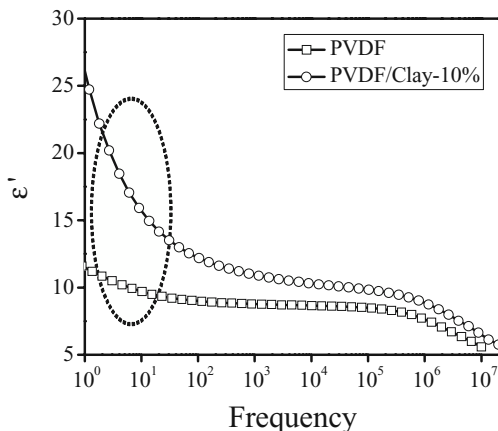
Figure 7.2 Frequency dependence of dielectric permittivity for PVDF/clay nanocomposites at 30 °C.

PVDF/clay system were investigated by Chanmal and Jog [31]. Figure 7.2 shows the frequency dependence of dielectric permittivity for PVDF and PVDF nanocomposites at 30 °C. As can be seen from the figure the dielectric permittivity increases as a result of the incorporation of clay.

For example, the dielectric permittivity at a frequency of 10^{+00} Hz increases from 11 for pristine PVDF to about 25 for 10% clay content in the nanocomposites. The increase in the permittivity with increasing clay loading, particularly in the low-frequency region, can be attributed to the interfacial polarization operative in low frequency end of the spectrum. In polymers and composites, interfacial polarization is present due to the difference in the permittivity values of the filler and polymer matrix and such interface can lead to an increase in dielectric permittivity, particularly in the low-frequency region.

7.3.2
Vo–Shi Model Fitting to Dielectric Permittivity

The variation of dielectric permittivity at 1 Hz with clay loading is shown in Figure 7.3. The dielectric permittivity increases monotonically with increasing clay loading. The experimental data were analyzed using a log law model proposed by Lichtenecker which takes into account the filler content [32]. As can be seen in the figure the predicted values using the log law model are significantly lower than the experimental values. This indicates that there is an additional contribution to observed dielectric permittivity. Vo and Shi presented a model to predict the dielectric permittivity of polymer nanocomposites which takes into account the contribution from the interface [33]. As can be seen from the figure, experimentally obtained permittivity values of PVDF/clay nanocomposites are in good agreement
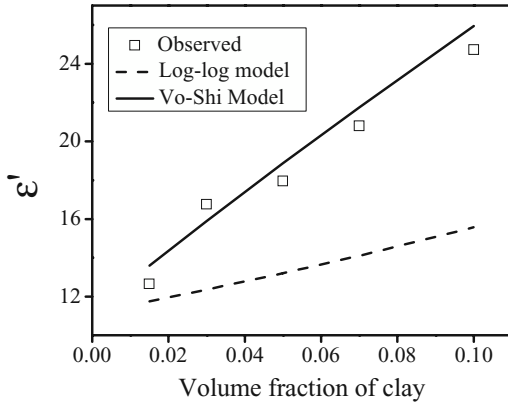
Figure 7.3 Composition dependence of dielectric permittivity for PVDF/clay nanocomposites at 1 Hz and fitting of the experimental data with Lichtenecker and Vo–Shi model.

with the values predicted by the Vo and Shi model. The parameters, namely the interface constant K of 7 and permittivity of the interface of 50, provide the best fit to the observed data.

The value of K represents a relative volume of the interphase region influenced by the surface area of the dispersed phase. The high value of interface constant suggests a high surface area and the presence of strong interfacial interactions between PVDF and clay [34, 35].

7.3.3
Role of Interface

The contribution of the interface was further elucidated by analyzing the data using Cole–Cole plots in impedance formalism as shown in Figure 7.4. Two incomplete arches are observed for nanocomposites at 30 °C. However, for pristine PVDF only one arch is evident in the frequency range of our measurements. The two semicircles in the case of nanocomposites represent the charge transport within the bulk and interface [36]. Since this kind of behavior is not observed in pristine PVDF, it can be ascribed to the presence of active interface between polymer and clay layers. This supports the contention that the interfacial effects become more evident and contribute toward the charge transport in clay nanocomposites.

7.3.4
Frequency Dependence of Dielectric Relaxation Spectra

Figure 7.5 shows the frequency dependence of dielectric permittivity loss (ε'') curves for PVDF and PVDF/clay nanocomposites. Two relaxations are clearly
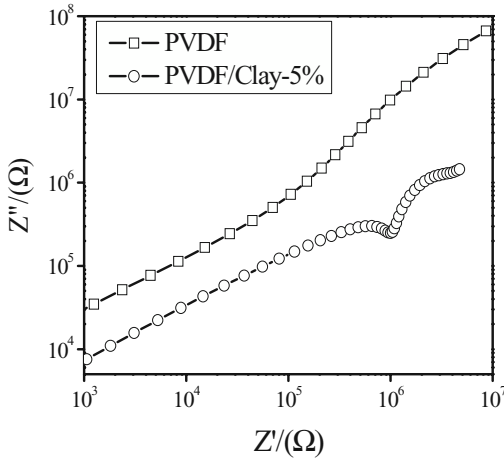
Figure 7.4 Cole–Cole plot for PVDF clay nanocomposites at 110 °C.
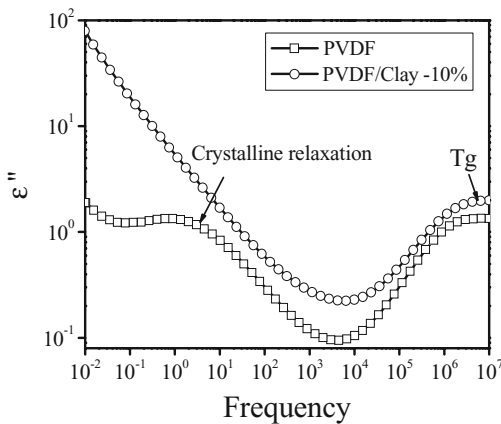
Figure 7.5 Dielectric relaxation spectra of PVDF/clay nanocomposites at 30 °C.

discernible from the dielectric permittivity loss spectra. The faster segmental relaxation seen at frequency 10^{+07} Hz is attributed to glass transition relaxation and is denoted as α_a relaxation. It is well reported that the peak at 10^{+07} Hz is related to the micro-Brownian cooperative motions of the main chain backbone and is dielectric manifestation of the glass transition temperature of PVDF [37].

In clay nanocomposites, the presence of clay, even up to 10%, does not affect the segmental process (glass transition relaxation-α process) confirming that the time scale and length scale of the α_a process are unaffected with the addition of clay. The slower relaxation peak at about 10^{+00} Hz is denoted as α_c relaxation and

is associated with the molecular motions in the crystalline region of PVDF in the nonpolar, that is, α form of PVDF [38]. The crystalline relaxation peak completely disappeared in PVDF/clay nanocomposites as seen in Figure 7.5. It is well documented that the crystalline relaxation peak disappears in nanocomposites exhibiting β crystalline form of PVDF [39, 40]. The absence of the crystalline relaxation peak in PVDF/clay nanocomposites thus can be recognized as a dielectric manifestation for β form in PVDF.

7.4
PVDF/BaTiO₃ Nanocomposites

Typically, polymers have low dielectric permittivity and are not suitable directly in capacitor applications and on the other hand, high permittivity ferroelectric ceramic requires higher processing temperature. The incorporation of various inorganic filler into polymer matrix offers a unique opportunity for the development of composite material with potential applications in charge storing devices and energy density devices [41].

7.4.1
Frequency Dependence of Dielectric Relaxation Spectra

The study of nanocomposites of PVDF with BaTiO₃ has been reported by Chanmal and Jog [42]. The composites were prepared by the melt compounding technique. Figure 7.6 shows the dielectric spectroscopic study of these nanocomposites at room temperature. As evident from the figure, both PVDF and nanocomposites show two relaxation processes corresponding to the crystalline relaxation and glass
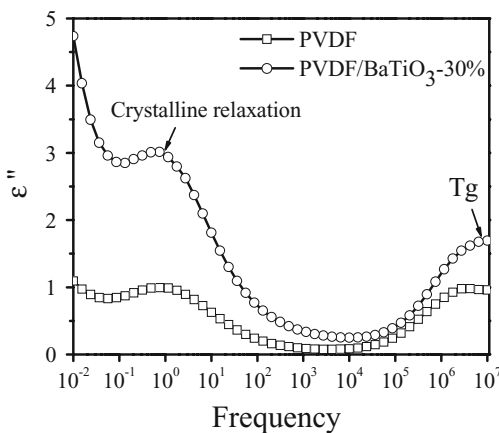
Figure 7.6 Frequency dependence of permittivity for PVDF/BaTiO₃ nanocomposites at 30 °C.
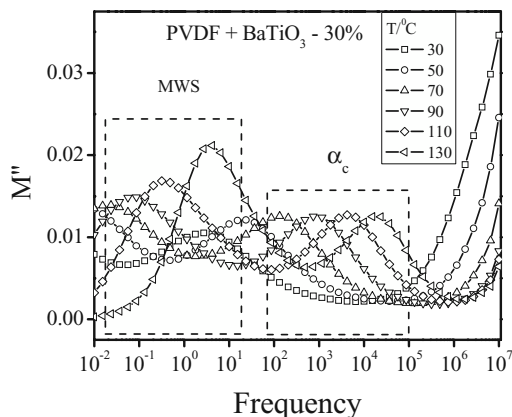
Figure 7.7 Temperature-dependent electric modulus spectra of PVDF/BaTiO₃ nanocomposites.

transition. Unlike in the PVDF/clay nanocomposites, crystalline relaxation is clearly seen in the nanocomposites. The presence of the crystalline peak indicates the nonpolar α-phase of PVDF in the nanocomposites. This is also confirmed with X-ray diffraction and IR spectroscopy (not shown in the figure). Thus in the case of PVDF-based nanocomposites, dielectric spectroscopy acts as a supporting tool to understand the phases present in the polymer.

7.4.2
Electric Modulus Presentation of Dielectric Relaxation Spectra

Dielectric relaxation spectra in Figure 7.6 show that, in nanocomposites, dielectric losses increase significantly with filler inclusion. It is therefore convenient to represent the data in modulus formalism. Figure 7.7 shows the temperature-dependent electric modulus (M'') spectra of PVDF and PVDF/BaTiO₃ nanocomposites. Two relaxation processes can be clearly observed in the modulus curves particularly on the higher temperature side. The M'' peaks for both relaxation processes shift to a higher frequency with increasing temperature. The relaxation peak at the high-frequency side is identified as fast symmetric crystalline relaxation (α_c). At high temperature, another peak appears in the modulus spectra. This is attributed to MWS polarization (also known as interfacial polarization) which can be seen in the heterogeneous materials. For heterogeneous composite, an interfacial polarization is almost always present because of filler additives or even impurities that migrate toward the interface [43]. This MWS relaxation is attributed to the trapping of ionic charges at the interface between the amorphous and the crystalline regions of the polymer.

It is observed from the figure that there is no significant change in the dielectric relaxation peak height in the crystalline relaxation process, whereas the intensity
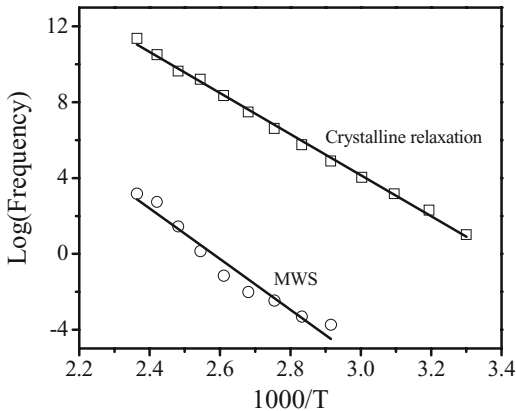
Figure 7.8 Arrhenius plots for crystalline and MWS relaxation in PVDF/BaTiO₃-30% nanocomposites.

of MWS relaxation peak increases with temperature and peak broadening decreases signify the asymmetric nature of MWS relaxation [44].

7.4.3
Activation Energy of Crystalline and MWS Relaxation Processes

Figure 7.8 shows the activation energy plots of PVDF nanocomposites for crystalline and MWS relaxation processes. For PVDF/BaTiO$_3$ nanocomposites, the relaxation time decreases with increasing temperature due to enhancement of mobility of charge carriers at high temperature. The activation energy for crystalline relaxation was calculated using the Arrhenius equation described in Eq. (7.4). The activation energy was found to be about 0.41 eV for PVDF as well as PVDF/BaTiO$_3$ nanocomposites. This value is in good agreement with the reported value of activation energy for crystalline relaxation (α_c) in PVDF [37]. The MWS relaxation also shows Arrhenius-type behavior indicating that relaxation is a thermally activated process. The activation energy plots for crystalline relaxation almost coincide which indicates that time scales of the relaxation process are independent of filler loading. However, the activation energy of MWS relaxation is slightly reduced in the nanocomposites.

7.5
PVDF/Fe₃O₄ Nanocomposites

Magnetic nanoparticle-embedded polymer matrices are studied extensively for potential application in microwave communication systems, magnetic recording media, etc. In this view, understanding their magneto-dielectric properties is
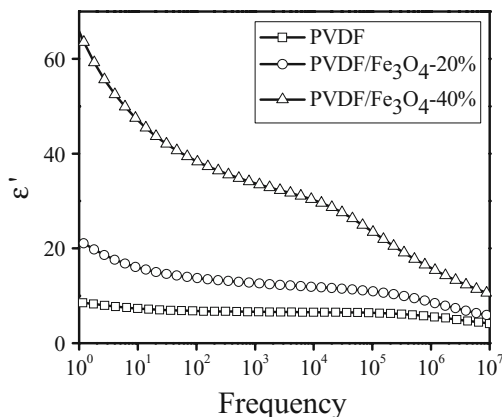
Figure 7.9 Frequency-dependent dielectric permittivity of PVDF/Fe$_3$O$_4$ nanocomposites at 30°C.

important to explore their candidature [45, 46]. Melt-compounded nanocomposites of PVDF with Fe$_3$O$_4$ have been presented in the present section [47]. The room-temperature frequency dependence of the dielectric properties of PVDF/Fe$_3$O$_4$ nanocomposites is shown in Figure 7.9. For both polymer and nanocomposites, dielectric permittivity decreases with increasing frequency. This is because at low frequency, dipoles have enough time to get polarized whereas at high frequency, dipoles do not have enough time to get polarized in the direction of the applied field. The dielectric permittivity is found to be dependent on both frequency and filler fraction loading. The dielectric permittivity increases to 65 at 40% of filler loading at frequency 1 Hz. The important point to be noted is that the dielectric permittivity is increased in the whole frequency range of measurement. The higher value of permittivity in the high-frequency region brings the interest of application of these materials in high-frequency electronic devices. The dispersion behavior of dielectric permittivity with frequency in nanocomposites is similar to that observed in neat PVDF, except an early onset of dielectric dispersion (around 10^{+04} Hz) for 40 wt% of filler loading. This is also reflected in the dielectric loss spectra of nanocomposites.

7.5.1
Low-Temperature Dielectric Relaxation Spectra

Figure 7.10 shows the dielectric loss spectra of PVDF/Fe$_3$O$_4$ nanocomposites at 10°C. The addition of Fe$_3$O$_4$ is found to increase the intensity of dielectric loss spectra in the nanocomposites and the relaxation peak corresponding to glass transition temperature shifts to lower frequency. This shifting of the relaxation peak to lower frequency is consistent with early onset of dispersion observed in
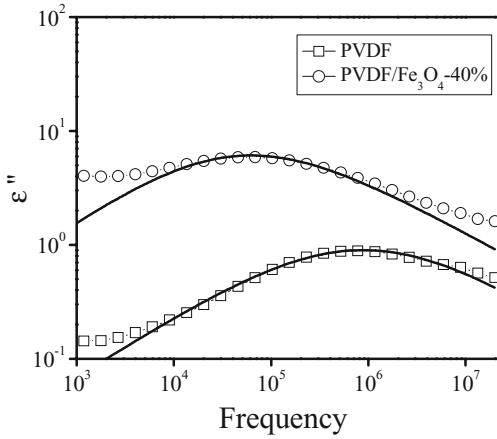
Figure 7.10 Glass transition relaxation of PVDF and PVDF/Fe$_3$O$_4$ nanocomposites at 10 °C.
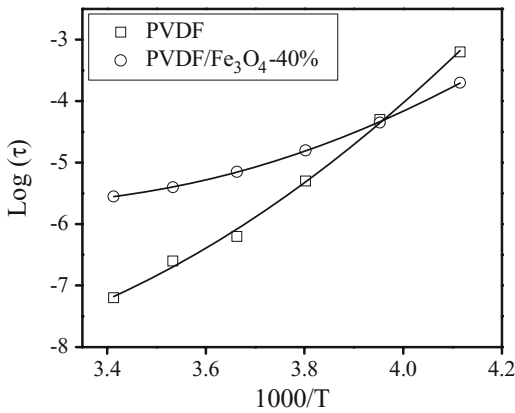
Figure 7.11 VFT plots of glass transition relaxation in PVDF and PVDF/Fe$_3$O$_4$ nanocomposites.

the dielectric permittivity spectra. This indicates the retardation of the glass transition relaxation process in the nanocomposites with longer relaxation time and lower mobility.

The frequency dependence of the dielectric permittivity for dielectric relaxation is further analyzed by the Havriliak–Negami (HN) function as described in Eq. (7.3). The solid line in Figure 7.11 shows that the experimental data are reasonably good fitted with the HN function. As evident from the figure, the glass transition of PVDF in PVDF/Fe$_3$O$_4$ nanocomposites shifts to lower frequencies as compared

to neat PVDF. The VFT analysis of the experimental data shown in figure also confirms the retardation of the process.

7.5.2
Activation Energy of Glass Transition Relaxation

The mean relaxation time of glass transition relaxation against reciprocal temperature can be fitted by the Vogel–Fulcher–Tammann (VFT) function described in Eq. (7.5). Figure 7.11 shows that relaxation time decreases with increasing temperature, indicating the enhancement of mobility of charge carriers at high temperature.

The activation energy obtained from VFT fitting is found to be 0.08 eV for PVDF and 0.19 eV for nanocomposites. The similar values of activation energy for PVDF are obtained by Bello *et al.* and Tuncer *et al.* [37, 38]. Activation energy of glass transition relaxation increases with increasing Fe_3O_4 loading. This result is indeed consistent with the frequency and temperature behavior of $PVDF/Fe_3O_4$ nanocomposites.

7.5.3
Normalized Spectra of Dielectric Relaxation

Figure 7.12 shows the normalized spectra of glass transition temperature. From the figure it is evident that peak broadening is reduced with Fe_3O_4 addition. Typically, the local relaxation processes are considered to have distribution of relaxation times which represent the heterogeneity in the materials under study. Wider distribution of relaxation times indicates higher heterogeneity in the system. From the normalized spectra, it indicates that our composites are less heterogeneous as evidenced by reduced width of distribution of relaxation times [48].
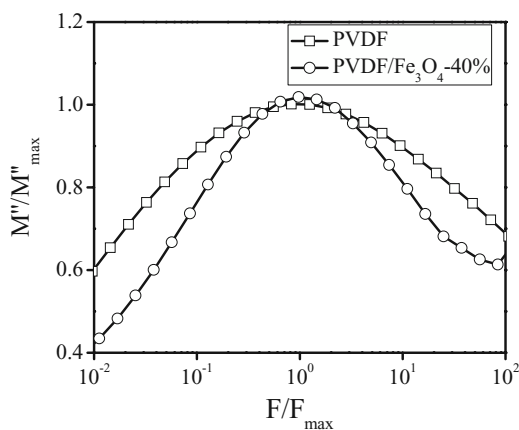
Figure 7.12 Normalized relaxation spectra of $PVDF/Fe_3O_4$ nanocomposites at −30°C.

7.6
Comparative Analysis of PVDF Nanocomposites

Figure 7.13 shows the comparative plot of dielectric permittivity variation in PVDF-based nanocomposites with filler inclusion. It is seen from the figure that permittivity variation depends on the type of filler loading. In the case of PVDF/Fe_3O_4 nanocomposites, a significant increase in the dielectric permittivity is observed. The permittivity increase in the high-frequency region is very important in different applications. Comparatively, a small increase in the permittivity is observed in the case of $BaTiO_3$ nanofiller, even though the filler itself has a high dielectric constant. Barium titanate-based polymer composites often require high filler loading to achieve the desirable dielectric properties. However, functionalization of nanoparticles can improve the permittivity significantly [49]. The solid line in the figure shows that the observed data can be fitted with the log law model. It can be recalled that for PVDF/clay nanocomposites this model showed lower values (Figure 7.3). Clay loading shows the maximum increase in the permittivity at comparatively lower filler loading. This can be attributed to the platelet structure of clay nanoparticles where interfacial effects are more dominant. The interface contribution leads to a significant increase in the permittivity.

In the case of PVDF/clay nanocomposites, a significant increase in the permittivity of PVDF/clay is observed which is attributed to the presence of active interface between the filler and polymer matrix. The variation of dielectric permittivity with filler content is best described by the Vo–Shi model, which takes into account the contribution of interface to permittivity. The presence of interface is confirmed by studying complex impedance analysis which shows a single semicircle in pristine PVDF whereas two semicircles are observed in nanocomposites indicating the presence of interface.
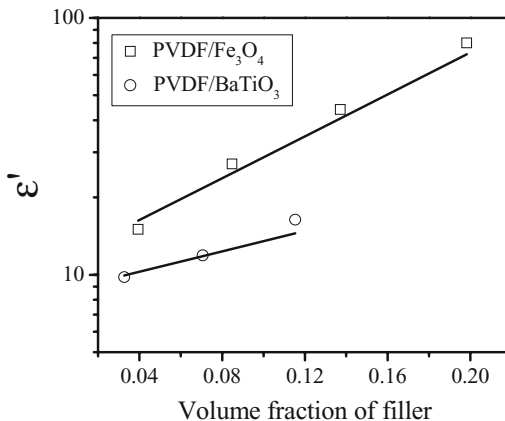
Figure 7.13 Comparative plot of variation of dielectric permittivity of PVDF with Fe_3O_4 and $BaTiO_3$. (Line represents fitting using the Lichtenecker model and symbols represent experimental data.)

In the dielectric relaxation spectra, overall three relaxations are observed in the PVDF-based nanocomposites. From the low-temperature to the high-temperature side, these relaxations were identified as glass transition temperature, crystalline chain relaxation, and MWS relaxation, respectively. It was found that crystalline relaxation is not affected with the addition of any of the three fillers studied. MWS relaxation showed retardation in $BaTiO_3$ addition and enhancement in the case of Fe_3O_4 addition. Glass transition relaxation is not affected significantly with clay and $BaTiO_3$ addition. However, Fe_3O_4 loading has shown retardation in the glass transition dynamics. Thus, additions of filler have a uniquely distinct impact on the relaxation dynamics of the polymer. The dynamics of all the relaxations was studied using the activation energy plot. In all the polymer nanocomposites systems, it was found that the dynamics of glass transition relaxation followed a nonlinear VFT equation whereas local crystalline and MWS relaxation follows the linear Arrhenius equation.

7.7
Conclusions

The results for dielectric behavior of various nanocomposites systems based on PVDF are presented in this chapter. The results indicate that the overall dielectric behavior of polymer nanocomposites can be understood by employing different formalisms, namely complex permittivity, complex impedance, and complex modulus. This analysis shows that dielectric spectroscopy provides a powerful technique to understand the molecular dynamics in polymer nanocomposites. In general, the analysis shows that the addition of nanoparticles has significant effect on the temperature and frequency dependence of dielectric relaxation behavior of the polymer.

Acknowledgment

Nomenclature

PVDF	– poly(vinylidene) fluoride
$BaTiO_3$	– barium titanate
Fe_3O_4	– iron oxide
f	– frequency
f_{max}	– frequency maximum in loss spectra
ω	– angular frequency
ε'	– real part of complex dielectric permittivity

ε'' – imaginary part of complex dielectric permittivity
M' – real part of electric modulus spectra
M'' – imaginary part of electric modulus spectra
σ_{dc} – dc conductivity
$\Delta\varepsilon$ – dielectric relaxation strength
α and β – shape parameters describing the symmetric and asymmetric broadening of relaxation
E_a – activation energy
τ – relaxation time
T – temperature
MWS   – Maxwell–Wagner–Sillars relaxation
T_g – glass transition temperature
α_c – crystalline relaxation
α_a – cooperative segmental relaxation

References

1 Kumar, S.K., and Krishnamoorti, R. (2010) *Annu. Rev. Chem. Biomol. Eng.*, **1**, 37–58.

2 Maity, P., Gupta, N., Parameswaran, V., and Basu, S. (2010) *IEEE Trans. Dielectr. Elect. Insul.*, **17**, 1665–1675.

3 Yangyang, S., Zhuqing, Z., and Wong, C.P. (2005) *Polymer*, **46**, 2297–2305.

4 Mijovic, J., Lee, H., Kenny, J., and Mays, J. (2006) *Macromolecules*, **39**, 2172–2182.

5 Kalgaonkar, R.A., and Jog, J.P. (2008) *Polym. Int.*, **57**, 114–123.

6 Xiao, Z., Li, Y., Ma, D., Schadler, L.S., and Akpalu, Y.A. (2006) *J. Polym. Sci. B Polym. Phys.*, **44**, 1084–1095.

7 Sebastian, M.T. (2010) *Int. J. Appl. Ceram. Technol.*, **7**, 415–434.

8 Pissis, P., Fragiadakis, D., Kanapitsas, A., and Delides, K. (2008) *Macromol. Symp.*, **265**, 12–20.

9 Kremer, F. (2002) *J. Non-Cryst. Solids*, **305**, 1–9.

10 Mijovic, J., and Sy, J.W. (2000) *Macromolecules*, **33**, 9620–9629.

11 Bergmann, A., and Owen, A. (2004) *Polym. Int.*, **53**, 863–868.

12 Wanjale, S.D., and Jog, J.P. (2006) *J. Macromol. Sci. B*, **45**, 1053–1064.

13 Couderc, H., Delbreilh, L., Saiter, A., Grenet, J., Souza, N.D., and Saiter, J.M. (2007) *J. Non-Cryst. Solids*, **353**, 4334–4338.

14 Bohning, M., Goering, H., Fritz, A., Brzezinka, K.W., Turky, G., Schonhals, A., and Schartel, B. (2005) *Macromolecules*, **38**, 2764–2774.

15 Mijovic, J., and Sy, J.W. (2002) *Macromolecules*, **35**, 6370–6376.

16 Patil, P.A., Wanjale, S.D., and Jog, J.P. (2008) *e-Polymers*, **79**, 1.

17 Havriliak, S. Jr. (1997) *Dielectric and Mechanical Relaxation in Materials: Analysis, Interpretation, and Application to Polymers*, Carl Hanser Verlag, Munich.

18 Frickel, N., Greenbaum, A.G., Gottlieb, M., and Schmidt, A.M. (2011) *J. Phys. Chem. C*, **115**, 10946–10954.

19 Johnstone, J.H.L., and Williams, J.W. (1929) *Phys. Rev.*, **34**, 1483.

20 Kyritsis, A., Vikelis, G., Maroulas, P., Pissis, P., Milosheva, B., Kotsilkova, R., Toplijska, A., Silvestre, C., and Duraccio, D. (2011) *J. Appl. Polym. Sci.*, **121**, 3613–3627.

21 Comer, A.C., Heilman, A.L., and Kalika, D.S. (2010) *Polymer*, **51**, 5245–5254.

22 Madbouly, S.A., and Otaigbe, J.U. (2007) *Polymer*, **48**, 4097–4107.

23 McCrum, N.G., Read, B.E., and Williams, G. (1967) *Anelastic and Dielectric Effects in Polymeric Solids*, John Wiley & Sons, Ltd, London.

24 Hammamia, H., Arous, M., Lagache, M., and Kallel, A. (2007) *J. Alloy Comp.*, **430**, 1–8.

25 Psarrasas, G.C., Manolakakib, E., and Tsangaris, G.M. (2003) *Compos. Appl. Sci. Manuf.*, **34**, 1187–1198.

26 Arous, M., Amor, I.B., Kallel, A., Fakhfakh, Z., and Perrier, G. (2007) *J. Phys. Chem. Solids*, **68**, 1405–1414.

27 Page, K.A., and Adachi, K. (2006) *Polymer*, **47**, 6406–6413.

28 Ding, Y., Pawlus, S., Sokolov, A.P., Douglas, J.F., Karim, A., and Soles, C.L. (2009) *Macromolecules*, **42**, 3201–3206.

29 Martin, J., Sanz, C.A.M., Ezquerra, T.A., and Nogales, A. (2009) *Macromolecules*, **42**, 5395–5401.

30 Priya, L., and Jog, J.P. (2003) *J. Appl. Polym. Sci.*, **89**, 2036–2040.

31 Chanmal, C.V., and Jog, J.P. (2009) *e-Polymers*, **112** (112), 1–8.

32 Lichtenecker, K. (1924) *Phys. Z.*, **25**, 225.

33 Vo, H.T., and Shi, F.G. (2002) *Microelectron. J.*, **33**, 409.

34 Todd, M.G., and Shi, F.G. (2002) *Microelectron. J.*, **33**, 627–632.

35 Murugaraj, P., Mainwaring, D., and Huertas, N.M. (2005) *J. Appl. Phys.*, **98**, 054304.

36 Lu, H., Zhang, X., and Zhang, H. (2006) *J. Appl. Phys.*, **100**, 054104.

37 Bello, A., Laredo, E., and Grimau, M. (1999) *Phys. Rev. B*, **60**, 12764–12774.

38 Tuncer, E., Wegener, M., and Multhaupt, R.G. (2005) *J. Non-Cryst. Solids*, **351**, 2917–2921.

39 Valetine, V.K., Inna, A.M., Grigory, V.M., Gavrilov, N.V., and Bessonova, N.P. (2007) *J. Appl. Polym. Sci.*, **105**, 1107–1117.

40 Oka, Y., and Koizumi, N. (1982) *Polym. J.*, **14**, 869–876.

41 Li, J., Claude, J., Franco, L.E.N., Seok, S., and Wang, Q. (2008) *Chem. Mater.*, **20**, 6304–6306.

42 Chanmal, C.V., and Jog, J.P. (2008) *Express Polym. Lett.*, **2**, 294–301.

43 Yu, S., Hing, P., and Hu, X. (2000) *J. Appl. Phys.*, **88**, 398–404.

44 Madbouly, S.A., Mansour, A.A., and Abdou, N.Y. (2007) *Eur. Polym. J.*, **43**, 1892–1904.

45 Ramajo, L.A., Cristobal, A.A., Botta, P.M., Lopez, J.M.P., Reboredo, M.M., and Castro, M.S. (2009) *Compos. Appl. Sci. Manuf.*, **40**, 388–393.

46 Yang, T.I., Brown, R.N.C., Kempel, L.C., and Kofinas, P. (2008) *J. Magn. Magn. Mater.*, **320**, 2714–2720.

47 Chanmal, C.V., and Jog, J.P. (2011) Dielectric relaxation dynamics in PVDF/Fe$_3$O$_4$ nanocomposites. (unpublished data).

48 Li, C., Wu, J., Zhao, J., Zhao, D., and Fan, Q. (2004) *Eur. Polym. J.*, **40**, 1807–1814.

49 Kim, P., Doss, N.M., Tillotson, J.P., Hotchkiss, P.J., Pan, M.J., Marder, S.R., Li, J., Calame, J.P., and Perry, J.W. (2009) *ACS Nano*, **3**, 2581–2592.

8
AFM Characterization of Polymer Nanocomposites

Ken Nakajima, Dong Wang, and Toshio Nishi

8.1
Atomic Force Microscope (AFM)

8.1.1
Principle of AFM

Atomic force microscope (AFM) was invented during the collaboration between Prof. Quate in Stanford University and Dr. Binnig and Dr. Gerber who developed scanning tunneling microscope (STM) at IBM Zurich [1]. In contrast to STM, it is not necessary to request conductivity in samples, which has led its development into many different scientific and industrial fields. The AFM has a cantilever as its most basic component, which has a very sharp probe at its free end in order to interact with samples' surfaces. The interaction force induces the deflection of the cantilever, which is the most important signal of concern. Since the interaction force between them is generally called "atomic force," the microscope was named as the atomic force microscope. The original AFM by the developers used STM to detect the cantilever deflection, while an optical beam method is mostly used nowadays due to easier handleness.

The force acting on two atoms separated by a certain finite distance is schematically depicted as shown in Figure 8.1. At a long distance, the attractive force acts which is called as dispersion force, a kind of van der Waals force. If these atoms are replaced by molecules, van der Waals force originated from the electric dipole is added to the interaction. The force acting on isolated atoms or molecules is proportional to the sixth power of the separation distance, while macroscopic objects such as probes and samples have a weaker dependence on distance. For instance, the long-range attractive force due to van der Waals interaction becomes proportional to the second power of distance when the contact between a sphere and a planer surface is taken into account. When the atoms approach more, the wavefunctions of electrons associated with these atoms start to overlap, which produces strong repulsive force (Pauli's exclusion principle). In general, the equilibrium atomic distance is determined as the balance point between these
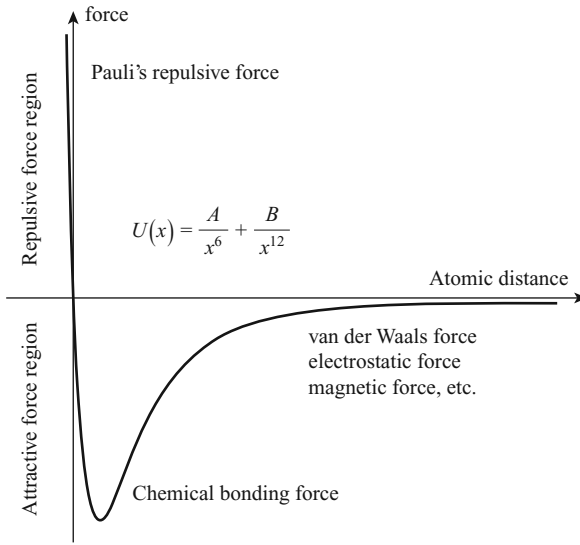
Figure 8.1 Atomic force acting between two atoms.
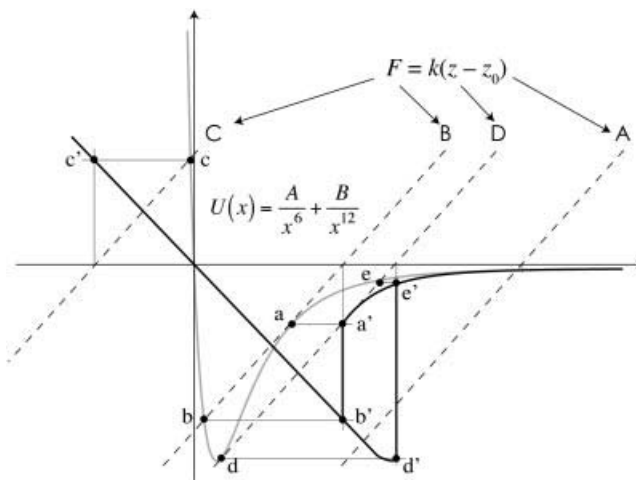
Figure 8.2 Force–distance curve.

attractive and repulsive forces. Other forces can occur in some cases such as the one originated from chemical bonding.

Figure 8.2 shows the response of an AFM cantilever near a sample's surface. The probe attached on the cantilever feels the force similar to the one shown in Figure 8.1. This force is rewritten in Figure 8.2 as a gray solid curve, which deflects the cantilever. If the deflection is small enough, the restoring force, F, obeys Hooke's law and is expressed as

$$F = k(z - z_0) \tag{8.1}$$

where k is the spring constant of the cantilever and $z - z_0$ is the cantilever deflection. The force balance is realized at the intersection points between the gray solid curve and the line expressed by Eq. (8.1), including points a to e in Figure 8.2. In the practical AFM measurement, since the force is measured as a function of the sample's displacement, which is controlled by the piezoelectric scanner placed beneath the sample, the black solid curve, including points from a' to e', is obtained. We call this curve the force–distance curve (or simply the force curve). When the cantilever approaches the sample from far away (line A), it starts to sense attractive force and gradually bends to the sample. Then, in the case of a sufficiently soft cantilever, the sudden jump-in (adhesion) to the sample's surface occurs from points a to b on line B. The force gradient on this point is equal to the spring constant, k. After that, it crosses the point of apparent zero force and further bends to come into the repulsive region. It is now to withdraw the cantilever from the sample. The cantilever deflection gradually decreases and reaches the attractive region passing through the repulsive region, the first adhesion point. Here, the cantilever bends to a totally opposite direction. Further withdrawal is followed by another sudden jump-out from points d to e on line D. The force at the maximum deflection before the jump-out is called the maximum adhesive force.

The so-called contact-mode operation uses the cantilever deflection as the feedback signal. In other words, the AFM probe traces the surface corrugation with keeping the deflection signal constant, commonly in the repulsive region by moving the sample up and down using a piezoelectric scanner (Figure 8.3). Then,
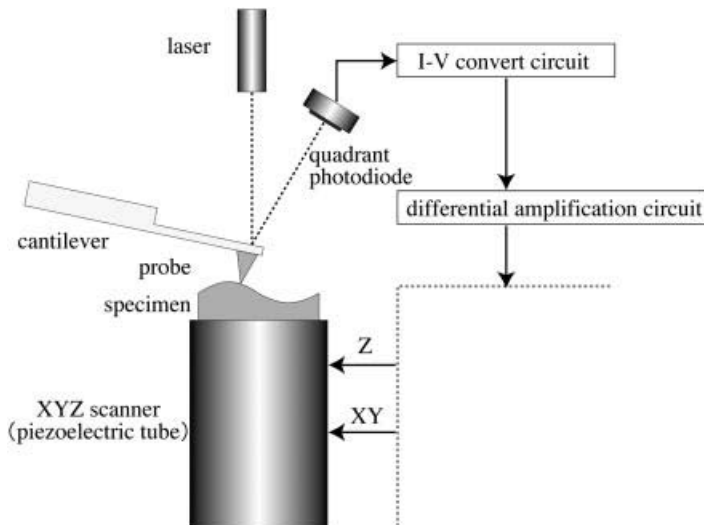
Figure 8.3 Contact-mode AFM.

the set of displacement signals in the z-direction can be regarded as the topographic image. However, this is only valid in an ideal situation. As reviewed in later sections, the z-displacement signal no longer represents the true topography when the sample's surface is soft enough to be deformed by the interaction force.

8.1.2
Principle of Tapping Mode AFM [2]

Contact mode had been adopted in old commercial AFM instruments because of its easy principle. Since the AFM probe is scanned over a sample's surface in contact, it makes the existence of frictional force inevitable. The damage by the frictional force is sometimes very serious. The interaction force is also larger than ones in the case of other later-developed modes, which makes atomic resolution imaging difficult. If the measurement is performed under ambient conditions, the water-adsorbed layer on the sample's surface produces capillary force between the AFM probe and the sample and therefore the subtle control of force is impossible. It is required to bring the measurement condition into liquid to avoid this problem. Although the invention of tapping mode is not so new, actually it was right after the invention of contact mode in the early 1990s, it has become the standard equipment of commercial AFM machines since the mode is developed to overcome problems seen in contact mode. In this section, we will review the principle of tapping mode (Figure 8.4).
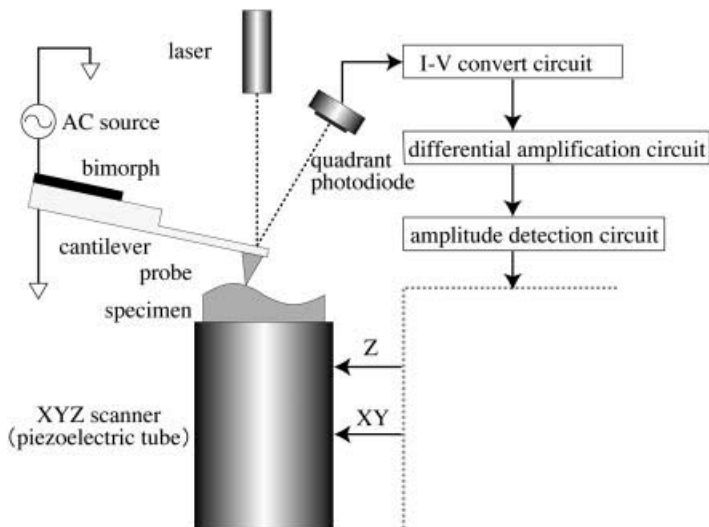
Figure 8.4 Tapping-mode AFM.

The AFM cantilever is now vibrated at a certain frequency near its resonant frequency. Upon an approach, when its probe starts to touch a sample's surface (namely the probe is placed in the repulsive interaction region) intermittently, the oscillation amplitude decreases. Tapping-mode operation uses this amplitude signal for feedback control. As indicated by the naming of "tapping," the contact between the probe and the sample is limited to a very short period during a vibration cycle, and many problems occurring in contact mode can be improved. As shown later, the contact force exerted to the sample can be minimized and the effect of frictional interaction becomes negligible even when harder cantilevers are used. The mode suits the measurement in liquids, which spreads the application field such as biology.

Since the principle of tapping mode is very complicated, it is not simple to understand the phenomena occurring at the interface between the probe and the sample. For example, the cantilever is usually vibrated at a pretty large oscillation amplitude of 20–50 nm. Then, the probe is cyclically placed into attractive and repulsive regions, bringing the cantilever oscillation into a nonlinear fashion. In spite of such difficulty, it is important to have a rough image of cantilever movement in order to interpret experimental results.

When the probe is placed sufficiently far away from the sample's surface so that there is no interaction, the cantilever vibrates at a constant oscillation amplitude, where the excess energy injected to the cantilever from the small bimorph located at its fixed end is dissipated by internal friction inside the cantilever and viscous interaction with a surrounding medium such as air or liquid.[1] While the probe approaches the sample's surface, the intermittent contact results in the decrease in the oscillation amplitude. The equation of motion for the cantilever receiving forced oscillation is written as follows:

$$m\frac{d^2z}{dt^2} + \gamma\frac{dz}{dt} + kz = mA_d\omega^2\cos\omega t \tag{8.2}$$

It is a well-known equation for a damped harmonic oscillator with forced oscillation excited by displacement. The bimorph displacement vibrated at the amplitude of A_d. This simplification can cause some essential arguments, while they are beyond the scope of this chapter. m and k are the point mass[2] and the spring constant of the cantilever, respectively. These two quantities define the resonant angular frequency ω_0 $(=2\pi f_0, f_0$: resonant frequency) as follows:

$$\omega_0 = \sqrt{\frac{k}{m}} \tag{8.3}$$

γ is the viscosity coefficient and written as

$$\gamma = \frac{m\omega_0}{Q} \tag{8.4}$$

1) The equation of motion for forced oscillation without damping term shows a divergence of the oscillation amplitude.

2) We call it as effective mass, which does coincide neither with the mass of the probe nor that of the cantilever.

where Q is the dimensionless parameter to express the resonance. Larger Q means the smaller energy dissipation and the oscillation bandwidth becomes narrower. When the external force is imposed at $t = 0$, the solution of Eq. (8.2) becomes

$$z(t) = \frac{\omega^2 A_d}{\sqrt{(\omega_0^2 - \omega^2)^2 + \left(\dfrac{\omega_0 \omega}{Q}\right)^2}} \left[\cos(\omega t - \varphi) - \frac{1}{2\omega_0}\{(\omega_0 + \omega)\cos(\omega_0 t - \varphi) \right.$$
$$\left. - (\omega_0 - \omega)\cos(\omega_0 t + \varphi)\} \right] \tag{8.5}$$

where the phase φ becomes

$$\varphi = \tan^{-1}\left(\frac{\omega_0 \omega}{Q(\omega_0^2 - \omega^2)}\right) \tag{8.6}$$

The first term in Eq. (8.5) expresses a steady solution and the second one expresses a transient solution. When the oscillation frequency $f\,(=\omega/2\pi)$ is approximately the same with the resonant frequency f_0, Eq. (8.5) can be simplified as follows:

$$z(t) = \frac{\omega^2 A_d}{\sqrt{(\omega_0^2 - \omega^2)^2 + \left(\dfrac{\omega_0 \omega}{Q}\right)^2}} \left(1 - e^{-\frac{\omega_0}{2Q}t}\right)\cos\left(\omega t - \frac{\pi}{2}\right)$$
$$= A_0\left(1 - e^{-\frac{\omega_0}{2Q}t}\right)\cos\left(\omega t - \frac{\pi}{2}\right) \tag{8.7}$$

A_0 is defined as the oscillation amplitude of free oscillation. Note that $A_0 \approx QA_d$ when $\omega \approx \omega_0$. Figure 8.5 shows the transient response of Eq. (8.7). Because of the
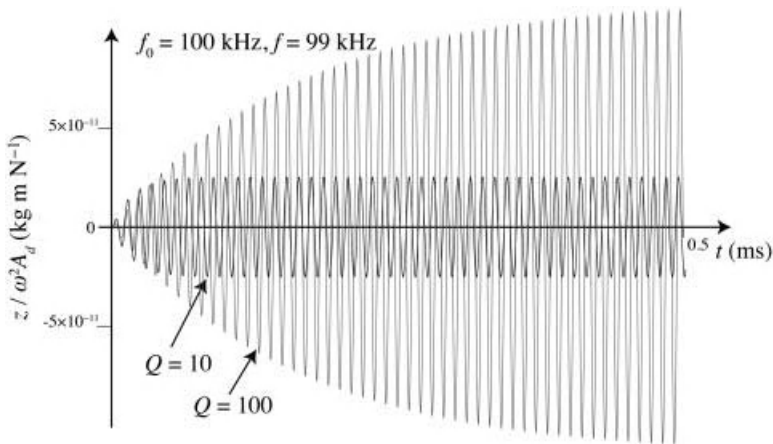
Figure 8.5 Transient response of cantilever oscillation.

transient term, it takes some time for the steady solution to be achieved, which strongly depends on Q.

Based on the above-mentioned knowledge, we derive the tapping force between the probe and the sample. Assume that the amplitude is reduced from A_0 to A due to the intermittent contact. The energy difference ΔE between these two states can be written as

$$\Delta E = \frac{1}{2} k (A_0^2 - A^2) \tag{8.8}$$

Here, imagine the situation when the sample is suddenly taken away. Then, the cantilever oscillation shows the transient response similar to Figure 8.5 because the energy injection from the bimorph is continuing. Note that the oscillation change is not from 0 but from A. Assume that the amplitude changes from A to $A + \Delta A$ during a single cycle; the energy increment at each cycle becomes

$$\frac{1}{2} k (A + \Delta A)^2 - \frac{1}{2} k A^2 \approx k A \Delta A \tag{8.9}$$

Since ΔE is compensated during Q oscillations, ΔA is calculated using Eqs. (8.8) and (8.9) as follows:

$$\Delta A = \frac{A_0^2 - A^2}{2QA} \tag{8.10}$$

In the practical situation, the sample is *not* taken away and therefore the oscillation amplitude is kept constant at A. This means that the amplitude increment ΔA decays at each cycle. Thus, the force acting on the system is written as

$$F = k \Delta A \tag{8.11}$$

For example, $\Delta A = 0.0042\,\text{nm}$ is obtained for $A_0 = 20\,\text{nm}$, $A = 18\,\text{nm}$, $k = 40\,\text{N/m}$, $Q = 500$. The equivalent force becomes 0.17 nN. It is possible to realize this force level using the contact-mode cantilever with the spring constant of 0.1 N/m. The deflection of 1.7 nm is merely required. The value is not impossible but normally difficult since there are contributions from frictional or capillary effects. It is worth keeping Eq. (8.11) in mind in performing the actual experiment. If you want to reduce tapping force, A must be approached to A_0 as much as possible. However, the feedback control becomes unstable in this case. Another method to decrease tapping force is achieved by bringing Q value higher, while the response speed becomes slower in this case. In general, sensitivity and response time are inconsistent with each other. Q becomes considerably small when the AFM instrument is placed in the liquid medium due to its higher viscosity. As a result, the tapping force in liquid becomes quite large.

8.1.3
Phase and Energy Dissipation

As shown in Eq. (8.7), the phase shift between cantilever oscillation and forced oscillation is 90° if the oscillation frequency is near the resonant frequency of the
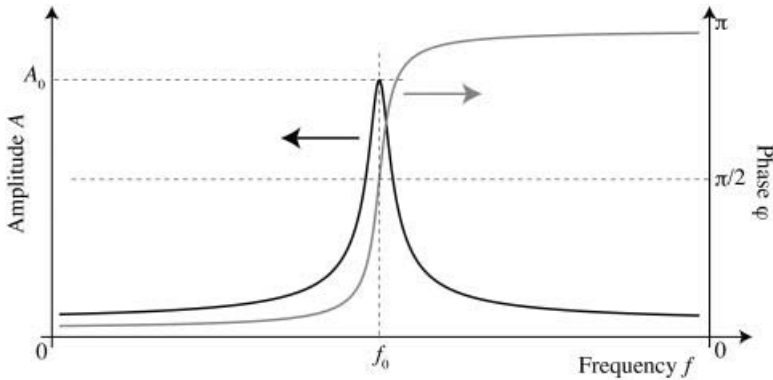
Figure 8.6 Frequency dependences of the oscillation amplitude and phase.

cantilever. The further understanding of this relationship is obtained by visualizing Eqs. (8.5) and (8.6) as shown in Figure 8.6. Although the existence of a real sample is not explicitly treated in Section 8.1.2, the interaction between the probe and the sample's surface makes the oscillation state much more complicated. It is natural that the phase shift is also affected by this interaction. The commercial instruments offer the so-called phase contrast imaging capability, which is based on the imaging of this quantity. Since the fact that the contrast in phase is usually clearer than that of topography, the imaging method has been widely used among users. However, the interpretation of phase contrast is not simple and sometimes misleads wrong conclusions. This is partly owing to the past advertisement by instrument vendors that phase contrast can reveal materials' stiffness difference. Here, we would like to look at what "phase" is. In short, "phase" expresses the energy dissipation between the probe and the sample.

In Eq. (8.2), the energy balance is attained between the energy injection from forced oscillation and the energy dissipation due to viscous force for the free oscillation condition. Here, the viscous force originated from the internal friction within the cantilever and the viscous interaction between the cantilever and the medium. As described in Eq. (8.4), these contributions have already been included in the Q-value. Such a simplification allows us to further assume that the interaction between the probe and the sample can also be incorporated into the equation if this interaction is simply regarded as viscous interaction even when the probe is touching to the sample's surface. This idea offers the energy dissipation image, which is much more sophisticated interpretation of "phase contrast." [3–5]

Although a precise derivation must be referred to [4, 5], we derive the formula of energy dissipation here. We assume that the following energy balance is valid even when the probe is interacting with the sample's surface:

$$E_{\text{ext}} = E_{\text{tip}} + E_{\text{dis}} \tag{8.12}$$

where E_{ext} is the work done by the external force per cycle. E_{probe} and E_{dis} are the energy dissipated by the viscous interaction and by interaction with the sample, respectively. E_{ext} is calculated as follows:

$$E_{ext} = \int_0^T F_{ext} \frac{dz}{dt} dt = \frac{\pi k}{Q} A_0 A \sin \varphi \tag{8.13}$$

During this derivation, we should note that $z(t) = A\cos(\omega t - \varphi)$. Similarly,

$$E_{probe} = \int_0^T \gamma \left(\frac{dz}{dt}\right)^2 dt = \frac{\pi k}{Q} \frac{\omega}{\omega_0} A^2 \tag{8.14}$$

Using Eqs. (8.12)–(8.14), we obtain

$$E_{dis} = \frac{\pi k}{Q} A_0 A \left(\sin \varphi - \frac{\omega}{\omega_0} \frac{A}{A_0} \right) \tag{8.15}$$

If we correct not only the phase image but also the amplitude image in tapping-mode operation, it becomes possible to convert these images into the energy dissipation image. It is worth mentioning that Eq. (8.15) must be regarded as the first approximation. Firstly, the cantilever under transient conditions is treated as that under steady conditions. Secondly, the equation is no more valid if the oscillation amplitude is not near the resonant frequency. The more essential problem is whether the phase change is simply expressed by viscous interaction. If there is adhesive interaction between the probe and the sample, adhesive hysteresis (corresponding to the difference in jump-in and jump-out force in static contact mode as discussed in Section 8.1.1) plays an important role in phase change.

8.2
Elasticity Measured by AFM

8.2.1
Sample Deformation

As mentioned above, the direct touch of the probe to the sample surface is inevitable in AFM. If this effect is negligible, an obtained image expresses a true surface topography. However, soft materials such as polymers and biomaterials are easily deformed even by a very weak force. For example, a 0.1–10 nN force exerted by a 10 nm diameter punch probe results in a stress of 1.3–130 MPa. Plastic materials having a GPa-order Young's modulus might not be deformed significantly by this range of force, whereas rubbery materials with a MPa-order modulus and gels with a kPa-order modulus undergo substantial deformation. The sharper the probe tip, the more serious is this effect.

Does this effect become a disadvantage or an advantage? This question can lead to different answers depending on the researcher's viewpoint. In this chapter, our

answer is an advantage; we can measure the surface Young's modulus because of this effect. Instrumentation to obtain a measure of "hardness" by pushing some kind of probe onto a surface began their history with the hardness indenter tester and the main stream of recent progress is seen in the nanoindenter system [6]. Although the lateral resolution achieved is far below that of the AFM, there are several advantages of the indenter compared to the AFM. Among them, it is the most essential one that the force-detection system is independent of the displacement-detection system. In contrast, AFM uses the deflection of the cantilever for the force detection. The sample deformation is also measured from the conversion of this quantity, resulting in a fundamental difficulty in analyzing the mechanical properties of materials. Probes coated with diamond-like carbon (DLC) are now commercially available, but there remain several problems such as durability and controllability of the probe shape. However, a two-dimensional high-resolution mapping capability is easily realized by AFM-based indentation. Like body palpation by medical doctors or masseurs, we can now perform nanopalpation with the AFM sharp probe enabling measurement of surface elasticity.

8.2.2
Contact Mechanics

It is necessary to classify materials into ideal elastic body, ideal plastic body, and elastoplastic body, when the contact between two bodies is discussed. In the case of an indenter system, a plastic contact is regarded as an ideal condition because of its historical background. Nowadays, it can also treat an elastoplastic contact [7]. On the other hand, when AFM is used to perform indentation without losing the capability of two-dimensional mapping, nondestructive measurement is ideal. Thus, let us start the discussion of an elastic contact. If the probe tip is mathematically sharp, the contact region feels strong stress concentration. Then, the plastic deformation occurs from the instant of the contact. However, this situation is never observed in the realistic measurement because the probe tip is not perfectly sharp. AFM probes are definitely sharper than those of indenters, while their tip can be regarded as round shape. Therefore, indentation measurement in the elastic deformation region below the yield stress becomes possible. The indenter uses a load cell to detect force. The current sensitivity of the load cell ranges from μN to mN. AFM has the advantage to detect forces below nN, even reaches to the pN range. This makes it possible to perform elastic measurement.

8.2.3
Sneddon's Elastic Contact

We describe the elastic contact between two bodies developed by Sneddon [8]. The probe with arbitrary shape $z = f(r)$ (solid line) is considered as shown in Figure 8.7. The restrictions for the function are $f(0) = 0$ and axisymmetric, where r is the distance from the symmetry axis. Sneddon solved the mathematical formula for the normal stress $\sigma(r)$ and normal sample displacement $u_z(r)$ when the probe is
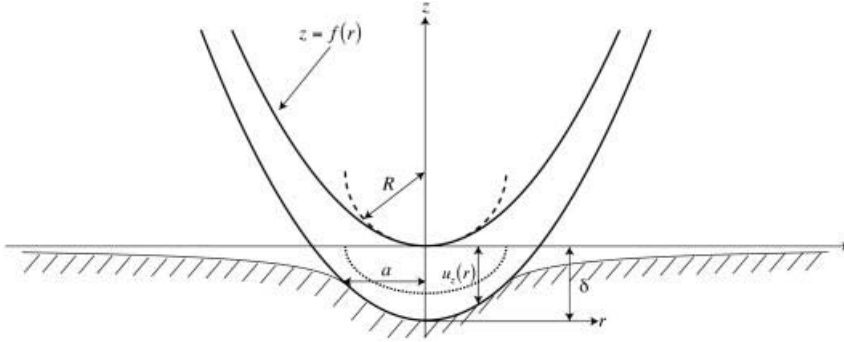
Figure 8.7 Coordinate system to describe elastic contact.

indented by the distance of δ. As for the stress, he assumed that there is no frictional effect at the contact interface. Thus, $\sigma_{rz}(r, 0) = 0$, where the second zero in the parentheses means the contact interface. He only treated $\sigma_{zz}(r, 0)$. For the simplicity, $\sigma_z(r)$ denotes $\sigma_{zz}(r, 0)$. We only introduce his results:

$$u_z(r) = \delta - f(r) \quad (r \le a) \tag{8.16}$$

$$u_z(r) = \int_0^1 \frac{\chi(t)}{\sqrt{\dfrac{r^2}{a^2} - t^2}} dt \quad (r > a) \tag{8.17}$$

$$\sigma_z(r) = -\frac{E}{2a(1 - v^2)}\left[\frac{\chi(1)}{\sqrt{1 - \dfrac{r^2}{a^2}}} - \int_{r/a}^1 \frac{\chi'(t)}{\sqrt{t^2 - \dfrac{r^2}{a^2}}} dt \right] \quad (r \le a) \tag{8.18}$$

$$\sigma_z(r) = 0 \quad (r > a) \tag{8.19}$$

where a is the radius of contact line. We adopt the variable transformation $x = r/a$ hereafter. E and v is the sample's Young's modulus and Poisson's ratio, respectively. $\chi(t)$ is defined as follows:

$$\chi(t) = \frac{2}{\pi}\left(\delta - t\int_0^t \frac{f'(x)}{\sqrt{t^2 - x^2}} dx \right) \tag{8.20}$$

Equations (8.16) and (8.19) are obvious. Thus, the main subject is solving Eqs. (8.17) and (8.18) from Eq. (8.20). Furthermore, by assuming $t = 1$ in Eq. (8.20), the sample deformation on the symmetry axis is written as

$$\delta = \int_0^1 \frac{f'(x)}{\sqrt{1 - x^2}} dx + \frac{\pi}{2}\chi(1) \tag{8.21}$$

Sneddon assumed $\chi(1) = 0$ to avoid the divergence of Eq. (8.18) at $x = 1$. This assumption brought several arguments during the development of later coming theories, while they are beyond our scope in this chapter [9].

The total load is obtained by integrating Eq. (8.18) as follows:

$$F = -2\pi \int_0^a r\sigma_z(r)\mathrm{d}r = -2\pi a^2 \int_0^1 x\sigma_z(x)\mathrm{d}x \tag{8.22}$$

By substituting Eq. (8.18) into Eq. (8.22),

$$F = -\frac{\pi a E}{1-v^2} \int_0^1 x \int_x^1 \frac{\chi'(t)}{\sqrt{t^2 - x^2}} \mathrm{d}t\mathrm{d}x \tag{8.23}$$

By using repeated integrals and integration by parts:

$$
\begin{aligned}
F &= \frac{\pi a E}{1-v^2} \int_0^1 \chi'(t) \int_0^t \frac{x}{\sqrt{t^2 - x^2}} \mathrm{d}x\mathrm{d}t = -\frac{\pi a E}{1-v^2} \int_0^1 t\chi'(t)\mathrm{d}t \\
&= -\frac{\pi a E}{1-v^2} \left\{ [t\chi(t)]_0^1 - \int_0^1 \chi(t)\mathrm{d}t \right\} = \frac{\pi a E}{1-v^2} \int_0^1 \chi(t)\mathrm{d}t
\end{aligned}
\tag{8.24}
$$

By substituting Eq. (8.18) into Eq. (8.24)

$$F = \frac{\pi a E}{1-v^2} \left[\delta - \int_0^1 \frac{xf(x)}{\sqrt{1-x^2}} \mathrm{d}x \right] \tag{8.25}$$

By substituting Eq. (8.21) into Eq. (8.25), we obtain the final formula,

$$F = \frac{\pi a E}{1-v^2} \int_0^1 \frac{x^2 f'(x)}{\sqrt{1-x^2}} \mathrm{d}x \tag{8.26}$$

Equations (8.21) and (8.26) are Sneddon's standard equations.

As an example, consider the conical probe. If the half-angle of the cone is regarded as Ψ,

$$f(x) = \frac{a}{\tan\Psi} x, \quad f'(x) = \frac{a}{\tan\Psi} \tag{8.27}$$

By substituting these equations into Eqs. (8.21) and (8.26),

$$F = \frac{2E\tan\Psi}{\pi(1-v^2)} \delta^2 \tag{8.28}$$

is obtained. The shape function for the spherical probe (dashed line in Figure 8.7) is written as

$$f(x) = R - \sqrt{R - a^2 x^2} \tag{8.29}$$

where R expresses the radius of the sphere. If we adopt the parabolic approximation ($R \gg a$),

$$f(x) = R - R\left(1 - \frac{a^2}{R^2}x^2\right)^{1/2} \cong R - R\left(1 - \frac{a^2}{2R^2}x^2\right) = \frac{a^2}{2R}x^2 \tag{8.30}$$

By substituting these equations into Eqs. (8.21) and (8.26),

$$F = \frac{4E\sqrt{R}}{3(1-v^2)}\delta^{\frac{3}{2}} \tag{8.31}$$

is obtained. Equations (8.28) and (8.31) are well known as the Hertzian contact solution [10, 11].

8.2.4
Nanopalpation Realized by AFM

Now, we will describe how AFM is used to perform nanoindentation, in other words, nanopalpation. We use the force–distance curve explained in Section 8.1.1 and the contact mechanics to analyze the curve [12]. Note that Sneddon or Hertzian contact mechanics cannot treat adhesive contact. Thus, these theories can only be applied when the adhesive interaction is negligible. Measurements under aqueous conditions are effective for polymeric materials if the materials have low water absorbability. A cantilever with a large spring constant also hides weak van der Waals forces.

Figure 8.8b is the schematic description of the force–distance curves for hard (dashed) and soft (solid) materials. Note that they are redraws of Figure 8.1 with no adhesive interaction. As shown in Figure 8.8a, the AFM cantilever and probe are treated as a spring with a spring constant of k and a sphere with a radius of curvature, R, respectively. The force, F, is expressed by Hooke's law,

$$F = k\Delta \tag{8.32}$$

Since recent developments in this field have included several reports on direct measurement of k and R [13, 14], it is expected to realize improved quantitative accuracy. If the sample surface is sufficiently rigid, the cantilever deflection, Δ, always coincides with the displacement, $(z - z_c)$, of the piezoelectric scanner measured from a contact point $(z_c, 0)$ as depicted in the dashed line in Figure 8.8b. However, if the sample surface undergoes elastic deformation as in the case of the solid line, we can estimate the sample deformation, δ, as follows:

$$\delta = (z - z_c) - \Delta \tag{8.33}$$

The δ–F plot, shown in Figure 8.8c, derived from the z–Δ plot is now fitted with the theory of Sneddon contact mechanics (Eq. (8.28) or Eq. (8.31)) to provide an estimation of Young's modulus. Note that the power exponents for δ are different depending on the probe shape.
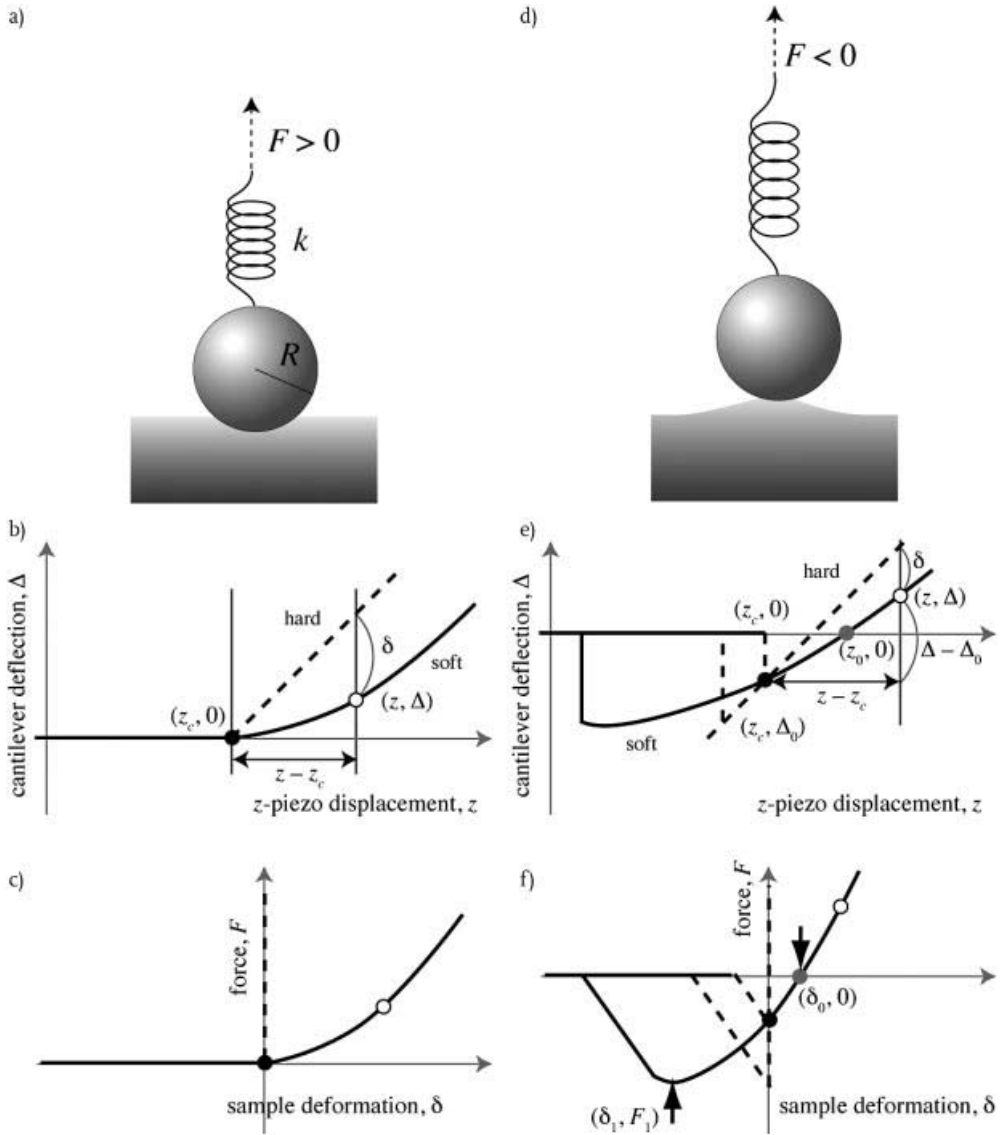
Figure 8.8 Elastic contact analysis for the force–distance curve.

8.2.5
Adhesive Contact

If the adhesive interaction is no longer negligible, we need to use the theory developed by Johnson, Kendall, and Roberts (JKR model) [15]. Their formula

can be correlated with "fracture mechanics" in considering $\chi(t)$ in Section 8.2.3, while we omit this argument in this chapter [16]. Figure 8.8d shows a schematic picture of adhesive contact during the unloading process. Figure 8.8e is the schematic force–distance curve for hard (dashed) and soft (solid) materials. Firstly, it is observed that an abrupt change in cantilever deflection occurs from the point $(z_c, 0)$ to the contact point (z_c, Δ_0) (jump-in explained in Section 8.1.1). After that, the force increases, crossing the horizontal axis $(z_0, 0)$ in Figure 8.8e, where the apparent force exerted on the cantilever becomes zero due to the balance between the elastic repulsive force caused by sample deformation and the adhesive attractive force, F_{adh} (balance point). During the unloading process, a much larger adhesive force is observed beyond the original contact point. The sample surface is raised up during this time (see Figure 8.8d). Finally, the maximum adhesive force is realized (maximum adhesion point) at (z_1, Δ_1) in Figure 8.8e, succeeded by a sudden decrease in the contact radius and jump-out of the cantilever. The sample deformation is calculated by the formula

$$\delta = (z - z_c) - (\Delta - \Delta_0) \quad (\Delta_0 < 0) \tag{8.34}$$

Using Eq. (8.34), the z–Δ plot in Figure 8.8e is converted into the δ–F plot shown in Figure 8.8f. The JKR contact is described as follows [15]:

$$F = \frac{K}{R}a^3 - 3w\pi R - \sqrt{6w\pi RF + (3w\pi R)^2} \tag{8.35}$$

$$\delta = \frac{a^2}{3R} + \frac{2F}{3aK} \tag{8.36}$$

$$K = \frac{4}{3}\frac{E}{1 - \nu^2} \tag{8.37}$$

where a, w, and K are the contact radius, the adhesive energy (or the work of adhesion), and the elastic coefficient, respectively.

Since Eq. (8.35) is the cubic equation of a, a closed-form expression similar to Eq. (8.31) cannot be deduced from Eqs. (8.35) and (8.36). Accordingly, curve-fitting analysis as in the case of the Sneddon contact is not usually possible. Thus, as an alternative, the so-called two-point method has been used, which was introduced by Walker et al. [17]. This method involves the use of two special points from the δ–F plot to calculate Young's modulus and adhesive energy algebraically. These points are the above-explained two points: the balance point; $(z_0, 0)$ in Figure 8.8e or $(\delta_0, 0)$ in Figure 8.8f, and the maximum adhesion point; (z_1, Δ_1) in Figure 8.8e or (δ_1, F_1) in Figure 8.8f. The maximum adhesive force, F_1, is calculated from Eq. (8.35) subject to the condition that the formula inside square root term becomes zero:

$$6w\pi RF_1 + (3w\pi R)^2 = 0$$
$$\therefore F_1 = -\frac{3}{2}\pi Rw \tag{8.38}$$

A simple transposition results in an expression for the adhesive energy,

$$w = -\frac{2F_1}{3\pi R} \tag{8.39}$$

The substitution of Eq. (8.39) for Eqs. (8.35) and (8.36), followed by the elimination of a from these equations, results in an expression of δ_1 as follows:

$$\delta_1 = -\frac{1}{3}\left(\frac{F_1^2}{K^2 R}\right)^{1/3} \tag{8.40}$$

Then, δ_0 can be similarly calculated, whereas an additional condition in this case is $F = 0$:

$$\delta_0 = \frac{1}{3}\left(\frac{16F_1^2}{K^2 R}\right)^{1/3} \tag{8.41}$$

These formulas finally lead to the following expression for the elastic coefficient:

$$K = \left(\frac{1+16^{1/3}}{3}\right)^{3/2} \frac{F_1}{\sqrt{R(\delta_0 - \delta_1)^3}} \tag{8.42}$$

8.2.6
Nanomechanical Mapping

To map the local mechanical properties of soft materials, force–volume (FV) measurement is the most appropriate method. In this mode, force–distance curve data are recorded until a specified cantilever deflection value (trigger set-point), Δ_{trig}, is attained for 128×128 points over a two-dimensional surface. At the same time, z-displacement values, z_{trig}, corresponding to the trigger set-point deflection are recorded to build an apparent topographic image. The topographic image taken in this mode is basically the same as that obtained by the conventional contact mode if the contact force set-point and the trigger set-point are identical. If all the points over the surface are rigid enough, the set of recorded displacements, z_{trig}, represents the topographic image (true height) of the sample. However, if the surface deforms as discussed earlier, it is no longer valid to regard the obtained data as the true topographic information. However, since we have a force–distance curve for each point, we can estimate the maximum sample deformation value for each point, referring to Eq. (8.34),

$$\delta_{\max} = (z_{\text{trig}} - z_c) - (\Delta_{\text{trig}} - \Delta_0) \quad (\Delta_0 < 0) \tag{8.43}$$

Consequently, two-dimensional arrays of sample deformation values can be regarded as the sample deformation image. The force–distance curve analyses for 16 384 data yield Young's modulus distribution and adhesive energy distribution images at the same time and the same location [18]. We now have apparent height (z_{trig}) and sample deformation ($\delta_{\max}$) images taken at the same time and Δ_{trig} is the preset value and therefore constant for all of the force–distance curves. Then, the

appropriate determination is performed for the contact point (the array of $[z_c, \Delta_0]$); this realizes the reconstruction of the "true" surface topography, free from sample deformation [19, 20].

8.3
Example Studies

8.3.1
Carbon Nanotubes-Reinforced Elastomer Nanocomposites [21]

Recent studies have shown that carbon nanotubes (CNTs)-filled elastomer nano-composites exhibit greatly increased electrical, mechanical, and thermal properties. This effect is usually attributed to the nanotube network structure [22–25], which is readily detected by electrical and rheological property measurements. In a well-dispersed composite, the large aspect ratio of the CNTs and their short-range attraction lead to the formation of a solid-like material with the network structure. This network superstructure, along with the ability to transfer stress from the continuous polymer matrix to the CNTs network, is responsible for the enhancement of the composites mechanical properties [25]. However, the information obtained by electrical and rheological measurements is usually qualitative and averaged over the sample volume, and therefore they lack some spatial information. In this section, we employed the nanomechanical mapping technique, by which mechanical properties as well as its distribution can be visualized at a micro or nanoscale.

Natural rubber (NR) with multiwalled carbon nanotubes (MWCNTs) loadings of 1, 3, 5, 10, 20, 60 phr was prepared using a 6-inch two-roll mill and named NR1, NR3, NR5, NR10, NR20, and NR60, respectively. The resulted compounds were sheeted into slabs and cured by compression molding. The sheet sample was then cut by a Leica EM FC6 ultramicrotome to obtain a flat surface. All AFM measurements were performed using a Veeco AFM multimode series with a NanoScope V controller under ambient conditions. The cantilever used for nanomechanical mapping, that is, force–distance curve measurements, is made of Si_3N_4 (Veeco-probes) with the spring constant of 0.38 N/m (nominal). An actual spring constant of 0.475 ± 0.018 N/m was measured by the thermal tune method. Force–distance curves were collected over randomly selected areas at a resolution of 128 × 128 pixels.

It is well known that the homogeneous dispersion of the filler and the strong interfacial interaction between the filler and the polymer matrix can effectively improve the mechanical, electrical, and thermal performances of the prepared nanocomposites. We first present several typical transmission electron microscope (TEM) and AFM tapping-mode images of MWCNTs/NR nanocomposites with different CNT loadings. As shown in Figures 8.9 and 8.10, the CNTs are well dispersed in the NR matrix, especially for the low CNT loading (≤20 phr). At very high loading content (60 phr), the CNTs show relatively homogeneous dispersion.
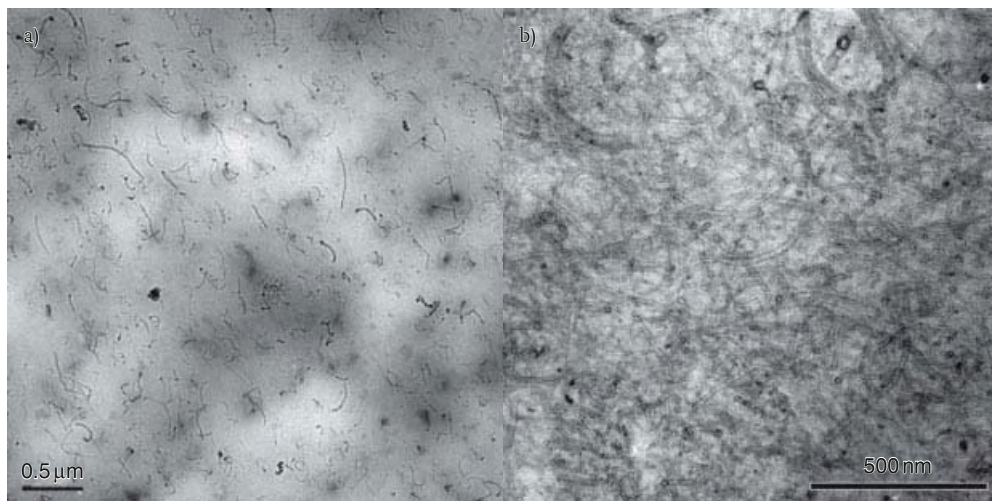
Figure 8.9 TEM images of NR3 (a) and NR60 (b) nanocomposites.

The fair dispersion of the pristine CNTs can be attributed to the high shear stress exerted during mixing. The compound gets very distorted by the large shearing force when it passes the roll. However, the rubber's recovery force occurs immediately after passing through the roll. By this kneading of repeated distortion and recovery, it is thought that the CNTs are taken from the cohesive group, thread by thread, and then are homogenously dispersed.

Figure 8.11 shows Young's modulus (a) and adhesive energy (b) maps obtained with nanomechanical mapping. Young's modulus and adhesive energy maps qualitatively resemble TEM and tapping-mode images (Figures 8.9 and 8.10). The fiber-like structure in the adhesive energy map represents components having lower adhesive energy but higher elastic modulus. Such structures are possibly assigned to the CNTs. The light green area shows higher adhesive energy but lower elastic modulus. Such an area is possibly assigned to the NR matrix. These results indicate that the nanomechanical mapping technique is successful for identifying and characterizing heterogeneity in nanocomposites containing various components. By comparing the scale of adhesive energy and Young's modulus maps of different samples, as expected, with the increase of the CNTs loading content, the adhesive energy gradually decreases and Young's modulus increase. As a comparison, Figure 8.12 shows Young's modulus histogram of the NR20 sample and Young's modulus peak values of the nanocomposites, indicating that the mechanical strength is greatly increased with the CNT loading.

In order to quantitatively measure the nanomechanical properties, the high-resolution maps with 400 nm scan size were investigated. As an example, Figure 8.13 shows Young's modulus and adhesive energy maps of the NR20 sample. Each

a)

2 µm

b)

2 µm

c)

2 µm
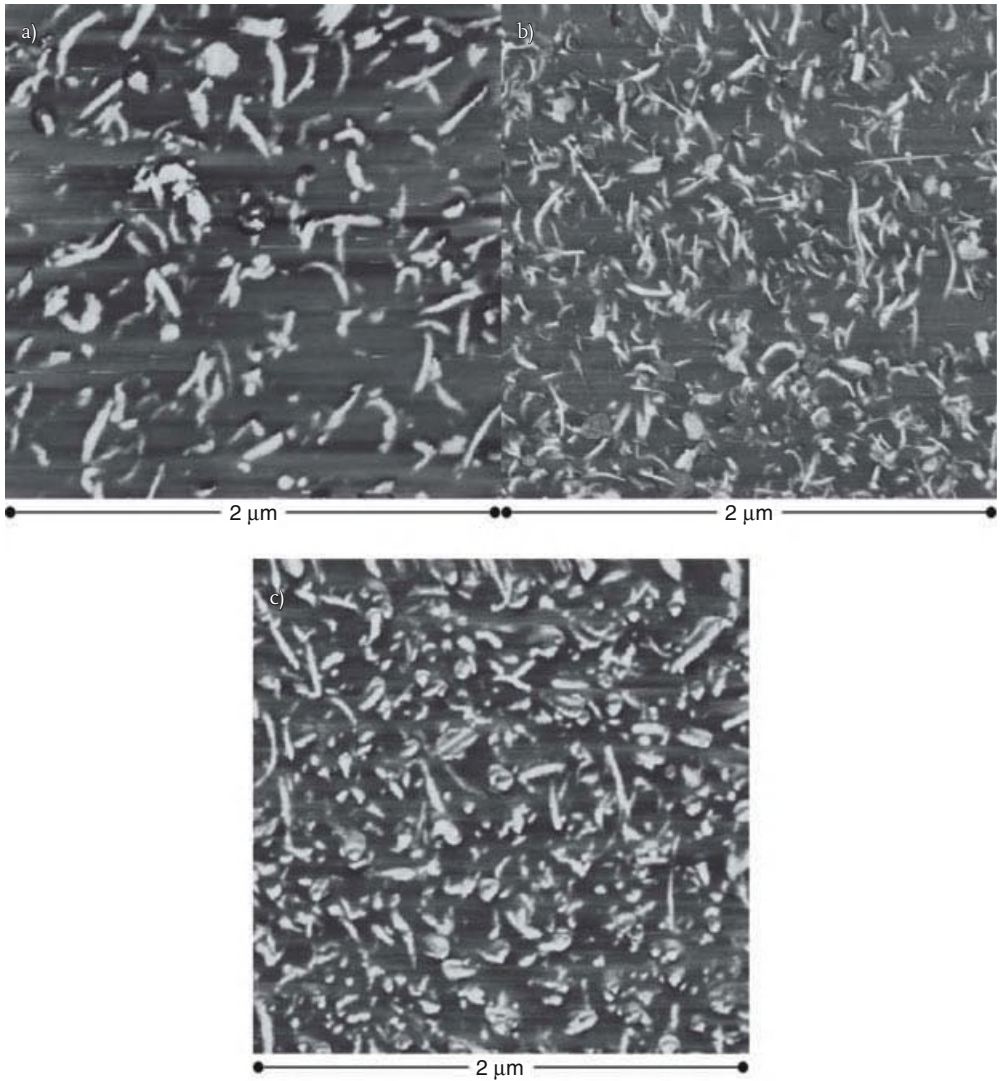
Figure 8.10 AFM tapping-mode phase images of NR5 (a), NR20 (b), and NR60 (c) nanocomposites.

of the images can be divided into three typical regions: three representative points are indicated by black circles and the corresponding force–deformation curves are shown in Figure 8.14. The curve fitting against the JKR contact is also superimposed in each case. The typical region indicated by the lowest circle on the fiber-like structure has Young's modulus of $148.6 \pm 13.6\,MPa$ (Figure 8.14a). Although this value is far lower than CNT's Young's modulus, we attribute this region as a
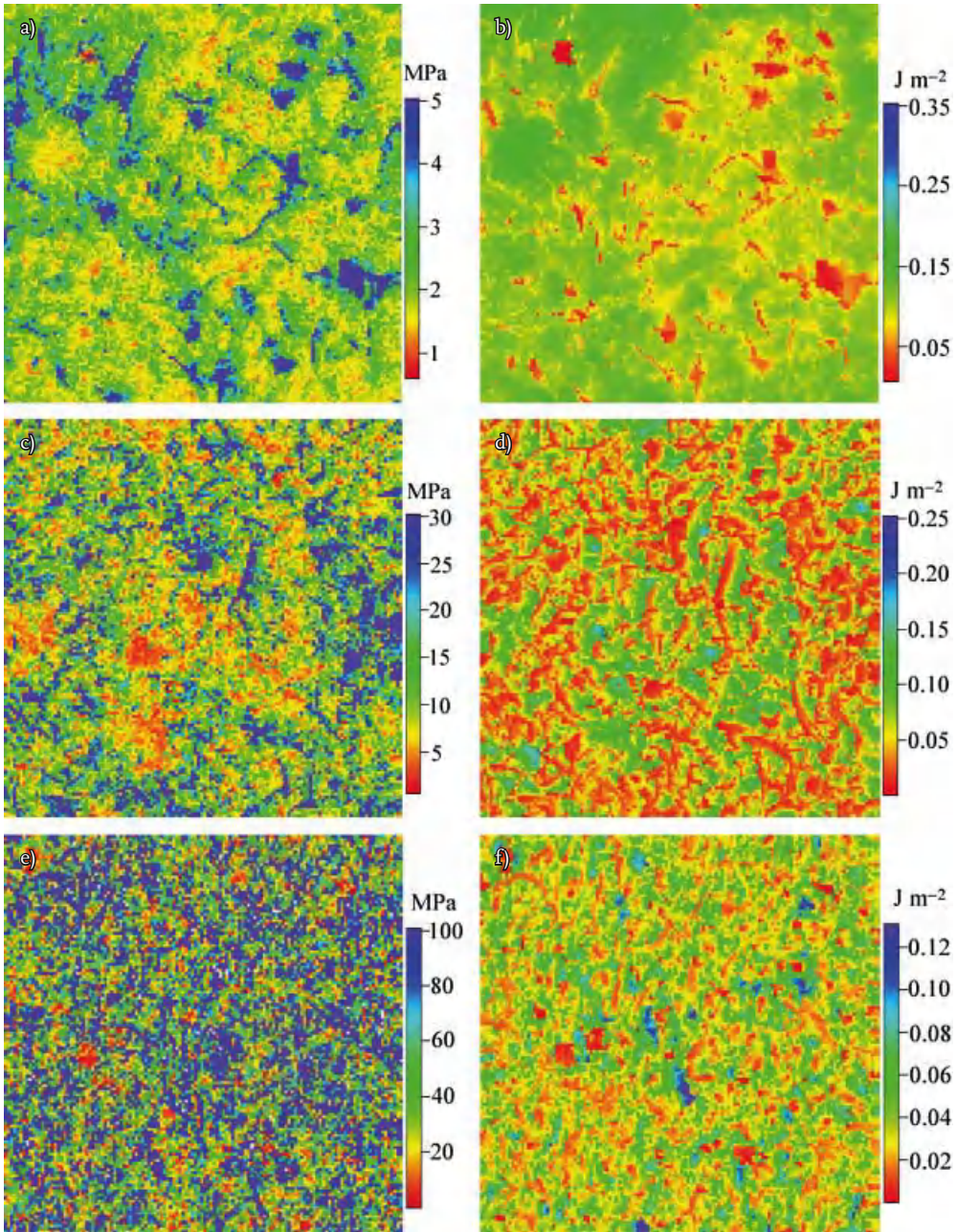
Figure 8.11 Nanomechanical mapping Young's modulus and adhesive energy maps of different NR nanocomposites. (a, b) NR5, (c, d) NR20, and (e, f) NR60. The scan size is 2.0 μm.

a)

b)
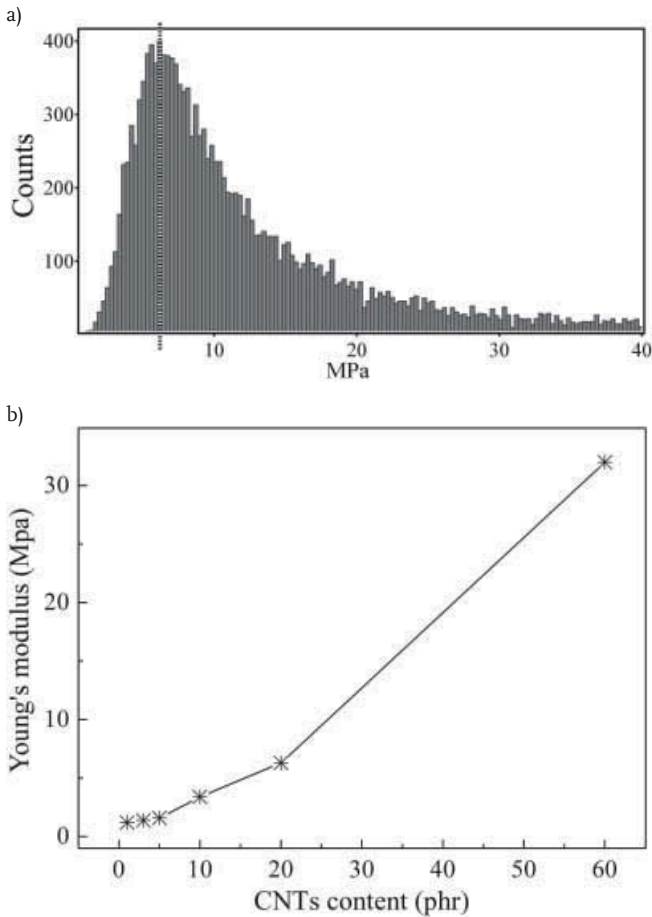
Figure 8.12 Young's modulus distribution of NR20 and Young's modulus peak values of the nanocomposites.

stiff CNT region. One possible reason for the low Young's modulus of CNTs is that the rubber surrounding CNTs is deformed. In this case, it is very difficult to know the real mechanical properties of stiff materials floating on a soft material. The typical region indicated by the highest circle shows higher adhesive energy but lower Young's modulus. Its corresponding value of Young's modulus is 9.2 ± 6.5 MPa (Figure 8.14c), a typical value for a NR bulk. Therefore, the nano-mechanical mapping results enabled us to recognize the CNTs region and NR matrix clearly. The most important is that, in addition to CNTs and NR regions, we also find another region in all samples. As marked by the middle circle in Figure 8.13, the area around CNTs shows Young' modulus of 24.6 ± 5.5 MPa (Figure 8.14b). That region is stiffer than the NR region but softer than the CNT
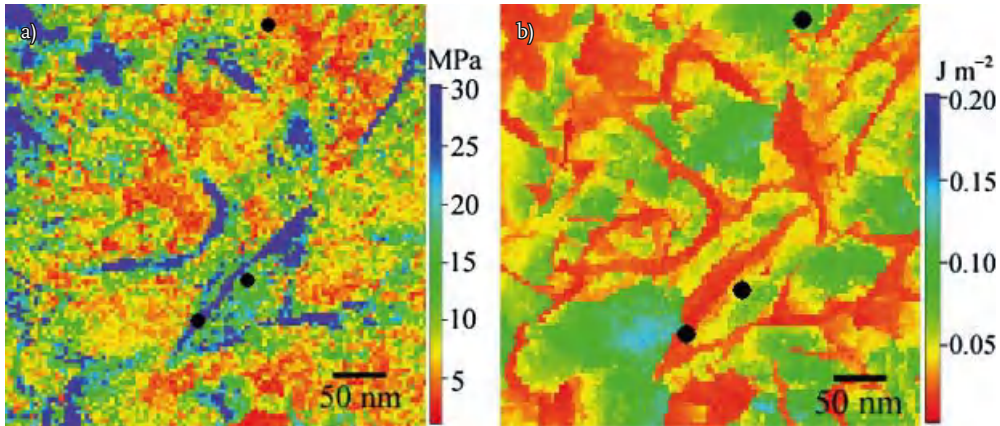
Figure 8.13 Magnified Young's modulus (a) and adhesive map (b) of the NR20 sample.
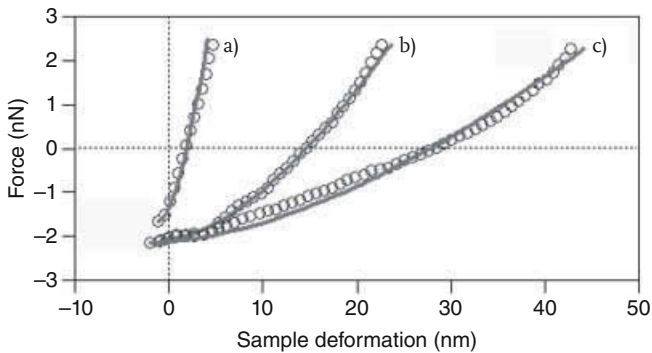
Figure 8.14 Force–deformation curves of local points indicated by open circles in Figure. 8.13. The curve fitting against the JKR contact was superimposed on each curve. (a) MWCNT region (lower circle), 148.6 ± 13.6 MPa, (b) interfacial region (middle circle), 24.6 ± 5.5 MPa, and (c) NR region (upper circle), 9.2 ± 6.5 MPa.

region. However, its adhesive energy is lower than that in the NR region but higher than that in the CNTs region. It is impossible to explain the results simply from the consideration of constituents. We call this intermediate modulus and adhesive energy region the mechanical interfacial region. By pulling out a single CNT from the poly(ethylene-butene) film, Barber also observed that the regions had anomalously high shear strength [26]. In MWCNTs/polycarbonate composites, both Ding [27] and Pötschke [28] observed thick (tens of nm) layers of polymer coating CNTs. This indicates that a layer with high shear strength is formed. For carbon black/rubber composites, bound rubber is well known as an interfacial rubber phase bound to carbon blacks [29–31], and the existence of the bound rubber phase has

been visualized by our nanomechanical mapping technique [32]. In order to examine the existence of interfacial rubber phases in CNTs-filled NR composites, noncured specimens were dissolved in toluene and, from a measurement of the weight of the gel that remained, 0.5 g of interfacial substance per 1 g of CNTs was obtained. This substance was thought to be the NR molecules which had been forming the interfacial regions bound to CNTs. Using the nanomechanical mapping technique, such regions were visualized with intermediate modulus and adhesive energy. Although a number of studies suggest that interactions with CNTs may result in a region around of the polymer with morphology and properties different from the bulk [22, 23, 33], the present work would be the first report to quantitatively evaluate the intermediate mechanical regions in real space.

Based on the above results, we proposed a schematic diagram of the "cellular structure" model formed in CNTs/elastomers nanocomposites illustrated in Figure 8.15. At low CNTs loading, the mechanical interfacial regions bounded to the CNTs and CNTs itself were uniformly and individually dispersed in the NR matrix (shown in Figure 8.15a). The mechanical property of such a composite is relatively low because there is no interaction among CNTs. With increasing CNTs loading, the CNTs as well as mechanical interfacial regions firmly connect to each other into a network and form three-dimensional structures. As a result, the NR matrix is considered to be divided into small units consisting of the mechanical interfacial regions and CNT itself. The three-dimensional interconnections among the mechanical interfacial regions and CNTs are named a "cellular structure." The mechanical interfacial region functions as cell walls, and the NR matrix is confined in the "cells." The CNTs/NR composites are considered to be, in a sense, an aggregation of cells. The cellular structure is formed when the loading amount of CNTs is high. The partial cellulation takes place when the loading amount of CNTs reaches 10 phr, as shown in Figure 8.15. When the loading amount of the CNTs is up to 60 phr, large numbers of cells are formed and distributed in the matrix (Figure 8.15c). The formation of the cellular structure is responsible for the greatly increased mechanical properties. It is worth mentioning that a cellular structure, formed promoted by 1-allyl-3-methyl imidazolium chloride (AMIC) ionic liquid, is also observed at low CNTs loading (~3 wt%) in rubber/MWCNT composites [34].

8.3.2
Investigation of the Reactive Polymer–Polymer Interface [35]

The achievement of compatibilization of immiscible polymer blends is a convenient and attractive way for obtaining high performance polymeric materials. For this purpose, the following two methods are usually adopted: one is the addition of the premade block or graft copolymer during the mixing process of the immiscible blends and the other is the reactive compatibilization in which the block or graft copolymer is formed *in situ* at the interfacial regions. It is believed that the preadded or *in situ* formed copolymer plays the role of an emulsifier, which promotes the compatibilization and increases the interfacial adhesion between the immiscible polymers. Therefore, the investigation of the polymer–polymer
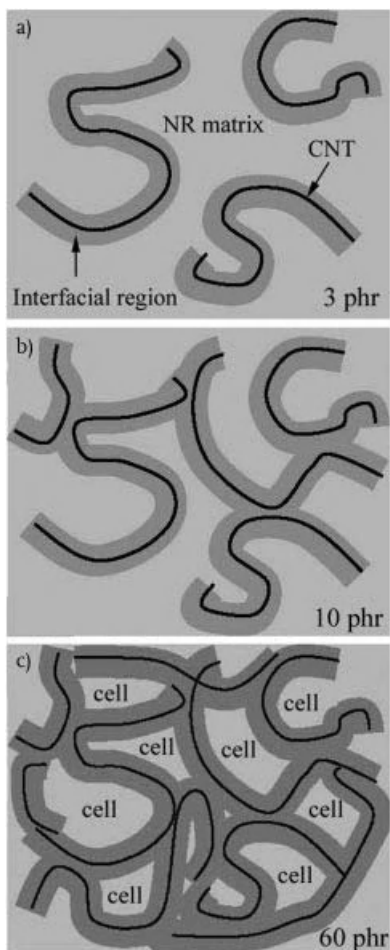
Figure 8.15 Schematic diagram of the cellulation model formed in CNTs/elastomer nanocomposites. (a) Percolation, (b) partial cellular structure, and (c) three-dimensional cellular structure.

interface in such blends has been a long-standing academic and technological challenge.

TEM and AFM are two important techniques for characterization of the interfacial morphology. With TEM, the interfacial thickness and emulsified region can be measured by examining the cross section of the interface [36–40]. With AFM, the roughened interface resulting from compatibilization can be observed by the investigation of the revealed surface after removing the top layer [38, 41, 42]. Forward recoil spectrometry (FRES) [39, 43], secondary ion mass spectrometry (SIMS) [44], and time-resolved ellipsometry [36] are other important techniques

for investigating the interfacial thickness and distribution of the copolymers at the interfacial regions. Although these techniques provide quantitative measurements at the interfacial regions, staining and deuterium labeling are usually necessary for contrast, limiting the types of model polymers available for testing. For some polymer pairs such as polyolefin/nylon and polyolefin elastomer/nylon, the double staining technique is necessary to deeply stain the interface to get better contrast [45]. Sample preparation, as well as the experiments themselves, may sometimes be difficult or inconvenient to perform. Thin film geometries do not permit the investigation of compatibilization under typical polymer processing conditions [46]. Most importantly, the above-mentioned techniques never catch mechanical information of the constituting polymers and interfacial regions.

In the present chapter, we employed a nanomechanical mapping technique to investigate the interface of the polymer blends. A reactive compatibilization blend, polyolefin elastomer (POE)/polyamide (PA6), is selected as a model system. The uncompatibilized POE/PA6 and reactive compatibilized POE-*g*-MA/PA6 blends with a composition of 80/20 (w/w) were prepared by melt compounding using a 5 mL DSM microcompounder that consists of a vertical barrel with two conical screws (screw diameter ranges from 0.43 to 1 cm, screw length = 10.75 cm). Before blending, PA6 was dried in a vacuum oven at 100 °C for 8 h and used immediately. The materials were added simultaneously and mixed at 100 rpm at a temperature of 240 °C for 10 min. The prepared blends were then cut by a Leica EM FC6 ultra-microtome at −120 °C to obtain a flat surface.

The reactive compatibilization of polyolefin/nylon blends has been widely studied to obtain high performance materials. The formation of a block or graft copolymer by coupling reaction between anhydride/amine leads to a fine morphology and increases the interfacial adhesion of such immiscible blends. Figure 8.16 presents Young's modulus map of uncompatibilized POE/PA6 and reactive
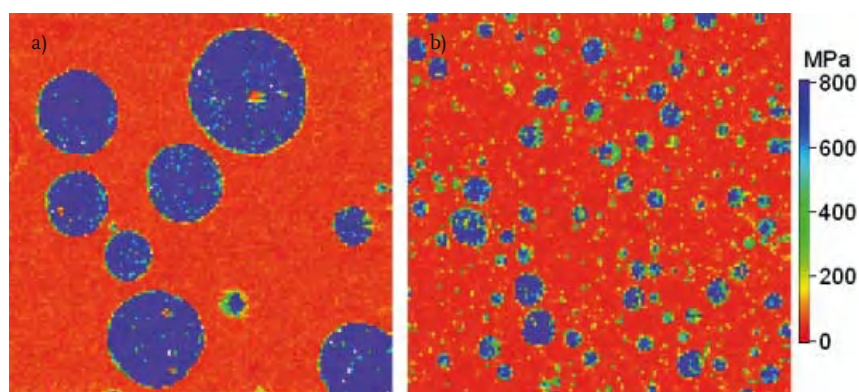
Figure 8.16 Young's modulus map of (a) uncompatibilized POE/PA6 and reactive compatibilized POE-*g*-MA/PA6 blends. Scan size is 12 μm.

compatibilized POE-*g*-MA/PA6 blends. The round and blue particles show that the higher Young's modulus are assigned to the disperse phase PA6 component, while the red areas show the lower one assigned to the POE or grafting POE component. Young's modulus calculated via force–deformation curves (Figure 8.17) are 2.9 ± 1.1 GPa for the PA6 component and 25.5 ± 10.3 MPa for the POE
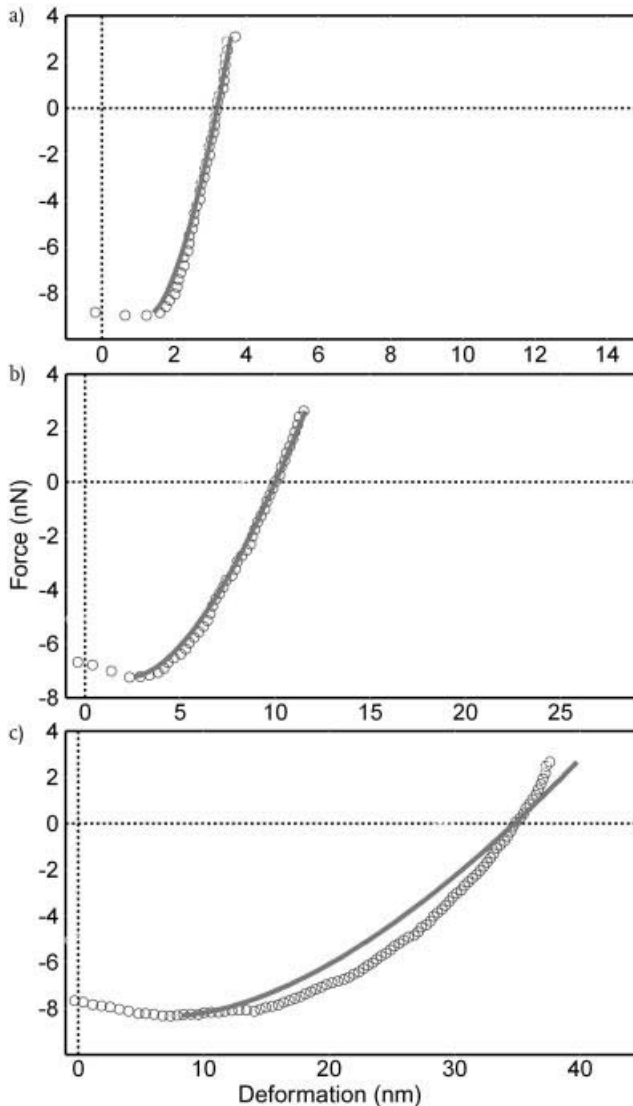
Figure 8.17 Typical force–deformation curves of (a) PA6, (b) POE, and (c) interfacial regions. The curve fitting against the JKR contact was superimposed on each curve. (a) PA6 region, 2.9 ± 1.1 GPa, (b) POE region, 25.5 ± 10.3 MPa, (c) interfacial region, 376 ± 69 MPa.

or grafting POE component. Young's modulus for both PA6 and POE components agree well with bulk modulus (PA6: 2.5 ± 0.9 GPa, POE and POE-g-MA: 23.5 ± 11.1 MPa). Thus, we may claim that the nanomechanical mapping technique is successful for identifying the composition in those blends. On the other hand, by comparing the two modulus maps, we may observe that the dispersion and particle size of the dispersed phase PA6 become homogeneous, displaying a very fine dispersion due to the reactive compatibilization. MA groups in compatibilizer react with amine groups in PA6 to form copolymers, which induces a drastic decrease in interfacial tension and suppression of coalescence between the originally immiscible polymer phases.

To obtain a more complete picture at the interfacial regions, Figure 8.18a and b shows Young's modulus map of the uncompatibilized POE/PA6 and compatibilized POE-g-MA/PA6 blends with the scan size of 500 nm. As shown, the interface between the POE and PA6 in uncompatibilized blend is smooth and flat, whereas as to the compatibilized blends, the interface becomes quite rough after the same processing. Some parts of the POE domain appear to have pinched off at the interface and moved into PA6. In Figure 8.18, we approximately localize the roughening zone with two dashed lines. The magnitude of the width of the
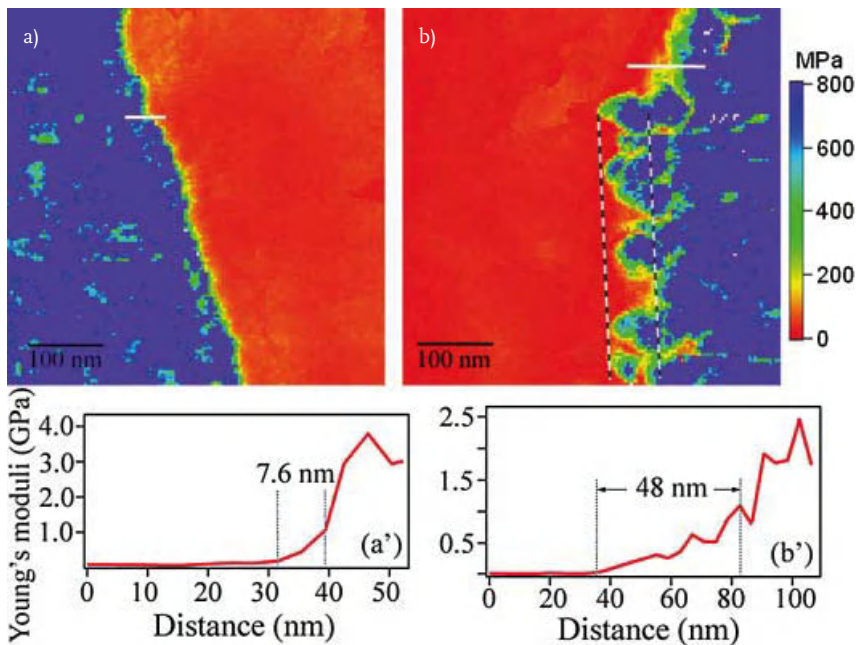
Figure 8.18 Young's modulus maps of POE/PA6 (a) and POE-g-MA/PA6 (b) blends. (c, d) Corresponding line sections across the interface indicated by the white line in Young's modulus maps.

roughening zone is about 70 nm. A line section across the interface indicated by the white line in Young's modulus map (Figure 8.18) shows that the transition between Young's modulus of the two polymer phases in uncompatibilized blend is sharp while becomes much wider in compatibilized blend (Figure 8.18c and d). We refer to the transition distance that Young's modulus increases from that of POE to that of PA6 as the interfacial width, which is ~7.6 nm for the uncompatibilized blend and, after reactive compatibilization, increases to ~48 nm. The width of the interface obtained from several line sections of different regions is 9.7 ± 3.6 nm for the uncompatibilized blend and 38.9 ± 19.7 nm for the reactive compatibilized blend. It should be noted that the occurrence of the interfacial width in the uncompatibilized blend is probably caused by the small Flory's interaction parameter, χ [41, 47], or thermal fluctuations [38, 41], but it is much less than that caused by the reactive compatibilization. It is worth mentioning that the interfacial width reported by Inoue *et al.* [36, 45] and Macosko *et al.* [38] is ~50 nm in polypropylene (PP-*g*-MA)/PA6 or polysulfone (PSU-*g*-MA)/PA6 blends and several hundreds of nm in amine-terminal polystyrene (PS-NH2)/anhydride-terminal poly(methylmethacrylate) (PMMA-anh) blends, respectively. It should also be noted that in the PA6 domain, both for the uncompatibilized and compatibilized blends as well as pure PA6 (Figure 8.19), we observe some light blue area, showing Young's modulus 400–700 MPa. The decreased modulus is probably caused by water absorption, which will greatly decrease the mechanical properties of PA6. However, besides measuring the interfacial width, the nanomechanical mapping also enables us to evaluate the interfacial strength. The measured Young's modulus in interfacial regions is about 375 ± 69 MPa and its corresponding force–deformation curve is shown in Figure 8.17b.

In conclusion, we have obtained the nanomechanical mapping on a model reactive polymer blend of POE/PA6. With this technique, we can not only measure the Young's modulus of the blend components but also map the morphology of the POE/PA6 blend based on Young's modulus of the constituting polymers.
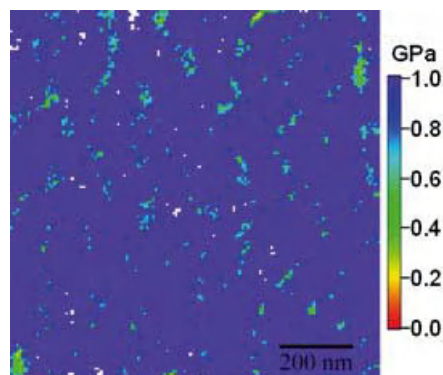
Figure 8.19 Young's modulus map of pure PA6.

Furthermore, the most important result is that the interfacial morphology, width, and mechanical property of the blends can be easily evaluated based on the Young's modulus map with several hundreds of nm scan size. By comparing these results obtained from the nanomechanical mapping with those of the classical characterization methods used for compatibilization, such as TEM, this technique is promising in operation without any staining or coating. It also enables us to directly link the mechanical properties and morphology of the polymer blends. Our results will be useful to the research of the interfacial reaction and structure of polymer blends as well as the composites.

8.3.3
Nanomechanical Properties of Block Copolymers [20, 48, 49]

Block copolymers (BCPs) have attracted increased interest in recent years. The highly ordered nanostructures formed by self-assembly can be found in a wide range of promising applications. To date, most of the studies on BCP nanostructures have been carried out using small angle X-ray scattering (SAXS) and electron microscopy with proper staining techniques [50]. However, neither SAXS nor electron microscopy techniques can be used to determine mechanical information on such materials. In order to understand and develop advanced BCP materials, it is very important to investigate these samples for identifying phase separated topography, composition, and mechanical properties of individual blocks. In this work, we employed the nanomechanical mapping technique to investigate a poly(styrene-*b*-ethylene-*co*-butylene-*b*-styrene) (SEBS) triblock copolymers. What we aim at is to characterize the compositional effect on surface morphology and nanomechanical properties of SEBS block copolymers. Herein we directly correlate the structures to the changes in mechanical properties (Young's modulus), which will enable us to have a deeper insight into the microstructure–property correlations.

Four types of SEBS samples were supplied by Asahi KASEI Corp. and used without further treatment. The characteristics of the sample are listed in Table 8.1, including component weight ratio, number-average molecular weight, M_n, and molecular weight distribution M_w/M_n. The film samples with the thickness of about $10\,\mu m$ were prepared by solvent casting a $0.004\,g\,mL^{-1}$ SEBS toluene solution onto cleaned glass slides. The as-prepared films were first dried in a fume hood

Table 8.1 SEBS sample characteristics.

Samples	Component weight ratio	M_n	M_w/M_n
SEBS (10/80/10)	10/80/10	75 000	1.1
SEBS (14.5/71/14.5)	14.5/71/14.5	75 000	1.1
SEBS (21/58/21)	21/58/21	74 000	1.1
SEBS (33.5/33/33.5)	33.5/33/33.5	70 000	1.1

for 1 day and then in vacuum at room temperature for another 3 days to remove residual solvent.

The triblock copolymer SEBS consisting of hard and soft blocks that usually exhibit a phase-separated morphology has been widely studied by AFM techniques. Figure 8.20 presents the tapping-mode phase image of the SEBS samples with different component weight ratios. The characteristic phase-separated mor-
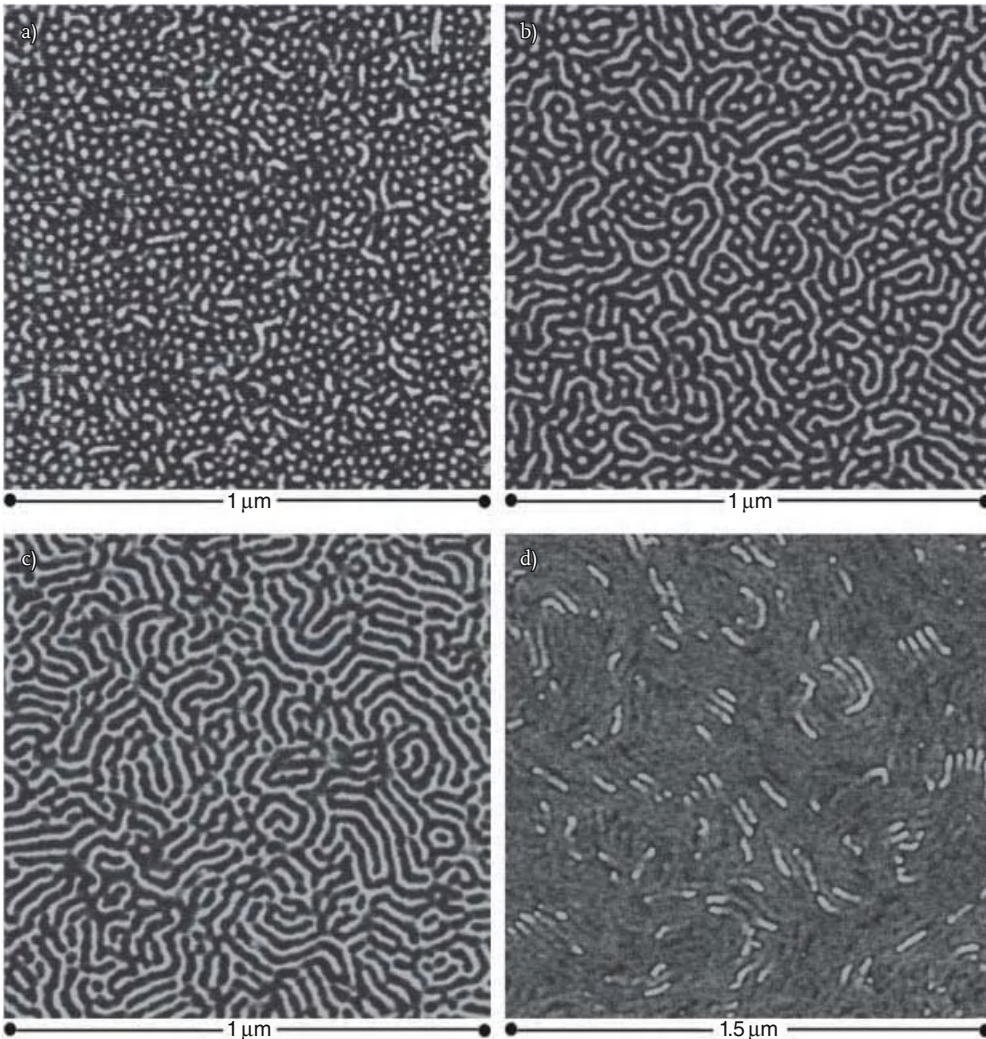
Figure 8.20 AFM tapping-mode phase images of thin films of (a) SEBS (10/80/10), (b) SEBS (14.5/71/14.5), (c) SEBS (21/58/21), and (d) SEBS (33.5/33/33.5). Note the different scales in the images.

phologies consisting of bright and dark nanophasic domains were observed. At a low PS component (SEBS [10/80/10]), a coexistence of the irregular short cylinders and spheres is observed. As the PS weight ratio increases, the microstructure changes from a rod like or an intermediate between the cylinder and lamellar structure for SEBS (14.5/71/14.5) to a well-ordered lamellar for SEBS (21/58/21). A further increase in the PS weight ratio (SEBS 33.5/33/33.5) induces such a great change in microstructure that only the EB cylinder remains clearly visible. A possible reason may be attributed to the high PS weight ratio, which increases the SEBS T_g a lot. The molecular mobility of PS decreases and it cannot form well phase-separated morphology during the experiment conditions. In such a case, it is difficult to get the clear PS features. It should be noted that such conclusions are drawn only from the results of the surface morphologies obtained by AFM tapping mode and the bulk morphologies of triblock copolymers are mainly governed by the volume ratio of the phases. Here we only make this statement to compare the results from AFM tapping mode with those from the nanomechanical mapping measurements. In any case, the topography data alone provide little information about the chemical and mechanical heterogeneity of the SEBS films, which is especially apparent in Figure 8.20a–c. Without further analysis, it is impossible to identify the bright or dark regions because some other researchers have assigned the bright regions to the hard PS component and dark regions to the soft rubbery PEB component [51, 52]. However, in general, it is difficult to assign the chemical composition to the features observed in height and phase images unless additional experimentation is conducted [53, 54]. Furthermore, the assignment of the bright or dark in contrast to the hard or soft domain in phase imaging is not always straightforward. For example, several studies have assigned the brighter contrast to the stiffer material and the darker one to the softer material [55, 56]. In other reports, the darker region has been attributed to the stiffer material and the lighter region to the softer material [54, 57]. Therefore, nanomechanical mapping measurements were performed in order to provide an easy and efficient method to identify the composition and investigate the mechanical properties of the different regions.

Figure 8.21 presents Young's modulus maps obtained from nanomechanical mapping measurements for SEBS samples with different compositions. As observed, Young's modulus maps show a variety of ordered structures resembling the surface topography observed in the tapping mode. The characteristic phase-separated morphologies consisting of high and low Young's modulus regions are clearly exhibited. For the SEBS (10/80/10) sample, a coexistence of irregular short cylinders and spheres is observed from Young's modulus map. As the PS weight ratio increases, Young's modulus maps show a well-ordered structure for the SEBS (14.5/71/14.5) and SEBS (21/58/21) samples. Young's modulus map of the SEBS (33.5/33/33.5) is also very similar to the image obtained by AFM tapping mode. Moreover, this result further demonstrates that it is only the PEB block that forms the well-ordered structure (the red areas with lower Young's modulus are considered to be the soft PEB blocks). The corresponding modulus profile across a section reveals that the two chemical blocks have a large difference in modulus
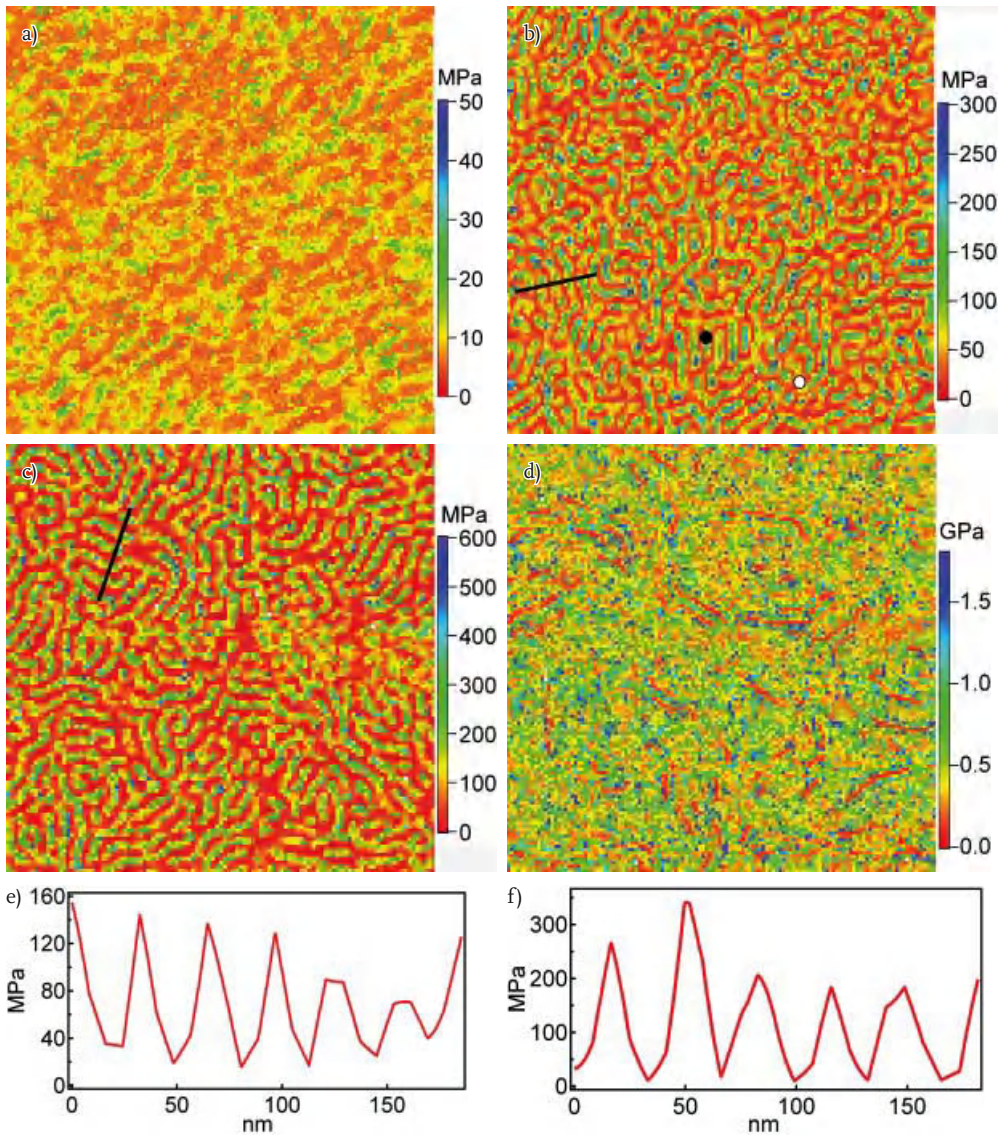
Figure 8.21 Young's modulus maps of (a) SEBS (10/80/10), (b) SEBS (14.5/71/14.5), (c) SEBS (21/58/21), and (d) SEBS (33.5/33/33.5). The scan size of (a) is 500 nm and (b–d) is 1 µm. Numerical values across the sections indicated by the line in (b) and (c) are given in (e) and (f), respectively.
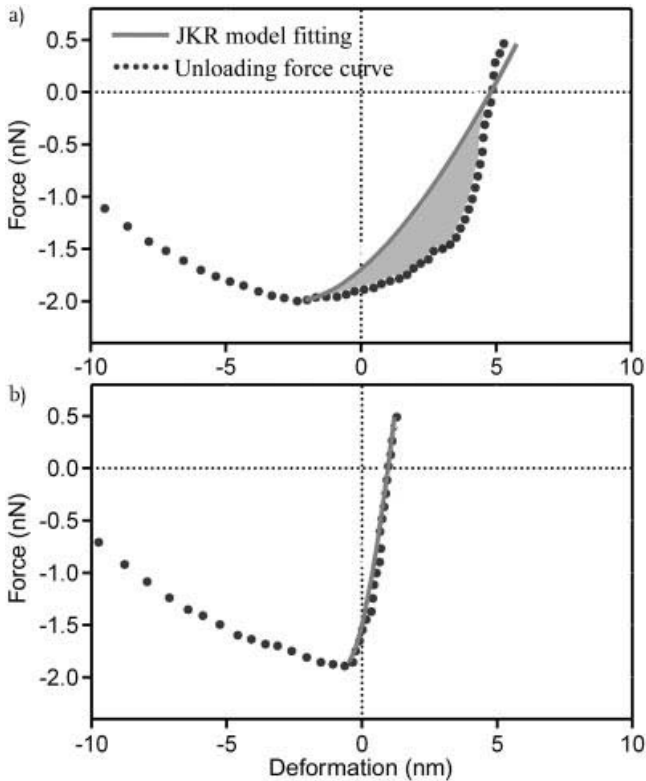
Figure 8.22 Force–deformation curves of (a) PEB and (b) PS regions. The curve fitting against the JKR contact is superimposed on each curve. The area enclosed by the force–deformation and JKR fitting curve represents the contribution of viscoelasticity to E_{dis}, as shown in Figure 8.22a.

values (Figure 8.21e and f). Therefore, such a map enables us to directly link the morphology and mechanical properties of the block copolymers. In Young's modulus maps, the light green areas with higher Young's modulus are considered to be the hard PS blocks (in the case of Figure 8.21d, the PS blocks are not clear), while the red areas with lower Young's modulus are the soft PEB blocks. Figure 8.22 displays the two typical force–deformation curves corresponding to the two points indicated by the white and dark circles in Young's modulus image (Figure 8.21b). The curve fit using JKR contact mechanics is also superimposed in each case. Here, the results demonstrate that JKR analysis of the withdrawing process fits well for the elastic PS component. However, deviations appear for the viscoelastic PEB component because of the viscoelastic effect. Young's modulus calculated from force–deformation curves are presented in Table 8.2. With the same evaluation method, we also investigated Young's modulus of the bulk PS and PEB films (Table 8.2). It is found that as the PS weight ratio increases, the modulus of

Table 8.2 Calculated Young's modulus of the PS and PEB blocks in SEBS samples[a].

Samples		SEBS (10/80/10)	SEBS (14.5/71/14.5)	SEBS (21/58/21)	SEBS (33.5/33/33.5)
Young's modulus (MPa)	PS	19.2 ± 2.5	133.3 ± 26.0	209.0 ± 29.3	823.0 ± 168.1
	PEB	8.7 ± 2.1	25.6 ± 9.2	42.4 ± 16.9	97.6 ± 17.8

a) The measured modulus value of pure PS and PEB is 2.02 ± 0.59 GPa and 10.1 ± 0.5 MPa, respectively.

both the PEB and PS blocks that we have observed also increase dramatically. Young's modulus of the PEB blocks of the SEBS (10/80/10) are almost the same as the bulk value but much lower than SEBS (14.5/71/14.5), SEBS (21/58/21), and SEBS (33.5/33/33.5). Although the PS blocks for the SEBS (33.5/33/33.5) approach the bulk value, there is a dramatic decrease in stiffness as to the other three SEBS samples. Previous work has shown that the hard substrate (usually, infinitely stiff solids compared to compliant polymer layers) is a critical issue that affects the measured nanomechanical response [58]. Usually, the research restricts the localized deformations (indentations) to the depths much smaller than the total thickness of the films (<20%) in order to eliminate the influence of the solid support. In our case, the trigger set point of 3 nm is much less than 1% of the film thickness (10 μm). Thus, the decreased modulus for the PS blocks and increased modulus for the PEB's mainly result from the microstructure change that is governed by the volume ratio of the phases. At the low volume fraction of PS, the soft PEB blocks surround and support the PS blocks underneath, while at the high volume fraction of PS, the microstructure changes appear to be more PS phase dominated. It should be noticed that Young's modulus reported by Tsukruk *et al.* [58] is 20 ± 7 MPa for the glassy domains PS and 7 ± 3 MPa for the rubber phase PEB of a molecularly thick SEBS layers. As to the one reported by Motomatsu *et al.* [52], it is 24 ± 3.1 MPa for the PS and 6.4 ± 0.3 MPa for the PEB of a SEBS (15/70/15) sample. The variation of the determined Young's modulus may result from the AFM measurement, such as the probe radius, probe geometry, and different contact model [52, 59]. Other possibilities include sample preparation such as film thickness.

Not only Young's modulus at nanoscale, but also the energy dissipation, E_{dis}, during probe–sample interactions can be evaluated by a recently developed amplitude–modulation AFM (AM-AFM) method as described in Section 8.1.3 [60–62]. By measuring the phase shift, Edis is calculated using Eq. (8.15). By plotting the measured E_{dis} as a function of the A/A_0, a characteristic energy dissipation curve can be obtained. Figure 8.23a shows the typical E_{dis} versus A/A_0 curves corresponding to the PEB and PS components. According to Garcia [61], the E_{dis} versus A/A_0 curves suggest that the viscoelastic force dominate the dissipation process between the AFM probe and sample. As can be seen, the dissipated energy

a)

b)
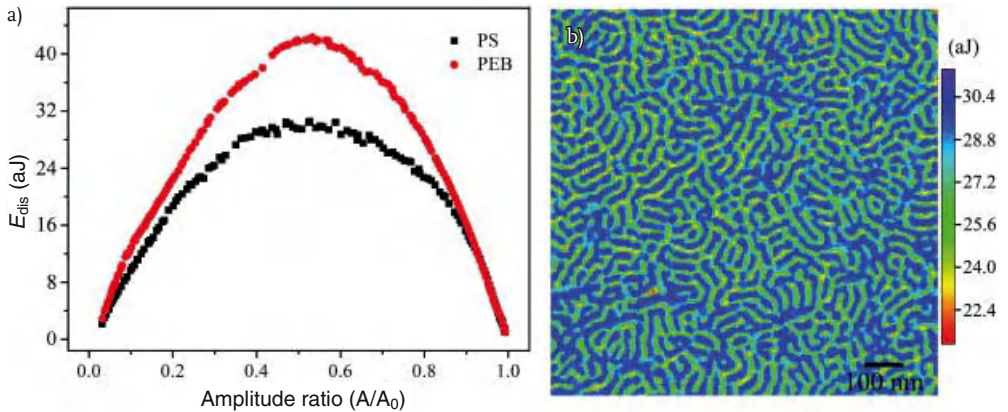
Figure 8.23 (a) Energy dissipation curve measured as a function of the amplitude ratio A/A_0. (b) Energy dissipation map converted according to Eq. (8.15).

of the PEB and PS is considerably different despite that the curve shape and the maximum are dependent on how close the AFM probe is located to the center of the components during the measurements. Locating probe at the center of the PS block yields lower maximum and larger difference from that on the PEB regions. Figure 8.23b is an E_{dis} map converted from two-dimensional arrays of E_{dis} values. The blue areas with higher dissipated energy are considered to be the soft PEB blocks, while the blue and green areas with lower dissipated energy are considered to be the hard PS blocks. Therefore, the result indicates that a map of E_{dis} can also clearly distinguish the two chemical blocks of the copolymer.

The statistic distribution of E_{dis} can be perfectly fitted by Gaussian curves (Figure 8.24a), and we evaluate the average dissipated energy at a different amplitude ratio A/A_0. E_{dis} is plotted as a function of the cantilever's oscillation amplitude A/A_0. As shown in Figure 8.24b, at $A/A_0 \sim 0.55$, the maximum E_{dis} for the PEB and PS are ~41.0 and ~33.2 aJ, respectively. Irrespective of the variation of E_{dis} with A/A_0, the $E_{dis}^{PEB}/E_{dis}^{PS}$ ratio remains to be constant value of ~1.2 ± 0.04 (the inset in Figure 8.24b). The average of difference in energy dissipation is estimated to be 3.3%. Please note that the Figure 8.23a is the typical E_{dis} versus A/A_0 curves for the PEB and PS components while the Figure 8.24b is (the statistic average of E_{dis}) versus A/A_0 curves. Thus, they show similar features.

The energy dissipated can also be measured by FV mode. Figure 8.25a and b shows typical cantilever deflection curves corresponding to the PEB and PS components, respectively. The force is deduced by multiplying the cantilever's deflection by its spring constant. Generally, the attractive force between the probe and sample shows similar features. But it is larger on PEB regions than that on PS, because PEB is more adhesive compared with PS [21]. In the repulsive force regime, the loading–unloading curves overlap, suggesting that the repulsive probe–sample interaction is managed by the elastic property of the sample (the

a)

b)
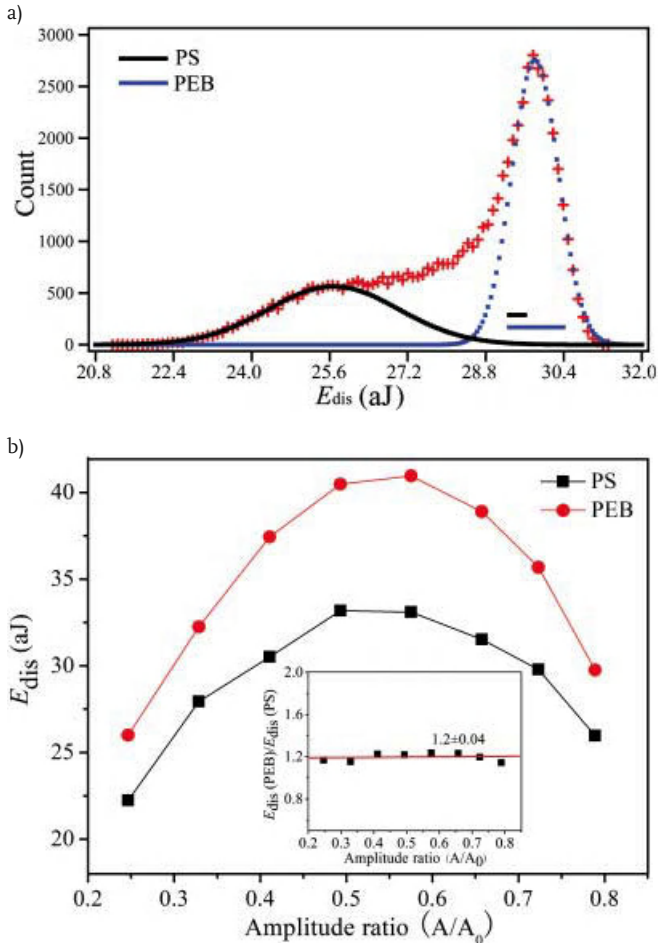
Figure 8.24 (a) Distribution of energy dissipation. The black and blue lines are the Gaussian fits of the experimental data points. (b) Statistic average energy dissipation as a function of the cantilever's oscillation amplitude A/A_0. The inset shows the variation of $E_{dis}^{PEB}/E_{dis}^{PS}$ with the amplitude ratio A/A_0. The average difference in the energy dissipation is estimated to be 3.3%.

elastic modulus of the probe is much higher than that of the PEB and PS). These characteristics of the force curves indicate that the probe–sample interactions are dominated by long-range attractive forces without mechanical instabilities of the cantilever and large-scale plastic deformation of the sample [4].

A large difference between loading and unloading force curves is found in the region dominated by attractive forces [4]. It indicates that the energy loss mainly originates from the adhesive forces between the probe and sample. The force for the pull-out of polymer chains and/or capillary force also contributes to the dis-
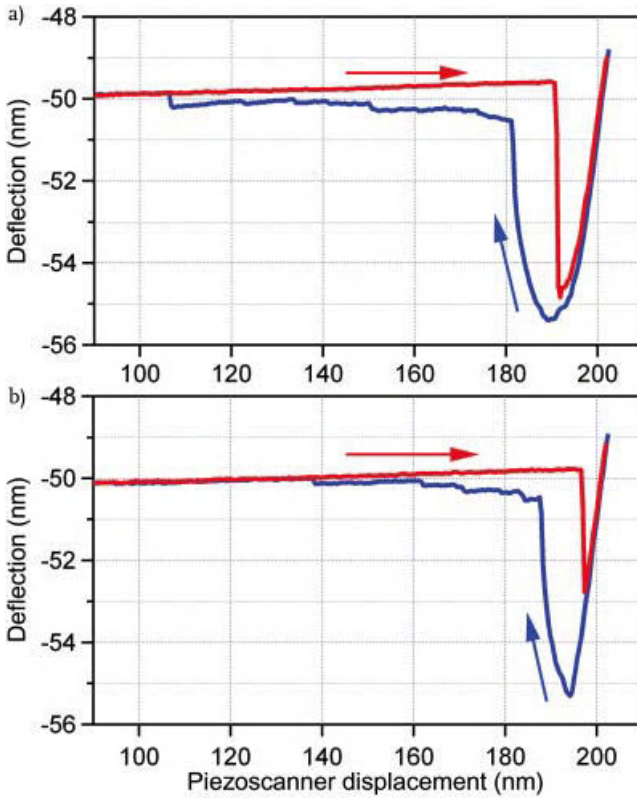
Figure 8.25 Cantilever deflection–distance curves on the (a) PEB and (b) PS region. The arrows indicate the direction of the relative tip–sample displacement. The area enclosed between loading–unloading curves is the dissipated energy.

sipated energy [63]. E_{dis} can be deduced by calculating the area enclosed by the force curves [4]. Therefore, based on the 2D array of the force–distance curves, an energy dissipation map can be obtained as shown in Figure 8.26a. The regions exhibiting larger E_{dis} can be identified as the soft PEB blocks, while the regions showing smaller E_{dis} correspond to the hard PS blocks. The difference in energy dissipation can be seen in the profile presented in Figure 8.26b, with $E_{dis}^{PEB} = 42.5 \pm 6.9$ aJ and $E_{dis}^{PS} = 31.8 \pm 2.4$ aJ. The $E_{dis}^{PEB}/E_{dis}^{PS}$ ratio is calculated to be ~1.3. In FV mode, the trigger threshold is about 0.5 nN, corresponding to an amplitude ratio of $A/A_0 \sim 0.8$ in AM-AFM (the tapping force is calculated to be ~0.5 nN at $A/A_0 \sim 0.8$ according to Eqs. (8.10) and (8.11), the contact pressure is much lower than the yield strength of the soft PEB). E_{dis} measured with AM-AFM at $A/A_0 \sim 0.8$ is 29.8 aJ for the PEB and 25.6 aJ for the PS. Although A/A_0 is lower in AM-AFM due to an unknown contact area and scan speed [64, 65], the $E_{dis}^{PEB}/E_{dis}^{PS}$ ratio ~1.2 is almost equal to that from FV measurements (~1.3). The consistent
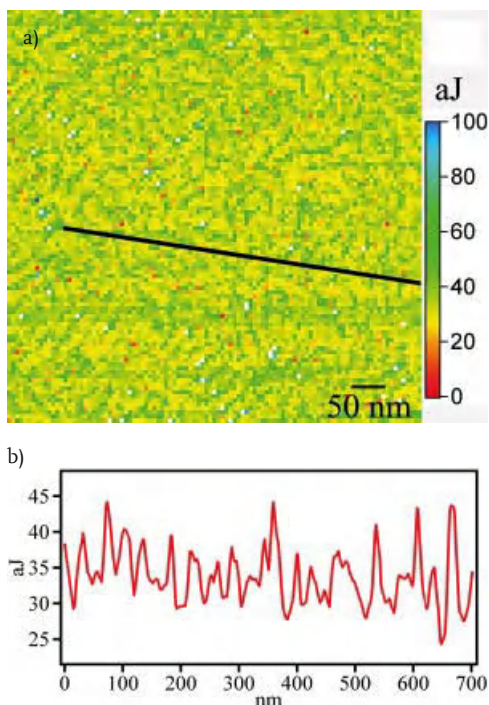
Figure 8.26 (a) Map of the dissipated energy of the SEBS sample calculated from the loading–unloading curves. (b) Numerical values across the section indicated by the line in (a).

$E_{dis}^{PEB}/E_{dis}^{PS}$ ratio suggests that characterization of E_{dis} by static AFM is quantitatively comparable with that by dynamic AFM.

It is noted that the measured E_{dis} by either static or dynamic AFM is basically qualitative and includes all probe–surface interactions such as viscoelasticity and adhesive energy. In order to distinguish the contribution of viscoelastic and adhesive, we fit the force–deformation curves with the JKR model. The curve fittings are also displayed in Figure 8.22. It is known that the JKR theory is derived for perfectly elastic solids and assumes reversible behavior in loading and unloading processes. Here, the viscoelasticity of the PEB components plays an important role during the unloading process which results in the occurrence of large deviation. Then, the area enclosed by the force–deformation and JKR fitting curves represents the contribution of viscoelastic behavior to E_{dis}, which is 4.5 ± 9.6 aJ for the PEB and 0.55 ± 0.12 aJ for the PS components. The ratio of viscoelasticity-induced E_{dis} for the two components is about 8.2, nearly one order of magnitude higher than that obtained by calculating the total E_{dis} ($E_{dis}^{PEB}/E_{dis}^{PS}$ is ~1.2 and 1.3 in dynamic and static AFM, respectively). This suggests that the imaging contrast can be significantly enhanced. Although E_{dis} is dependent on experimental parameters,
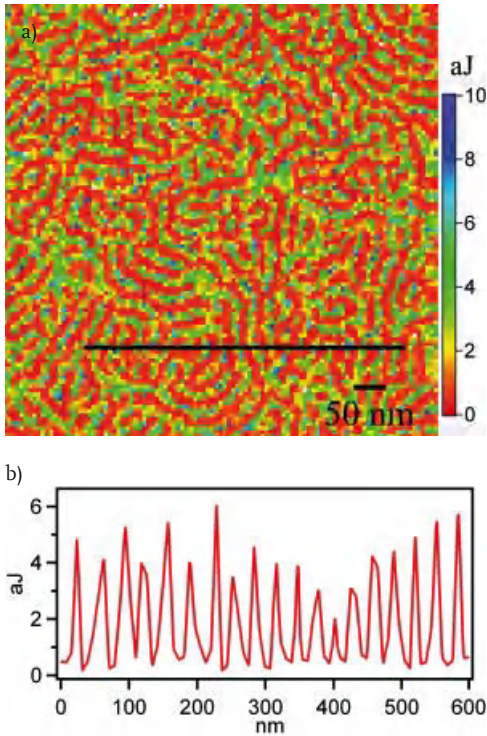
Figure 8.27 (a) Map of the viscoelastic property of the SEBS sample. (b) Numerical values across the section indicated by the line in (a).

the two chemical blocks of the SEBS copolymer can be unambiguously identified as shown in Figure 8.27.

Besides nanomechanical properties, we can also obtain the deformation image and true surface morphology of the block copolymers at the same time with the nanomechanical mapping technique. It is well known that the height images obtained from tapping mode and FV are affected by the sample deformation, which results from the force between the probe tip and the sample as discussed in Section 8.2.6. However, here we will show the true height images obtained by using the nanomechanical mapping technique. Figure 8.28 shows the generated original height, sample deformation, and true height images. Shown in Figure 8.28a is the original height image directly obtained from the FV mode. It contains artifacts due to the low elastic modulus of the rubbery PEB component. The sample deformation δ is calculated from Eq. (8.43). Then, two-dimensional arrays of sample deformation values can be regarded as a sample deformation image (Figure 8.28b). The true height image can be considered as the superimposition of the original height image and the sample deformation image. The weak contrast of the true height image is due to large compensation of the deformation at soft
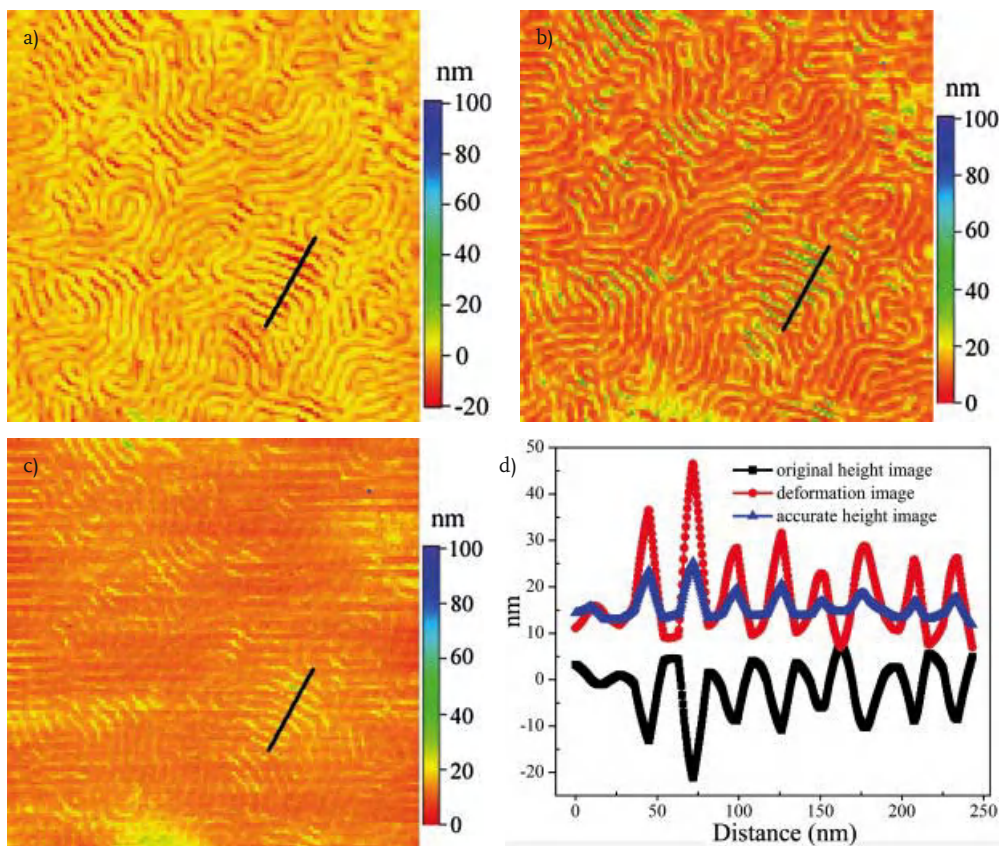
Figure 8.28 (a) Original height image, (b) deformation image, and (c) true height image obtained with nanomechanical mapping, (d) Section analysis on the original height, deformation, and true height image.

PEB regions. Even though, it reveals the real surface topography of the SEBS films prepared by the solvent casting technique. By comparing the section analysis of the original height and true height images (Figure 8.28d), it is found that the topography is totally reversed. The higher and lower regions in the original height image become lower and higher regions in the true height image. The height contrast reverses is due to the large deformation caused by the force between the probe tip and the sample. On the other hand, the calculated tapping force in the tapping mode experiment is about 0.35–0.45 nN, which is almost equal to one-third of the trigger threshold of 1.2 nN in the FV mode. The corresponding deformation in the tapping mode is calculated to be almost half of the deformation in FV mode. It indicates that the deformation of PS and PEB blocks are about 5 and 15 nm, respectively. Considering that the apparent height difference in the tapping-

mode height image is ~4.5 nm, it can be concluded that the true topography should be the inverse of the tapping-mode height image. Then, similar to the original height image obtained from FV mode, the tapping-mode height image is also an artifact due to the large deformation. However, the reconstructed true height image reveals the true surface topography and shows that the softer PEB blocks are actually higher than the stiffer PS blocks. This finding clearly demonstrates that both the tapping-mode height image and the FV original height image of SEBS films are artifacts. Therefore, we may conclude that the reconstruction procedure is valid enough to claim that the obtained height image represents the true topographic feature free from sample deformation.

8.4
Conclusion

In summary, we have investigated the surface mechanical properties including Young's modulus, adhesion, viscoelasticity, and energy dissipation during probe–sample interactions by employing AFM nanomechanical mapping. The ability of nanomechanical mapping for identifying the composition and evaluating the mechanical properties at nanoscale will open a new way to study surface properties and explore the microstructure–properties relationship in a large range of polymeric and biological materials.

References

1 Binning, G., Quate, C.F., Gerber, C.H., and Weibel, E. (1986) Atomic force microscope. *Phys. Rev. Lett.*, **56** (9), 930–933.

2 Sugawara, Y. (2006) Atomic force microscopy, in *Roadmap of Scanning Probe Microscopy* (ed. S. Morita), Springer, Berlin, p. 16.

3 García, R., and Pérez, R. (2002) Dynamic atomic force microscopy methods. *Surf. Sci. Rep.*, **47**, 197–301.

4 Tamayo, J., and García, R. (1998) Relationship between phase shift and energy dissipation in tapping-mode scanning force microscopy. *Appl. Phys. Lett.*, **73** (20), 2926–2928.

5 Anczykowski, B., Gotsmann, B., Fuchs, H., Cleveland, J.P., and Eling, V.B. (1999) How to measure energy dissipation in dynamic mode atomic force microscopy. *Appl. Surf. Sci.*, **140**, 376–382.

6 Oliver, W.C., and Pharr, G.M. (2004) Measurement of hardness and elastic modulus by instrumented indentation: advances in understanding and refinements to methodology. *J. Mater. Res.*, **19**, 3–20.

7 Oliver, W.C., and Pharr, G.M. (1992) An improved technique for determining hardness and elastic modulus using load and displacement sensing indentation experiments. *J. Mater. Res.*, **7** (6), 1564.

8 Sneddon, I.N. (1965) The relation between load and penetration in the axisymmetric Boussinesq problem for a punch of arbitrary profile. *Int. J. Eng. Sci.*, **3**, 47–57.

9 Maugis, D., and Barquins, M. (1981) Adhesive contact of a conical punch on an elastic half-space. *J. Phys. Lett.*, **42** (5), L95–L97.

10 Landau, L., and Lifchitz, E. (1967) *Theory of Elasticity, Mir*, Moscow, Russia.

11 Johnson, K. (1989) *Contact Mechanics*, Cambridge University Press, Cambridge, pp. 84–106.

12 Nakajima, K., and Nishi, T. (2010) Nanorheology of polymer nanoalloys and nanocomposites, in *Polymer Physics: from Suspensions to Nanocomposites and Beyond* (eds L.A. Utracki and A.M. Jamieson), Wiley, New Jersey, pp. 129–160.

13 Hutter, J.L., and Bechhoefer, J. (1993) Calibration of atomic-force microscope tips. *Rev. Sci. Instrum.*, **64** (7), 1868–1873.

14 Villarrubia, J.S. (1997) Algorithms for scanned probe microscope image simulation, surface reconstruction, and tip estimation. *J. Res. Natl. Inst. Stand. Technol.*, **102**, 425–454.

15 Johnson, K.L., Kendall, K., and Roberts, A.D. (1971) Surface energy and the contact of elastic solids. *Proc. R. Soc. Lond., A*, **324**, 301–313.

16 Maugis, D., and Barquins, M. (1980) Fracture mechanics and adherence of viscoelastic solids, in *Adhesion and Adsorption of Polymers* (ed. L.H. Lee), Plenum, New York, pp. 203–277.

17 Sun, Y., Akhremitchev, B., and Walker, G.C. (2004) Using the adhesive interaction between atomic force microscopy tips and polymer surfaces to measure the elastic modulus of compliant samples. *Langmuir*, **20** (14), 5837–5845.

18 Nagai, S., Fujinami, S., Nakajima, K., and Nishi, T. (2009) Nanorheological investigation of polymeric surfaces by atomic force microscopy. *Compos. Interface*, **16**, 13–25.

19 Nukaga, H., Fujinami, S., Watabe, H., Nakajima, K., and Nishi, T. (2005) Nanorheological analysis of polymer surfaces by atomic force microscopy. *Jpn. J. Appl. Phys.*, **44** (7B), 5425–5429.

20 Wang, D., Fujinami, S., Nakajima, K., and Nishi, T. (2010) True surface topography and nanomechanical mapping measurements on block copolymers with atomic force microscopy. *Macromolecules*, **43**, 3169–3172.

21 Wang, D., Fujinami, S., Nakajima, K., and Nishi, T. (2010) Production of a cellular structure in carbon nanotube/

natural rubber composites revealed by nanomechanical mapping. *Carbon*, **48**, 3708–3714.

22 Moniruzzaman, M., and Winey, K.I. (2006) Polymer nanocomposites containing carbon nanotubes. *Macromolecules*, **39**, 5194–5205.

23 Coleman, J.N., Khan, U., Blau, W.J., and Gun'ko, Y.K. (2006) Small but strong: a review of the mechanical properties of carbon nanotube-polymer composites. *Carbon*, **44**, 1624–1652.

24 Du, F.M., Scogna, R.C., Zhou, W., Brand, S., Fischer, J.E., and Winey, K.I. (2004) Nanotube networks in polymer nanocomposites: rheology and electrical conductivity. *Macromolecules*, **37**, 9048–9055.

25 Chatterjee, T., and Krishnamoorti, R. (2008) Steady shear response of carbon nanotube networks dispersed in poly(ethylene oxide). *Macromolecules*, **41**, 5333–5338.

26 Barber, A.H., Cohen, S.R., and Wagner, H.D. (2003) Measurement of carbon nanotube-polymer interfacial strength. *Appl. Phys. Lett.*, **82**, 4140–4142.

27 Ding, W., Eitan, A., Fisher, F.T., Chen, X., Dikin, D.A., Andrews, R., Brinson, L.C., Schadler, L.S., and Ruoff, R.S. (2003) Direct observation of polymer sheathing in carbon nanotube–polycarbonate composites. *Nano Lett.*, **3**, 1593–1597.

28 Pötschke, P., Fornes, T.D., and Paul, D.R. (2002) Rheological behavior of multiwalled carbon nanotube/polycarbonate composites. *Polymer*, **43**, 3247–3255.

29 Kaufman, S., Slichter, W.P., and Davis, D.D. (1971) Nuclear magnetic resonance study of rubber–carbon black interactions. *J. Polym. Sci. [A-2]*, **9**, 829–839.

30 Nishi, T. (1974) Nuclear magnetic resonance study of rubber–carbon black interactions. *J. Polym. Sci. Polym. Phys. Ed.*, **12**, 685–693.

31 O'Brien, J., Cashell, E., Wardell, G.E., and McBrierty, V.J. (1976) NMR investigation of interaction between carbon-black and *cis*-polybutadiene. *Macromolecules*, **9**, 653–660.

32 Nishi, T., Nukaga, H., Fujinami, S., and Nakajima, K. (2007) Nanomechanical mapping of carbon black reinforced natural rubber by atomic force microscopy. *Chin. J. Polym. Sci.*, **25**, 35–41.

33 Coleman, J.N., Khan, U., and Gun'ko, Y.K. (2006) Mechanical reinforcement of polymers using carbon nanotubes. *Adv. Mater.*, **18**, 689–706.

34 Das, A., Stöckelhuber, K.W., Jurk, R., Fritzsche, J., Klüppel, M., and Heinrich, G. (2009) Coupling activity of ionic liquids between diene elastomers and multi-walled carbon nanotubes. *Carbon*, **47**, 3313–3321.

35 Wang, D., Fujinami, S., Nakajima, K., and Nishi, T. (2010) Investigation of reactive polymer–polymer interface using nanomechanical mapping. *Macromolecules*, **43**, 5521–5523.

36 Koriyama, H., Oyama, H.T., Ougizawa, T., Inoue, T., Weber, M., and Koch, E. (1999) Studies on the reactive polysulfone–polyamide interface: interfacial thickness and adhesion. *Polymer*, **40**, 6381–6393.

37 Adedeji, A., Lyu, S., and Macosko, C.W. (2001) Block copolymers in homopolymer blends: interface vs. micelles. *Macromolecules*, **34**, 8663–8668.

38 Zhang, J.B., Lodge, T.P., and Macosko, C.W. (2005) Interfacial morphology development during PS/PMMA reactive coupling. *Macromolecules*, **38**, 6586–6591.

39 Jiao, J.B., Kramer, E.J., Vos, S.D., Möller, M., and Koning, C. (1999) Morphological changes of a molten polymer/polymer interface driven by grafting. *Macromolecules*, **32**, 6261–6269.

40 Yin, Z., Koulic, C., Pagnoulle, C., and Jérôme, R. (2003) Probing of the reaction progress at a PMMA/PS interface by using anthracene-labeled reactive PS chains. *Langmuir*, **19**, 453–457.

41 Kim, H.Y., Jeong, U., and Kim, J.K. (2003) Reaction kinetics and morphological changes of reactive polymer–polymer interface. *Macromolecules*, **36**, 1594–1602.

42 Jones, T.D., Schulze, J., Macosko, C.W., Moon, B., and Lodge, T.P. (2003) Effect of thermodynamic interactions on reactions at polymer/polymer interfaces. *Macromolecules*, **36**, 7212–7219.

43 Schulze, J.S., Cernohous, J.J., Hirao, A., Lodge, T.P., and Macosko, C.W. (2000) Reaction kinetics of end-functionalized chains at a polystyrene/poly(methyl methacrylate) interface. *Macromolecules*, **33**, 1191–1198.

44 Harton, S.E., Stevie, F.A., and Ade, H. (2005) Diffusion-controlled reactive coupling at polymer–polymer interfaces. *Macromolecules*, **38**, 3543–3646.

45 Li, H.G., Chiba, T., Higashida, N., Yang, Y., and Inoue, T. (1997) Polymer–polymer interface in polypropylene/polyamide blends by reactive processing. *Polymer*, **38**, 3921–3925.

46 Schulze, J.S., Moon, B., Lodge, T.P., and Macosko, C.W. (2001) Measuring copolymer formation from end-functionalized chains at a PS/PMMA interface using FRES and SEC. *Macromolecules*, **34**, 200–205.

47 Russell, T.P., Menelle, A., Hamilton, W.A., Smith, G.S., Satija, S.K., and Majkrzak, C.F. (1991) Width of homopolymer interfaces in the presence of symmetric diblock copolymers. *Macromolecules*, **24**, 5721–5726.

48 Wang, D., Fujinami, S., Liu, H., Nakajima, K., and Nishi, T. (2010) Investigation of true surface morphology and nanomechanical properties of poly(styrene-*b*-ethylene-*co*-butylene-*b*-styrene) using nanomechanical mapping: effects of composition. *Macromolecules*, **43**, 9049–9055.

49 Wang, D., Liang, X.B., Liu, Y.H., Fujinami, S., Nishi, T., and Nakajima, K. (2011) Characterization of surface viscoelasticity and energy dissipation in a polymer film by atomic force microscopy. *Macromolecules*, **44**, 8693–8697.

50 Lynd, N.A., Meuler, A.J., and Hillmyer, M.A. (2008) Polydispersity and block copolymer self-assembly. *Prog. Polym. Sci.*, **33**, 875–893.

51 Ganguly, A., Sarkar, M.D., and Bhowmick, A.K. (2007) Morphological mapping and analysis of poly[styrene-*b*-(ethylene-*co*-butylene)-*b*-styrene] and its clay nanocomposites by atomic force microscopy. *J. Polym. Sci. [B]*, **45**, 52–66.

52 Motomatsu, M., Mizutani, W., and Tokumoto, H. (1997) Microphase domains of poly (styrene-block-ethylene/butylene-block-styrene) triblock copolymers studied by atomic force microscopy. *Polymer*, **38**, 1779–1785.

53 Raghavan, D., Gu, X., Nguyen, T., VanLandingham, M.R., and Karim, A. (2000) Mapping polymer heterogeneity using atomic force microscopy phase imaging and nanoscale indentation. *Macromolecules*, **33**, 2573–2583.

54 Bar, G., Thomann, Y., Brandsch, R., Cantow, H.J., and Whangho, M.H. (1997) Factors affecting the height and phase images in tapping mode atomic force microscopy. Study of phase-separated polymer blends of poly(ethene-*co*-styrene) and poly(2,6-dimethyl-1,4-phenylene oxide). *Langmuir*, **13**, 3807–3812.

55 Sauer, B.B., McLean, R.S., and Thomas, R.R. (1998) Tapping mode AFM studies of nano-phases on fluorine-containing polyester coatings and octadecyltrichlorosilane monolayers. *Langmuir*, **14**, 3045–3051.

56 Magonov, S.N., Elings, V., and Papkov, V.S. (1997) AFM study of thermotropic structural transitions in poly(diethylsiloxane). *Polymer*, **38**, 297–307.

57 Magonov, S.N., Ellings, V., and Whangbo, M.H. (1997) Phase imaging and stiffness in tapping-mode atomic force microscopy. *Surf. Sci.*, **375**, L385–L391.

58 Tsukruk, V.V., Sidorenko, A., Gorbunov, V.V., and Chizhik, S.A. (2001) Surface nanomechanical properties of polymer nanocomposite layers. *Langmuir*, **17**, 6715–6719.

59 Kopycinska-Müller, M., Geiss, R.H., and Hurley, D.C. (2006) Contact mechanics and tip shape in AFM-based nanomechanical measurements. *Ultramicroscopy*, **106**, 466–474.

60 Cleveland, J.P., Anczykowski, B., Schmid, A.E., and Elings, V.B. (1998) Energy dissipation in tapping-mode atomic force microscopy. *Appl. Phys. Lett.*, **72**, 2613–2615.

61 García, R., Gómez, C.J., Martínez, N.F., Patil, S., Dietz, C., and Magerle, R. (2006) Identification of nanoscale dissipation processes by dynamic atomic force microscopy. *Phys. Rev. Lett.*, **97**, 016103.

62 Dietz, C., Zerson, M., Riesch, C., Franke, M., and Magerle, R. (2008) Surface properties of elastomeric polypropylenes studied with atomic force microscopy. *Macromolecules*, **41**, 9259–9266.

63 Nakajima, K., Yamaguchi, H., Lee, J.C., Kageshima, M., Ikehara, T., and Nishi, T. (1997) Nanorheology of polymer blends investigated by atomic force microscopy. *Jpn. J. Appl. Phys.*, **36**, 3850–3854.

64 Bar, G., Delineau, L., Brandsch, R., Bruch, M., and Whangbo, M.H. (1999) Importance of the indentation depth in tapping-mode atomic force microscopy study of compliant materials. *Appl. Phys. Lett.*, **75**, 4198–4200.

65 Tamayo, J., and García, R. (1997) Effects of elastic and inelastic interactions on phase contrast images in tapping-mode scanning force microscopy. *Appl. Phys. Lett.*, **75**, 2394–2397.

9
Electron Paramagnetic Resonance and Solid-State NMR Studies of the Surfactant Interphase in Polymer–Clay Nanocomposites

Gunnar Jeschke

9.1
Introduction

Property improvement of polymers by reinforcement with clay minerals or other layered silicates crucially depends on nanodispersion of the filler [1, 2]. The most common engineering and mass polymers are nonpolar or only weakly polar and thus tend to segregate from the ionic layered silicates. The thermodynamic reason for this separation is an increase in Coulomb energy on separation of the silicate layers from their counterions that is not compensated by favorable interactions of the polymer with the silicate surface [3]. This problem can be overcome by organic modification of the layered silicate with cationic surfactants, most commonly tri-methylammoniumalkyl (TMA) or the more thermally stable [4] tributylphospho-niumalkyl (TBP) surfactants. In such polymer-layered-silicate nanocomposites (PLSNs) interaction between the silicate layers and the polymer, which is important for morphology and mechanical properties, is mediated by the surfactant layer. This layer can be considered as an interphase between the silicate and polymer components of the composite.

Direct experimental evidence on structure and dynamics of this interphase is hard to obtain with bulk techniques that integrate over all components of the composite. First insight into the interplay of surfactant orientation on the silicate surface, surfactant conformation, and interlayer spacing in organically modified layered silicates (OMLSs) was achieved by combining information on interlayer spacing from X-ray diffraction (XRD) with information on surfactant conforma-tion from Fourier transform infrared (FTIR) spectroscopy [5]. The surfactant layer can be directly addressed by labeling a small fraction of surfactant molecules with a free radical [6]. These spin probes are then studied by electron paramagnetic resonance (EPR) spectroscopy, which can characterize molecular motion on pico-second to microsecond time scales and structure on length scales between a few tenths of a nanometer and 10 nm. Alternatively, surfactant molecules can

be isotope-labeled for selective observation by NMR spectroscopy or, in the case of TBP surfactants, can be selectively observed by NMR at natural isotope abundance.

This chapter provides an overview of the information that can be obtained on the surfactant interphase by such NMR and EPR techniques and is organized as follows. In Section 9.2 the characterization techniques and their relative advantages and disadvantages are explained. In Section 9.3 information from NMR and EPR on structure and dynamics of surfactant molecules in OMLS is reviewed to provide a solid foundation for discussion of the more complex interphase behavior in the nanocomposites in Section 9.4. The conclusion summarizes the main findings.

9.2
NMR, EPR, and Spin Labeling Techniques

9.2.1
Solid-State NMR Spectroscopy

In modern NMR spectroscopy frequencies of transitions between nuclear spin states are measured and correlated by excitation with radiofrequency pulses, subsequent detection of the free induction decay, and Fourier transformation that yields a spectrum [7]. The transition frequencies are dominated by the nuclear Zeeman interaction between the spins and a static external magnetic field of up to 20 T in strength. Modification of the local field at the nucleus due to the surrounding electrons causes the chemical shift, which provides structural resolution. The NMR line of a given nucleus may split into a multiplet or may broaden due to coupling to neighboring nuclear spins. In solution-state NMR, splittings are observed from J couplings, which are mediated by bond electrons and thus provide information on connectivity of atoms. The dipole–dipole couplings, which act through space and decay with the third power of spin–spin distance, are averaged in solution by fast tumbling of the molecules. In solid-state NMR [6], these dipole–dipole couplings can be measured at distances up to a few tenths of a nanometer and provide information on spatial structure of the molecule. On the other hand, dipole–dipole couplings cause strong line broadening, which hides chemical shift information. This broadening can be suppressed by fast rotation of the sample about an axis that includes the magic angle θ_m with the magnetic field axis, where $3\cos^2\theta_m - 1 = 0$. Such magic-angle spinning (MAS) improves resolution at the cost of losing the distance information. This information can be reintroduced by suitable sequences of radiofrequency pulses.

The most widely studied nuclei, ^1H, ^{13}C, ^{15}N, ^{31}P, and ^{19}F, have a nuclear spin quantum number of $I = 1/2$. If the spin quantum number is larger, for instance $I = 1$ in the case of deuterons (^2H), the nuclei have an electric quadrupole moment that interacts with an electric field gradient. The electric field gradient arises from

the bond electrons, so that this nuclear quadrupole interaction also provides information on molecular structure. Moreover, the nuclear quadrupole interaction is orientation dependent and thus is averaged by molecular motion. Partial averaging of this interaction is often observable in solid-state ^{2}H NMR spectra. Analysis of such spectra provides information on the type and time scale of molecular motion around the microsecond range. Relatively simple ^{2}H NMR experiments and data analysis can provide rather detailed information on molecular dynamics [8]. These advantages come at the expense of somewhat cumbersome sample preparation, which involves site-specific isotope labeling.

9.2.2
EPR Spectroscopy

In EPR spectroscopy transitions of the electron spin with spin quantum number $S = 1/2$ are excited by microwave irradiation and observed either by continuous-wave (CW) [9] or pulse techniques [10]. The Pauli principle mandates that the two electrons in a bond electron pair have different spin state. Hence, the magnetic moment of electron spins compensates on bonding and EPR is observable only for unpaired electrons. This restricts applicability of EPR spectroscopy to the minority of paramagnetic compounds. The strict requirement for unpaired electrons allows for using EPR spectroscopy as a *probe* technique in complex diamagnetic materials (Section 9.2.3). Due to the 580 times larger magnetic moment of the electron spin compared to the proton spin, EPR spectroscopy is much more sensitive than NMR spectroscopy and a small fraction of spin probes in such a material can easily be detected.

Unless several electron spins couple to a group spin $S > 1/2$, transition frequencies in EPR spectroscopy are dominated by the electron Zeeman interaction between the electron spin and a static magnetic field that typically is only 0.35 T and rarely exceeds 5 T. The electron Zeeman interaction is modified by spin–orbit coupling, which leads to a shift of the g value of bound electrons with respect to the g value of the free electron $g_e = 2.002\,319$. The g shift is the EPR equivalent to the chemical shift in NMR. It is dominated by covalent or coordinative bonding, but may be influenced by noncovalent interactions, such as hydrogen bonding, and by polarity of the environment.

The coupling between electron spins and nuclear spins is called hyperfine interaction and is caused by spin density of the unpaired electron in *s* orbitals on the nucleus (Fermi contact interaction) or by dipole–dipole interaction of the magnetic moments of the two spins. Dipole–dipole interaction arises from spin density in orbitals that are not spherically symmetric (p, d, f orbitals) or from through–space interaction. For protons (^{1}H) the former contribution vanishes and dipolar hyperfine couplings can be directly interpreted in terms of distances. Such analysis is a good approximation for nuclei of other elements, if the electron spin and nuclear spin belong to different molecules, since in this case the through–space interaction is much larger than the one from spin density transfer.

If spin densities on the nucleus of interest exceed a few percent, the hyperfine couplings are often resolved in EPR spectra, even in the solid state, where lines are broadened due to anisotropy of the g value. Very small hyperfine couplings can be measured by exciting and observing nuclear spin transitions. For sensitivity reasons this is not done by NMR techniques, but rather by transferring spin polarization from the electron spin to the nuclei [10]. In electron spin echo envelope modulation (ESEEM) techniques this transfer is achieved solely by microwave pulses, taking advantage of the nonzero transition moment of formally forbidden electron-nuclear spin transitions. Due to line shape deformations and very low transition moments at long distances, ESEEM techniques are not the method of choice for measuring ^{31}P-electron distances on TBP surfactants. Such distances can be measured more precisely and with better sensitivity by direct irradiation of the nuclear spin transitions with a radiofrequency pulse in an electron nuclear double resonance (ENDOR) experiment [11].

Electron spins couple to each other by overlap of orbitals (exchange coupling) or through space (dipole–dipole coupling). These couplings are often negligible in EPR spectroscopy, since electron spins are rare or intentionally diluted. In PLNS the spin labels on the surfactant molecules are confined to the interphase, which is only a small fraction of the total material. This confinement reduces average interspin distances and thus increases average dipole–dipole couplings between electron spins. These couplings are still much too small to be resolved in EPR spectra and do not even lead to noticeable line broadening. However, they can be measured by the electron electron double resonance technique DEER.

Dipole–dipole couplings between spins and the spin–orbit interaction are generally anisotropic. Hence, the EPR spectrum depends on orientation of the molecule with respect to the static magnetic field. Typically the anisotropy of the electron Zeeman interaction and the anisotropy of the largest hyperfine couplings are as large as a few tens to a few hundreds of megahertz. This leads to a sensitivity of spectral line shape to motion around nanosecond time scales, which nicely complements the information that is accessible by deuterium NMR.

9.2.3
Spin Label EPR

To use EPR spectroscopy as a probe technique, unpaired electrons need to be introduced into a diamagnetic system in the form of spin labels (covalent attachment to the site of interest), spin tracers (spin-carrying molecules that substitute for a component of the system), or spin probes (paramagnetic substances with some specificity for the site of interest due to noncovalent interaction). In the following, we use the commonly accepted term spin labeling, although work on PLNS mostly involves spin tracers for surfactant molecules.

Good spin labels are chemically stable and they are small, so that they can provide site-specific information without unduly disturbing the system under
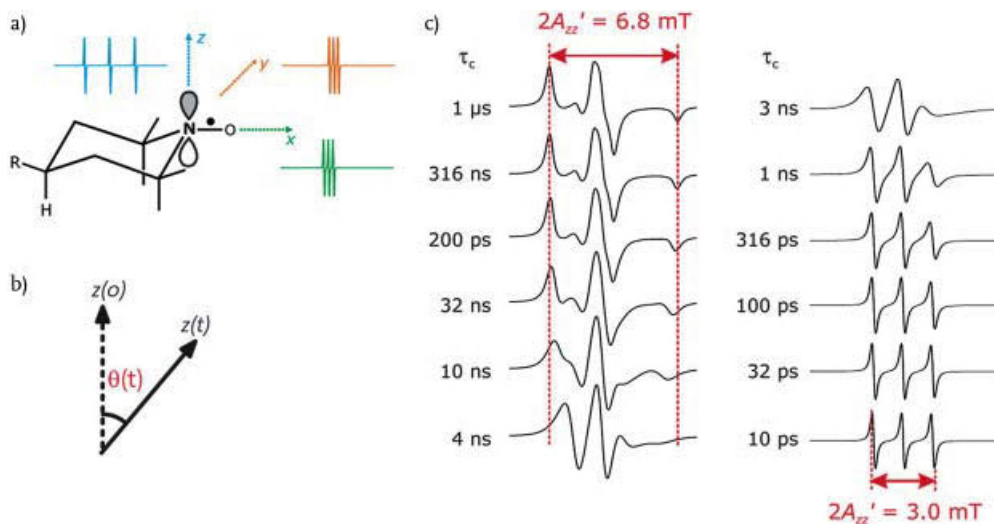
Figure 9.1 Nitroxide EPR spectrum at X band frequencies. (a) Definition of the molecular frame and spectra along the principal directions. (b) For a tumbling nitroxide in soft matter or liquid solution, the direction of the z axis changes by angle θ in a time t. The stochastic function $\theta(t)$ can be characterized by the rotational correlation time τ_c during which the ensemble average $\langle \cos \theta(t) \rangle$ decreases from $\langle \cos \theta(0) \rangle = 1$ to $1/e$. (c) Spectral line shapes and outer extrema splitting A'_{zz} depend on τ_c, with maximum sensitivity at $\tau_c \approx 3.5$ ns, where the character changes from a solid-state spectrum (left column) to a liquid-state spectrum (right column).

study. Furthermore, their EPR spectrum should depend on label environment, for example, polarity, and should not be too broad, as a wide spectral spread reduces sensitivity. Finally, the spectrum should depend on label dynamics on the time scales of interest.

Nitroxide radicals (Figure 9.1a) fulfill all these requirements and are synthetically well accessible. Their exceptional thermal stability up to temperatures of 160 °C in the absence of catalytically active surfaces or other reactive species and up to 140 °C in the presence of silicates and surfactants allows for studying the order–disorder transition of surfactant interphase as well as the melting of crystalline domains of polymers or their glass transitions. In fact, the native TMA and TBP surfactant molecules in nanocomposites themselves decompose below or near the decomposition temperature of nitroxides, when they are in contact with a silicate surface.

The nitroxide spectrum at the standard EPR frequency (X band, ~9.6 GHz) is dominated by the hyperfine coupling to the ^{14}N nucleus in the N–O bond and modified by an anisotropic g shift that comes primarily from spin density at

the oxygen atom of this bond. As ^{14}N has nuclear spin $I = 1$, a hyperfine triplet is observed. Splitting between the lines is maximal along the lobes of the p_π orbital on the nitrogen, which define the z axis of the molecular frame (Figure 9.1a, $A_{zz} \approx 3.4\,mT \approx 95\,MHz$). To a good approximation the much smaller hyperfine coupling perpendicular to these lobes is invariable within the xy plane, $A_{xx} \approx A_{yy} \approx 0.55\,mT \approx 7\,MHz$. In contrast, the g shift is maximal along the N–O bond (x direction of the molecular frame, $g_{xx} \approx 2.0090$, $\delta g_{xx} \approx 6700\,ppm$), about half as large perpendicular to both the N–O bond and the p_π lobes (y direction, $g_{yy} \approx 2.0058$, $\delta g_{yy} \approx 3500\,ppm$), and close to zero along the p_π lobes. At the X band the anisotropic g shift leads to a slight, but clearly visible asymmetry of the powder spectrum. This powder spectrum arises from superposition of the spectra along all orientations in the molecular frame (Figure 9.1c, top of left column).

The electron spin is strongly localized to the N–O bond, with almost 45% spin density at the nitrogen and almost 55% at the oxygen atom. Localization of the unpaired electron at the oxygen atom corresponds to a mesomeric structure without formal charges, whereas localization at the nitrogen atom corresponds to a formal positive charge on that atom and a formal negative charge on the oxygen atom. Polar environments favor this charge separation and thus lead to larger spin density on the ^{14}N nucleus. This in turn leads to a larger ^{14}N hyperfine coupling, which is most strongly visible in A_{zz}. In contrast, the g shift is reduced by more polar environments, which is most strongly visible in δg_{xx}. Precise measurements of δg_{xx} require at least W-band frequencies (94 GHz).

In soft matter, the molecular frame of the nitroxide reorients with respect to the external magnetic field due to Brownian rotational diffusion of the whole molecule or conformational transitions of the nitroxide group. At X-band frequencies, reorientation of the molecular frame z axis influences spectral line shapes most strongly. EPR measurements are performed on large ensembles (typically $10^{15} \ldots 10^{16}$ molecules). The reorientation angle $\theta(t)$ of the z axis at time t with respect to the orientation at zero time (Figure 9.1b) differs for the different molecules in the ensemble, since molecular motion is stochastic. With the approximation that the ensemble average $\langle \cos \theta(t) \rangle$ decays exponentially, time scale of the motion can be characterized by a single rotational correlation time τ_c. This is the time when $\langle \cos \theta(t) \rangle$ has decayed from its initial value 1 to $1/e$.

The simplest way of obtaining information on molecular motion from EPR spectra of tumbling nitroxides (Figure 9.1c) is acquisition of a series of spectra as a function of temperature and measurement of the outer extrema separation $2A'_{zz}$. An extrema separation of 5 mT approximately corresponds to the crossover between the slow- and fast-tumbling regimes at $\tau_c \approx 3.5\,ns$. The temperature $T_{5\,mT}$ of this crossover is sometimes referred to as an EPR glass transition temperature, although it generally differs from the glass transition temperature T_g of the matrix and should not be interpreted without taking into account structure of the nitroxide-carrying molecule and interaction of this molecule with the matrix. Changes of $T_{5\,mT}$ for the same spin label during variation of a system parameter can be safely discussed, for instance, the change observed when intercalating a polymer into
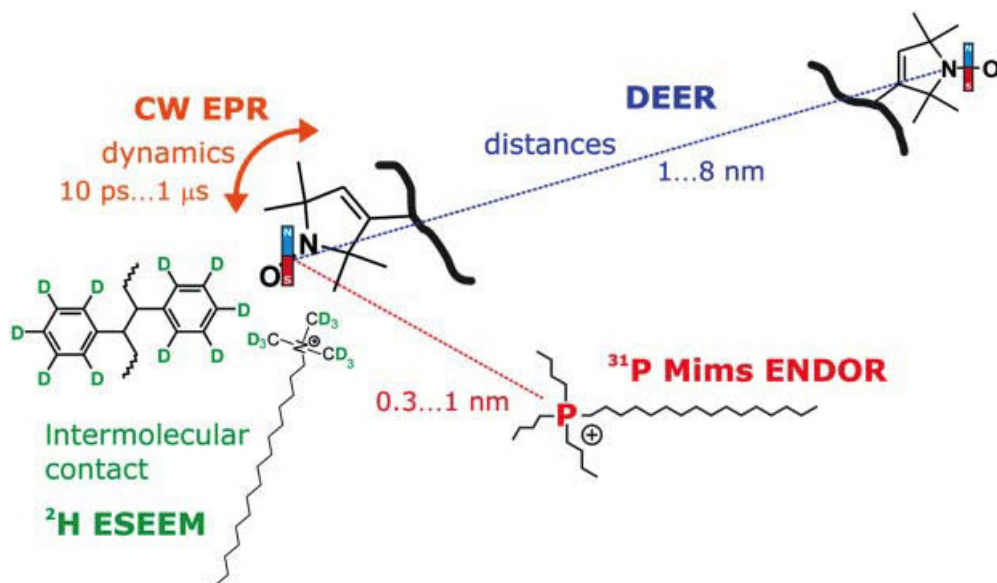
Figure 9.2 Information that can be obtained on spin-labeled systems by different EPR techniques.

the galleries of an OMLS. More information is obtained by fitting simulated spectra [12] to the experimental ones over the whole temperature range, which provides the dependence of τ_c on T. Arrhenius plots of $-\ln \tau_c$ versus $1/T$ or Vogel-Fulcher–Tamman fits [13] reveal whether the motion corresponds to a thermally activated process or to glass transition behavior.

Structural information in the vicinity of a spin label can be obtained by measuring couplings to electron spins or nuclear spins in neighboring molecules or in the silicate (Figure 9.2) [6]. Such intermolecular distances are broadly distributed unless the material is highly ordered. For instance, distance distributions on a nanometer length scale between spin-labeled surfactant molecules in OMLS or PLNS measured by DEER usually correspond to a homogeneous spatial distribution where information concerns only local concentration and confinement of the surfactant to a low-dimensionality phase (usually two-dimensional) [14].

In contrast, partial order of the surfactant layer on subnanometer length scales leads to resolved distributions of the distance between the electron spin and ^{31}P nuclei in surfactant headgroups [14]. Qualitative information on surfactant interphase structure can be derived from ESEEM spectra, which provide a type of local elemental analysis [6]. Nuclear isotopes can be recognized by their characteristic nuclear Zeeman frequencies. In particular, for deuterated components of OMLS or PLNS this information can be quantified by analysis of modulation depths,
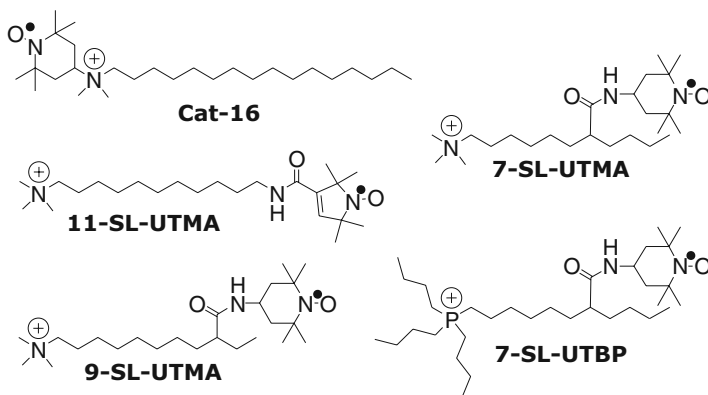
Scheme 9.1 Spin tracers for surfactant molecules in OMLS and PLSN.

which are proportional to the number of nuclei and to the inverse sixth power of the distance between the electron and nuclear spin [10, 15].

9.2.4
Spin Labeling of the Surfactant Interphase

The layer of cationic surfactants can be addressed by spin tracers that are themselves cationic surfactants. One such compound (Cat-16 in Scheme 9.1) is commercially available. Cat-16 incorporates in OMLS and PLSN, as evidenced by ^{19}F hyperfine coupling to fluorine nuclei in the fluoromica Somasif ME-100 [6] and is sensitive to surfactant loading and the presence of the polymer [15]. However, this compound has the disadvantage of headgroup modification with respect to the native surfactants. Such headgroup modification leads to an unnecessary perturbation of the material, even if surfactant–silicate interaction remains largely intact, since only about 1% of the surfactant molecules is substituted by spin tracers. More importantly, the observer surfactant molecule has an interaction energy with the silicate surface that is different from the one of the native surfactant molecules, which presumably leads to different dynamics and may lead to different local structure.

To overcome these disadvantages, we designed surfactant spin tracers with unmodified headgroups [15, 16]. These spin tracers are based on an undecyl chain and either TMA or TBP headgroups, so that both types of cationic surfactants can be matched. The spin label is 4-hydroxy-2,2,6,6-tetramethyl-piperidin-1-oxyl (TEMPOL), which is attached by an amide linkage at position 7 or 9 of the undecyl chain or a 3-carbamoyl-2,2,5,5-tetramethyl-3-pyrrolin-1-oxyl label that is attached to the chain end by an amide linkage (Scheme 9.1). The different label positions allow for addressing different locations in the surfactant interphase without coming too close to the silicate surface.

9.3
Characterization of Organically Modified Layered Silicates

9.3.1
Heterogeneity of Organoclays

The first spectra of Cat-16 and 11-SL-UTMA in OMLS based on the fluoromica Somasif ME-100 and synthetic Laponites revealed two or three dynamic components, respectively [6]. The slow-motion EPR spectra at ambient temperature revealed variation of the outer extrema separation $2A'_{zz}$ with surfactant loading, as quantified by the ratio R of surfactant concentration to cation exchange capacity (CEC) of the silicate (Figure 9.3a).

This variation can have two reasons. First, the polarity of the spin label environment is larger in the first adsorption layer on the ionic silicate which leads to larger A_{zz}. Second, mobility is higher for surfactant molecules whose headgroups are not directly attached to the silicate surface, which leads to a reduction in $2A'_{zz}$ as compared to $2A_{zz}$. Surprisingly, variation is already observed at surfactant loadings $R < 1$, which indicates that the headgroups interact with surface sites of different polarity or different surface energy.

In the ^{31}P NMR spectra of Somasif ME-100 modified with hexadecyl-TBP (HTBP) a second component with different chemical shift arises for surfactant loadings $R > 1$ (Figure 9.3b). This component can be interpreted as a fraction of surfactant molecules without direct headgroup contact to the silicate surface (remote surfactant molecules). The chemical shift difference is presumably due to susceptibility differences near to and remote from the silicate. A close look reveals that the chemical shift of the peak assigned to directly silicate-attached
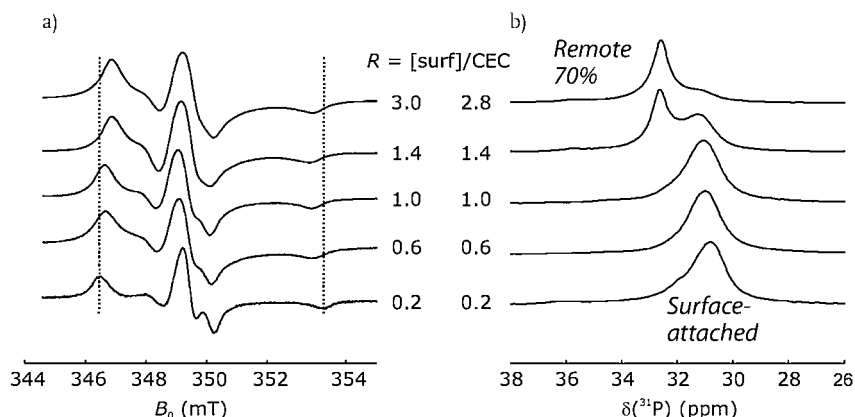
Figure 9.3 Variation of EPR spectra of Cat-16 (a) and ^{31}P NMR spectra of HTBP in Somasif ME-100 organically modified by HTMA (a) or HTBP (b). Spectra are shown for different surfactant loadings. Dotted lines in (a) are guides to the eyes to point out variation of $2A'_{zz}$.

surfactant varies with surfactant loading for $R < 1$. This again indicates the presence of different surface sites.

When a surfactant-deficient sample ($R = 0.8$) was studied by variable-temperature NMR, the narrow peak at larger chemical shift appeared at about 320 K and dominated the spectrum at 400 K [15]. This leads to the notion of a temperature-dependent CEC. Headgroups of HBP surfactants appear to dissociate from the silicate surface at higher temperatures.

This relatively simple picture needs to be modified in the face of evidence from small-angle x-ray scattering (SAXS) on heterogeneous layer stacking in surfactant-excess ($R = 2.8$) Somasif organoclays [17]. Analysis of temperature-dependent SAXS profiles indicates an AB superstructure in layer stacking, with alternating thick (A) and thin (B) surfactant layers, at ambient temperature. In as-prepared organoclay this structure exists beside AA-type stacks with only thick layers. On heating, the AB superstructure vanishes, the fraction of AA-type stacks increases, and BB-type stacks form. On subsequent cooling, AB-type stacks reform, but now at the expense of AA-type stacks. After one thermal cycle the organoclay consists of a mixture of AB-type stacks with superstructure and BB-type stacks with thin surfactant layers.

This behavior and the heterogeneous morphology of Somasif ME-100, revealed by transmission electron microscopy (TEM) in the same study [17], complicate analysis of the NMR and EPR results. Therefore, we performed further studies [14, 18] with the synthetic layered silicate magadiite that is morphologically uniform, exhibits only one interlayer peak in wide-angle x-ray scattering (WAXS) profiles, and has the additional advantage of being free from paramagnetic iron(III) impurities [18].

9.3.2
Heterogeneity and Position Dependence of Surfactant Dynamics

Surfactant dynamics was found to be heterogeneous, independently of the position of the spin label in the surfactant and of structural heterogeneity of the layered silicate [16, 18]. This heterogeneity is most clearly visible for the headgroup-labeled spin tracer Cat-16 (Figure 9.4a), where at $R = 2.8$ and a temperature of 433 K about 90% of the nitroxide labels still exhibit a rigid-limit spectrum (blue component), whereas the remaining 10% are highly mobile (red component). The large fraction of immobilized TMA surfactant compared to the NMR results for TBP surfactant [15] suggest that at 400 K most headgroups are mobile on the NMR time scale (longer than a microsecond), but rigid at the EPR time scale (shorter than 10 ns). Note that the results cannot be directly compared, since the headgroups differ. Comparison of data for TMA and TBP probes in [16] does however suggest that HTBP layers are less mobile at a given temperature than hexyl-TMA (HTMA) layers. This is consistent with lifetimes of surfactant-silicate contact at 400 K on the order of 100 ns.

For labels attached *near* the chain end, the slow component (blue arrow) is more mobile and the fast component (red arrow) less mobile than for the headgroup
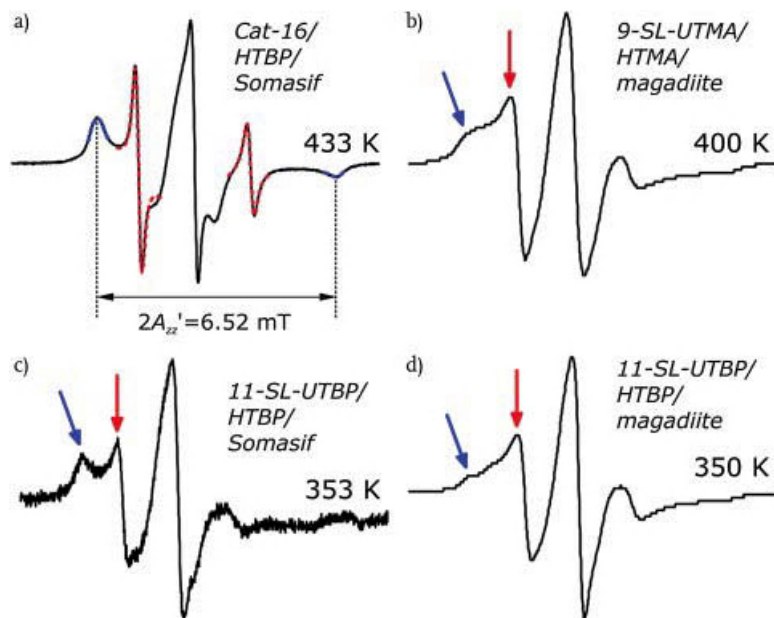
Figure 9.4 CW EPR spectra in OMLS at elevated temperatures for different surfactant spin tracers (see Scheme 9.1) combined with different native surfactants and layered silicates.

label (Figure 9.4b). If the label is attached *at* the chain end, a very similar spectrum is observed already at 50 K lower temperature (Figure 9.4d). This suggests that mobility of the major, slowly moving fraction of surfactants steadily increases from the headgroup toward the chain end. Complete analysis of the data supports this conclusion [16], which was also confirmed by others by NMR for TBP surfactants in different OMLS [19]. Comparison of Figure 9.4c and d indicates that surfactant immobilization on Somasif ME-100 surfaces is slightly stronger than on the surface of synthetic magadiite.

9.3.3
Further Features of Surfactant Dynamics

Molecular motion of TMA surfactants in organomagadiites was studied in more detail by variable-temperature ^{2}H solid-state NMR [18]. For this study HTMA was specifically deuterated either in the headgroup methyl groups (d$_9$HTMA, see Figure 9.2) or in one of the two methylene groups that are closest to the headgroup (dαHTMA, 1-position and dβHTMA, 2-position). The NMR results thus complement the EPR results for labeling positions 7, 9, and 11 of UTMA.

At ambient temperature (298 K) the NMR spectrum of d$_9$HTMA is much narrower than the ones of dαHTMA and dβHTMA (Figure 9.5), although the
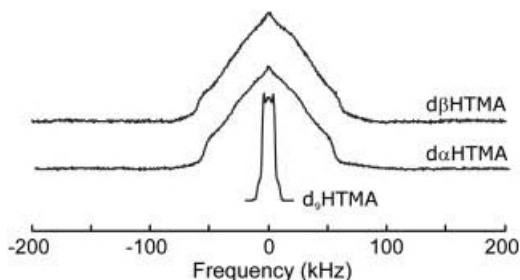
Figure 9.5 ^{2}H solid-echo NMR spectra of hexadecyl-TMA organomagadiites at 298 K.

rigid-limit linewidths for methyl and methylene deuterons hardly differ. This is explained by fast three-site jumps of the methyl groups around the CD_3–N bond concomitant with fast three-site jumps of the complete headgroup around the $(CD_3)_3$N–C bond. Superposition of these two rotations leads to a narrowing by a factor of about nine with respect to the rigid-limit spectrum. Three-site jumps of the complete headgroup may also explain why the fast component in the EPR spectra of Cat-16 corresponds to a more mobile nitroxide label than the fast components in spectra of the other spin labels.

The ^{2}H NMR spectra of dαHTMA and dβHTMA at 298 K hardly differ from each other (Figure 9.5), but differ significantly from the rigid-limit spectra observed at 233 K and below [18]. This can be assigned to rotation of the alkyl chain around its long axis, which affects the methylene protons in all positions along the chain in the same way. At 353 K all three spectra further narrow and a slight, but clearly significant difference becomes visible between dαHTMA and dβHTMA [18]. This can be assigned to a wiggling motion of the alkyl chain with respect to the headgroup, which causes a mobility gradient along the chain, with the chain end being more mobile. Such motion again is in agreement with the EPR results that also imply increasing mobility toward the chain end. Arrhenius plots of CW-EPR-derived rotational correlation times for TBP surfactant spin tracers show activation of a motional component at the order–disorder transition of the surfactant layer of 328 K. This component can be identified with the wiggling motion, whose molecular origin is trans-gauche transitions along the alkyl chain.

9.3.4
Structural Aspects of the Surfactant Layer

Contact between the headgroups of native surfactant molecules and spin labels at different positions along the alkyl chain of surfactant spin tracers was studied by ^{2}H ESEEM [14, 16]. The spectra clearly prove contact between a label at the chain end and the headgroup layer, suggesting that the alkyl chains lie almost flatly on the surface (Figure 9.6). This confirms a surfactant layer structure that had been
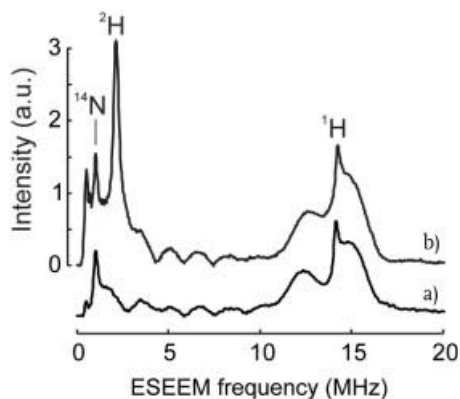
Figure 9.6 ^{2}H ESEEM spectra of 11-SL-UTMA in HTMA layers of organomagadiites. (a) Control with protonated HTMA. (b) Spectrum obtained with d$_9$HTMA.
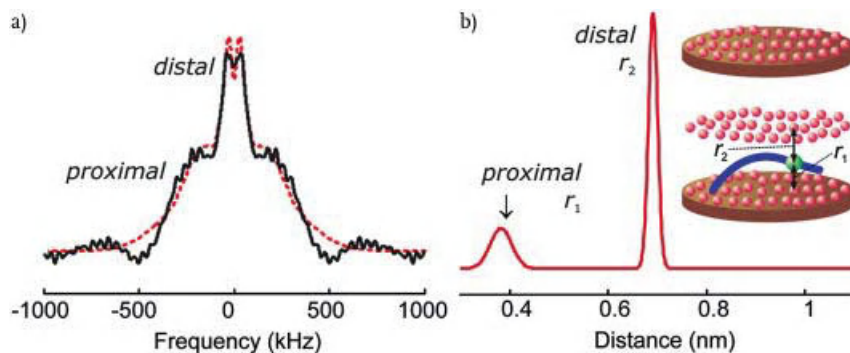
Figure 9.7 ^{31}P ENDOR on 11-SL-HTBP in HTBP/magadiite OMLS. (a) Matrix Mims ENDOR spectrum (black) and fit (red). (b) Distance distribution that fits the experimental spectrum. The inset shows interpretation of the distances with silicate platelets indicated as brown disks, surfactant headgroups as red spheres, the alkyl chain of the surfactant spin tracer as a blue string, and the spin label as a green sphere.

proposed before on the basis of less direct evidence [5]. Closer inspection of ^{2}H ESEEM intensities shows that in both Somasif-based [16] and magadiite-based [14] OMLS the contact between label and headgroups is even somewhat stronger at the chain end than closer to the center of the chain (positions 7 and 9). Note that headgroup contact of the label is revealed in the ESEEM spectra also by the narrow ^{14}N peak that can be assigned to nitrogen in a nearly tetrahedral environment (Figure 9.6), that is, to the quaternary ammonium group [20]. Therefore, such contact can also be proved without resorting to specifically deuterated surfactants.

Conformation of the surfactant tracers with respect to the headgroup layer in HBP surfactants was investigated by ^{31}P ENDOR [14]. Invariably, the spectra show two clearly distinguishable signals (for example, see Figure 9.7), corresponding to

a proximal distance (0.36 . . . 0.48 nm) and a distal distance (0.69 . . . 0.88 nm). In agreement with the ^{2}H ESEEM experiments, the proximal distance is slightly shorter for the chain-end label in 11-SL-UTBP than for the labels closer to the chain center in 9- and 7-SL-UTBP [14].

The distal distance does not agree with expectations for the distance to the surfactant layer on the opposing silicate platelet in a stack, which should be about twice as long according to WAXS data on basal spacing [14, 18]. This distance of about 1.9 nm to the next platelet is outside the sensitive range of ^{31}P matrix Mims ENDOR [21]. The same applies to the distance of more than 1 nm to the headgroup layer on the opposite side of the same silicate plate-let. Occurrence of a distance slightly less than half the distance to the next platelet suggests a multilayer surfactant structure. As sketched in Figure 9.7, one center layer in between the surface attached layers can explain the results. Such trilayer formation had been predicted before from molecular dynamics simulations of OMLS with alkyl chains grafted to the surface, for cases where the ratio between chain length and CEC is sufficiently large [22]. According to these predictions, multilayer formation may not depend on surfactant excess. Our samples were, however, surfactant-saturated ($R = 3.4$ for hexadecyl-TMA and $R = 2.8$ for hexadecyl-TBP surfactants) [18], so that we cannot draw a con-clusion on this point. Note also that our data cannot exclude a quadrilayer struc-ture [14].

Further information on surfactant distribution in OMLS can be obtained from DEER experiments. Primary DEER data are stretched exponential decays that cor-respond, within experimental error, to confinement of the label to two dimensions on the DEER background length scale below 20 nm [14]. On first sight, two-dimensional confinement is expected for surface-attached species. However, simu-lations show that dimensionality should approach three for stacks of five or more layers of such surfaces at the basal distance of 3.2 nm measured by WAXS. The DEER results thus imply an average stack thickness of less than 16 nm, which is in agreement with the large width of the d_{001} peak in WAXS and the strong attenu-ation of the d_{002} peak with respect to the d_{001} peak [14].

9.4
Characterization of Nanocomposites

9.4.1
Intercalated Nanocomposites and Nonintercalated Composites

We have studied composite formation by melt intercalation under 70 MPa pres-sure at a temperature of 433 K that exceeds the glass transition or melting tem-perature of the applied polymers poly(styrene) (PS), poly(caprolactone) (PCL), poly(ethylene oxide), poly(vinylidene fluoride), poly(ethyl methacrylate) (PEMA), poly(4-vinylpyridine) [6, 14–16, 18]. No shear stress was applied, so that exfoliation of the silicate stacks was unlikely to occur.

Virtually complete intercalation of PS with a molecular weight of 10 kDa (PS-10k) into an OMLS prepared from HTMA and Somasif ME-100 was observed by WAXS [15]. The d_{001} peak of the OMLS (basal spacing 2.16 nm) completely vanished and was replaced by a d_{001} peak at basal spacing of 3.38 nm. For PS with a molecular weight of 30 kDa we found partial intercalation (spacing of 3.26 nm) and only a slight widening of the basal spacing to 2.21 nm for the remaining, nonintercalated fraction of the OMLS. At a molecular weight of 100 kDa, only the slight widening was observed. For an OMLS prepared from HTBP and Somasif ME-100, only the slight widening was seen with both protonated and deuterated PS-10k [15]. We concluded that no significant intercalation occurred in these cases. PS-10k did not intercalate into OMLS prepared from synthetic magadiite and either HTMA or HTBP [18].

Composite formation for all other polymers was tested with the magadiite/ HTMA and magadiite/HTBP systems. Only PCL with molecular weight of 24 kDa intercalated into both systems, while PEMA with molecular weight of 250 kDa intercalated to a smaller extent in the HTMA system, but did not intercalate into the HTBP system. Taken together these results indicate that the thermally more stable HTBP surfactant is somewhat inferior to HTMA with respect to compatibilization between polymers and layered silicates. No correlation was found between glass transition temperature or dielectric constant of the polymer on the one hand and degree of intercalation on the other hand. Large molecular weight may hinder intercalation, as seen for PS; however, under the same conditions PEMA with an even higher molecular weight and only slightly lower glass transition temperature did intercalate. The fact that PCL and PEMA intercalate into magadiite OMLS, while none of the other polymers does, may suggest a favorable interaction of hydrogen-bond accepting carbonyl groups with the hydrogen-bond donating silicate surface.

In the following we distinguish between intercalated nanocomposites (INCs) and nonintercalated composites (NICs). The latter were designated as microcomposites in some of our earlier work [15, 16, 18]. This was a misnomer, since the DEER data obtained in [14] indicate a silicate stack thickness of less than 16 nm. It may well be possible that both INC and NIC could be extruded to exfoliated nanocomposites, but we did not test for this.

9.4.2
Influence of the Polymer on Surfactant Dynamics

In all cases, for both INC and NIC, composite formation strongly changes surfactant dynamics as observed in CW EPR spectra. In the absence of polymer, the fraction of fast surfactant molecules strongly increases above the order–disorder transition temperature T_{ODT} of HTBP (343 K), whereas in the NIC with PS such increase is observed only above the glass transition temperature of PS (370 K) [15]. Hence, composite formation with PS immobilizes the surfactant interphase. This is also observed for the INC obtained with OMLS prepared from HTMA and Somasif ME-100.
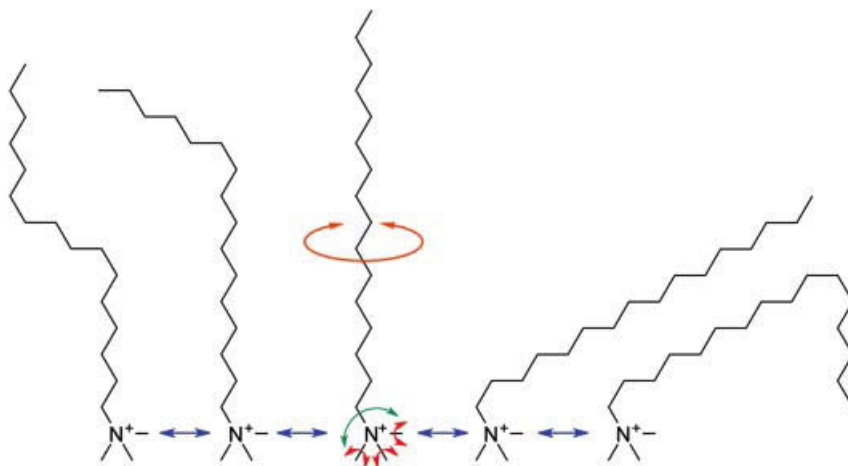
Figure 9.8 Schematic picture of surfactant dynamics in OMLS and PLSN. Rotation of the methyl groups in the headgroup (red arrows) and of the headgroup as a whole (green arrow) with respect to the alkyl chain persist to temperatures as low as −80 °C. Rotation of the molecule as a whole (orange arrow) is initiated between −40 °C and ambient temperature. Trans-gauche transitions in the alkyl chain (blue arrows), which lead to stronger dynamics toward the alkyl chain end, are activated at the order–disorder transition of the surfactant layer (OMLS) or at the glass transition temperature of the polymer (PLNS).

In contrast, formation of INC with PCL leads to mobilization of the surfactant interphase [18]. Arrhenius plots indicate that the character of surfactant motion changes near the melting temperature of PCL for 11-SL-UTBP and near the glass transition temperature of PS for all surfactant spin tracers in HTBP/magadiite NIC. Thus, dynamics of the polymer matrix governs dynamics of the surfactant interphase in both INC and NIC. For the NIC this may result from the pressure exerted by the rigid, glassy polymer matrix on the OMLS stacks below the glass transition temperature of PS. This pressure impedes the expansion of the stacks with increasing temperature that occurs in pure OMLS according to SAXS data [17].

An increase in dynamics from the headgroup toward the chain end, as observed before in pure OMLS, is also seen in INC and NIC [16, 18]. We can conclude that CW EPR senses the wiggling motion that is visualized in Figure 9.8 by an example set of trans-gauche conformational transitions. Activation of this wiggling motion is impeded by the high-T_g polymer PS as a matrix for the silicate stacks and eased by intercalation of the low-T_g polymer PCL.

9.4.3
Influence of the Polymer on Surfactant Layer Structure

Contact between the polymer and surfactant tracers was assessed by ^{2}H ESEEM for composites prepared with perdeuterated PS with a molecular weight of 10 kDa

Table 9.1 Normalized ^{2}H ESEEM peak intensities in composites prepared with perdeuterated PS and Somasif ME-100. ESEEM intensity has an experimental error of $\pm$0.30 due to noise level[a].

Surfactant	*R*	Tracer	ESEEM intensity
HTMA	3[b]	Cat-16	8.87
HTBP	0.8[c]	Cat-16	1.32
HTBP	1.7[c]	Cat-16	2.01
HTMA	3[b]	11-SL-UTMA	3.13
HTBP	1.7[c]	11-SL-UTMA	0.76

a) Surfactant saturation is characterized by the ratio *R* between surfactant concentration and CEC.
b) Nominal surfactant ratio in preparation.
c) Surfactant amount determined by quantitative ^{31}P NMR.

[15]. We have reprocessed these data using software developed in [14, 23] to quantify differences between INC and NIC and between different labels (Table 9.1). As expected, polymer/surfactant contact as accessed by the same spin tracer is much stronger for the INC prepared with HTMA surfactant than for the NIC prepared with HTBP surfactant. The ratio of ^{2}H ESEEM intensities between INC and NIC for surfactant-excess OMLS ($R > 1$) is about 4.3 and does not differ within experimental uncertainty for the head-labeled tracer Cat-16 and the tail-labeled tracer 11-SL-UTMA. The significant polymer/surfactant contact in NIC is further evidence for a large specific surface of OMLS particles in these samples, that is, for the small thickness of silicate stacks suggested by the DEER results (Section 4.1). Surfactant excess OMLS exhibit stronger polymer/surfactant contact than surfactant-deficient OMLS, indicating that part of the excess surfactant in NIC disperses in the polymer.

The same ^{2}H ESEEM technique can be applied to assess dilution of the surfactant layer by the polymer when using headgroup-deuterated native surfactant in conjunction with surfactant spin tracers and nondeuterated polymer [14]. In the INC obtained with PCL, the dilution ratio is approximately 3 near the surfactant chain end (tracers 11-SL-UTMA and 9-SL-UTMA) and approximately 7 closer to the alkyl chain center (7-SL-UTMA). By thermal gravimetric analysis (TGA) the HTMA fraction in the corresponding OMLS was determined as 85 mmol/100 g [24]. In composites prepared from 75% by weight polymer and 25% by weight OMLS, this corresponds to a polymer-repeat-unit-to-surfactant ratio of about 10 for both PS and PCL. The ^{2}H ESEEM results thus indicate rather intimate mixing of the surfactant interphase with the polymer, in particular, near the center of the alkyl chain.

Surprisingly, dilution ratios as large as 2.5 . . . 3 are found in the NIC prepared with PS. Even assuming that the silicate stacks are on average less than five layers thick, these results are hard to explain without assuming that composite formation leads to reorganization of the surfactant layer inside the stacks. Since contact

between the headgroups of the native HTMA surfactant on the one hand and the centers and tails of the surfactant spin tracers on the other hand decreases, the reorganization is most likely an increase in the tilt angle of the surfactant alkyl chains with respect to the silicate surface and, thus, to the attached headgroup layer.

Further information on the influence of polymers on surfactant orientation as well as on localization of the polymer chains was obtained with ^{31}P Mims matrix ENDOR (Figure 9.7) [14]. The mean proximal distance r_1 remains the same within experimental error on INC formation with PCL for all three tested surfactant spin tracers (11-, 9-, and 7-SL-UTBP). This indicates that the almost parallel orientation of the surfactant alkyl chains with respect to the silicate surface is maintained in these INC. In contrast, a significant increase of r_1 by 0.05 . . . 0.08 nm is observed with all tracers on NIC formation with PS. This is consistent with the hypothesis of an increase in tilt angle of the alkyl chains. Note, however, that the increase in mean distance r_1 is small with respect to the distance between the headgroup and the labeling sites (1.42, 1.17, and 0.91 nm). Thus, the average tilt angle of the alkyl chains with respect to the surface is still only about 20° in the NIC with PS, whereas it is about 15° in the OMLS and the INC with PCL. Since ^{31}P ENDOR overemphasizes short distances, these tilt angles have to be interpreted as lower limits.

The distal distance r_2 does not change significantly on formation of NIC with PS. This is expected, as for the magadiite NIC no significant increase in basal spacing is observed [24]. In contrast, the distal distance increases by 0.15 nm for 9-SL-UTBP and by 0.17 nm for 7-SL-UTBP on formation of INC with PCL. When comparing these changes to the increase in basal spacing by 0.6 nm, one might favor a surfactant quadrilayer model rather than the trilayer model indicated in the inset of Figure 9.7b. However, the layers are expected to be somewhat diffuse and ^{31}P Mims matrix ENDOR detects the distance of closest approach. If the center layer in a trilayer structure is diluted by the polymer, as is suggested by the ESEEM results, it becomes thicker and the distances of closest approach between this layer and the surface layers increases by less than half of the increase in basal spacing. In a quadrilayer model, such a dilution effect would need to be rather weak, since without any dilution the distance increase should be 0.2 nm. Hence, we slightly favor the trilayer model, but cannot exclude a quadrilayer model or the coexistence of models with different numbers of surfactant layers between a pair of silicate platelets.

In any case, the peak in the distance distribution at r_2 does not vanish or diminish in relative intensity on INC formation. This implies that the center layer does not dissolve. Rather the polymer chains are sandwiched between the existing surfactant layers. This finally leads to the schematic structural pictures of OMLS and INC shown in Figure 9.9. Surfactant chains are only moderately tilted away from the silicate surface and at least one, relatively well defined center layer of surfactant headgroups exists. Polymer intercalation leads to a moderate increase in headgroup layer distances. The polymer chains insert in both alkyl chain layers.
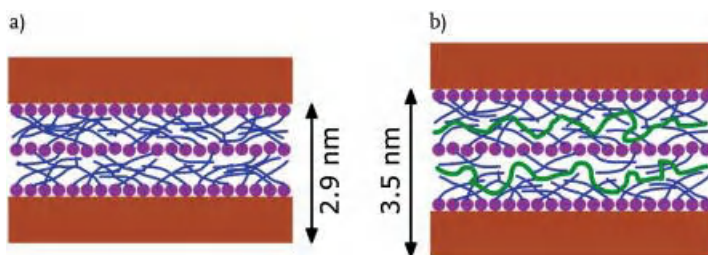
Figure 9.9 Schematic drawing of structural models of OMLS (a) and intercalated PLSN (b). Clay platelets (1 nm thickness) are shown in brown, surfactant headgroups in magenta, surfactant alkyl chains in blue, and polymer chains in green color. Dimensions are given for the OMLS and ICN prepared from HTBP, synthetic magadiite, and PCL, with reduced radii of surfactant headgroups and alkyl chains as well as the polymer chain to enhance clarity.

9.5
Conclusion

EPR spectroscopy on surfactant spin tracers and solid-state NMR spectroscopy can provide a wealth of data on surfactant dynamics and the structure of surfactant layers on a molecular level. In OMLS, surfactant headgroups rotate down to temperatures of $-80\,°C$, while rotation of the surfactant molecule as a whole about its long axis is activated between $-40\,°C$ and ambient temperature. Wiggling motion of the surfactant chain leads to a dynamic gradient along the alkyl chain with higher mobility at the chain end. This motion, whose molecular origin is trans-gauche transitions along the alkyl chain, is activated at the order–disorder transition of the surfactant layer. The long axes of the surfactant molecules are tilted by an angle of only about 15° with respect to the silicate surface. In the surfactant-excess OMLS, which provide better results in nanocomposite formation than stochiometric or surfactant-deficient OMLS, a center layer of surfactant headgroups exists. In the temperature range between ambient temperature (298 K) and the decomposition temperature of the surfactants (above 433 K), thermally activated dissociation of the surfactant headgroups from the silicate surface is observed. The OMLS, prepared by precipitation of layered silicate dispersions with cationic surfactants, are characterized by a mean stack thickness of not more than 16 nm (five layers).

Melting of the OMLS with polymers under a moderate pressure of 70 MPa leads to intercalation of the carbonyl-group-containing polymers PCL and PEMA, but not of poly(ethylene oxide), poly(vinylidene fluoride), or poly(4-vinylpyridine). PS exhibits borderline behavior with respect to intercalation. This polymer, which presumably is compatibilized by surfactant headgroups via cation-π interactions, intercalates at sufficiently low molecular weight into OMLS prepared from Somasif ME-100 and HTMA, but not in those prepared from HTMA with HTBP or from synthetic magadiite with any of the two surfactants. The lower propensity of HTBP

to compatibilize PS is in line with the expected weaker cation-π interactions due to screening of the charge by the bulkier alkyl chains.

Significant contact between polymer and surfactant molecules in NIC confirms the small stack size, which leads to a large fraction of surfactant molecules on the silicate stack surface. Furthermore, activation of the wiggling motion of the surfactants in NIC sets in at the glass transition temperature T_g of the polymer, if T_g is above the order–disorder transition temperature T_{ODT} of the surfactant layer in pure OMLS. Formation of NIC leads to reorganization of the surfactant layer with a slight increase in tilt angle of the surfactant layer with respect to the silicate surface. This effect may result from a temperature dependence of mean tilt angle together with solidification of the stacks at a higher temperature when they are dispersed in a matrix of high-T_g polymer.

INCs are characterized by a significant increase in basal spacing of the silicate stacks. The activation temperature of surfactant wiggling dynamics is set by the glass transition temperature of the intercalated polymer, both for $T_g > T_{ODT}$ and for $T_g < T_{ODT}$. The mean tilt angle of the surfactant alkyl chains with respect to the silicate surface is hardly affected by intercalation. Headgroups, chain centers, and chain ends of the surfactants are all in contact with the polymer, at least for PS. The polymer chains insert in the alkyl chain bilayers between the surface-attached surfactant headgroup layer and the surfactant headgroup center layer, forming a double-decker sandwich structure.

Acknowledgments

References

1 Ray, S.S., and Okamoto, M. (2003) *Prog. Polym. Sci.*, **28**, 1539–1641.

2 Utracki, L.A., Sepehr, M., and Boccaleri, E. (2007) *Polym. Adv. Technol.*, **18**, 1–37.

3 Cygan, R.T., Greathouse, J.A., Heinz, H., and Kalinichev, A.G. (2009) *J. Mater. Chem.*, **19**, 2470–2481.

4 Xie, W., Xie, R.C., Pan, W.P., Hunter, D., Koene, B., Tan, L.S., and Vaia, R. (2002) *Chem. Mater.*, **14**, 4837–4845.

5 Vaia, R.A., Teukolsky, R.K., and Giannelis, E.P. (1994) *Chem. Mater.*, **6**, 1017–1022.

6 Jeschke, G., Panek, G., Schleidt, S., and Jonas, U. (2004) *Polym. Eng. Sci.*, **44**, 1112–1121.

7 Schmidt-Rohr, K., and Spiess, H.W. (1994) *Multidimensional Solid-State NMR and Polymers*, Academic Press.

8 Spiess, H.W. (1985) *Adv. Polym. Sci.*, **66**, 23–58.

9 Weil, J.A., Bolton, J.R., and Wertz, J.E. (1994) *Electron Paramagnetic Resonance*, John Wiley & Sons, Inc., New York.

10 Schweiger, A., and Jeschke, G. (2001) *Principles of Pulse Electron Paramagnetic*

Resonance, Oxford University Press, Oxford.

11 Jeschke, G., and Schlick, S. (2006) Advanced ESR methods in polymer research, in *Continuous-Wave and Pulsed ESR Methods* (ed. S. Schlick), John Wiley & Sons, Inc., New York.

12 Schneider, D.J., and Freed, J.H. (1989) *Biol. Magn. Reson.*, **8**, 1–76.

13 Santangelo, M.G., Levantino, M., Cupane, A., and Jeschke, G. (2008) *J. Phys. Chem. B*, **112**, 15546–15553.

14 Mao, Q., Schleidt, S., Zimmermann, H., and Jeschke, G. (2008) *Phys. Chem. Chem. Phys.*, **10**, 1156–1167.

15 Panek, G., Schleidt, S., Mao, Q., Wolkenhauer, M., Spiess, H.W., and Jeschke, G. (2006) *Macromolecules*, **39**, 2191–2200.

16 Schleidt, S., Spiess, H.W., and Jeschke, G. (2006) *Colloid Polym. Sci.*, **284**, 1211–1219.

17 Gelfer, M.Y., Burger, C., Nawani, P., Hsiao, B.S., Chu, B., Si, M., Rafailovich, M., Panek, G., Jeschke, G., Fadeev, A.Y., and Gilman, J.W. (2007) *Clays Clay Miner.*, **55**, 140–150.

18 Mao, Q., Schleidt, S., Zimmermann, H., and Jeschke, G. (2007) *Macromol. Chem. Phys.*, **208**, 2145–2160.

19 Mirau, P.A., Serres, J.L., Jacobs, D., Garrett, P.H., and Vaia, R.A. (2008) *J. Phys. Chem. B*, **112**, 10544–10551.

20 Hinderberger, D., Spiess, H.W., and Jeschke, G. (2004) *J. Phys. Chem. B*, **108**, 3698–3704.

21 Zanker, P.P., Jeschke, G., and Goldfarb, D. (2005) *J. Chem. Phys.*, **122**, 024515.

22 Hackett, E., Manias, E., and Giannelis, E.P. (1998) *J. Chem. Phys.*, **108**, 7410–7415.

23 Volkov, A., Dockter, C., Bund, T., Paulsen, H., and Jeschke, G. (2009) *Biophys. J.*, **96**, 1124–1141.

24 Mao, Q. (2007) Synthesis and Characterization of Structurally Well-Defined Polymer-Layered Silicate Nanocomposites. PhD thesis, University of Mainz.

10
Characterization of Rheological Properties of Polymer Nanocomposites

Mo Song and Jie Jin

10.1
Introduction

Over the last 20 years, considerable efforts around the world have been devoted to the development of a new class of polymer nanocomposites, in which nanofillers are dispersed at a molecular level in the polymer matrix to reinforce and provide novel characteristics [1–3]. The various types of nanofillers such as layered silicate, graphite nanosheets, carbon nanotubes (CNTs), nanofibers, metal oxide nanoparticles, and layered titanate have been used to produce a variety of polymer nanocomposites for many industry applications [1–10]. Polymer nanocomposites with very low filler loadings have shown a number of impressive property enhancements, including mainly increased tensile strength, modulus, hardness and fracture toughness, decreased gas permeability and flammability, improved thermal stability and specific heat resistivity, and electrical and optical properties [1, 11–17]. However, such property enhancements depend on effective dispersion of these nanofillers in the polymer matrix and the ability of the particle surface to alter polymer segment dynamics [1–3]. The state of dispersion is sensitive to the forces that act between particles dispersed in polymer and how these forces drive particle organization. These conditions can be created in a solvent medium or in molten state using mixing processes governed by the flow pattern and rheology of the systems [18]. Generally, the introduction of nanofillers within a polymeric matrix causes more difficulties in the processing. The mobility of the particles is reflected by viscosity, viscoelasticity, moduli, etc. Accordingly, understanding of the rheological properties of such nanocomposites is of significant importance for mastering the process parameters that lead to controlled microstructure, which in turn enables design of the properties of the end-use products [19, 20].

Rheology has been extensively used in the study of nanocomposite systems in conjunction with basic characterization techniques such as XRD, SEM, and TEM [21]. A large number of rheological studies on polymer nanocomposites have been

published in the last few years. It is believed that rheology offers an effective way to assess the state of nanofiller dispersion and to detect the presence of interconnecting microstructure of the nanocomposites in molten state directly. In this chapter, the authors will introduce some basic rheological theories and give a brief review of the current study on understanding of the rheological properties of polymer nanocomposites.

10.2
Fundamental Rheological Theory for Studying Polymer Nanocomposites

Rheology is science that deals with the way materials deform when forces are applied to them. Similar to those of general multiphase systems, rheological behavior of polymer nanocomposites is affected by discontinuity of material properties in the material domains, the presence of concentration gradient due to nonhomogeneity, and orientation of the flow element due to the presence of dispersed phases. In particular, for polymer nanocomposites the rheological properties are influenced by the nature of structure formed, depending on the state of nanofillers dispersion in the matrix, the polymer–nanofiller interactions, imposed stress, and orientation of flow domains. In rheological measurements, three types of flow are often applied: the steady-state shear, dynamic shear, and external flow. The steady-state shearing is important for predicting processability and performance of polymer nanocomposites. It can provide some information of flow-induced changes of morphology, indicating a great diversity of structures within the nanocomposite family. Dynamic measurements are very useful in analyzing the viscoelastic response of nanostructured dispersion, used to predict interconnecting microstructure of the samples. Dynamic testing of a material may be conducted by creep and creep recovery, stress relaxation, or oscillatory deformation. Most studies on polymer nanocomposite flow focused on the linear viscoelastic behavior. The solid-like behavior at small deformation rates claim that the nonterminal flow region is the most important characteristic of polymer nanocomposites. The extensional flow leads to uniform deformation under well-controlled conditions recording the stress growth function at constant deformation rate. This can provide valuable information regarding the orientation of the dispersed phase in the form of particles.

In practice, understanding of the steady flow is essential in polymer rheology because many industrial processes encounter shear flow behavior. There are three important rheological parameters measured with imposition shear: viscosity, η, shear stress, σ, and the first normal stress difference, N_1. Each of these parameters depends on the shear rate and the dependences are associated with particle rotations in shear flow [22]. Commonly, three geometric arrangements are used to measure fluid viscosity, capillary, coquette, and cone and plate. In capillary instruments, the fluid is forced though the capillary by application of pressure. For steady-state shear, viscosity can be determined by Poiseuile's equation. For a dilute solution, this may be written as follows [23]:

$$\eta = \frac{\pi r_c^4 \Delta P t}{8 V L_c} \tag{10.1}$$

where r_c and L_c are the radius and length of the capillary, respectively, ΔP is the pressure drop, V is the volume of fluid that passes through the capillary, and t is the flow time. The corresponding shear stress at the capillary wall is

$$\sigma = \frac{r_c P}{2 L_c} \tag{10.2}$$

and the rate of shear at the wall for a Newtonian fluid is

$$\dot{\gamma} = \frac{\sigma}{\eta} \tag{10.3}$$

$$\dot{\gamma} = \frac{4V}{\pi r_C^3} \frac{1}{t} \tag{10.4}$$

In nanocomposite systems, the rheological properties of particulate suspensions are sensitive to the particle size, shape, and surface characteristics of the dispersed phase. The relative viscosity, η_r, of suspensions in a Newtonian medium as a function of the volume fraction of the suspended particles, φ, might be expressed as [24]

$$\eta_r = 1 + [\eta]\varphi + k_1([\eta]\varphi)^2 + \cdots + k_{n-1}([\eta]\varphi)^n \tag{10.5}$$

where the intrinsic viscosity, $[\eta]$, depends on the rigidity and shape of the suspended particles and k is an interaction constant. In a shear field the particles rotate with a period dependent on the rate of shearing, $\dot{\gamma}$, and aspect ratio, p:

$$t = \frac{2\pi}{\dot{\gamma}}\left(p + \frac{1}{p}\right) \tag{10.6}$$

where a customary definition of the aspect ratio is used ($p > 1$), p being defined as the ratio of the largest to the smallest dimension, that is, for rods, $p =$ length/diameter, and for disk $p =$ diameter/thickness. The experimental data of $[\eta]$ versus p for disks polydispersed in size and shape with $p \leq 300$ followed the empirical dependence [23].

$$[\eta] = 2.5 + 0.025\left(1 + p^{1.47}\right) \tag{10.7}$$

The effect of concentration on viscosity can be explained by a mean field equation [24, 25]. In the mean field theory, the incremental viscosity changes with the volume fraction, $d\varphi$, of nanofillers added into suspension, and the viscosity, $\eta(\varphi)$, becomes [24, 25]

$$\eta(\varphi + d\varphi) = \eta(\varphi)[1 + d(\ln\varphi)] \tag{10.8}$$

Assuming that $\eta(\varphi)$ obeys Einstein's theory of intrinsic viscosity $[\eta]$, then the equation can be written as

$$\eta = \eta(\varphi = 0)\left(1 - \varphi/\varphi_\infty\right)^{-[\eta]\varphi_\infty} \tag{10.9}$$

Here, $\eta(\varphi = 0)$ is the viscosity of the suspending medium, φ_∞ is the viscosity percolation threshold corresponding to the critical volume fraction at which particles are packed such that the viscosity of the suspension becomes infinite, showing no Newtonian plateau at low shear rates. For suspensions of spherical particles a monotonic increase was observed. Experimentally, in the polymer/clay nanocomposites the critical volume fraction $\varphi_\infty = 0.62$ for monodispersed hard spheres and $\varphi_\infty = 0.78$ to 0.87 for polydispersed spheres [26, 27]. Within this concentration range the disks show two regions of behavior, the first stretching from zero up to the limit of the free rotation, corresponding to φ_∞, and the second above it. Within the first, the disks are free to assume a random orientation; thus, in molten polymer they present exfoliated polymer nanocomposites. Within the second, $\varphi > \varphi_\infty$ free rotation is impossible; thus, the platelets align. In geometrical consideration, the limiting concentration, corresponding to the critical volume fraction φ_∞, can be calculated by the following equation:

$$\varphi_\infty = \frac{a_0}{p} \tag{10.10}$$

where a_0 is constant. For monodispersed and polydispersed oblate ellipsoids a_0 is 0.93 or 1.24, respectively [26, 27]. Empirically, for $p < 100$ the following dependence was suggested [28]:

$$\frac{1}{\varphi_\infty} = 1.55 + 0.0598p \tag{10.11}$$

or

$$\frac{1}{\varphi_\infty} = 0.136 + 1.401p^{1/3} \tag{10.12}$$

The two empirical relations have been used to describe most of nanocomposite systems. For low p the geometrical dependence offers reasonable maximum volume fraction prediction [27, 29].

The shear viscosity of the nanocomposites increased monotonically with nanofiller loading and displayed shear thinning behavior at higher shear rates. This non-Newtonian behavior is of tremendous practical importance in processing and fabrication of polymer nanocomposites. The decreased viscosity makes melt polymer easier to process. In order to quantify this effect, a large number of equations have been developed, both empirically and theoretically. The Herschel–Bulkley model [30] is commonly used to describe the thinning behavior of fluids such as mud and clay suspensions [31]. Herschel–Bulkley equations are given by

$$\sigma = \sigma_y + k\dot{\gamma}^n \tag{10.13}$$

$$\eta = \frac{\sigma_y}{\dot{\gamma}} + k\dot{\gamma}^{n-1} \tag{10.14}$$

Equation (10.14) is used to calculate the viscosity, η, of suspensions or fluid in consideration. Here σ is shear stress, σ_y, is yield stress, $\dot{\gamma}$ is shear rate, k is a

constant, and n is the flow behavior index, which depends on the type of fluid. When $n > 1$, the fluid exhibits a shear thickening behavior; when $n = 1$, the fluid exhibits a Bingham plastic behavior; when $n < 1$, the fluid exhibits a shear thinning behavior, which is a case that is commonly observed with polymer nanocomposites. The model reduces to a power law model when σ_y is equal to zero. It is well known that the n, k, σ_y values are functions of the type fluid. Typical curves for the viscosity as a function of shear rate for different temperatures can be found in Figure 10.7.

The steady-shear viscosities for the nanocomposites exhibit enhanced shear-thinning behavior at low shear rates. At high shear rates the viscosities show more decreased values from the zero-shear viscosities with increasing filler loading and the values are almost identical to those of unfilled polymers. To examine the relationship between shear viscosity (η) and shear rate ($\dot{\gamma}$), the Carreau equation is used [23]:

$$\eta = \frac{\eta_0}{\left[1 + (\dot{\gamma}\lambda)^2\right]^{(1-n)/2}} \tag{10.15}$$

Here, η_0 is the zero-shear rate viscosity, λ is a characteristic (or relaxation) time, and n is the dimensionless parameter, where the slope of η versus $\dot{\gamma}$ in the power law region is given by $n - 1$. Note that, in the special case of $n = 1$ or $\dot{\gamma}\lambda \to 0$, Eq. (10.15) reduces to the Newtonian fluid model. For $n < 1$, the equation predicts shear-thinning behavior. A crossover from a Newtonian plateau to a shear-thinning region occurs at the critical shear rate $\dot{\gamma}_c$. $\dot{\gamma}_c$ is approximately equal to the inverse of the characteristic time, which is the longest relaxation time required for the elastic structures.

Nanofiller size, shape, and concentration have a strong influence on the elasticity of polymer nanocomposite, which can be characterized by the first normal stress difference, N_1, resulting from the filler orientation and extension of polymer chain segments. In steady shear measurements, first normal stress difference, N_1, of polymer melt or polymer solution at fixed concentration depends on both temperature and shear rate. The Maxwell equations are generally used [24]:

$$N_1 = \frac{2t\sigma^2}{\eta} \tag{10.16}$$

$$t = \frac{K\eta_S M^3/2\alpha^3}{T} \tag{10.17}$$

where t and η are, respectively, the constant-relaxation time and shear viscosity and α is expansion factor whose value depends on temperature and corresponds to the behavior in linear viscosity range. The maximum observed value of α is 2. There are some reports regarding the effect of nanofillers on the elasticity of polymer nanocomposites [32, 33]. For the nanocomposite containing near isotropic fillers, such as TiO_2, $CaCO_3$, and carbon black, the first normal stress difference, N_1, decreases compared with that of unfilled polymers. But in the case of

anisometric fillers, for example, fibers, the normal stresses are higher, leading to higher elasticity of the nanocomposites. This is due to hydrodynamic particle effects as a result of strong orientation in flow direction. Increasing filler concentration showed a decrease of the elasticity of the nanocomposite, which was resulted from reducing mobility of the polymer chains in the presence of the filler and leading to increased rigidity [32].

The dynamic shear measurements have been used for characterization of a large number of nanocomposites. Because of the complications caused by the stress-induced orientation of nanofillers resulting in different rheological responses, small deformation amplitude oscillatory shear measurements are generally performed by applying a time-dependent strain and measuring the resultant shear stress [23, 24],

$$\gamma(t) = \gamma_0 \sin(\omega t) (1) \tag{10.18}$$

$$\sigma(t) = \sigma_0 (\sin \omega t + \delta) \tag{10.19}$$

where $\gamma(t)$ is the sinusoidal strain; γ_0 is the strain amplitude; ω is the frequency of oscillation; $\sigma(t)$ is the sinusoidal stress; σ_0 is the stress amplitude; and δ is the phase lag angle. The elastic (storage) modulus G', viscous (loss) modulus G'', and η^* complex viscosity can be derived as follows:

$$G' = \left(\frac{\sigma_0}{\gamma_0} \right) \cos \delta \tag{10.20}$$

$$G'' = \left(\frac{\sigma_0}{\gamma_0} \right) \sin \delta \tag{10.21}$$

$$\eta^* = \sqrt{\left(\frac{G'}{\omega} \right)^2 + \left(\frac{G''}{\omega} \right)^2} \tag{10.22}$$

Generally, the region of linear viscoelascity is very sensitive in the presence of nanofillers, especially at low frequencies. These viscoelastic parameters directly correspond to the presence of the interconnecting structure. The viscoelastic response can predict the boundary of intense interparticle connectivity or physical cross-linking often offered to as the rheological percolation threshold. From a rheological viewpoint, evaluation of the percolation threshold can be characterized by a zero-slope plateau in the tan δ versus frequency curve at low frequency. The zero-slope plateau in the tan δ versus frequency curve reflects the boundary between two opposing factors: the negative value of the slope of the tan δ curve for melts and the positive value for solid. This critical percolation point is dependent on the filler loading and temperature. The low percolation threshold for a polymer nanocomposite system is directly related to the high aspect ratio of nanofillers.

In small deformation amplitude oscillatory shear measurements, strain sweeps can determine a range of variables where the linear viscosity is to be found. The experimental data can be described by KBKZ's model [34]:

$$G'(\gamma) = \frac{G_0'}{1 + G_1'\gamma_f^2 - G_2'\gamma_f^3} \tag{10.23}$$

$$G''(\gamma) = \frac{G_0'}{1 + G_1'\gamma_f^2 - G_2'\gamma_f^3} \tag{10.24}$$

where γ_f is the strain fraction and G_i are equation parameters with G_0 defining the linear viscoelastic values of G' and G''.

Extensional viscosity is the measure of resistance of a material subjected to stretching flow under well-controlled conditions and is identified by the extensional stress recording the stress growth function at a constant Hencky strain rate and temperature. In a typical extensional viscosity profile the extensional viscosity as a function of time shows two behaviors; the first corresponds to a gradual viscosity increase known as the linear region and the second to a rapid viscosity increase known as the nonlinear region [24]. In the nonlinear region of deformation, a strain hardening effect is observed. The extensional viscosity η_E at a constant Hencky strain rate $\dot{\varepsilon}$ is defined as

$$\eta_E(t) = \frac{\sigma_E(t)}{\dot{\varepsilon}} \tag{10.25}$$

Strain hardening (SH) is defined as a logarithm of a ratio of the stress growth function in elongation to three times that for the linear viscoelastic response in shear, with both values taken at the same temperature and time [35].

$$SH \equiv \log\left(\frac{\eta_E^+}{3\eta_S^+}\right) \tag{10.26}$$

Nanocomposite systems respond differently to extensional stresses. For example, exceptionally, diluted suspensions show strain softening [36]. This behavior can be applied to trace disturbance of the stress distribution around filler particles during extensional flow.

10.3
Characterization of Rheological Properties of Polymer Nanocomposites

Over the last few years, the rheological behavior of polymer/clay nanocomposites has been investigated extensively. The state of the dispersion of nanofiller studied is at two levels: (i) the macroscopic level, which involves the measurements of the rheological properties of the bulk blend, or (ii) the microscopic level, which investigates the detailed dynamics of the individual particles [37]. The steady shear viscoelasticity provides complementary information to the linear and nonlinear dynamic oscillatory shear measurements regarding the quiescent structure and ability of shear to deform and reorient nanoparticles in the nanocomposites. Generally, the shearing thinning behavior of polymer nanocomposites is that their viscosities are comparable with those pure polymers at high shear rate resulted by

the reorientation of nanofillers to the flow direction. At low shear rate and frequency, the shear thinning behavior is always minimal as observed in pure polymers. Pronounced shear thinning has been found to be a characteristic feature of truly nanodispersed composites. The degree of shear thinning behavior in response to extremely applied flow controls the viscoelastic properties of the nanocomposites. The rheological properties are influenced by many factors, including the filler content, the additives used, processing temperature, and the nature of polymer matrices [21].

Krishnamoorti and coworkers [38] first described the steady shear rheological behavior of intercalated or exfoliated nanocomposites based on poly(dimethyldiphenyl siloxane) (PDS) and layered silicate. Figure 10.1 represents steady shear rheological behavior for a series of intercalated nanocomposites with varying silicate contents. The viscosity of the nanocomposites was enhanced considerably at low shear rate and increased monotonically with increasing silicate loading. In the low shear rate region neat polymer showed Newtonian behavior, whereas the intercalated nanocomposites displayed a shear thinning behavior and this behavior was more prominent with high silicate loading. At a high shear rate, both neat polymer and its nanocomposites showed strong shear thinning behavior. Figure 10.2 shows the steady shear viscosity behavior for a series of exfoliated nanocomposites. The viscosity systematically increases with silicate loading but still obeys the Newtonian behavior in the lower shear rate region, even at the highest silicate loadings. In contrast between two types of the nanocomposite systems, the results indicate that highly anisotropic intercalated layered silicate
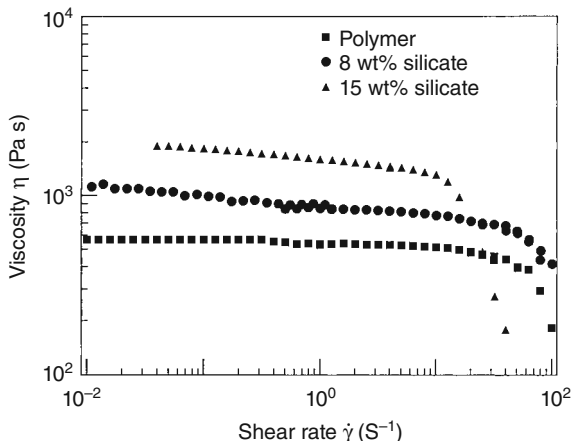
Figure 10.1 The steady shear rheological behavior for a series of intercalated nanocomposites of a copolymer of dimethylsiloxane and diphenylsiloxane with a dimethylditallow- montmorillonite with varying levels of silicate loadings at $T = 28\,°C$. Reproduced from reference [38] with permission.
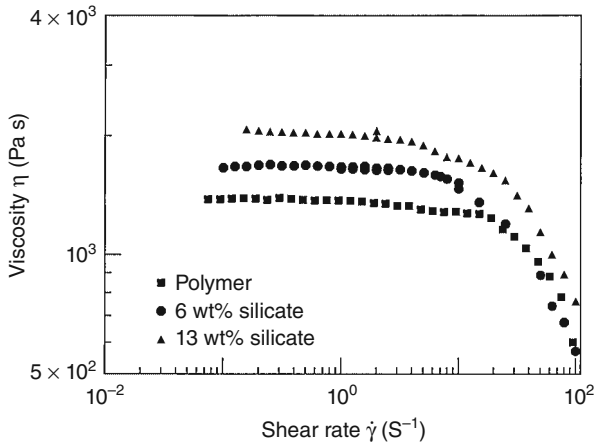
Figure 10.2 The steady shear viscosity behavior for a series of delaminated nanocomposites of poly(dimethylsiloxane) with dimethyl ditallow montmorillonite at 28 °C. Reproduced from reference [38] with permission.

particles alter the relaxation dynamics of the polymer chains, leading to the non-Newtonian behavior.

The shear viscosity behavior of intercalated nanocomposites based on biodegradable aliphatic polyesters (BAP) and organophilic montmorillonite (OMMT) was also reported by Lim and coworkers [39]. Figure 10.3 shows the shear viscosity as a function of the shear rate for BAP and its nanocomposites. Like other nanocomposite systems, the viscosities of BAP/OMMT nanocomposites were decreased with increasing shear rate. At very lower shear rates, the viscosity behaved a Newtonian plateau even for high OMMT content. However, at a high shear rate, these nanocomposites exhibited higher degrees of shear thinning behavior compared to the pure polymer. The degree of shear thinning increases with clay loading because of the alignment of clay layers under shear; the suspension microstructure changes from a random orientation to a shear-induced ordered orientation [40]. This observation suggests that the clay layers are strongly oriented toward the flow direction at high shear rates and that the shear thinning behavior observed at a high shear rate is dominated by that of the pure polymer. The scaling curves as shown in Figure 10.3b demonstrate a Newtonian plateau at low shear rates and power law behavior at high shear rates. The shear viscosities for BAP/OMMT were well represented by the Carreau model. From the measured shear viscosities, the critical shear rate for each sample was obtained as 0.18, 0.12, 0.08, 0.02, and 0.007 s^{-1} for BAP00, BAP03, BAP06, BAP09, and BAP15, respectively. It was observed that, at $\lambda \dot{\gamma}_c = 1$, a departure from the plateau region begins. The degree of shear thinning and relaxation time λ increased with OMMT loading.

a)

b)
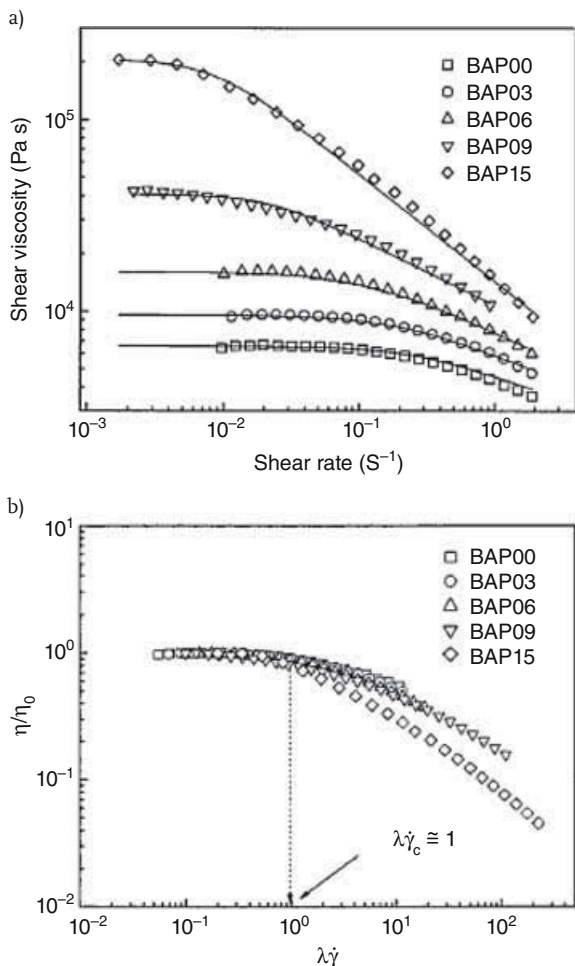
Figure 10.3 (a) Shear viscosity versus shear rate of BAP/OMMT for various OMMT loadings at 140 °C. Symbols represent the experimental data. Solid lines represent the Carreau model. (b) Scaled plot for η/η_0 versus $\lambda\dot{\gamma}$. Reproduced from reference [39] with permission.

Song and coworker [41] studied the effect of temperature on rheological behavior for a variety of polyol/clay mixtures during *in situ* polymerization of polyurethane/clay nanocomposites. By combining XRD technique a relationship between shear thinning behavior of polyol/clay dispersion and the intercalation or exfoliation state of the clay in the matrix was established. Based on the experimental results, a possible layer-by-layer exfoliation mechanism was proposed. The variation of the viscosity of polyol/clay dispersions with mixing time at various temperatures was examined for three different kinds of clay systems. At higher temperatures, the
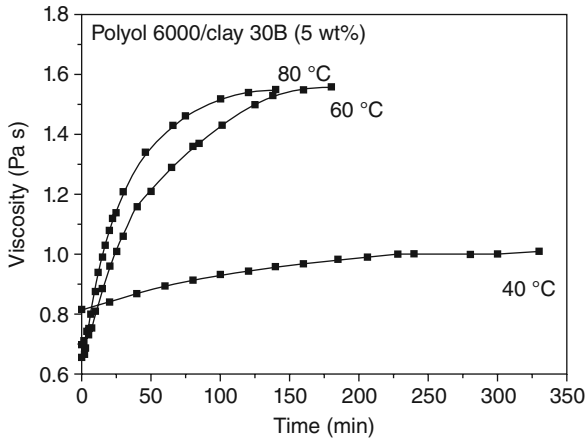
Figure 10.4 Variation of viscosity of polyol/clay C30B dispersions with mixing time at various temperatures. Reproduced from reference [41] with permission.
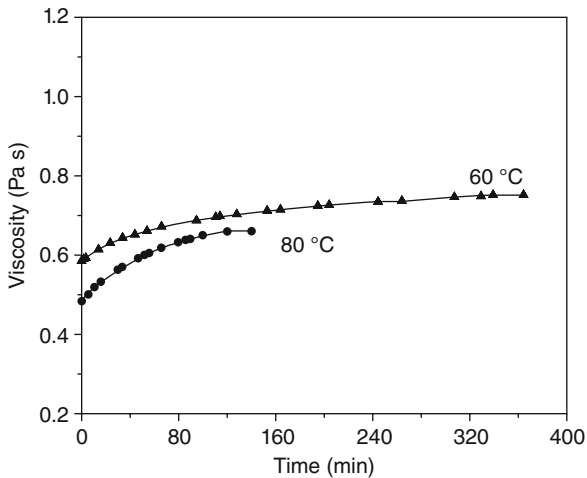
Figure 10.5 Variation of viscosity of polyol/clay 20A dispersions with mixing time at 60 and 80 °C. Reproduced from reference [41] with permission.

viscosity of the polyol/clay C30B dispersions increased significantly with mixing time as shown in Figure 10.4. For the polyol/clay 20A system, the viscosity of the dispersion practically did not change at 20 °C and slightly increased at 60 °C and 80 °C with mixing time as shown in Figure 10.5.

In comparison between two different clay systems, the viscosity for polyol/clay 20A dispersions increased slightly with mixing time. At 80 °C, after 90 min, the
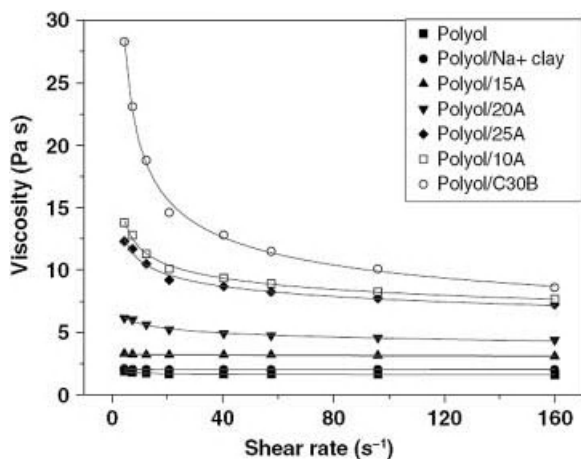
Figure 10.6 Viscosity versus shear rate for polyol/clay dispersions with various clays (viscosity determined at 20 °C). Reproduced from reference [41] with permission.

viscosity of the polyol/clay 20A dispersion reached a plateau value of 0.65 Pa s, which was much lower than that of the polyol/C30B system. For the original unmodified Na^+ clay, the viscosity of polyol/Na^+ clay dispersions remained almost unchanged with mixing time at various temperatures.

The effect of clay on viscous behavior was quite different for three systems. A rapid increase in viscosity at higher temperatures for the clay C30B system was noticed. In order to understand this phenomenon, further investigation was done. Figure 10.6 shows the rheological behavior of blank polyol and polyol/clay dispersions with different kinds of clay determined at 20 °C. Figure 10.4 shows the viscosity versus shear rate for polyol/clay C30B dispersions prepared at various temperatures.

The shear thinning parameter n was obtained according to Herschel–Bulkley models listed in Tables 10.1 and 10.2. For polyol/Na^+ clay and polyol/15A dispersions, the viscosity was low. The shear thinning parameter, n, was found to be 1.00, which is similar to that of the blank polyol dispersions. For polyol/20A, polyol/25A and polyol/10A dispersions, the viscosity was relatively high, and n decreased to ~0.9. For polyol/C30B dispersions, the viscosity was the highest, and n was found to be 0.77. When combined with the XRD data, the state of clays in polyol could be evaluated as shown in Tables 10.1 and 10.2 (Figure 10.7).

The results demonstrate that there was good correlation between the rheological behavior and the dispersion state of the clays. In particular, the shear thinning exponent, n, could be used to semiquantitatively characterize the state of the clay layers. A lower n value corresponded to high shear thinning behavior and a high exfoliation state of clay layers in the polymer matrix. If there was no intercalation or exfoliation, the viscosity increased slightly owing to the increase in the

Table 10.1 Relationship between rheological data and clay state, evaluated from XDR (reproduced from reference [41] with permission)[a].

Dispersion	η_L (Pa s)	η_H (Pa s)	n	Clay state (XRD evaluation)
Blank polyol	1.87	1.63	0.99	–
Polyol/N$_a^+$ clay	2.10	2.03	1.00	Low intercalation
Polyol/15A	3.30	3.09	0.99	Low intercalation
Polyol/20A	6.15	4.39	0.90	High intercalation
Polyol/25A	12.30	7.24	0.87	High intercalation
Polyol/10A	13.80	7.67	0.87	High intercalation
Polyol/30B	28.30	8.60	0.77	Exfoliation

a) η_L and η_H are the viscosity values at a low shear rate (4.45 s^{-1}) and at a high shear rate (159.8 s^{-1}), respectively.

Table 10.2 Relationship between rheological data and clay state, evaluated from XDR (reproduced from reference [41] with permission)[a].

Mixing temperature (°C)	η_L (Pa s)	η_H (Pa s)	n	Clay state (XRD evaluation)
20	2.53	2.22	1.02	No intercalation or exfoliation
40	13.4	5.3	0.86	Medium exfoliation
60	18.5	7.04	0.85	Medium exfoliation
80	28.3	8.60	0.77	High exfoliation
100	29.2	8.60	0.76	High intercalation

a) η_L and η_H are the viscosity values at a low shear rate (4.45 s^{-1}) and at a high shear rate (159.8 s^{-1}), respectively.
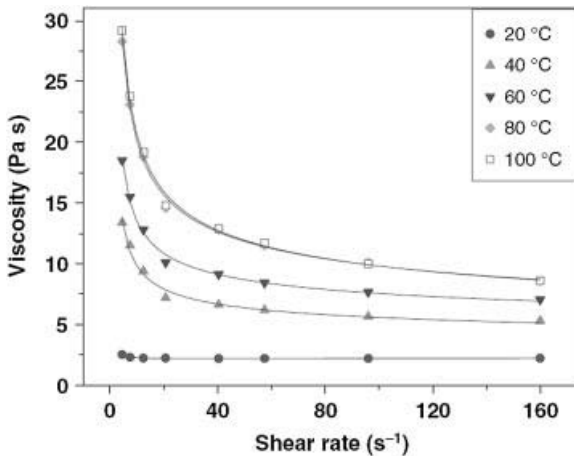
Figure 10.7 Viscosity versus shear rate for polyol/clay C30B dispersions after mixing for 4 h at 20, 40, 60, 80, and 100 °C. Reproduced from reference [41] with permission.

concentration of the dispersed phase, and the shear thinning behavior should be similar to that of the blank polyol. When the clay layers were intercalated, clay tactoids with a larger size formed, and viscosity increased markedly compared with the blank polyol. This was due to the increase in the size and concentration of the dispersed phase together with the increase in the interactions between polyol and clay. When the clay was exfoliated, many separated layers of clay formed. These exfoliated individual clay layers with a large surface area formed a network gel structure, leading to a significant increase in viscosity. Once the network structure is formed, at a relatively high shear rate the viscosity decreases owing to the alignments and disentanglements of clay layers, and thus the shear thinning behavior will appear more obviously. Clearly, this behavior only occurred in the clay C30B system, indicating that the interactions between clay and polyol play a key role in clay exfoliation. There are thus different rheological behaviors for intercalated and exfoliated polyol/clay dispersions. The viscosity and the shear thinning exponent *n* can be used to characterize the dispersion state of clay in polyols.

The interaction between the polyol and clay and the mixing temperature plays an important role in the occurrence of exfoliation and intercalation. The relationship between rheological behavior of polyol/clay dispersion and the intercalation or exfoliation state of the clay was established. This provides a convenient and efficient way to evaluate the dispersion state of the clay. Based on the experimental results, a possible layer-by-layer exfoliation mechanism was proposed [41].

Choi and coworkers [42] also described the effect of the dispersion of silicate layers and the interaction between the organoclay surface and the polymer matrix on the melt-state rheological properties of polymer/clay nanocomposites. They prepared a series of poly(ethylene oxide) (PEO)/organoclay nanocomposites, using three types of surfactants modified montmorillonite (Cloisite 15A, 20A, and 25A). First, they selected two different organoclays, which have different modifier concentration but the same alkylamonium salts. Secondly, they differentiated the types of alkylamonium salts having the same organic modifier. All nanocomposites were fabricated by the solvent casting method. The rheological properties of these nanocomposites differed with varying modifier concentration and surfactant size (chain length). The PEO/Cloisite 25A nanocomposites with Cloisite 25A loading exhibit higher zero shear rate viscosities and more rapid shear thinning behavior than the pure PEO, which results from the reorientation of dispersed clay particles. The mean-field equation was applied to examine the effect of concentration of clay on viscosity. The results indicate that the rheological properties of nanocomposite systems depend on interactions between clay platelets and on interactions between the clay surface and the polymer matrix.

Some studies have demonstrated that the rheological behavior of polymer/clay nanocomposites is correlated with the microstructures of the nanocomposites and that microstructure changes cause temporal behavior. The rheological behavior of polymer/clay nanocomposites depends not only on the parent components but also on the composite phase morphology and interfacial characteristics. Different phase morphologies (intercalated or exfoliated) of polymer/clay were obtained according to interfacial characteristics between polymer chains and clay [2]. Lim

and Park [43] in their quantitative analysis reported these effects on rheological behavior based on different characteristic polymer/clay nanocomposites. Three polymer resins with different characteristics were used to fabricate the nanocomposites with clay: polystyrene (PS), polystyrene-*co*-maleic anhydride (PS-*co*-ma), and polyethylene-graft-maleic anhydride (PE-*g*-ma). Commercialized organophilic clay M6A was used. Three different series of PS/clay, PS-*co*-ma/clay, and PE-*g*-ma/clay nanocomposites were produced by melt intercalation. The final interfacial properties and phase morphology were examined by XRD and TEM. Both PS/M6A and PS-*co*-ma/M6A composites have intercalated structure, the original ordered structure of M6A is delaminated, and in the case of the PE-*g*-ma/M6A nanocomposite, exfoliated structure is formed. The results show that the rheological behavior of the PS-*co*-ma/M6A nanocomposites at low frequency is very different from that of the PS/M6A nanocomposites. In particular, the enhancement of the storage modulus of the PS-*co*-ma/M6A nanocomposites is very large compared to that of the PS/M6A nanocomposites and, unlike the PS/M6A nanocomposites, the PS-*co*-ma/M6A nanocomposites also exhibited plateau-like behavior. The results indicate that once clay loading exceeds 7 wt%, the liquid-like behavior of PS-*co*-ma/clay gradually changes to a pseudo solid-like behavior. For the PE-*g*-ma/M6A nanocomposites the storage and loss moduli increased and the frequency dependence of both moduli decreased with clay loading compared to those of the matrix polymer. The enhancement of both moduli in PE-*g*-ma/M6A is larger than those of PS/M6A and of PS-*co*-ma/M6A nanocomposites at all frequencies. These nanocomposites also exhibited a distinct plateau-like behavior at low frequency.

The interfacial interactions between polymer chains and clay layers, and the large contacting interfacial area are responsible for the rheological behavior. In the fabrication of PS/clay nanocomposites by melt intercalation, the main driving force of PS intercalation to the gallery of clay is the weak Levis acid–base interaction between the PS and the silicate surface. The PS-*co*-ma chains have a maleic anhydride group which functions as a strong active site with the silicate layer. The PS-*co*-ma chains in the silicate gallery, as a result, stick to the silicate layers more strongly than PS chains at the same silicate loading. In addition, as detected by TEM observations, the more uniform dispersion of clay particles was formed in PS-*co*-ma nanocomposites. As the micro-sized stacked clay particles are delaminated into smaller particles, the contacting area with polymer chains increases in the PS-*co*-ma nanocomposites. In order to fabricate PE/clay nanocomposites a function polar group should be introduced to the PE backbone, because of the absence of any interacting moieties leads to an immiscible state between the PE and clay. When the PE-*g*-ma chain intercalates into the interlayer of the layered silicate due to the interaction of the maleic anhydride group with the silicate surface, this forces the adjacent silicate layers to separate and leads to a fully exfoliated structure. In exfoliated nanocomposites, when the single layers of clay are dispersed in the polymer matrix, more polymer chains come into contact with the silicate surface and filler–filler interactions between clay particles are also very important, even at low clay loading. The PE-*g*-ma/M6A nanocomposites, which have exfoliated structure, showed large enhancement of the storage modulus both

at low and high frequency. The PS/clay nanocomposites showed a slight enhancement at low frequency because of its simple intercalated structure and weak interfacial interaction. The PS-*co*-ma/clay nanocomposites, which have a similar intercalated structure to PS/clay nanocomposites, showed a distinct plateau-like behavior at low frequency, as a result of the PS-*co*-ma having strong interactions with clay layers. Although strong interactions between maleic anhydride and clay also exist in both PS-*co*-ma/clay and PE-*g*-ma/clay nanocomposites, the rheological properties of polymer/layered silicate nanocomposites are also strongly dependent on their microstructures.

The effects of phase morphology and interfacial properties on the rheological behavior of polymer/clay nanocomposites were also studied by small amplitude oscillatory frequency tests after larger amplitude oscillatory shear. The larger amplitude oscillatory shear was conducted at $\gamma = 120\%$, $\omega = 1 \, \text{rad/s}$. The G' of shear-aligned PS/M6A nanocomposite was lower than that of the initially unaligned sample and close to that of the matrix polymer. A large decrease of G' was observed in the PS-*co*-ma/M6A nanocomposites, while the G' at low frequency was larger than that of PS/M6A. This indicates that strong interactions between the PS-*co*-ma and clay layer existed. This also suggests randomly oriented silicate layers and some particle network structure were formed. For the shear-aligned PE-*g*-ma/M6A nanocomposite, a decrease of G' was only in the high frequency region and was not large compared to that of PS/M6A or PS-*co*-ma/M6A nanocomposites. This suggests that the exfoliated structure still remains in the PE-*g*-ma/M6A nanocomposite after large amplitude oscillatory shear. These studies demonstrate that the strong clay–clay interaction and the large interfacial area between polymer chains and clay are primarily responsible for the rheological behavior of polymer nanocomposites.

Besides clays, carbon nanotubes (CNTs) are recognized as potentially valuable nanofillers. They have been known since the 1990s and being produced as multi-walled nanotubes (MWNTs) or single-walled nanotubes (SWNTs). In preparation of CNT nanocomposites the first challenge is the ability to control the dispersion of CNT in polymeric matrices due to its smaller diameter and strong van der Waals interactions [44]. Recently, some research has reported that when the loading of CNTs is at above critical value, a network structure can form in the nanocomposite system during mixing [45–47]. This can be used as a physical signal with which to monitor the level of nanoparticle dispersion in the matrix. Elastic gel, forming from such an entangled nanotube network, may prevent individual tube motion and such serves as an alternative mechanism of stabilization [48, 49]. Rheological behavior of a dispersion of MCNTs in a viscous polydimethylsiloxane (PDMS) matrix was studied by Huang and coworkers [50]. The rheological responses of the composite as a function of the dispersion mixing time and conditions indicate that a critical mixing time t^* needs to be exceeded to achieve satisfactory dispersion of CNTs in a polymer melt, this time being a function of CNT concentration and the mixing shear stress. Below this characteristic time, the composite system is full of dense tube clusters. The nonequilibrium feature characteristics, for example, colloidal glass and jamming of clusters, exist. The rheological features at the well-
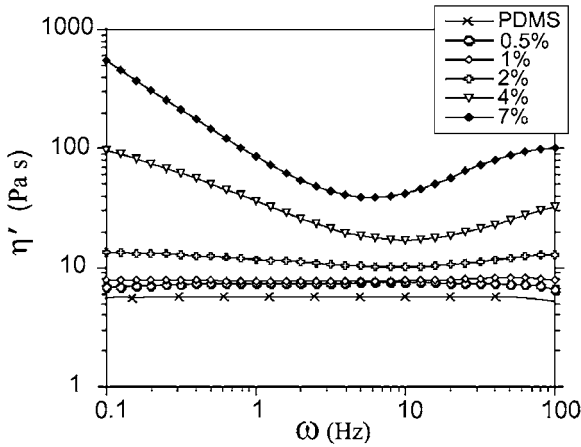
Figure 10.8 Summary for the dynamic viscosity against frequency for well-dispersed samples of different concentrations. Reproduced from reference [50] with permission.
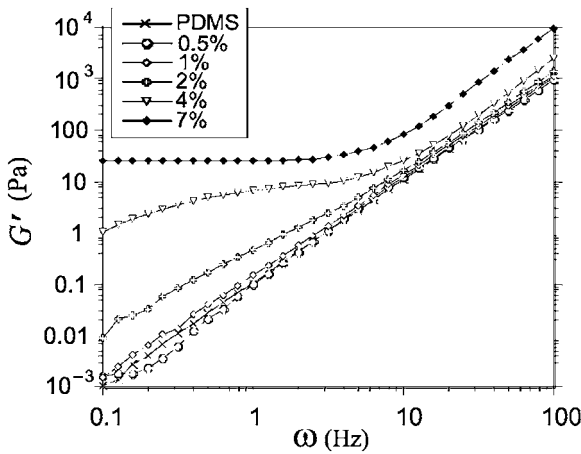
Figure 10.9 Summary for the storage modulus against frequency for well-dispersed samples of different concentrations. Note the emerging low-frequency rubber plateau in at high tube concentrations. Reproduced from reference [50] with permission.

dispersed systems possess very different rheological properties below and above the concentration characteristic value. The reproducible profiles of the rheological linear response are shown in Figures 10.8 and 10.9. Increasing CNT concentration increases the values of η', and also makes it more frequency dependent. The samples with 0.5, 1, and 2 wt% CNTs, just like the pristine PDMS, exhibit a nearly frequency independent. At CNT concentration above a characteristic value $n_c \sim 2$–3
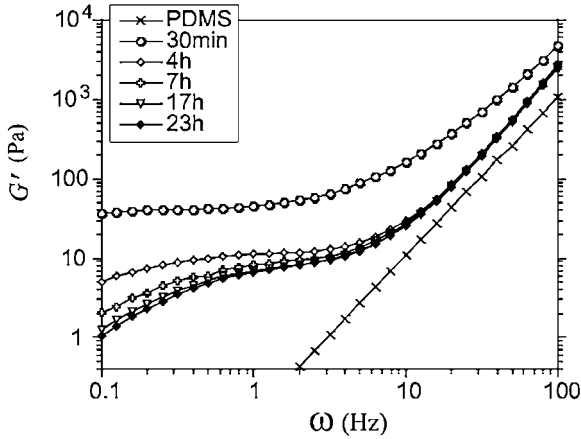
Figure 10.10 G' against frequency for 4 wt% samples mixed for different times. Reproduced from reference [50] with permission.
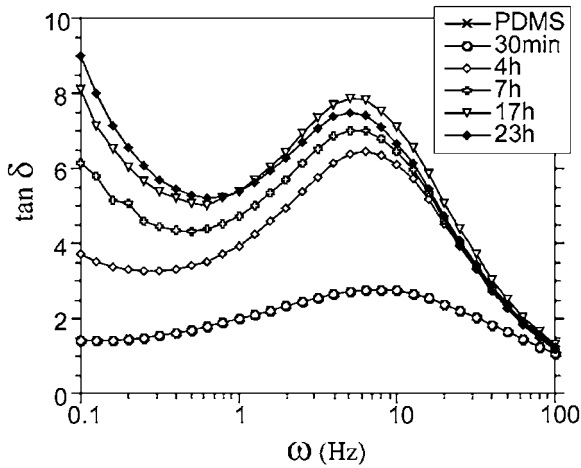
Figure 10.11 Tan δ' against frequency for 4 wt% samples mixed for different times. Reproduced from reference [50] with permission.

wt%, there is a significant change in viscosity profiles, which suggests a major change in nanocomposite structure. The presence of an entangled elastic network structure was evidenced by the rubber plateau in the storage modulus at $\omega \to 0$ and also in the peaks in the loss factor tan δ shown in Figures 10.10 and 10.11, while the low-concentration composite remains a viscous liquid.

It is concluded that the shear viscosity behavior of the polymer is characterized by two distinct regions, called the Newtonian and shear thinning regions. At low

shear rate, the Newtonian with independence of the shear rate is observed followed by the shear thinning region where the viscosity linearly decreases with an increase in the shear rate. Song further studied the steady shear viscosities of PEO/CNTs systems [51]. It was found that the shear viscosity of the nanocomposites was drastically increased with an increase in the CNT content especially at a low shear rate. As the CNT loadings increase, the Newtonian region disappears and only the shear thinning region remains throughout the entire shear rate. The effective volume fraction of CNT evaluated based on the Krieger–Dougherty equation is found to be about 10 times higher than the real particle volume fraction. It is believed that in the PEO/CNT system, particle–polymer and particle–particle inter-actions strongly existed. Remarkable shear thinning behavior has been reported in various nanocomposites embedded with nanofillers such as nanoclay, nanofib-ers, carbon blacks, and silica [37, 52]. It is posted that the particle–particle interac-tions, which result in an increase in the shear viscosity without the Newtonian plateau region, play a dominant role in the rheological behavior for the nanocomposites.

Du *et al.* [53] studied rheological behavior of poly(methyl methacrylate) PMMA nanocomposites containing single-walled carbon nanotube (SWNT) at a nonter-minal low frequency. Viscoelastic properties of the SWNT/PMMA nanocompos-ites are presented in Figure 10.12 for a range of SWNT weight fractions. The measurement of strain sweep was performed at 200 °C. Nanotube bundles have a dramatic influence on the rheological behavior, even at loading as low as 0.2 wt%. As the loading increases, both storage shear modulus G' and loss shear modulus G'' significantly increase, especially at low frequencies. At low frequencies, PMMA chains are fully relaxed and exhibit typical homo-polymer-like terminal behavior with the scaling properties of approximately $G' \sim \omega^2$ and $G'' \sim \omega$. However, at SWNT loadings higher than 0.2 wt %, this terminal behavior disappears, and the dependence of G' and G'' on ω at low frequency is weak. Thus, large-scale polymer relaxations in the nanocomposites are effectively restrained by the presence of the SWNT. That G' is independent of ω at low frequencies when the SWNT loading is higher than 0.2 wt% is indicative of a transition from liquid-like to solid-like viscoelastic behavior. This nonterminal low-frequency behavior can be attributed to a nanotube network, which restrains the long-range motion of polymer chains. The three-dimensional SWNT network appears to exist, in which nanotube bundles randomly intersect one another. Similar rheological behavior has been observed in polymer nanocomposites containing clays or MWNTs [37, 54, 55]. At high frequencies, the effect of the nanotubes on the rheological behavior is rela-tively weak. This suggests that the SWNTs do not significantly influence the short-range dynamics of the PMMA chains. Therefore, the presence of nanotubes has a substantial influence on polymer chain relaxations. Terminal rheological behav-ior is affected by the CNT dispersion state as shown in Figure 10.13. 1.0NT with good dispersion has the smallest low-frequency slope of G' versus ω and the highest G' at low frequencies. 1.0dwNT with intermediate dispersion also exhibits nonterminal rheological behavior, but 1.0dNT with poor dispersion has terminal behavior as does pure PMMA. Nanocomposites with poor nanotube dispersion

a)

b)
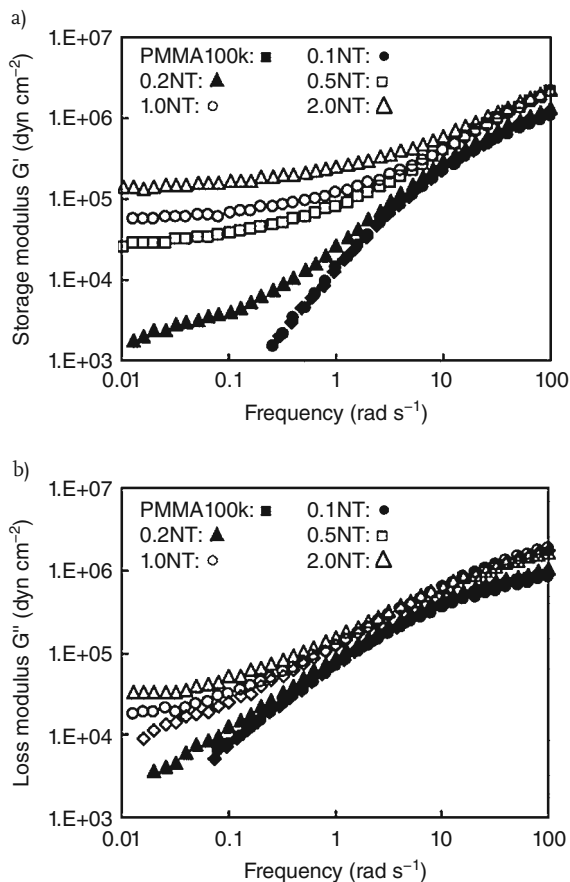
Figure 10.12 (a) Storage modulus and (b) loss modulus of SWNT/PMMA nanocomposites with various nanotube loadings. Rheology performed at 200 °C and 0.5% strain. Reproduced from reference [53] with permission.

have discrete nanotube-rich domains rather than a nanotube network, such that the polymer chains flow independent of the nanotubes.

Recent studies mentioned that along with dispersion, orientation of nanoplatelets also plays a major role in property enhancements in polymer nanocomposite systems. Kojima *et al.* [56] studied the effect of shear on the orientation of clay platelets and polymer unit cell as a function of depth in a 3 mm thick injection molded samples of nylon–clay nanocomposites. They concluded that the orientation of clay platelets affected the strength of the nanocomposites along different directions. Krishnamoorti *et al.* [57] proposed that rheological behavior of nanocomposites strongly depends on filler orientation.

The effect of the nanofiber aspect ratio on rheological properties for several polymer systems has been reported [58–60]. They proposed that the carbon
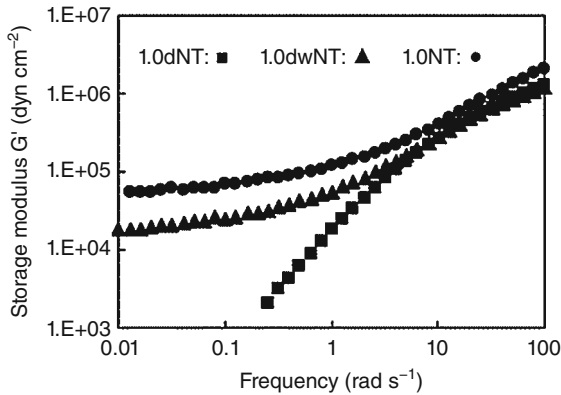
Figure 10.13 Frequency response of the storage modulus for SWNT/PMMA nanocomposites with 1 wt% SWNT with improving nanotube dispersion from 1.0dNT (poor dispersion) to 1.0NT (good dispersion). Reproduced from reference [53] with permission.

nanofibers were found to be well aligned with the direction of flow during processing, and, correspondingly, nanocomposite stiffness, yield stress, and fracture strength improved with respect to neat polymer. Very recently, the rheological properties of two different nanocomposite systems consisting in the dispersion of carbon nanofibers (CNFs) in polypropylene (PP) were reported by Tabuani [61]. The length of one CNF in low density is about 100–200 µm (LD-CNFs) and other in high density is about 50–100 µm (HD-CNFs). Both dynamic and steady-state shear rheology of the nanocomposites were studied. The results demonstrate that linear viscoelasticity shows the formation of a network structure for both systems above a critical composition value. The nanocomposite characterized by CNFs with larger aspect ratios shows a more pronounced increase of moduli and a lower critical composition. The presence of low aspect ratio (HD-CNFs) fibers produces a small increase in moduli up to 3 wt%, where G' and G'' data are closely pure PP throughout the frequency range. At low filler loading, the storage modulus enhancement is usually attributed to stiffness imparted by the solid particles that allow efficient stress transfer, which is mainly controlled by the matrix/filer–matrix interface. At higher loading the moduli increase deeply. At above a threshold value (above 3 wt%), a pseudo-solid-like behavior is observed at low frequencies, that is, G' and G'' data show the appearance of a plateau, suggesting the formation of some interconnected nanofiber network within the matrix. In comparison, the increase of both moduli is much larger for the LD–CNF system at the same loading, and the pseudo-solid-like plateau is observed at lower concentration of 2 wt%. The enhancement of moduli due to the presence of LD-CNF is significantly higher at lower frequencies, and the increase is more pronounced in the storage modulus. Thus, as it could be expected, the system with a lower aspect ratio shows a larger percolation concentration. This effect was also found in other polymer/

filler systems [62]. In order to view their peculiar response in linear viscoelasticity, steady shear measurements for LD–CNF nanocomposites were also studied. At lower concentrations, a Newtonian plateau is found at low shear rates. Nanocomposites with filler fraction above 2 wt% exhibit strong shear thinning throughout the investigated shear rate range, again suggesting the formation of some network structure. Shear thinning behavior of the viscosity can be associated at low shear rates with the breakdown of the network structure and at large shear rates with the possible alignment of the fibers along the flow direction.

The first normal stress difference, N_1, for the PP and LD–CNF nanocomposites was measured during the startup of steady shear tests with the rotational rheometer equipped with cone and plate fixture. N_1 transient for a sample with 6 wt% large respect ratio CNF at two different shear rates (5 and $10\,s^{-1}$) and the average steady-state value of the first normal stress difference as a function of the shear rate were discussed [61]. Clearly, long and oscillating N_1 transients were observed for the nanocomposites with above 1 wt% CNF loading. Normal stress signals become measurable only at high shear rates. At larger LD-CNF composition (6 and 10 wt%), N_1 attains negative steady-state values. These indicate typical features of lyotropic rod-like polymers in the nematic phase.

The effects of the addition of nanoparticles to a polymer matrix on the transient shear and transient extensional rheology of the composite in the melt phase were investigated by Miyazono *et al.* [63]. In order to result in fibers with larger aspect ratios, two methods were used to prepare PS/CNFs composites: melt blending (MB) and solvent casting (SC). The characteristics of CNFs in the nanocomposites prepared by two methods were given [63]. The melt blending process creates more shear forces than sonication, resulting in shorter fibers and a smaller distribution of CNF length in the MB samples.

Figure 10.14 shows the master curves of the elastic modulus, G', of MB and SC composites as well as pure PS samples prepared by the same methods. The small
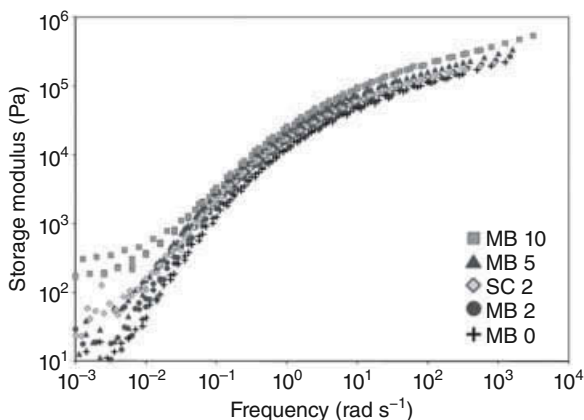
Figure 10.14 Master curve of the elastic modulus (G0) for MB and SC composites. Reproduced from reference [63] with permission.

amplitude oscillatory shear measurements were performed over the temperature range of 140–220 °C. The master curves were generated by shifting the measured data to 200 °C following the principles of time–temperature superposition; the shift factors (a_T) of PS and its composites are linear with temperature.

Effects of the CNFs on the linear viscoelastic moduli, especially at low frequencies, were observed. For both melt blended and solvent cast composites, the elastic modulus G' increases monotonically with increasing CNF concentration. The effect of CNF on G' of the nanocomposite prepared by the casting method was greater than that of those prepared by the melt blending method due to the aspect ratio of the CNFs. It was found that the temperature shift factors were almost independent of the CNF concentration and length, and the same as those of the pure polystyrene. The theoretical foundation of time–temperature superposition is that the relaxation times of the polymer chains have the same temperature dependence [62]. It shows that the addition of CNFs to the PS does not alter the shift factors, indicating that the mobility of the polymer chains is not constrained by the CNFs.

To further reveal the effects of CNF concentration and length on the rheology of the melt composites, the transient extensional flow behavior was also investigated. Typical transient extensional viscosity profiles are shown in Figure 10.15: the characteristic transient shear rheological behavior observed for these composites, decreasing viscosity with increasing shear rate, increasing viscosity with increasing CNF concentration. It was suggested that the CNFs create a network structure and as nanofiber concentration increases this network becomes stronger due to the increased contact between fibers. This network structure causes the increase in viscosity with increasing nanofiber concentration. The network structure is affected by the shear flow. At low shear rates, the flow of the polymer is
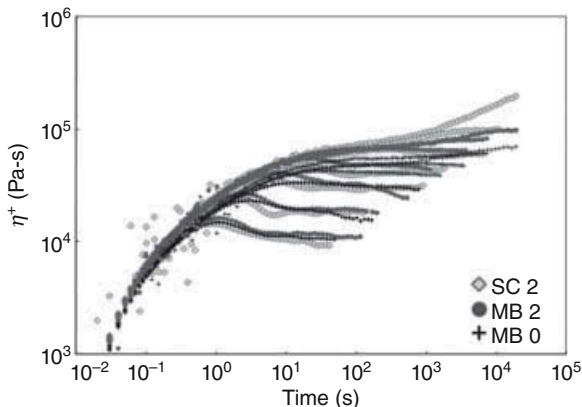
Figure 10.15 Comparison of transient-shear viscosity among MB0, MB2, and SC2 composites at shear rates 0.0001–3.0 s^{-1} and at T ¼ 160 °C. Reproduced from reference [63] with permission.
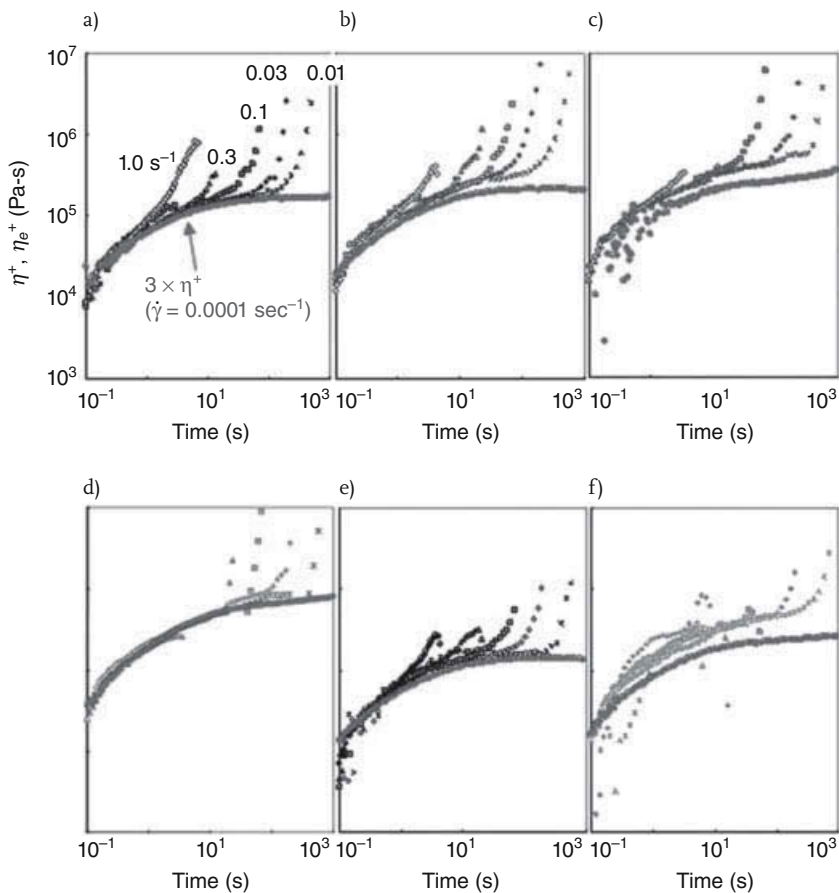
Figure 10.16 Transient-extensional viscosity of (a) MB0, (b) MB2, (c) MB5, (d) MB10, (e) SC0, and (f) SC2 at shear rates 0.01 (circle), 0.03 (triangle), 0.1 (square): 0.3 (diamond), and 1.0 s⁻¹ (asterisk) at *T*¼ 160 °C. The solid circle is three times the transient shear viscosity of the same polymer or PS/CNF composite measured at a shear rate of 0.000 s⁻¹. Reproduced from reference [63] with permission.

slow enough to cause little disruption to the network while at high shear rates the structure is destroyed; hence, at high shear rates the viscosities of all composites are similar.

Figure 10.16 shows the transient extensional viscosity η_e^+ of pure PS (MB0 and SC0), MB2, MB5, MB10, and SC2 composites over the extension rate range 0.01–1.0 s⁻¹. A comparison of transient shear viscosity with transient extensional viscosity of the MB2, MB5, and MB10 composites shows Trouton's ratio (η_e/η) in the linear viscoelastic regime for each to be greater than 3 and was calculated. The pure PS shows the ratio to be precisely equal to 3. With the addition of CNF

the transient extensional viscosity and Trouton's ratio increased. In comparison, the degree of the increase in extensional viscosity for the solution-casted composite is significantly greater than in melt-blended composites. The transient extensional viscosity of the SC2 sample is almost identical to the extensional viscosity of the MB5 sample; moreover, Trouton's ratio of SC2 is greater than that of MB5. The data of steady-state shear viscosity, η, and steady-state extensional viscosity, η_e, in the linear viscoelastic regime and Trouton's ratio for MB2 and SC2 composites were analyzed. The results show that the ratio of the steady-state extensional viscosities of SC2–MB2 (1.68) is significantly greater than the ratio of the steady-state shear viscosities of SC2–MB2 (1.14), which indicates that the fiber length has a greater effect on extensional deformation than shear deformation.

At higher loading of clay platelets in the nanocomposites, the tendency of the particles to form a percolating network arises [64, 65]. Galgali *et al.* [64] have studied the creep behavior of PP–clay nanocomposites containing high loading of clay on rheological response. The results of various creep measurements presented in their article show the viscosity of the nanocomposite as a function of shear stress. The material creeps at low stress in a Newtonian manner followed by apparent yielding at about 1000 Pa, in which the viscosity drops by three orders of magnitude in a very narrow range of shear stress. This clearly indicates that large zero-shear viscosity of material arises from frictional interactions of silicate layers that form a percolation networks. This caused the material to flow to an increasingly greater extent. At low shear rates a Newtonian response was observed in which shear rate increased linearly with increased shear stresses, followed by plateau for shear stress for a wide range shear rate. The complex modulus matched the yield stress value in the low frequency region, indicating the nonterminal region. The viscosity decreased steadily with preshearing. These results of creep experiments demonstrate that the frictional interaction between the clay layers could be one reason for the solid-like rheological behavior of the nanocomposite systems.

A relaxation of orientation for PP-based polymer nanocomposites with PP-MA was reported by Lele *et al.* [65]. The system was presheared, followed by disorientation with XRD. The results show that the relaxation time was faster than expected from the theory of Brownian motion. The disorientation was governed by the stress relaxation of macromolecules. There are many reports on studies of stress growth and flow reversal behavior of nanocomposites. In summary, two mechanisms are responsible for stress overshoots after rest. The first is based on randomization of the orientation imposed by Brownian motion and relaxation of the matrix. The second assumes that the three-dimensional structure is broken by shear and reforms under quiescent conditions. The former mechanism is expected to be applicable to exfoliated polymer/clay nanocomposites, where platelets are still able to rotate freely. The second mechanism dominates the intercalated nanocomposite systems, especially those with large low-aspect-ratio stacks.

Solomon *et al.* [37] studied the flow-induced structure change in PP-based polymer nanocomposites by measuring the stress growth and flow reversal behavior. The stress growth was measured at shear rates of $0.005–1.0 \, \text{s}^{-1}$. Results for the
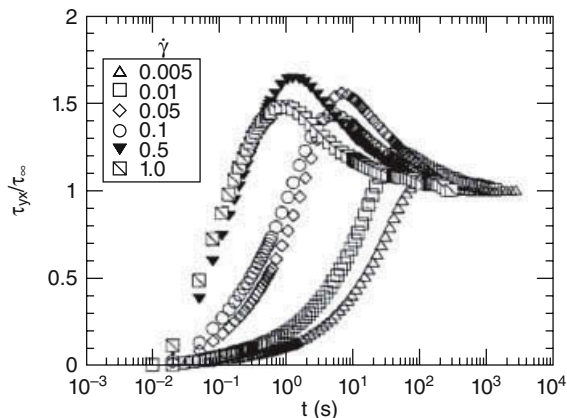
Figure 10.17 Transient shear stress measured during the startup of steady shear for the 4.8 wt% hybrid material. Reproduced from reference [37] with permission.
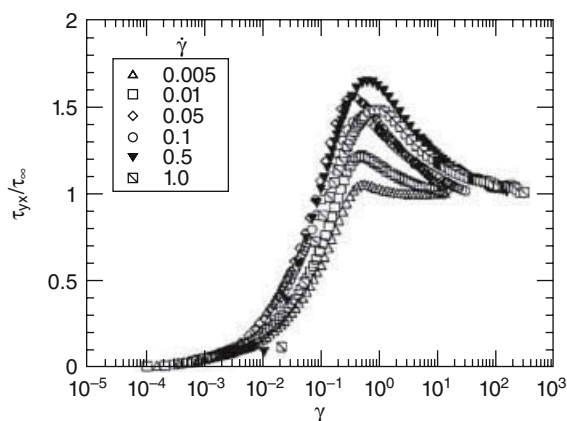
Figure 10.18 Transient shear stress versus strain for the 4.8 wt% hybrid material. Reproduced from reference [37] with permission.

4.8 wt% hybrid material are plotted in Figures 10.17 and 10.18. The magnitude of the overshoot was strong functions of the shear rate. The stress versus strain curves reached a maximum at strain $\gamma \approx 0.6 \pm 0.3$. The empirical observation that the onset of the stress overshoot in the startup of steady shear depends on the strain applied to the material, as opposed to the time after the flow has been imposed. Measurements of the flow reversal stress overshoot were carried out at shear rate of $0.1\,\mathrm{s}^{-1}$. The overshoot increased regularly with the rest time, t_{rest} (interval between preshearing and flow reversal). The data followed the scaled
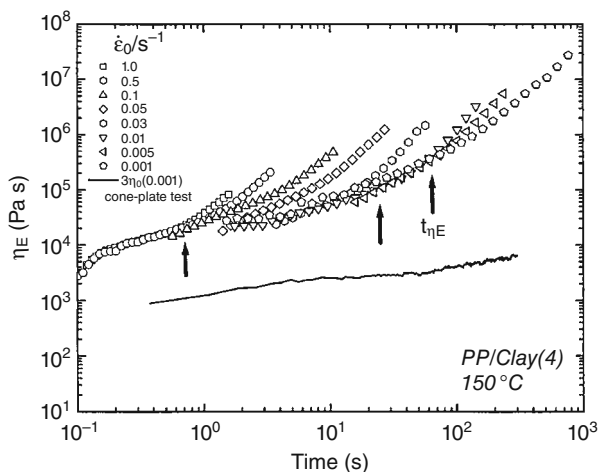
Figure 10.19 Time variation of elongational viscosity $\eta_E(\dot{\varepsilon}_0; t)$ for PP/4 wt% clay melt at 150 °C. The upward arrows indicate the uprising time t_{η_E} for $\dot{\varepsilon}_0 = 1.0, 0.01$ and $0.001\,\mathrm{s^{-1}}$. The solid line shows three times the shear viscosity, $3\eta_0(\dot{\gamma}; t)$, taken at a low shear rate $\dot{\gamma} = 0.001\,\mathrm{s^{-1}}$ on a cone-plate rheometer. Reproduced from reference [29] with permission.

relation versus t_{rest}. Thus, by means of the strain scaling of the transient stress in the startup of steady shear, it is concluded that Brownian relaxation processes do not significantly contribute to the hybrid rheological response.

Okamoto and coworkers [29] first investigated elongation flow behavior of PP-based nanocomposites at constant Hencky strain rate, $\dot{\varepsilon}_0$. Figure 10.19 shows double-logarithmic plots of transient elongational viscosity $\eta_E(\dot{\varepsilon}_0; t)$ versus time t observed for PP nanocomposite with 4 wt% clay at 150 °C with different Hencky strain rates $\dot{\varepsilon}_0$ ranging from 0.001 to 1.0 s^{-1}. The solid curve represents threefold shear viscosity $3\eta_0(\dot{\gamma}; t)$, with a constant shear rate of 0.001 s^{-1} at 150 °C. A strong tendency of strain-induced hardening was detected. At early stage, $\eta_E(\dot{\varepsilon}_0; t)$ gradually increased with time, but independent of $\dot{\varepsilon}_0$, which is called the linear region of the $\eta_E(\dot{\varepsilon}_0; t)$ curve. After a certain time t_{η_E} generally called the uprising time (marked with the upward arrows), there is a rapid upward deviation of $\eta_E(\dot{\varepsilon}_0; t)$ from the curves of the linear region. On other hand, two distinctive features were observed in the shear viscosity curve. First the extended Trouton rule is not valid for this system and secondly, the nanocomposite shows time-dependent thickening behavior called rheopexy behavior. This response revealed the difference in the shear flow-induced versus elongation-induced internal structures formation for the nanocomposite in the molten state. Furthermore, the same experiments were also studied for a PP-MA matrix without clay. In this system both strain-induced hardening and rheopexy behavior were not observed. The authors traced the strong soft hardening for the nanocomposite containing 4 wt% of clay. On the

basis of experimental results and two-directional TEM observations they concluded that the formation of a "house-of-cards" like structure was observed under slow elongational flow. The strong strain-induced hardening and rheopexy features are originated from the perpendicular alignment of the silicate layers to the stretching direction.

Ray and coworker [66] conducted extensional rheology studies on polylactide (PLA)/C_{18}MMT clay nanocomposites in melt state at a constant Hencky strain. Figure 10.20a shows double-logarithmic plots of transient elongational viscosity (η_E) against time (t) observed for PLA nanocomposite with 5 wt% of clay at 170 °C with different Hencky strain rates $\dot{\varepsilon}_0$ ranging from 0.01 to $1\,s^{-1}$. The results
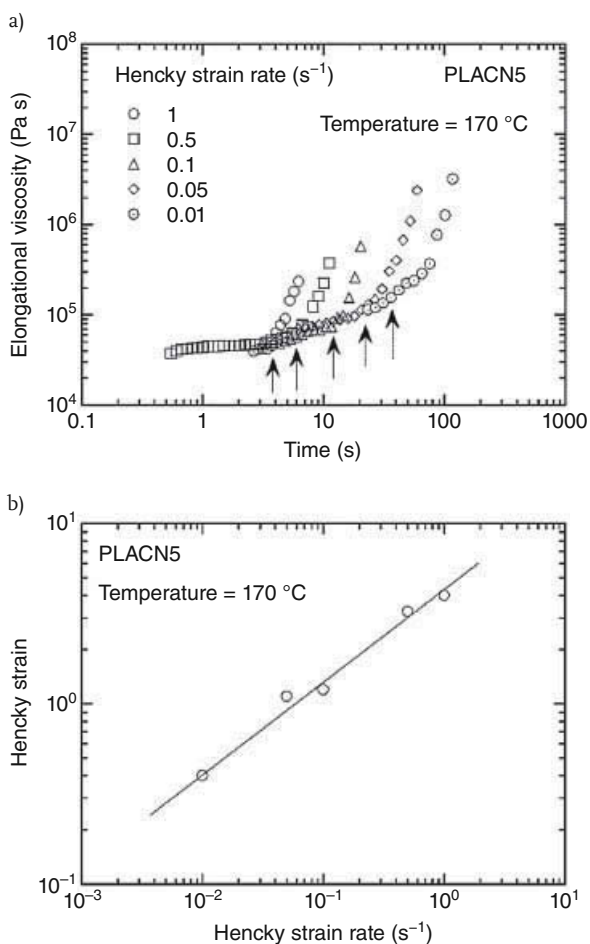
Figure 10.20 (a) Time variation of elongational viscosity for PLACN5 melt at 170 °C. (b) Strain rate dependence of uprising Hencky strain. Reproduced from reference [66] with permission.

were similar to that of the PP/clay nanocomposites. The figure shows a strong strain-induced hardening behavior for the nanocomposite. Like PP nanocomposite systems, the extended Trouton rule, $\eta_E(\dot{\varepsilon}_0; t) = 3\eta_0(\dot{\gamma}; t)$, does not hold for PLA/clay melt, as opposed to the melt of pure polymer melt [67]. The results indicate that although there are flow-induced internal structural changes in the case of extension, they are different compared to the structural changes taking place under shear flow. In the case of PLA/clay samples, the effect of strain hardening was observed at higher strain rates and show similarity with the behavior of the sample under shear measurements. The strong rheopexy observed in shear measurements at a very low shear rate reflected a fact that the shear-induced structural change involved a process with an extremely long relaxation time. The clay particles are aligned in the flow direction. The alignment of clay particles leads to more restricted motion of the polymer chains, subsequently increasing the viscosity.

As to the elongation-induced structure development, Figure 10.20b shows the Hencky strain rate dependence of the uprising Hencky strain $(\varepsilon_{\eta E}) = \varepsilon_0 \times t_{\eta E}$ taken for PLA nanocomposite with 3 wt% of clay at 170 °C. The $\varepsilon_{\eta E}$ values increase systematically with ε_0. The lower the value of ε_0, the smaller the value of $\varepsilon_{\eta E}$. This tendency probably corresponds to the rheopexy of PLA/5 wt% clay nanocomposite under slow shear flow.

10.4
Conclusions

Rheological properties of polymer nanocomposites with various types of nanofillers such as nanoclay, carbon nanotube, and nanofibers have been widely studied in the last 20 years. The most significant results of these works and relative theories were summarized in this chapter. The incorporation of nanofillers into the polymer matrix dramatically alters the rheological behavior of polymer chains. Pronounced shear thinning was found to be a characteristic feature of truly nanodispersed composites. The rheological properties are directly related to the degree of dispersion of nanofillers in the polymer matrix and also level of interfacial interactions between the particle surface and polymer chains or segments. The linear rheological properties are strongly correlated with mesoscopic structure of the nanocomposite.

A transition from liquid-like to solid-like rheological behavior for the nanocomposites at relatively low filler loadings was observed. Prolonged application of large amplitude oscillatory shear leads to a significant decrease of the linear viscoelastic modulus and elimination of solid-like behavior of the nanocomposites. Rheological property measurements revealed that an increase in shear viscosity and storage and loss moduli of nanocomposites with nanofiller loadings. It is believed that rheology offers an effective way to assess the state of nanofiller dispersion and to detect the presence of interconnecting microstructure of the nanocomposites in molten state directly.

References

1 Hussain, F., Hojjati, M., Okamoto, M., and Gorga, R.E. (2006) *J. Compos. Mater.*, **40**, 1511.

2 Bhattacharya, S.T., Kamal, M.R., and Gupta, R.K. (eds) (2007) *Polymeric. Nanocomposites*, Hanser.

3 Pinnavaia, T.J., and Beall, G.W. (eds) (2000) *Polymer-Clay Nanocomposites*, John Wiley & Sons Inc., New York.

4 Itagaki, T., Matsumura, A., Kato, M., Usuki, A., and Kuroda, K. (2001) *J. Mater. Sci. Lett.*, **20**, 1483–1484.

5 Chen, C., and Curliss, D. (2003) *J. Appl. Polym. Sci.*, **90**, 2276.

6 Dresselhaust, M.S., and Dresselhaust, G. (1981) *Adv. Phys.*, **30**, 139.

7 Subramoney, S. (1998) *Adv. Mater.*, **10**, 1157–1171.

8 Cui, X., Engellard, M.H., and Lin, Y. (2006) *J. Nanosci. Nanotechnol.*, **5**, 547.

9 Rafiq, R., Cai, D., Jin, J., and Song, M. (2010) *Carbon*, **48**, 4309.

10 Cai, D.Y., and Song, M. (2009) *Nanotechnology*, **20**, 085712.

11 Okada, A., Kawasumi, M., Usuki, A., Kojima, Y., Kurauchi, T., and Kamigaito, O. (1990) *Mater. Res. Soc. Symp. Proc.*, **171**, 45.

12 Zilg, C., Muelhaupt, R., and Finnter, J. (1999) *Macromol. Chem. Phys.*, **200**, 661.

13 Qin, S.H., Oin, D.Q., Ford, W.T., Resasco, D.E., and Herrera, J.E. (2004) *J. Am. Chem. Soc.*, **126**, 171.

14 Andrews, R., Jacques, D., Minot, M., and Rantell, T. (2002) *Macromol. Mater. Eng.*, **7**, 395.

15 Yao, K.J., Song, M., Hourston, D.J., and Luo, D.Z. (2002) *Polymer*, **43**, 1017–1020.

16 Xia, H., and Song, M. (2005) *Soft Matter*, **1**, 386.

17 Zou, W., Du, Z.J., Liu, Y.X., Yang, X.P., Li, H.Q., and Zhang, C. (2008) *Compos. Sci. Technol.*, **68**, 3259.

18 Bousmina, M. (2006) *Macromolecules*, **39**, 4259.

19 Eslami, H., Grmela, M., and Bousmina, M. (2009) *Rheol. Acta*, **48**, 317.

20 Eslami, H., Grmela, M., and Bousmina, M. (2009) *J. Polym. Sci.*, **47**, 1728.

21 Ray, S.S. (2006) *J. Ind. Eng. Chem.*, **6**, 811.

22 Hsieh, C.C., and Larson, R.G. (2004) *J. Rheol.*, **48**, 995–1021.

23 Utracki, L.A., and Jamieson, A.M. (eds) (2010) *Polymer Physics, Part I*, John Wiley & Sons, Inc., New Jersey.

24 Gupta, R.K. (ed.) (2000) *Polymer and Composite Rheology*, 2nd edn, Marcel Dekker, Inc., New York.

25 Laason, R.G. (ed.) (1999) *The Structure and Rheology of Complex Fluids*, Oxford University Press, Oxford.

26 Utracki, L.A. (2004) *Clay-Containing Polymeric Nanocomposites*, vol. 2, Monograph, RAPRA, Shawbury, UK.

27 Jogun, S.M., and Zukoski, C.F. (1999) *J. Rheol.*, **43**, 847.

28 Uracki, L.A., and Fisa, B. (1982) *Polym. Compos.*, **3**, 193.

29 Okamoto, M., Nam, P.H., Maiti, P., Kotaka, T., Hasegawa, N., and Usuki, A. (2001) *Nano Lett.*, **1**, 295.

30 Herschel, W.H., and Bulklery, R. (1926) *Proc. Am. Test. Mater.*, **26**, 621.

31 Matijaˇsi'c, G., and Glasnovi'c, A. (2002) *Chem. Biochem. Eng. Q.*, **16**, 165.

32 Tanaka, H., and White, J.L. (1980) *Polym. Eng. Sci.*, **20**, 949.

33 Shenoy, A.V. (1999) *Rheology of Filled Polymer Systems*, Kluwer Academic Publisher, London.

34 Utracki, L.A., and Lyngaae-Jørgensen, J. (2002) *Rheol. Acta*, **41**, 397.

35 Sammut, P. (2007) Elongational Flow of Polymeric Nanocomposites. Paper presented at the 4th International Symposium on Polymer Nanocomposites Science and Technology.

36 Takahashi, S. (1996) Studies on the effect of macromolecular chain structure on elongational rheology. PhD dissertation, Yamagata University, Yonezawa, Japan.

37 Solomon, M.J., Almusallam, A.S., Seefeldt, K.F., Somwangthanaroj, A., and Varadan, P. (2001) *Macromolecules*, **34**, 1864.

38 Krishnamoorti, R., Vaia, R.A., and Giannelis, E.P. (1996) *Chem. Mater.*, **8**, 1728.

39 Lim, S.T., Hyun, Y.H., and Choi, H.J. (2002) *Chem. Mater.*, **14**, 1839.

40 Choi, H.J., Kim, S.K., Hyun, Y.H., and Jhon, M.S. (2001) *Macromol. Rapid Commun.*, **22**, 320.

41 Xia, H., and Song, M. (2006) *Polym. Int.*, **55**, 229.

42 Hyun, Y.H., Lim, S.T., Choi, H.J., and Jhon, M.S. (2001) *Macromolecules*, **34**, 8084.

43 Lim, Y.T., and Park, O.O. (2001) *Rheol. Acta*, **40**, 220.

44 Grossiord, N., Loos, J., and Koning, C.E. (2005) *J. Mater. Chem.*, **15**, 2349.

45 Potschke, P., Fornes, T.D., and Paul, D.R. (2002) *Polymer*, **43**, 3247.

46 Du, F.M., Scogna, R.C., Zhou, W., Brand, S., Fischer, J.E., and Winey, K.I. (2004) *Macromolecules*, **37**, 9048.

47 Shaffer, M.S.P., Fan, X., and Windle, A.H. (1998) *Carbon*, **36**, 1603.

48 Kanai, H., Navarrete, R.C., Macosko, C.W., and Scriven, L.E. (1992) *Rheol. Acta*, **31**, 333.

49 Kharchenko, S.B., Douglas, J.F., Obrzut, J., Grulke, E.A., and Migler, K.B. (2004) *Nat. Mater.*, **3**, 564.

50 Huang, Y.Y., Ahir, S.V., and Terentjev, E.M. (2006) *Phys. Rev. B*, **73**, 125422.

51 Song, Y.S. (2006) *Rheol. Acta*, **46**, 231.

52 White, J.L., Czarnecki, I., and Tanaka, H. (1980) *Rubber Chem. Technol.*, **53**, 823.

53 Du, F., Scogna, R.C., Zhou, W., Brand, S., Fischer, J.E., and Winey, K.I. (2004) *Macromolecules*, **37**, 9048.

54 Lim, S.T., Lee, C.H., Choi, H.J., and Jhon, M.S. (2003) *J. Appl. Polym. Sci.*, **41**, 2052.

55 Meincke, O., Hoffmann, B., Dietrich, C., and Friedrich, C. (2003) *Macromol. Chem. Phys.*, **204**, 823.

56 Kojima, Y., Usuki, A., Kawasumi, M., Okada, A., Kurauchi, Y., Kamigaito, O., and Kaji, K. (1995) *J. Polym. Sci. B*, **33**, 1039.

57 Krishnamoorti, R., and Yurekli, K. (2001) *Curr. Opin. Colloid Interface Sci.*, **6**, 464.

58 Song, W., and Windle, A.H. (2005) *Macromolecules*, **38**, 6181.

59 Shen, J., Han, X.M., and Lee, L.J. (2006) *J. Cell. Plast.*, **42**, 105.

60 Choi, Y.K., Sugimoto, K.I., Song, S.M., and Endo, M. (2005) *Mater. Lett.*, **59**, 3514.

61 Tabuani, S.C.D., Ferri, D., and Maffettone, P.L. (2008) *Rheol. Acta*, **47**, 425.

62 Wang, Y.R., Xu, J.H., Bechtel, S.E., and Keolling, K.W. (2006) *Rheol. Acta*, **45**, 919.

63 Miyazono, K., Kagarise, C.D., Koelling, K.W., and Mahboob, M. (2011) *J. Appl. Polym. Sci.*, **119**, 1940.

64 Galgali, G., Ramesh, C., and Lele, A. (2001) *Macromolecules*, **34**, 852.

65 Lele, A., Mackley, M., Galgali, G., and Ramesh, C. (2002) *J. Rheol.*, **46**, 1091.

66 Ray, S.S., and Okamoto, M. (2003) *Macromol. Mater. Eng.*, **288**, 936.

67 Cox, W.P., and Merz, E.H. (1958) *J. Polym. Sci.*, **28**, 619.

11
Segmental Dynamics of Polymers in Polymer/Clay Nanocomposites Studied by Spin-Labeling ESR

Yohei Miwa, Shulamith Schlick, and Andrew R. Drews

11.1
Introduction

Polymer/clay nanocomposites, which are obtained by dispersing nanosized clay fillers in a polymer matrix, have received intense attention in both scientific and industrial fields due to their improved properties (mechanical, thermal, optical, electrical, and gas and liquid barriers) even at low inorganic content, typically 2–5 wt% [1, 2]. The clay fillers may be e*xfoliated*, in which discrete clay layers are dispersed in the polymer matrix, *intercalated*, in which polymer chains occupy the interlayer spaces between silicate platelets that remain in a crystalline association, or exist as undispersed, unintercalated particles. Polymer dynamics have a major impact on nanocomposites properties and a proper understanding of these processes is important for designing optimized materials. However, polymer dynamics in nanocomposites is complicated and depends on the polymer structure, composition, and morphology. For example, while some papers reported no change in the glass transition temperature, T_g, commonly evaluated as a standard of segmental dynamics of polymers [3], others reported an increase in T_g [4, 5], the total disappearance of the transition [6, 7], or a decrease in the T_g for nanocomposites [8, 9]. To understand the dynamics process, it is crucial to explore "local" interactions where the polymer/clay interface is expected to play an important role.

Our work is centered on the electron spin resonance (ESR) spin-labeling technique to study local interactions and dynamics of polymer chains in polymer/clay nanocomposites. This is a powerful technique for discerning properties of specific labeled regions or components in complex systems and can provide information on the dynamics on time scales in the range 10^{-11}–10^{-7} s [10, 11]. After a brief introduction to the method of spin labeling in Section 11.2, we present a summary of our studies on the segmental dynamics of polymers in *exfoliated* poly(methyl acrylate)/clay nanocomposite [12] and *intercalated* poly(ethylene oxide) (PEO)/clay nanocomposite [13] in Sections 11.3 and 11.4, respectively; new insights on polymer dynamics at the polymer/clay interface are presented and the effects of

confinement and interaction with the clay platelets on polymer dynamics are discussed.

11.2
Spin Labeling: Basic Principles

The ESR spin-labeling method in synthetic polymers has been applied to study the local segmental motion, electrostatic interactions, and molecular orientations at the labeled sites [14]. Nitroxide radicals are widely used as labels because of their availability, high chemical and thermal stability, and detailed spectral analysis. In this section, we describe the ESR spectrum of nitroxides, the analysis of their ESR spectra, and the deduction of motional details.

11.2.1
ESR Spectra of Nitroxide Radicals

The ESR spectrum of nitroxides is dominated by the hyperfine interaction of the electron spin with the nuclear spin of the ^{14}N nucleus ($I = 1$) and by g-shifts due to spin–orbit coupling mainly in the $2p_z$ orbital of the lone pair on the oxygen nucleus. The anisotropic contribution comes from the spin density in the nitrogen $2p_z$ orbital, as illustrated in Figure 11.1. If the external magnetic field is parallel to the z axis, the hyperfine interaction and the splitting is large; if it is perpendicular to the lobes, the splitting is small (Figure 11.1a). The g-shifts are also shown;
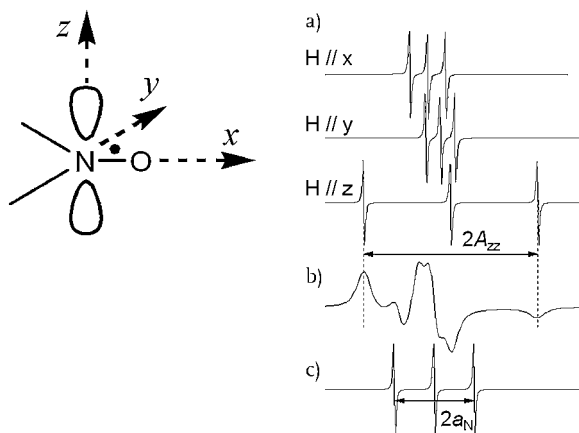
Figure 11.1 Anisotropic interactions for a nitroxide. (a) Immobilized and perfectly oriented nitroxide for the indicated orientations of the external magnetic field with respect to the nitroxide axis system. (b) Powder spectrum from immobilized nitroxides in disordered samples. (c) Fast motional spectrum in a solvent of low viscosity. $2A_{zz}$ is the extreme separation and a_N is the isotropic splitting.

the strongest shift is observed when the field is parallel to the N–O bond, which defines the x axis of the molecular frame. Thus, the triplets of lines at different orientations of the molecule with respect to the field not only have different splittings, but their centers are also shifted with respect to each other.

11.2.2
Line Shape Analysis of Nitroxide Radicals

When a nitroxide is attached to a polymer backbone via a short tether, the mobility of the nitroxide is strongly influenced by the segmental motion of the host polymer. Usually, all orientations of nitroxides have the same probability and a "powder" spectrum is obtained when the rotational motion is frozen on the time scale of the experiment (Figure 11.1b). On the other hand, the spectral anisotropy can be completely averaged for the fast thermal Brownian rotational diffusion possible in solutions of low viscosity and three equidistant lines of equal intensities width are observed in the ESR spectra (Figure 11.1c).

The mobility of nitroxides can be quantified by the rotational correlation time τ_R, which is the time during which a molecule maintains its spatial orientation. Examples of simulated ESR spectra with different τ_R values are shown in Figure 11.2. The ESR spectrum of nitroxide is sensitive to τ_R values in the range 10^{-11}–10^{-7} s. When τ_R is longer than 10^{-7} or shorter than 10^{-11} s, the ESR spectrum provides no dynamics information. Within the broad range of relaxation times that ESR is sensitive to, there are three subranges that must be considered separately. For
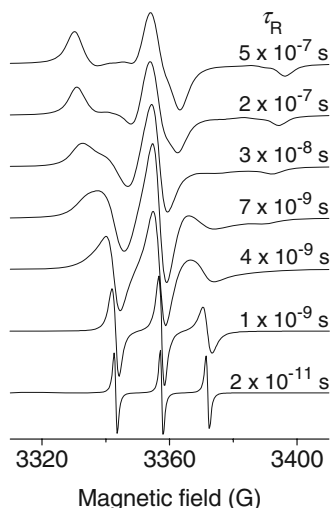
Figure 11.2 Simulated X-band ESR spectra of nitroxide and corresponding rotational correlation times, τ_R.
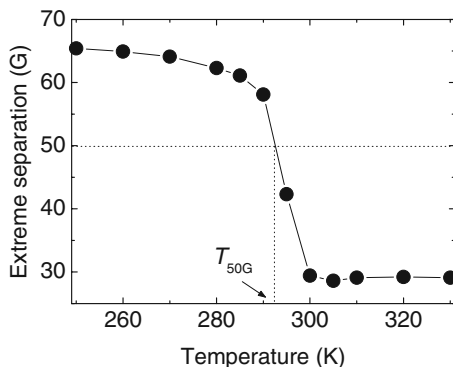
Figure 11.3 Plots of the ES against temperature. T_{50G} where ES is equal to 50 G is shown.

$10^{-11} < \tau_R < 10^{-9}$ s, the transverse relaxation and thus the line width are dominated by effects of rotational motion and the spectrum consists of three derivative Lorentzian lines with different widths. In this regime, the rotational correlation time can be inferred from the ratio of the line amplitudes [15]. In the range $10^{-9} < \tau_R < -10^{-8}$ s, the spectral shape changes with τ_R and the spectra are best analyzed visually and by simulation. When τ_R is longer than 10^{-8} s, the anisotropy is only moderately reduced by motion and a powder spectrum with a slightly reduced extreme separation (ES) results corresponding to $2A_{zz}$. Determination of τ_R in this regime has been described elsewhere [16].

A plot of ES as a function of temperature is shown in Figure 11.3, which gives a clear visual indicator of local dynamics and is often the simplest method to compare the dynamics in a series of materials. The temperature T_{50G} (or $T_{5.0\,mT}$) at which ES is 50 G (or 5.0 mT) is often used as a reference temperature for dynamics. The T_{50G} of a spin-labeled polymer is usually 50–100 K higher than the glass transition temperature (T_g) determined by DSC due to the higher frequency of ESR measurements [17]. The relaxation mode of polymers detected by the spin-label method has been described in more detail in reference [13].

11.3
Exfoliated Poly(methyl acrylate) (PMA)/Clay Nanocomposites

11.3.1
Preparation of Exfoliated Nanocomposites in the Absence of Surfactants

Exfoliated nanocomposites are usually more desirable for industrial applications compared to intercalated ones because the isotropic interactions between the polymer and the clay layers can be controlled [1, 2]. In the preparation of polymer/clay nanocomposites, the clay platelet surface is often modified with alkyl surfactants to enhance the miscibility between the components. In these systems, the
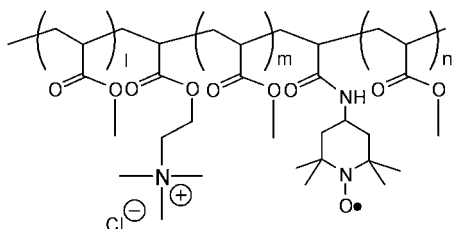
Figure 11.4 Spin-labeled PMA with attached trimethylammonium chloride groups.

nature of the polymer/clay interface as well as polymer dynamics can be strongly affected by the surfactants [1, 2]. The variable strength of the surfactant effect is one of the reasons why contradictory conclusions about the T_g of polymers in composites have often been reported. Detailed analyses of the structure and dynamics of surfactants have been carried out using advanced ESR techniques [18] and are described in more detail in another chapter of this volume.

Our approach has been to prepare poly(methyl acrylate) (PMA)/clay nanocomposites in the absence of surfactants in order to estimate the direct interactions between polymer segments and the clay platelet surface [12]. PMA was modified by attachment of nitroxide radicals and trimethylammonium chloride (TMC) groups in low concentrations ($\approx 1\,mol\%$), as shown in Figure 11.4; ion exchange between the TMC moiety and the clay platelet surface allowed the preparation of exfoliated nanocomposites even *in the absence of* surfactants. In our ESR study, a synthetic fluoromica (Somasif, ME-100) was chosen as the clay component. Somasif ($Na_{0.66}Mg_{2.68}(Si_{3.98}Al_{0.02})O_{10.02}F_{1.96}$) is appealing because it has negligible paramagnetic impurities and an exchange capacity of $115\,mequiv/g$. In addition to PMA/Somasif nanocomposites, the interaction of PMA with Somasif modified with a methyl tallow bis-2-hydroxyethylammonium (MEE) surfactant was also examined, as well as a conventional PMA/Somasif composite in which clay particles were dispersed without delamination was also prepared for comparison. The syntheses of these samples are given in reference [12]. As described below, the type of composite was determined by ESR, differential scanning calorimetry (DSC), and X-ray diffraction (XRD). We use the term "composites" to refer to materials in which the dispersion of the clay is on a scale significantly larger that the nanoscale. The notations used for the various types of composites are SPn for nanocomposites based on Somasif, COMPn for conventional composites based on Somasif, and MEEPn for nanocomposites based on MEE (modified Somasif), where n is the wt% clay.

11.3.2
Structure of Exfoliated Nanocomposites

As seen in Figure 11.5, neat Somasif clay exhibits two XRD peaks, at $2\theta = 7.2°$ ($d_{001} = 1.23\,nm$) and $9.3°$ ($0.95\,nm$) attributed to hydrated and dehydrated
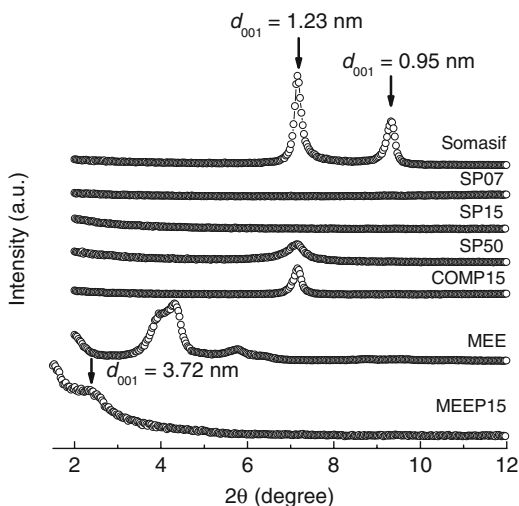
Figure 11.5 X-ray diffraction (XRD) patterns of the indicated samples. Reprinted with permission from Ref. [12a]. Copyright 2006 American Chemical Society.

crystallites, respectively [19]. The original Somasif peaks disappeared in SP07 and SP15, suggesting complete clay exfoliation and dispersion in the polymer matrix. Although XRD measurements were not carried out for SP03, it is reasonable to assume that the exfoliated structure also exists in SP03 based on the results for SP07 and SP15. The SP50 and the COMP15 showed the diffraction peak at $2\theta = 7.2°$, indicating the presence of crystalline hydrated Somasif. Based on the analyses of DSC and ESR, we conclude that SP50 consisted of both exfoliated and unexfoliated Somasif crystallites. The MEE system showed at least four distinct diffraction peaks due to crystallization of the intercalated clay with different spacings of the MEE layers, while MEEP15 showed only one peak, at $2\theta = 2.4°$ ($d_{001} = 3.72$ nm). Although ordering of intercalants has been observed in a variety of systems, the structure of the various intercalated MEE forms is not certain in this case and a detailed interpretation of the *d*-spacing MEE is speculative at this point.

11.3.3
Segmental Dynamics of PMA in Nanocomposites

11.3.3.1 The Glass Transition Temperature
The T_g and ΔT_g values determined by DSC are listed in Table 11.1. While T_g values did not vary significantly with Somasif content for most of the nanocomposites, ΔT_g of SP50 was larger than that of PMA, indicating that the segmental mobility

Table 11.1 Characteristics of samples.

Sample	Somasif (wt%)	T_g (K)[a]	ΔT_g (K)[a]	Structure[b]
PMA		287 ± 1	14 ± 1	
SP03	3	287 ± 1	15 ± 1	
SP07	7	287 ± 1	15 ± 1	Exfoliated
SP15	15	286 ± 1	15 ± 1	Exfoliated
SP50	50	285 ± 1	17 ± 1	Partially exfoliated
COMP15	15	287 ± 1	14 ± 1	Composite
MEEP15	15	285 ± 1	14 ± 1	Intercalated

a) Determined by DSC.
b) From XRD data.
Reprinted with permission from Ref. [12a]. Copyright 2006 American Chemical Society.
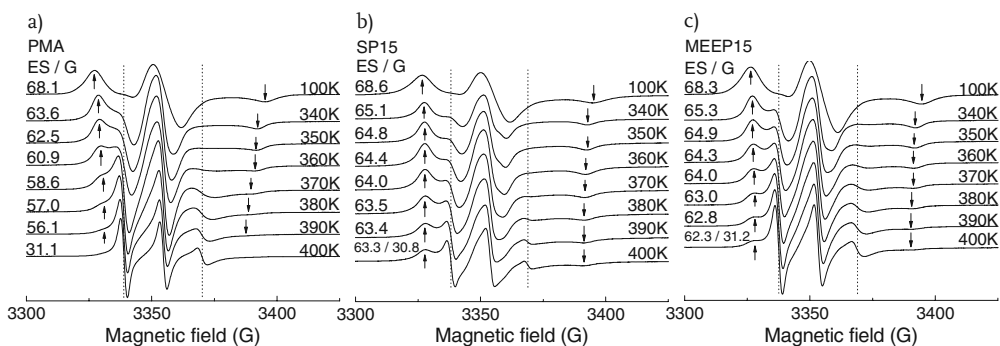
Figure 11.6 Temperature variation of ESR spectra for PMA (a), SP15 (b), and MEEP15 (c). The ES is indicated by arrows and given on the left. The $2a_N$ value is indicated in each set of spectra by dotted lines and given for $T = 400$ K. Reprinted with permission from Ref. [12a]. Copyright 2006 American Chemical Society.

of PMA became more heterogeneous in SP50 because of the larger amount of clay. This interpretation is also supported by the extra breadth in the d_{001} XRD peak when compared to other compositions, which is an indication of a higher level of disorder along the clay platelet normal direction.

11.3.3.2 Restricted Molecular Motion at the PMA/Clay Interface

Selected ESR spectra of spin-labeled PMA, SP15, and MEEP15 in the temperature range 100–400 K are shown in Figure 11.6a–c, respectively. The dotted vertical lines indicate the values of the isotropic hyperfine splitting from the ^{14}N nucleus a_N. By comparing the three sets of spectra, it is apparent that the mobility of PMA is

considerably restrained by the presence of Somasif: at 400 K the ESR spectrum of PMA is in the motionally narrowed regime (fast component), but a superposition of slow and fast components [20] is observed for SP15. The restricted molecular motion is caused primarily by attachment of the trimethylammonium groups on the Somasif surface and by the polar interaction between the ester groups and the siloxane oxygen on the basal surfaces of the silicate layers. The "anchoring" effect on a solid surface not only constrains the motion, but also increases the thickness of the restricted interfacial layer [21]. Moreover, the density of the polymer increases in the vicinity of the Somasif surface, leading to a lower polymer mobility [22]. The more constrained and denser layers of PMA at the clay surface are responsible for the improved mechanical properties and better thermal and dimensional stabilities of matrix polymers. Moreover, the lower molecular mobility inhibits diffusion of oxygen and unstable intermediates that can initiate degradation.

The increasing trend in ESs of the slow component for the SP03, SP07, SP15, and SP50 at 400 K with Somasif concentration (58.5, 63.1, 63.3, and 68.0 G, respectively) [12] indicates an increasing interaction between the polymer and the clay at the interface [12]. This increase is contrary to the expectation that the constraining effect be independent on Somasif content, provided that the clay platelets are well separated, and may be due to overlap of interfacial regions of different platelets with an increase in the Somasif content, as shown in Figure 11.7: polymer chains in interfacial regions confined by two or more Somasif platelets have lower
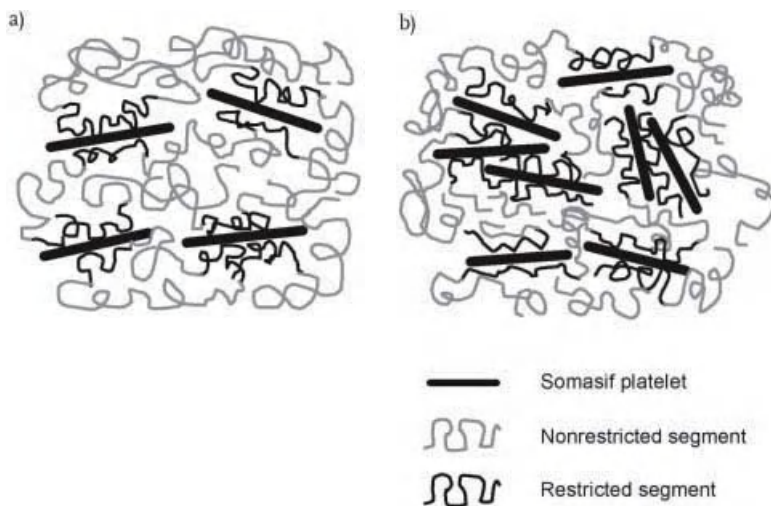
Figure 11.7 Schematic representation of PMA/Somasif nanocomposites with low (a) and high (b) Somasif content. PMA chains restricted due to their proximity to the Somasif surface and unrestricted chains are represented with black and gray lines, respectively. Reprinted with permission from Ref. [12a]. Copyright 2006 American Chemical Society.

mobility than those restricted by one platelet only. In addition, TMC groups can act as crosslinkers between Somasif platelets, leading to closer proximity between Somasif platelets. In contrast to chains at the polymer/clay interface, the $2a_N$ values, representing the fast component in the nanocomposites, are comparable to those in neat PMA (Figure 11.6), and indicate constant polymer mobility in regions distant from the Somasif surface.

Although ESR results point to a region of restricted polymer mobility near the interface that is significantly separated from the bulk region, no distinct glass transition of the interfacial region was detected by DSC. The absence of a distinct glass transition for the polymer in the interfacial region can be rationalized by the difference in the frequency dependence of glass transitions in the bulk and interfacial regions. For example, the difference in the dynamic glass transition modes in the bulk and interfacial regions of poly(dimethylsiloxane) filled with silica nanoparticles increased with an increase in frequency [23]. While the relaxation time, τ_c, detected by DSC ($\approx 100\,s$) implies a frequency $\nu = (2\pi\tau_c)^{-1} \approx 2 \times 10^{-3}\,Hz$ [24]; the ESR X-band frequency is $\approx 9 \times 10^9\,Hz$ and the dynamics of the polymer in the interfacial region can be detected by ESR and but not by DSC.

11.3.3.3 Thickness of the Interfacial Region
With the exception of PMA, the ESR spectra at 400 K (Figure 11.8) all contain fast and slow components; the relative intensities of the two spectral components were deduced by spectral deconvolution [12] and the percentage slow component
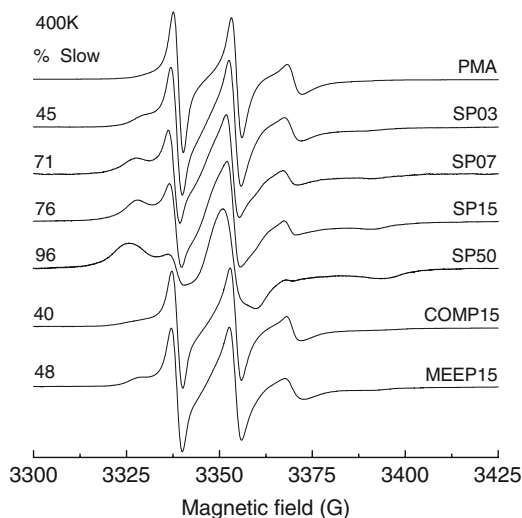
Figure 11.8 ESR spectra for the indicated systems measured at 400 K. The relative intensity of the slow component in percentage is given on the left (see text). Reprinted with permission from Ref. [12a]. Copyright 2006 American Chemical Society.

Table 11.2 Average distance between Somasif platelets, *D*, and thickness of the rigid interface, t_{int}.

Sample	*D* (nm)	t_{int} (nm)
SP03	67	15 ± 1.0
SP07	28	10 ± 0.5
SP15	12	5 ± 0.3

Reprinted with permission from Ref. [12a]. Copyright 2006 American Chemical Society.
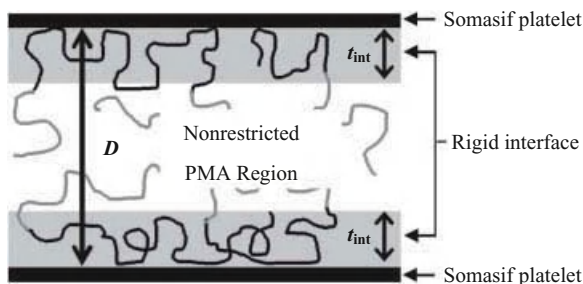
Figure 11.9 The average thickness of the polymer/clay interface, t_{int}, and the average distance between exfoliated clay platelets, *D* (see the text). Reprinted with permission from Ref. [12a]. Copyright 2006 American Chemical Society.

is indicated for each spectrum in Figure 11.8. For the SP*n* nanocomposites, the relative intensity of the slow component in the ESR spectra increased with increasing Somasif content, due to the larger rigid interfacial region. This implies that the slow component reflects the mobility in the interfacial region, and correlates with the size of the interfacial region in the nanocomposites. In COMP15 and MEEP15, the slow component intensities are much lower than those in SP15.

The average thickness of the interface, t_{int}, listed in Table 11.2 for SP03, SP07, and SP15 at 400 K was calculated from Eq. (11.1),

$$t_{int} = (I_{slow})D/200 \tag{11.1}$$

where I_{slow} is the relative intensity of the slow component, and *D* is the average distance between exfoliated Somasif platelets in the nanocomposites, as shown in Figure 11.9. The *D* was calculated from Eq. (11.2),

$$D = 2(1-w)/d_{PMA}Sw \tag{11.2}$$

where *w* is the weight fraction of Somasif in the SP*n* sample, d_{PMA} is the density of PMA, which was assumed to be equal to that of pure PMA ($\approx 1.2\,g\,cm^{-3}$), and

S is the specific surface area of Somasif platelets. Using a clay density of $2.6\,g\,cm^{-3}$, an average lateral size of platelets of $\approx 450\,nm$ as reported by the manufacturer and the thickness ($0.95\,nm$) deduced from XRD (Figure 11.5), S was estimated to be $\approx 800\,m^2\,g^{-1}$ by assuming that the Somasif platelets are 450-nm diameter disks.

Depending on Somasif content, the estimated interfacial thickness is ≈ 5–$15\,nm$ and decreases with increasing Somasif content (Table 11.2). This trend is most likely the result of some overlap of interfacial regions of different Somasif platelets as illustrated in Figure 11.7 and is consistent with a lower mobility in the interfacial region for increasing Somasif content.

11.4
Intercalated Poly(ethylene oxide) (PEO)/Clay Nanocomposites

11.4.1
Preparation of Intercalated PEO/Clay Nanocomposites

Nanocomposites consisting of polymers intercalated in layered inorganic compounds have attracted great interest in recent years, both as novel materials with enhanced properties, as well as ideal systems for the study of polymer behavior in nanoscopically confined media [1, 2]. In particular, PEO/clay nanocomposites have been widely studied because of their unique electronic, ionic (without counterions), structural, thermal, and mechanical properties [25–30]. In this system, PEO chains are confined in narrow, $<1\,nm$, galleries between the inorganic layers *in the absence of* surfactants. The intercalated PEO shows unique conformation and mobility compared to bulk PEO because of limited space and interactions with the charged surface of inorganic host layers and interlayer cations, such as Na^+ or Li^+. We have applied the ESR spin-labeling technique for the detection of the local environment in the galleries and for the direct and quantitative analysis of the dynamics of PEO chains intercalated and confined in the nanoscopic galleries between silicate platelets. The motivation for this study was to reveal effects of gallery width and molecular weight on the segmental mobility of polymer chains located between inorganic walls.

Two PEO samples with MW = 400 and 4000 Da were spin-labeled and intercalated into Somasif clay by either the solution intercalation [25] or melt intercalation methods [26] as shown in Figure 11.10. Nonintercalated components were completely removed by washing with benzene. For comparison, nonintercalated composites were also prepared via casting from a benzene solution. The notation used for the composites is NANO(m)n for intercalated nanocomposites and COMP(m)n for nonintercalated composites, where m and n are the molecular weight of PEO and the Somasif wt%, respectively; the n values were determined by thermal gravimetric analysis (TGA). The characteristics of the samples used in this work are listed in Table 11.3.
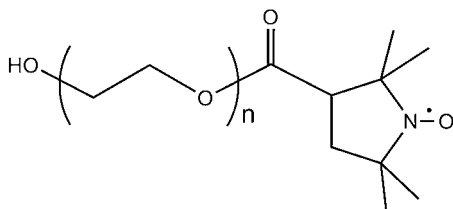
Figure 11.10 The chemical structure of spin-labeled PEO.

Table 11.3 Characteristics of samples.

Sample	Somasif (wt%)[a]	$d_{gallery}$ (nm)[b]	T_g (K)[c]	T_m (K)[c]
PEO4k	–	–	–	338
PEO400	–	–	205	279
NANO(4k)96	96	0.33	–	–
NANO(4k)82	82	0.83	–	–
COMP(4k)99.8	99.8	–	–	–
NAO(400)77	77	0.78	–	–

a) Determined by TGA.
b) The gallery width in which PEO chains were intercalated (estimated from XRD data).
c) Determined by DSC.

11.4.2
Structure of Intercalated Nanocomposites

11.4.2.1 Intercalation of PEO in Clay Galleries of Thickness <1 nm

XRD profiles for the samples measured in the 2θ range 3–10° at ambient temperature are shown in Figure 11.11. As noted above, the Somasif has two peaks, at 2θ = 7.2° (d_{001} = 1.23 nm) and 9.3° (0.95 nm), indicative of hydrated and dehydrated phases, respectively. On intercalation of PEO, an increase in d was observed for NANO(m)n samples: the galleries in which PEO is intercalated are 0.33 nm in NANO(4k)96, 0.83 nm in NANO(4k)82, and 0.78 nm in the NANO(400)77. For COMP99.8, no shift from the original diffraction peak position of neat Somasif was detected, indicating no PEO intercalation in the clay galleries. Intercalation also manifested itself in NANO(4k)96, NANO(4k)82, and NANO(400)77 with an increase in the PEO decomposition temperatures when compared to either PEO4k or PEO400, based on TGA measurements. An increase in the decomposition temperature is most likely because the diffusion of oxygen molecules is inhibited in the clay galleries and is additional evidence for the intercalation of PEO [13].
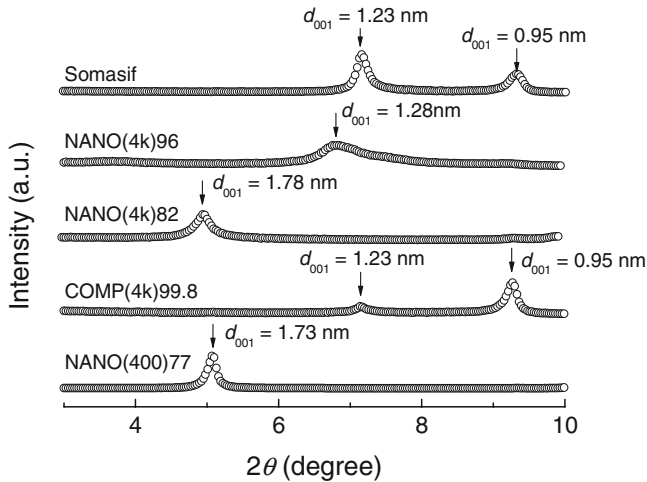
Figure 11.11 XRD patterns of Somasif (clay), NANO(4k)96, NANO(4k)82, COMP(4k)99.8, and NANO(400)77 in the 2θ range 3–10°.

Moreover, the decomposition temperature of NANO(4k)96 was higher than that of NANO(4k)82, indicating slower oxygen diffusion in the narrower galleries.

11.4.2.2 Inhibited Crystallization

XRD of crystalline PEO should show strong peaks at about 19° and 24° due to a combination of the (112) and (032) reflections and the (120) reflection, respectively [31]. However, these diffraction peaks are absent in the NANO(4k)82, indicating inhibited crystallization of the intercalated PEO (see reference [13a]). Inhibited crystallization for intercalated PEO is also supported by DSC and FTIR results. In the DSC traces (Figure 11.12), a distinct melting transition is observed for PEO400 and PEO4k at 279 and 338 K, and with 52% and 91% crystallinity, respectively, using 222.2 J g^{-1} as the fusion enthalpy of PEO crystallites [32]. On the other hand, melting transitions were not detected for any of the intercalated nanocomposite and nonintercalated composite samples. Moreover, FTIR spectra for the NANO(4k)96 and NANO(4k)82 did not show peaks at 1360 and 1343 cm^{-1} associated with the CH$_2$ wagging motion in crystalline PEO [33], suggesting that the PEO chains in the NANO(4k)96 and NANO(4k)82 were amorphous (see Ref. [13a]). Based on the XRD, DSC, and FTIR results, it is obvious that the crystallization is inhibited and PEO is amorphous in such narrow clay galleries.

11.4.2.3 Disappearance of the Glass Transition

Although PEO400 showed a clear glass transition at 279 K (Figure 11.12), no glass transition was detected for PEO4k because of its high crystallinity, ca. 91%. On the other hand, no glass transition was detected for the NANO(m)n samples by
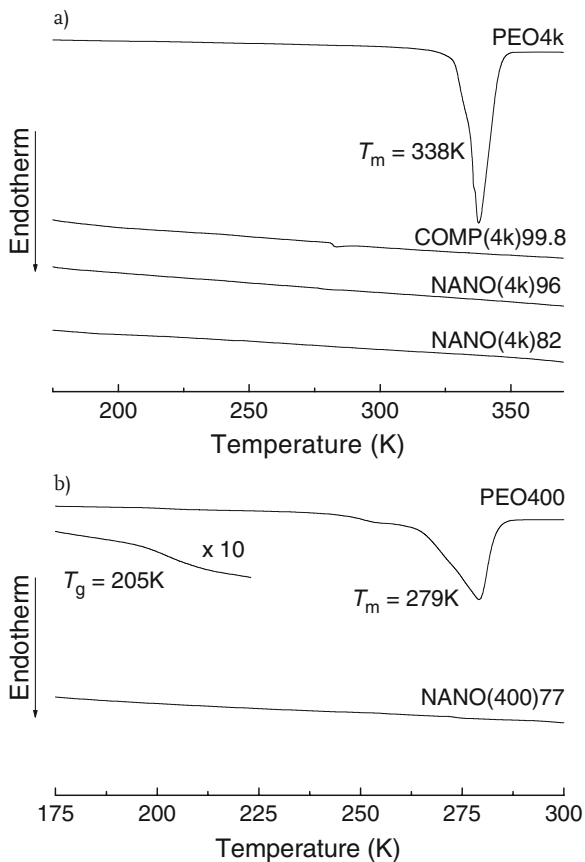
Figure 11.12 DSC traces.

DSC even though the PEO was amorphous in the galleries as described above. Based on recent research, it is now understood that a glass transition is a relaxation mode based on the cooperative interactions between neighboring segments [34]. The length-scale of the cooperative motion near T_g for bulk glass has been determined by various methods [35]. Although the length-scale is material dependent, the values are on the order of 1–4 nm. Therefore, it is reasonable to assume that the reduced cooperative motion in NANO(4k)82, NANO(4k)96, and NANO(400)77 is a result of PEO confinement in narrow galleries, <1 nm.

11.4.2.4 Hindered Hydrogen Bonding

ESR spectra at 100 K reflect the local environment around the spin labels because their motion is frozen. Selected experimental and simulated ESR spectra of the samples in the range 100–410 K are shown in Figure 11.13. The A and g tensors determined from the simulation of the spectra at 100 K are listed in Table 11.4.
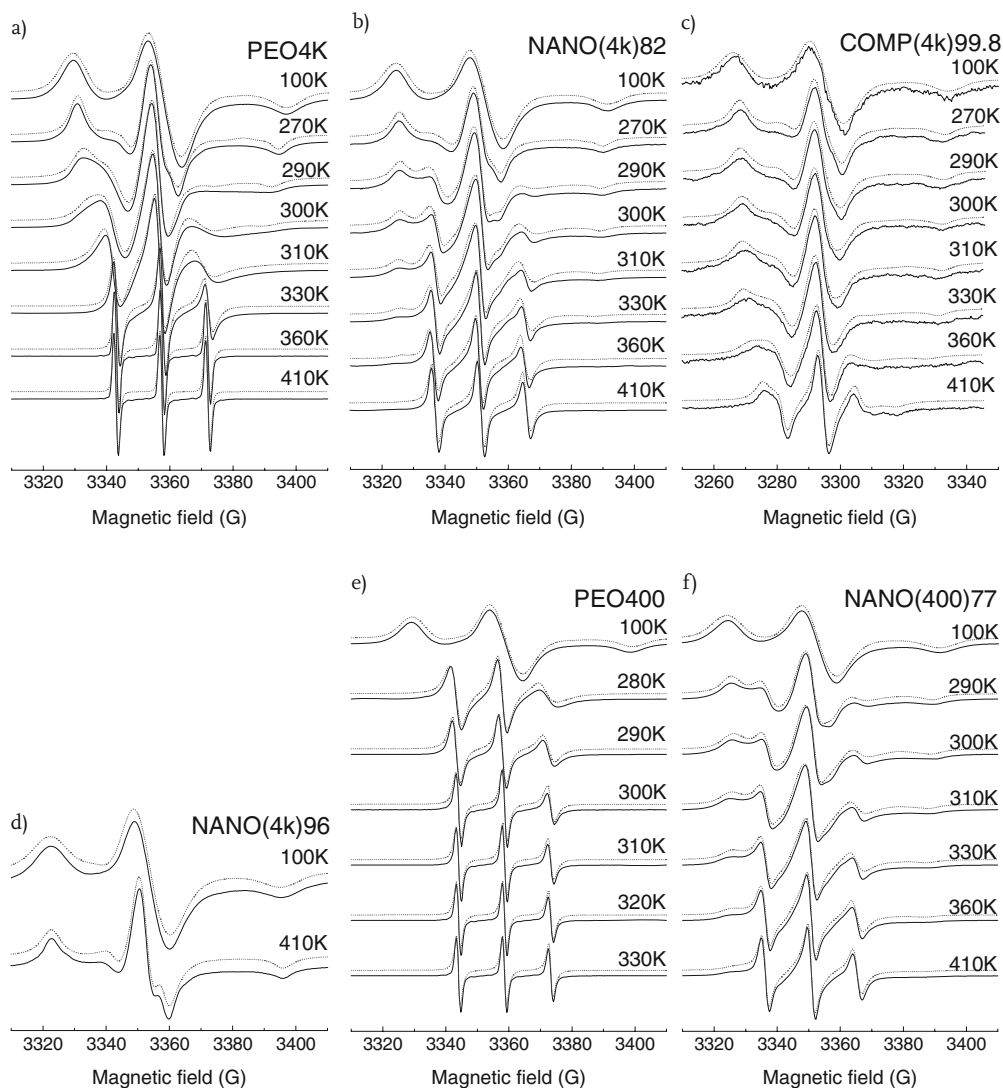
Figure 11.13 Temperature variation of ESR spectra (experimental spectra–full black lines; simulated spectra–red dotted lines) for PEO4k (a), NANO(4k)82 (b), COMP(4k)99.8 (c), NANO(4k)96 (d), PEO400 (e), and NANO(400)77 (f).

For PEO400, A_{zz} is significantly larger than that of the PEO4k (34.8 G vs. 33.6 G) due to the higher concentration of hydroxyl groups at the chain ends in PEO400. The increase in the hydroxyl group concentration increases the polarity of PEO, and because the hydroxyl group forms a hydrogen bond with a nitroxide, the result is a significant increase in A_{zz} [14]. Thus, the nitroxide labels are good indicators

Table 11.4 Magnetic parameters determined by simulation of ESR spectrum at 100 K.

Sample	g_{xx}	g_{yy}	g_{zz}	A_{xx}/G	A_{yy}/G	A_{zz}/G
PEO4k	2.0088	2.0068	2.0025	5.7	4.0	33.6
NANO(4k)96	2.0084	2.0052	2.0021	7.7	4.3	36.8
NANO(4k)82	2.0088	2.0067	2.0026	5.9	4.2	33.4
COMP(4k)99.8	2.0090	2.0070	2.0028	5.7	4.0	33.9
PEO400	2.0087	2.0067	2.0020	5.5	3.7	34.8
NANO(400)77	2.0088	2.0067	2.0025	5.9	4.2	33.6

for hydrogen bonding. For NANO(400)77, A_{zz} is significantly smaller than that of the PEO400 (33.6 G vs. 34.8 G), suggesting a decrease in the hydroxyl group concentration around the nitroxide labels. Although the number of hydroxyl groups in the galleries for NANO(400)77 is greater than that for NANO(4k)82, their A_{zz} values are very similar (33.6 G vs. 33.4 G), suggesting that the hydroxyl group concentration around the nitroxide labels did not increase. This can only occur if the interactions between PEO segments are negligible in the galleries, and suggests that the PEO segments are physically isolated.

11.4.3
Segmental Dynamics of PEO in Clay Galleries

11.4.3.1   Simulation of ESR Spectra and Determination of Dynamic Parameters
The segmental dynamics of spin-labeled PEO intercalated in clay galleries was analyzed in detail by simulations of experimental ESR spectra using a model known as "microscopic order with macroscopic disorder" (MOMD), which includes spin-label rotational diffusion [36]. The model assumes that the spin labels undergo microscopic molecular ordering with respect to a local director and that the local directors in the sample are randomly oriented in the laboratory frame. Pilar has recently summarized the successful application of the MOMD model for analyzing ESR line shapes of spin-labeled polymers [37]. The rotational diffusion of nitroxide spin labels attached to polymer chain segments can be approximated as a superposition of the isotropic rotational diffusion of the polymer chain segment with a rotational diffusion coefficient, R_S, and the internal rotation of the spin label with the rotational diffusion coefficient, R_I [37]. When the nitroxide spin label is attached to a polymer chain via a short tether, we can assume that $R_{prp} = R_S$ and $R_{pll} = R_I + R_S$. Here, the R_{pll} and R_{prp} are the parallel and perpendicular rotational diffusion coefficients, respectively. The results of the simulation of experimental spectra are shown in Figure 11.13. ESR spectra of all samples were simulated with a single spectral component, with the exception of NANO(4k)82 and NANO(400)77: two distinct spectral components, fast and slow, were necessary to fit spectra for these samples. Arrhenius plots of R_S are shown in Figure 11.14 and the activation energies E_S are listed in Table 11.5.
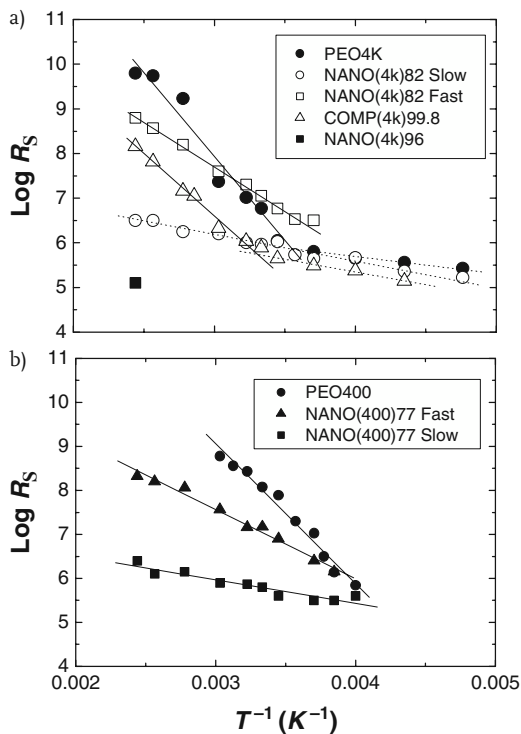
Figure 11.14 Arrhenius plots of the rotational diffusion coefficients R_S.

Table 11.5 Activation energies.

Sample	E_S (kJ mol^{-1})
PEO4k	69[a], 8[b]
PEO400	61
NANO82 (slow component)	11
NANO82 (fast component)	37
NANO(400)77 (slow component)	10
NANO(400)77 (fast component)	30
COMP99.8	54[c], 11[d]

a) $T^{-1} < 0.0035$.
b) $T^{-1} > 0.004$.
c) $T^{-1} < 0.003$.
d) $T^{-1} > 0.0037$.

11.4.3.2 **Effect of Gallery Thickness on the Segmental Mobility of Intercalated PEO**

The polymer chains in NANO(4k)96 are intercalated into galleries only 0.33 nm wide (comparable to the thickness of a PEO chain) and show a very low log R_S value (5.1) even at 410 K, compared to 9.8 for PEO4k. This is likely because the PEO chains are more constrained in these extremely narrow galleries (Figure 11.14a). The restriction is weaker in NANO(4k)82 with its larger gallery width (0.83 nm), and the ESR spectra show a superposition of fast and slow spectral components. The slow component clearly represents PEO segments interacting with the solid surface, leading to both a high A_{zz} and a low mobility. On the other hand, the R_S value of the fast component in NANO(4k)82 is higher than that for PEO4k for $T^{-1} < 0.0032$. The accelerated dynamics of the fast component represents both the weaker interactions with the polar clay surface and a lower PEO segmental density. This conclusion is consistent with computer simulations which show the coexistence of fast and slow segmental relaxations and a higher segmental density with a slower segmental relaxation near the inorganic surfaces [19, 27b, 28–30]. Although dynamic cooperativity between unconfined polymer segments generally increases with a decrease in temperature [34], this increase should be suppressed for polymer chains confined in galleries. Therefore, the fast relaxing component in the NANO(4k)82 retains a high mobility even at relatively low temperatures.

11.4.3.3 **Effect of Molecular Weight on the Segmental Mobility of Intercalated PEO**

The glass transition temperature of polymers generally decreases with a decrease in the molecular weight because of an increase in the concentration of chain ends [38]. Because the spin-labeled sites move cooperatively with neighboring segments in the bulk, their mobility increases with an increase in the chain-end concentration even when the chain ends are spin-labeled [17] (Figure 11.4). As expected, PEO400 has a higher mobility than PEO4k (Figure 11.14a) because of the higher chain-end concentration. However, NANO(400)77 showed mobility comparable with NANO(4k)82, where the log R_S values of the fast motional component in the NANO(400)77 and NANO(4k)82 at 410 K were 8.3 and 8.8, respectively (Figure 11.14a). This indicates that the mobility of the spin-labeled sites of the intercalated PEO was *not* enhanced by the increased chain-end concentration and is further evidence that the cooperative segmental motion of PEO is reduced in the galleries (Figure 11.10).

11.5
Conclusions

We have presented applications of ESR spin-labeling to estimate the "local" static interactions and dynamics of polymer chains in *exfoliated* and *intercalated* nanocomposites. The ESR spectra indicated heterogeneities in the structure and dynamics of polymer segments in nanocomposites. In particular, the relative

intensity of the spectral component of polymer chains restricted at the polymer/clay interface was accurately determined from deconvolution of ESR spectra. This approach is promising for predicting some important properties of nanocomposites, such as gas and liquid permeability, dimensional stability, and mechanical properties.

Our results also indicated that the dynamics of polymer segments in the vicinity of the clay platelets was restricted due to the electrostatic interactions between the polymer segments and charged clay surface. Detailed analysis of ESR spectra by computer simulations revealed that when PEO was confined in clay galleries of 0.8 nm, some segments were released from the restriction at the clay-wall surface and showed a *lower* activation energy compared to bulk PEO, most likely because of reduced intersegmental cooperativity in the limited narrow galleries.

From these results, we conclude that the ESR spin-labeling method is capable of describing "local" interactions and dynamics of polymers in nanocomposites.

Acknowledgments

References

1 Pinnavaia, T.J., and Beall, G.W. (2000) *Polymer-Clay Nanocomposites*, John Wiley & Sons, Ltd, Chichester, UK.

2 Ajayan, P.M., Schadler, L.S., and Braun, P.V. (2004) *Nanocomposite Science and Technology*, Wiley-VCH Verlag GmbH, Weinheim, Germany.

3 Tyan, H., Liu, Y., and Wei, K. (1999) *Chem. Mater.*, **11**, 1942–1947.

4 Vyazovkin, S., and Dranca, I. (2004) *J. Phys. Chem. B*, **108**, 11981–11987.

5 Tran, T.A., Saïd, S., and Grohens, Y. (2005) *Macromolecules*, **38**, 3867–3871.

6 Vaia, R.V., Jandt, K.D., and Giannelis, E.P. (1996) *Chem. Mater.*, **8**, 2628–2635.

7 Weimer, M.W., Chen, H., Giannelis, E.P., and Sogah, D.Y. (1999)

J. Am. Chem. Soc., **121**, 1615–1616.

8 Liu, T., Lim, K.P., Tjiu, W.C., Pramoda, K.P., and Chen, Z.-K. (2003) *Polymer*, **44**, 3529–3535.

9 Lee, Y.-H., Bur, A.J., Roth, S.C., and Start, P.R. (2005) *Macromolecules*, **38**, 3828–3837.

10 Miller, W.G. (1979) Chapter 4, in *Spin Labeling II – Theory and Applications* (ed. L.J. Berliner), Academic Press, New York, pp. 173–221.

11 Jeschke, G., and Schlick, S. (2006) Chapter 1, in *Advanced ESR Methods in Polymer Research* (ed. S. Schlick), John Wiley & Sons, Inc., Hoboken, NJ, pp. 3–24.

12 (a) Miwa, Y., Drews, A.R., and Schlick, S. (2006) *Macromolecules*, **39**, 3304–3311.; (b)

Miwa, Y., Drews, A.R., and Schlick, S. (2006) *Polym. Prepr. Am. Chem. Soc. Div. Polym. Chem.*, **47** (2), 839.

13 (a) Miwa, Y., Drews, A.R., and Schlick, S. (2008) *Macromolecules*, **41**, 4701–4708.; (b) Miwa, Y., Drews, A.R., and Schlick, S. (2009) *Macromolecules*, **42**, 8907–8913.

14 Jeschke, G., and Schlick, S. (2006) Chapter 7, in *Advanced ESR Methods in Polymer Research* (ed. S. Schlick), John Wiley & Sons, Inc., Hoboken, NJ, pp. 165–195.

15 Kivelson, D.J. (1960) *Chem. Phys.*, **33**, 1094–1106.

16 Freed, J.H. (1976) Chapter 3, in *Spin Labeling – Theory and Applications* (ed. L.J. Berliner), Academic Press, New York, pp. 53–132.

17 Miwa, Y., Tanase, T., Yamamoto, K., Sakaguchi, M., Sakai, M., and Shimada, S. (2003) *Macromolecules*, **36**, 3235–3239.

18 (a) Jeschke, G., Panek, G., Schleidt, S., and Jonas, U. (2004) *Polym. Eng. Sci.*, **44**, 1112–1121.; (b) Panek, G., Schleidt, S., Mao, Q., Wolkenhauer, M., Spiess, H.W., and Jeschke, G. (2006) *Macromolecules*, **39**, 2191–2200.

19 Chen, B., and Evans, J.R.G. (2004) *J. Phys. Chem. B*, **108**, 14986–14990.

20 Griffith, O.H., and Jost, P.C. (1976) in *Spin Labeling Theory and Applications* (ed. L.J. Berliner), Academic Press, New York, pp. 453–523.

21 Berriot, J., Lequeux, F., Monnerie, L., Montes, H., Long, D., and Sotta, P. (2002) *J. Non Cryst. Solids*, **307–310**, 719–724.

22 Mansfield, K.F., and Theodorou, D.N. (1989) *Macromolecules*, **22**, 3143–3152.

23 Fragiadakis, D., Pissis, P., and Bokobza, L. (2005) *Polymer*, **46**, 6001–6008.

24 Santangelo, P.G., and Roland, C.M. (1998) *Macromolecules*, **31**, 4581–4585.

25 (a) Aranda, P., and Ruiz-Hitzky, E. (1992) *Chem. Mater.*, **4**, 1395–1403.; (b) Wu, J., and Lerner, M.M. (1993) *Chem. Mater.*, **5**, 835–838.

26 Wong, S., Vaia, R.A., Giannelis, E.P., and Zax, D.B. (1996) *Solid State Ionics*, **86–88**, 547–557.

27 (a) Bujdák, J., Hackett, E., and Giannelis, E.P. (2000) *Chem. Mater.*, **12**, 2168–2174.; (b) Hackett, E., Manias, E., and Giannelis, E.P. (2000) *Chem. Mater.*, **12**, 2161–2167.

28 Kuppa, V., Menakanit, S., Krishnamoorti, R., and Manias, E. (2003) *J. Polym. Sci. B*, **41**, 3285–3298.

29 Kuppa, V., and Manias, E. (2003) *J. Chem. Phys.*, **18**, 3421–3429.

30 Lorthioir, C., Lauprêtre, F., Soulestin, J., and Lefebvre, J.-M. (2009) *Macromolecules*, **42**, 218–230.

31 Fraisse, F., Morlat-Thérias, S., Gardette, J.-L., Nedelec, J.-M., and Baba, M. (2006) *J. Phys. Chem. B*, **110**, 14678–14684.

32 Braun, W., Hellwege, K.-H., and Knappe, W. (1967) *Kolloid-Z. Z. Polym.*, **215**, 10–15.

33 Hoffmann, C.L., and Rabolt, J.F. (1996) *Macromolecules*, **29**, 2543–2547.

34 (a) Kauzmann, W. (1948) *Chem. Rev.*, **9**, 219–256.; (b) Adam, G., and Gibbs, J.H. (1965) *J. Chem. Phys.*, **28**, 373–383.

35 (a) Tracht, U., Wilhelm, M., Heuer, A., Feng, H., Schmidt-Rohr, K., and Spiess, H.W. (1998) *Phys. Rev. Lett.*, **81**, 2727–2730.; (b) Qiu, X.H., and Ediger, M.D. (2003) *J. Phys. Chem. B*, **107**, 459–464.; (c) Berthier, L., Biroli, G., Bouchard, J.-P., Cipelletti, L., El Masri, D., L'Hote, D., Ladieu, F., and Pierno, M. (2005) *Science*, **310**, 1797–1800.

36 (a) Meirovitch, E., Nayeem, A., and Freed, J.H. (1984) *J. Phys. Chem.*, **88**, 3454–3465.; (b) Xu, D., Budil, D.E., Ober, C.K., and Freed, J.H. (1996) *J. Phys. Chem.*, **100**, 15867–15872.; (c) Liang, Z., and Freed, J.H. (1999) *J. Phys. Chem. B*, **103**, 6384–6396.; (d) Earle, K.A., and Budil, D.E. (2006) Chapter 3, in *Advanced ESR Methods in Polymer Research* (ed. S. Schlick), John Wiley & Sons, Inc., Hoboken, NJ, pp. 53–83.

37 Pilar, J. (2006) Chapter 6, in *Advanced ESR Methods in Polymer Research* (ed. S. Schlick), John Wiley & Sons, Inc., Hoboken, NJ, pp. 133–163, and references therein.

38 Jin, X., Zhang, S., and Runt, J. (2002) *Polymer*, **43**, 6247–6254.

12
Characterization of Polymer Nanocomposite Colloids by Sedimentation Analysis

Vikas Mittal

12.1
Introduction

Organic–inorganic hybrid colloidal nanoparticles are synthesized in order to synergistically combine the functional properties of the organic and inorganic constituents [1–12]. This results in the final properties of the composite particles which are better than the constituent phases. Different types of hybridization processes are possible, namely, encapsulation of the inorganic materials by the various polymer matrices, or the immobilization of the inorganic phase on the surface of the polymer particles. This immobilization can also be physical or chemical in nature thus leading to varying extents of bonding strength of the phases. To achieve such composite particles, inorganic phase is predispersed in the continuous phase in which the monomer is also dispersed. The polymerization of monomer in the presence of the inorganic phase either by emulsion or miniemulsion polymerization method leads to the hybrid particles if the interactions between the two phases are controlled. Also, the conditions need to be optimized that lead to nanoscale dispersion of the inorganic particles, such that the resulting hybrid particles are also nanoparticles and do not contain aggregated inorganic particles. The enhancement of the properties thus results into the expansion of the spectrum of applications for such hybrid nanoparticles. Inorganic phase provides strength, dimensional, and heat stability to the particles, whereas, the organic component is helpful in providing intraparticle compatibility as well as enhanced interactions of the particles with various substrates.

The performance of the hybrid particles is dependent on the success of hybridization processes thus requiring the efficient characterization of the system. It is important to quantify if the whole amount of both the components are present together in the hybrid particles or if small amount of these phases exist separately. Apart from that, the particle size and size distribution of these colloidal particles

are also important drivers of their commercial applications; thus, it is necessary to study these characteristics in order to analyze the evolution of hybrid particles as a function of reaction parameters. There are a number of analytical methods which can provide information on the size of the particles like analytical ultracentrifugation, hydrodynamic chromatography, field flow fractionation, and dynamic light scattering, etc. Analytical ultracentrifugation (AUC), in which the particles are sedimented at high rotational speeds, is a method of choice for such analyses owing to its very high statistical analytical ability [13–23]. Additionally, in this method, the characterization of the colloidal system can be achieved not only in terms of particle size distribution, but the density distributions in the colloidal particles can also be accurately detected, which is otherwise not possible in the other analytical methods. As a result, analytical ultracentrifuge has been extensively used for the study of the polymer or inorganic particles [13–26]. The analysis of the complex hybrid colloidal systems with advanced morphologies like inorganic–organic core shell particles, polymer particles with inorganic particles grafted on the surface etc. as well as study of evolution of hybrid particles as a function of time poses a much bigger challenge and the use of analytical ultracentrifuges for such systems has not been fully developed.

Owing to its high potential, analytical ultracentrifuge can be used to synergistically characterize various aspects of hybrid particles. This information can be used to generate structure property correlations which can thus help to tune the synthesis processes as well as to design new ones. To achieve this, information from various detection modes using Schlieren, turbidity, and interference optics available in ultracentrifuge can be combined to generate in-depth analysis into the characterization of extent or success of hybridization, growth of hybrid composites as a function of time etc. For example, by following the distribution of the density of the particles, it is possible to detect the presence of single components present in the hybrid latex and subsequently from the density of the hybrid particles, it is also possible to generate information on the extent of the hybridization process. The sedimentation profiles of the particles generated by turbidity and interference optics under the action of centrifugal field in the ultracentrifuge can also be analyzed in order to generate this information. Apart from that, the use of preparative ultracentrifugation can also be incorporated in the analysis to follow the evolution of the hybridization process as a function of time by following the changes in the density as well as size of the particles. The use of preparative ultracentrifugation though provides qualitative information on the system, however, it has a strong advantage of the ability to generate fractions of the various components which can be further characterized by other analysis methods. Combination of analytical ultracentrifugation with filed flow fractionation has also been reported for the hybrid particle analysis [27].

The current study reports the characterization of the above-mentioned aspects of polymer inorganic hybrid colloidal particles by the use of analytical and preparative ultracentrifugation. Both the hybrid types with organic core or inorganic core were studied and the systems included polystyrene-layered silicate hybrids,

polyurethane–pigment hybrids, polyacrylate–calcium carbonate, and polystyrene–silica hybrids. All these systems though were hybrid colloidal particles, but completely differ from each other in their synthesis methodologies (compatibilization of organic and inorganic phases for the composite synthesis has different considerations for each system), interactions between the particles and the dispersion medium and final morphologies, thus representing different characterization complexities. The goal of the current chapter is, thus, twofold: first to establish the insights into the different systems chosen for this study by correlating the information from different detection optics available in ultracentrifuge, thus to lessen the dependence on the other characterization methodologies, and secondly, to act as a reference for the characterization of other complex colloidal systems.

12.2
Materials and Experimental Methods

12.2.1
Hybrid Colloid Dispersions

The hybrid polystyrene-layered silicate, polyurethane-pigment, and polystyrene-silica colloid dispersions used in the study were achieved by either emulsion or miniemulsion polymerization of the polymer phase. These synthesis processes resulted in hybrid colloids in which either the inorganic particles were encapsulated by the polymer phase or the polymer particles formed the core and the inorganic particles adhered to the surface of the particles forming the shell. The amount of inorganic content was also varied in the hybrid particles. In another example of hybrid particles, the preformed organic (polyacrylate-based latex) and inorganic (calcium carbonate) particles were also mixed with each other which results into the adsorption of the polymer particles on the surface of large inorganic particles.

12.2.2
Turbidity and Interference AUC

OPTIMA XL ultracentrifuge from Beckman Coulter fitted with turbidity or interference detection optics was used for the sedimentation analysis of the hybrid particles [13]. The user-made turbidity detection optics employed a green detection light with a wavelength of 546 nm which was generated using a stabilized incandescent lamp as light source and a monochromatic light filter. The light was focused to 0.5 mm at mid-cell. The dispersion is placed in the centerpiece of a mono-sector cell and the change in the intensity of the light beam as a function of running time is recorded. The intensity of the incident light reduces owing to the scattering by the dispersion particles in the measurement cell, according to Mie's light scattering theory. This signal is then recorded by the photomultiplier

as a function of time and is converted into the diameter information after inserting the values of density as well as refractive index of the particles as well as suspension medium. The interference detection optics, on the other hand, is based on the principle of Rayleigh interferometer. A laser diode with a wavelength of 675 nm was used as a light source. The detection is based on the principle that velocity of light depends on the refractive index of the medium through which it passes. Thus, refractive index difference between the solution and the solvent, which is proportional to the corresponding concentration at this radial position, can be efficiently monitored by using this optics and subsequently converted to diameter information. Concentrations of roughly $10 \, \mathrm{g \, l^{-1}}$ were used for the sedimentation analysis. Interference optics was operated by running the rotor at 10 000 rpm, whereas a ramp in the speed of the rotor was used for the turbidity detection. Measurements were carried out at room temperature and distilled water was used for the dilution of the dispersions.

12.2.3
Static Density Gradients

OPTIMA XL model of the AUC from Beckman Coulter fitted with user-made Schlieren detection optics was used to analyze the density distribution of the dispersion particles by using static density gradient analysis [28, 29]. Schlieren optics set-up was similar to the set-up of Rayleigh interferometer on which the interference detection optics is based, but it had a phase plate in the focus of the condenser lens. Flash lamp was used as light source and light of well-defined wavelength of 546 nm was generated. As mentioned above, in the case of interference optics, the vertical fringe shift is proportional to the difference in the refractive index, whereas, in Schlieren optics, the vertical shift is proportional to the radial refractive index gradient. Mono sector cells containing −2° horizontal wedge windows to compensate the steep radial optical refractive index gradient were used. Water nycodenz density gradient system covering the complete range of measurable density (1.05–1.415 $\mathrm{g \, cm^{-3}}$) was used. A small amount of emulsifier was also added to water in order to inhibit any aggregation of the particles. The rotor speeds in the range of 30 000–40 000 rotations per minute were chosen. The concentration of particles was adjusted to roughly $0.1 \, \mathrm{g \, l^{-1}}$. The samples were generally run for 22 h at room temperature.

12.2.4
Preparative Ultracentrifugation

Preparative ultracentrifuge from Beckman Coulter was used for the preparative fractionation of various hybrid colloid dispersions. Depending on the systems, fractionation time in the range of 25–70 h and sedimentation speeds in the range 20 000–44 000 rotations per minute were used. Similarly, different amounts of nycodenz were also employed, the most common permutations being 25% nycodenz in water or 50% nycodenz in D_2O [30].

12.3
Results and Discussion

Multidirectional characterization of the hybrid colloidal nanoparticles is important to confirm the success of hybridization reaction and to quantify its extent in the hybrid particles. Such characterization also helps to control the reaction conditions in order to achieve optimal hybrid formation, only which can realize the synergistic improvement in the properties as compared to the constituents. Different modes of detection as well as different set of experiments possible in the ultracentrifuge provide opportunities for the analysis of a combination of different characteristics of the particles, which otherwise is not possible from any other single technique. Although a combination of different analytical methods would most probably be required for the complete analysis of hybrid particles, but the use of centrifugation is still suitable to answer many questions pertaining to the hybridization reaction success, the evolution of hybrid particles as a function of time, extent of hybridization, etc. by accurately following the size and density distributions of the particles.

The comparison of the sedimentation velocity profiles of polystyrene-layered silicate hybrid particles consisting of 1.25 vol% of the inorganic content as well as pure polymer and inorganic particles, generated by using interference detection optics at 10 000 rotations per minute, revealed qualitative information about the polydispersity in the samples. The later scans in the case of hybrid and pure polymer particles were broad or flattening thus indicating that a well-defined sedimentation plateau was not formed which indicated the presence of polydispersity in the particle size. In case the particles were more monodisperse, the sedimentation profile would have a well-defined plateau with similar slopes in the scans in the beginning as well as in the end. The sedimentation profile of the pure inorganic particles showed on the other hand a more uniform sedimentation plateau indicating that the particles in this case sedimented almost at the same time. It would mean that the particles may be more monodisperse in size if the density of the particles is fairly constant. The changes in the sedimentation profiles of the pure inorganic particles after hybridization reaction already signaled that these particles may be bound with the organic phase, which needed to be further analyzed by quantitative analysis.

Figure 12.1 shows the differential and cumulative sedimentation coefficient distributions for the pure polystyrene polymer and inorganic silicate particles as well as polystyrene-layered silicate hybrid particles [31]. The sedimentation coefficients of the hybrid particles synthesized by using different amounts of inorganic fractions were observed to decrease as compared to pure inorganic particles. As the sedimentation coefficient of the particles is a direct function of the density as well as size of the particles, therefore, the reduction in the sedimentation coefficient of the hybrid particles confirms the expected decrease in the density of the inorganic particles ($2.5\,g\,cm^{-3}$) owing to the association with the organic phase. Even though the resulting hybrid particles are larger in size as compared to the pure inorganic particles thus requiring the sedimentation coefficient of these

a)

b)
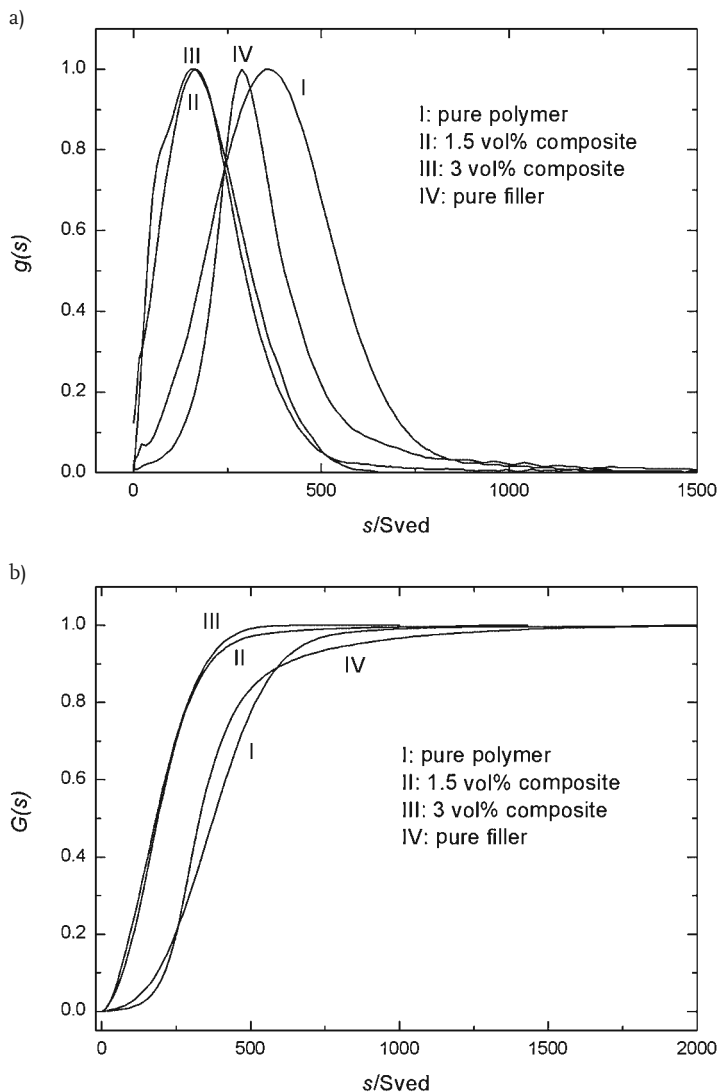
Figure 12.1 (a) Differential and (b) cumulative sedimentation coefficient distributions of polystyrene-layered silicate hybrid particles (filler volume fractions of 1.25% and 2.5%) and pure components measured by interference detection optics. Reproduced from reference [31] with permission from Springer.

particles to be higher than that of the inorganic particles, but the impact of decreased density in the case of hybrid particles takes precedence. The pure polymer particles were observed to have higher sedimentation coefficient probably owing to the higher particle sizes. However, the polymer fraction in the hybrid particles is not a true representative of the pure polymer particles owing to the

generation of hybrid particles by *in-situ* polymerization of monomer in the presence of inorganic filler. Thus, it is of interest to achieve information on the hybridization process solely by the characterization of the hybrid particles. Apart from that, absence of sedimentation peak signal corresponding to pure inorganic particles in the case of hybrid particles may indicate the absence of free inorganic particles in the hybrid latexes. However, as the sedimentation curves of the pure and hybrid particles still overlap to some extent, therefore the absence of any pure inorganic particles need to be further confirmed by other analysis methods like turbidity optics and the preparative ultracentrifugation. Similarly, it is also important to quantify the presence of any pure polymer particles formed during the hybridization process. The sedimentation coefficient distribution of the hybrid particles synthesized with 2.5 vol% of the filler fraction was similar to the hybrids with 1.25 vol% of filler indicating that either the effect of increasing the amount of filler did not significantly affect the characteristics of the particles or there was a small fraction of free inorganic particles which need to be detected by using the above mentioned analysis methods. Figure 12.2 also shows the corresponding differential and cumulative particle size distributions of the hybrid as well as pure polymer and inorganic colloids [31]. The hybrid particles were broad in size distribution as compared to the pure inorganic particles which also confirms the earlier observations from sedimentation profiles. The increase in the particle size distribution also confirms the hybrid formation which subsequently leads to the reduction in the density of the particles resulting in the shifting of the particles to lower sedimentation coefficient range. It can also be argued that the size may also increase by the aggregation of the inorganic particles with each other, but in such cases, the sedimentation coefficient of the aggregates would be even higher than the singly inorganic particles. Similarly, the higher diameter signal may also arise from the generation of only pure polymer particles free from any inorganic particles, but in such a case too, the sedimentation coefficient distribution would exhibit the signals corresponding to both the pure components. Therefore, the increased sizes as well as decreased density in the case of hybrid particles clearly confirm the formation of hybrid particles. The pure polymer particles were also observed to have broad particle size distribution as compared to the pure inorganic particles as indicated by the sedimentation velocity data. The higher diameter of these particles earlier observed from sedimentation coefficient distributions was also confirmed indicating that the polymer particles containing the filler have smaller particle as compared to the pure polymer particles formed in the absence of filler particles. The broadness in sizes in the case of pure polymer and hybrid particles was also very similar indicating that the polymer chains formed during the polymerization tended to generate polydispersity in the size of the particles irrespective of the presence or absence of filler in the system. Similar to the case of sedimentation coefficient mentioned above, the absence of lower diameter peaks in the size distributions of the hybrid particles corresponding to pure inorganic particles cannot be taken as a confirmation of the absence of any pure inorganic particles in the hybrid latexes owing to the partial overlap of diameter distributions. Apart from that, a shoulder at low diameter range is also observed

a)

b)
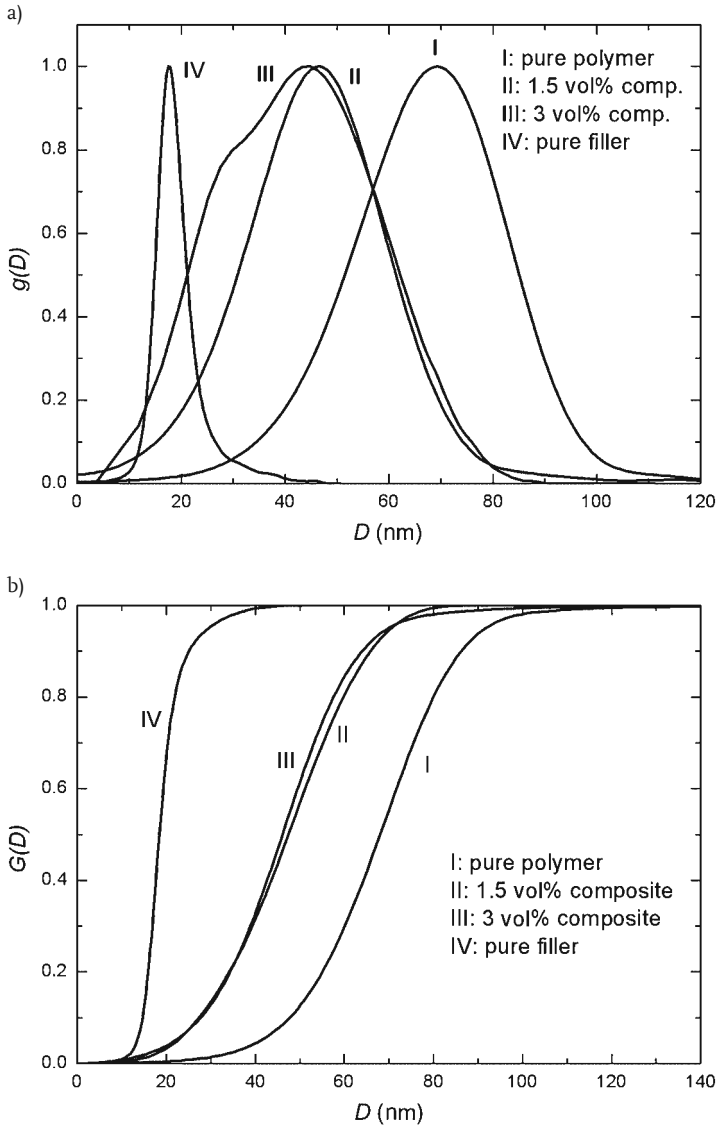
Figure 12.2 (a) Differential and (b) cumulative particle size distributions of polystyrene-layered silicate hybrid particles (filler volume fractions of 1.25% and 2.5%) and pure components, when measured by interference optics in ultracentrifuge. Reproduced from reference [31] with permission from Springer.
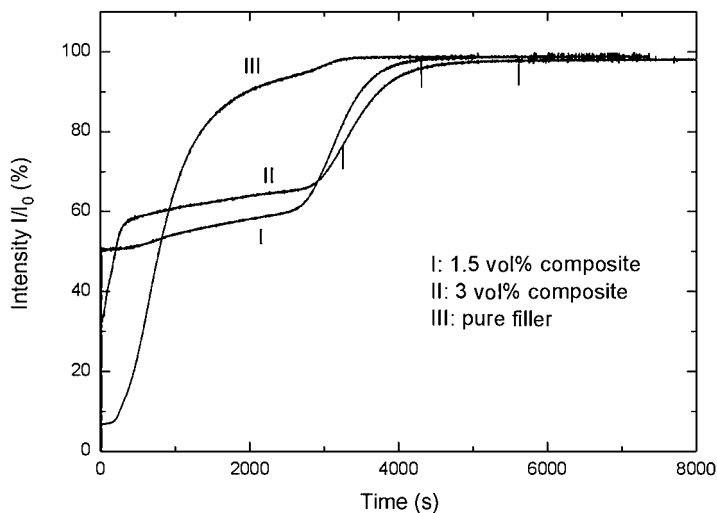
Figure 12.3 Intensity versus time profiles of the polystyrene-layered silicate hybrid and pure inorganic particles detected by turbidity optics. Reproduced from reference [31] with permission from Springer.

in the case of hybrid particles containing 2.5 vol% of filler, which may also indicate the presence of a small amount of free inorganic particles in the latex. Also, as the pure polymer particles do not completely represent the polymer fraction formed in the presence of filler, the absence of free polymer particles formed during the hybridization reaction needs to be confirmed separately.

Analytical ultracentrifugation analysis of the dispersion particles was also carried out by using turbidity detection optics, in which the change in the intensity of the incident light beam at mid-radius position can be plotted as a function of time. Figure 12.3 demonstrates these analyses for inorganic as well as hybrid particles [31]. The filler particles were observed to sediment faster as compared to hybrid particles owing to the higher density. The absence of sedimentation of particles in the hybrid dispersions in the range of pure inorganic particles would confirm the absence of any free inorganic particles fraction in the dispersions. In the case of hybrid dispersion containing 1.25 vol% of inorganic fraction, no such signal is observed. However, in the case of hybrid particles with 2.5 vol% of the filler fraction, a sharp fast-occurring sedimentation peak with a slope similar to the sedimentation of pure inorganic particles was observed. This peak may signify a small amount of free inorganic particles in the system and as the peak was observed at sedimentation times earlier than the sedimentation of pure inorganic particles, therefore, it may also signify the presence of aggregates of such inorganic particles which then sediment faster than the pure inorganic particles. The aggregates of pure polymer or hybrid particles can also lead to such signal, but they need to be much bigger to sediments at such high rate and these would have been easily

a)

b)
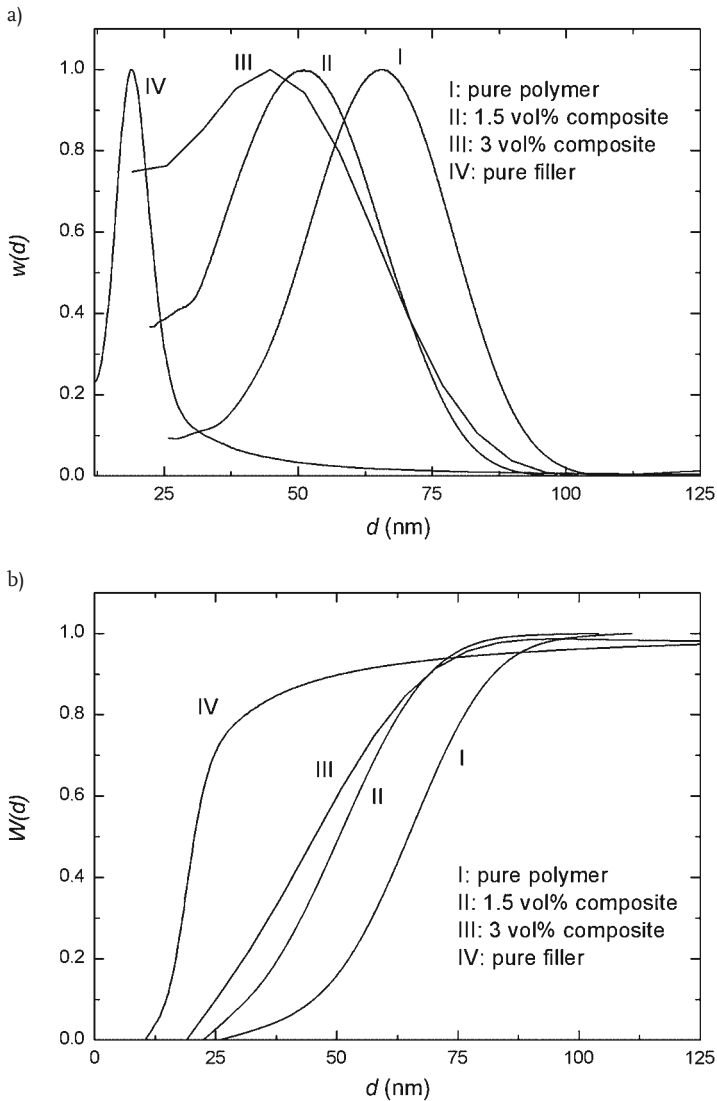
Figure 12.4 (a) Differential and (b) cumulative particle size distributions of the polystyrene-layered silicate hybrid particles along with pure polymer and inorganic filler particles when measured with turbidity optics in ultracentrifuge. Reproduced from reference [31] with permission from Springer.

noticed in the dispersions. Thus, this peak is more attributable to the inorganic fraction aggregated to small extent. It may also correlate with the shoulder observed in the particle size distributions of the hybrid particles when 2.5 vol% filler fraction was used. Figure 12.4 also shows the differential and cumulative size distributions of the pure and hybrid particles measured by turbidity detection optics [31]. The
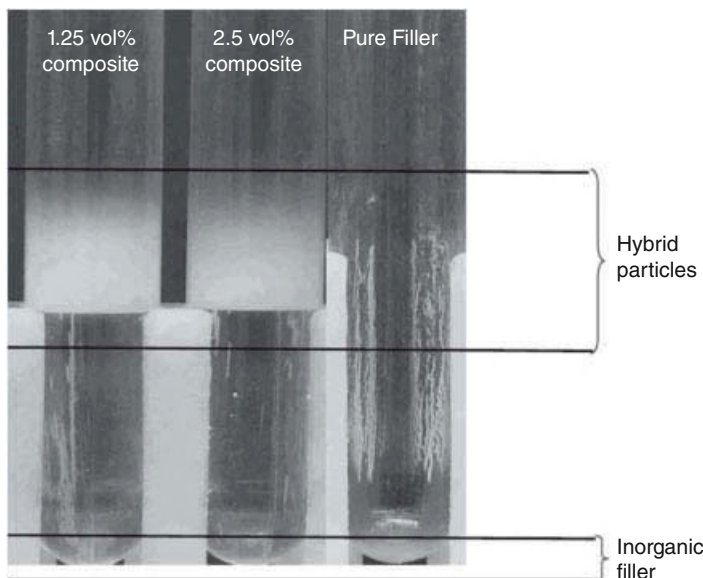
Figure 12.5 Use of preparative ultracentrifuge for the detection of pure inorganic layered silicate particles remaining in the colloidal system after hybridization reaction. Reproduced from reference [31] with permission from Springer.

peak diameters as well as diameter distributions were similar as compared to interference detection optics thus exhibiting the robustness of the analytical ultracentrifugation method in characterization of the hybrid latex particles.

Preparative ultracentrifugation was also carried out to confirm the observations from the turbidity detection as shown in Figure 12.5 [31]. The results were collected after sedimentation for 77 h at 40 000 rotations per minute by forming a density gradient containing 25% nycodenz in water. The pure filler particles sedimented completely at the bottom of the sedimentation tube. The composite dispersion with 1.25 vol% of the filler had one band corresponding to the hybrid particles and no sedimentation of the pure inorganic particles was observed at the bottom of the tube. In the case of dispersion with 2.5 vol% of filler fraction, similar band corresponding to the hybrid particles was observed but a small amount of filler was also observed at the bottom of the tube. It thus confirms the earlier observation that in the composite particles synthesized with higher fraction of filler, a small amount of filler particles was free in the dispersion. Also no other low-density band corresponding to pure polymer fraction was observed. The pure polymer particles formed in the absence of the filler are not compared owing to their completely different sedimentation coefficients as well as particle sizes. Also, both the hybrid particle dispersions were observed to have similar bands (and thus density) also confirming the earlier findings.
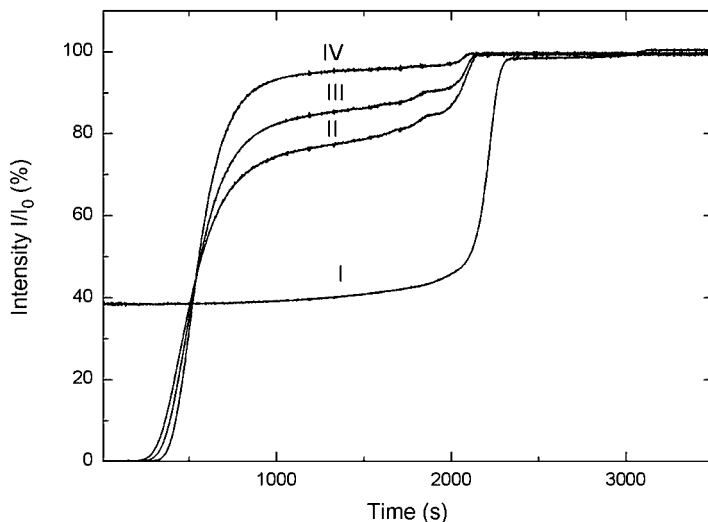
Figure 12.6 Intensity versus time plots of sedimentation profile of pure acrylate based polymer latex (curve I) compared with the profiles of polymer–CaCO$_3$ hybrid particles (curves II–IV) in order to determine the amount of hybridization in the particles. Reproduced from reference [31] with permission from Springer.

Turbidity detection optics can also be used for the quantification of free polymer particles in the hybrid latex, apart from free inorganic particles. An example of CaCO$_3$ pigment hybrid with polyacrylate-based polymer binder particles is demonstrated in Figure 12.6, where the transmission of the incident beam resulting from the scattering by the particles is plotted as a function of time for pure polymer latex (curve I) as well as for hybrid latexes (curves II–IV) synthesized by using different mixing ratios of polymer and the pigment particles [31]. The pure polymer particles sediment slowly owing to lower density and only one sedimentation plateau was observed in this case. In the case of hybrid latexes, two sedimentation plateaus were observed. The first plateau corresponded to the pure pigment or hybrid latex particles which owing to their higher densities sediment much faster. The presence of second plateau corresponded with the sedimentation behavior of pure polymer particles thus indicating the presence of free binder particles in the hybrid latexes. The height of this signal could be correlated with the signal height corresponding to the pure polymer latex particles which allowed the quantification of amount of free polymer particles in the hybrid latex. It was thus calculated from the plateau heights of curves II–IV that an amount of 4%, 14%, and 21% of the total binder was free, respectively, in the hybrid latexes.

Density gradient analysis in analytical ultracentrifugation is also an important tool for the quantification of the hybridization processes. By comparing the exact density distributions of the hybrid particles with that of pure components, it is possible to ascertain the extent of hybridization.
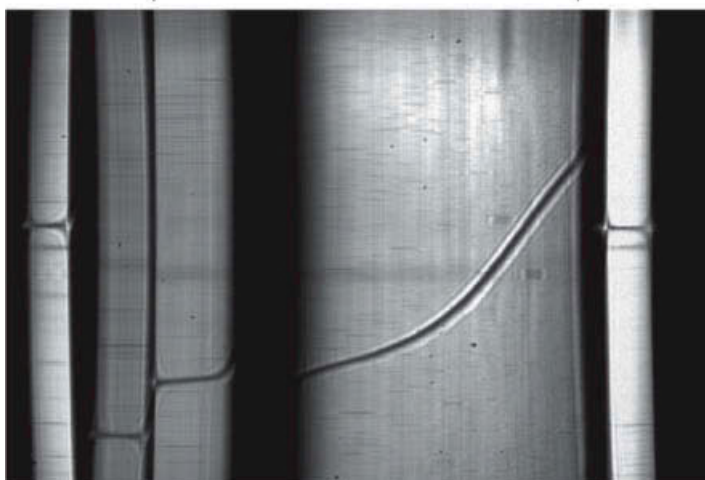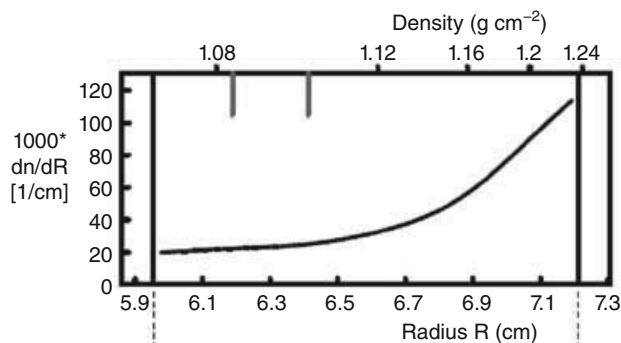
Figure 12.7 Schlieren images representing the density distribution of polystyrene silica hybrid particles (density gradients, after 22 h at 30 000 rpm, 25 °C, 20 wt% nycodenz in water). Reproduced from reference [31] with permission from Springer.

Although the upper density in the case of aqueous gradients is limited to 1.415 g cm^{-3}, it is still suitable in many cases to detect the hybrid particles as well as free polymer particles. The extent of hybridization in the hybrid particles can then be used to calculate the amount of free inorganic particles in the dispersion, if any. Figure 12.7 shows the density distribution of polystyrene silica hybrid particles measured in the gradient with a density range of 1.07–1.24 g cm^{-3} using 20 wt% nycodenz in water at 30 000 rotations per minutes for 22 h at room temperature [31]. The particles were observed to have a density in the range of 1.083–1.099 g cm^{-3} (mean values of 1.090 g cm^{-3}). As the density of pure polymer (1.055 g cm^{-3}) and pure silica particles (2.3 g cm^{-3}) was known, therefore, the combination of the component densities with the densities of the hybrid particles resulted to the observation that the hybrid particles have 5–8 wt% silica particles. This value can then be compared with the initially added silica particles during

Figure 12.8 Schlieren image of the hybrid latex containing polyurethane encapsulated pigment particles (density gradients, after 22 h at 40 000 rpm, 25 °C, 20 wt% nycodenz in water). The first band shows the free polymer (density 1.066 g cm^{-3}), whereas the second broad band (density 1.083–1.165 g cm^{-3}) indicates the encapsulated pigment. Reproduced from reference [31] with permission from Springer.

the hybridization process thus helping in control and tuning of the hybridization reactions. The absence of a signal at 1.055 g cm^{-3} in the hybrid particles corresponding to pure polymer indicated the absence of any free polymer in the dispersion. The size distribution of the particles using the mean density of 1.090 g cm^{-3} was also measured indicating that the particles contained the distributions in both density as well as particle size and analytical ultracentrifuge is the most efficient method to characterize such complex heterogeneities in the particles.

Figure 12.8 depicts another example of characterization of the pigment polyurethane hybrid particles by the use of density gradient analysis [31]. The nycodenz density gradient (20 wt% nycodenz in water) after 22 h at 40 000 rotations per minute at room temperature was used. Two bands were observed in the density gradient, the first band at a density value of 1.066 g cm^{-3} corresponded to the pure polymer, whereas the second band in the density range 1.083–1.165 g cm^{-3} corresponded to the hybrid particles. The broadness of the density band also signified that the hybridization was not uniform and there existed a distribution in the amount of the inorganic content in the particles. By combining this density range with density of pure polymer and pure pigment particles, it was observed that the hybrid particles had 3–22% of the pigment particles incorporated in them. Thus, the use of analytical ultracentrifugation provides valuable insights into the state of hybridization of the system.
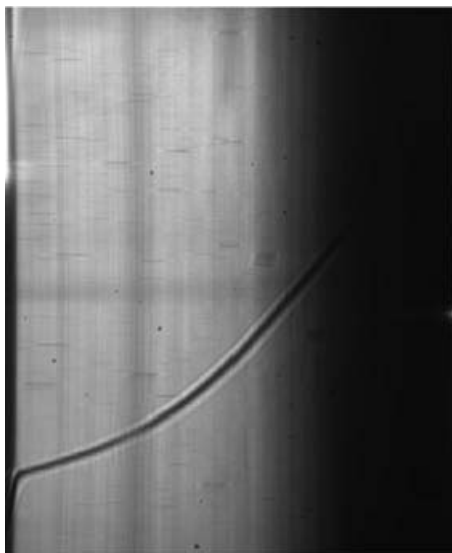
Figure 12.9 Schlieren image representing the density distribution of the polyurethane encapsulated pigment particles, when the density of the hybrid particles lies beyond the detectable range of the density gradient. The particles shown in the image have density values from 1.246 to >1.415 g cm^{-3}. Reproduced from reference [31] with permission from Springer.

Figures 12.7 and 12.8 represented the cases where the whole of the hybrid particles could be observed in the density gradient range possible with aqueous gradients. However, as the amount of the inorganic content increase in the hybrid particles, their density falls out of the measurable range using aqueous gradients. Figure 12.9 shows one such example of pigment encapsulation by polymer [31]. The hybrid particles lie in the density range of 1.246 to >1.415 g cm^{-3} which indicates that it was not possible to analyze all the hybrid particles by using the density gradient in analytical ultracentrifuge. The particles with density higher than 1.415 g cm^{-3} sedimented very fast and settled at the bottom of the cell. By combining the densities of pure components with that of hybrid particles, it was observed that the hybrid particles contained 38% to >66% of the inorganic fraction. The pure polymer fraction was absent as no signal was observed in the hybrid particles which corresponded with the density of the polymer. Such cases where the density of the hybrid particles lies out of the measurable range of the aqueous density gradient column can be qualitatively analyzed in preparative ultracentrifuge. The use of preparative ultracentrifuge also yields information on the presence or absence of free inorganic particles. Figure 12.10a shows the characterization of the particles shown in Figure 12.9 when performed in preparative ultracentrifuge [31]. The density gradient was generated by 50% nycodenz in D$_2$O and the particles
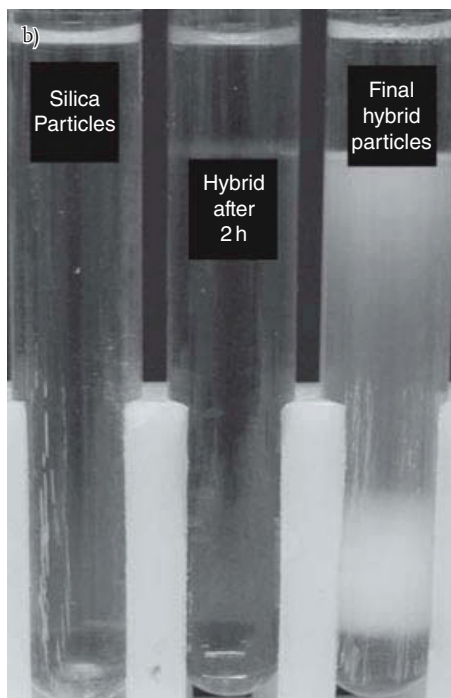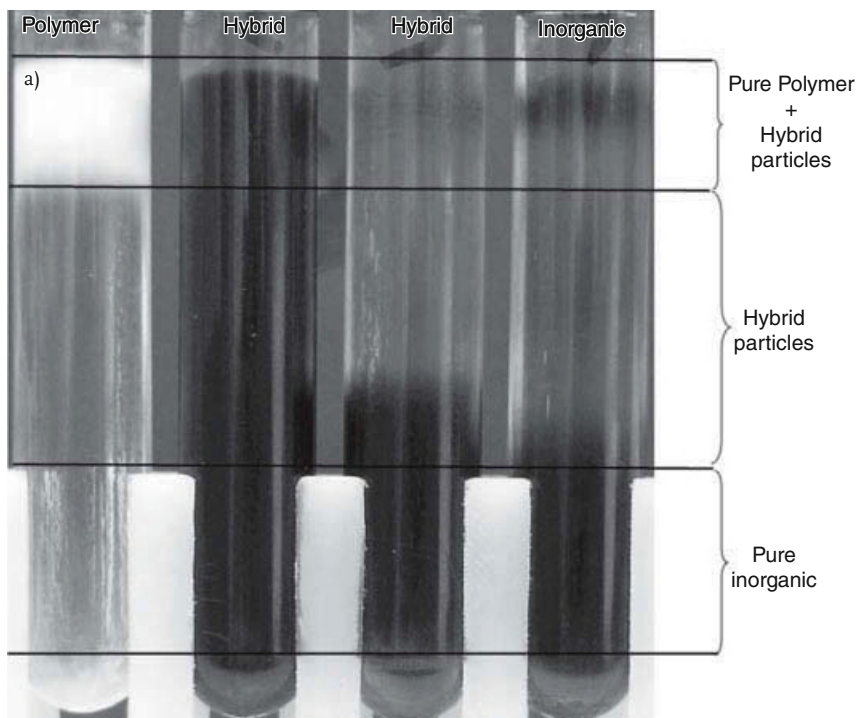
Figure 12.10 Preparative ultracentrifugation (a) of the polyurethane encapsulated particles to qualitatively analyze the system which otherwise is not possible in density gradient analysis and (b) of hybrid silica-polystyrene particles to follow the evolution of hybridization process as a function of time. Reproduced from reference [31] with permission from Springer.

were sedimented for 70 h at a speed of 40 000 rotations per minutes followed by 25 h at 44 000 rotations per minute. The pure polymer particles lie at the top of the tube owing to the least density and the pure pigment particles lie at the bottom of the tube owing to the highest density. The fractions in between these two pure components in the case of hybrid dispersions corresponded to the hybrid particles with varying extents of hybridization depending on their place in the density gradient in the tube. Thus, the use of preparative centrifuge not only confirms the presence or absence of any free polymer particles in the hybrid latexes, it also provides information on the free inorganic particles, thus covering the whole range of density of the system, which is otherwise not possible in density gradients. The additional advantage of the preparative ultracentrifugation is that the fractions of various pure and hybrid components can be separated and further analyzed for their characteristics.

The use of preparative ultracentrifugation also allows one to follow the synthesis of hybrid particles as a function of time. Figure 12.10b shows such an example of silica polystyrene hybrid synthesis (25 wt% nycodenz, 30 h at 20 000 rotations per minute) [31]. The monomer is polymerized in the presence of silica particles in such a process. The first tube is the nanodispersion of silica particles after sedimentation, and thus is completely transparent, even though silica particles settle at the bottom of the tube. The second tube corresponds to the hybrid dispersion after 2 h of polymerization, whereas the third tube is the final hybrid latex. The presence of very light band both in the upper and lower halves of the tube corresponded to pure polymer and hybrid latex particles. The third tube also corresponded similarly to the presence of pure polymer particles in the upper half of the tube, and the hybrid particles in the lower half of the tube. The presence of any free silica particles could not be visually detected. The fractions obtained at different times during the polymerization process can be separated and further analyzed to understand the reaction mechanisms or effect of parameters etc. thus helping to tune the hybrid particles according to the need.

12.4
Conclusions

Complex organic–inorganic hybrid materials need to be analyzed to ascertain the level of hybridization of the two components of the system as well as to fine tune the synthesis methodologies by understanding the evolution of hybrid morphology as a function of time or other reaction parameters. In this regard, multidirectional characterization possibilities available in analytical and preparative ultracentrifugation methods are immensely beneficial. The state of the hybridization of the colloidal particles can be quantified by the synergistic combination of interference, turbidity, and Schlieren (density gradient analysis) detection optics. These methods also provide information on the presence of free polymer as well as inorganic particles and also help to characterize the hybrid particles for the distribution of organic and inorganic parts thus helping to control or tune the hybrid synthesis.

These methods also allow us to characterize the distributions both in the size as well as density of the particles; such complex heterogeneities in the particles are otherwise not very straightforward to characterize in other analysis methods. Qualitative analysis of the hybrid particles, in the cases especially where the density is above the range covered by the density gradients, is possible in preparative ultracentrifuge. Apart from that, its use for the study of the growth of hybrid particles as a function of time could also be demonstrated. These fractions can also be separated for further analysis. These synergistic combinations of the various possibilities in ultracentrifuge can thus help to design and control the hybrid systems more efficiently.

It also lessens the dependence on multiple characterization methods for the analysis of hybrid systems.

Acknowledgments

References

1 Bechtold, N., Tiarks, F., Willert, M., Landfester, K., and Antonietti, M. (2000) *Macromol. Symp.*, **151**, 549.

2 Templeton-Knight, R. (1990) *Chem. Ind.*, **16**, 512.

3 Templeton-Knight, R. (1990) *J. Oil Colour Chem. Assoc.*, **731**, 459.

4 Bourgeat-Lami, E., and Lang, J. (1998) *J. Colloid Interface Sci.*, **197**, 293.

5 Bourgeat-Lami, E., and Lang, J. (1999) *J. Colloid Interface Sci.*, **210**, 281.

6 Barthet, C., Hickey, A.J., Cairns, D.B., and Armes, S.P. (1999) *Adv. Mater.*, **11**, 408.

7 Luna-Xavier, J.-L., Guyot, A., and Bourgeat-Lami, E. (2002) *J. Colloid Interface Sci.*, **250**, 82.

8 Butterworth, M.D., Corradi, R., Johal, J., Lascelles, S.F., Maeda, S., and Armes, S.P. (1995) *J. Colloid Interface Sci.*, **174**, 510.

9 Schmid, A., Fujii, S., and Armes, S.P. (2005) *Langmuir*, **21**, 8103.

10 Schmid, A., Fujii, S., Armes, S.P., Leite, C.A.P., Galembeck, F., Minami, H., Saito, N., and Okubo, M. (2007) *Chem. Mater.*, **19**, 2435.

11 Schmid, A., and Armes, S.P. (2009) *Langmuir*, **25**, 2486.

12 Nguyen, D., Zondanos, H.S., Farrugia, J.M., Serelis, A.K., Such, C.H., and Hawkett, B.S. (2008) *Langmuir*, **24**, 2140.

13 Mächtle, W., and Börger, L. (2006) *Analytical Ultracentrifugation of Polymers and Nanoparticles*, Springer, Berlin.

14 Mächtle, W. (1984) *Makromol. Chem.*, **185**, 1025.

15 Mächtle, W. (1988) *Angew. Makromol. Chem.*, **162**, 35.

16 Müller, H.G. (1989) *Colloid Polym. Sci.*, **267**, 1113.

17 Mächtle, W. (1992) *Analytical Ultracentrifugation in Biochemistry and Polymer Science* (eds S.E. Harding, A.J. Rowe, and J.C. Horton), The Royal Society of Chemistry, Cambridge.

18 Cölfen, H. (2005) *Analytical Ultracentrifugation: Techniques and Methods* (eds D.J. Scott, S.E. Harding,

and A.J. Rowe), The Royal Society of Chemistry, Cambridge.

19 Cölfen, H. (2004) *Polym. News*, **29**, 101.

20 Cölfen, H. (2004) *Particle Sizing and Characterization* (eds T. Provder and J. Texter), American Chemical Society, Washington.

21 Jamison, J.A., Krueger, K.M., Yavuz, C.T., Mayo, J.T., LeCrone, D., Redden, J.J., and Colvin, V.L. (2008) *ACS Nano*, **2**, 311.

22 Dieckmann, Y., Colfen, H., Hofmann, H., and Petri-Fink, A. (2009) *Anal. Chem.*, **81**, 3889.

23 Calabretta, M.K., Colvin, V., and Matthews, K.S. (2004) *Biophys. J.*, **86**, 21A.

24 Colfen, H., Volkel, A., Shinichi, E., Kobold, U., Kaufmann, J., Puhlmann, A., Goltner, C., and Wachernig, H. (2002) *Langmuir*, **18**, 7623.

25 Gohon, Y., Giusti, F., Prata, C., Charvolin, D., Timmins, P., Ebel, C., Tribet, C., and Popot, J.L. (2006) *Langmuir*, **22**, 1281.

26 Joralemon, M.J., Murthy, K.S., Remsen, E.E., Becker, M.L., and Wooley, K.L. (2004) *Biomacromolecules*, **5**, 903.

27 Colfen, H., and Volkel, A. (2003) *Eur. Biophys. J.*, **32**, 432.

28 Mächtle, W., and Lechner, M.D. (2002) *Prog. Colloid Polym. Sci.*, **119**, 1.

29 Börger, L., Lechner, M.D., and Stadler, M. (2004) *Prog. Colloid Polym. Sci.*, **127**, 19.

30 Börger, L., and Lechner, M.D. (2006) *Colloid Polym. Sci.*, **284**, 405.

31 Mittal, V. (2010) *Colloid Polym. Sci.*, **288**, 621.

13
Biodegradability Characterization of Polymer Nanocomposites

Katherine M. Dean, Parveen Sangwan, Cameron Way, and Melissa A.L. Nikolic

13.1
Introduction

Biodegradable polymers and nanocomposites can be exposed to a wide variety of natural, simulated, or artificial environments to measure or monitor their extent of degradation. These environments are not discrete to just nanocomposites, but can be used to assess the biodegradation nature of most materials that contain biodegradable polymers. These environments typically include soil, compost, marine substrates (sludge, water), and sewage. Each environment contains different microorganisms (in terms of species diversity and population), different physical and chemical parameters (in terms of temperature, moisture, pH, aeration, and nutrients) that influence rates of microbial activity that in turn affect the rate of degradation seen in the nanocomposites. Consequently, the biodegradation of nanocomposites should always be evaluated in their intended environment of "end usage," as different environments are not always comparable.

In this chapter, the methodologies used to measure and understand biodegradation of nanocomposites are discussed. In Section 13.1, the broader picture of biodegradation is discussed. In Section 13.2, the methods for measuring biodegradation are explained in detail. In Section 13.3, the standards associated with methods are listed and described, and finally in Section 13.4 the biodegradation of a number of nanocomposites types are discussed.

13.2
Methods of Measuring Biodegradation

An ideal biodegradation test method should include conditions expected during period of application of the nanocomposites and the disposal environment at the end of their life-cycle. A number of standard on-field and lab-based test methods are currently available to measure the biodegradability of a range of polymers including nanocomposites. A series of test methods listed below are generally performed for the assessment of biodegradation.

13.2.1
Analytical Techniques

13.2.1.1 Morphological

Physical appearance of polymers (color, shape, size, any visible holes or cracks on polymer surface, and/or biofilm formation) is recorded before and after biodegradation [1]. A colorimeter is commonly used for color measurements (yellowness, whiteness, light transmission, and haze).

13.2.1.2 Microscopic

Polarizing optical microscopy (POM) and scanning electron microscopy (SEM) techniques are commonly used to investigate surface morphology of polymers and to detect growth of microorganisms on polymers during biodegradation. Transmission electron microscopy (TEM) is primarily used for characterization of internal structure and spatial distribution of the various phases of polymer [2–6].

13.2.1.3 Gravimetric

Polymer samples are weighed before and after biodegradation and the percentage weight loss is determined as follows:

$$\% \text{ weight loss} = \frac{(W_{to} - W_{ts})}{W_{to}} \times 100$$

where, W_{to} and W_{ts} refer to the weight of samples at time 0 (before exposure) and at specific sampling time, respectively [1, 2, 4, 7–9].

13.2.1.4 Physical and Thermal

Tensile tests (strength, modulus, and elongation at break) are used to determine changes in mechanical properties during biodegradation. X-ray diffraction (XRD)/wide-angle XRD (WAXRD) technique is often used to measure degree of crystallinity and morphology of polymer nanocomposites. Differential scanning calorimetry (DSC) and thermogravimetric analysis (TGA) are used to investigate thermal transitions of polymers by measuring their glass transition and melting-point temperatures. Dynamic-mechanical thermal analysis (DMTA) measures the response of a given material to a cyclic deformation as a function of the temperature.

13.2.1.5 Spectroscopic

Fluorescence and UV-visible spectrometry are used to determine the transmission of light through polymer films. Transparency measurements are important for selecting appropriate packaging materials as UV and visible light can have a negative effect on the quality of packaged food products. Fourier transform infrared spectroscopy (FTIR), nuclear magnetic resonance (NMR), and mass spectrometry (MS) are routinely used to obtain qualitative information on changes in chemical structure or formation of functional groups on polymers during biodegradation. A combination of two or more of these methods is used to gain better insights

on the extent and homogeneity of nanoscale fillers dispersed within the polymer matrix.

13.2.1.6 Chromatographic

Gel permeability chromatography (GPC) is often used to determine changes in average molecular weights (M_n and M_w) and polydispersity index (M_w/M_n) of polymer nanocomposites during biodegradation. High-performance liquid chromatography (HPLC) and gas-phase chromatography (GC) techniques are used to detect presence of monomers and oligomers formed in an aqueous or gas phases during biodegradation.

13.2.1.7 Respirometry

Evolution of CO_2 and Oxygen Demand The biodegradation of nanocomposites can be indirectly evaluated, by more than just the direct methods. These methods primarily focus on the aerobic or anaerobic digestion of the biomaterial and the evolution of carbon dioxide or consumption of oxygen (aka oxygen demand). This is measured *in situ* to the test and is quantified either discretely or continuously, then related back to the original material through compound stoichiometry and chemical structure to determine an estimate of biodegradation.

Note: There are other compounds, such as methane in anaerobic environments

$$\textbf{Aerobic}: C_{SAMPLE} + O_2 \rightarrow CO_2 + C_{BIOMASS} + C_{RESIDUAL} \tag{13.1}$$

$$\textbf{Anaerobic}: C_{SAMPLE} + H_2 \rightarrow CO_2 + CH_4 + C_{BIOMASS} + C_{RESIDUAL} \tag{13.2}$$
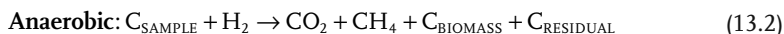
Some samples (i.e., dumbbells and other simple shapes) that have undergone, or are still undergoing, these types of tests can also be simultaneously tested for visual or physical changes, such as weight loss, mechanical or electrical testing. However, such tests must be treated with caution when interpolating or extrapolating the data due to the complex nature of interactions that are occurring and the possibility of residual contamination from the medium.

Respirometers "Respirometers" is the term given to most custom-built (see Figure 13.1) or commercially available test units that measure aerobic degradation of materials. They commonly pass a controlled flow rate of air through a sample-medium mix to maintain an aerobic environment (i.e., oxygen concentration above 6–10%). The sample-medium mixture are contained within test vessels (sometimes called "bioreactors") and may be subjected to artificial heating to follow a constant or desired temperature profile. These units then focus on measuring the evolution of carbon dioxide from the test vessels in order to estimate the percentage biodegradation of the sample.

The evolved gases can be directly analyzed by gas chromatography, infrared spectroscopy, or absorbed into alkaline solutions (such as $Ba(OH)_2$ and NaOH) for liquid titrations. The gas profile of the sample-medium mix is converted into a

Figure 13.1 Custom-built respirometer used by Commonwealth Scientific Industrial Research Organization (CSIRO), Australia.

percentage biodegradation by subtracting the medium-only profile (contained discretely in other test vessels) and dividing by the theoretical CO_2 that could be produced if all organic carbon in the sample was converted to CO_2 (see Eq. (13.3))

$$\text{Sample degradation (\%)} = \frac{\text{Vol}(CO_{2,\text{SAMPLE+MEDIUM}}) - \text{Vol}(CO_{2,\text{MEDIUM}})}{\text{Theoretical Vol}(CO_{2,\text{SAMPLE}})} \quad (13.3)$$

Recent publications in this area focus on (i) a detailed outline of the construction of their units designed to comply with the biodegradation testing standards [10–12]; (ii) the stability and accuracy of the chosen setup, such as CO_2 determination by IR, alkaline solutions, and gas chromatography [13, 14], or improved control through the additional of a pycnometer [15]; (iii) the environmental and physio-chemical properties [16] of the media to produce the most stable or optimum biodegradation kinetics, such as aeration rates [12, 17–19], compost moisture, pH, temperature profiles [20, 21] (using both constant temperature and a temperature profile); (iv) the use of vermiculite or pearlite [22–27] to improve the signal-to-noise ratio between the compost/soil baseline and compost/soil-sample mix; and (v) design considerations of the unit that can effect in the compost stability and conditioning during the test [28].

AS ISO 14855   The Australian test standard AS ISO 14855 [29] is closely related to the European (ISO 14855) and American (ASTM D5338) test methods. The AS ISO 14855 test method regulates the aerobic biodegradation of plastic materials under controlled composting conditions using the analysis of evolved

carbon dioxide. It sets clear requirements for the mature compost used at the start of the test that must also produce 50–150 mg of CO_2 per gram of volatile solids over the first 10 days of the test. Test samples can be in a variety of forms (including granules, powders, film, or simple shapes) to a maximum surface area of 2×2 cm. The evolution of CO_2 can be measured directly, by continuous infrared analyzer or gas chromatograph, or cumulatively in a CO_2 trap. Each test vessel typically contains 100 g of sample material and 600 g of compost (both on a dry weight basis) and placed in the test environment maintained at $58 \pm 2\,°C$ for the maximum duration of 6 months. Test is performed in triplicate (three test vessels for test material, reference, and the blank). At the end of test, samples are described as biodegradable if they have exceeded 90% biodegradation. Each test is validated against both compost and sample requirements, mentioned above, as well as positive reference (i.e., microcrystalline cellulose) and possibly a negative reference. To pass the validation, the positive reference must also achieve more than 70% biodegradation after 45 days and the difference between the percentage biodegradation in the replicate samples is less than 20% at the end of the test.

Modified Sturm Test   The modified sturm test is another aerobic test available for polymeric materials. The test requires addition of the test substance at two concentrations (10 and 20 mg l^{-1}) to a solution of defined mineral nutrient (free of organic carbon) and sewage microorganisms (1–20×10^6 ml^{-1}). The test is run for 28 days, without any acclimatization period, and is incubated at ambient temperatures with stirring. The CO_2 evolved is trapped in alkali and measured as carbonate by either titration or with the use of a carbon dioxide analyzer. Similarly to AS ISO 14855, the biodegradation of the sample is estimated according to Eq. (13.3) listed above. A sample is regarded as readily biodegradable, if it produced greater than 60% of its theoretical total carbon within 28 days while maintaining a variation between samples of less than 5%.

13.2.2
Oxygen Demand

Oxygen demand (or consumption) is another method for quantifying biodegradation of polymers under an aerobic environment. Like CO_2 evolution, this test can be performed in various mediums and commonly inside a closed vessel where the oxygen is consumed via microbial respiration producing CO_2. These CO_2 gases are absorbed (i.e., by soda lime pellets) causing an overall pressure drop in the gas environment of the vessel (i.e., detected by manometer). Oxygen is then generated back into the vessel (via coulometric oxygen production unit) until the pressure is restored. The oxygen demand profile (i.e., equivalent to the oxygen consumed by respiration) is recorded and related against a theoretical oxygen demand (TOD) of the sample, determined either analytically (i.e., elemental analyzer) or from the chemical formula, and used to determine an estimated degree of biodegradation (see Eq. (13.4)).
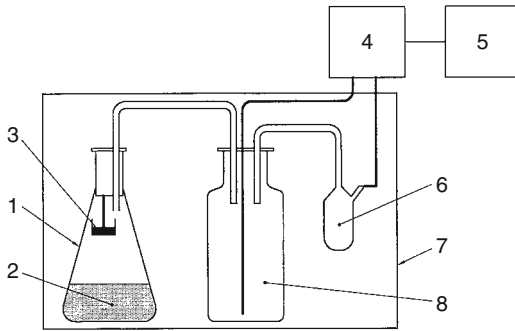
Figure 13.2 Schematic diagram of a manometric respirometer (adapted from ISO 17556)
1. Test Flask; 2. Test mixture; 3. CO_2 absorber; 4. Monitor; 5. Computer; 6. Manometer;
7. Thermostatted enclosure; 8. Oxygen-generating unit.

$$\text{Sample degradation (\%)} = \frac{O_{2,\text{PROD SAMPLE+MEDIUM}} - O_{2,\text{PROD MEDIUM}}}{\text{Theoretical } O_{2,\text{SAMPLE}}} \tag{13.4}$$

ISO 17556 (referred to in Table 13.2) is one such test method that uses oxygen demand (see Figure 13.2). Approximately 100–300 mg of test material is added to 100–300 g of soil in a closed vessel. The vessel can be maintained at any constant temperature (±1 °C), preferably between 20 and 25 °C for a maximum period of 6 months. Samples are tested in duplicate, and the oxygen demand and degree of biodegradation is measured as mentioned above.

13.2.3
Microbiological Techniques

Microbial degradation of materials is assessed either by subjecting the test materials to a huge diversity of environmental microorganisms found in compost, soil, marine, fresh water, and activated sludge samples or to selected pure cultures of bacteria or fungi that are known to possess biodegradation potential.

13.2.3.1 Direct Cell Count
Total number of bacteria growing on the surface of test materials can be estimated by epifluorescence microscopy using ethidium bromide and SYBR Green II. LIVE/DEAD *Bac* viability staining kits are also commercially available for detecting viable bacterial cells.

13.2.3.2 Clear-Zone
According to this method, test material is placed on a solid media in Petri dish containing no additional C source and sprayed on with a mixed inoculum of known bacteria and fungi. After incubation at specified test conditions (say 30 or 50 °C for a period of 3–4 weeks) the test material is visualized for any surface

growth and/or formation of clear zone (inhibition zone) indicating susceptibility or resistance of test material to microbial degradation [30].

13.2.3.3 Pour Plate/Streak Plate

These methods are frequently used for enumeration and isolation of biodegrading microorganisms. Samples are taken from the surface of degraded material (previously exposed to environmental or pure cultures) and serial dilutions are made with sterile solution. Pour plate method involves adding an aliquot of the dilution into a Petri plate, pouring measured amount of agar media and mixing the two by gently swirling and then incubation at suitable conditions to allow growth of microorganisms. In the streak plate method, an aliquot is added to agar media in a Petri plate and microbial cells are spread across the plate using a wire loop or a spreader to physically separate the cells so that each grows into a separate colony (visible microbial growth on media plate) during incubation [1, 31].

13.2.3.4 Turbidity

Bacterial growth on the biodegraded test materials can be quantified by using spectrophotometer. Particulate objects such as bacterial cells absorb or scatter light in proportion to their cell mass or number. An increase in the turbidity of liquid media and broths indicates an increase in the number of microbial cells capable of utilizing the test material as a sole carbon source [32].

13.2.4
Enzymatic Techniques

Enzymes catalyze breakdown of specific bonds in the polymers generating monomers and oligomers, thus resulting into gravimetric and molecular weight loss. Enzymatic degradation of polymer nanocomposites is reportedly carried out under defined set of laboratory conditions. The method involves incubation of sterilized film samples in a buffer solution or medium broth containing one or more relevant enzymes. Enzymatic activity is measured spectrophotometrically in the liquid medium and the percent weight loss over period of time is calculated [33, 34].

13.2.5
Molecular Techniques

Molecular ecological techniques are considered powerful diagnostic and quantitative tools for the study of microorganisms directly in their natural habitats. These methods target functional genes, phylogenetically informative genes, or RNA to extract genetic information from microorganisms without culturing them, and to relate the information on microbial structure and diversity to ecosystem functions. In particular, the use of 16S rRNA and its genes are frequently used as phylogenetic markers for detection and identification of different microbial species involved in biodegradation of test material under natural as well as simulated environmental conditions [35] (Table 13.1).

Table 13.1 Summary of characterization techniques for biodegradation.

Characterization techniques	Properties analyzed	References
Gravimetric	% Weight loss	[1, 2, 4, 7]
Tensile	Mechanical strength, modulus, and elongation	[4, 5]
XRD/WAXRD	Crystallinity, interlayer spacing and dispersion degree of nanoscale fillers, kinetics of the polymer melt intercalation process	[3–5, 36–38]
DSC	Crystallization and melting behavior	[2, 3, 31]
TGA	Thermal stability	[2, 3, 5, 6]
DMTA	Thermal transitions	[2, 3, 6]
Oxygen gas permeability	Oxygen gas transmission rates	[6]
POM	Surface characteristics	[2–4]
UV-visible spectrometry	Transmittance of UV and visible light	[39]
Fluorescence microscopy	Enumeration and viability of bacterial cells	[40, 41]
AFM	Particle size and distribution, surface morphology and microstructure, degree of crystallization	[37]
FTIR	Chemical analysis, crystallization and orientation of polymer, interfacial interactions	[2, 38]
NMR	Chemical analysis	[42]
GPC/SEC	Average molecular weights	[2, 3, 6, 31, 38]
SEM	Surface morphology	[2–5]
TEM	Internal structure and morphology of nanoscale fillers in composites	[3, 5, 6]
Clear-zone	Resistance or susceptibility of plastics to microbial degradation	[30]
Pour plate or Streak plate	Enumeration and isolation of degrading microorganisms	[1, 31]
Turbidity	Estimation of microbial growth and abundance	[32]
Enzymatic	Weight loss and enzymatic activity in the liquid medium containing test material and enzymes	[33, 34]
Molecular	Detection, identification of degrading microorganisms	[35]

13.3
Standards for Biodegradation

There are several standard test methods and drafts available (Table 13.2), which are frequently used to assess biodegradability of polymers by measuring molecular weight and molecular weight distribution, tensile properties, weight loss, extent of fragmentation, enzyme assays, biochemical oxygen demand, carbon dioxide production, and ecotoxicity. A combination of test procedures can be used during evaluation to confirm that biodegradation has actually occurred. The selection of test methodology should be based on potential fields of application of the test polymer and its fate at the end of its purpose, that is, compost, soil, fresh or marine water. Some of the widely used standards are AS4736; ASTM D5338; ASTM D6002; EN 13432; ISO 14855 (for compost exposure) and ASTM D5988; ISO 17556 (for soil exposure) and ASTM D6691; ASTM D6692; ISO 15314; ISO 16221 (for marine exposure) (Table 13.2).

The European standard for biodegradability is EN 13432. This norm standard is a reference point for all European producers, authorities, facility managers, and consumers. The standard specifies requirements and procedures to determine the compostability of plastic packaging materials based on four main areas – biodegradability; disintegration during biological treatment; effect on the biological treatment process; and effect on the quality of the resulting compost. This standard can be applied to other packaging materials in addition to polymers, and incorporates following tests and standards: ISO 14855; ISO 14852; ASTM D5338-92; ASTM D5511-94; ASTM D5152-92; ASTM E1440-91; modified OECD 207; and CEN TC 261/SC4/WG2.

In this test procedure polymers are exposed to environments in standard biometric test methods to measure the rate and degree of biodegradation. After this biodegradation stage, the end residues are subjected to aquatic and terrestrial toxicity tests (E 1440, OCED guideline 207 and OCED guideline 208) to ensure that they are environmentally benign and not persistent. Each degradation stage must be independently evaluated to allow a combined evaluation of a polymer's environmental performance under controlled laboratory conditions. According to the standard, the results of laboratory exposure cannot be directly extrapolated to estimate absolute rate of deterioration by the environment because the acceleration factor is material dependent and can be significantly different for each material and for different formulations of the same material. However, exposure of a similar material of known outdoor performance, such as a control material, at the same time as the test specimens during the trial, allows for comparison of the material durability relative to that of the control under the test conditions utilized.

13.4
Biodegradable Nanocomposites

A number of authors have investigated the effects of different nanoparticles on the biodegradation rates of the nanocomposites they form. The results were shown

Table 13.2 Selected list of published standards for biodegradation.

Standard	Description
AS 4736-2006	Biodegradable plastics – biodegradable plastic suitable for composting and other microbial treatment
ASTM D6954-04	Standard guide for exposing and testing plastics that degrade in the environment by a combination of oxidation and biodegradation.
ASTM D5338-11	Standard test method for determining aerobic biodegradation of plastic materials under controlled composting conditions. Incorporating thermophillic temperatures
ASTM D5526-94(2011)e1	Standard test method for determining anaerobic biodegradation of plastic materials under accelerated landfill conditions.
ASTM D5988-03	Standard test method for determining aerobic biodegradation in soil of plastic materials or residual plastic material after composting
ASTM D6340-98(2007)	Standard test methods for determining aerobic biodegradation of radiolabeled plastic materials in an aqueous or compost environment
ASTM D6400-99	Standard specifications for compostable plastics
ASTM D6691-09	Standard test method for determining aerobic biodegradation of plastic materials in the marine environment by a defined microbial consortium or natural sea water inoculum
ASTM D7081-05	Standard specifications for nonfloating biodegradable plastics in the marine environment
EN 13432:2000	Requirements for packaging recoverable through composting and biodegradation – test scheme and evaluation criteria for the final acceptance of packaging
EN 14045:2003	Packaging – evaluation of the disintegration of packaging materials in practical oriented tests under defined composting conditions
EN 14046:2003	Packaging – evaluation of the ultimate aerobic biodegradability of packaging materials under controlled composting conditions – method by analysis of released carbon dioxide
EN 14047:2002	Packaging – determination of the ultimate aerobic biodegradability of packaging materials in an aqueous medium – method by analysis of evolved carbon dioxide
EN 14048:2002	Packaging – determination of the ultimate aerobic biodegradability of packaging materials in an aqueous medium – method by measuring the oxygen demand in a closed respirometer
EN 14806:2005	Packaging – preliminary evaluation of the disintegration of packaging materials under simulated composting conditions in a laboratory-scale test

Table 13.2 (*Continued*)

Standard	Description
ISO 14851:1999	Determination of the ultimate aerobic biodegradability of plastic materials in an aqueous medium – method by measuring the oxygen demand in a closed respirometer
ISO 14852:1999	Determination of the ultimate aerobic biodegradability of plastic materials in an aqueous medium – method by analysis of evolved carbon dioxide
ISO 14855-1:2005	Determination of the ultimate aerobic biodegradability of plastic materials under controlled composting conditions – method by analysis of evolved carbon dioxide. Part 1: General method
ISO 14855-2:2007	Determination of the ultimate anaerobic biodegradability of plastic materials under controlled composting conditions – method by analysis of evolved carbon dioxide. Part 2: Gravimetric measurement of carbon dioxide evolved in a laboratory-scale test
ISO 14593:1999	Water quality – evaluation of the ultimate aerobic biodegradability of organic compounds in aqueous medium – method by analysis of inorganic carbon in sealed vessels (CO_2 headspace test)
ISO 16221:2001	Water quality – guidance for the determination of biodegradability in the marine environment
ISO 16929:2002	Plastics – determination of the degree of disintegration of plastic materials under defined composting conditions in a pilot-scale test
ISO 17556:2003	Plastics – determination of the ultimate aerobic biodegradability in soil by measuring the oxygen demand in a respirometer or the amount of carbon dioxide evolved
ISO 20200:2004	Plastics – determination of the degree of disintegration of plastic materials under simulated composting conditions in a laboratory-scale test
CEN/TR 15822:2009	Plastics – biodegradable plastics in or on soil – recovery, disposal, and related environmental issues

to vary depending on the biodegradation environment, nanoparticle type, and loading.

13.4.1
PLA Nanocomposites

Previously, it has been reported how the biodegradation rate of polylactic acid (PLA) is affected by the incorporation of nanoparticles [1, 31, 35, 36, 43–45]; these have generally reported that the incorporation of nanoparticles (generally those which are more hydrophilic than the PLA itself) lead to more rapid rates of

biodegradation with the exception of Ozkoc and Kemaloglu [44] who find the opposite.

Ozkoc and Kemaloglu [44] have investigated PLA and polyethylene glycol (PEG) plasticized PLA nanocomposite films (containing 0%, 3%, and 5% montmorillonite clay [Cloisite 30B]). They found the order of rate of biodegradation in composting medium PLA > PLA/PEG > 3%, clay/PLA/PEG > 5%, clay/PLA/PEG > 3%, clay/PLA. The rate of biodegradation was monitored using weight loss of the PLA films. Ozkoc and Kemaloglu [44] claimed that although the nanoclays they used were more hydrophilic than the PLA and the composites absorbed more water, the enhanced crystallinity from the inclusion of the nanoclays led to slower rates of biodegradation.

Ray *et al.* [36, 46] have also investigated the biodegradability of PLA nanocomposites comprising of different kinds of layered silicates. They found that the biodegradability of neat PLA was improved significantly after the inclusion of clays and depended upon both the nature of the pristine layered silicates and the type of surfactants used for modification of the layered silicate. Unlike Ozkoc and Kemaloglu [44], Ray *et al.* [36, 46] monitored the biodegradation via carbon dioxide evolution and loss of molecular weight. Figure 13.3 shows the rates of biodegradation monitored via carbon dioxide evolution and loss of molecular weight of PLA and various PLA/ modified clay nanocomposites.

Fukuishima *et al.* [31] also studied the effects of varying types of organically modified montmorillonites (OMMT) at 5% w/w loading in PLA nanocomposites on degradation in a commercial compost. The addition of montmorillonites was found to increase the PLA degradation rate based on gravimetric analysis, especially for the highest dispersed clay in the polymer matrix. Samples of each material were removed from the compost, washed with water, and dried at room temperature for 24h to constant weight. Fukishima *et al.* [31] also studied the microorganisms isolated from the compost and showed that the presence of bacterium *Bacillus licheniformis* significantly impacted on PLA biodegradation in compost.

Sangwan *et al.* [35] completed a more comprehensive study of the changes in microbial community structure and population during degradation of polylactide (PLA)/organically modified layered silicates (OMLS) nanocomposites, using methods of gravimetric analysis, molecular weight, and biodegradation via evolution of CO_2 to measure biodegradation. Sangwan *et al.* [35] found that cloned gene sequences belonging to members of the phyla *Actinobacteria* and *Ascomycota* were the most dominant groups of microorganisms during biodegradation of PLA/ OMLS nanocomposites. Sangwan *et al.* [35] used novel molecular ecological techniques for *in situ* identification of new microorganisms involved in biodegradation of these PLA nanocomposite materials.

Sabet *et al.* [47] also studied the biodegradability of PLA and PLA/PCL with an OMLS montmorillonite and evaluated in a compost environment at 58°C [47] via gravimetric methods. Sabet *et al.* [47] showed that the incorporation of a nanoclay

a)

b)
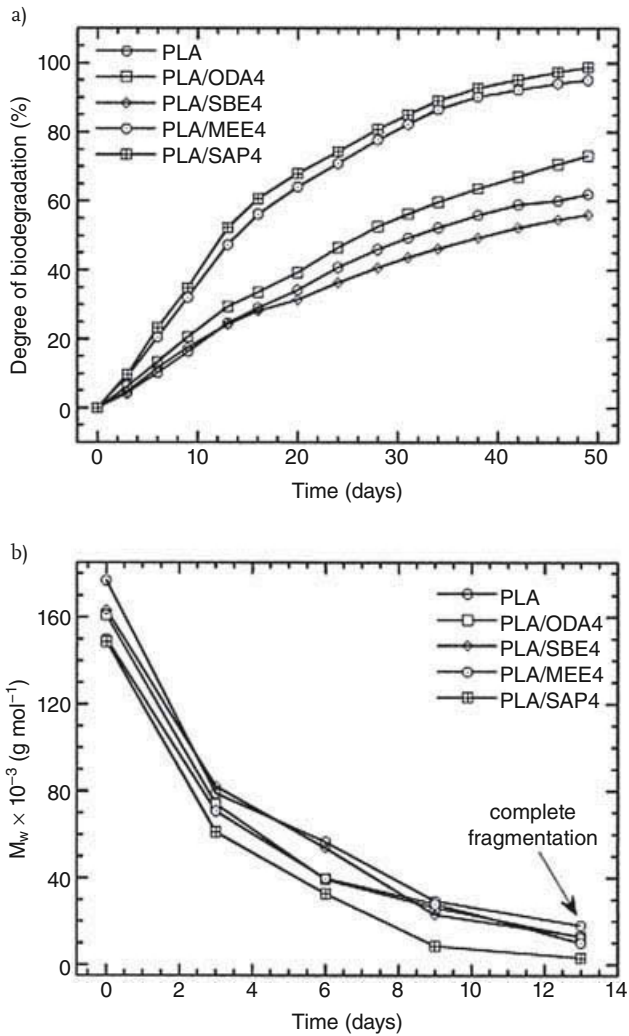
Figure 13.3 (a) Degree of biodegradation measured via CO_2 evolution and (b) change of matrix M_w of pure PLA and PLA in various nanocomposites under compost. Reproduced from Sinha Ray *et al*. [46] with permission from Elsevier.

increased the rate of hydrolytic degradation of PLA and PLA/PCL blended material, compared to neat PLA and PLA/PCL with no nanoclay.

Paul *et al*. [45] studied the hydrolytic degradation of polymer layered silicate nanocomposites based on polylactide matrix (PLA) and OMLS montmorillonites in phosphate buffer solution for more than 5 months. While natural unmodified

montmorillonite-Na$^+$ led to the formation of a microcomposite, mainly intercalated nanocomposites were prepared by melt blending PLA with montmorillonites modified with either by 2-ethylhexyl (hydrogenated tallow alkyl) ammonium cations (Cloisite® 25A) or by bis-(2-hydroxyethyl) methyl tallow alkyl ammonium cations (Cloisite® 30B). The hydrolytic degradation of the PLA chains was strongly effected by the relative hydrophilicity of the clay layers.

13.5
Starch Nanocomposites

The biodegradation rates of nanocomposites based on starch have also been studied by a number of authors. Biodegradation has been monitored and measured by a number of different methods and biodegradation has been shown to depend on biodegradation environment, nanoparticle type, and loading.

Tang *et al.* [9] studied the biodegradation (via gravimetric methods) of several starch/polyvinyl alcohol (PVOH)/nano-silicon dioxide (nano-SiO$_2$) blend films. Tang *et al.* [9] showed via gravimetric analysis using soil burial testing that the addition of 5 wt% nano-SiO$_2$ has no significant influence to the overall amount of biodegradation, but decreased the initial rate of biodegradation of the films in soil.

Nayak *et al.* [48] have investigated the biodegradation of thermoplastic starch/polybutylene adipate-*co*-terephthalate (TPS/PBAT) blends at starch content with two different organically modified nanoclays – Cloisite C20A and Cloisite C30B – at various clay loadings. The PBAT was further modified by grafting maleic anhydride (MA) to improved interfacial adhesion with the starch and nanoclay. The biodegradability of the following film samples was evaluated in controlled compost at 58 °C: PBAT, PBAT/TPS, PBAT/TPS/C30B, and PBAT/MA-g-PBAT/TPS, with cellulose being used as the positive reference and polyethylene as the negative control in the experiment. After incubation for 130 days, only a slight increase in the rate of biodegradation was observed for the PBAT/TPS/C30B formulation. Therefore, it was observed that the rate of degradation of PBAT matrix increased with the incorporation of TPS/nanoclay.

The role of α-amylase in PVA/starch nanocomposite degradation was studied by Spiridon *et al.* [8]. Preweighed films of blends or nanocomposites were immersed in a 20-mL solution containing 6 IU α-amylase/g material. The mass loss (for both wet and dry samples) was monitored at set time intervals. The amount of nondegraded residual blends containing nanoparticles suggested the possibility to optimize the material degradability by incorporation of nanoparticles. Spiridon *et al.* [8] discussed that biodegradation is mainly controlled by dissolution/erosion, while enzymatic degradation of starch also occurs. The susceptibility of nanocomposite films to enzymatic degradation was shown to vary in the following order: PVA/starch/nanocore > PVA/starch/Bentonite > PVA/starch/Peruvian clay, as also supported by the water adsorption capacity, which is one of the main conditions for biodegradation. Figure 13.4 illustrates the key mass loss results for the nanocore series of materials.
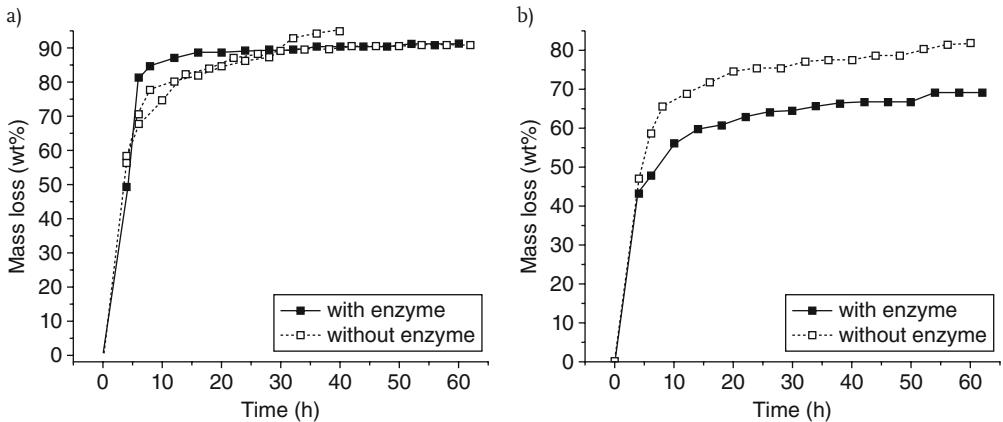
Figure 13.4 Mass loss versus degradation time for PVA/starch/1 wt% nanocore (a) and PVA/starch/5 wt% nanocore I28 nanocomposites (b). Reproduced from Spiridon *et al*. [8] with permission from Elsevier.

13.6
PCL Nanocomposites

A number of authors have studied the biodegradability PCL containing nanocomposites in a range of different biodegradation environments.

Ratto *et al*. [49] studied the biodegradability of a range of PCL/clay nanocomposite materials in soil, where the amount of clay was varied from 5% to 25%. The biodegradability results showed that mineralization reached 50% in 50 days for PCL/clay combinations, whereas after the same time period, neat PCL had only reached 10%.

Farrell *et al*. [50] have also studied the rate of biodegradation of PCL and organically modified clay nanocomposite in soil, compost, and marine environments. PCL was mixed with OMMT clay at 2 and 5 wt% loading, followed by extrusion in a twin screw extruder into pellets. In soil, the biodegradation results of these materials illustrated that the rate of biodegradation was significantly accelerated with the incorporation of particular nanoparticles into the PCL.

Fukushima *et al*. [1] have evaluated the biodegradation of PCL-sepiolite in compost. The PCL-sepiolite material was prepared by melt mixing the components in an internal mixer at 75 °C for 5 min, manually extracted from the mixer, air cooled, then milled into a fine powder using a rotary mill. Films of thickness 0.6 mm were obtained by compression molding at 120 °C for 5 min.

During the compost biodegradation study of PCL–sepiolite composites (dimensions $20 \times 6 \times 0.6 \, mm^3$), the temperature was kept constant at 40 °C and relative humidity 50–70%. At set time intervals, samples were extracted from the compost (composed of pruning residues, wood chips, dried leaves, and straw), washed with water, and dried at room temperature until constant sample weight was obtained.

Several analytical methods and techniques were used to evaluate the overall bio-degradation of the PCL–sepiolite materials; these included optical microscopy, FTIR, SEC, and DSC. Figure 13.5 illustrates the change in appearance for neat PCL and PCL–sepiolite film, after burial in compost for 35 and 58 days, respectively.

Figure 13.6 shows that approximately 50% weight loss of PCL and PCL–sepiolite samples was achieved after 100 days in compost. The extent and rate of PCL degradation was not significantly affected by the addition of sepiolite at 5 wt% to the PCL.

Fukushima *et al.* [2] have investigated the biodegradation fumed silica-PCL based nanocomposites. Fumed silica was primarily used as a filler to improve the UV resistance of the polymer. The residual mass data for PCL and PCL-fumed silica samples indicate that the presence of fumed silica did not significantly affect the rate of PCL degradation in compost.
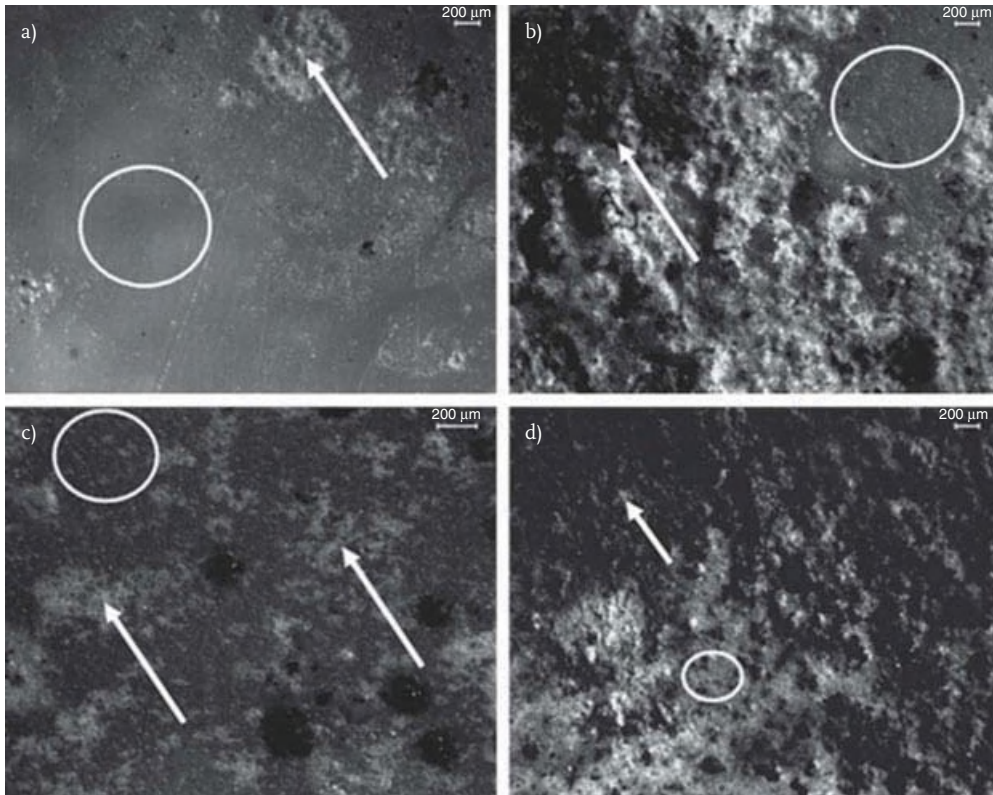
Figure 13.5 Optical micrographs of PCL after (a) 35 days and (b) 58 days; and PCL + SEPS9 after (c) 35 days and (d) 58 days in compost. Reproduced from Fukushima *et al.* [1] with permission from Elsevier.
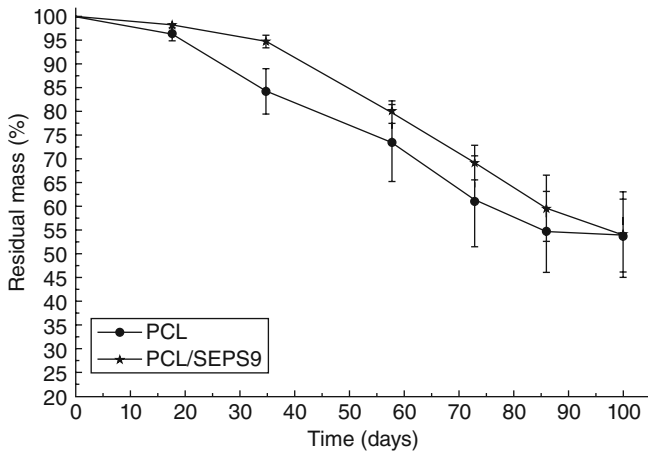
Figure 13.6 Residual mass for PCL and PCL-sepiolite with progression in degradation time in compost. Reproduced from Fukushima [1] with permission from Elsevier.

The biodegradation of PCL nanocomposites have also been investigated in marine environments [50]. Farrel *et al.* [50] studied the weight loss of PCL and PCL/5% clay nanocomposites in aerated natural seawater, where the seawater remained aerobic throughout the incubation period. The films were evaluated under two nutrient conditions: (i) unsupplemented and (ii) supplemented with 5.0 mg l^{-1} nitrogen (as NH_4Cl) and 1.0 mg l^{-1} phosphorous (as KH_2PO_4).

The neat PCL films showed a 90% weight loss after 8 days while being agitated. The PCL/5% clay film exhibited an 80% weight loss after 2 days, significantly higher than that observed for neat PCL of the same thickness after 2 days incubation. Films that were not agitated during incubation exhibited a considerably lower mass.

13.7
PHA/PHB Nanocomposites

Wang *et al.* [7] have studied the biodegradability of poly(3-hydroxybutyrate-*co*-3-hydroxyvalerate) based organically modified montmorillonite (PHBV/OMMT) nanocomposites in a soil suspension. The soil sample was combined and dispersed in a salt solution. Each PHBV/OMMT sample was placed in the soil suspension and incubated at 28 °C under aerobic conditions. Once samples were removed from the soil suspension, the films were washed with 75% ethanol in water, to prevent the continuation of microbial attack to the material, and then dried to constant weight under vacuum. Dried films were weighed and morphological changes were studied using SEM. A bacterial count
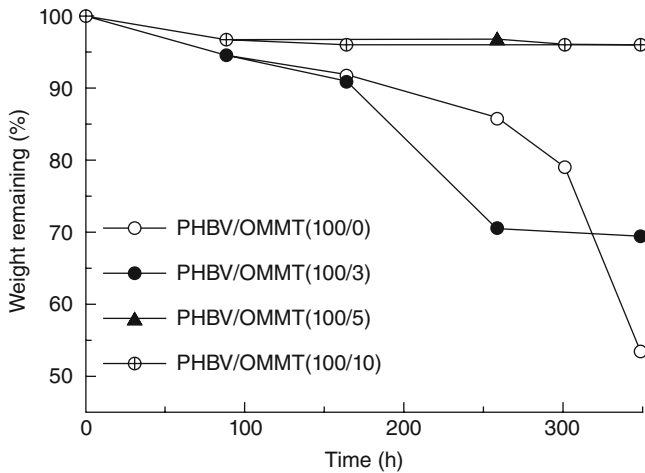
Figure 13.7 Sample mass remaining of PHBV and PHBV/OMMT nanocomposites after biodegradation trials in soil suspension. Reproduced from Wang *et al.* [7] with permission from Elsevier.

on the number of PHBV-degrading microorganisms in the soil was also performed.

Figure 13.7 illustrates that after exposing PHBV/OMMT samples to biodegradation condition in the soil suspension for up to 350 h, the weight loss of neat PHBV was around 45% and for PHBV/OMMT samples 100/3, 100/5, and 100/10 were 30%, 4%, and 4%, respectively. These results indicate that the rate and extent of PHBV biodegradability in a soil suspension decreased as the amount of OMMT added was added to PHBV. This result was in agreement with biodegradability results seen by Lee *et al.* [51], for another aliphatic polyester/OMMT material investigated in activated soil, although different to what is typically seen on other biopolymer systems in composting or conventional soil environments as discussed elsewhere in this chapter.

Maiti *et al.* [3] investigated the biodegradation of polyhydroxybutyrate (PHB) containing an organically modified fluoromica clay at 2 wt%, in compost. The biodegradation of the neat PHB and corresponding nanocomposite was investigated at two different temperatures, room temperature and 60 °C, in a sealed chamber at constant humidity of approximately 85% in compost manure. The degradation of the polymer was monitored by measuring the mass loss of the polymer, SEM, and changes in the spherulite size with biodegradation.

PHB biodegradation in compost was shown to be significantly enhanced with the inclusion of the organically modified fluoromica – see Figure 13.8 – with close to 100% biodegradation at room temperature within 7 weeks for the nanocomposite. Additionally, the degradation profile of neat PHB compared with the nanocomposite are different, where there is more enhanced lag phase initially for the biodegradation of neat PHB compared with nanocomposite.

a)

b)
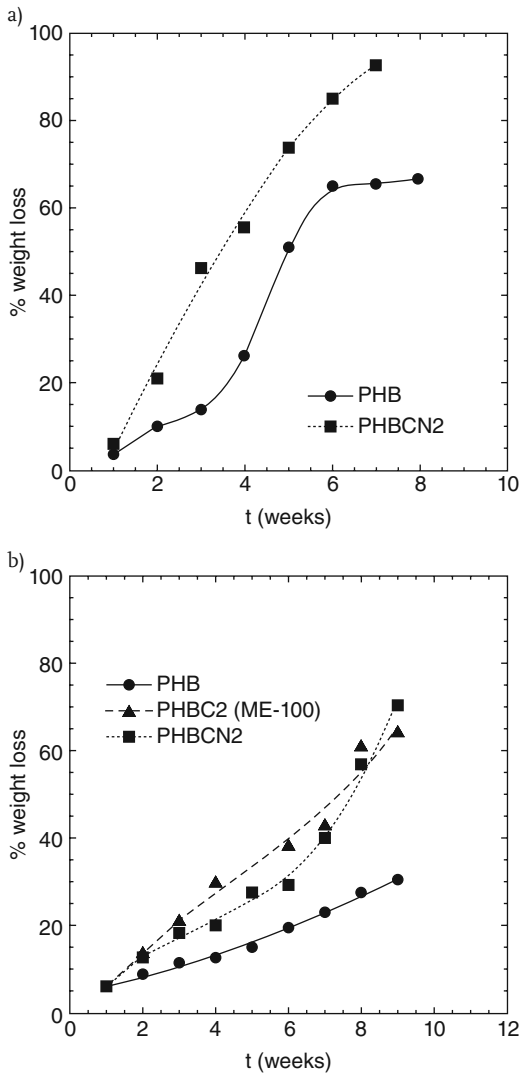
Figure 13.8 Percentage weight loss during biodegradation in the compost media (a) at room temperature (RT) and (b) at 60 °C. Reproduced from Maiti *et al.* [3] with permission from American Chemical Society.

Maiti *et al.* [3] also investigated the effect of crystallinity on the biodegradation. They showed that when the PHB and PHB nanocomposite were crystallized at 100 °C, the spherulites of the PHB nanocomposite were much smaller than those of neat PHB crystallized at the same temperature. Figure 13.9 shows the polarized optical images illustrating the difference in spherulite size for PHB and the PHB nanocomposite crystallized at 100 °C, before and after 6 weeks biodegradation in
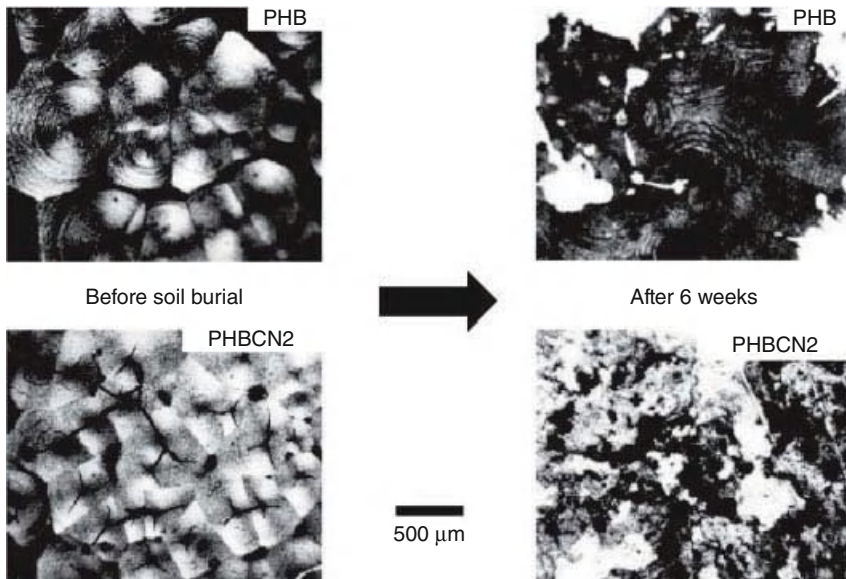
Figure 13.9 Polarizing optical images of PHB and PHBCN2 before and after 6 weeks of biodegradation. The samples were crystallized at 100 °C prior to composting. Reproduced from Maiti *et al.* [3] with permission from the American Chemical Society.

compost. Figure 13.9 clearly shows that the PHB nanocomposite is more biodegraded compared with neat PHB. The basic spherulite morphology of neat PHB appears intact. Maiti *et al.* [3] proposed that the more rapid rate of biodegradation of PHB nanocomposite could be attributed to the higher interspherulitic area and smaller spherulites.

13.8
Nanocomposites of Petrochemical-Based Polymer

In a study by Reddy *et al.* [52], film samples of oxobiodegradable polyethylene (OPE) and oxobiodegradable polyethylene nanocomposite (OPENac) were subjected to abiotic oxidation followed by microbial degradation using microorganism *Pseudomonas aeruginosa*. The progress of degradation was followed by monitoring the chemical changes of the samples using high-temperature GPC and FTIR. The growth of bacteria on the surface of the polymer was monitored using environmental SEM. GPC data and FTIR results indicated that the abiotic oxidation of polyethylene was influenced significantly by the pro-oxidant but not by nanoclay. However, the changes in molecular weight distribution and FTIR spectra for the biodegraded samples indicate that the growth rate of *P. aeruginosa* on the OPENac

was significantly greater than that on OPE. Reddy *et al.* [52] proposed that the nanoclay provided a favorable environment to microorganisms, helping them to proliferate [52]

13.9
Conclusions

There are numerous techniques that can be used to characterize the biodegradation of polymers and nanocomposites. These range from simple gravimetric analysis to measuring the amount of evolved CO_2 from microorganisms to advanced analytical techniques, all of which offer us an understanding of biodegradation.

Just as critical as the techniques are the environments in which polymers and nanocomposites can be exposed, these can include to a wide variety of natural, simulated, or artificial environments. These environments typically include soil, compost, marine substrates (sludge, water), and sewage. Each environment contains different microorganisms (in terms of species, diversity, and population), different physical parameters (in terms of temperature, moisture, pH, aeration) that influence the rate of microbial activity that in turn affect the rate of degradation seen in the nanocomposite. Consequently, the biodegradation of nanocomposites should always be evaluated in their intended environment of "end usage," as different environments are not always comparable.

References

1 Fukushima, K., Tabuani, D., Abbate, C., Arena, M., and Ferreri, L. (2010) Effect of sepiolite on the biodegradation of poly(lactic acid) and polycaprolactone. *Polym. Degrad. Stab.*, **95**, 2049–2056.

2 Fukushima, K., Tabuani, D., Abbate, C., Arena, M., and Rizzarelli, P. (2011) Preparation, characterization and biodegradation of biopolymer nanocomposites based on fumed silica. *Eur. Polym. J.*, **47**, 139–152.

3 Maiti, P., Batt, C.A., and Giannelis, E.P. (2007) New biodegradable polyhydroxybutyrate/layered silicate nanocomposites. *Biomacromolecules*, **8**, 3393–3400.

4 Someya, Y., Kondo, N., and Shibata, M. (2007) Biodegradation of poly(butylene adipate-*co*-butylene terephthalate)/ layered-silicate nanocomposites. *J. Appl. Polym. Sci.*, **106**, 730–736.

5 Li, Q., Yoon, J.-S., and Chen, G.-X. (2011) Thermal and biodegradable properties of poly(l-lactide)/poly(epsilon-caprolactone) compounded with functionalized organoclay. *J. Polym. Environ.*, **19**, 59–68.

6 Ray, S.S., and Okamoto, M. (2003) Biodegradable polylactide and its nanocomposites: opening a new dimension for plastics and composites. *Macromol. Rapid Commun.*, **24**, 815–840.

7 Wang, S.F., Song, C.J., Chen, G.X., Guo, T.Y., Liu, J., Zhang, B.H., and Takeuchi, S. (2005) Characteristics and biodegradation properties of poly(3-hydroxybutyrate-*co*-3-hydroxyvalerate)/ organophilic montmorillonite (PHBV/ OMMT) nanocomposite. *Polym. Degrad. Stab.*, **87**, 69–76.

8 Spiridon, I., Popescu, M.C., Bodârlau, R., and Vasile, C. (2008) Enzymatic degradation of some nanocomposites of poly(vinyl alcohol) with starch. *Polym. Degrad. Stab.*, **93**, 1884–1890.

9 Tang, S., Zou, P., Xiong, H., and Tang, H. (2008) Effect of nano-SiO_2 on the

performance of starch/polyvinyl alcohol blend films. *Carbohydr. Polym.*, **72**, 521–526.

10 Jayasekara, R., Lonergan, G.T., Harding, I., Bowater, I., Halley, P., and Christie, G.B. (2001) An automated multi-unit composting facility for biodegradability evaluations. *J. Chem. Technol. Biotechnol.*, **76**, 411–417.

11 Kijchavengkul, T., Auras, R., Rubino, M., Ngouajio, M., and Thomas Fernandez, R. (2006) Development of an automatic laboratory-scale respirometric system to measure polymer biodegradability. *Polym. Test.*, **25**, 1006–1016.

12 Kale, G., Auras, R., Singh, S.P., and Narayan, R. (2007) Biodegradability of polylactide bottles in real and simulated composting conditions. *Polym. Test.*, **26**, 1049–1061.

13 Calmon, A., Dusserre-Bresson, L., Bellon-Maurel, V., Feuilloley, P., and Silvestre, F. (2000) An automated test for measuring polymer biodegradation. *Chemosphere*, **41**, 645–651.

14 Drímal, P., Hoffmann, J., and Druzbík, M. (2007) Evaluating the aerobic biodegradability of plastics in soil environments through GC and IR analysis of gaseous phase. *Polym. Test.*, **26**, 729–741.

15 Berthe, L., Druilhe, C., Massiani, C., Tremier, A., and de Guardia, A. (2007) Coupling a respirometer and a pycnometer, to study the biodegradability of solid organic wastes during composting. *Biosyst. Eng.*, **97**, 75–88.

16 Grima, S., Bellon-Maurel, V., Feuilloley, P., and Silvestre, F. (2000) Aerobic biodegradation of polymers in solid-state conditions: a review of environmental and physicochemical parameter settings in laboratory simulations. *J. Polym. Environ.*, **8**, 183–195.

17 de Guardia, A., Petiot, C., and Rogeau, D. (2008) Influence of aeration rate and biodegradability fractionation on composting kinetics. *Waste Manag.*, **28**, 73–84.

18 Sundberg, C., and Jönsson, H. (2008) Higher pH and faster decomposition in biowaste composting by increased aeration. *Waste Manag.*, **28**, 518–526.

19 Száraz, L., and Beczner, J. (2003) Optimization processes of a CO_2 measurement set-up for assessing biodegradability of polymers. *Int. Biodeterior. Biodegradation*, **52**, 93–95.

20 Liang, C., Das, K.C., and McClendon, R.W. (2003) The influence of temperature and moisture contents regimes on the aerobic microbial activity of a biosolids composting blend. *Bioresour. Technol.*, **86**, 131–137.

21 Pagga, U., Beimborn, D.B., Boelens, J., and De Wilde, B. (1995) Determination of the aerobic biodegradability of polymeric material in a laboratory controlled composting test. *Chemosphere*, **31**, 4475–4487.

22 Bellia, G., Tosin, M., Floridi, G., and Degli-Innocenti, F. (1999) Activated vermiculite, a solid bed for testing biodegradability under composting conditions. *Polym. Degrad. Stab.*, **66**, 65–79.

23 Chiellini, E., and Corti, A. (2003) A simple method suitable to test the ultimate biodegradability of environmentally degradable polymers. *Macromol. Symp.*, **197**, 381–396.

24 Degli-Innocenti, F., Tosin, M., and Bastioli, C. (1998) Evaluation of the biodegradation of starch and cellulose under controlled composting conditions. *J. Polym. Environ.*, **06**, 197–202.

25 Solaro, R., Corti, A., and Chiellini, E. (1998) A new respirometric test simulating soil burial conditions for the evaluation of polymer biodegradation. *J. Polym. Environ.*, **06**, 203–208.

26 Starnecker, A., and Menner, M. (1996) Assessment of biodegradability of plastics under simulated composting conditions in a laboratory test system. *Int. Biodeterior. Biodegradation*, **37**, 85–92.

27 Tosin, M., Degli-Innocenti, F., and Bastioli, C. (1998) Detection of a toxic product released by a polyurethane-containing film using a composting test method based on a mineral bed. *J. Polym. Environ.*, **06**, 79–90.

28 Way, C., Wu, D.Y., Dean, K., and Palombo, E. (2010) Design considerations for high-temperature respirometric

biodegradation of polymers in compost. *Polym. Test.*, **29**, 147–157.

29 Standards (2005) AS ISO 14855-2005. *Plastic Materials – Determination of the Ultimate Aerobic Biodegradability and Disintegration under Controlled Composting Conditions – Method by Analysis of Evolved Carbon Dioxide*. Standards Australia, Sydney, NSW Australia.

30 Rhim, J.-W., Hong, S.-I., Park, H.-M., and Ng, P.K.W. (2006) Preparation and characterization of chitosan-based nanocomposite films with antimicrobial activity. *J. Agric. Food Chem.*, **54**, 5814–5822.

31 Fukushima, K., Abbate, C., Tabuani, D., Gennari, M., and Camino, G. (2009) Biodegradation of poly(lactic acid) and its nanocomposites. *Polym. Degrad. Stab.*, **94**, 1646–1655.

32 Shimpi, N., Borane, M., Mishra, S., and Kadam, M. (2012) Biodegradation of polystyrene (PS)-poly(lactic acid) (PLA) nanocomposites using Pseudomonas aeruginosa. *Macromol. Res.*, **20**, 181–187.

33 Shih, Y.-F., and Wu, T.-M. (2009) Enzymatic degradation kinetics of poly(butylene succinate) nanocomposites. *J. Polym. Res.*, **16**, 109–115.

34 Arena, M., Abbate, C., Fukushima, K., and Gennari, M. (2011) Degradation of poly(lactic acid) and nanocomposites by *Bacillus licheniformis*. *Environ. Sci. Pollut. Res.*, **18**, 865–870.

35 Sangwan, P., Way, C., and Wu, D.-Y. (2009) New insight into biodegradation of polylactide (PLA)/clay nanocomposites using molecular ecological techniques. *Macromol. Biosci.*, **9**, 677–686.

36 Ray, S.S., Yamada, K., Okamoto, M., and Ueda, K. (2003) Control of biodegradability of polylactide via nanocomposite technology. *Macromol. Mater. Eng.*, **288**, 203–208.

37 Zeng, Q.H., Yu, A.B., Lu, G.Q., and Paul, D.R. (2005) Clay-based polymer nanocomposites: research and commercial development. *J. Nanosci. Nanotechnol.*, **5**, 1574–1592.

38 Kumanayaka, T.O., Parthasarathy, R., and Jollands, M. (2010) Accelerating effect of montmorillonite on oxidative degradation of polyethylene nanocomposites. *Polym. Degrad. Stab.*, **95**, 672–676.

39 Petersson, L., and Oksman, K. (2006) Biopolymer based nanocomposites: comparing layered silicates and microcrystalline cellulose as nanoreinforcement. *Compos. Sci. Technol.*, **66**, 2187–2196.

40 Horiba, Y., Khan, S.T., and Hirashi, A. (2005) Characterization of the microbial community and culturable denitrifying bacteria in a solid-phase denitrification process using poly(ε-caprolactone) as the carbon and energy source. *Microbes Environ.*, **20**, 25–33.

41 Hajiali, H., Karbasi, S., Hosseinalipour, M., and Rezaie, H.R. (2010) Preparation of a novel biodegradable nanocomposite scaffold based on poly (3-hydroxybutyrate)/bioglass nanoparticles for bone tissue engineering. *J. Mater. Sci. Mater. Med.*, **21**, 2125–2132.

42 Okamoto, M. (2005) Biodegradable polymer/layered silicate nanocomposites: a review, in *Handbook of Biodegradable Polymeric Materials and Their Applications* (eds S. Mallapragada and B. Anarasimhan), American Scientific Publishers. Valencia, CA.

43 Maiti, P., Yamada, K., Okamoto, M., Ueda, K., and Okamoto, K. (2002) New polylactide/layered silicate nanocomposites: role of organoclays. *Chem. Mater.*, **14**, 4653–4661.

44 Ozkoc, G., and Kemaloglu, S. (2009) Morphology, biodegradability, mechanical, and thermal properties of nanocomposite films based on PLA and plasticized PLA. *J. Appl. Polym. Sci.*, **114**, 2481–2487.

45 Paul, M.A., Delcourt, C., Alexandre, M., Degée, P., Monteverde, F., and Dubois, P. (2005) Polylactide/montmorillonite nanocomposites: study of the hydrolytic degradation. *Polym. Degrad. Stab.*, **87**, 535–542.

46 Sinha Ray, S., Yamada, K., Okamoto, M., Fujimoto, Y., Ogami, A., and Ueda, K. (2003) New polylactide/layered silicate nanocomposites: 5. Designing of materials with desired properties. *Polymer*, **44**, 6633–6646.

47 Sabet, S.S., and Katbab, A.A. (2009) Interfacially compatibilized poly(lactic acid) and poly(lactic acid)/

polycaprolactone/organoclay nanocomposites with improved biodegradability and barrier properties: effects of the compatibilizer structural parameters and feeding route. *J. Appl. Polym. Sci.*, **111**, 1954–1963.

48 Nayak, S.K. (2010) Biodegradable PBAT/ starch nanocomposites. *Polym. Plast. Technol. Eng.*, **49**, 1406–1418.

49 Ratto, J.A., Steeves, D.M., Welsh, E.A., and Powell, B.E. (1999) A study of polymer clay nanocomposites for biodegradable applications. *Antec '99: Plastics Bridging the Millennia, Conference Proceedings, Vols I–III– Vol I: Processing; Vol II: Materials; Vol III: Special Areas.* Brookfield Center, Soc Plastics Engineers.

50 Farrell, R., Goodwin, S., Wirsen, C., Lucciarini, J., Martinez, M., and Ratto, J.A. (2000) A biodegradation study of co-extruded nanocomposites consisting of polycaprolactone and organically modified clay. *Antec 2000: Society of Plastics Engineers Technical Papers, Conference Proceedings, Vols I–III.* Lancaster, Technomic Publ Co Inc.

51 Lee, S.-R., Park, H.-M., Lim, H., Kang, T., Li, X., Cho, W.-J., and Ha, C.-S. (2002) Microstructure, tensile properties, and biodegradability of aliphatic polyester/clay nanocomposites. *Polymer*, **43**, 2495–2500.

52 Reddy, M.M., Deighton, M., Bhattacharya, S., and Parthasarathy, R. (2009) Biodegradation of montmorillonite filled oxo-biodegradable polyethylene. *J. Appl. Polym. Sci.*, **113**, 2826–2832.

Index